A Multi-Frequency VLA Continuum Investigation of Starburst and AGN Activity in Local U/LIRGs

Yiqing Song
Beijing, China

B.S. Physics, University of California, Los Angeles, 2016
M.S. Astronomy, University of Virginia, 2018

A Dissertation Presented to the
Graduate Faculty of the

University of Virginia

in Candidacy for the Degree of

Doctor of Philosophy

Department of Astronomy

University of Virginia
August 2022

Committee Members:
Aaron S. Evans
Eric J. Murphy
Loreto Barcos-Muñoz
Shane W. Davis
Robert E. Davis

Abstract

The rates at which galaxies form stars have been declining since ~ 3 billion years after the Big Bang. Massive stars that drive the chemical enrichment of the Universe are now being produced at much lower rates in the Milky Way and most other galaxies in our local Universe, compared to galaxies at $z \sim 1-2$, when most stars formed. During this distant era of rapid growth, a significant fraction of star formation took place in Luminous and Ultra-luminous Infrared Galaxies (U/LIRGs), where UV and optical light from newly formed massive stars are largely absorbed by thick layers of dust in these systems and re-emitted at infrared wavelengths. At $z \sim 0$, U/LIRGs are relatively rare but they are the most extreme star-forming galaxies in the local Universe. While these local U/LIRGs do not fully resemble their high-z counterparts, they provide an excellent opportunity for a detailed assessment of the properties of extreme activity that may have been taking place at the peak of cosmic star formation.

Many local U/LIRGs are observed to be interacting and merging gas-rich spiral galaxies, during which process molecular gas in the system is driven towards the galaxy centers, triggering intense nuclear starbursts and/or accretion of the supermassive black holes (i.e. Active Galactic Nuclei; AGN). Meanwhile, the large amounts of dust generated in the starburst prohibit a direct view of the most energetic regions in local U/LIRGs with UV/optical/near-IR observations.

In this dissertation, I characterize the starburst and AGN activity in a representative sample of 68 local U/LIRGs from the multi-wavelength Great Observatories All-sky LIRG Survey (GOALS), using 3 – 33 GHz radio continuum observations from the GOALS "equatorial" Survey (GOALS-ES) conducted with the Karl G. Jansky Very Large Array (VLA), described in Chapter 2. These multi-frequency observations of the optically-thin radio continuum provide a highly-detailed and extinction-free view of the most energetic yet often dust-obscured star-forming and AGN activity in these extreme local systems.

Using the 33 GHz radio continuum as a direct tracer of star formation rates (SFR), in Chapter 3 I studied the star-forming properties of nuclear rings in four GOALS-ES systems and found that these nuclear rings all contribute to more than 50% of the total star formation of their host U/LIRGs, and the individual regions residing in these rings have star formation rate surface densities that rival star-forming clumps observed at $z = 1 - 4$ with much larger sizes. Looking beyond the nuclear rings, in Chapter 4 I identified and characterized the size and luminosity of over 100 individual regions of compact 15 and/or 33 GHz radio continuum emission in the full GOALS-ES sample on 100 pc scales. On average, the individual star-forming regions identified in these U/LIRGs have 100 times higher star formation rates and surface densities compared to those in nearby normal star-forming disk galaxies that are of similar sizes. I also identified a sample of luminous galactic nuclei that appear to be forming stars near the maximal capacity as predicted by theoretical models for star-forming disks supported by dust-reprocessed radiation pressure. Several of these nuclei have been identified to host AGN, and the rest may be going through a key phase of heavily obscured co-evolution between supermassive black holes and nuclear star formation that is thought to precede the formation of luminous quasars. Detection of high brightness temperature radio cores indicative of AGN activity via follow-up VLBI observations will directly verify this scenario. Lastly in Chapter 5, I modeled the 3 – 33 GHz spectral energy distribution observed in these local U/LIRGs on kpc scales and found that the radio continuum emission of star-forming regions and nuclei in these systems, compared to those originating from AGN activity, indeed have higher contributions from thermal free-free emission from HII regions, particularly at 33 GHz, validating the usage of 33 GHz as a direct tracer of recent star formation. The 3 – 33 GHz radio continuum is also strongly correlated with mid- and far-IR dust emission observed on ~ 10 kpc scales for star-forming regions, especially at 70μm, indicating their shared origin.

Acknowledgements

"Physics is not the universe. Rather, it is one very human attempt to get at its innards."

– Chanda Prescod-Weinstein, *The Disordered Cosmos: A Journey into Dark Matter, Spacetime, & Dreams Deferred*

This very human attempt to peek into the dusty hearts of local U/LIRGs would not have been possible without the company, guidance and support of many wonderful people.

My biggest thanks go to my advisor Aaron, who has taught me not only the excitement of galaxy evolution research, but also the importance of collaboration and teamwork in this field. Aaron's caring patience and unwavering cheerfulness repeatedly helped me rise above my tendency to procrastinate and doubt myself, which only became worse during the pandemic. Over the years I have also greatly benefited from the support from my academic siblings - Sean, for teaching me how to reduce VLA data and for always being the first one to give feedback on my proposal/paper drafts; Loreto, for inspiring me with countless proposal and project ideas, for believing me and encouraging me to believe myself; George, for sharing endless knowledge on simulations, multi-wavelength observations and statistics (everything!). I am fortunate to have worked alongside a very large array of radio experts at NRAO - including Eric, Emmanuel, Amanda, Ilsang, Dong-chan, Bjorn, John, Dave, Devaky, Kim, Andy - whose input and feedback have helped me focus on a clearer picture while also expanding my horizon. I also thank my GOALS collaborators elsewhere in the world - Lee, Kirsten, Joe, Vassilis, Tanio, Hanae, Vivian, Thomas, Jason S. Jason C., Jed, Claudio, Justin, Jeff. Although most or all our interactions have been online, your honest feedback, encouragement and willingness to help have shown me that people are the hearts of research. I look forward to continuing to work with and learn from you all in the coming years.

I feel extremely lucky to have been surrounded by many wonderful women in astronomy throughout grad school: Loreto, Amanda, Vivian and Hanae, Devaky and Kim – your enthusiasm, dedication and encouragement will always inspire me; Pallavi, Kim, Sun Meng, Xiaoshan and Ceci – your kindness, authenticity and silliness allowed me to be myself. I would also like to thank my cohort (Luca, Robby, Andy, David and Hannah), professors and classmates, the DSBK Assessment Team (Sandy, Brian, Chris, Allison, Anne, Renato, Bri et al.), my office mates at UVa and NRAO (Sun Meng, Pallavi, Matt, Bruce, Andy, Ceci, Mark, Alejandro) and fellow junior GOALS members (Jed, James, Alejandro, Tianmu, Will, Shunshi) – I enjoyed working with/alongside you all.

I want to thank Ed, John, Peter, Dana, Gabby, Ricky, Jamila and the rest of the evolving DEI Committee for their time and effort to keep the conversation going. I deeply appreciate Whitney, Barbara, Gabby and Jackie for all that they do to keep everything organized and make the department a better working space. I thank Connie, Pearl and Dale at NRAO for dealing with my forgetfulness, and the custodians at the department and NRAO for providing a clean and tidy environment to work in.

I thank my astronomy friends and allies from UCLA (Vanshree, Brittany, Jennifer, Xinnan, Jason, Cicero and Sam), my first astronomy professors (Prof. Mike

Jura, Prof. Andrea Ghez) and research mentors (Prof. Jean Turner, Dr. Chao-Wei Tsai), with whose support and encouragement I headed for graduate school. While it turned out to be rather stressful, hanging out with Sun Meng, Luca, Pallavi, Xiaoshan, Kim, Pedro, Andreas, Alma, Alejandro, Lianis and many others have made it all less daunting. I also thank my friends Vanshree, Xiaoyun, Mandy, Yuqi, Anni, Ruby, Alex, Xiaoyi and Zhuowa, who always managed to talk me out of my stubbornness and cheer me up whenever I'm feeling down.

I owe my persisting motivation to Caroline. Thank you for being there for me always, for bringing me out of my shell to see the world with an open mind, for introducing me to all the wonderful people from App and the Anthro Dept., who have shown me the many more possibilities of life, for bringing me into the Gianiny and Noel families, who made me feel at home far away from home, and for bringing Ellie to me – she is the best. I look forward to our new adventures together!

I am forever indebted to my parents who, despite our many differences and disagreements, have always loved and supported me, provided me with a space where my impractical interest in astronomy was allowed to grow. I'll always be thankful for my brother, his positive attitude towards everything and extraordinary calmness for a teenager has been a great comfort in the past few years.

Last but not least, thank you to my committee members – Aaron, Eric, Loreto, Shane for guiding me over the years with both knowledge and kindness, and Rob for hopping on board the U/LIRG train once again to help me get to the end.

To medical workers around the world, who fought hard on the ground so we can look up and appreciate the stars.

Table of Contents

List of Figures

List of Tables

Chapter 1

Introduction

This dissertation investigates the properties of the most extreme star-forming galaxies in the local Universe (i.e. $z \sim 0$) – (Ultra-)Luminous Infrared Galaxies (U/LIRGs) – using radio continuum observations. In this Chapter, I will provide a general overview of the connections between stars and galaxies, and introduce U/LIRGs as well as their significance in the evolution of our Universe. I will describe what we have learned so far about U/LIRGs in the local Universe, and what radio continuum observations can help further our understanding of these extreme galaxies.

1.1 Stars, Galaxies & the Universe

The complex array of elements that produce and sustain life as we know it, mostly come from the intricate process of nucleosynthesis in stars – the burning and fusion of hydrogen atoms into heavier elements (Burbidge et al., 1957). While all stars participate in this process, massive stars that are born with more than $\sim$8 solar masses ($M_\odot$) play particularly critical roles in populating our periodic table, as illustrated in Figure 1.1 from Johnson (2019). Many elements heavier than oxygen are exclusively produced in massive stars, either during their lifetime under the immense gravita-

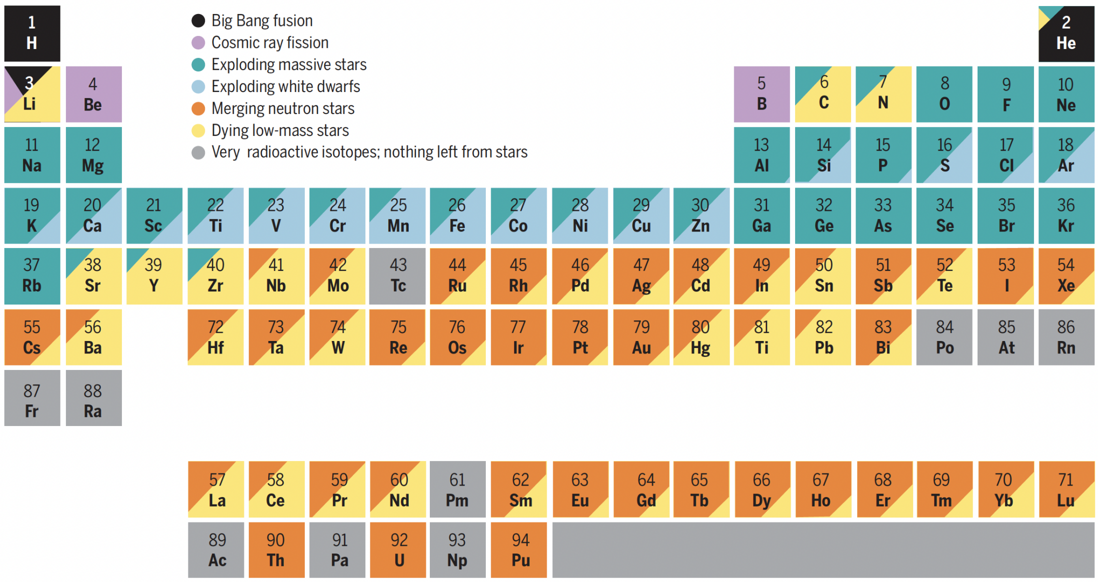

Figure 1.1: The sources of elements found in the Solar System, from Johnson (2019). Massive stars ($\gtrsim 8\,\mathrm{M}_\odot$) play critical roles in populating our periodic table.

tional potential in their extremely hot cores (Burbidge et al., 1957), in the strong shock waves produced in their spectacular demise as supernovae explosion (e.g. Hoyle & Fowler, 1960; Meyer et al., 1992; Vartanyan et al., 2019) or even afterwards via mergers of the remnant neutron stars (e.g. Freiburghaus et al., 1999; Korobkin et al., 2012). Numerous low-mass stars formed from materials enriched by these massive stars then go on to produce additional heavy elements during their much longer lifetime (i.e. billions of years), since their formation till today (e.g. Karakas & Lattanzio, 2014).

With only $\sim 1\,\mathrm{M}_\odot$ produced every year in the Milky Way (Robitaille & Whitney, 2010), massive stars capable of dramatically enriching the interstellar medium within only a few million years are extremely rare. The rates at which stars form in galaxies in the local Universe at redshift $z \sim 0$ are in general rather low compared to at $z \sim 1-2$ (about 3 Gyrs after the Big Bang), when half of the observed stellar mass today were formed (Figure 1.2 (left); Madau & Dickinson, 2014). In this era of rapid growth, a dominant fraction of star formation is thought to take place in Luminous Infrared Galaxies (LIRGs; $L_{\rm IR} > 10^{11} L_{\odot}$) and Ultra-Luminous Infrared Galaxies (ULIRGs; $L_{\rm IR} > 10^{12} L_{\odot}$), as shown in Figure 1.2 (right). The extraordinary IR luminosities of these galaxies largely come from the thick layers of dust particles that reprocess the intense UV radiation from newly-formed (< 10 Myr) luminous massive stars to the IR regime. The large amounts of dust present in LIRGs and ULIRGs also come from these short-lived massive stars: with each of them expelling all the heavy elements synthesized during its lifetime in the form of supernova after only a short few million years, dust particles formed from these heavy elements are allowed to quickly accumulate.

How extreme were the star-forming activities in these distant galaxies? How do these activities compare to those taking place in Milky Way-like galaxies in our local Universe? To search for answers to these questions, we turn to U/LIRGs in the local Universe ($z \sim 0$). While local U/LIRGs do not fully resemble their high-z counterparts (e.g. Tacconi et al., 2020), they are one of the few places that allow us a close-up assessment of the properties of extreme star formation observed across cosmic time.

1.2 (Ultra-)Luminous Infrared Galaxies at $z \sim 0$

While U/LIRGs in the early Universe are now widely recognized as the dominant contributors of co-moving dust-obscured star formation rates at $z \sim 1-2$ (e.g. Murphy et al., 2011a; Magnelli et al., 2011, 2013), it is the discovery and subsequent studies of U/LIRGs in the local Universe that laid (and continue to establish) the foundation of studies of distant dusty star-forming galaxies at high-z. From the first ever IR all-sky survey conducted with the InfraRed Astronomical Satellite (IRAS; Neuge-

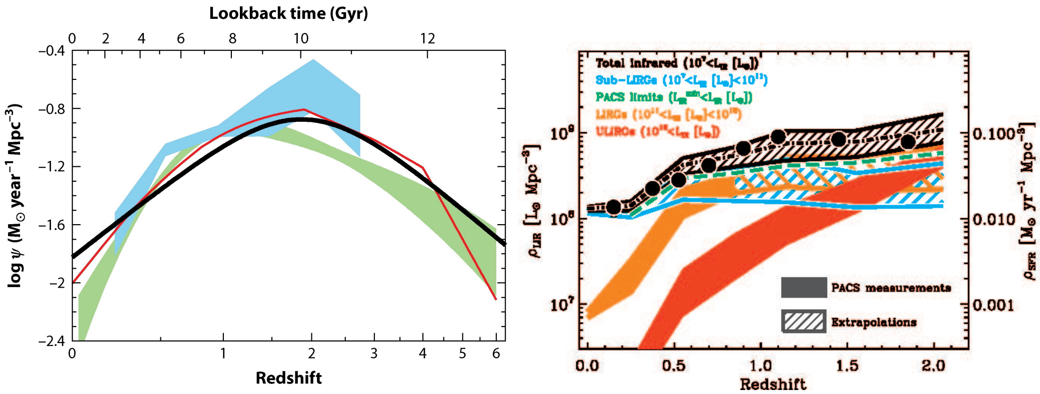

Figure 1.2: (Left) Evolution of the cosmic star formation rate (black curve) derived from UV and IR surveys, from Madau & Dickinson (2014). Both galaxy star formation and black hole accretion [red curve - from X-ray Shankar et al. (2009); green shaded area - from hard X-ray analysis by Aird et al. (2010); blue shaded area - from IR analysis by Delvecchio et al. (2014)] reached peak activity at $z \sim 1-2$. (Right) from Magnelli et al. (2013): Relative contributions to the co-moving total IR luminosity density and obscured star formation rate density (black hatched area) from sub-LIRGs, LIRGs and ULIRGs at $z = 1--2$, derived from Herschel observations of the Great Observatories Origins Deep Survey (GOODS Elbaz et al., 2011) field.

bauer et al., 1984), Sanders et al. (2003) identified 629 bright extra-galactic sources with total 60μm flux greater than $5.24\,$Jy (Janskys; 1 Jy $= 10^{-26}\mathrm{W\,m^{-2}\,Hz^{-1}}$) and at absolute Galactic Latitude $|b| > 5°$ that form the Bright Revised Galaxies Sample (BRGS), within which 181 are LIRGs and 21 are ULIRGs (Armus et al., 2009). While U/LIRGs only contribute $\sim 6\%$ of the total IR luminosity of the local Universe (Soifer & Neugebauer, 1991), these local U/LIRGs at $z < 0.08$ are the most extreme star-forming galaxies at $z \sim 0$, with specific star formation rates (sSFR; i.e. SFR per stellar mass) around $3.9 \times 10^{-10}\,\mathrm{yr^{-1}}$, about an order of magnitude higher than nearby normal spiral galaxies with similar stellar masses, as estimated using UV and IR measurements by Howell et al. (2010).

Deep optical follow-up studies revealed that at least 30% of LIRGs and almost all ULIRGs are interacting/merging gas rich spiral galaxies (see Figure 1.3 for examples), and systems with higher IR luminosities also have smaller separations between

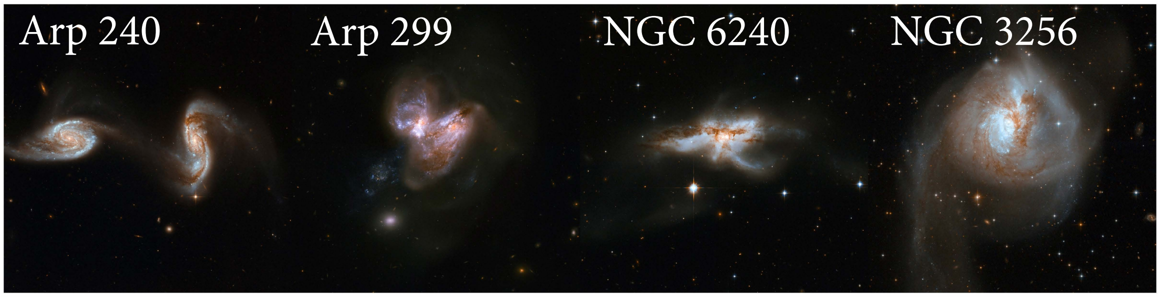

Figure 1.3: HST color-composite images of four local U/LIRGs: (left to right) Arp 240 (D_L =108 Mpc, $L_{\rm IR}$ =$10^{11.6}L_{\odot}$), Arp 299 (51 Mpc, $10^{11.9}L_{\odot}$), NGC 6240 (116 Mpc, $10^{11.9}L_{\odot}$) and NGC 3256 (39 Mpc, $10^{11.6}L_{\odot}$). *Credit: NASA, ESA, the Hubble Heritage Team (STScI/AURA)-ESA/Hubble Collaboration and A. Evans (University of Virginia, Charlottesville/NRAO/Stony Brook University).*

the merging galaxies (e.g. Larson & Tinsley, 1978; Armus et al., 1987; Sanders & Mirabel, 1996). Meanwhile, numerical simulations of gas-rich galaxy mergers predict the triggering of intense starburst activity (i.e. a "burst" in the SFR of duration 10 - 100 Myrs, involving up to 5% of the total stellar mass; Larson & Tinsley, 1978) during the process, due to accumulation of star-forming molecular gas towards the galaxy centers driven by tidal torques produced in the asymmetric gravitational potential (e.g. Mihos & Hernquist, 1996). Along with an intense nuclear starburst, the molecular gas may also feed the supermassive black holes (SMBH) residing in the galaxy centers (e.g. Di Matteo et al., 2005; Springel et al., 2005). This feeding generates powerful radiation that span the entire electromagnetic wavelengths (e.g. see review by Padovani et al., 2017). Such energetic events, termed as the Active Galactic Nuclei (AGN), have been observed in many LIRGs and ULIRGs, especially those at the final coalescing stages that also have the highest IR luminosities (e.g. Ricci et al., 2017; Koss et al., 2018; Ricci et al., 2021).

These results from observations and simulations together suggest that the interacting/merging local U/LIRGs may represent an important transitional phase in the hierarchical evolution of many massive galaxies, as illustrated in Figure 1.4: gas-rich

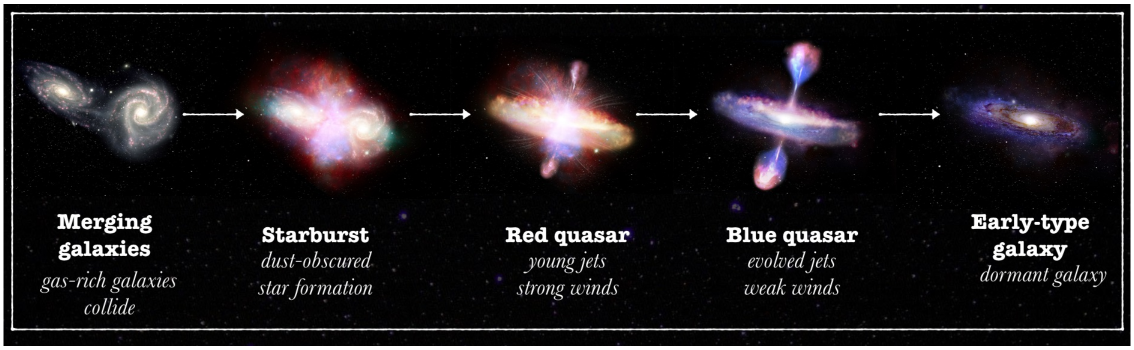

Figure 1.4: An artist's conception of the transition from gas-rich mergers of spiral galaxies to a dormant elliptical galaxy. With this model the rare population of local interacting LIRGs and ULIRGs represent a brief transitional starburst phase between galaxy mergers and the blue quasar phase during which winds and/or jets drive away the obscuring dust, revealing an unobscured AGN, and ultimately shutting down the star formation to form a dormant early-type galaxy. *Credit: Gemini Observatory, GMOS-South, NSF, adapted by S. Munro.*

mergers trigger nuclear starburst and AGN activity, the latter of which subsequently expels interstellar materials away from the galaxy, quenching star formation first and eventually the AGN itself, leaving behind a quiescent elliptical galaxy with old stars and little molecular gas (e.g. Sanders et al., 1988; Di Matteo et al., 2005; Springel et al., 2005; Hopkins et al., 2006). The tight correlations observed between the masses of SMBH and the properties of their host galaxies (e.g. stellar mass, stellar velocity dispersion, stellar bulge mass; Kormendy & Ho, 2013; McConnell & Ma, 2013) among elliptical galaxies in the local Universe infers that regulatory processes that help set the mass ratio of the central SMBH and the stellar bulge mass (for an example) must have taken place in the early Universe. While many high-z U/LIRGs are not observed to be galaxy mergers (e.g. Tacconi et al., 2020), some regulatory processes must be in effect during merger events. Studying U/LIRGs in the local Universe hence provides an opportunity to investigate star formation and AGN activity in rapidly-evolving galaxies which ultimately could lead to the production of an elliptical galaxy that abides by the observed relations between SMBH and their host galaxies.

1.2.1 The Great Observatories All-sky LIRG Survey (GOALS)

Numerous efforts have been dedicated to study local U/LIRGs at many different wavelengths since their discovery, and it quickly becomes evident that to fully understand the nature of these extremely dusty systems, observations across the electromagnetic spectrum are required. Figure 1.5 below demonstrates such necessity: the eastern galaxy in the merging galaxy pair VV 114 (a local LIRG) is very faint at visible wavelengths but actually dominates the emission from the entire system at mid-IR and radio wavelengths. Traditional diagnostics of the star-forming activity that rely on direct observations of the UV and optical photons from young massive stars would therefore significantly underestimate the total SFR of such a system. Furthermore, it would be impossible to characterize the nuclear starburst and potential AGN activity triggered during the merger – which are critical for understanding the galaxy evolutionary process – without accounting for the light extinguished by foreground dust.

While IRAS allowed the discovery of a large number of local U/LIRGs, observations that spatially-resolve the dust emission from different interacting components were only later made available with the Infrared Space Observatory (Kessler et al., 1996) and the Spitzer Space Telescope (Werner et al., 2004). This advancement motivated the Great Observatories All-sky Survey (GOALS), which combines data from NASA's great observatories operating at X-ray (Chandra), optical/Near-IR (HST) and Mid-IR (Spitzer), as well as those from state-of-the-art UV (GALEX) and far-IR facilities (Herschel), to conduct a comprehensive census of the star-forming and AGN activity in all 202 local U/LIRGs identified from the RBGS (e.g. see detailed description in Armus et al., 2009). These systems span a range in IR luminosity ($10^{11-12.5} L_\odot$), distance ($20-400\,\mathrm{Mpc}$) and represent both isolated galaxies and

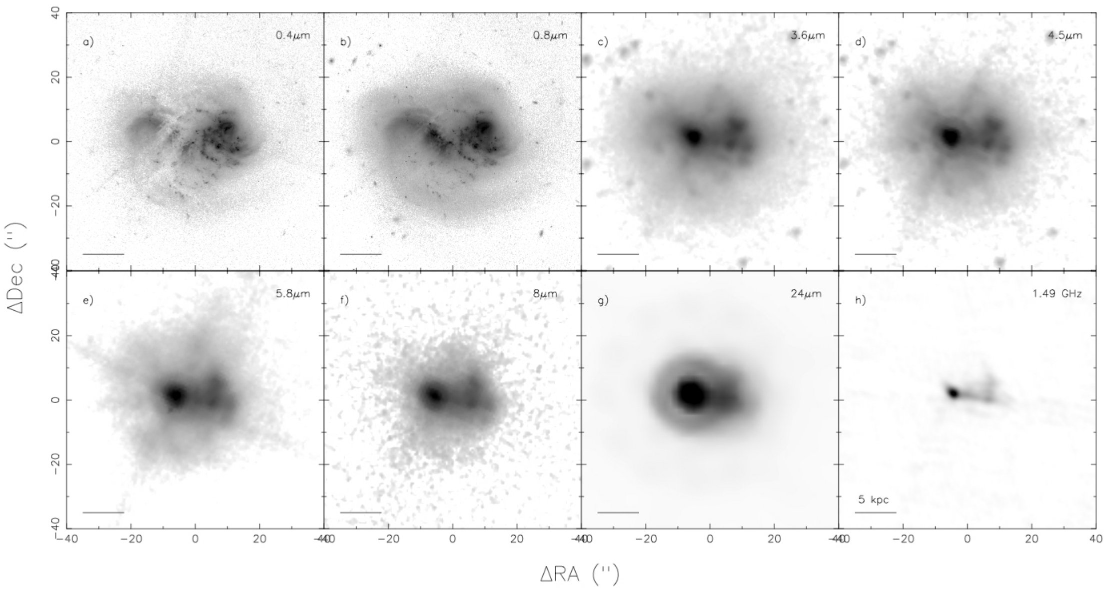

Figure 1.5: Multi-wavelength images of a local LIRG VV 114 (87 Mpc, $10^{11.6}L_{\odot}$), a merging galaxy pair. Dust lanes heavily obscures emission from the eastern galaxy at visible wavelength (i.e. 0.4μm), which is only revealed at longer wavelengths (mid-IR: $3.6 - 24\mu$m, radio: 1.49 GHz) to be energetically dominant. Observations were taken with the HST (optical; Evans et al. in prep.), Spitzer (MIR; Mazzarella et al. in prep.) and the VLA (radio; Condon et al., 1991). *Credit: T. Vavilkin.*

galaxy interaction/mergers at various stages (Stierwalt et al., 2013). Using GOALS observations, Howell et al. (2010) showed that on average, up to 95% of star-forming activity in local U/LIRGs are buried behind dust that would be missed with UV-only observations, confirming the importance of a multi-wavelength approach in studying local U/LIRGs.

Aside from mapping the kpc-scale dust continuum emission in local U/LIRGs across a wide wavelength range, the Spitzer and Herschel GOALS observations also provided the IR spectra of the central few kpc of these extreme systems that allowed robust characterizations of the nuclear starburst and/or AGN activity based on the associated IR line emission and absorption features. For an example, MIR line emission from polycyclic aromatic hydrocarbons (PAH) – an important component of interstellar dust grains – can be used to trace properties of star formation (i.e. strength of UV radiation field, density, etc.), as they are abundant in photo-dissociation regions (PDRs) around sites of newly-formed massive stars (e.g. Hollenbach & Tielens, 1999). The PAH line emission hence is typically weak around powerful AGN, which can also be directly identified if high ionization lines such as [Ne V] 14.3μm (ionizing potential of 96 eV) are present (e.g. Armus et al., 2004). The combination of several other line signatures are also used to assess the strength of AGN relative to starburst (e.g. Inami et al., 2013; Díaz-Santos et al., 2017), as well as the properties of photo-dissociation regions in these intense starbursts (e.g. Díaz-Santos et al., 2017; McKinney et al., 2021). The special advantage of the MIR diagnostics is that they allow identification of AGN activity that is obscured by dust, whose X-ray/UV/optical emission could be significantly absorbed and weakened. The 9.7μm absorption feature associated with silicate dust grains also provides a direct assessment of the severeness of foreground dust obscuration in local U/LIRGs (Spoon et al., 2006). Analysis of these IR observations revealed that the nuclear activity in a majority of local U/LIRGs are dominated by recent starburst ($< 6\,\mathrm{Myr}$) (e.g. Petric et al., 2011; Inami et al., 2013; Stierwalt et al., 2013, 2014; Díaz-Santos et al., 2017) that are likely more compact and have stronger radiation field compared to star-forming regions in nearby normal galaxies (Díaz-Santos et al., 2017), but the level of AGN contribution possibly increases towards the final coalescing stage where the dust obscuration becomes most severe, limiting direct AGN identification (Stierwalt et al., 2013). These studies, combined with those at shorter wavelengths (e.g. Howell et al., 2010; Iwasawa et al., 2011; Torres-Albà et al., 2018; Ricci et al., 2017, 2021), have demonstrated the diversely extreme nature of the local U/LIRG population relative to nearby normal galaxies on kpc scales and provided a solid foundation for more detailed exploration of the immediate circumnuclear region around AGN or nuclear starburst, on the scales of individual Giant Molecular Clouds ($10 - 100\,\mathrm{pc}$), which are the fundamental units of galaxy star formation.

1.3 The Radio Continuum Perspective

While the IR wavelengths harbor a wealth of information on the physical conditions of the interstellar medium in galaxies, ground-based observations at $10 - 100\ \mu$m often suffer from atmosphere absorption. Space missions, until very recently (with the launch of the James Webb Space Telescope), have been limited to relatively small apertures that can only resolve large-scale galaxy structures (>few kpc). Observations of the optically-thin radio emission with interferometers like the Very Large Array, as shown in the last panel of Figure 1.5, provide an excellent alternative path for characterizing the most compact and dust-obscured regions that dominate the energy output of local U/LIRGs.

Radio continuum emission from star-forming regions are directly associated with massive stars: as high-energy photons from young massive stars ionize the surrounding gas, electrons accelerated in ionized plasma emit thermal free-free emission; electrons accelerated in supernovae of massive stars emit synchrotron emission. When the electron opacity is low, the former is weakly dependent on the observing frequency ($S_{\rm ff} \propto \nu^{-0.1}$) while the latter quickly diminishes towards higher observing frequencies ($S_{\rm syn} \propto \nu^{-0.8}$) due to quicker energy loss of electrons accelerated to higher energy. These two types of radio continuum emission, together with cold dust emission at above $\sim$ 90 GHz, depict well the observed radio/sub-millimeter continuum spectra of star-forming galaxies, such as that of M82, as shown in Figure 1.6 from Condon (1992). Therefore, radio continuum emission provides an excellent extinction-free tracer of recent star formation, and the power-law slope of the optically-thin radio continuum spectrum, or the spectral index (α as described by $S \propto \nu^{\alpha}$), measured between two radio frequencies ($\sim 1 - 90$ GHz) can be used to separate the relative contribution of thermal free-free and synchrotron emission (Condon, 1992; Murphy et al., 2011b, 2012).

Meanwhile, when AGN are present, their strong magnetic field can also accelerate cosmic ray electrons to very high energy which emit synchrotron radiation. The radio continuum emission of powerful AGN is largely dominated by synchrotron emission. Because the highly energetic emission from AGN occurs very close to the SMBH, on scales less than 1 pc, radio continuum emission from AGN itself is extremely compact. Hence, if observations have sufficiently-high resolutions (using Very Long Baseline Interferometry), AGN can be identified directly based on compact unresolved morphology and high brightness temperatures T_b, as defined by the Rayleigh-Jean approximation for a black body emitter: $S_\nu = 2kT_b\nu^2/c^2$, where c is the speed-of-light and k is the Boltzmann constant. At high electron opacity, stellar emission can be approximated as thermal blackbody emission, and thus the maximum brightness temperatures that can be achieved in even the most powerful starbursts cannot ex-

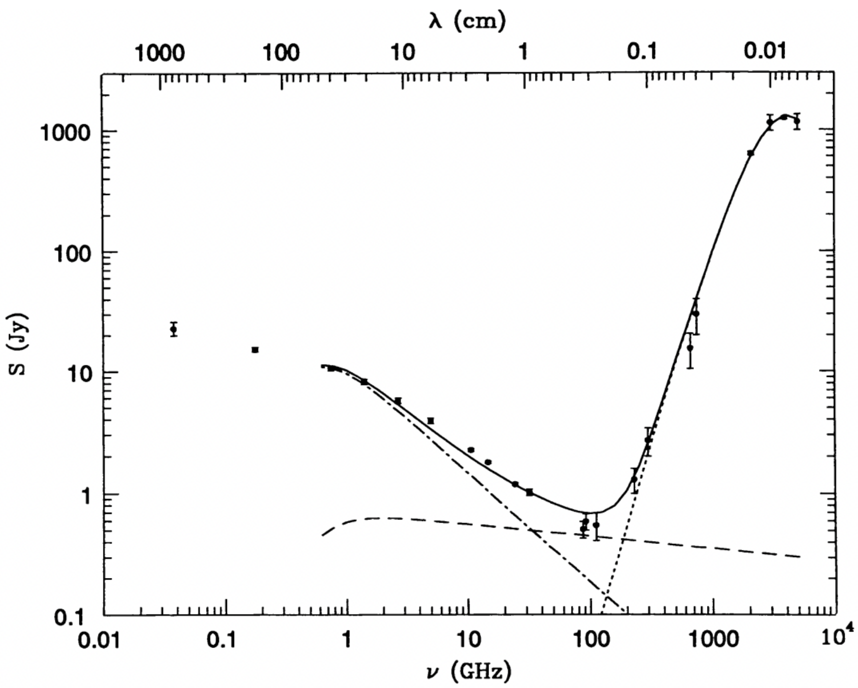

Figure 1.6: Radio/Sub-millimeter spectrum of the nearby starburst galaxy M82 (solid line), from Condon (1992). The spectrum is well described by the sum of three continuum emission components: synchrotron (dot-dash line), thermal free-free (dashed line), cold dust (dotted line).

ceed the electron temperatures of the HII regions (i.e. regions of hydrogen ionized by young massive stars) at $\sim 10^4$ K (Condon et al., 1991; Condon, 1992). Thus, compact radio sources with $T_b > 10^5\,K$ would indicate a powerful non-thermal origin - AGN activity.

On larger physical scales, many AGN are uniquely identified at radio wavelengths via their luminous synchrotron-dominated radio jets that can span kpc to even Mpc in length. These jets are thought to be generated by SMBH with rapid spin and highly-magnetized disk (e.g. Blandford et al., 2019). These AGN are often classified as "radio-loud" (RL), classically-defined as those with total 5 GHz (radio)/ 4400 (optical) flux ratio over 10 (Kellermann et al., 1989). For "radio-quiet" (RQ) AGN with moderate radio luminosity and without visible jets or lobes on kpc scales, the interpretation of their 100- pc to kpc-scale radio continuum emission becomes a lot more complicated, as illustrated in Figure 1.7 from Panessa et al. (2019), and requires thorough comparison and analysis of multi-wavelength observations and/or radio observations on (sub-)pc scales. Therefore, caution must be taken when using radio continuum to infer the star-forming properties of extreme systems like local U/LIRGs, many of which host RQ AGN that are not necessarily detected in the optical due to heavy dust obscuration (e.g. Stierwalt et al., 2013; Ricci et al., 2021).

1.3.1 The Karl G. Jansky Very Large Array (VLA)

Since its first observation in the 1970s, the Very Large Array located in Socorro, New Mexico, has been the most productive radio telescope in the world, capturing radio emission of various astronomical objects near and far. Composed of 27 25m-antenna that observe simultaneously, VLA utilizes radio interferometry and functions as a giant hypothetical single-dish radio telescope operating at $1-50$ GHz that is capa-

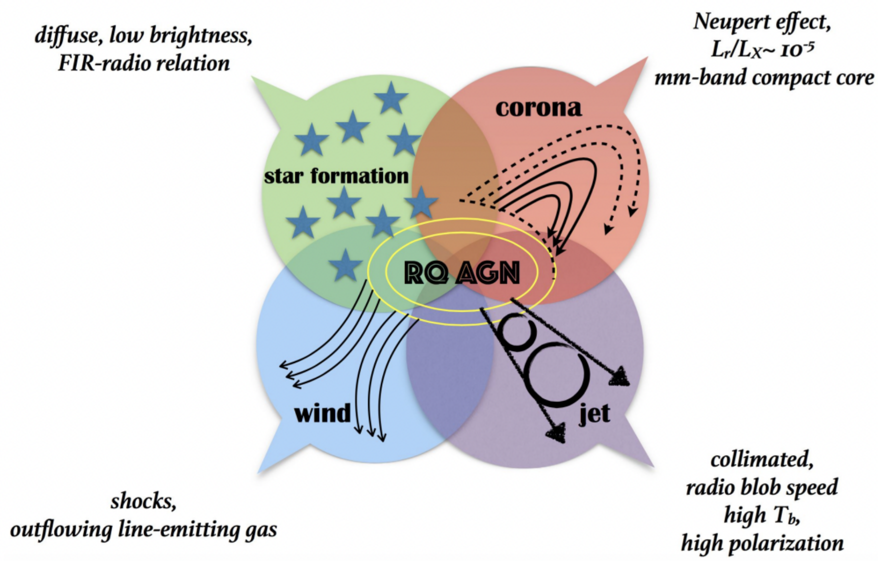

Figure 1.7: Possible origins of observed radio continuum emission from radio-quiet AGN, from Panessa et al. (2019): star formation, AGN wind/jets/outflows, AGN accretion disk coronae. Signatures and methods that may be used to identify these different mechanisms are also listed. See Panessa et al. (2019) for details.

ble of resolving highly-detailed structures of extended objects such as local U/LIRGs while also recovering diffuse emission on large physical scales. This is achieved by moving the antennas around into four different configurations – changing the spacing between antennas, from up to 0.6 to 22 miles apart. Each two antennas form a so-called "baseline", and each baseline is sensitive to radio sources with specific sizes at a given observing frequency, with longer baseline (i.e. greater distance between the antenna pair) more sensitive to more compact sources and shorter baselines more sensitive to larger sources. Therefore, by using different VLA antenna configurations, we can study radio emission occurring on a wide range of physical scales in local U/LIRGs, from individual star-forming regions to galaxy-scale tidal tails.

1.3.2 VLA Surveys of local U/LIRGs

Surveys of local U/LIRGs conducted with the VLA have unveiled and characterized the most energetically-dominating regions in these systems, which greatly advanced our understanding of their extreme nature. During early operation of the VLA, Condon et al. (1990) conducted a 1.49 GHz survey of all galaxies in the RBGS using all four VLA configurations, and found close resemblance between the observed radio and far-IR brightness distribution and morphology for very extended systems larger than $\sim$ 8' (resolution limit of IRAS). Based on this finding, and the tight empirical correlation between FIR and radio luminosities of galaxies of various types spanning six orders of magnitude in luminosity (de Jong et al., 1985; Helou et al., 1985; Yun et al., 2001), the authors proposed that in the absence of high-resolution FIR observations that can resolve IR-luminous galaxies smaller than 8' (which were later provided by Herschel), radio maps are excellent alternatives for indicating the sizes and locations of the FIR-emitting regions in local U/LIRGs.

A follow-up survey at 8.49 GHz was conducted for 40 local U/LIRGs with the highest FIR luminosities by Condon et al. (1991) using the most extended VLA A-configuration, reaching a high angular resolution of 0".25 ($\sim$ 100 pc at a median $D_L \sim 100$ Mpc). The authors showed that a large fraction of the FIR radiation from these galaxies likely originate from compact starbursts with sizes $\sim$ 100 pc, which appear to be common in these systems. They also found moderately flat radio spectral indices between 1.49 and 8.49 GHz for many of the compact starbursts, which indicate high electron opacity. Building upon these results, Clemens et al. (2008) investigated the 1.4 – 22.5 GHz radio spectra of 31 of the most luminous local U/LIRGs with the VLA, and found some of them to be steeper than expected from a simple combination of optically-thin free-free and synchrotron emission, which may be attributed to energy losses of high-energy synchrotron (Condon, 1992). This trend was later confirmed and extended to up to 36 GHz by Leroy et al. (2011). However, Murphy (2013) showed that sources with steepest spectral indices at ~ 10 GHz were also associated with ongoing galaxy mergers, which suggest that galaxy-scale tidal shocks rather than supernovae in compact starbursts may be responsible for the apparent excess of synchrotron emission. Despite this, these studies all confirmed that the most compact sources show flatter 1.49 – 8.49 GHz spectral indices that are indicative of absorption of synchrotron photons by dense ionized gas. Using observations from Condon et al. (1991), Vardoulaki et al. (2015) compared the radio morphology and 1.49 – 8.49 GHz spectral indices of 35 local U/LIRGs with multi-wavelength AGN diagnostics and identified proposed radio diagnostics of AGN based on spectral index distribution.

The above studies largely utilized VLA observations conducted before the upgrade in 2009, when spectral coverage from 1 – 50 GHz was only 20% and the instantaneous bandwidths of the VLA receivers were less than 1 GHz. The upgraded VLA enabled up to 8 GHz of instantaneous bandwidths, 10 times higher sensitivity and 100% frequency coverage, which allowed efficient mapping of the multi-frequency radio emission in local U/LIRGs. Using high-resolution 6 – 33 GHz observations of 22 of the most luminous local U/LIRGs taken with the upgraded VLA, Barcos-Muñoz et al. (2015) and Barcos-Muñoz et al. (2017) were able to robustly constrain the sizes, SFR and surface densities of the compact, energetically-dominant nuclei of these extreme systems on $\sim$ 100 pc to sub-kpc scales, and found that many of them are possibly forming new stars near the maximal capacity that is allowed by the balance between gravitational potential and radiation pressure (Thompson et al., 2005). In particular, the west nucleus of Arp 220 is estimated to have a SFR surface density of $10^{4.1}\ M_\odot\,\mathrm{yr}^{-1}\ \mathrm{kpc}^{-2}$, the highest value ever measured among known star-forming systems (Barcos-Muñoz et al., 2015).

Most studies in the radio have focused on the most luminous systems, where the compact nuclei completely dominate the radio continuum emission. The upgraded VLA not only provided a window to more sensitively probe the fainter high-frequency radio emission (> 10 GHz) that is dominated by thermal free-free emission, but also has allowed a larger survey including local U/LIRGs that are less luminous with intrinsically fainter radio emission – the GOALS "Equatorial" VLA Survey (see Chapter 2 for details) – to provide a more representative view of their most energetic activities, which is the main motivation behind this dissertation. First analysis of the survey, led by Linden et al. (2019), focused on the bright kpc-scale extra-nuclear star-forming regions detected in the spiral arms or tidal tails of 22 local LIRGs at 3 - 33 GHz, which are found to have elevated star formation rates compared to those in nearby normal galaxies. This study also confirmed the robustness of 33 GHz radio continuum as an extinction-free tracer of ongoing star-forming activities in dusty local U/LIRGs, and paved the road for subsequent studies presented in this dissertation.

1.4 This Dissertation

This dissertation built upon results from previous VLA surveys of local U/LIRGs and normal galaxies to provide a new multi-frequency (3, 15, 33 GHz) view of the starburst and AGN activity in a representative sample of these extreme systems, using observations from the recently-completed GOALS "Equatorial" VLA Survey carried out between 2014 and 2020. A detailed description of the goals of the survey as well as information on sample selection, observations and data reduction is provided in Chapter 2. Chapter 3 and 4 summarizes results and analysis of the most compact radio continuum sources identified and characterized mainly using 15 and 33 GHz observations from the survey, with Chapter 3 specifically focusing on nuclear star-forming rings detected in the survey. Chapter 5 presents the spatially-resolved 3 - 33 GHz radio spectra observed in local U/LIRGs, as well as comparisons between resolved radio and IR flux measurements for these systems. Chapter 3 has been published in the Astrophysical Journal (ApJ, 916, 73S), and Chapter 4 has been submitted to AAS Journals and is currently under review. Chapter 5 will be submitted later this year including the image atlas and basic aperture photometry for the entire survey.

The survey is led by my advisor Prof. Aaron Evans, following the design of the Star Formation in Radio Survey (SFRS) led by Dr. Eric Murphy, as described in Chapter 2. Data reduction and imaging for the survey were carried out by Dr. Sean Linden and myself using the Common Astronomy Software Applications (CASA, v4.7.0; McMullin et al., 2007), each of us focusing on half of the observations taken with VLA/14A-471 (PI: A. Evans) and VLA/16A-204 (PI: S. Linden). Dr. Sean Linden worked with Dr. Emmanuel Momjian closely for weeks learning the necessary data reduction techniques, which he taught me upon his return. This and my training at the 16th Synthesis Imaging Workshop helped laid foundation for the work presented in this dissertation. ALMA archival data presented in Chapter 3 were re-calibrated and re-imaged by me, with valuable guidance from NRAO staff at the 2018 ALMA Reduction Workshop. Dr. Linden, Dr. Eric Murphy and Dr. Loreto Barcos-Muñoz generously provided reduced VLA images from Murphy et al. (2018); Linden et al. (2020); Barcos-Muñoz et al. (2015, 2017) used in Chapter 3 and 4. Dr. John Hibbard offered valuable advice on identifying locations of galactic nuclei using multi-wavelength datasets during the drafting of Chapter 4. William Meynardie contributed many of the preliminary analysis of Herschel IR images from Chu et al. (2017) that led to Chapter 5. I have led two VLA proposals (20A-401, 20B-313) to complete the survey with technical support from Dr. Emmanual Momjian, and have reduced and imaged the resulted observations myself, used in Chapter 4. I produced all data analysis presented in this dissertation as well as drafted the manuscripts, with helpful inputs from Prof. Aaron Evans, Dr. Sean Linden, Dr. Loreto Barcos-Muñoz, Dr. Eric Murphy, Dr. George Privon, Dr. Ilsang Yoon, Dr. Devaky Kunneriath and many other members from the GOALS collaboration including Dr. Lee Armus, Dr. Tanio Díaz-Santos, Dr. Joseph Mazzarella, Prof. Vassilis Charmandaris, Dr. Vivian U and Prof. Hanae Inami.

The work presented in this dissertation is funded by the National Science Foundation through the Grote Reber Fellowship Program administered by Associated Universities, Inc./National Radio Astronomy Observatory and the NSF grant AST 1816838. Travel to relevant training, workshops and conferences were partially supported via the Professional Development Fund from the UVa Graduate School of Arts and Science.

Chapter 2

The GOALS "Equatorial" VLA Survey

2.1 Introduction

The GOALS "equatorial" VLA survey (hereafter GOALS-ES; see also Linden et al., 2019) is a multi-frequency, multi-resolution snapshot survey carried out with the upgraded Karl G. Jansky Very Large Array designed to map the brightest radio continuum emission in 68 U/LIRGs from GOALS (see Chapter 1) that have declination of $|\delta| < 20^\circ$, at 3, 15 and 33 GHz. The equatorial selection allows detailed follow-up studies using ground-based facilities from both Hemispheres, and each target was observed with the VLA in both A-(or B-) and C-configurations to capture both compact emission on $\sim 100\,\mathrm{pc}$ scales as well as diffuse emission on $\sim$ kpc scales.

Importantly, the GOALS-ES observations serve as a companion to the Star Formation in Radio Survey (SFRS), which imaged 56 nearby ($D_L < 30\,\mathrm{Mpc}$) normal star-forming galaxies (i.e. non-U/LIRGs with $L_{\mathrm{IR}} < 10^{11} L_\odot$) from SINGS (Kennicutt et al., 2003) and KINGFISH (Kennicutt et al., 2011) at matched frequencies and also at both kpc (Murphy et al., 2012) and $\sim$ 100 pc scales (Murphy et al., 2018; Linden et al., 2020). These studies also demonstrated that in nearby galaxies, the 33 GHz radio continuum is strongly dominated by thermal free-free emission from HII regions and hence can be used as a direct tracer of recent star formation. However, existing 6 – 33 GHz VLA survey of 22 of the most luminous local U/LIRGs by (Barcos-Muñoz et al., 2017) reveals that their 33 GHz radio emission is dominated by non-thermal synchrotron emission. Build upon the SFRS and existing 33 GHz VLA survey of 22 of the most luminous local U/LIRGs by (Barcos-Muñoz et al., 2017), the GOALS-ES aims to provide a more representative view of the star-forming and AGN activity in U/LIRGs in the local Universe, and investigate the following main science questions:

• Where does the brightest 3 - 33 GHz radio continuum emission come from in local U/LIRGs? Are they powered by AGN or star formation?

• How much does thermal free-free emission from recent star formation contribute to the 33 GHz continuum emission of these systems on $\sim$ 100 pc and $\sim$ kpc scales?

• What are the star-forming properties of local U/LIRGs on the scales of Giant Molecular Clouds? How do they compare to those measured in nearby normal galaxies (as observed by the SFRS)?

These questions are addressed in the subsequent chapters in this dissertation.

2.2 Sample

The GOALS-ES sample of 68 local U/LIRGs covers the entire range of $L_{\rm IR}$ ($10^{11} - 10^{12.5}$L$_\odot$), distances ($V_{\rm H}$ = 1137 - 26249 km/s), and merger stages spanned by the full GOALS sample of 202 systems, as shown in Figure 2.1. A two-sample Kolmogorov-Smirnov (K-S) test on the $L_{\rm IR}$ and $V_{\rm H}$ distributions of GOALS and the equatorial sample yields p-values of 0.86 and 0.74, respectively. Hence, this equatorial sample serves as a statistically robust representation of the local U/LIRG population. Table

2.1 lists the basic properties of the GOALS-ES sample. In total, 18 systems are in (a) "pre-mergers", 10 in (b) "early-stage" mergers, 4 in (c) "mid-stage" mergers, 21 in (d) "late-stage" mergers, and 15 are (N) "non-mergers", based on visual classification by Stierwalt et al. (2013) using *Spitzer* imaging.

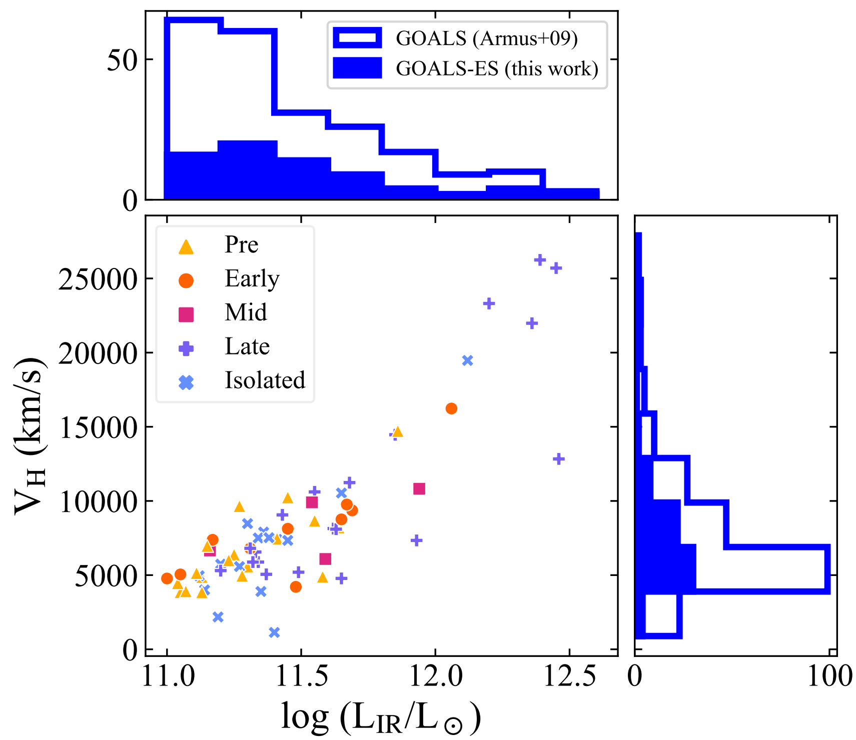

Figure 2.1: Basic properties (Heliocentric velocity and 8-1000μm IR luminosity) of the GOALS-ES sample. Each system is color-coded by its merger stage, using visual classification by Stierwalt et al. (2013). The sample covers the full range of IR luminosities, distances and merger stages represented by the GOALS sample of all 202 local U/LIRGs.

2.3 Observation & Reduction

The VLA observations for the GOALS-ES utilizes three receiver bands: *S*-band (2–4 GHz), *Ku*-band (12–18 GHz) and *Ka*-band (26.5–40 GHz), which has enabled us to sample a wide frequency range for characterizing the radio spectral energy distribution (SED). Each target was observed at each band in both *A*-configuration (synthesized beam FWHM $\sim 0''.06 - 0''.6$) and C-configuration (synthesized beam FWHM $\sim 0''.6 - 7''.0$) to detect bright compact regions on $\sim 100\,\mathrm{pc}$ scales as well as large-scale diffuse structures on $\sim kpc$ scales at the distances of the U/LIRGs in the sample. Ten systems in the sample were additionally observed with Ka-band in B-configuration (beam FWHM $\sim 0''.2$) due to poor A-configuration detections. All A- and C-configuration observations were initially carried out during 2014 March 06 – December 04 in 14A-471 (PI: A. Evans). Observations with Ka-band were incomplete due to limited availability of the required observing conditions, and were later completed in 2016 October 7 - 12 in 16A-204, (PI: S. Linden). Additionally, Ku-band observations for six systems from 14A-471 were unsuccessful due to temporary malfunction of the requantizer, and were re-observed on December 10 in 20B-313 (PI: Y. Song). For the $A-$configuration observations, each galaxy was observed with 5-minute on-source time at S-band and Ku-band, and 10 minutes at Ka-band. For the $C-$configuration observations, each galaxy was observed with 5-minute on-source time at all three Bands.

Additional B-configuration observations at Ka-band were carried out during 2020 June 27 – 2022 January 3 in 20A-401 (PI: Y. Song). These observations focused on ten systems with extended emission that were clearly detected at Ku-band during the 14A-471 campaign, but had poor detections at Ka-band due to limited sensitivity of the snapshots. Therefore, these ten systems were observed with longer on-source time ($\gtrsim 30$ minutes) to ensure good detections for comparison with Ku-band observations. The project codes for the observations of each system used in this work are provided in Table 2.2 and 2.3.

All raw datasets from project 14A-471 and 16A-204 were first reduced and calibrated into Measurement Sets (MS) using the Common Astronomy Software Applications (CASA; McMullin et al., 2007) VLA data calibration pipeline (v4.7.0). For observations from 20A-401 and 20B-313, we acquired the calibrated Measurement Sets directly from the NRAO Science Ready Data Products (SRDP) data archive (CASA v5.6.2 for 20A-401, v5.4.2 for 20B-313).

We then visually inspected the calibrated MS, flagged bad data related to RFI and specific antennae or channels, and then re-ran the appropriate versions of VLA pipelines on the flagged MS without Hanning smoothing. We repeated this procedure until all bad data were removed from the Measurement Sets.

We proceeded to image each science observation using `tclean` in CASA, utilizing the same versions that calibrations were performed with. In general, we adopted Briggs weighting with a robust parameter of 0.5, using the Multi-Term (Multi-Scale) Multi-Frequency Synthesis deconvolving algorithm (Rau & Cornwell, 2011) with `scales` = [0, 10, 30] pixels and `nterm` = 2. In cases where sensitivity was poor (peak S/N $<$ 10), Natural weighting or a robust parameter of 1.0 was adopted instead to enhance sensitivity at the expense of the angular resolution. Cleaning masks were determined visually using the CASA `viewer`. In cases where detection is strong (S/N $>$ 50), we further performed iterative phase-based self-calibration on the calibrated MS and before re-imaging to achieve better sensitivity. The characteristics of the final native resolution images used in this dissertation are listed in Table 2.2 and 2.3.

Table 2.1: Basic Properties of the GOALS-ES Sample

ID (1)	IRAS (2)	Galaxy Name (3)	RA (J2000) (4)	DEC(J2000) (5)	$\log(\frac{L_{IR}}{L_{\odot}})$ (6)	V_H(km/s) (7)	D_L(Mpc) (8)	Scale (pc/") (9)	Stage (10)
1	F00085-1223	NGC 0034	00h11m06.56s	-12°0628".2	11.34	5881	84	393	d
2	F00163-1039	MCG -02-01-052	00h18m50.90s	-10°2236".7	11.45	8125	117	540	b
3	F01053-1746	IC 1623 (VV 114)	01h07m47.59s	-17°3024".2	11.59	6087	87	400	c
4	F01076-1707	MCG -03-04-014	01h10m08.93s	-16°5109".9	11.65	10536	152	689	N
5	F01173+1405	CGCG 436-030	01h20m02.63s	+14°2142".3	11.69	9362	134	612	b
6	F01364-1042		01h38m52.79s	-10°2712".1	11.85	14464	211	931	d
7	F01417+1651	III Zw 035	01h44m30.56s	+17°0609".0	11.64	8214	117	539	a
8	F02071-1023	NGC 0838	02h09m38.66s	-10°0847".2	11.05	3851	54	257	a
9	F02114+0456	IC 0214	02h14m05.56s	+05°1023".7	11.43	9061	130	592	d
10	F02152+1418	NGC 0877	02h17m53.26s	+14°3118".4	11.07	3913	55	261	a
11	F02281-0309	NGC 0958	02h30m42.84s	-02°5620".5	11.20	5738	81	379	N
12	F02401-0013	NGC 1068	02h42m40.72s	-00°0047".9	11.40	1137	17	80	N
13	F02435+1253	UGC 02238	02h46m17.46s	+13°0544".6	11.33	6560	93	433	d
14	F02512+1446	UGC 02369	02h54m01.75s	+14°5836".4	11.67	9761	140	640	b
15	F03359+1523		03h38m47.07s	+15°3254".1	11.55	10613	153	693	d
16	F03514+1546	CGCG 465-012	03h54m15.95s	+15°5543".4	11.16	6662	95	442	c
17	F04097+0525	UGC 02982	04h12m22.68s	+05°3249".1	11.20	5305	76	355	d
18	F04191-1855	ESO 550-IG02	04h21m20.02s	-18°4839".6	11.27	9652	140	637	a
19	F04315-0840	NGC 1614	04h33m59.95s	-08°3446".6	11.65	4778	69	323	d
20	F04326+1904	UGC 03094	04h35m33.81s	+19°1018".0	11.41	7408	107	493	N
21	F05053-0805	NGC 1797	05h07m44.84s	-08°0108".7	11.04	4457	65	304	a
22	F05054+1718	CGCG 468-002	05h08m21.21s	+17°2208".0	11.05	5049	73	340	b
23	F05187-1017		05h21m06.53s	-10°1446".2	11.30	8474	123	566	N
24	05442+1732		05h47m11.2s	+17°3346".4	11.30	5582	81	381	a
25	F06295-1735	ESO 557-G002	06h31m47.2s	-17°3716".6	11.25	6385	94	439	a
26	07251-0248		07h27m37.62s	-02°5454".8	12.39	26249	401	1643	d
27	F07329+1149	MCG +02-20-003	07h35m43.44s	+11°4234".8	11.13	4873	74	345	a
28	F09111-1007		09h13m37.69s	-10°1924".6	12.06	16231	246	1073	b

Table 2.1 continued

Table 2.1: Basic Properties of the GOALS-ES Sample (continued)

ID (1)	IRAS (2)	Galaxy Name (3)	RA (J2000) (4)	DEC(J2000) (5)	$\log(\frac{L_{IR}}{L_\odot})$ (6)	V_H(km/s) (7)	D_L(Mpc) (8)	Scale (pc/") (9)	Stage (10)
29	F09437+0317	Arp 303 (IC 0563/4)	09h46m20.70s	+03°0330".4	11.23	6002	93	430	a
30	F10015-0614	NGC 3110	10h04m02.11s	-06°2829".5	11.37	5054	80	372	d
31	F10173+0828		10h20m00.24s	+08°1332".8	11.86	14716	224	986	a
32	F11186-0242	CGCG 011-076	11h21m12.24s	-02°5902".5	11.41	7464	117	538	a
33	F11231+1456	IC 2810	11h25m45.07s	+14°4036".0	11.45	10243	158	714	a
34	F12112+0305		12h13m46.02s	+02°4842".2	12.36	21980	340	1427	d
35	F12224-0624		12h25m03.9s	-06°4052".1	11.36	7902	124	570	N
36	F12243-0036	NGC 4418	12h26m54.6s	-00°5239".6	11.19	2179	36	170	N
37	F12592+0436	CGCG 043-099	13h01m50.28s	+04°2000".8	11.68	11237	174	782	d
38	F12596-1529	MCG -02-33-098	13h02m19.66s	-15°4604".2	11.17	4773	77	359	b
39	F13188+0036	NGC 5104	13h21m23.09s	+00°2033".2	11.27	5578	90	419	N
40	F13197-1627	MCG -03-34-064	13h22m24.45s	-16°4342".4	11.28	4959	80	375	a
41	F13373+0105	Arp 240 (NGC 5257/8)	13h39m55.34s	+00°5009".5	11.62	6798	108	500	b
42	F13497+0220	NGC 5331	13h52m16.32s	+02°0618".0	11.66	9906	154	699	c
43	F14348-1447		14h37m38.28s	-15°0024".2	12.39	24883	387	1596	d
44	F15107+0724	CGCG 049-057	15h13m13.07s	+07°1332".1	11.35	3897	64	302	N
45	F15276+1309	NGC 5936	15h30m00.85s	+12°5922".1	11.14	4004	66	310	N
46	F15437+0234	NGC 5990	15h46m16.41s	+02°2455".6	11.13	3839	63	297	a
47	F16164-0746		16h19m11.75s	-07°5403".0	11.62	8140	127	583	d
48	F16284+0411	CGCG 052-037	16h30m56.53s	+04°0458".7	11.45	7342	115	531	N
49	F16399-0937		16h42m40.11s	-09°4313".7	11.63	8098	126	579	d
50	F16504+0228	NGC 6240	16h52m58.9s	+02°2403".3	11.93	7339	115	529	d
51	F16516-0948		16h54m23.72s	-09°5320".9	11.31	6807	107	495	d
52	F17138-1017		17h16m35.68s	-10°2040".5	11.49	5197	83	386	d
53	17208-0014		17h23m21.97s	-00°1700".7	12.46	12834	197	874	d
54	17578-0400		18h00m31.86s	-04°0053".4	11.48	4210	67	317	b
55	18090+0130		18h11m33.41s	+01°3142".4	11.65	8759	134	610	b
56	F19297-0406		19h32m22.30s	-04°0001".1	12.45	25701	394	1619	d
57	19542+1110		19h56m35.78s	+11°1904".9	12.12	19473	294	1257	N

Table 2.1 continued

Table 2.1: Basic Properties of the GOALS-ES Sample (continued)

ID (1)	IRAS (2)	Galaxy Name (3)	RA (J2000) (4)	DEC(J2000) (5)	$\log(\frac{L_{IR}}{L_{\odot}})$ (6)	V_H(km/s) (7)	D_L(Mpc) (8)	Scale (pc/") (9)	Stage (10)
58	F20304-0211	NGC 6926	20h33m06.13s	-02°0138".9	11.32	5880	88	412	d
59	F20550+1655	II Zw 096	20h57m24.38s	+17°0739".2	11.94	10822	160	724	c
60	F22287-1917	ESO 602-G025	22h31m25.48s	-19°0204".0	11.34	7507	110	506	N
61	F22491-1808		22h51m49.35s	-17°5224".9	12.20	23312	351	1466	d
62	F23007+0836	NGC 7469	23h03m15.64s	+08°5225".5	11.58	4892	71	332	a
63	F23024+1916	CGCG 453-062	23h04m56.55s	+19°3307".1	11.38	7524	109	502	N
64	F23157+0618	NGC 7591	23h18m16.25s	+06°3509".1	11.12	4956	71	335	N
65	F23157-0441	NGC 7592	23h18m22.19s	-04°2457".4	11.40	7380	107	490	b
66	F23254+0830	NGC 7674	23h27m56.71s	+08°4644".3	11.55	8671	125	573	a
67	23262+0314	NGC 7679	23h28m46.62s	+03°3041".4	11.11	5138	74	346	a
68	F23394-0353	MCG -01-60-022	23h42m00.91s	-03°3654".4	11.15	6966	100	464	a

NOTE — (1): Unique identifier for each IRAS system. (2): IRAS system name; (3): Commonly used galaxy name; (4) & (5): J2000 coordinates for galaxy based on *Spitzer* IRAC 8μm imaging (Mazzarella, in prep.; Chu et al., 2017). (6): 8 - 1000 μm infrared luminosity in solar units. (7) Heliocentric velocity from the NASA/IPAC Extragalactic Database (NED). (8) & (9): Luminosity distance of the system and physical scale corresponding to 1"at the distance of the system, calculated using the 3-attractor model (Mould et al., 2000) and Ned Wright's Cosmology Calculator (Wright, 2006), based on values from (4), (5) and (7). (10): Merger stage based on visual classification, from Stierwalt et al. (2013): a - pre-merger; b - early-merger; c - mid-merger; d - late-merger; N - isolated galaxy; see Stierwalt et al. (2013) for more details.

Table 2.2: Characteristics of Native-Resolution GOALS-ES Images ($A-/B-$configuration)

ID (1)	Project Code (2)	$\theta^{33\mathrm{GHz}}_{M\times m}$ ($''\times''$) (3)	P.A.$^{33\mathrm{GHz}}$ (°) (4)	$\sigma^{33\mathrm{GHz}}_{\mathrm{rms}}$ (μJy) (5)	$\theta^{15\mathrm{GHz}}_{M\times m}$ ($''\times''$) (6)	P.A.$^{15\mathrm{GHz}}$ (°) (7)	$\sigma^{15\mathrm{GHz}}_{\mathrm{rms}}$ (μJy) (8)	$\theta^{3\mathrm{GHz}}_{M\times m}$ ($''\times''$) (9)	P.A.$^{3\mathrm{GHz}}$ (°) (10)	$\sigma^{3\mathrm{GHz}}_{\mathrm{rms}}$ (μJy) (11)
1	14A-471	0″.14 × 0″.06	−41	21.5	0″.17 × 0″.11	−6	21.3	0″.79 × 0″.56	10	19.7
2	14A-471	0″.14 × 0″.06	−40	20.9	0″.19 × 0″.12	−7	11.6	0″.66 × 0″.47	7	23
3	20A-401∗,14A-471	0″.28 × 0″.18	16	8.0	0″.19 × 0″.1	−15	13.6	0″.8 × 0″.57	−2	27.5
4	20A-401∗,14A-471	0″.28 × 0″.19	−15	6.0	0″.22 × 0″.13	−15	11.7	0″.87 × 0″.52	0	18.5
5	14A-471	0″.09 × 0″.06	−41	16.0	0″.14 × 0″.12	42	15.6	0″.61 × 0″.55	1	21.6
6	14A-471	0″.16 × 0″.05	−43	21.3	0″.16 × 0″.13	−7	12.9	0″.77 × 0″.55	−8	17
7	14A-471	0″.08 × 0″.05	−44	18.4	0″.11 × 0″.1	−18	13.2	0″.6 × 0″.52	−4	13
8	14A-471	0″.20 ×″ .06	−43	18.9	0″.2 ×″ .12	−26	12.3	0″.74 × 0″.49	−15	23
9	14A-471	0″.11 × 0″.05	−48	16.6	0″.14 × 0″.11	−39	13.6	0″.65 × 0″.55	−16	15.5
10	14A-471	0″.11 × 0″.06	−42	14.5	0″.13 × 0″.12	−28	11.4	0″.59 × 0″.52	−12	16.5
11	14A-471,16A-204	0″.12 × 0″.06	1	11.5	0″.18 × 0″.14	14	8.6	0″.94 × 0″.58	44	13.6
12	14A-471	0″.1 ×″ .06	1	35.3	0″.14 × 0″.11	12	120.0	0″.87 × 0″.57	46	116
13	20A-401∗,16A-204	0″.24 × 0″.18	−65	5.2	0″.16 × 0″.14	15	10.4	0″.74 × 0″.57	64	15.7
14	14A-471,16A-204	0″.09 × 0″.06	−6	11.7	0″.13 × 0″.11	8	9.9	0″.74 × 0″.57	58	13.7
15	14A-471	0″.09 × 0″.06	12	15.8	0″.13 × 0″.11	−174	9.4	0″.65 × 0″.57	47	11.8
16	14A-471,16A-204	0″.1 ×″ .07	7	15.3	0″.13 × 0″.11	0	9.8	0″.64 × 0″.57	46	14
17	14A-471,16A-204	0″.1 ×″ .06	12	12.2	0″.13 × 0″.11	5	9.7	0″.72 × 0″.55	36	16.7
18	14A-471,16A-204	0″.15 × 0″.07	12	13.7	0″.22 × 0″.12	−5	11.2	1″.14 × 0″.53	25	13.3
19	14A-471,16A-204	0″.12 × 0″.06	16	13.7	0″.17 × 0″.11	0	15.1	0″.86 × 0″.55	27	18.3
20	14A-471	0″.07 × 0″.07	58	15.0	0″.13 × 0″.11	8	10.4	0″.57 × 0″.53	12	18.4
21	20A-401*,14A-471	0″.27 × 0″.19	−34	4.0	0″.16 × 0″.11	13	10.4	0″.8 × 0″.54	7	18.5
22	14A-471	0″.08 × 0″.06	63	15.3	0″.14 × 0″.13	−3	13.0	0″.55 × 0″.49	12	18.7
23	14A-471	0″.1 ×″ .06	33	19.3	0″.18 × 0″.13	17	11.5	0″.79 × 0″.55	6	18.4
24	20A-401*,14A-471	0″.27 × 0″.18	−69	7.2	0″.13 × 0″.11	−178	10.6	0″.59 × 0″.53	8	11.6
25	14A-471	0″.15 × 0″.06	29	23.9	0″.19 × 0″.1	−2	12.7	0″.93 × 0″.54	−2	14.1
26	14A-471,30B-313	0″.08 × 0″.06	6	17.8	0″.15 × 0″.11	−5	13.9	0″.69 × 0″.58	−2	15.5
27	14A-471,30B-313	0″.08 × 0″.07	24	17.8	0″.14 × 0″.11	−10	9.8	0″.62 × 0″.54	−2	15.9
28	14A-471,30B-313	0″.1 ×″ .07	−12	16.4	0″.24 × 0″.13	−19	11.2	0″.87 × 0″.54	−24	15.9
29	14A-471,30B-313	0″.08 × 0″.07	−17	15.5	0″.19 × 0″.13	−22	11.4	0″.72 × 0″.59	−38	13.8
30	14A-471,30B-313	0″.09 × 0″.06	−13	17.5	0″.23 × 0″.13	−25	11.8	0″.86 × 0″.53	−32	17.9
31	14A-471,30B-313	0″.07 × 0″.06	−15	16.5	0″.14 × 0″.11	−24	15.9	0″.71 × 0″.57	−47	14.9
32	14A-471	0″.08 × 0″.06	−11	12.1	0″.28 × 0″.13	47	19.3	0″.76 × 0″.58	24	14
33	14A-471,30B-313	0″.07 × 0″.06	−37	17.0	0″.15 × 0″.12	−41	13.5	0″.8 × 0″.57	−62	15.6
34	14A-471	0″.07 × 0″.06	−20	12.0	0″.18 × 0″.13	48	11.8	0″.66 × 0″.56	14	15.1
35	14A-471	0″.09 × 0″.06	−28	15.6	0″.2 ×″ .12	33	11.4	0″.79 × 0″.55	4	15.7
36	14A-471	0″.08 × 0″.06	−19	20.6	0″.19 × 0″.13	41	27.4	0″.69 × 0″.57	11	12.2
37	14A-471	0″.08 × 0″.06	−22	12.8	0″.16 × 0″.13	40	11.3	0″.65 × 0″.56	6	12
38	14A-471	0″.1 × 0″.06	−16	14.9	0″.25 × 0″.12	31	14.5	0″.88 × 0″.53	5	16.7
39	20A-401*,14A-471	0″.23 × 0″.17	−39	7.3	0″.14 × 0″.12	11	11.9	0″.7 × 0″.57	29	24.8
40	14A-471	0″.1 × 0″.06	−14	12.9	0″.26 × 0″.12	31	11.1	0″.91 × 0″.53	3	41
41	14A-471	0″.08 × 0″.06	18	13.4	0″.14 × 0″.11	14	9.7	0″.7 × 0″.59	31	16.6
41	14A-471	0″.08 × 0″.06	18	13.3	0″.14 × 0″.11	14	9.7	0″.7 × 0″.59	31	16.6
42	20A-401*,14A-471	0″.21 × 0″.18	63	6.2	0″.14 × 0″.11	11	9.8	0″.7 × 0″.57	24	18.9
43	14A-471	0″.11 × 0″.06	−26	18.4	0″.21 × 0″.12	16	13.5	0″.88 × 0″.54	−13	16.8
44	14A-471	0″.07 × 0″.06	0	31.1	0″.13 × 0″.11	−7	55.2	0″.64 × 0″.58	5	22.8
45	14A-471	0″.08 × 0″.06	−7	15.0	0″.13 × 0″.11	−7	10.2	0″.6 × 0″.57	12	22.8
46	14A-471	0″.08 × 0″.06	−1	13.5	0″.14 × 0″.11	−8	10.0	0″.65 × 0″.59	0	15.8
47	14A-471	0″.08 × 0″.06	−1	15.4	0″.16 × 0″.11	−12	19.3	0″.79 × 0″.57	−15	21
48	20A-401*,14A-471	0″.2 ×″ .18	51	9.1	0″.14 × 0″.11	−10	9.8	0″.64 × 0″.59	−21	16.6
49	14A-471	0″.08 × 0″.06	−1	16.1	0″.17 × 0″.11	−14	14.0	0″.81 × 0″.56	−17	18.9

Table 2.2 continued

Table 2.2: Characteristics of Native-Resolution GOALS-ES Images ($A-/B-$configuration) (continued)

ID (1)	Project Code (2)	$\theta_{M\times m}^{33\mathrm{GHz}}$ ($''\times''$) (3)	P.A.$^{33\mathrm{GHz}}$ (°) (4)	$\sigma_{\mathrm{rms}}^{33\mathrm{GHz}}$ (μJy) (5)	$\theta_{M\times m}^{15\mathrm{GHz}}$ ($''\times''$) (6)	P.A.$^{15\mathrm{GHz}}$ (°) (7)	$\sigma_{\mathrm{rms}}^{15\mathrm{GHz}}$ (μJy) (8)	$\theta_{M\times m}^{3\mathrm{GHz}}$ ($''\times''$) (9)	P.A.$^{3\mathrm{GHz}}$ (°) (10)	$\sigma_{\mathrm{rms}}^{3\mathrm{GHz}}$ (μJy) (11)
50	14A-471	$0''.07\times0''.06$	0	28.7	$0''.14\times0''.11$	−13	54.7	$0''.66\times0''.57$	−25	37.8
51	14A-471	$0''.09\times0''.06$	11	16.6	$0''.23\times0''.14$	26	10.0	$0''.75\times0''.52$	3	16.5
52	20A-401*,14A-471	$0''.27\times0''.18$	31	9.8	$0''.19\times0''.11$	23	10.3	$0''.77\times0''.53$	2	20
53	14A-471	$0''.07\times0''.06$	9	24.9	$0''.16\times0''.11$	26	11.7	$0''.67\times0''.54$	3	23.4
54	14A-471	$0''.08\times0''.07$	−48	24.6	$0''.15\times0''.11$	16	11.4	$0''.7\times0''.57$	−6	176
55	14A-471,16A-204	$0''.08\times0''.06$	−2	16.7	$0''.14\times0''.11$	15	10.9	$0''.67\times0''.6$	3	16.7
56	14A-471	$0''.08\times0''.06$	−11	16.4	$0''.15\times0''.11$	−1	10.1	$0''.79\times0''.53$	−28	17.7
57	14A-471	$0''.07\times0''.06$	−9	16.5	$0''.15\times0''.13$	−11	11.4	$0''.65\times0''.58$	−47	13.4
58	14A-471	$0''.08\times0''.06$	−19	16.1	$0''.18\times0''.11$	−7	11.5	$0''.89\times0''.56$	−41	19.4
59	14A-471	$0''.07\times0''.06$	−37	17.1	$0''.16\times0''.13$	60	10.2	$0''.54\times0''.49$	5	39.9
60	14A-471	$0''.12\times0''.05$	−29	20.4	$0''.21\times0''.11$	−12	9.8	$1''.1\times0''.5$	−29	20.9
61	14A-471	$0''.12\times0''.05$	−31	20.9	$0''.21\times0''.11$	−15	9.2	$1''.2\times0''.51$	−32	22.2
62	14A-471	$0''.09\times0''.06$	−27	20.7	$0''.13\times0''.12$	−5	9.3	$0''.65\times0''.52$	−47	24.6
63	14A-471	$0''.07\times0''.06$	−37	17.9	$0''.12\times0''.11$	−31	10.8	$0''.63\times0''.54$	−58	19.2
64	20A-401*,14A-471	$0''.3\times''.17$	55	7.9	$0''.13\times0''.11$	−18	9.3	$0''.69\times0''.53$	−46	22.5
65	14A-471	$0''.09\times0''.06$	−23	19.0	$0''.15\times0''.11$	−19	9.9	$0''.8\times0''.52$	−32	19.6
66	14A-471	$0''.08\times0''.05$	−34	20.8	$0''.13\times0''.11$	−19	12.2	$0''.7\times0''.53$	−46	42
67	14A-471	$0''.09\times0''.06$	−26	17.7	$0''.13\times0''.11$	−13	9.3	$0''.72\times0''.54$	−46	20.9
68	14A-471	$0''.09\times0''.06$	−23	15.7	$0''.15\times0''.11$	−12	9.9	$0''.8\times0''.53$	−36	20.7

* 20A-401 observations were taken with VLA $B-$configuration

NOTE — (1) Identifier for the IRAS system, corresponding to column (1) in Table 2.1. (2) VLA project code for the $A-/B-$configuration observations used for imaging. (3) - (5): Characteristics of Ka-Band (33 GHz) images: FWHM (major × minor) and position angle of the synthesized beam and image noise, as quantified by the root-mean-square value measured in an emission-free region of the image before primary beam correction. (6) - (8): Characteristics of Ku-Band (15 GHz) images. (9) - (11): Characteristics of S-Band (3 GHz) images.

Table 2.3: Characteristics of Native-Resolution GOALS-ES Images ($C-$configuration)

ID (1)	Project Code (2)	$\theta^{33\mathrm{GHz}}_{M\times m}(''\times'')$ (3)	P.A.$^{33\mathrm{GHz}}$ (°) (4)	$\sigma^{33\mathrm{GHz}}_{\mathrm{rms}}$ (μJy) (5)	$\theta^{15\mathrm{GHz}}_{M\times m}(''\times'')$ (6)	P.A.$^{15\mathrm{GHz}}$ (°) (7)	$\sigma^{15\mathrm{GHz}}_{\mathrm{rms}}$ (μJy) (8)	$\theta^{3\mathrm{GHz}}_{M\times m}(''\times'')$ (9)	P.A.$^{3\mathrm{GHz}}$ (°) (10)	$\sigma^{3\mathrm{GHz}}_{\mathrm{rms}}$ (μJy) (11)
1	14A-471	$0''.89\times0''.6$	7	23.1	$1''.92\times1''.1$	−24	13.7	$10''.1\times5''.9$	−24	27.8
2	14A-471	$0''.83\times0''.5$	7	18.8	$1''.9\times1''.2$	−24	14.8	$10''.4\times6''.5$	−36	100
3	14A-471	$0''.94\times0''.51$	1	20	$2''.62\times1''.18$	−31	13.7	$13''.4\times5''.9$	−32	28.4
4	14A-471	$0''.93\times0''.52$	4	17.2	$3''.05\times1''.54$	−37	17.9	$12''.1\times5''.6$	−31	35
5	14A-471	$0''.6\times0''.53$	−2	21	$1''.42\times1''.2$	−29	12.5	$6''.92\times6''.28$	−44	24.8
6	14A-471	$0''.83\times0''.52$	1	31	$2''.4\times1''.2$	−35	12.7	$11''.8\times5''.7$	−36	32.8
7	14A-471	$0''.63\times0''.56$	18	20	$1''.4\times1''.2$	−27	13.1	$6''.65\times6''.2$	−48	21
8	14A-471	$0''.81\times0''.52$	−2	17	$2''.5\times1''.1$	−39	18	$13''.2\times5''.8$	−41	60
9	14A-471	$0''.65\times0''.53$	2	16	$1''.8\times1''.2$	−43	13	$9\times6''.2$	−50	38.3
10	14A-471	$1''.73\times1''.64$	28	26	$1''.5\times1''.2$	−47	11.5	$7''.4\times6''.1$	−66	20.7
11	14A-471	$0''.68\times0''.51$	75	50	$1''.76\times1''.24$	29	9.9	$8''.7\times6''.1$	12	20.1
12	14A-471	$0''.83\times0''.59$	36	95.3	$1''.7\times1''.2$	28	68.6	$8''.12\times5''.8$	8	342
13	14A-471	$0''.72\times0''.59$	50	15.4	$1''.5\times1''.3$	38	10.2	$7''.3\times6$	5	29.1
14	14A-471	$0''.7\times0''.59$	53	17.3	$1''.4\times1''.2$	38	10.8	$7''.1\times5''.9$	4	25.7
15	14A-471	$0''.65\times0''.59$	40	16.2	$1''.4\times1''.2$	19	10.5	$6''.8\times5''.5$	1	24.2
16	14A-471	$0''.65\times0''.58$	42	16.5	$1''.4\times1''.2$	15	9.5	$6''.6\times5''.4$	−1	24.5
17	14A-471	$0''.77\times0''.58$	39	16.8	$1''.5\times1''.2$	23	10	$7''.7\times6''.1$	4	28.5
18	14A-471	$1''.19\times0''.53$	26	20.2	$2''.3\times1''.1$	16	11	$11''.1\times5''.5$	0	28.1
19	14A-471	$1\times0''.57$	31	22	$1''.8\times1''.1$	18	19	$9''.5\times5''.9$	3	120
20	14A-471	$0''.65\times0''.55$	−15	16.6	$1''.4\times1''.2$	0	9.8	$6''.3\times5''.6$	−1	40.3
21	14A-471	$0''.77\times0''.57$	14	17	$1''.77\times1''.2$	5	9.8	$9\times5''.7$	2	29.8
22	14A-471	$0''.59\times0''.58$	6	17	$1''.4\times1''.2$	−2	12.2	$6\times5''.4$	−13	67.6
23	14A-471	$0''.8\times0''.54$	12	19.4	$1''.79\times1''.12$	−178	11.6	$9''.1\times5''.7$	−1	32
24	14A-471	$0''.6\times0''.57$	−5	16.3	$1''.4\times1''.2$	0	12	$6''.5\times5''.6$	−1	45.5
25	14A-471	$0''.96\times0''.54$	14	17.9	$2''.1\times1''.1$	−1	12	$10''.42\times5''.6$	−10	38.8
26	14A-471	$0''.71\times0''.55$	7	17.2	$1''.7\times1''.1$	−8	11	$8''.1\times5''.6$	0	33
27	14A-471	$0''.62\times0''.56$	−4	16.3	$1''.4\times1''.1$	−5	11	$7\times5''.9$	1	23.9
28	14A-471	$0''.8\times0''.55$	−8	16.2	$2''.1\times1''.2$	−25	12.6	$9''.3\times5''.7$	−18	19.1
29	14A-471	$0''.66\times0''.56$	−24	15.1	$1''.7\times1''.2$	−32	11	$7''.9\times6$	−24	20.5
30	14A-471	$0''.78\times0''.55$	−15	15.8	$2''.1\times1''.2$	−31	11.5	$9''.3\times5''.8$	−25	27.5
31	14A-471	$0''.65\times0''.55$	−18	15.8	$1''.6\times1''.2$	−36	12.8	$7''.6\times5''.9$	−28	21.5
32	14A-471, 16A-204	$0''.71\times0''.62$	−1	12.6	$1''.7\times1''.2$	−9	45.6	$8''.3\times6''.6$	8	40
33	14A-471	$0''.64\times0''.56$	−32	15.1	$1''.8\times1''.3$	−54	12	$7''.83\times6''.3$	−52	21.9
34	14A-471, 16A-204	$0''.72\times0''.63$	−38	17.3	$1''.7\times1''.3$	−16	48	$7''.6\times6''.1$	−13	24.3
35	14A-471, 16A-204	$0''.78\times0''.63$	−20	13.5	$2\times1''.3$	−26	52.3	$9\times6''.2$	−9	21.3
36	14A-471, 16A-204	$0''.69\times0''.62$	−25	16.5	$1''.7\times1''.2$	−21	55	$8''.1\times6''.1$	−10	44.2
37	14A-471, 16A-204	$0''.68\times0''.59$	−36	13.3	$1''.7\times1''.3$	−28	39	$7''.7\times6''.1$	−18	23
38	14A-471, 16A-204	$0''.9\times0''.6$	2	13.9	$2''.5\times1''.2$	−22	33	$10\times5''.8$	−8	31.5
39	14A-471, 16A-204	$0''.71\times0''.58$	24	12.8	$1''.6\times1''.2$	20	12.3	$9''.1\times5''.82$	26	59.2
40	14A-471, 16A-204	$0''.93\times0''.6$	4	14.7	$2''.49\times1''.2$	−23	30.7	$10''.4\times5''.8$	−9	67
41	14A-471, 16A-204	$0''.78\times0''.57$	37	10.2	$1''.6\times1''.2$	21	8.8	$7''.8\times5''.8$	19	34
41	14A-471, 16A-204	$0''.78\times0''.57$	37	10.2	$1''.6\times1''.2$	21	8.8	$7''.8\times5''.8$	19	34
42	14A-471, 16A-204	$0''.73\times0''.59$	37	10.3	$1''.5\times1''.2$	20	10	$7''.8\times6''.3$	19	37
43	14A-471, 16A-204	$0''.9\times0''.59$	−13	11.7	$3''.06\times1''.4$	−33	63.1	$10''.3\times5''.6$	−23	28
44	14A-471, 16A-204	$0''.65\times0''.57$	17	10.1	$1''.4\times1''.2$	1	32	$6''.7\times5''.3$	−5	35
45	14A-471, 16A-204	$0''.64\times0''.56$	25	13.1	$1''.4\times1''.2$	−1	11.3	$6''.5\times5''.4$	−4	26
46	14A-471, 16A-204	$0''.68\times0''.57$	24	12.7	$1''.5\times1''.2$	0	10	$6''.6\times5''.3$	−1	33
47	14A-471, 16A-204	$0''.82\times0''.61$	24	13.8	$1''.8\times1''.2$	−6	21	$8\times5''.2$	−10	34
48	14A-471, 16A-204	$0''.71\times0''.57$	32	13	$1''.5\times1''.2$	1	11	$6''.6\times5''.5$	−11	27.8
49	14A-471, 16A-204	$0''.84\times0''.56$	21	12.2	$1''.8\times1''.2$	−10	9.5	$8''.5\times5''.4$	−10	25.3

Table 2.3 continued

Table 2.3: Characteristics of Native-Resolution GOALS-ES Images ($C-$configuration) (continued)

ID (1)	Project Code (2)	$\theta^{33\mathrm{GHz}}_{M\times m}$ ($''\times''$) (3)	P.A.$^{33\mathrm{GHz}}$ (°) (4)	$\sigma^{33\mathrm{GHz}}_{\mathrm{rms}}$ (μJy) (5)	$\theta^{15\mathrm{GHz}}_{M\times m}$ ($''\times''$) (6)	P.A.$^{15\mathrm{GHz}}$ (°) (7)	$\sigma^{15\mathrm{GHz}}_{\mathrm{rms}}$ (μJy) (8)	$\theta^{3\mathrm{GHz}}_{M\times m}$ ($''\times''$) (9)	P.A.$^{3\mathrm{GHz}}$ (°) (10)	$\sigma^{3\mathrm{GHz}}_{\mathrm{rms}}$ (μJy) (11)
50	14A-471, 16A-204	$0''.71 \times 0''.57$	31	35.1	$1''.51 \times 1''.18$	−9	11	$7''.7 \times 6''.1$	−11	85.3
51	14A-471, 16A-204	$0''.84 \times 0''.55$	17	13.7	$2 \times 1''.1$	25	12.5	$9''.6 \times 5''.7$	−23	25.6
52	14A-471, 16A-204	$0''.85 \times 0''.55$	20	15.3	$1''.9 \times 1''.1$	22	15.2	$10''.3 \times 5''.9$	−26	28.8
53	14A-471, 16A-204	$0''.71 \times 0''.58$	23	12.2	$1''.62 \times 1''.2$	24	13.6	$8''.7 \times 5''.9$	−30	57.2
54	14A-471, 16A-204	$0''.73 \times 0''.57$	17	23.4	$1''.6 \times 1''.1$	20	32.8	$10''.1 \times 5''.7$	−32	40.5
55	14A-471, 16A-204	$0''.67 \times 0''.58$	19	13.5	$1''.5 \times 1''.1$	21	13.1	$9''.3 \times 6$	−32	40.1
56	14A-471, 16A-204	$0''.71 \times 0''.56$	−5	13.8	$1''.6 \times 1''.1$	−174	12	$16 \times 6''.6$	−48	64
57	14A-471, 16A-204	$0''.63 \times 0''.57$	−7	10.6	$1''.3 \times 1''.1$	−1	11.5	$11 \times 6''.1$	−57	30.6
58	14A-471, 16A-204	$0''.71 \times 0''.56$	−11	13.8	$1''.6 \times 1''.1$	−10	14.2	$24''.5 \times 6''.1$	−53	11.7
59	14A-471	$0''.73 \times 0''.6$	62	18.3	$1''.3 \times 1''.1$	−1	12.7	$6''.7 \times 6''.2$	20	15.9
60	14A-471	$0''.99 \times 0''.5$	−11	19	$2''.5 \times 1''.1$	−28	16.1	$11''.2 \times 5''.7$	−11	20.9
61	14A-471	$0''.97 \times 0''.5$	−13	19.6	$2''.4 \times 1''.1$	−31	17.6	$10''.7 \times 5''.5$	−14	20.8
62	14A-471	$0''.74 \times 0''.61$	−171	18.8	$1''.4 \times 1''.1$	−31	20.1	$7 \times 5''.7$	−13	53.3
63	14A-471	$0''.6 \times 0''.53$	−2	21.3	$1''.3 \times 1''.2$	−48	12.1	$6''.7 \times 5''.8$	−10	21.4
64	14A-471	$0''.63 \times 0''.51$	−4	17.7	$1''.5 \times 1''.1$	−36	13.2	$7''.1 \times 6$	−13	20.5
65	14A-471	$0''.74 \times 0''.53$	4	20	$1''.7 \times 1''.1$	−26	16.4	$8''.1 \times 5''.5$	−11	18.2
66	14A-471	$0''.62 \times 0''.51$	−16	18.4	$1''.4 \times 1''.1$	−36	12.7	$7''.3 \times 5''.9$	−15	43
67	14A-471	$0''.66 \times 0''.53$	−1	16.5	$1''.5 \times 1''.1$	−33	14	$7''.6 \times 6$	−15	24.3
68	14A-471	$0''.69 \times 0''.54$	2	16.8	$1''.7 \times 1''.1$	−31	12.3	$8 \times 5''.8$	−13	18.5

NOTE — (1) Identifier for the IRAS system, corresponding to column (1) in Table 2.1. (2) VLA project code for the $C-$configuration observations used for imaging. (3) - (5): Characteristics of Ka-Band (33 GHz) images: FWHM (major × minor) and position angle of the synthesized beam and image noise, as quantified by the root-mean-square value measured in an emission-free region of the image before primary beam correction. (6) - (8): Characteristics of Ku-Band (15 GHz) images. (9) - (11): Characteristics of S-Band (3 GHz) images.

2.4 Image Atlas

We detected emission with SNR$\gtrsim$ 5 in all but one GOALS-ES systems at at least one frequency. Due to incorrect pointing setup, we did not detect emission in MCG - 01-60-022. In 63 of the 68 GOALS-ES systems, we detected emission with SNR$\gtrsim$ 5 at a resolution of $\sim$ 0".1 – 0".2 at 15 (Ku) and/or 33 GHz (Ka), corresponding to $\sim$ 10 – 160 pc at the distances of these systems. To our knowledge, this is the largest sample of local U/LIRGs that have been observed at high ($>$ 10 GHz) radio frequencies on $\sim$ 100 pc scales.

Below we display all the native resolution images from the GOALS-ES. To help visualize the spatial distribution of the radio continuum emission, for each system we also show the optical y-band image from PanSTARRS1 (Flewelling et al., 2020) in grey scales, with 3, 5, 10$\sigma_{\rm rms}$ contours from the 3 GHz A-configuration images overlaid on top in magenta. For each set of radio images, 3, 15, and 33 GHz images are displayed from left to right, and A-configuration images are displayed below the C-configuration images. Images from the same configuration also share the same field-of-view. In each image, the synthesized beam is represented with a red hatched ellipse on the lower left corner.

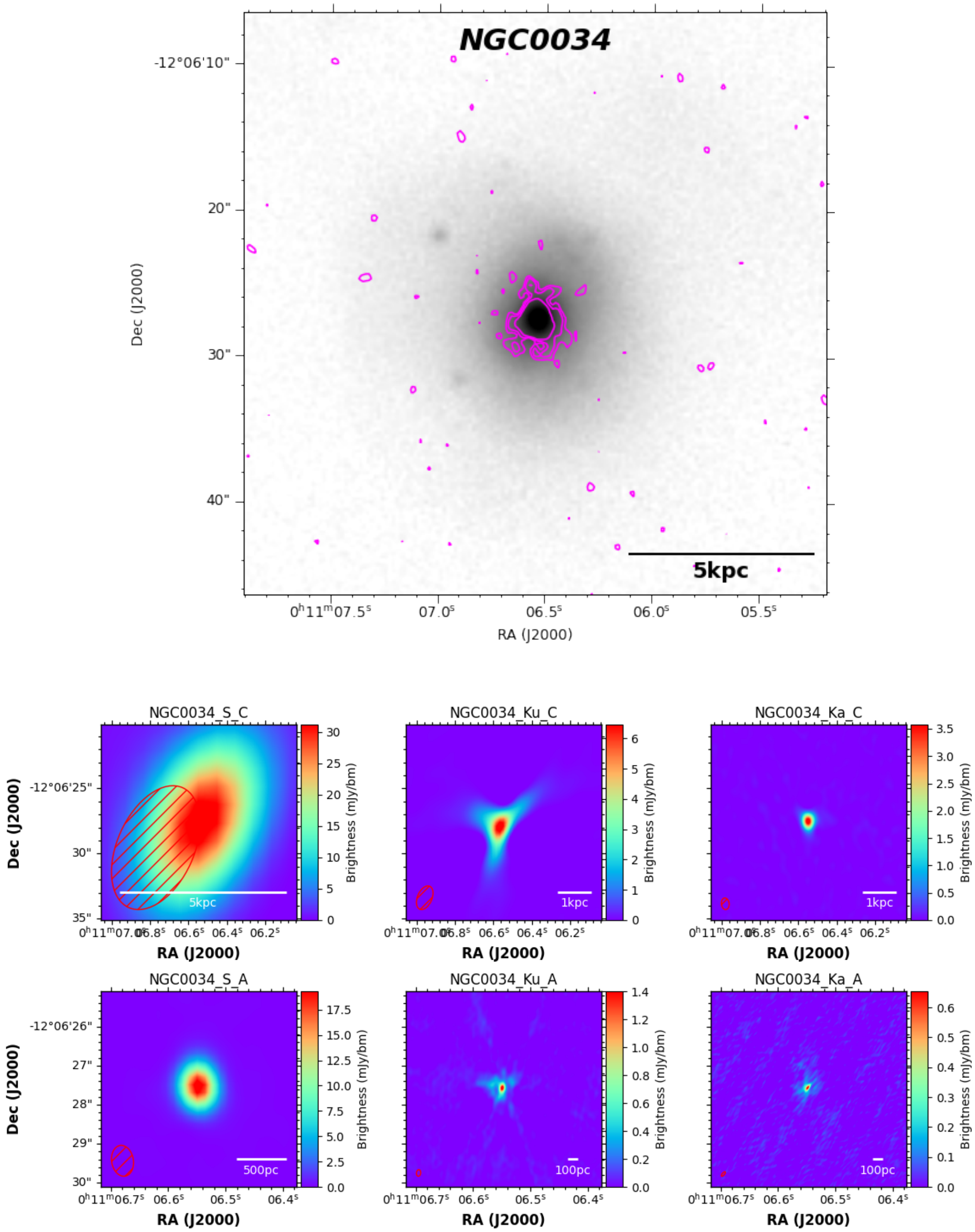

Figure 2.2: NGC 0034

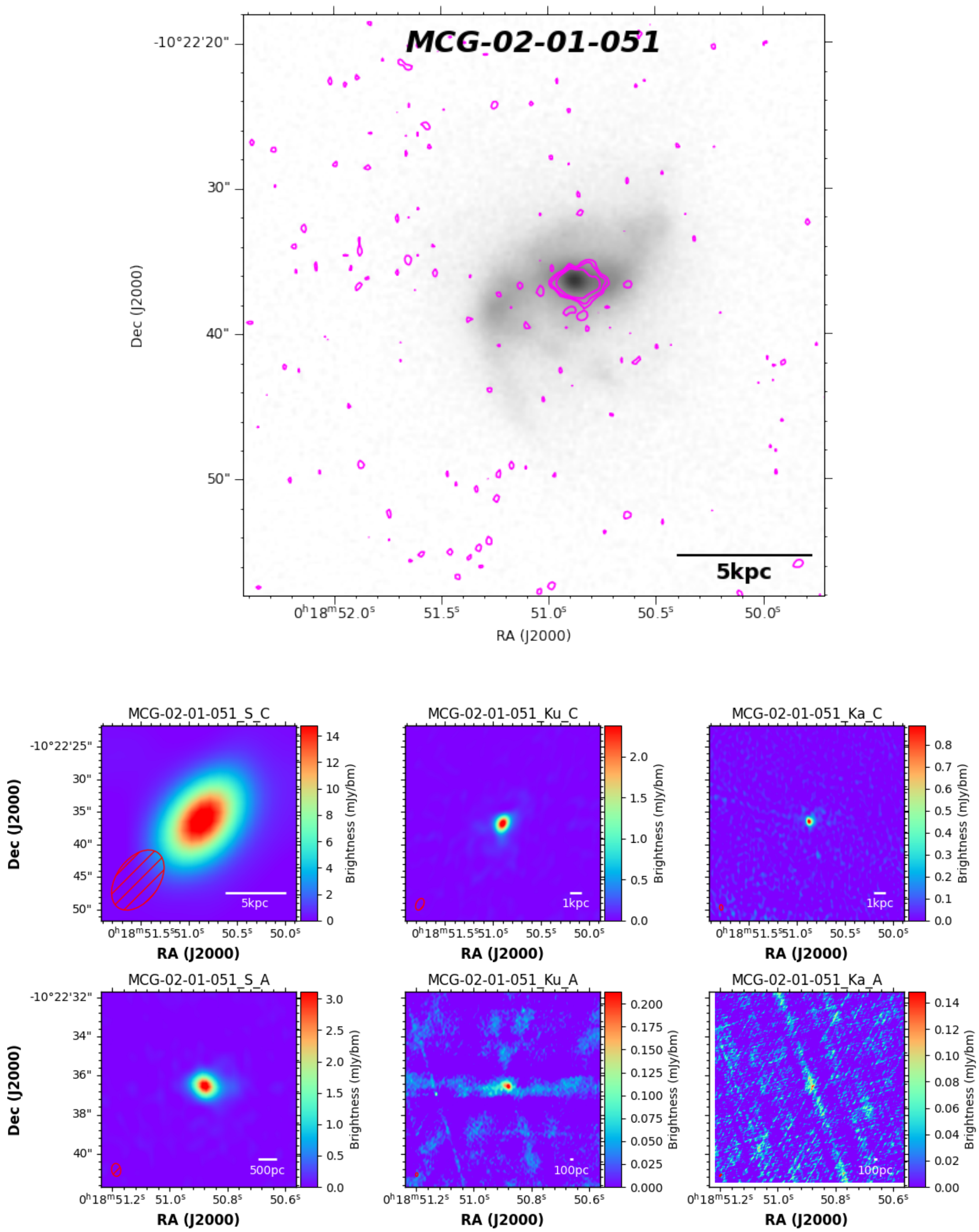

Figure 2.3: MCG-02-01-051

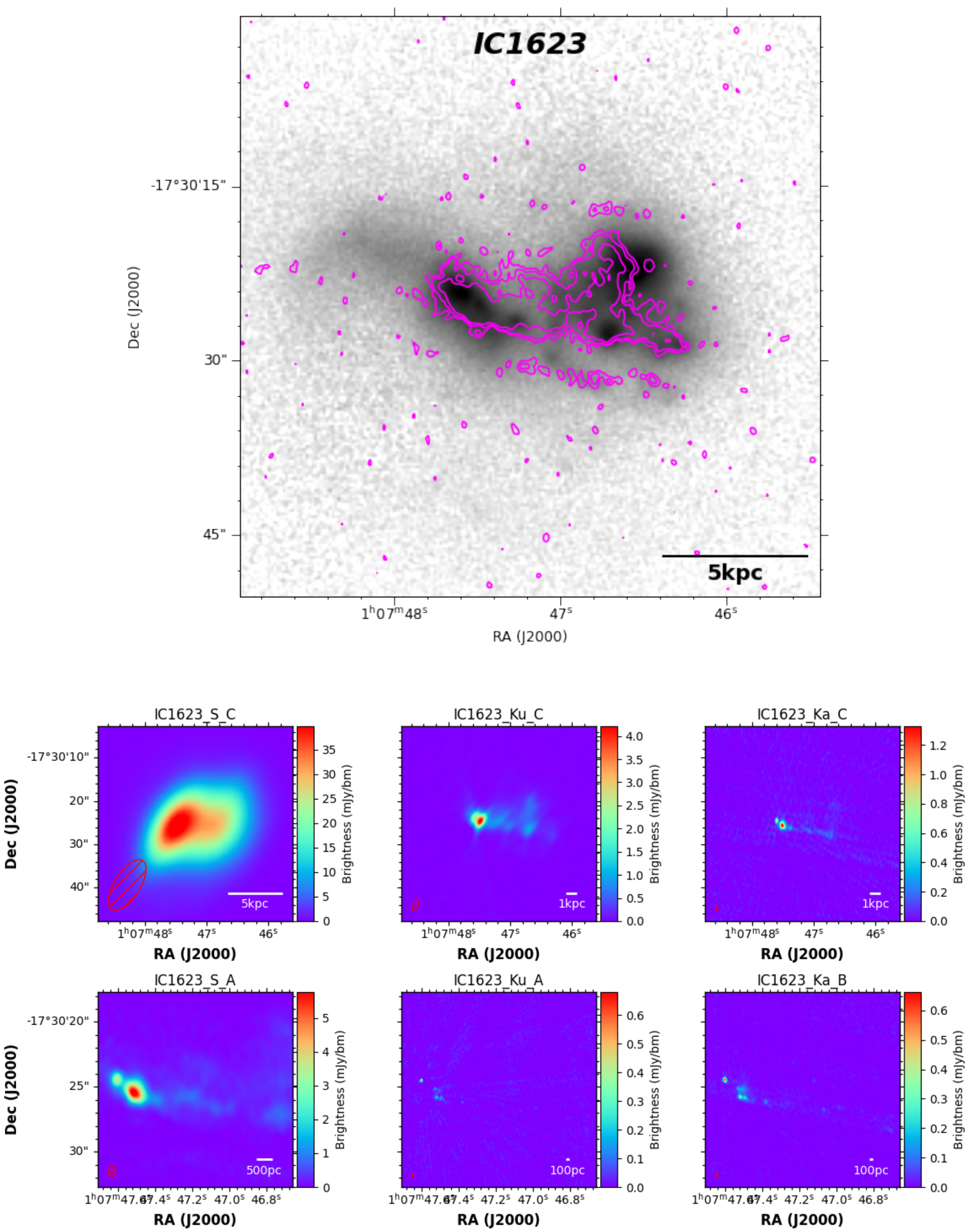

Figure 2.4: IC 1623

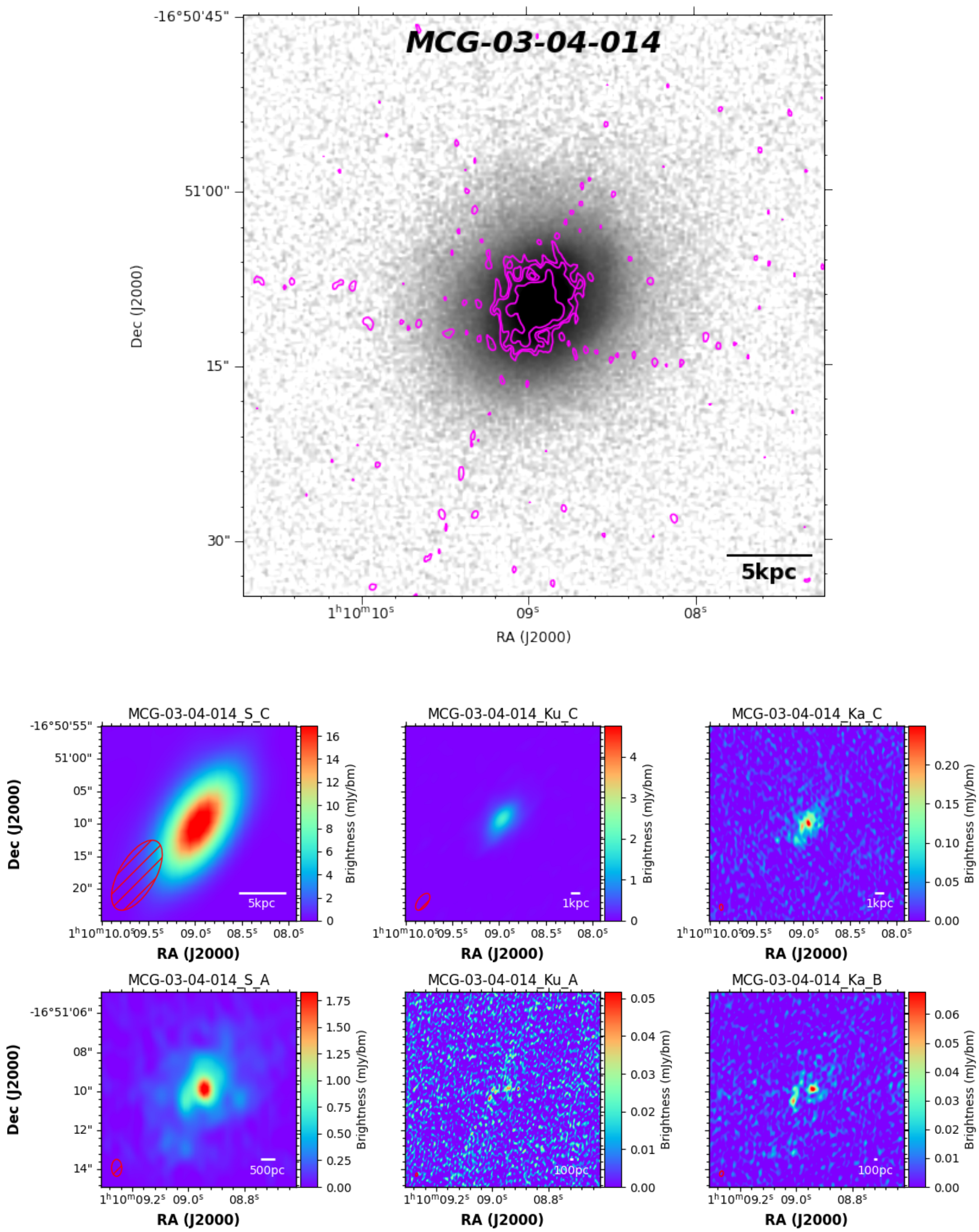

Figure 2.5: MCG-03-04-014

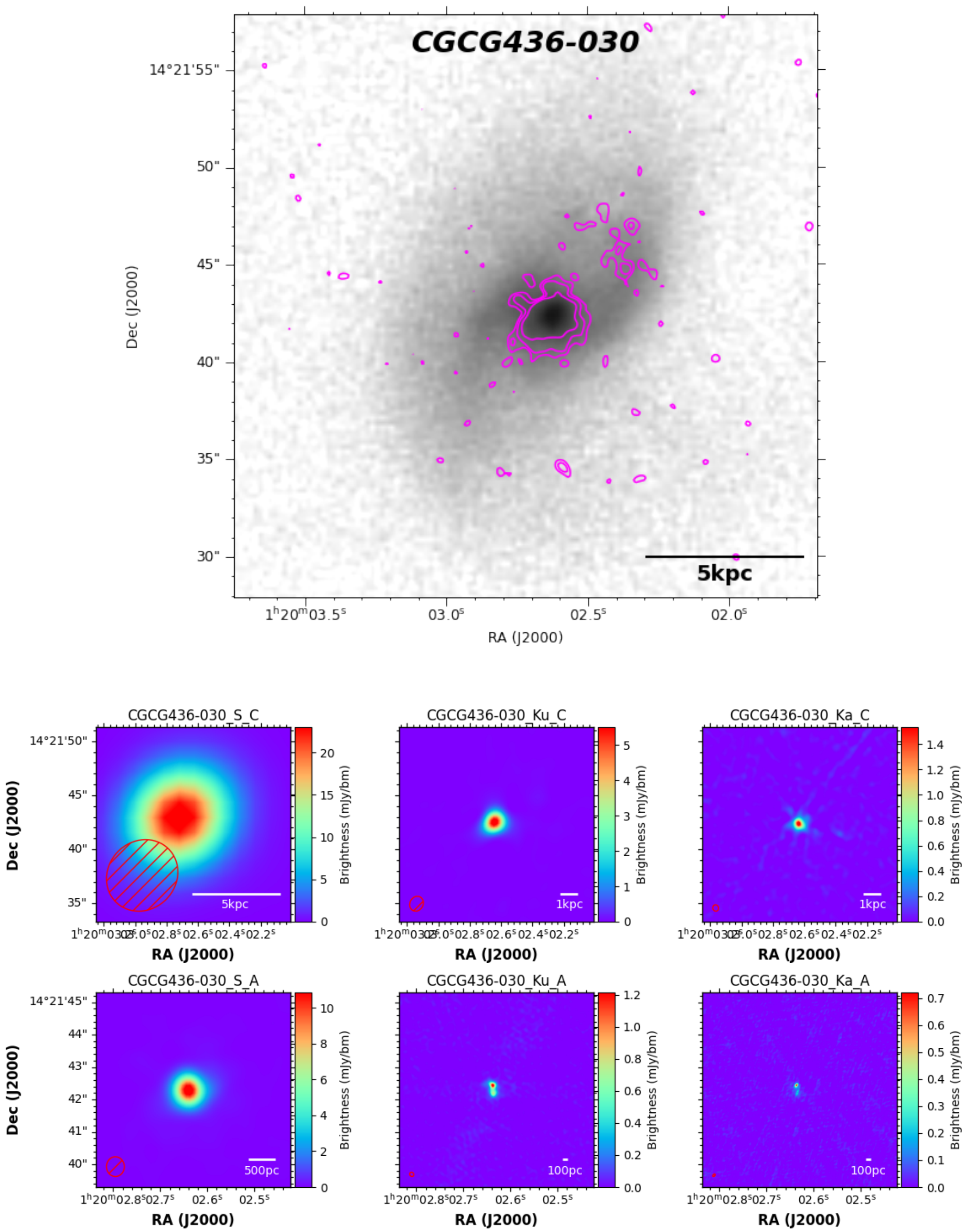

Figure 2.6: CGCG 436-030

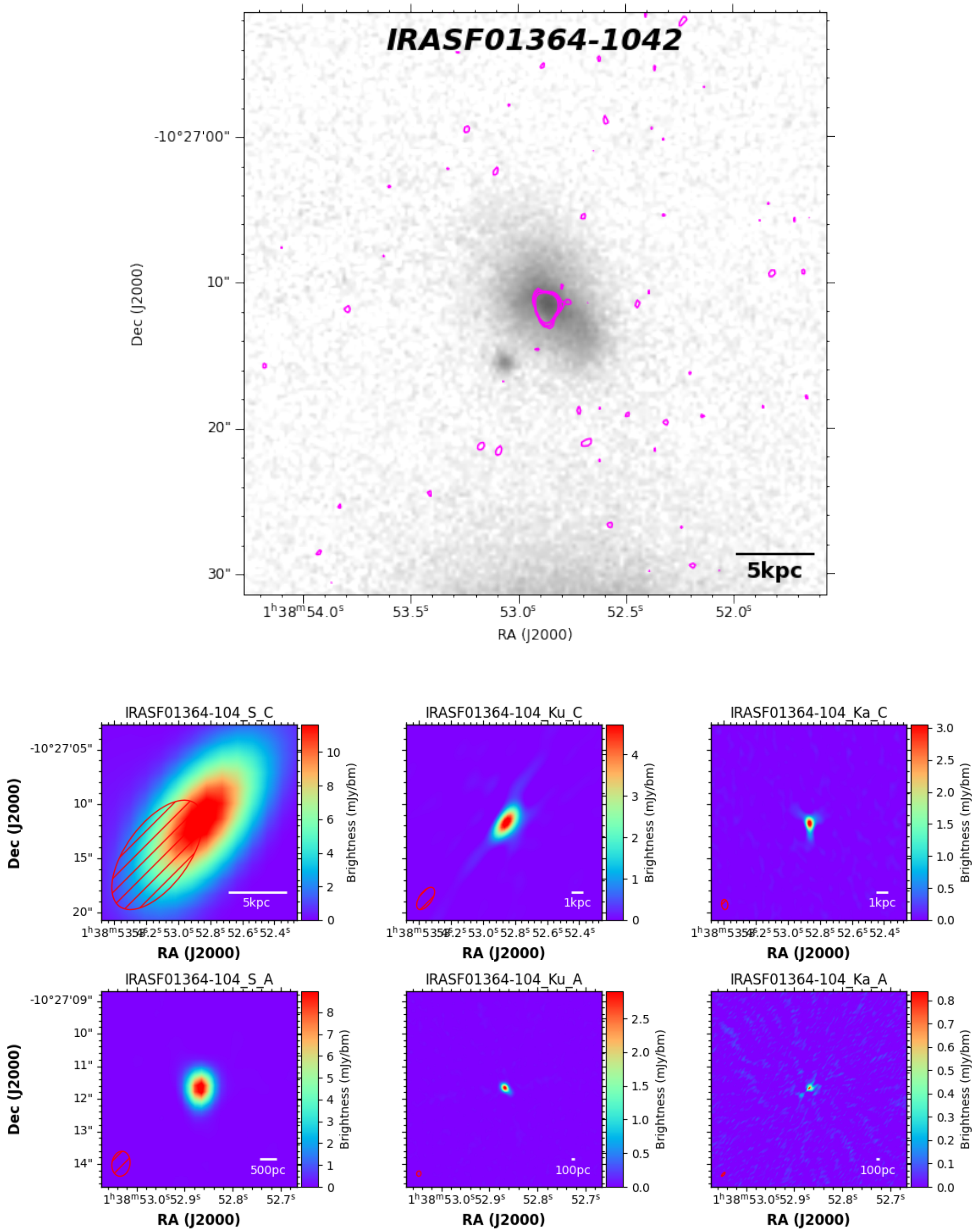

Figure 2.7: IRAS F01364-1042

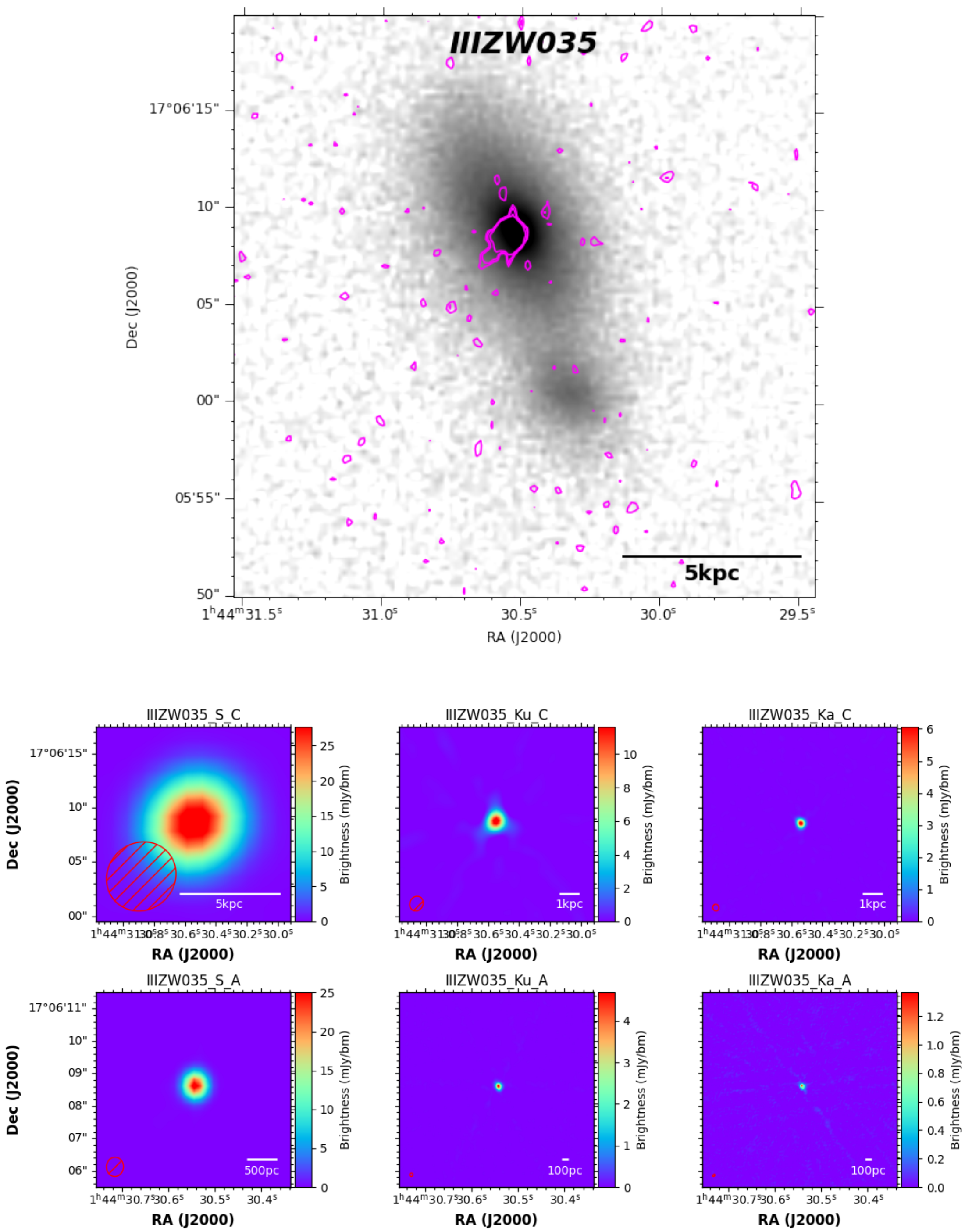

Figure 2.8: IIIZw 035

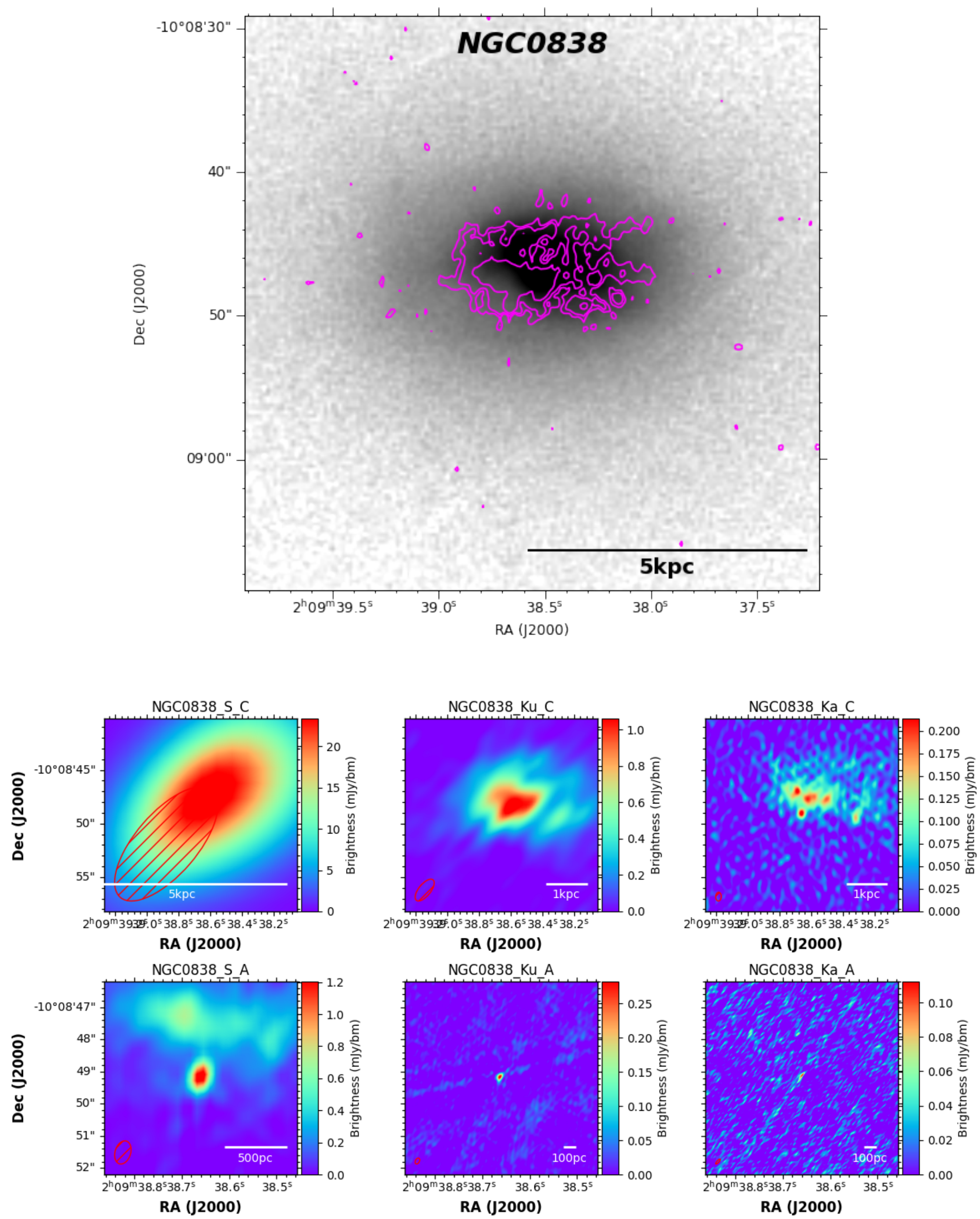

Figure 2.9: NGC 0838

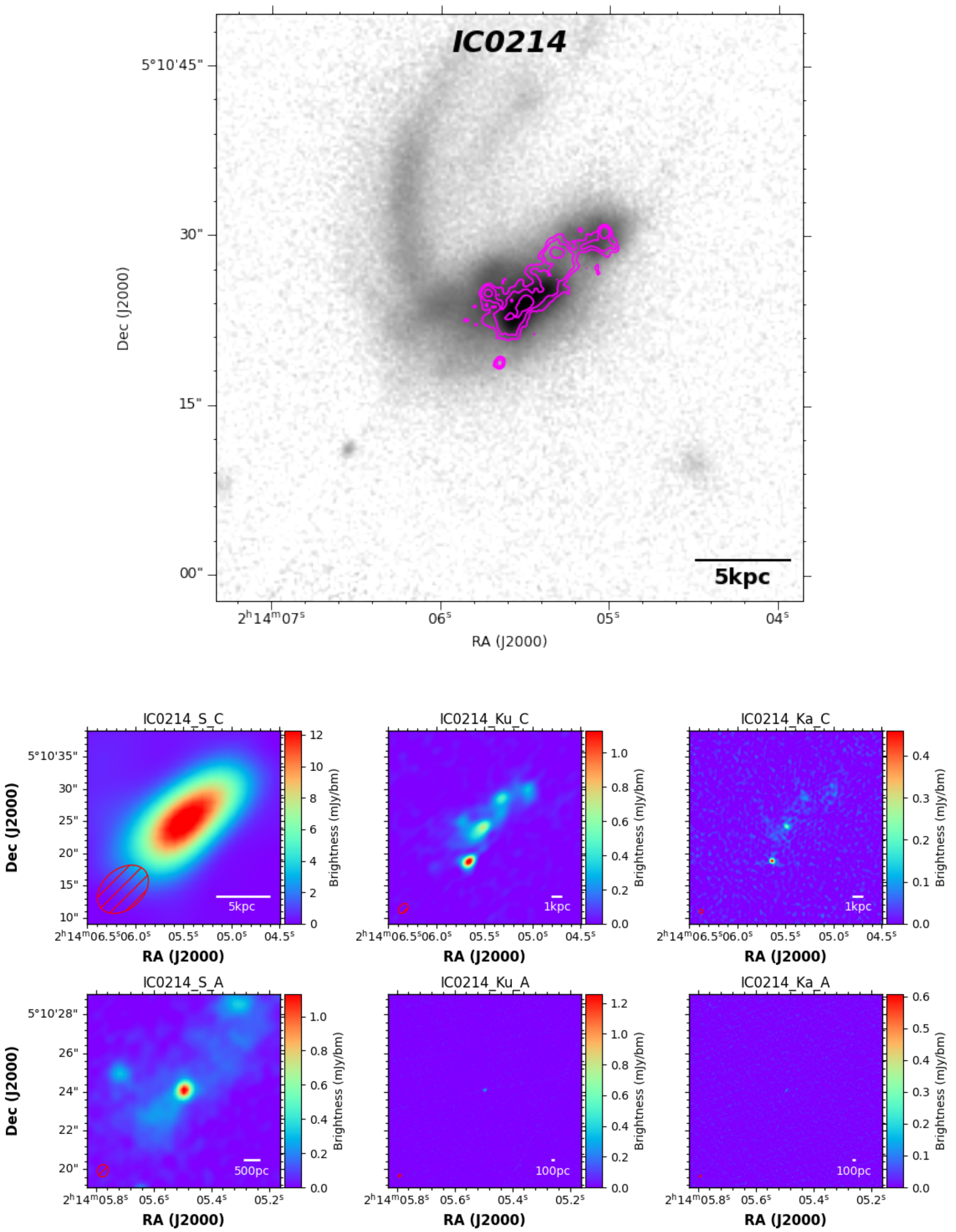

Figure 2.10: IC 0214

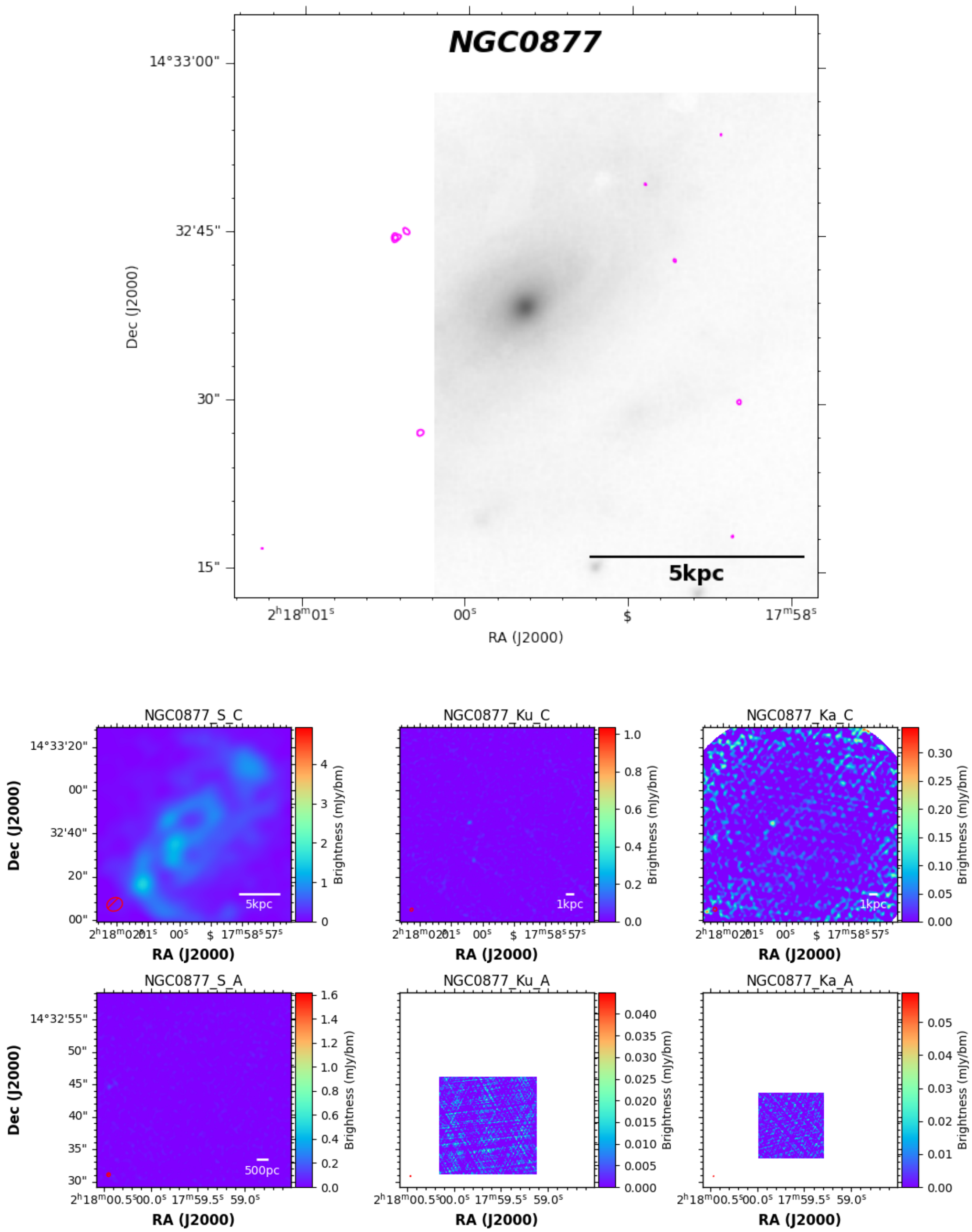

Figure 2.11: NGC 0877

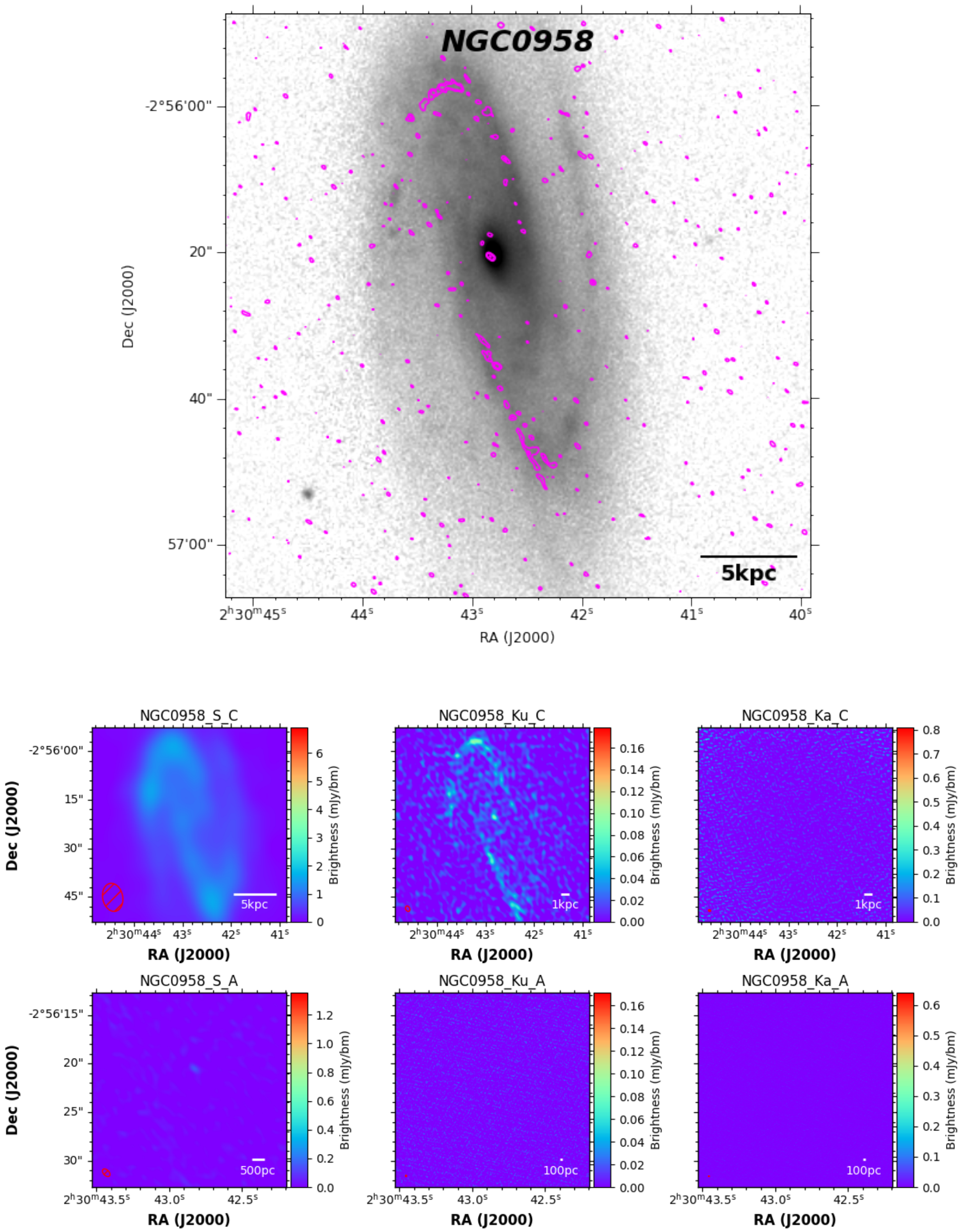

Figure 2.12: NGC 0958

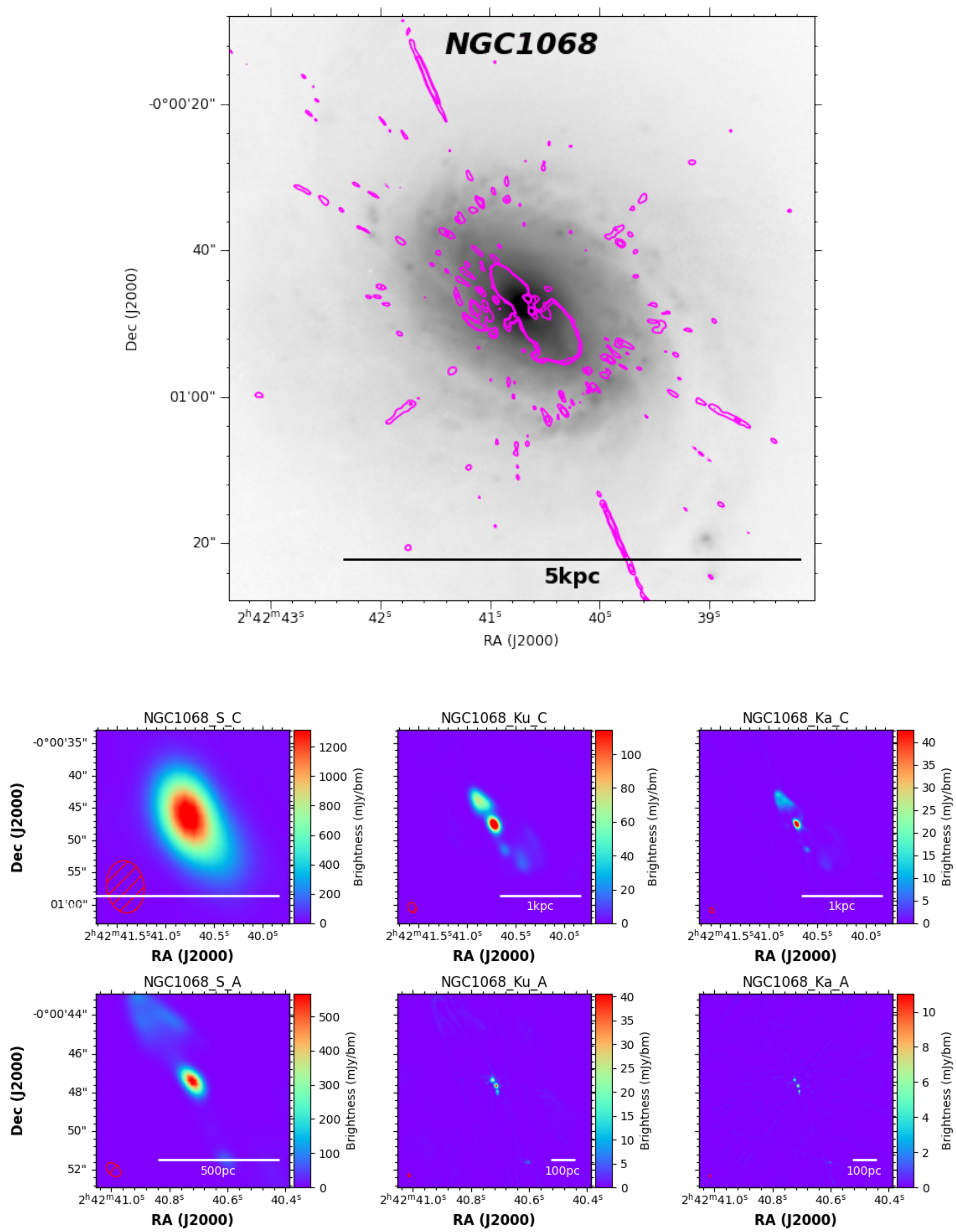

Figure 2.13: NGC 1068

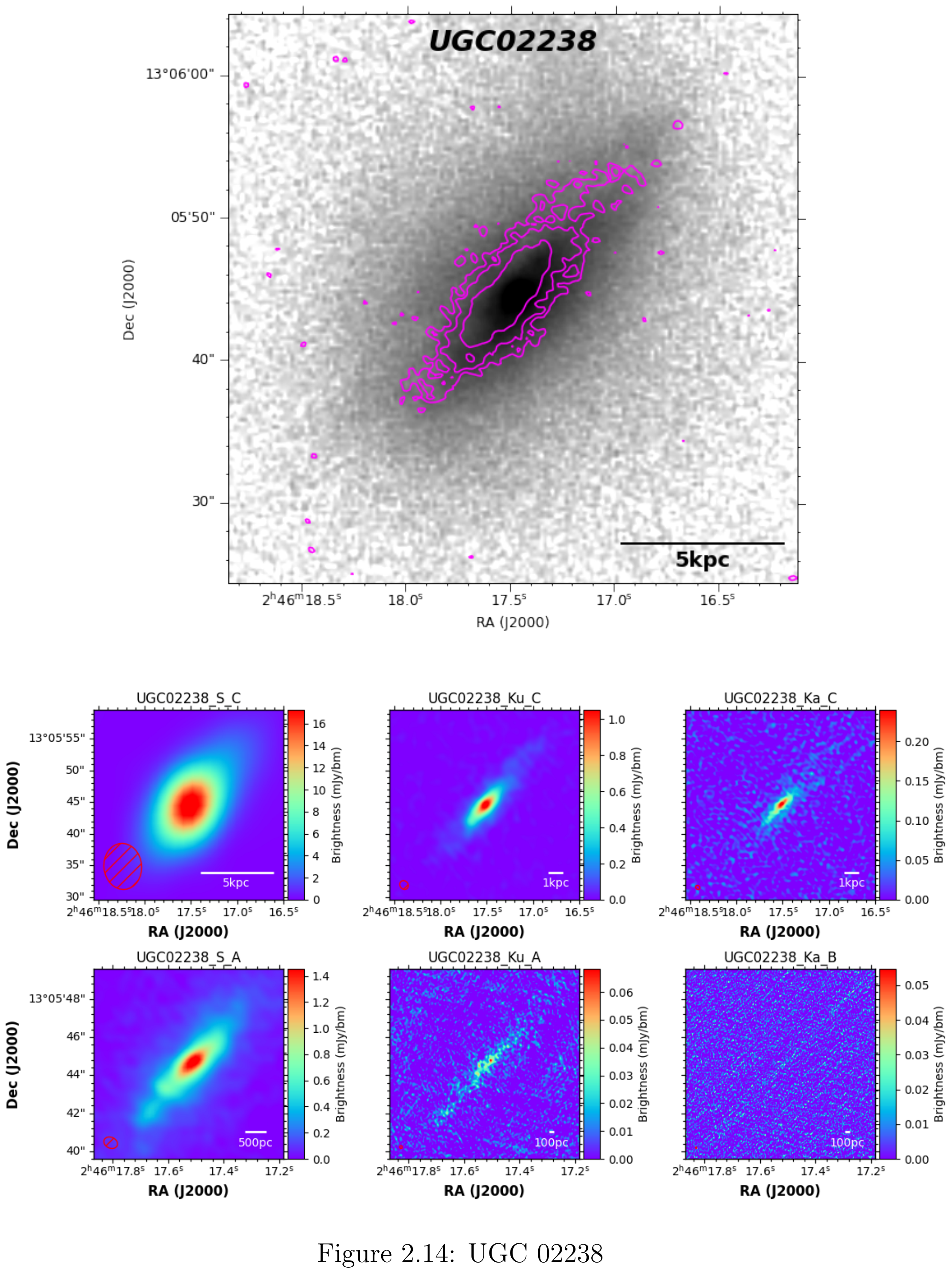

Figure 2.14: UGC 02238

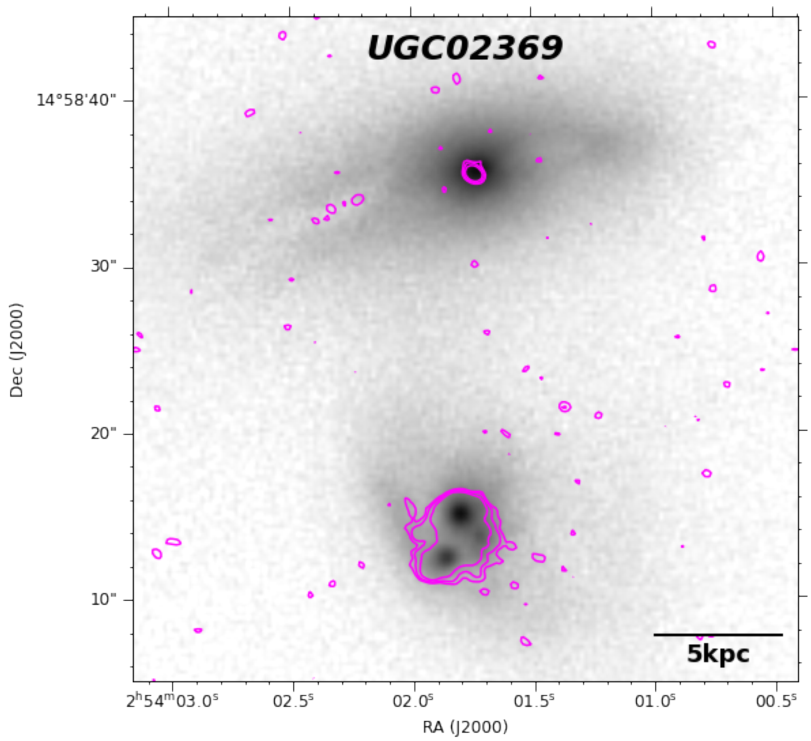

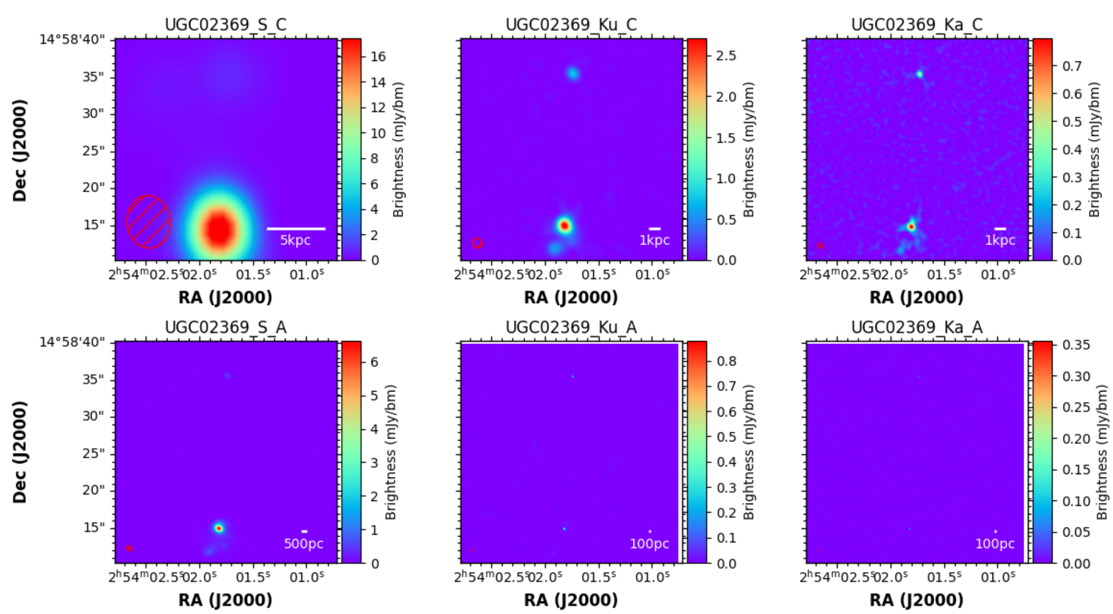

Figure 2.15: UGC 02369

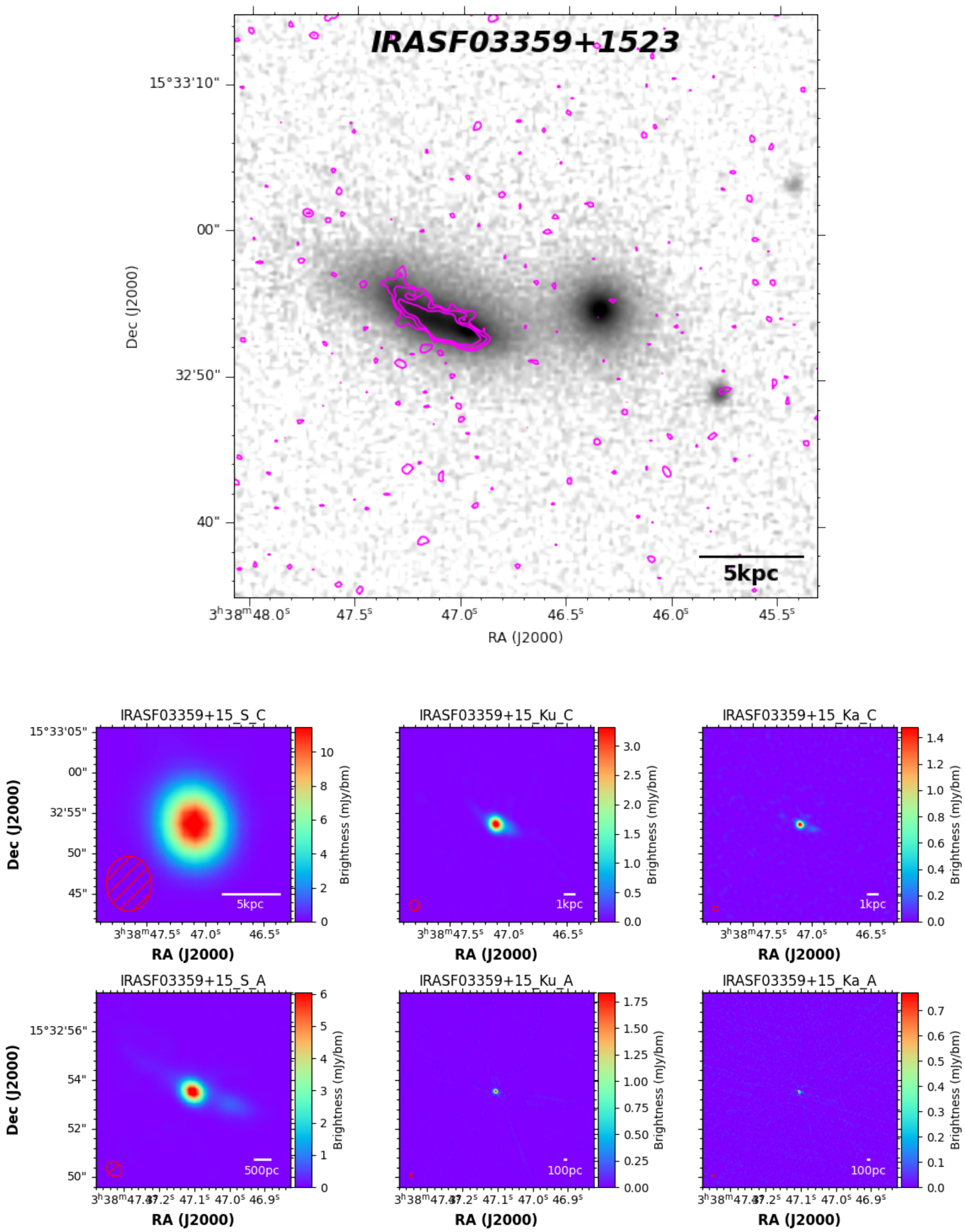

Figure 2.16: IRASF 03359+1523

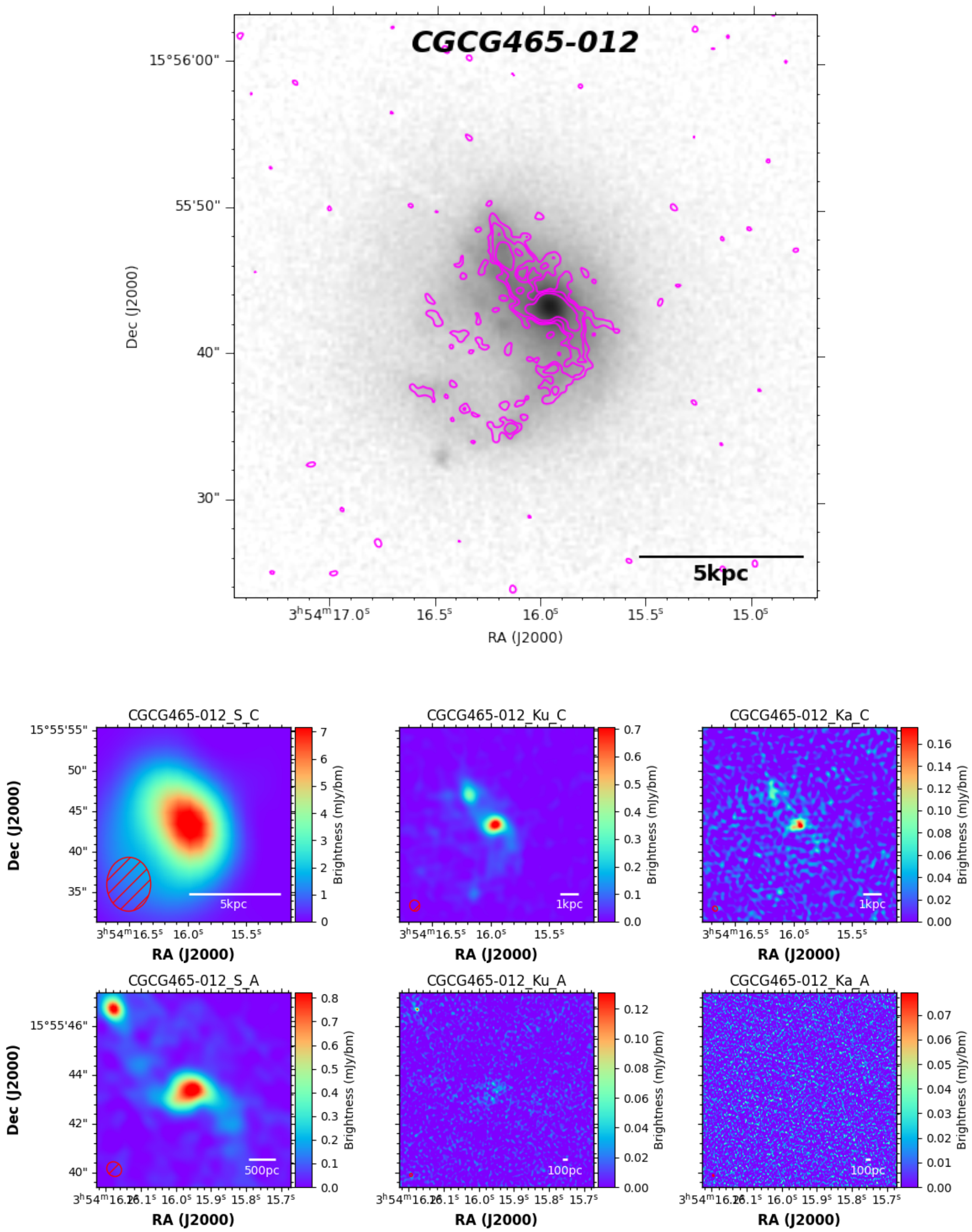

Figure 2.17: CGCG 465-012

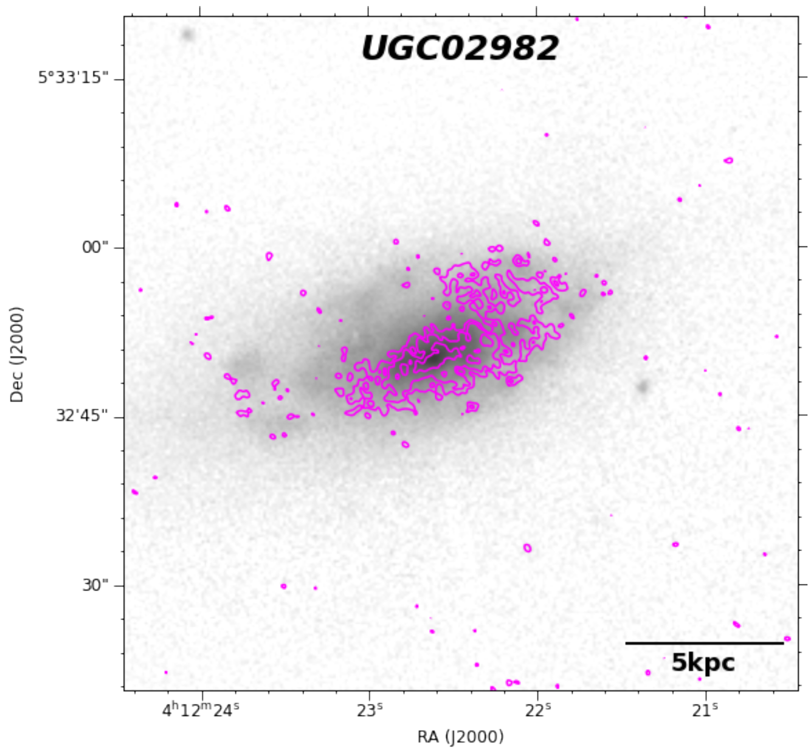

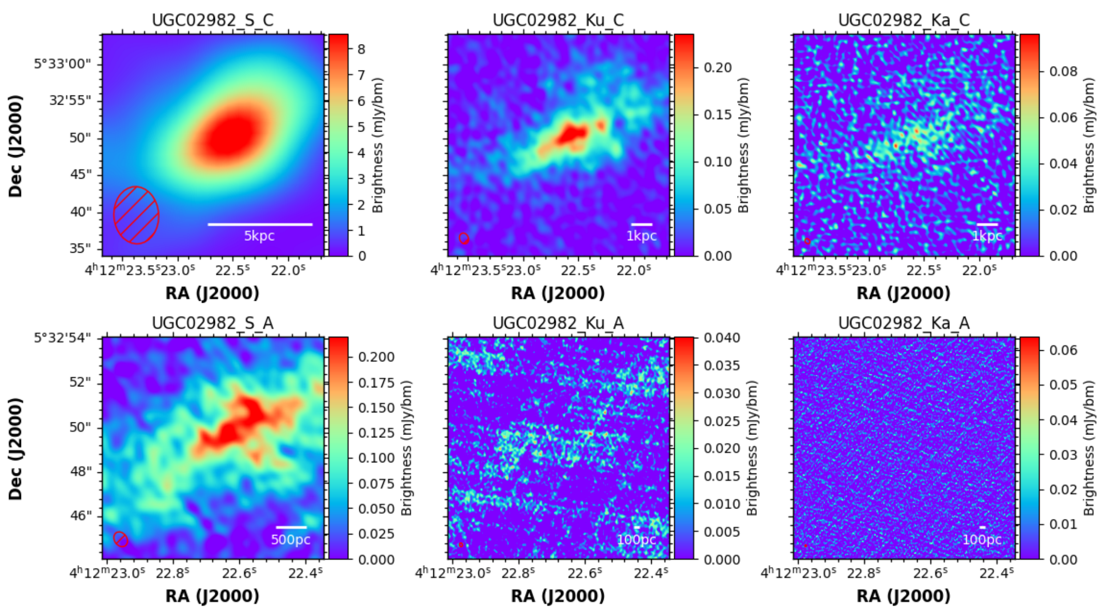

Figure 2.18: UGC 02982

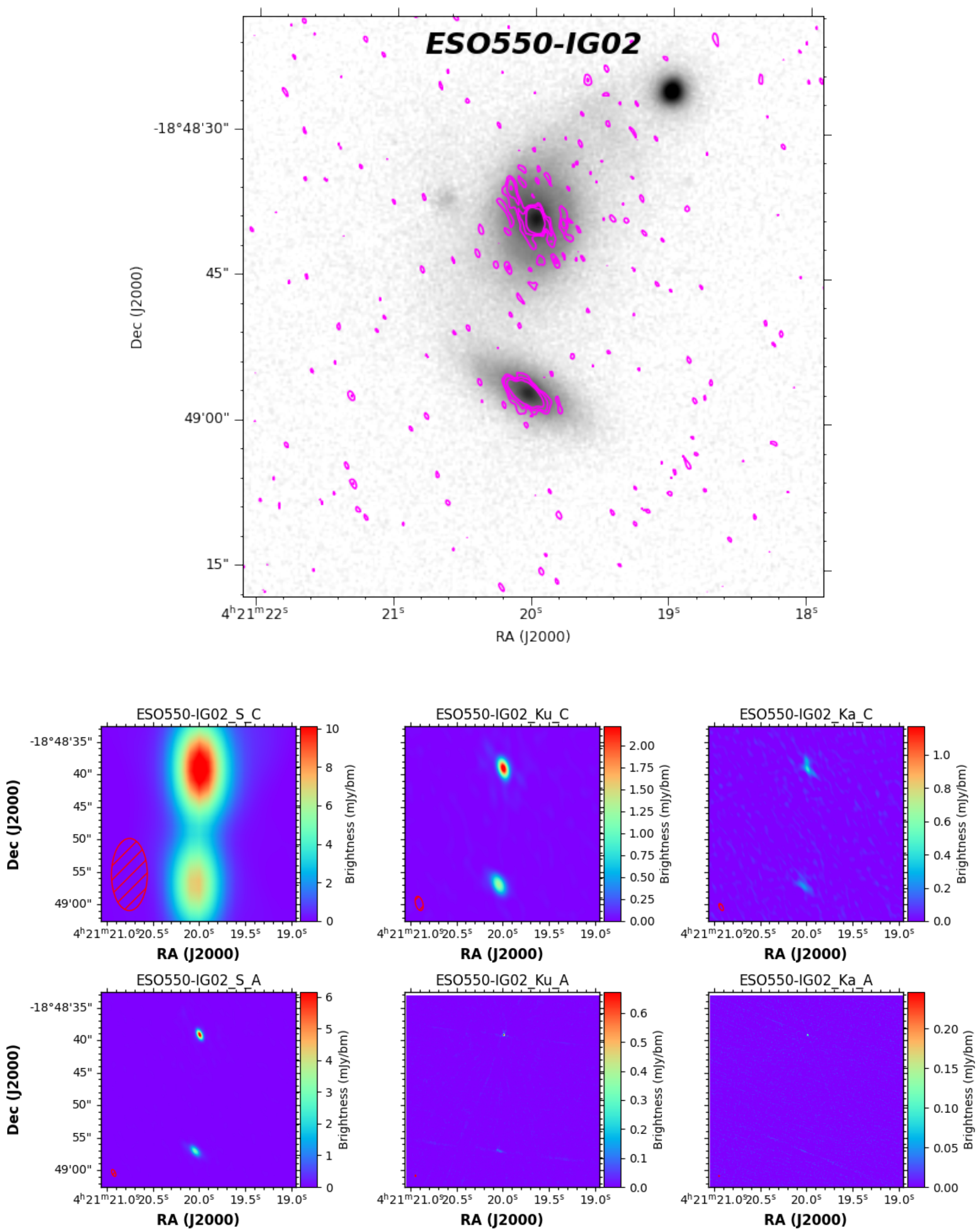

Figure 2.19: ESO 550-IG02

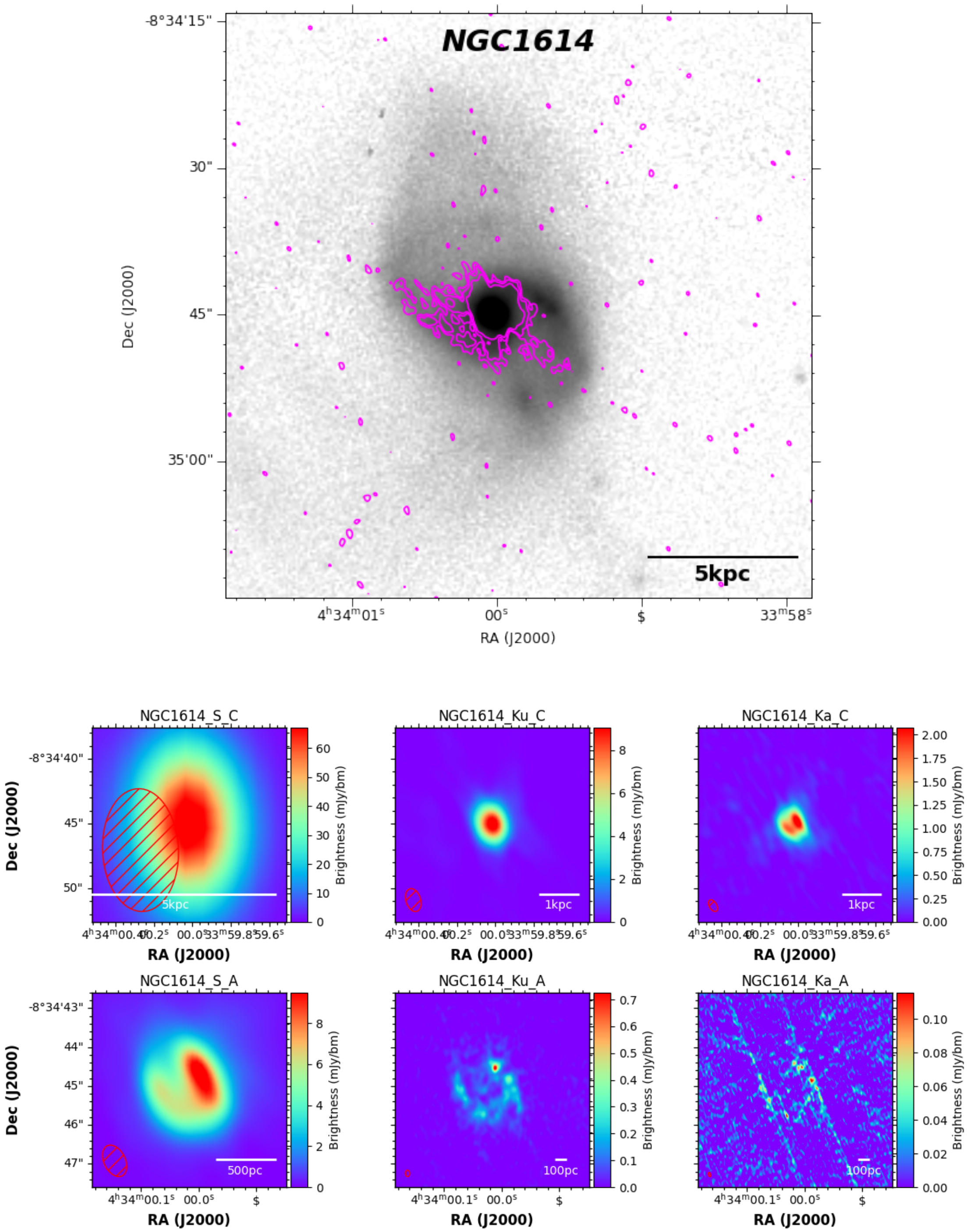

Figure 2.20: NGC 1614

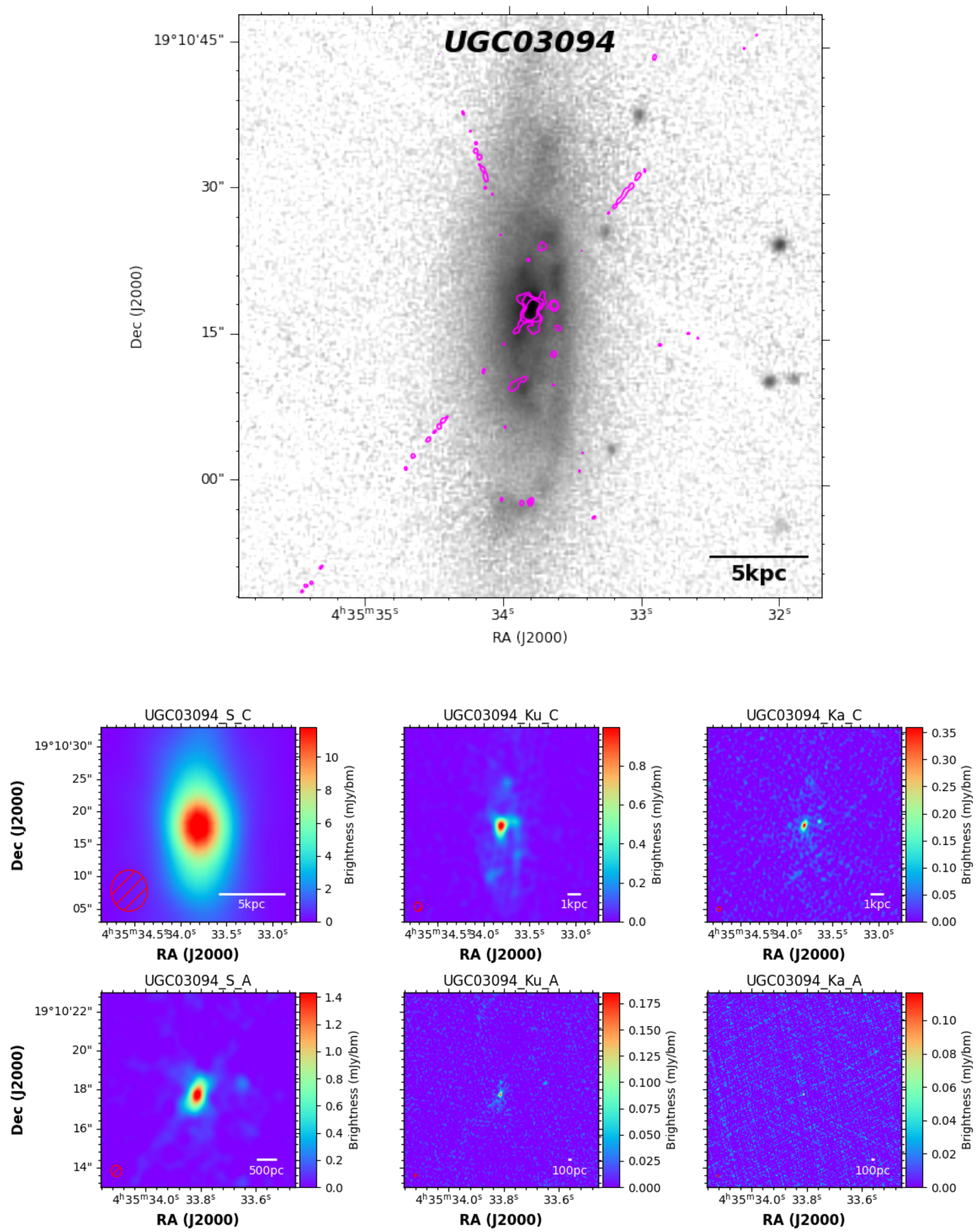

Figure 2.21: UGC 03094

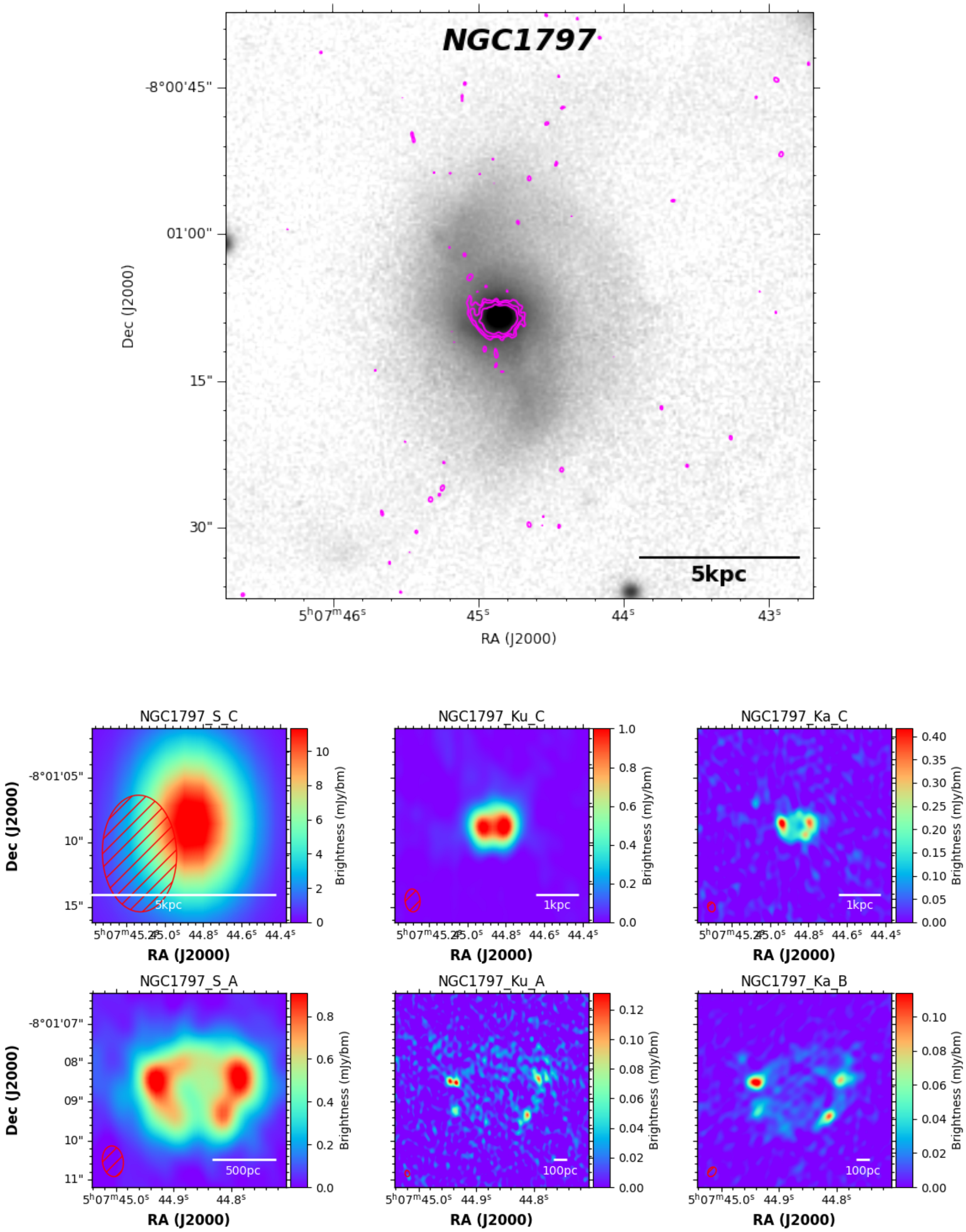

Figure 2.22: NGC 1797

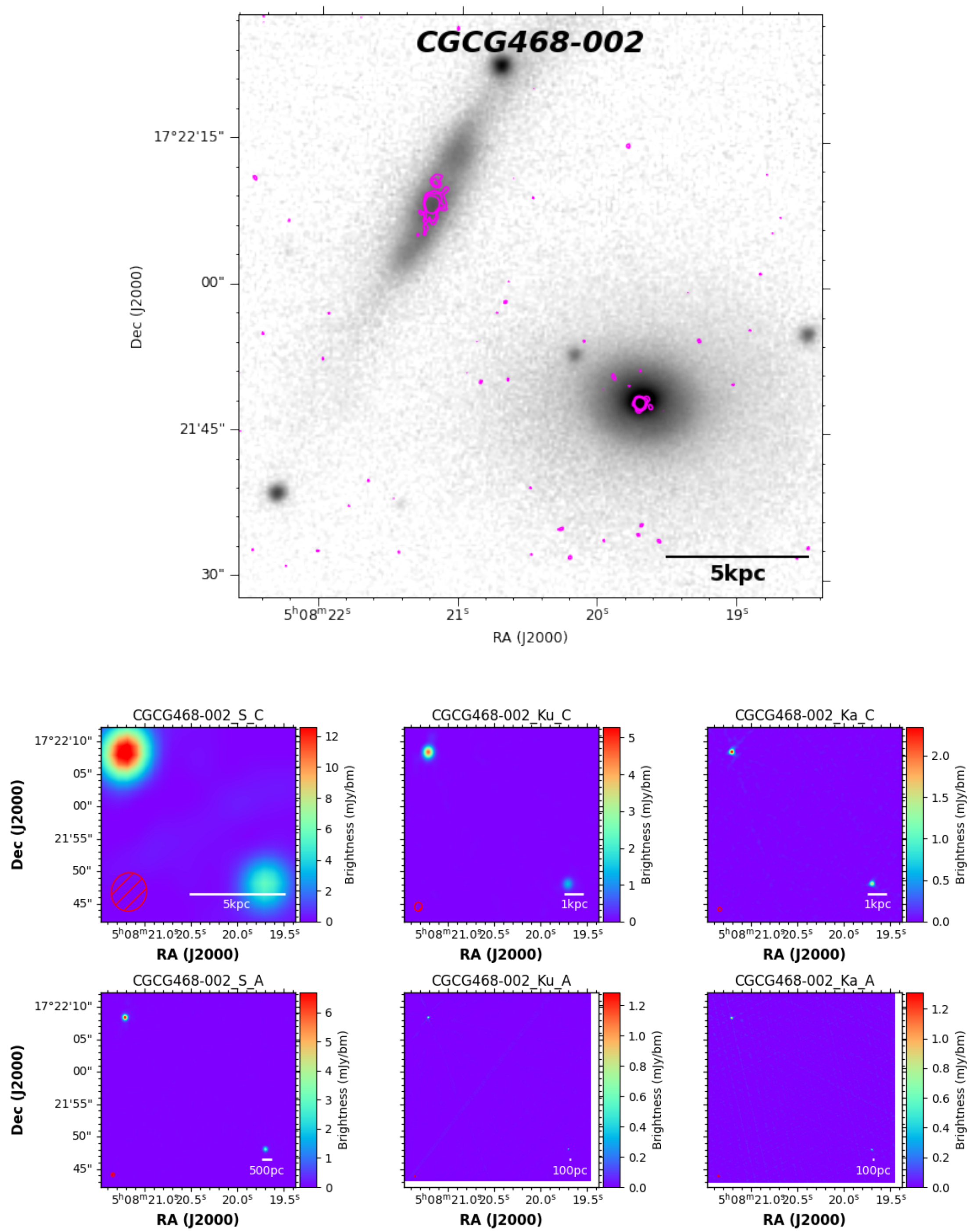

Figure 2.23: CGCG 468-002

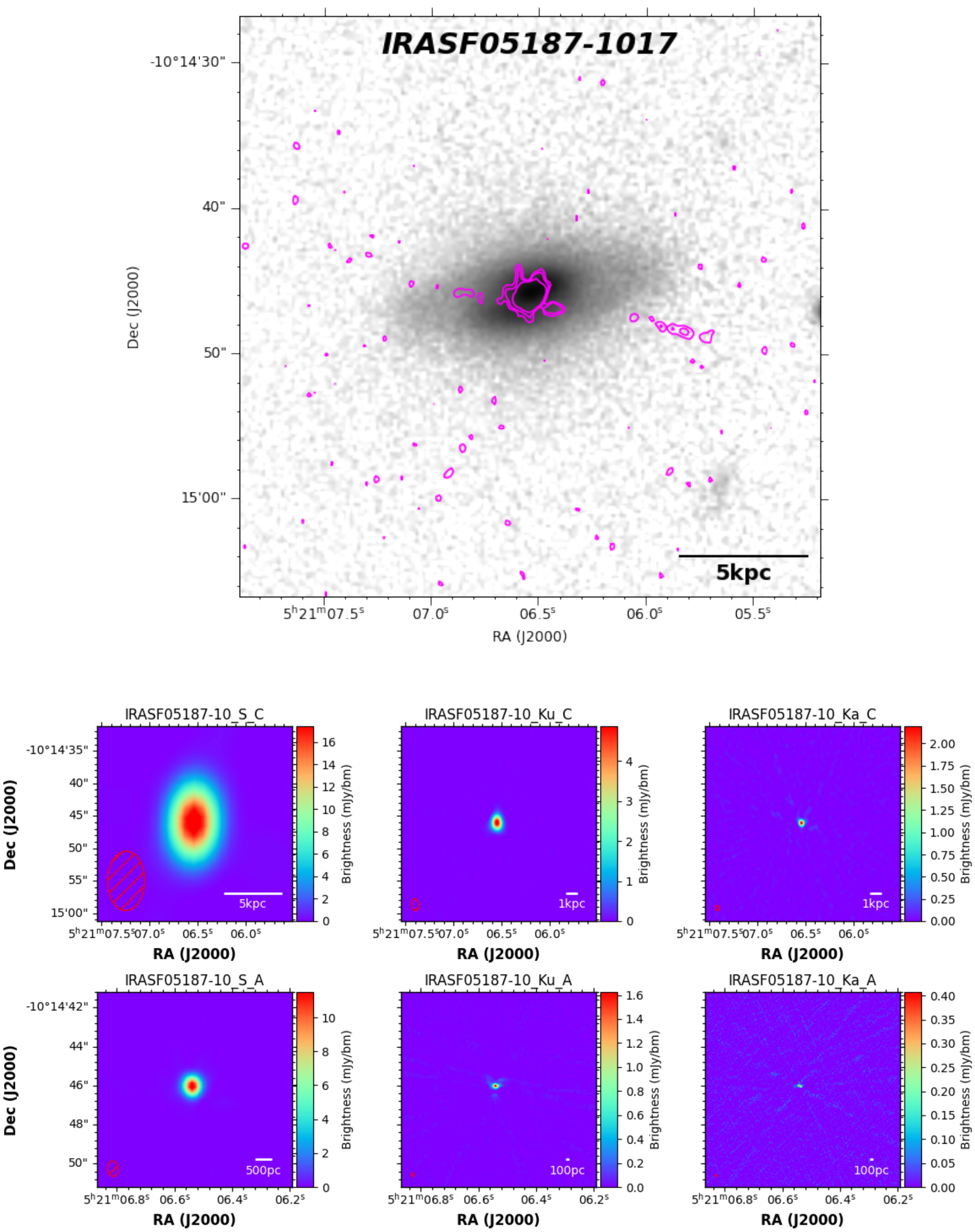

Figure 2.24: IRAS F05187-1017

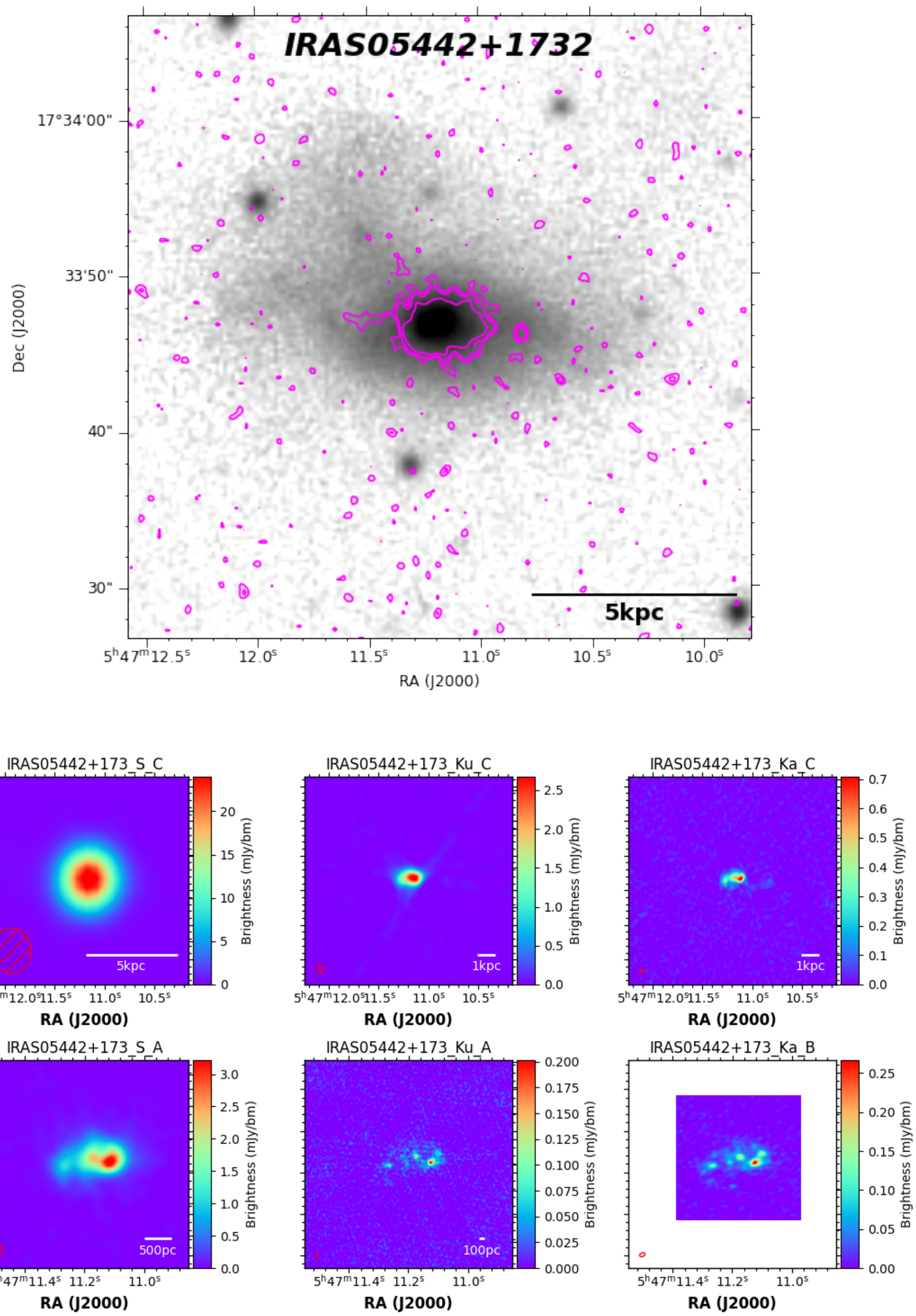

Figure 2.25: IRAS 05442+1732

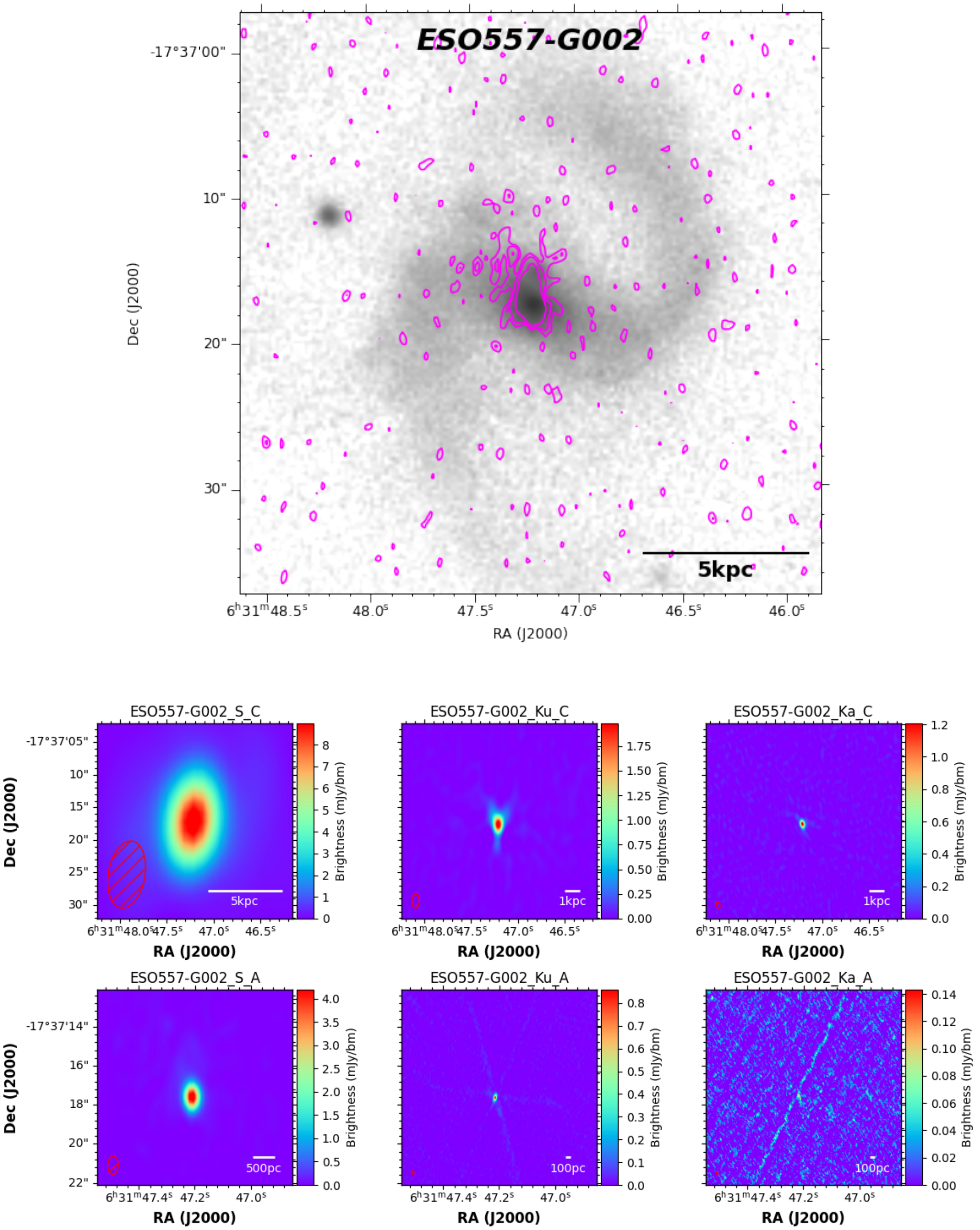

Figure 2.26: ESO 557-G002

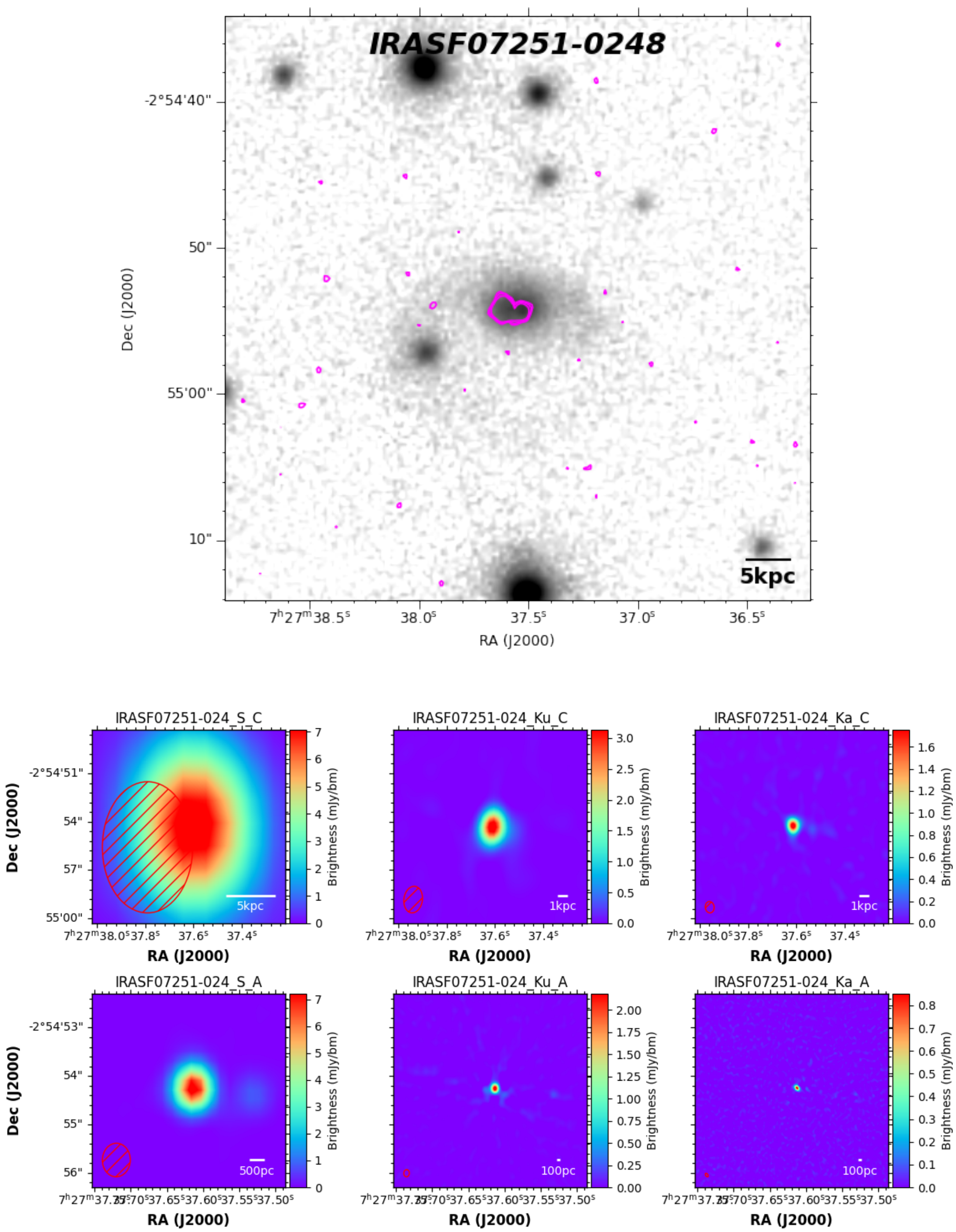

Figure 2.27: IRAS F07251-0248

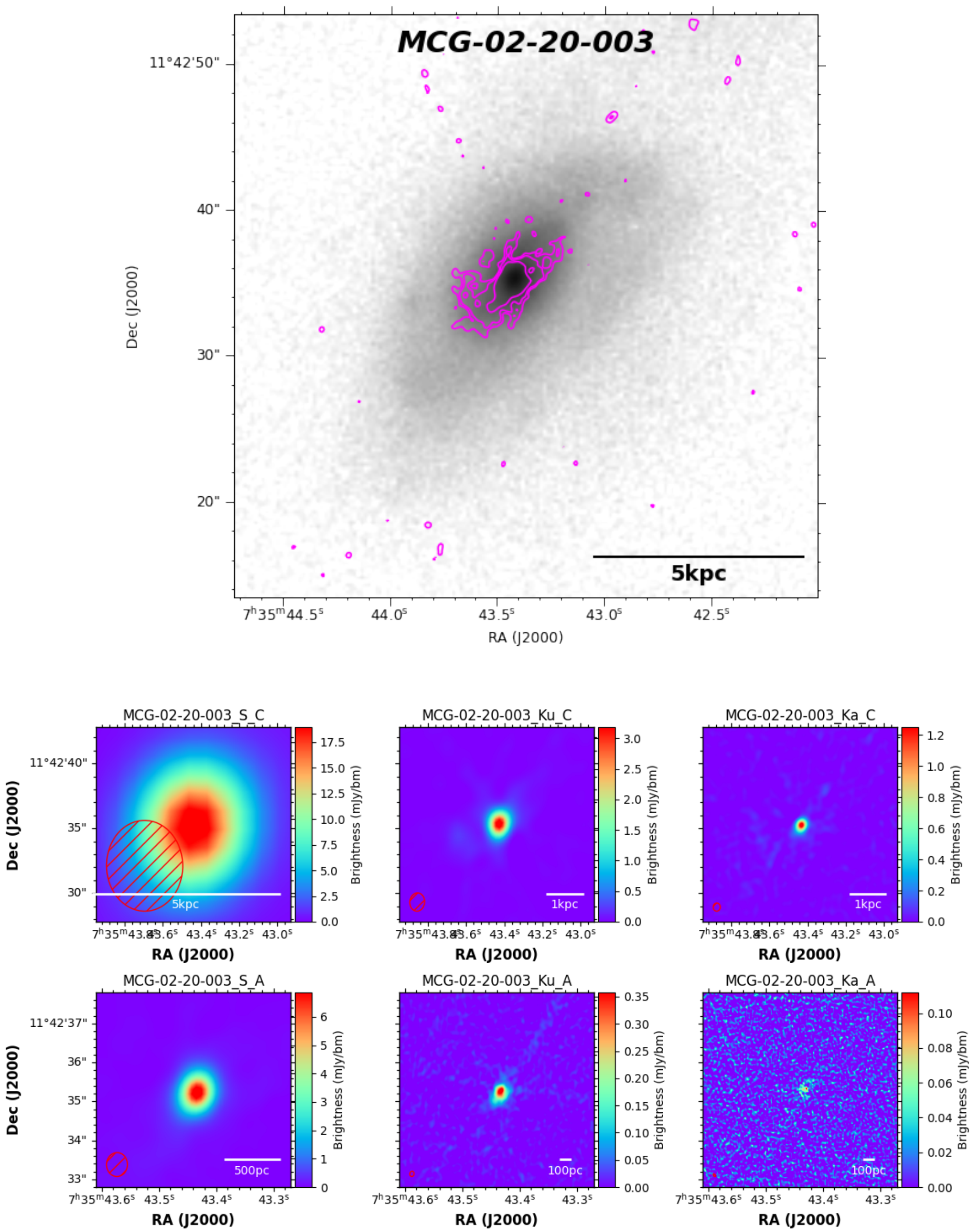

Figure 2.28: MCG-02-20-003

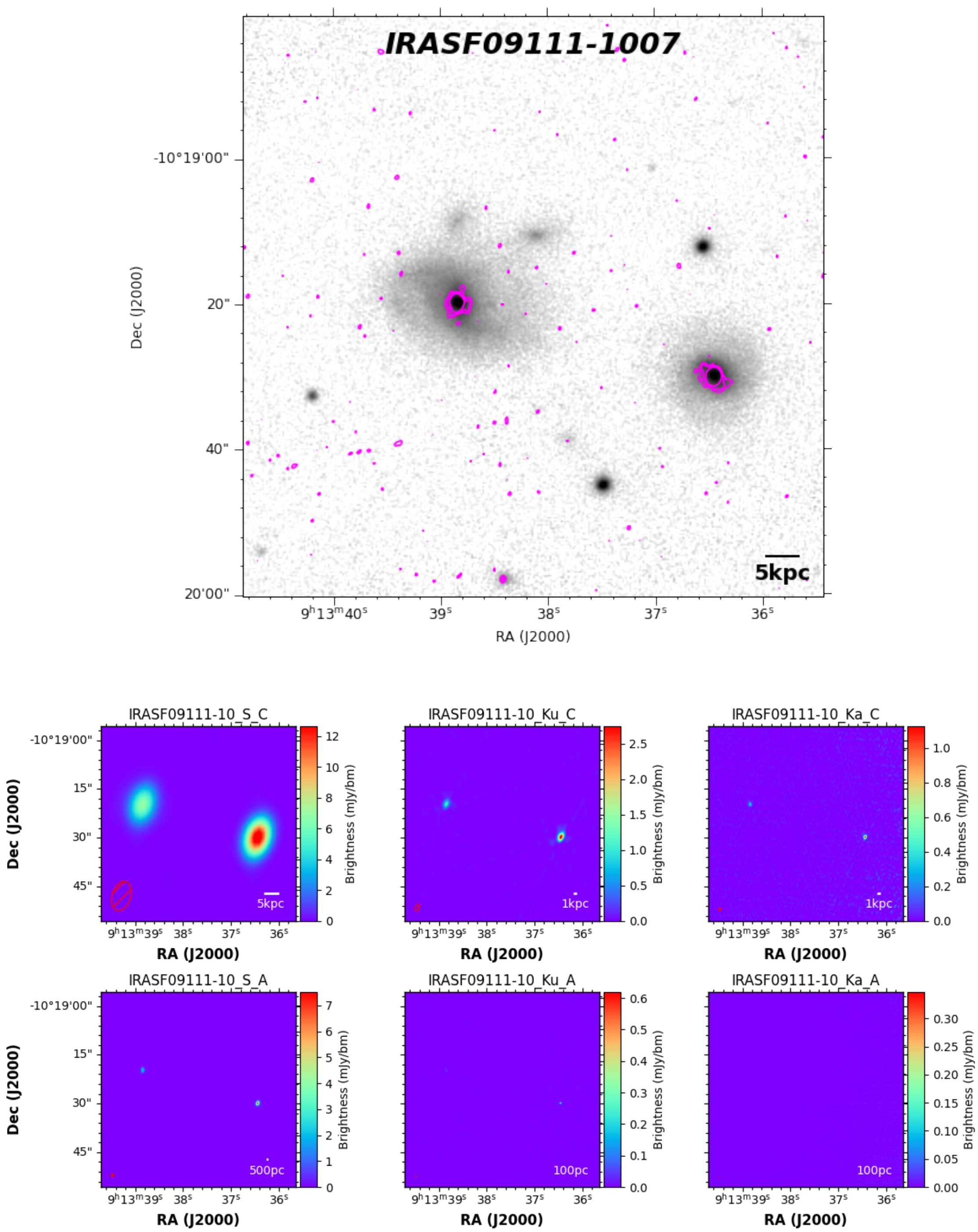

Figure 2.29: IRAS F09111-1007

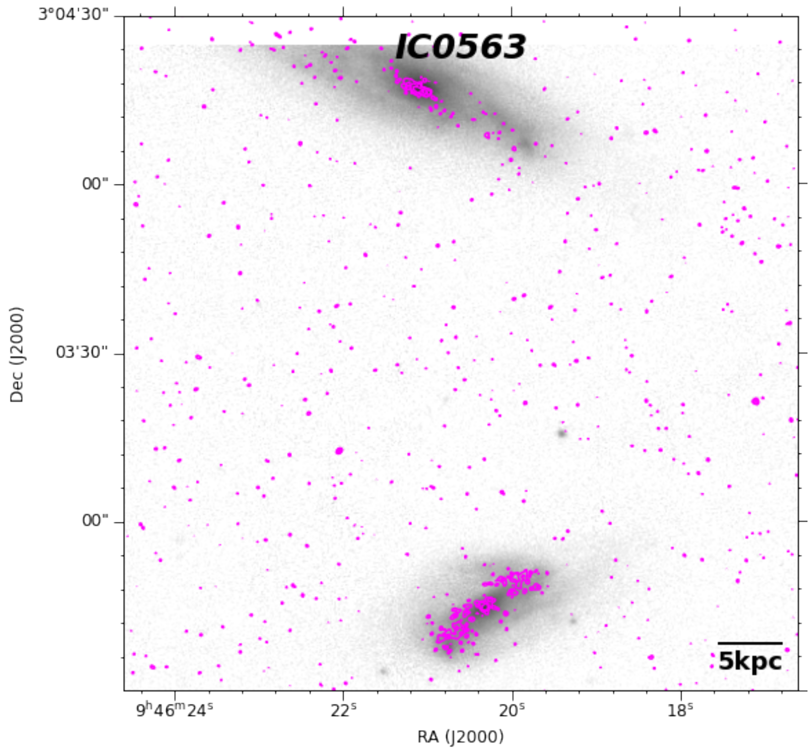

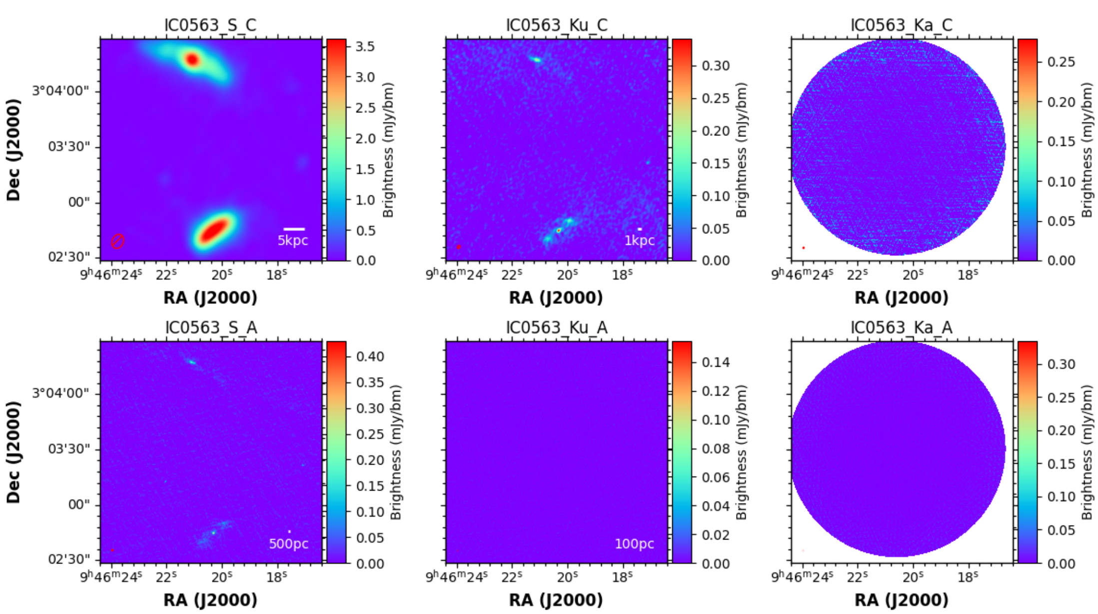

Figure 2.30: IC 0563

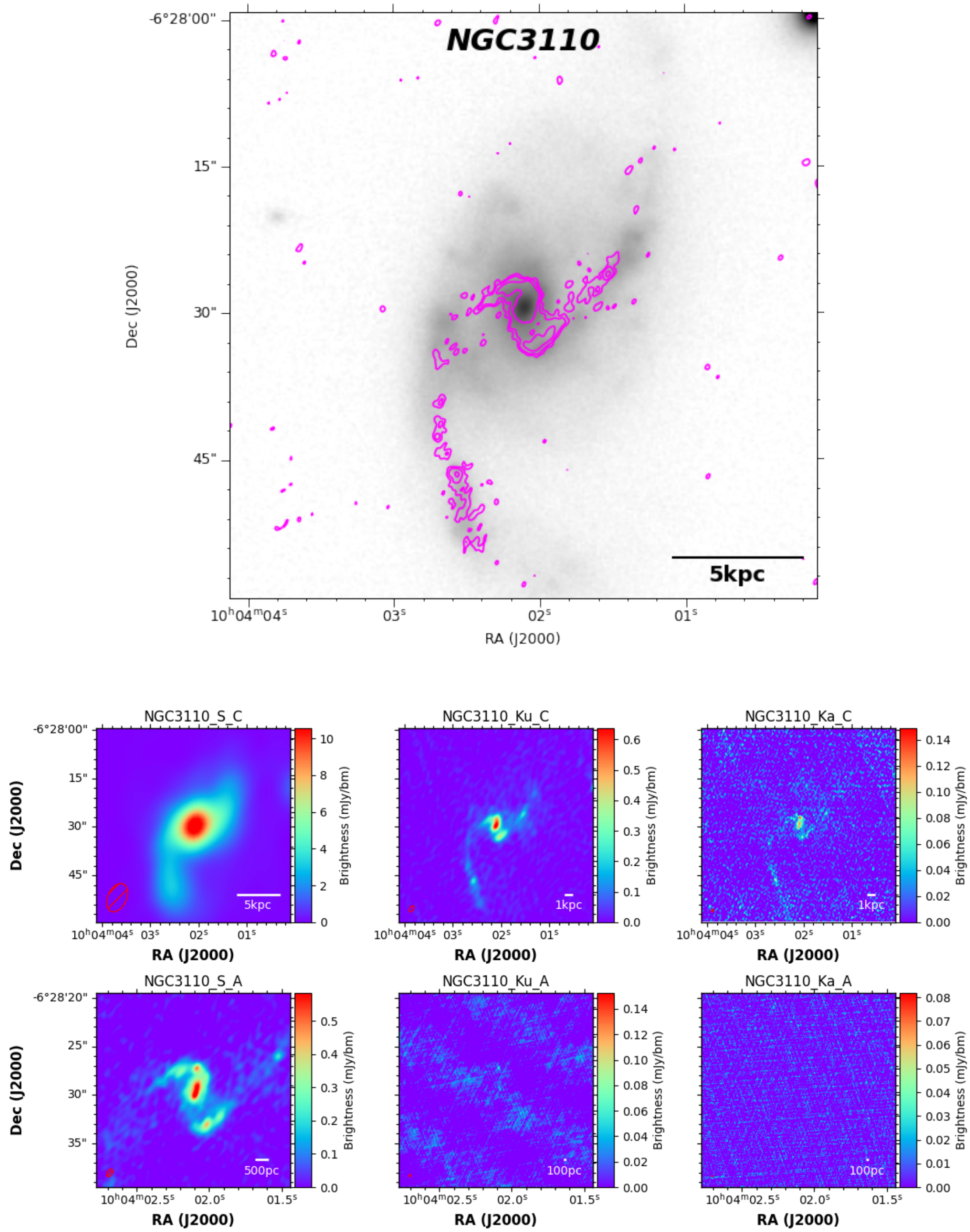
NGC3110
5kpc
-6°28'00"
15"
30"
45"
Dec (J2000)
10h04m04s
03s
02s
01s
RA (J2000)
NGC3110_S_C
NGC3110_Ku_C
NGC3110_Ka_C
NGC3110_S_A
NGC3110_Ku_A
NGC3110_Ka_A
Brightness (mJy/bm)
5kpc
1kpc
500pc
100pc
-6°28'20"
25"
35"
10h04m02.5s
02.0s
01.5s

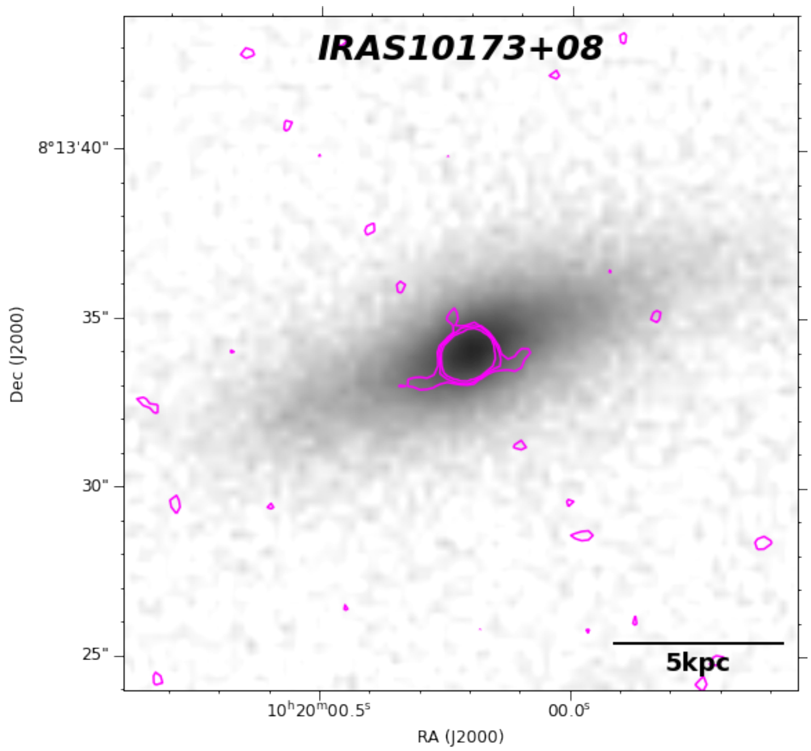

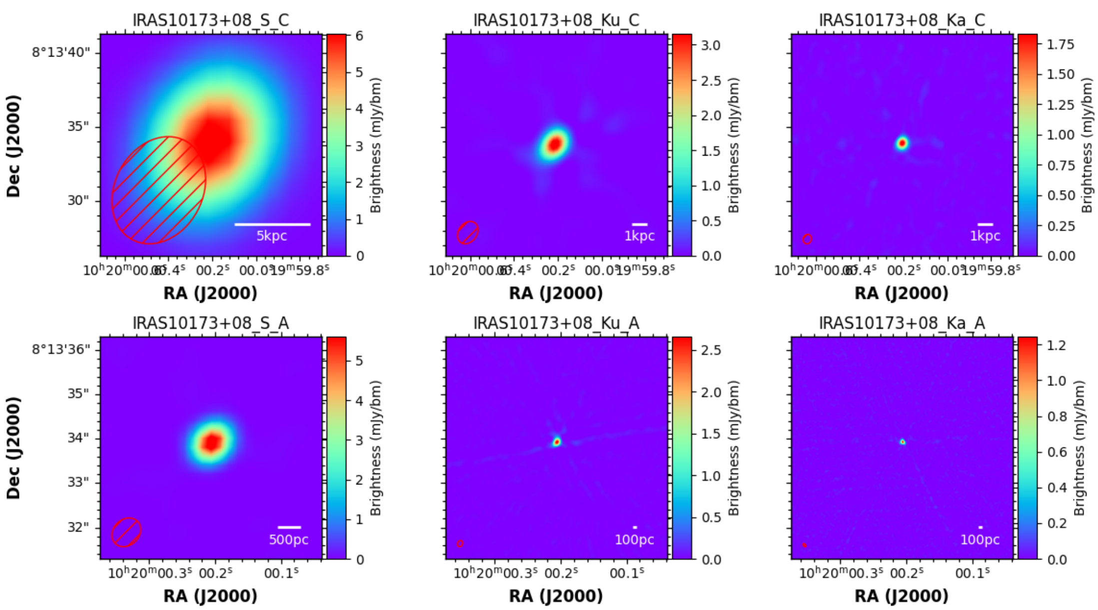

Figure 2.31: IRAS 10173+0828

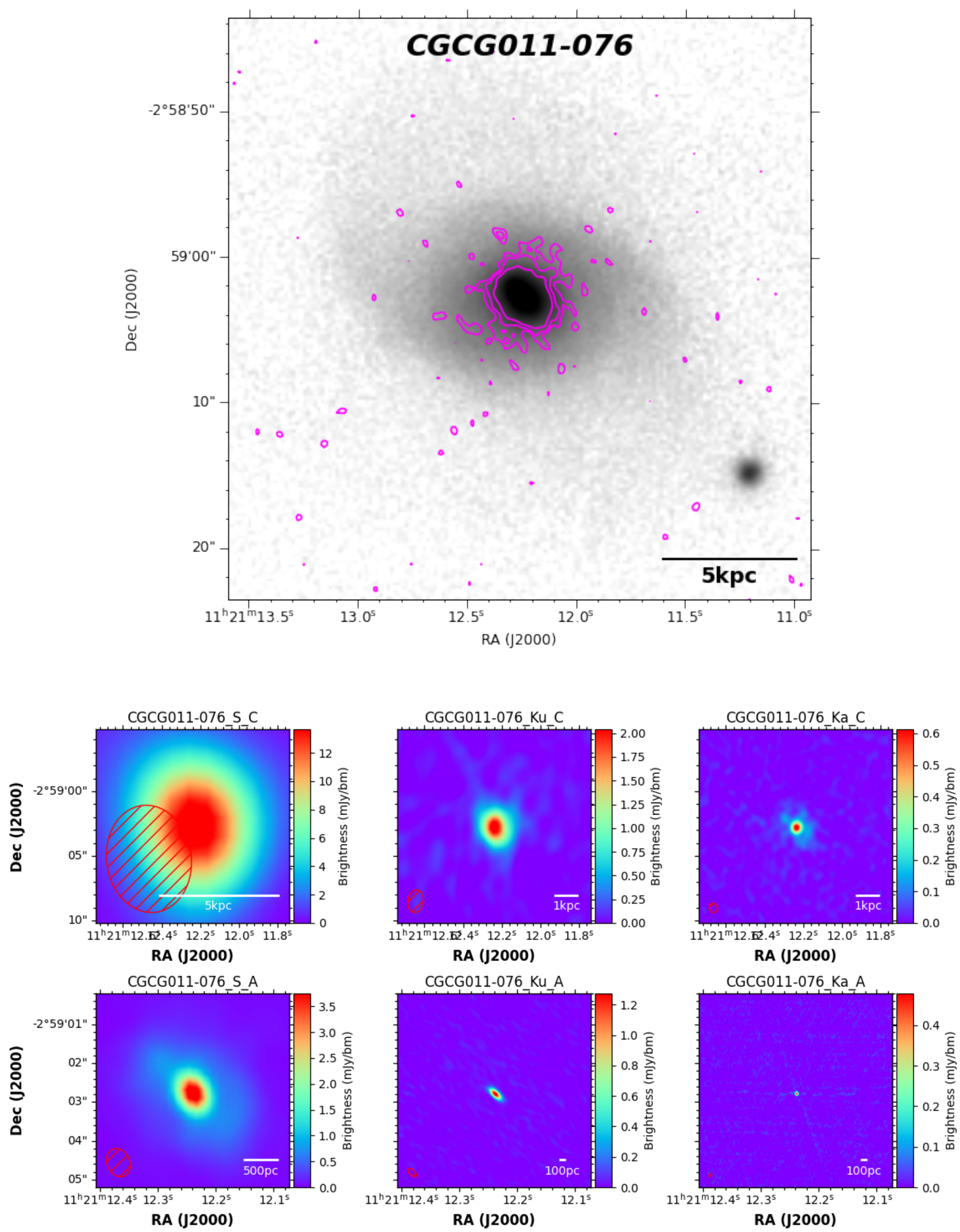

Figure 2.32: CGCG 011-076

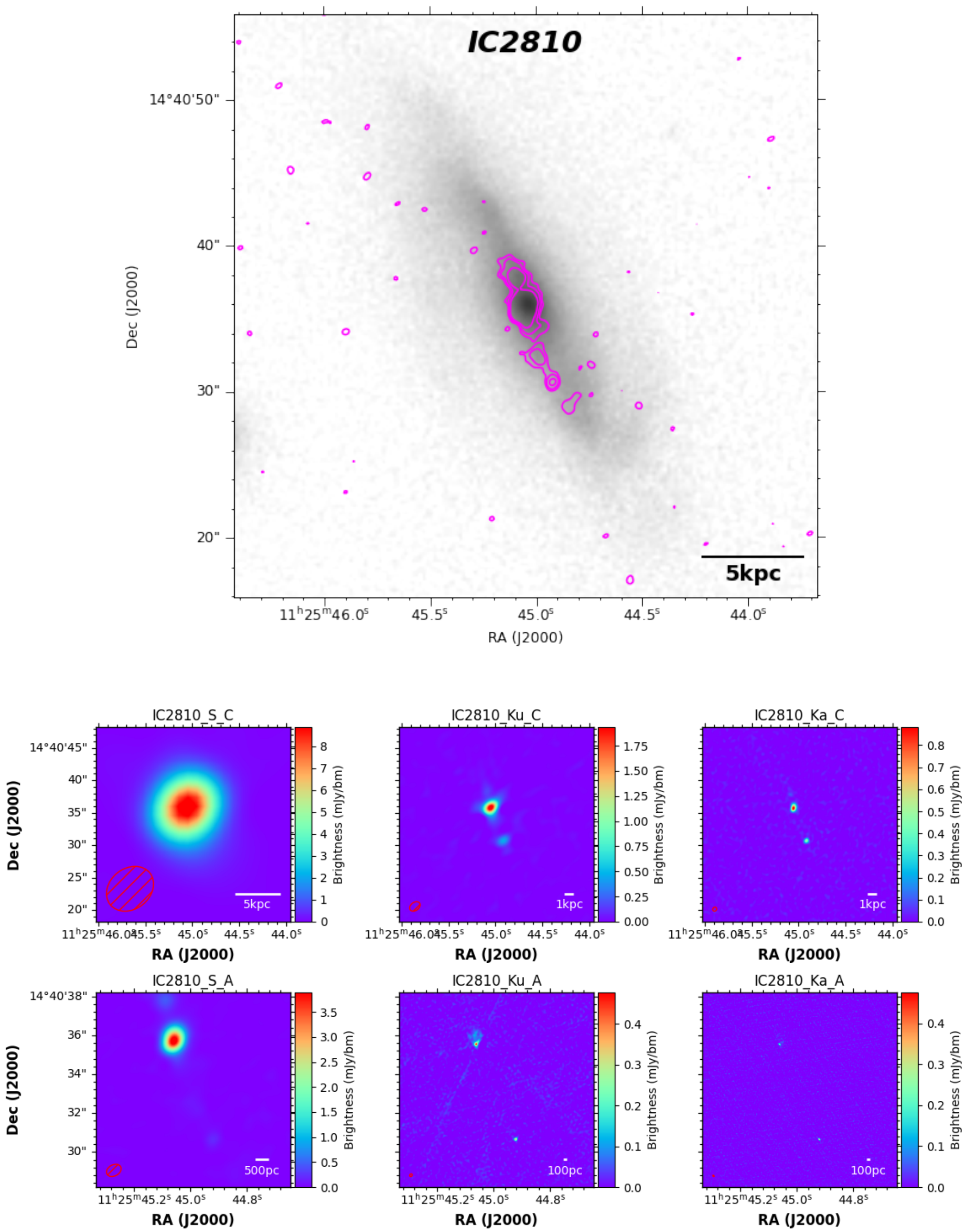

Figure 2.33: IC 2810

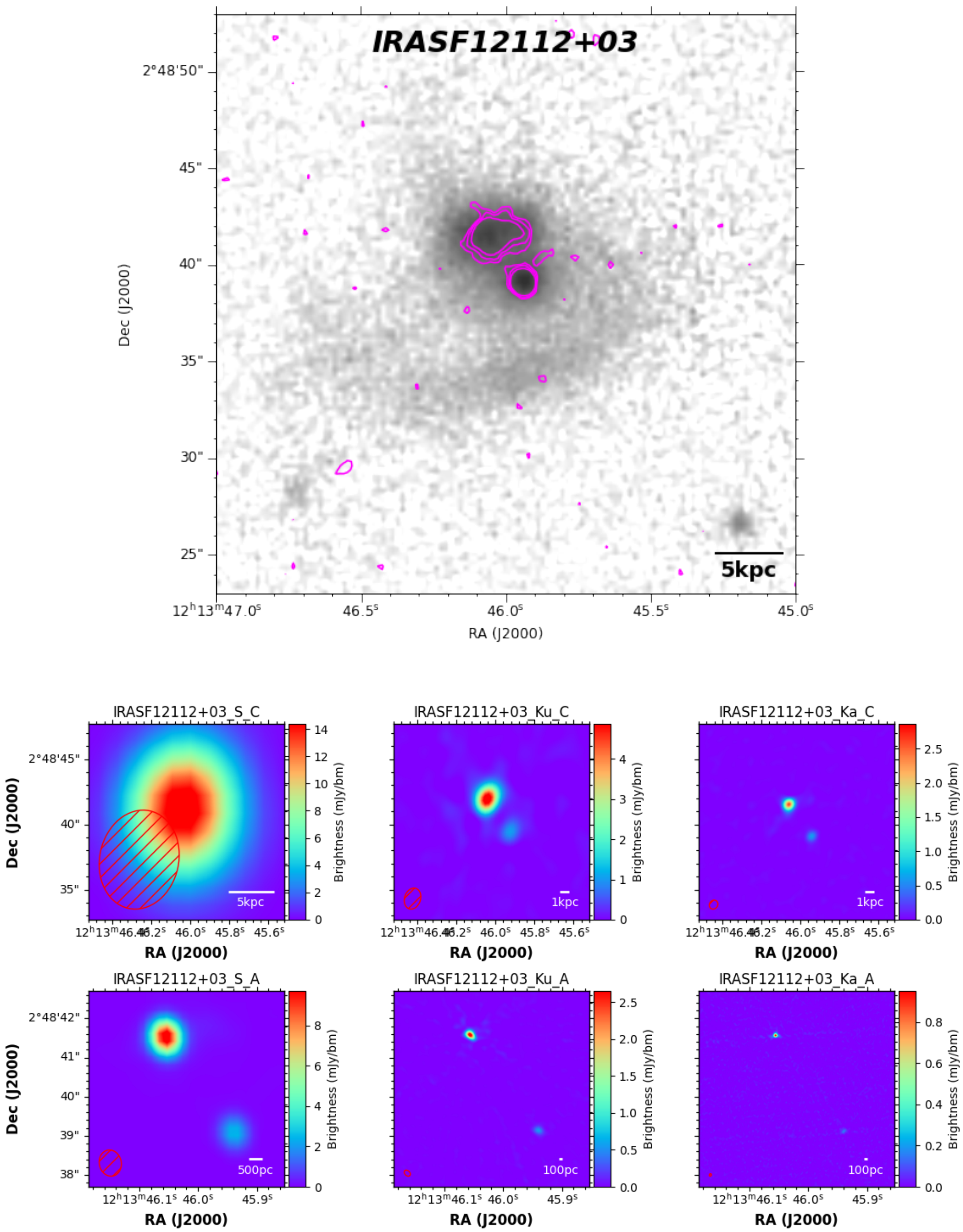

Figure 2.34: IRAS F12112+0305

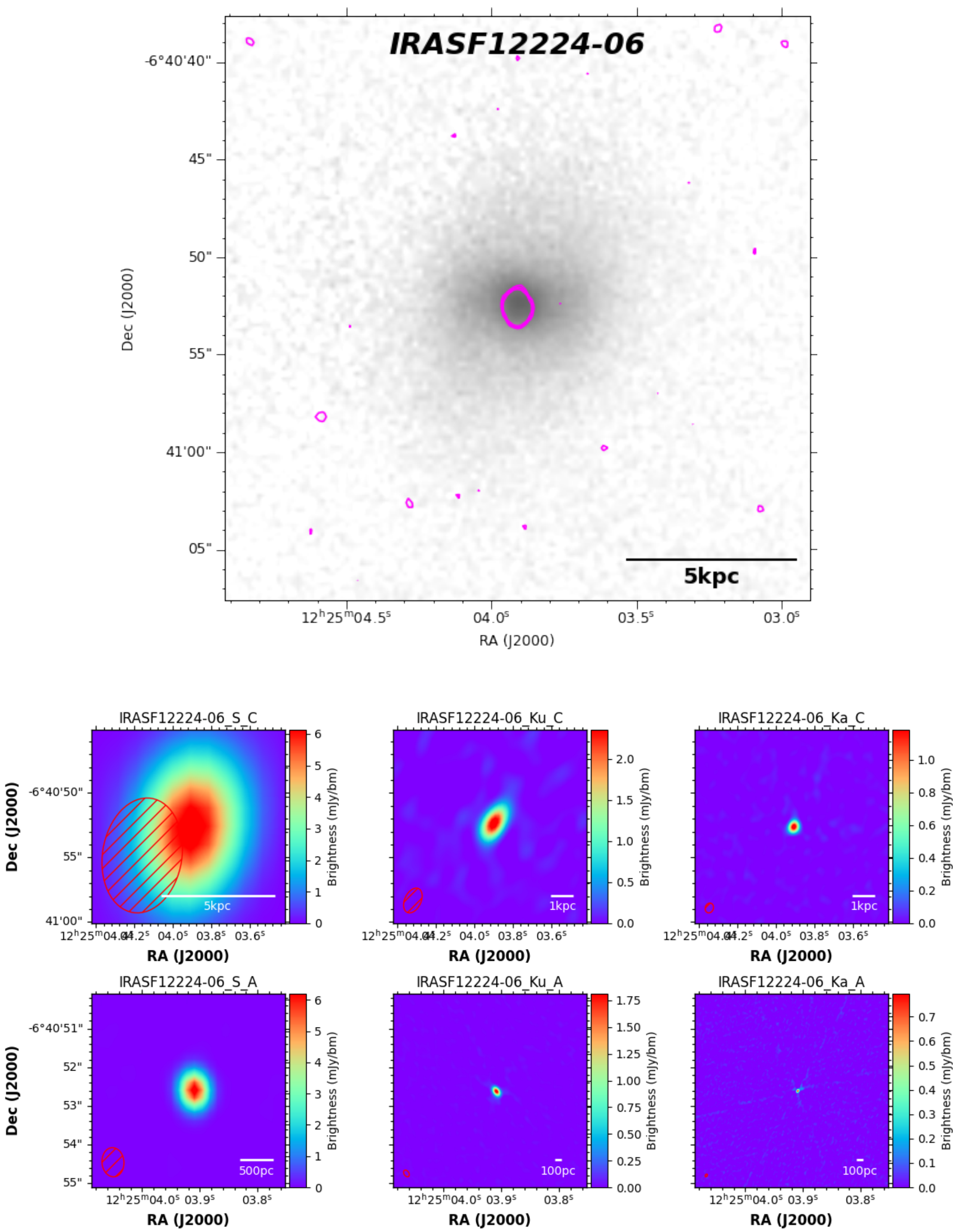

Figure 2.35: IRAS F12224-0624

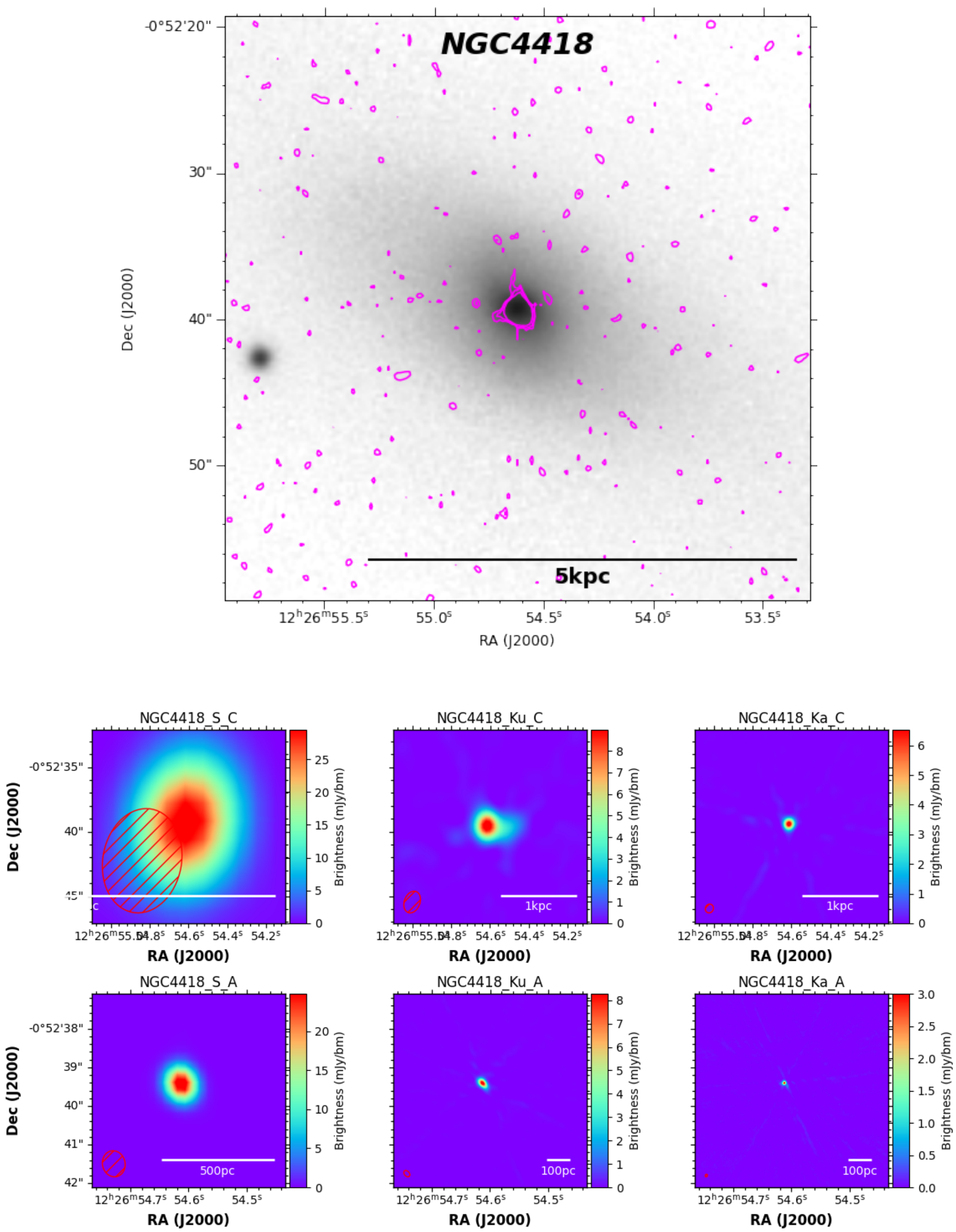

Figure 2.36: NGC 4418

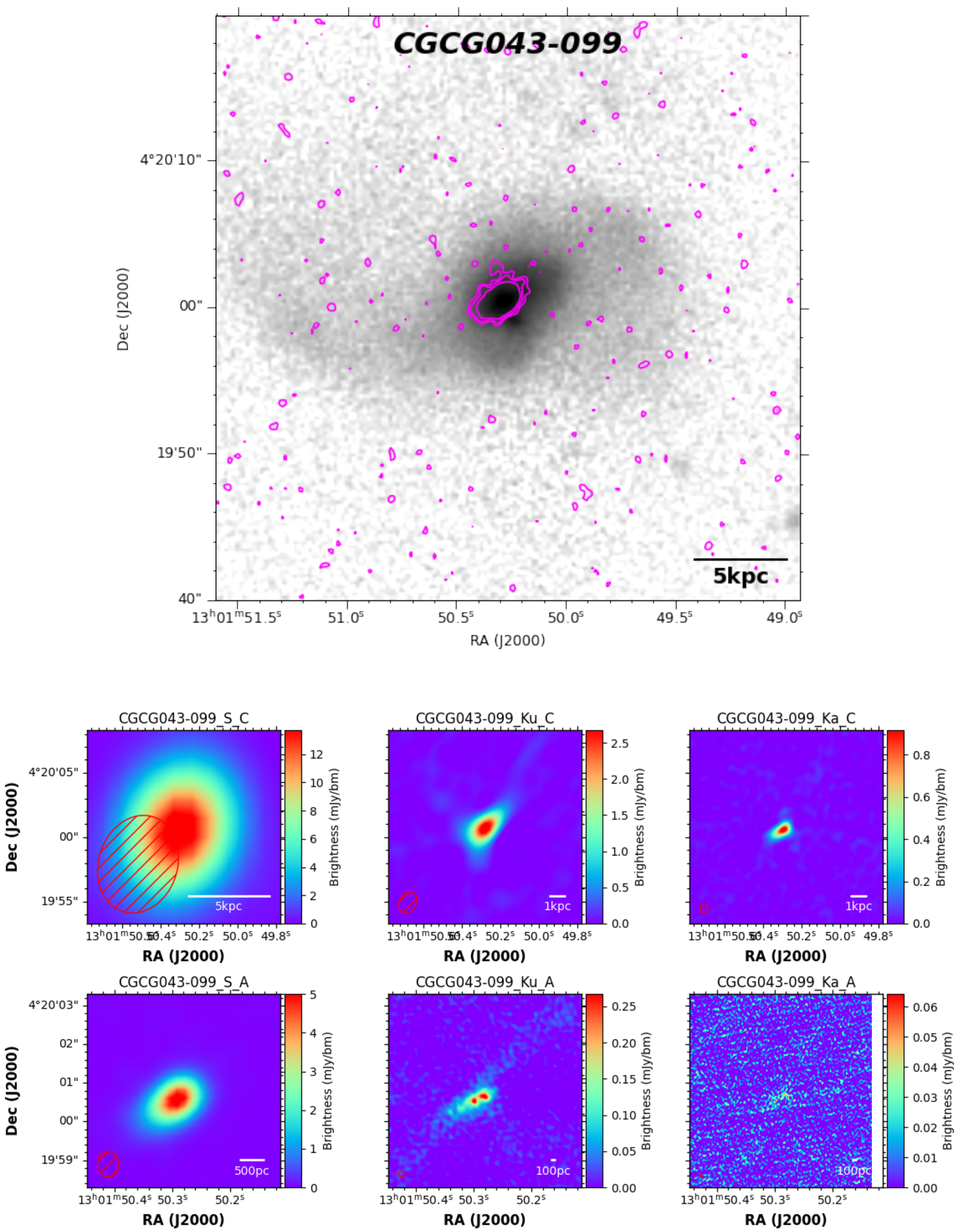

Figure 2.37: CGCG 043-099

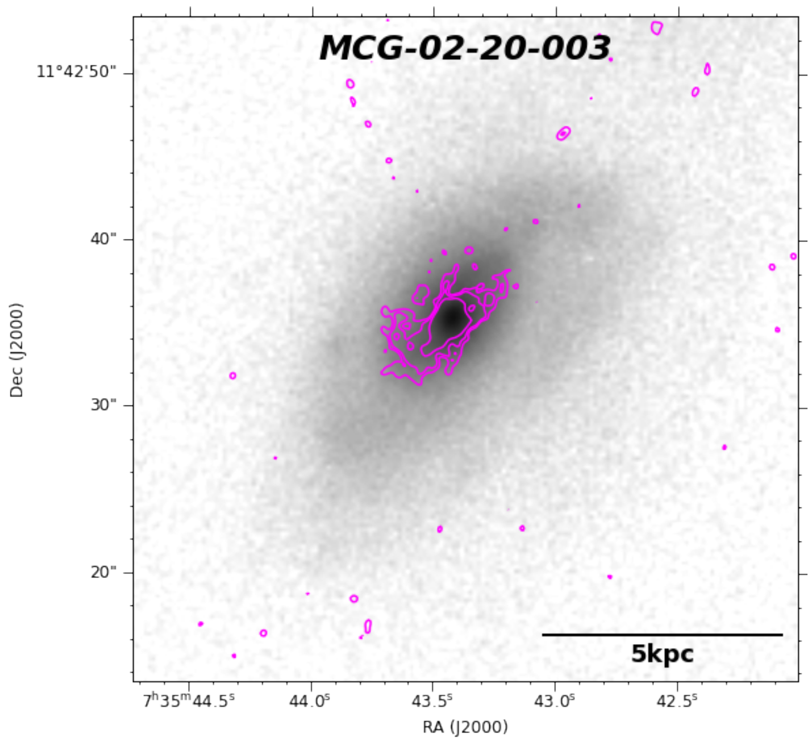

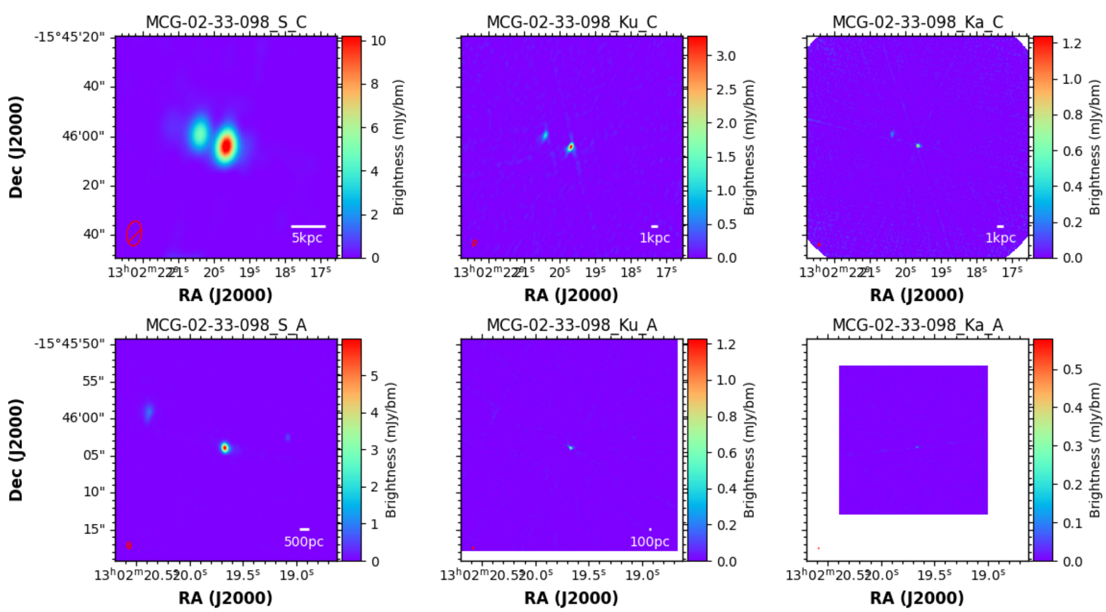

Figure 2.38: MCG -02-33-098

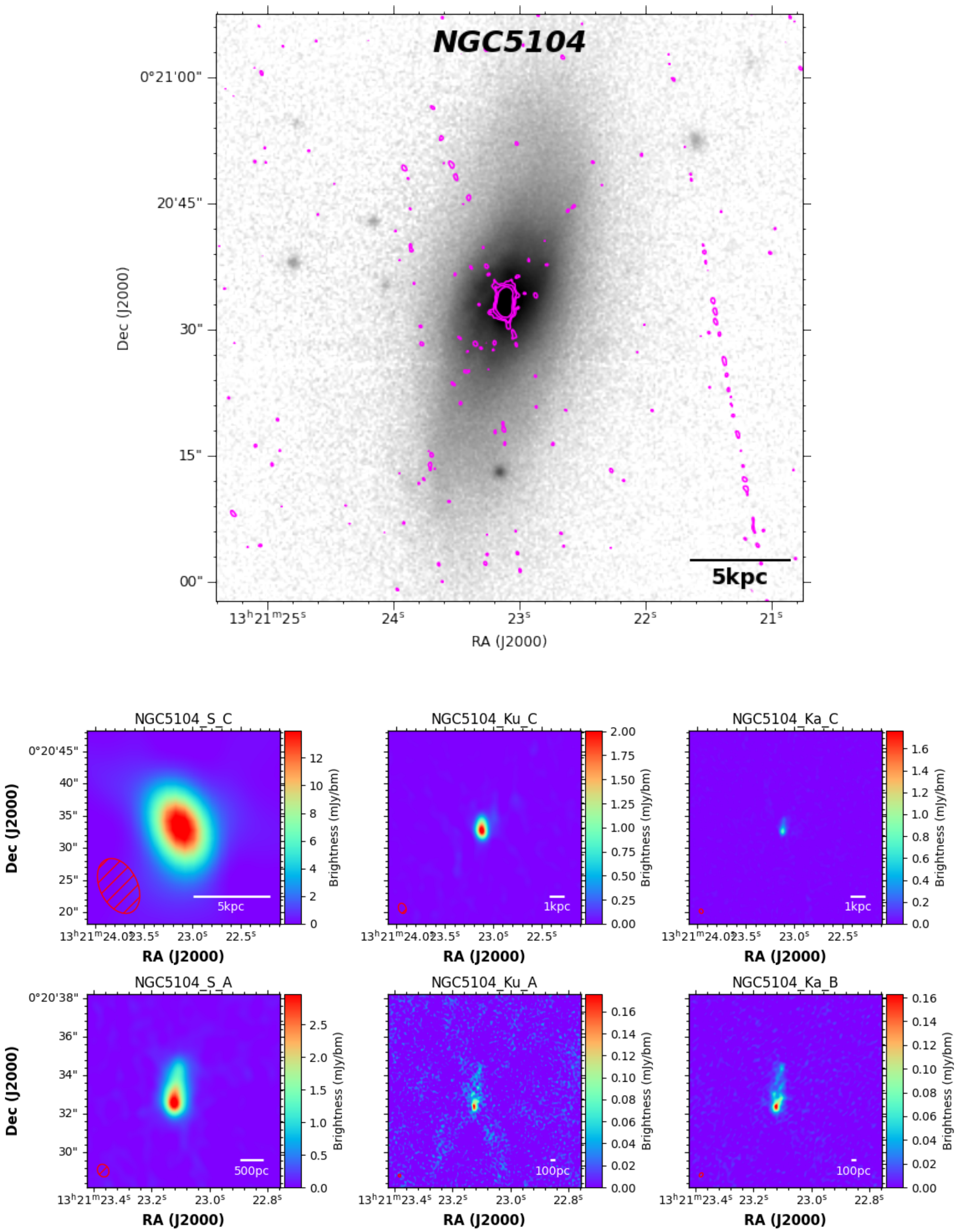

Figure 2.39: NGC 5104

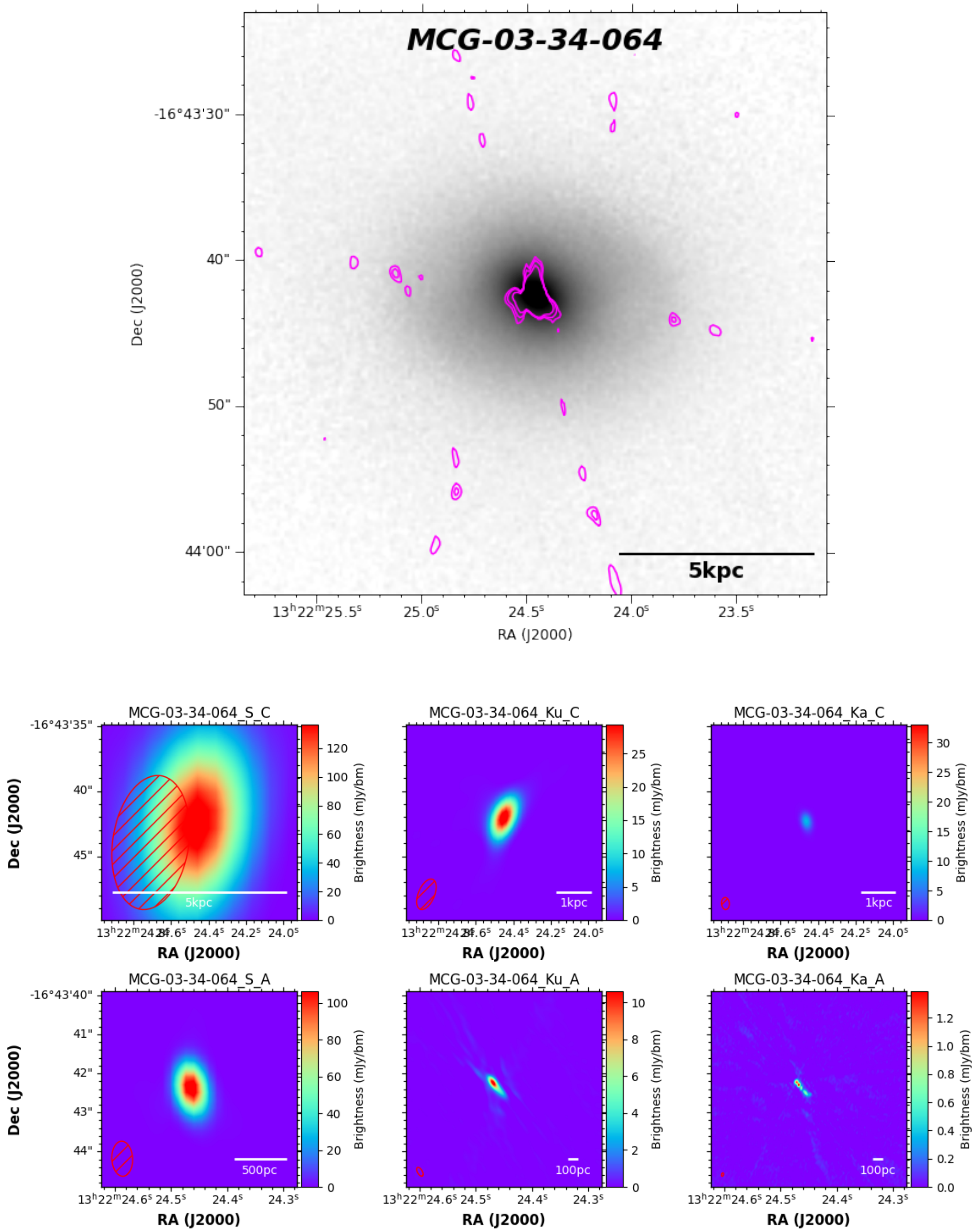

Figure 2.40: MCG-03-34-064

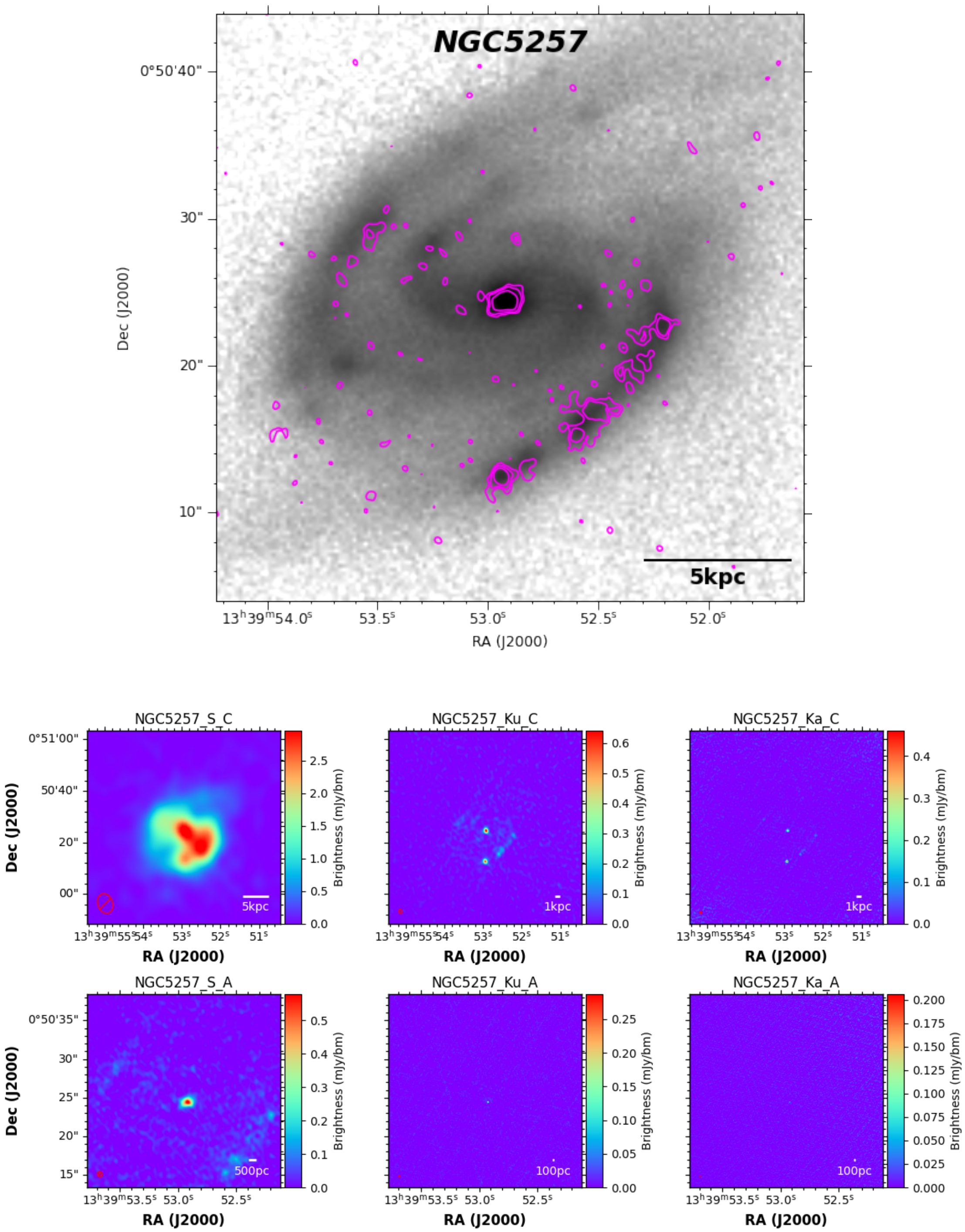

Figure 2.41: NGC 5257

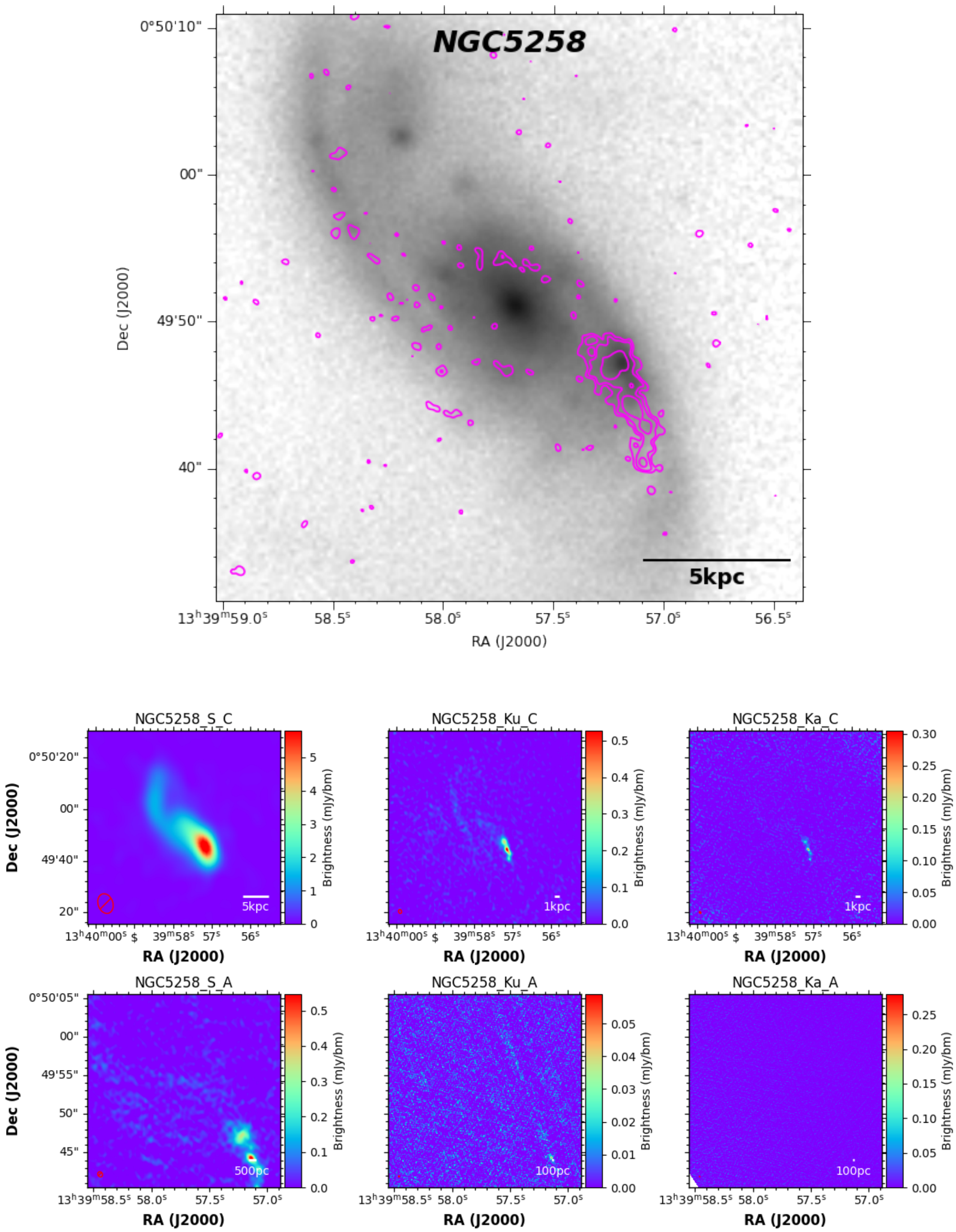

Figure 2.42: NGC 5258

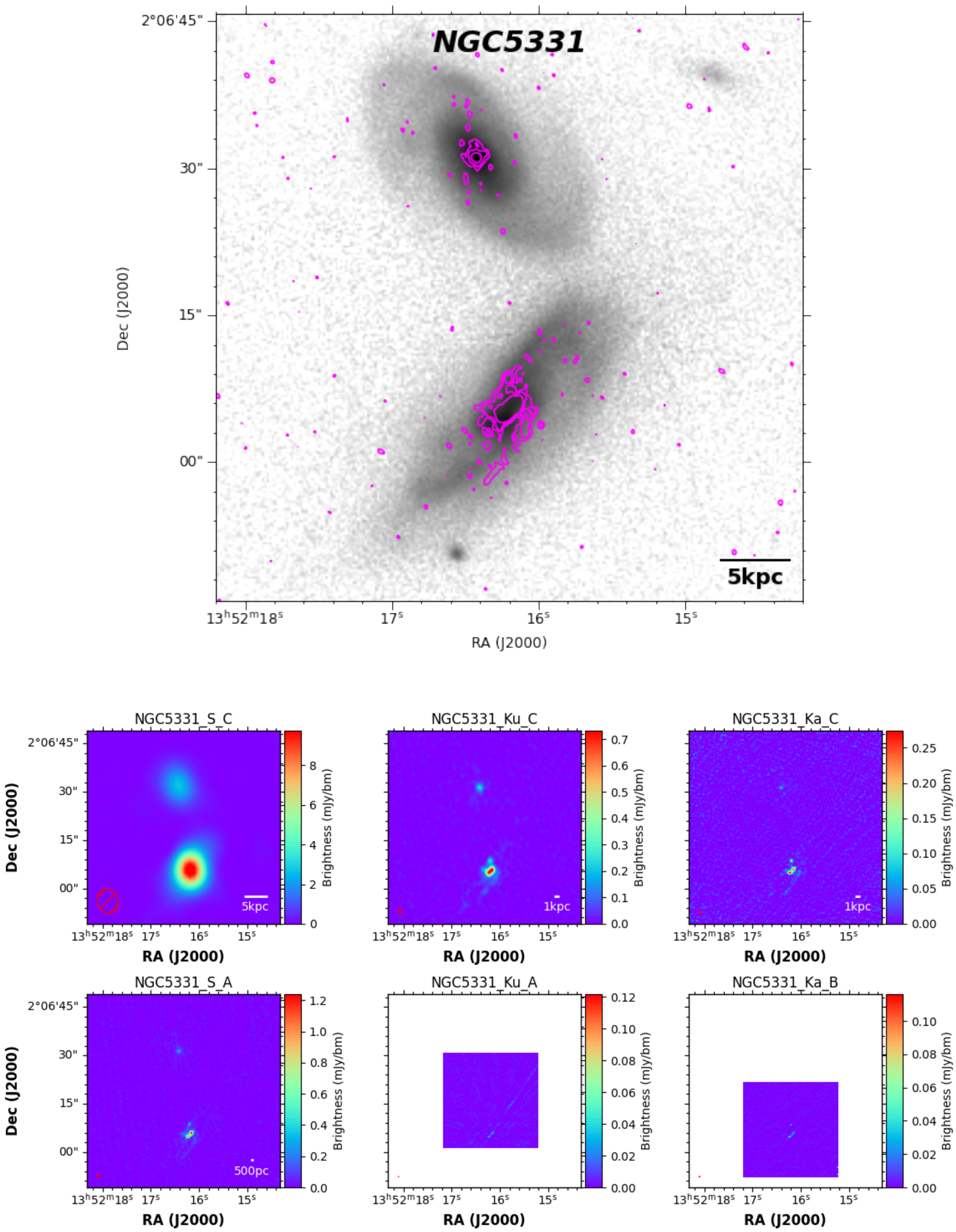

Figure 2.43: NGC 5331

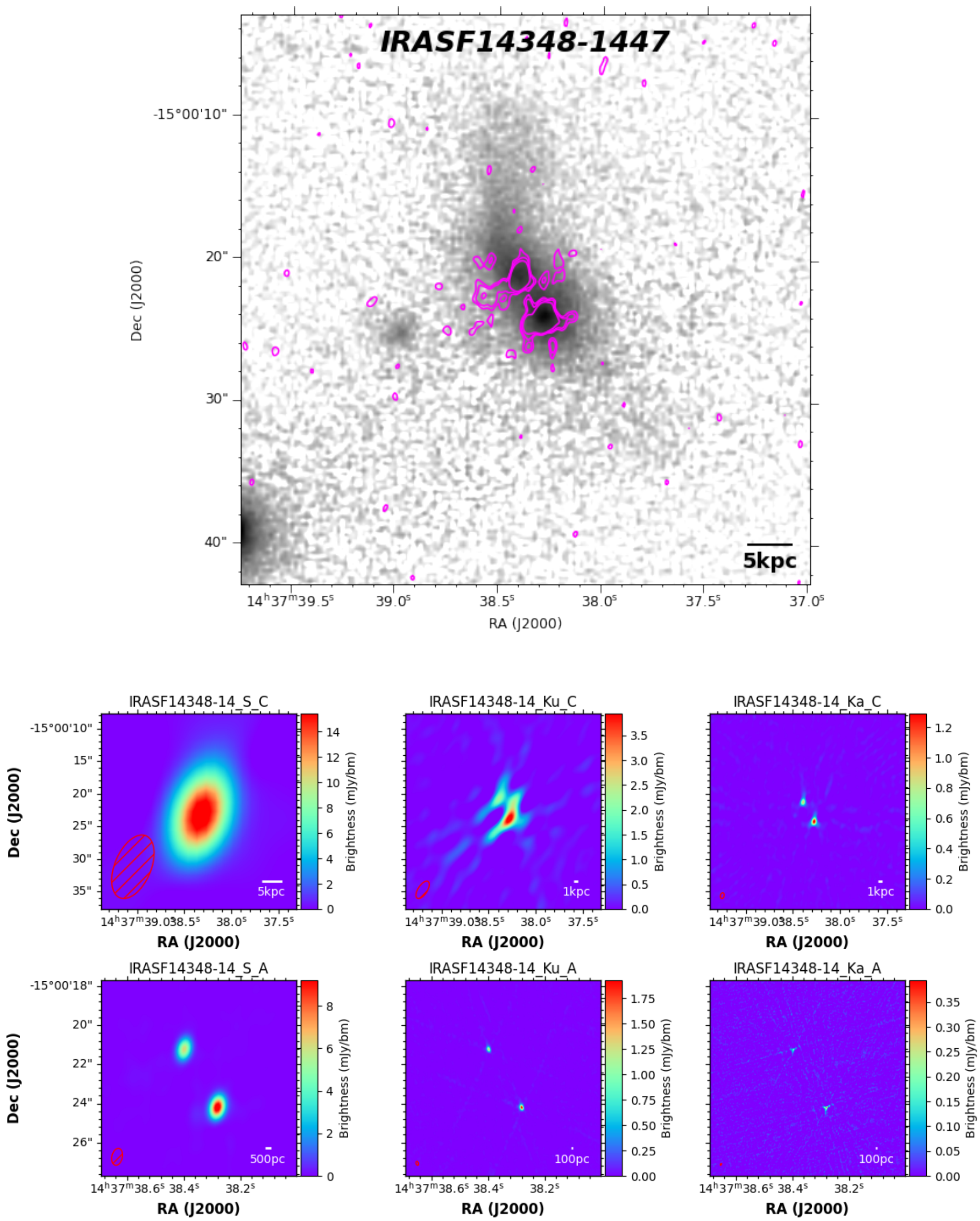

Figure 2.44: IRAS F14348-1447

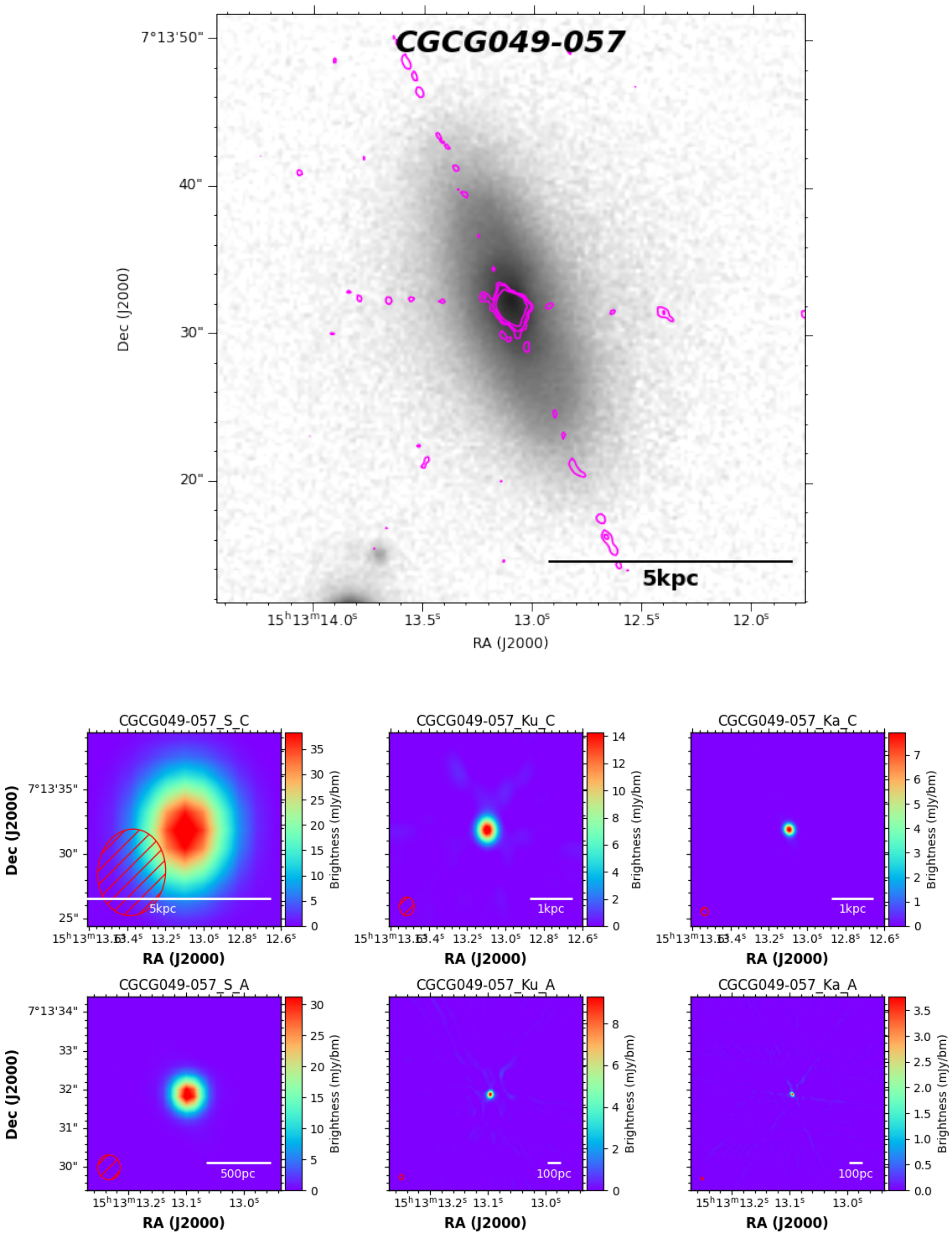

Figure 2.45: CGCG 049-057

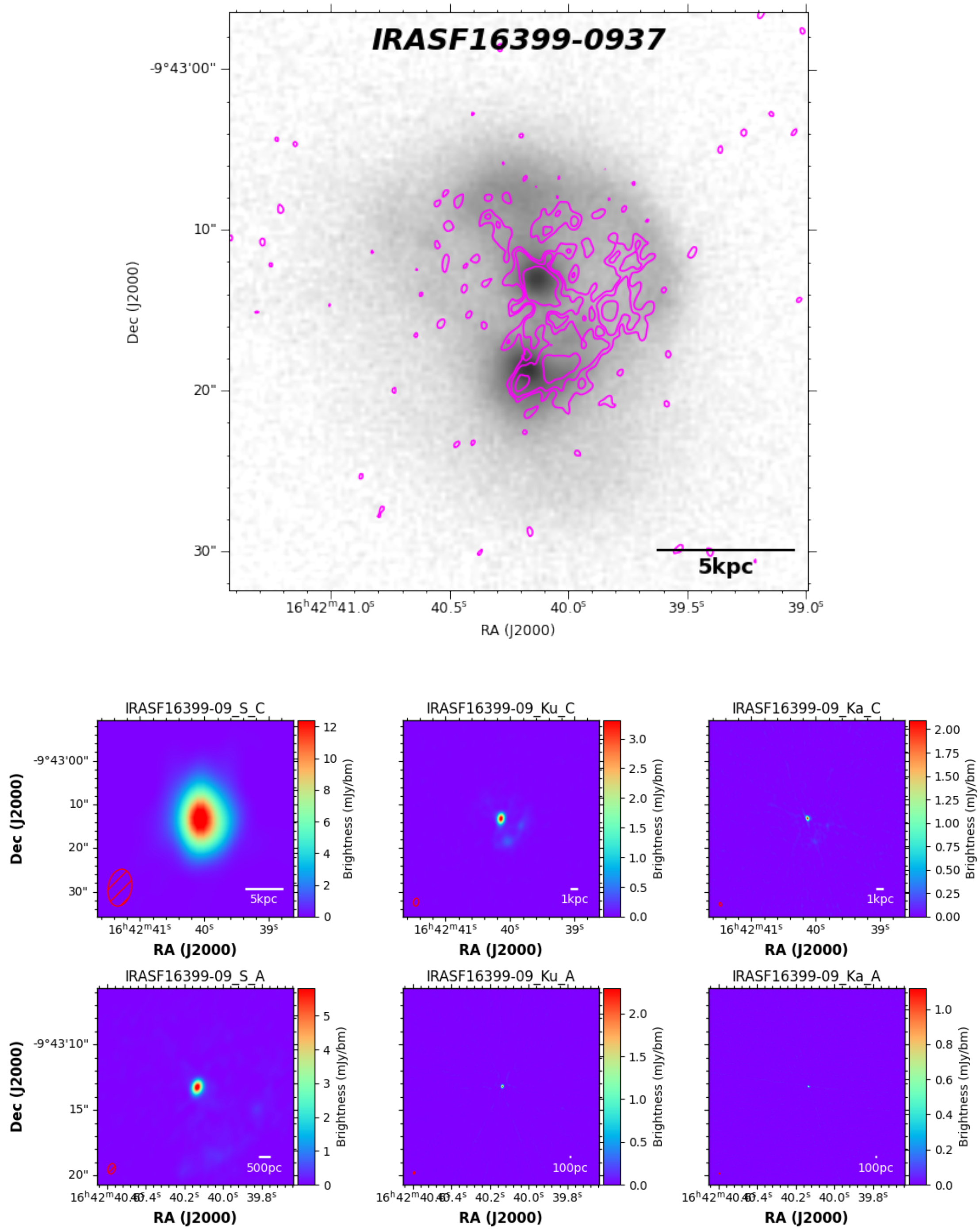

Figure 2.46: IRAS F16399-0937

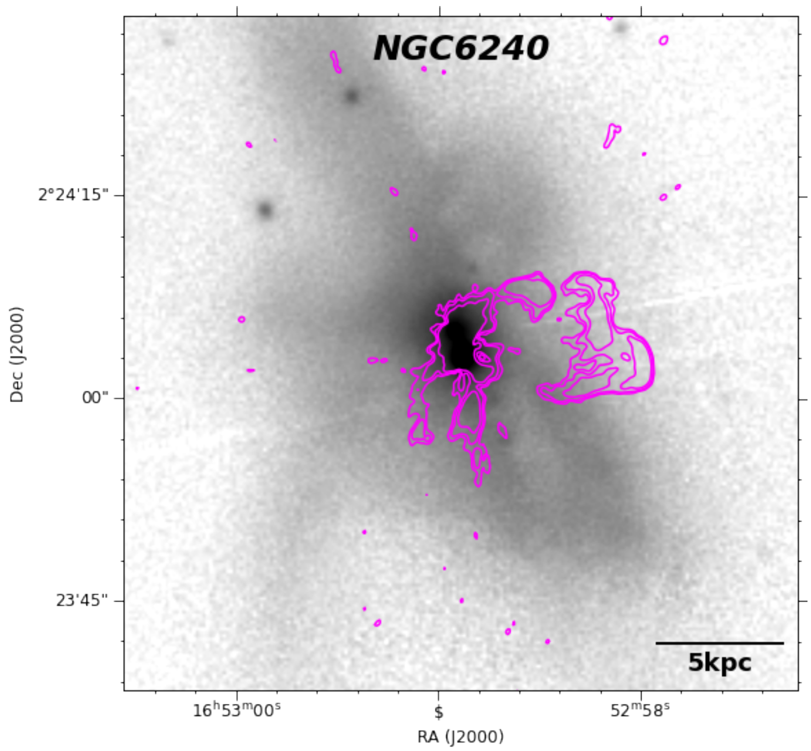

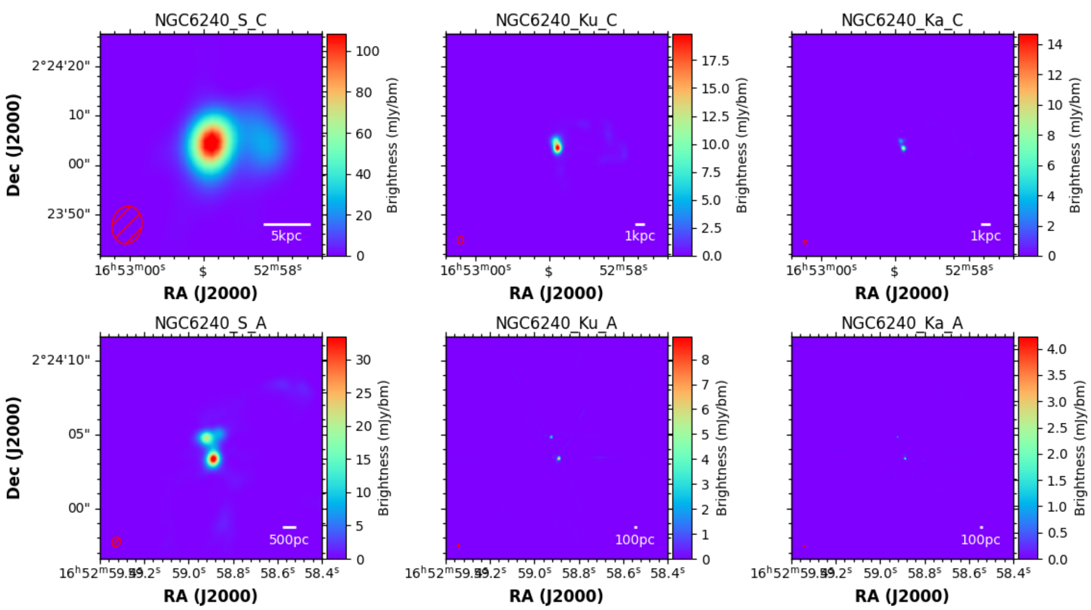

Figure 2.47: NGC 6240

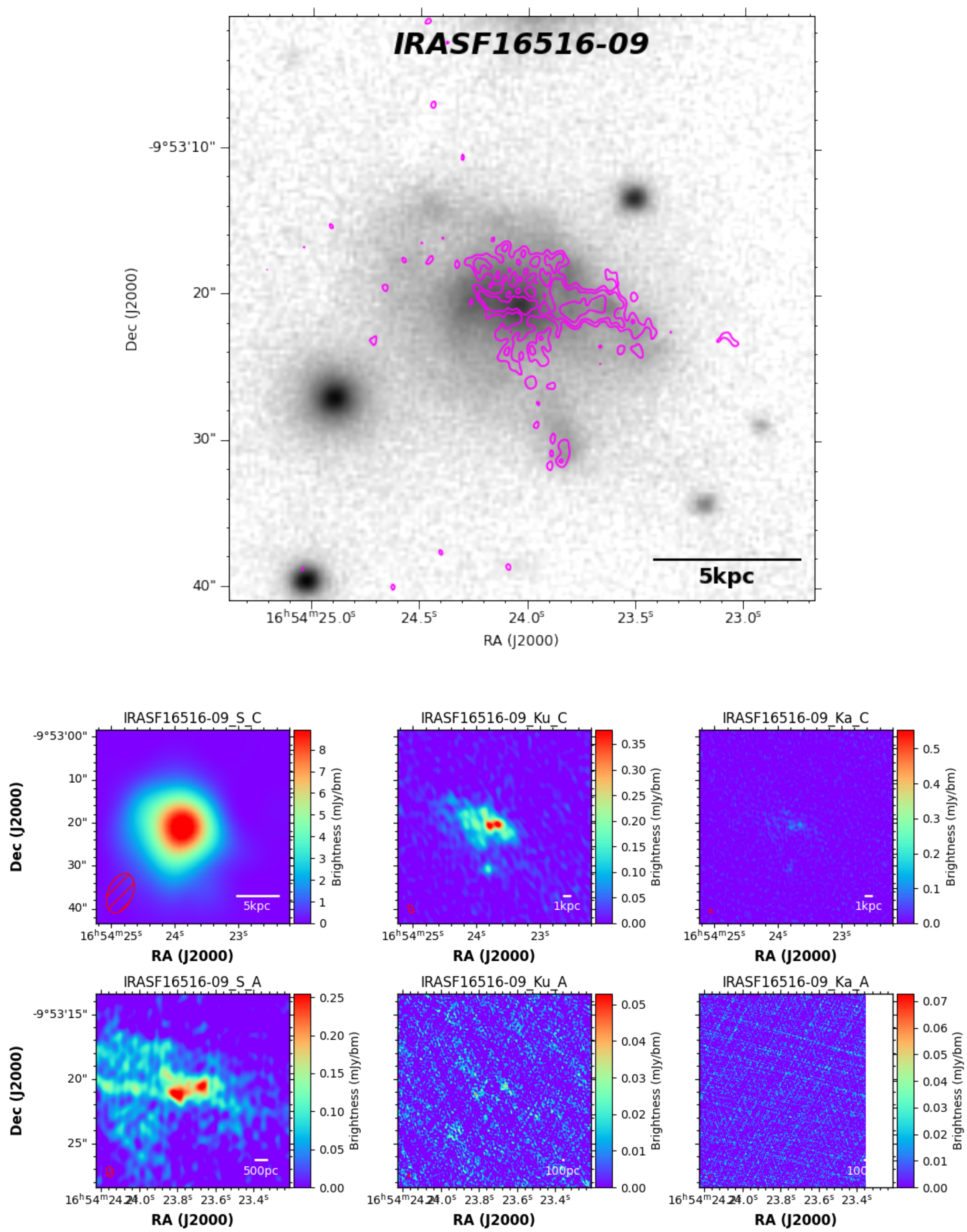

Figure 2.48: IRAS F16516-0948

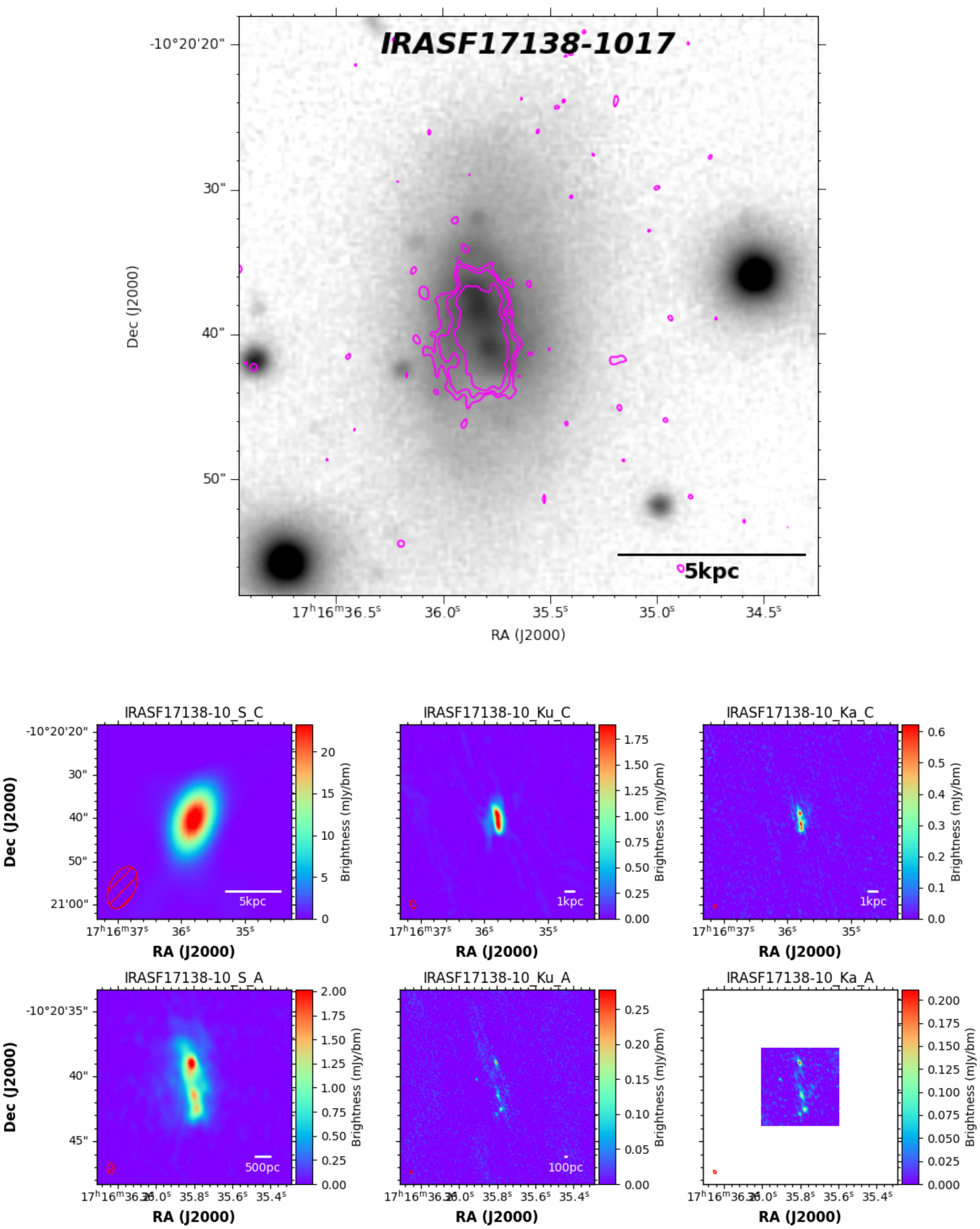

Figure 2.49: IRAS F17138-1017

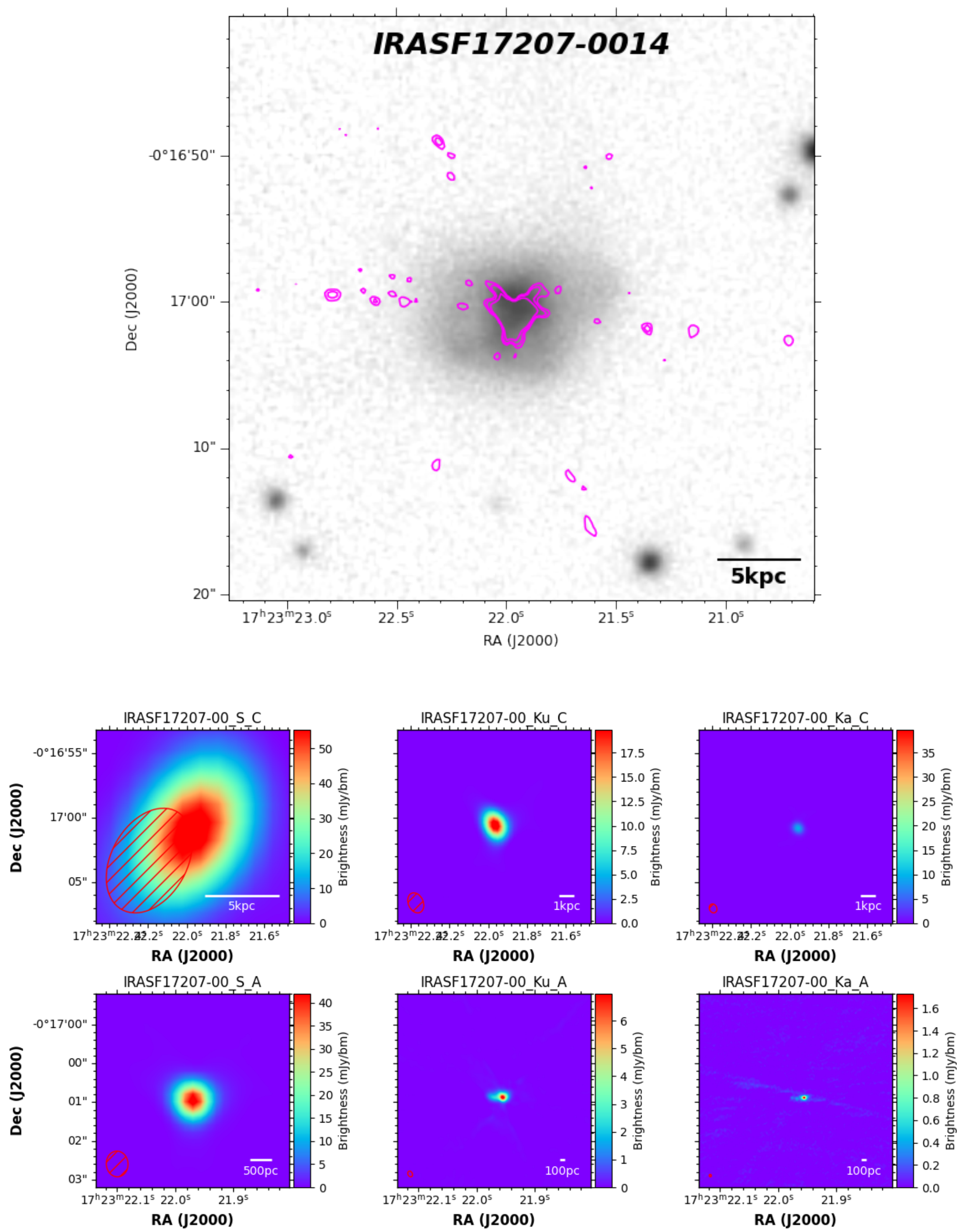

Figure 2.50: IRAS F17207-0014 (or IRAS 17208-0014)

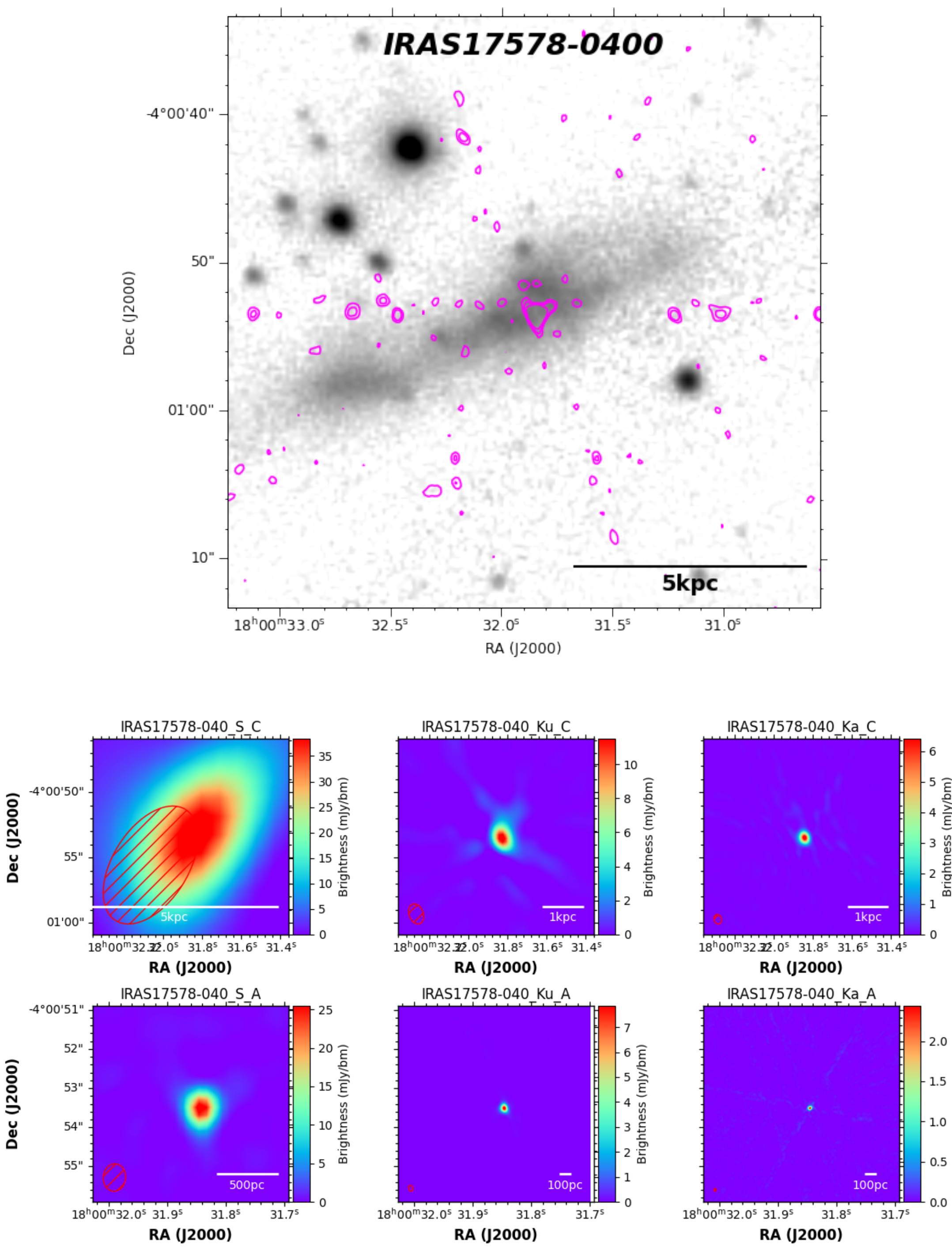

Figure 2.51: IRAS 17578-0400

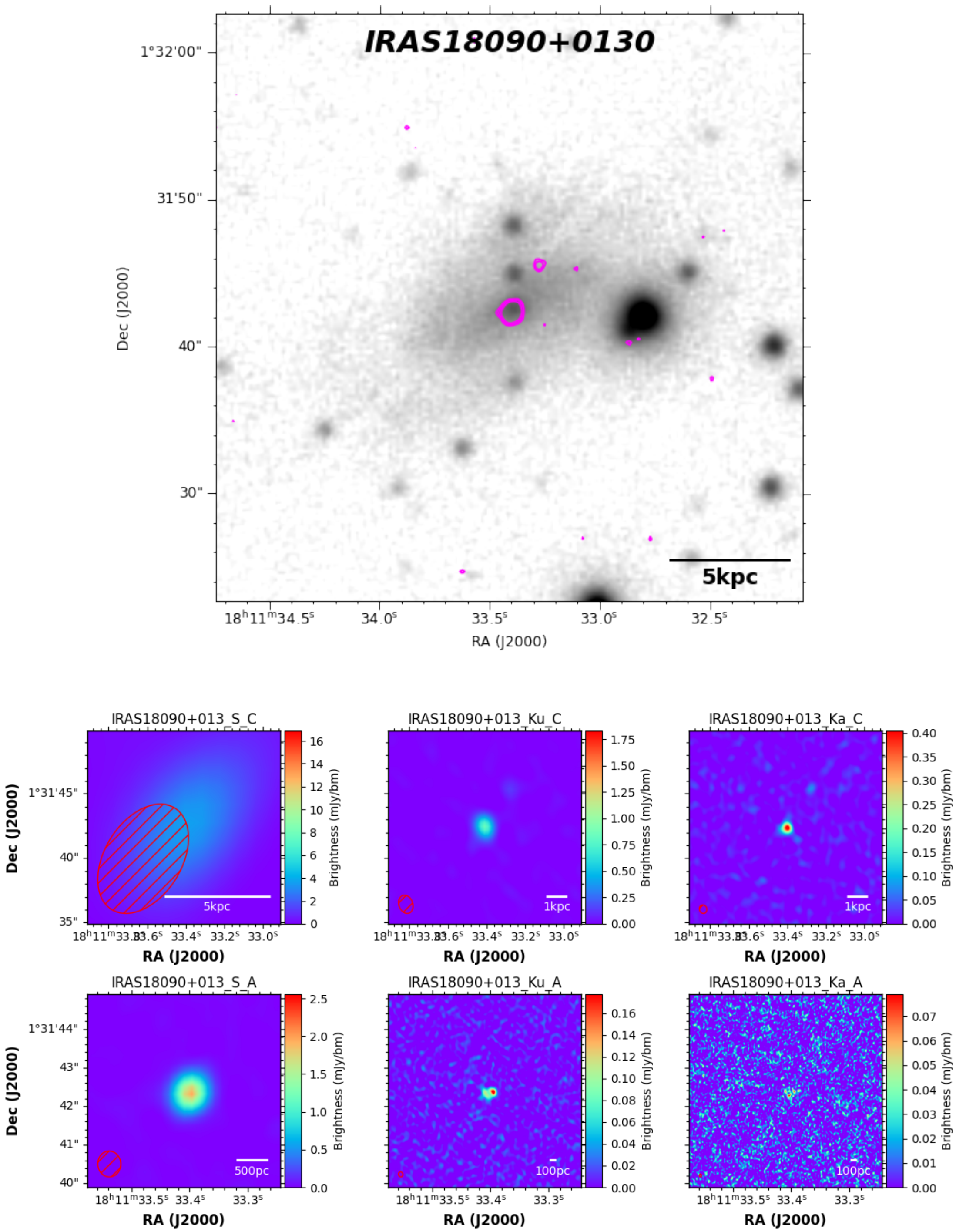

Figure 2.52: IRAS 18090+0130

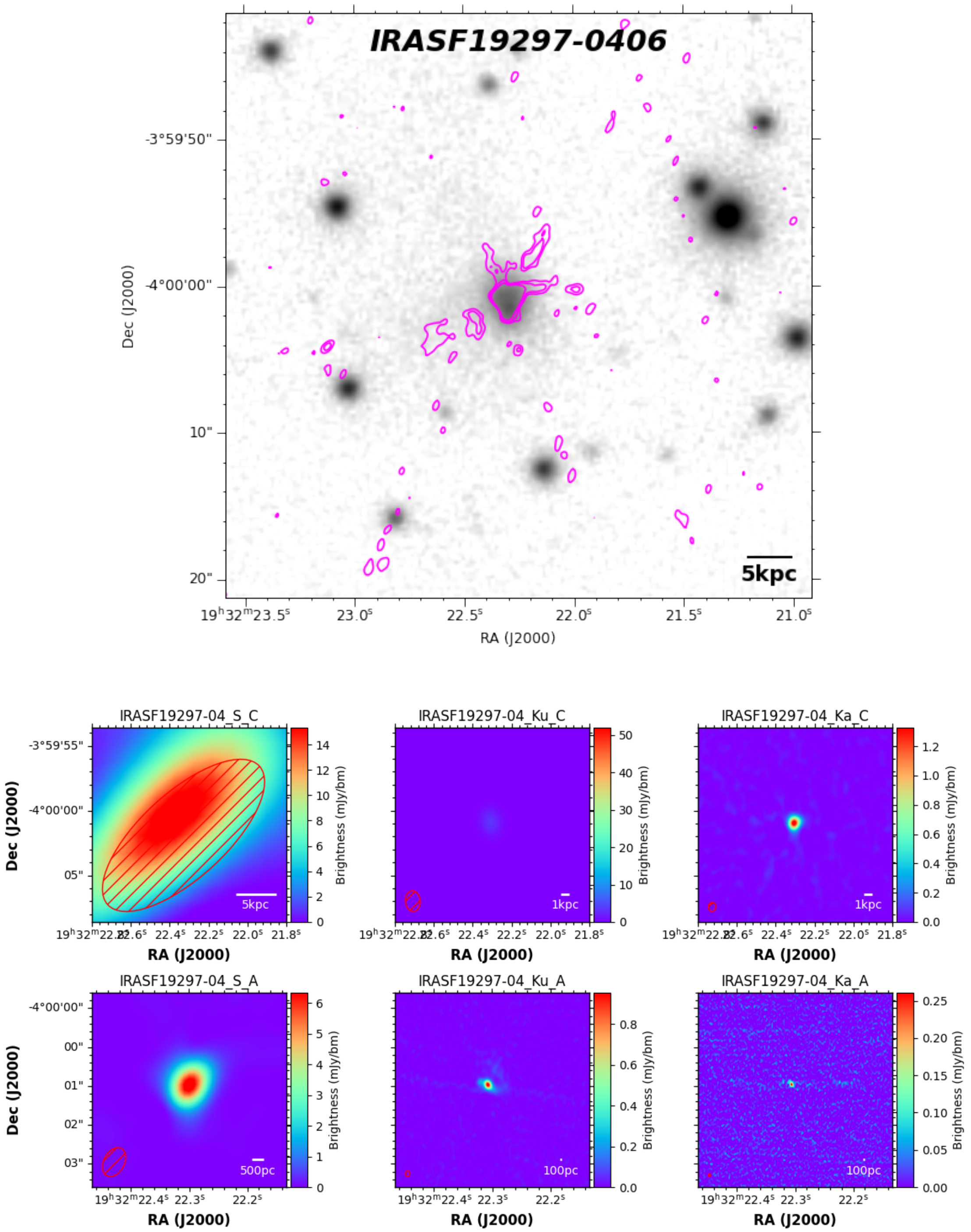

Figure 2.53: IRAS F19297-0406

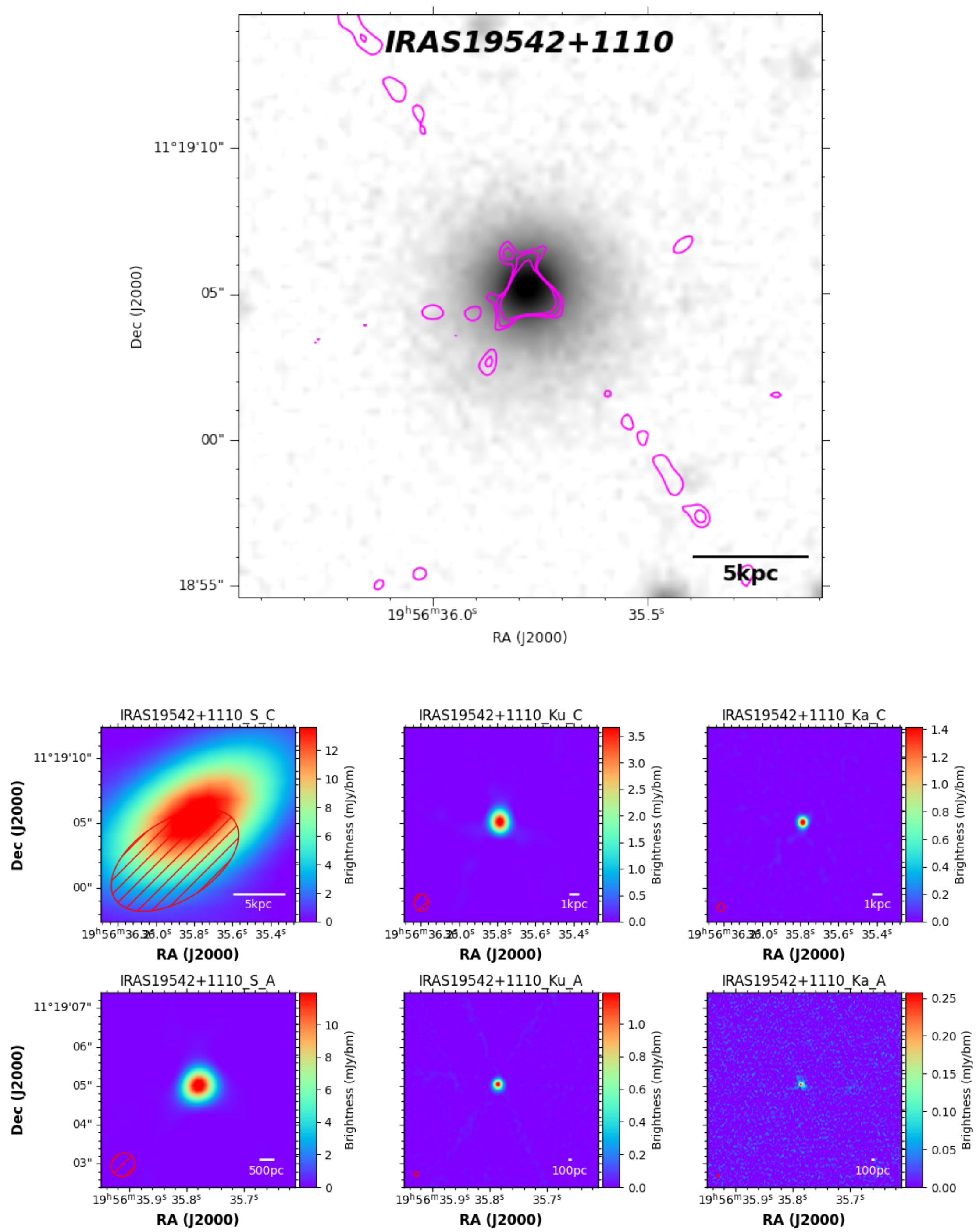

Figure 2.54: IRAS 19542+1110

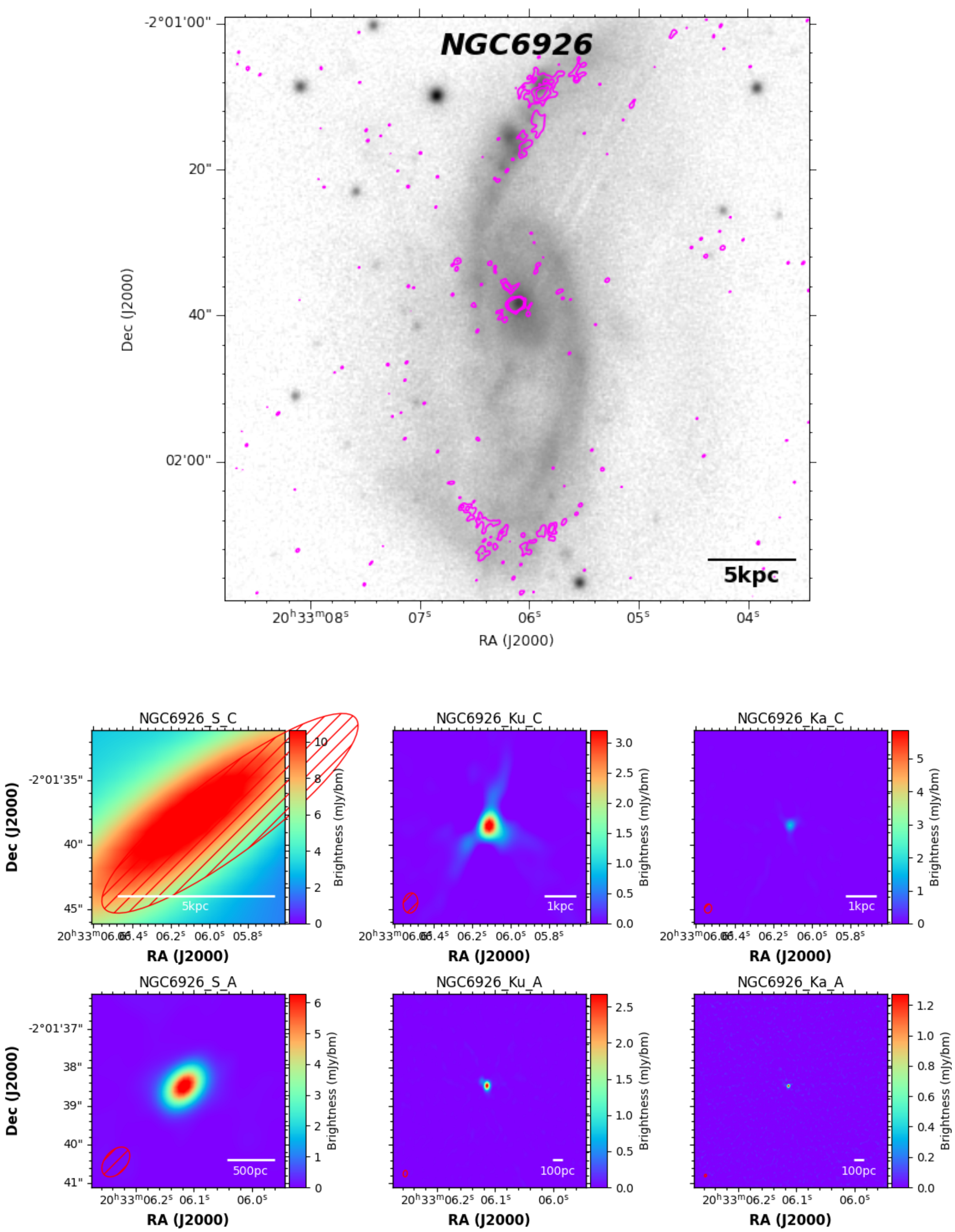

Figure 2.55: NGC 6926

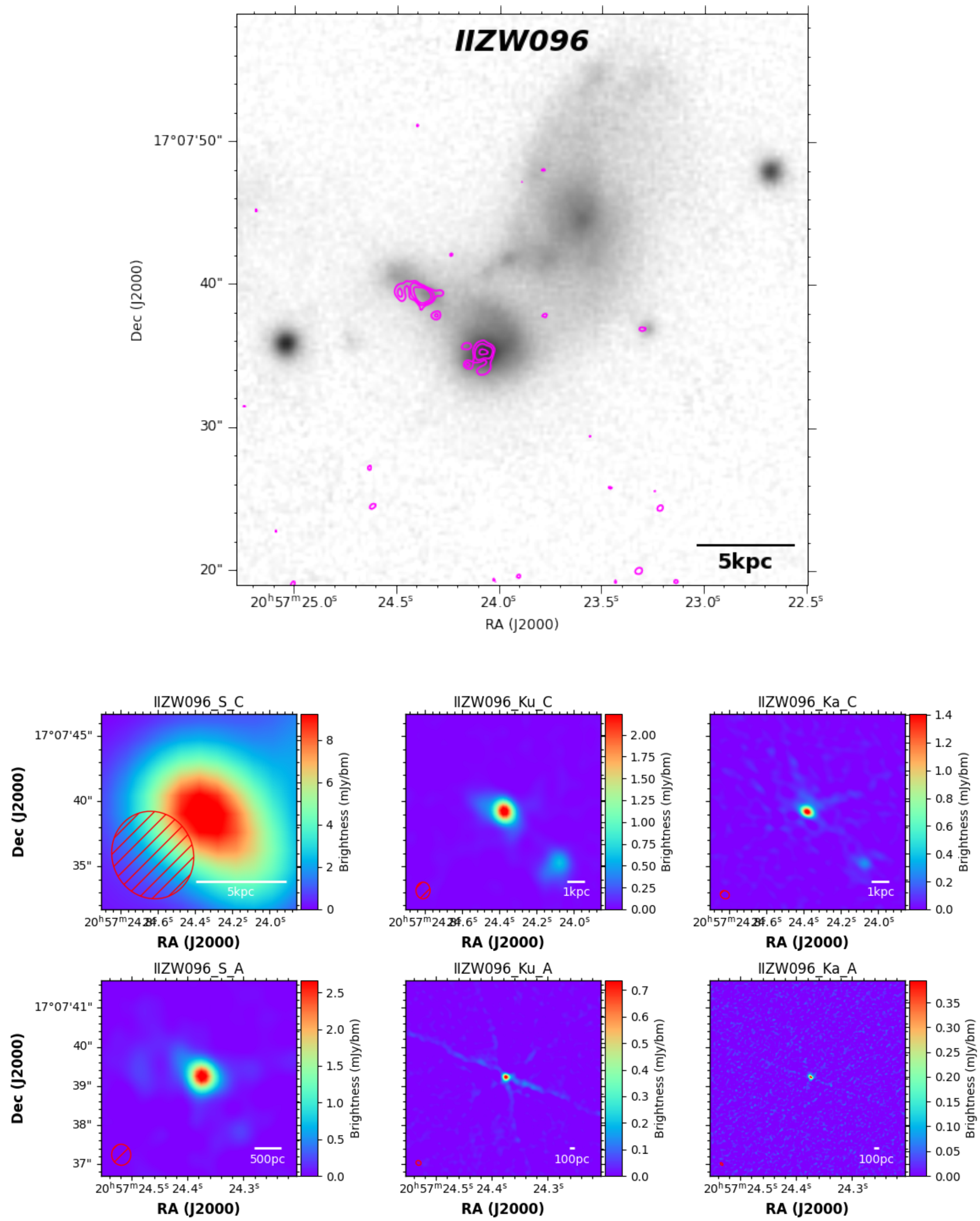

Figure 2.56: IIZw 096

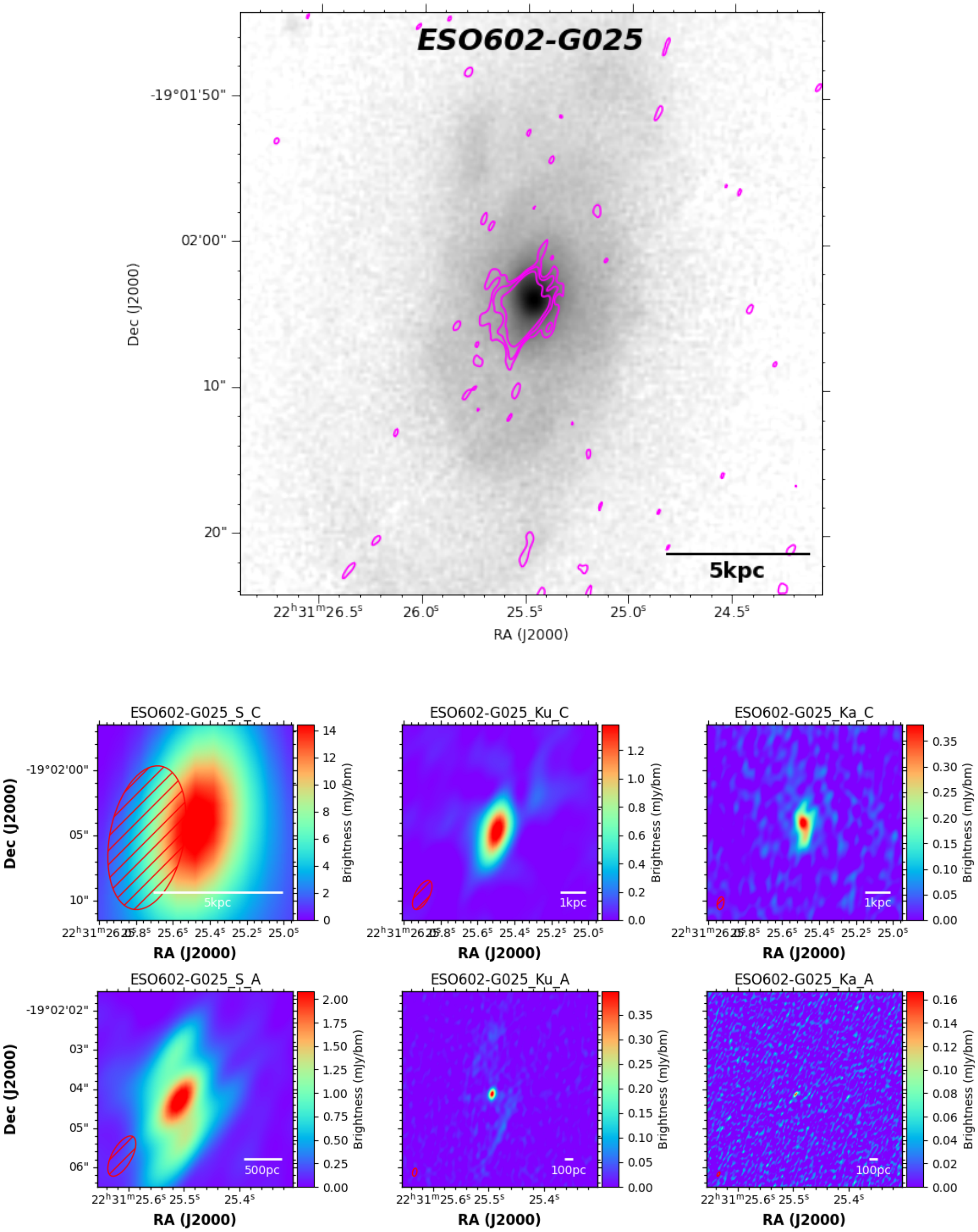

Figure 2.57: ESO 602-G025

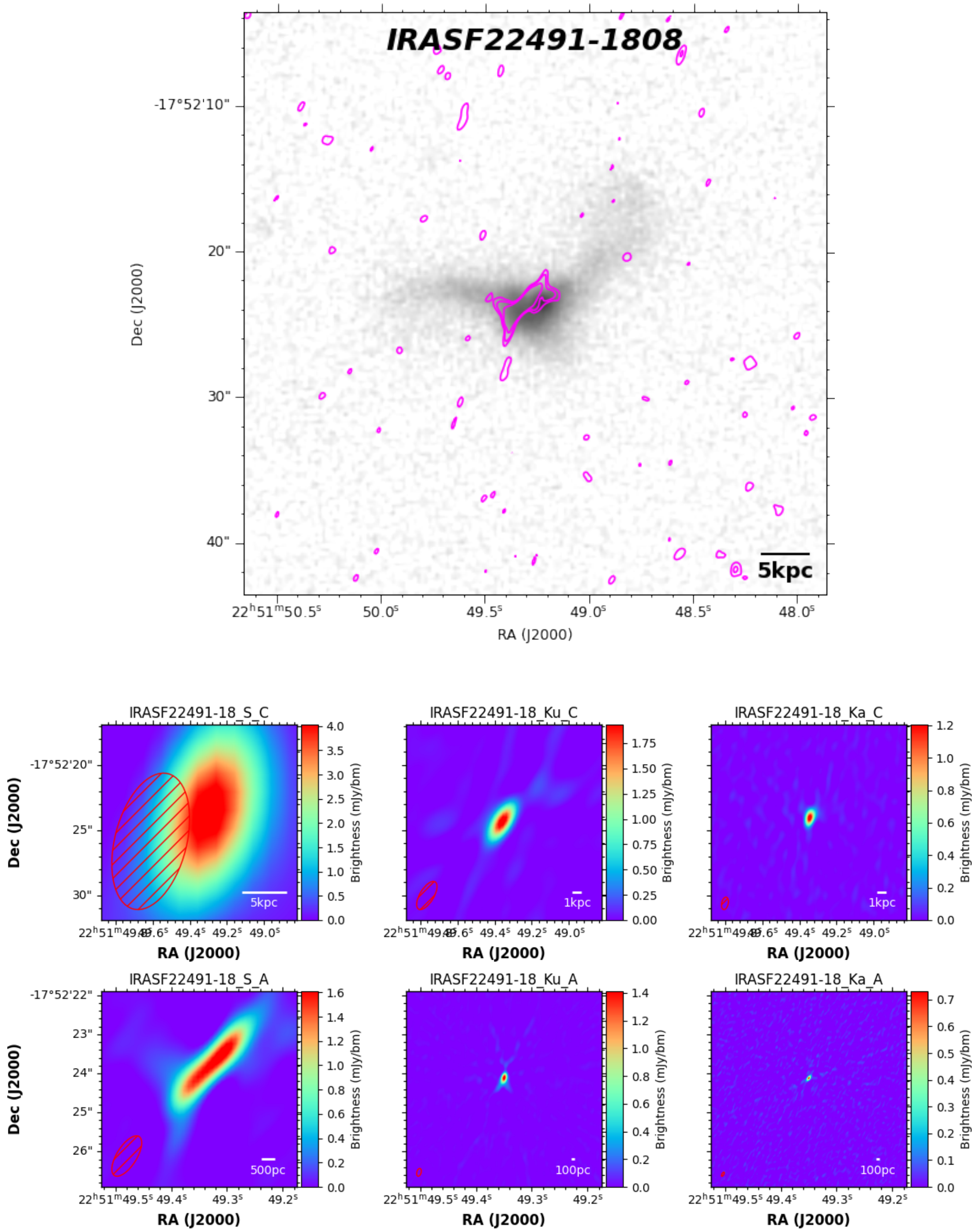

Figure 2.58: IRAS F22491-1808

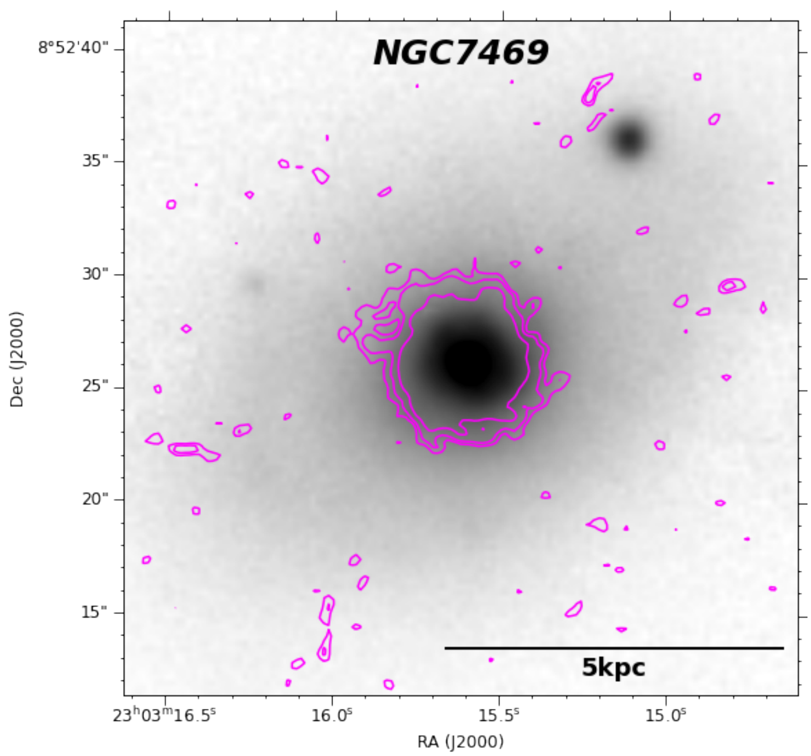

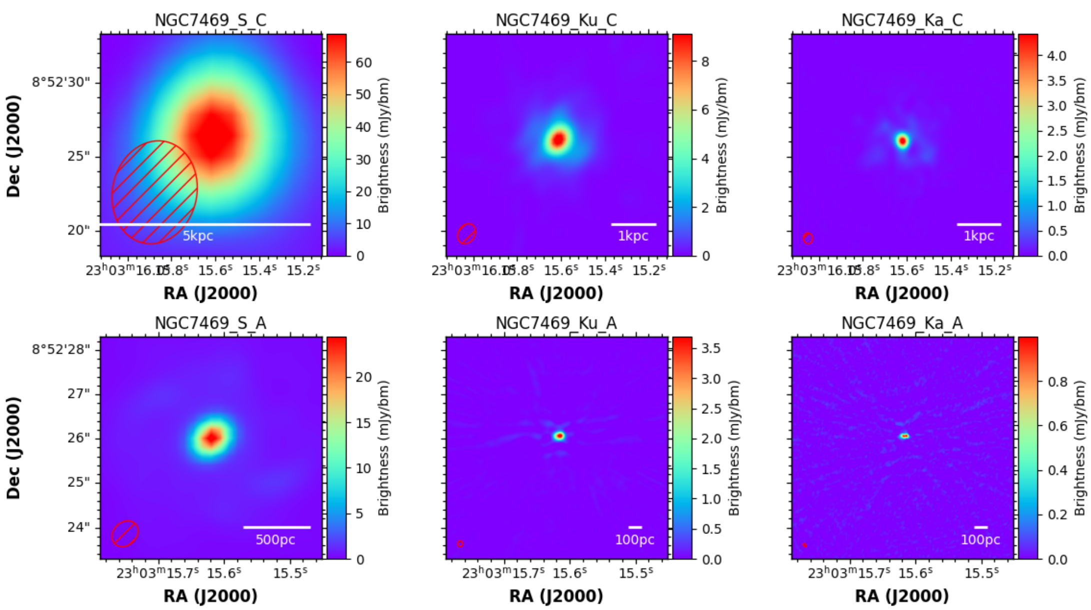

Figure 2.59: NGC 7469

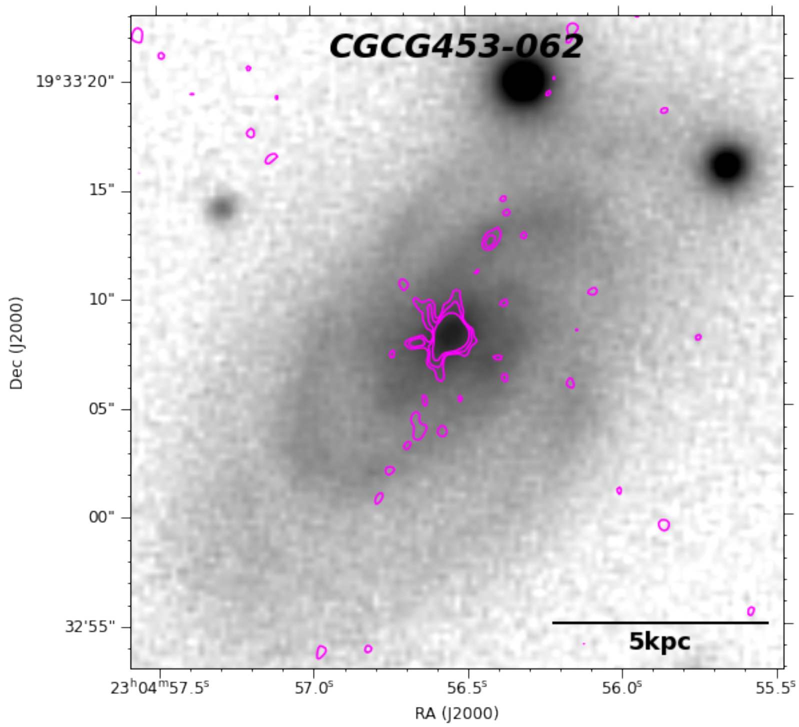

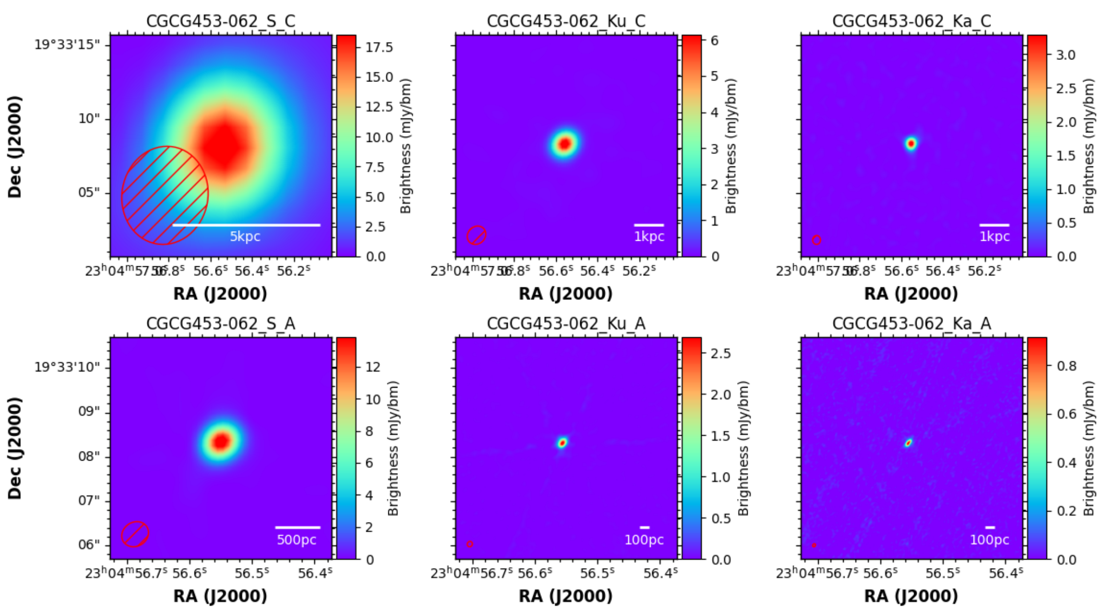

Figure 2.60: CGCG 453-062

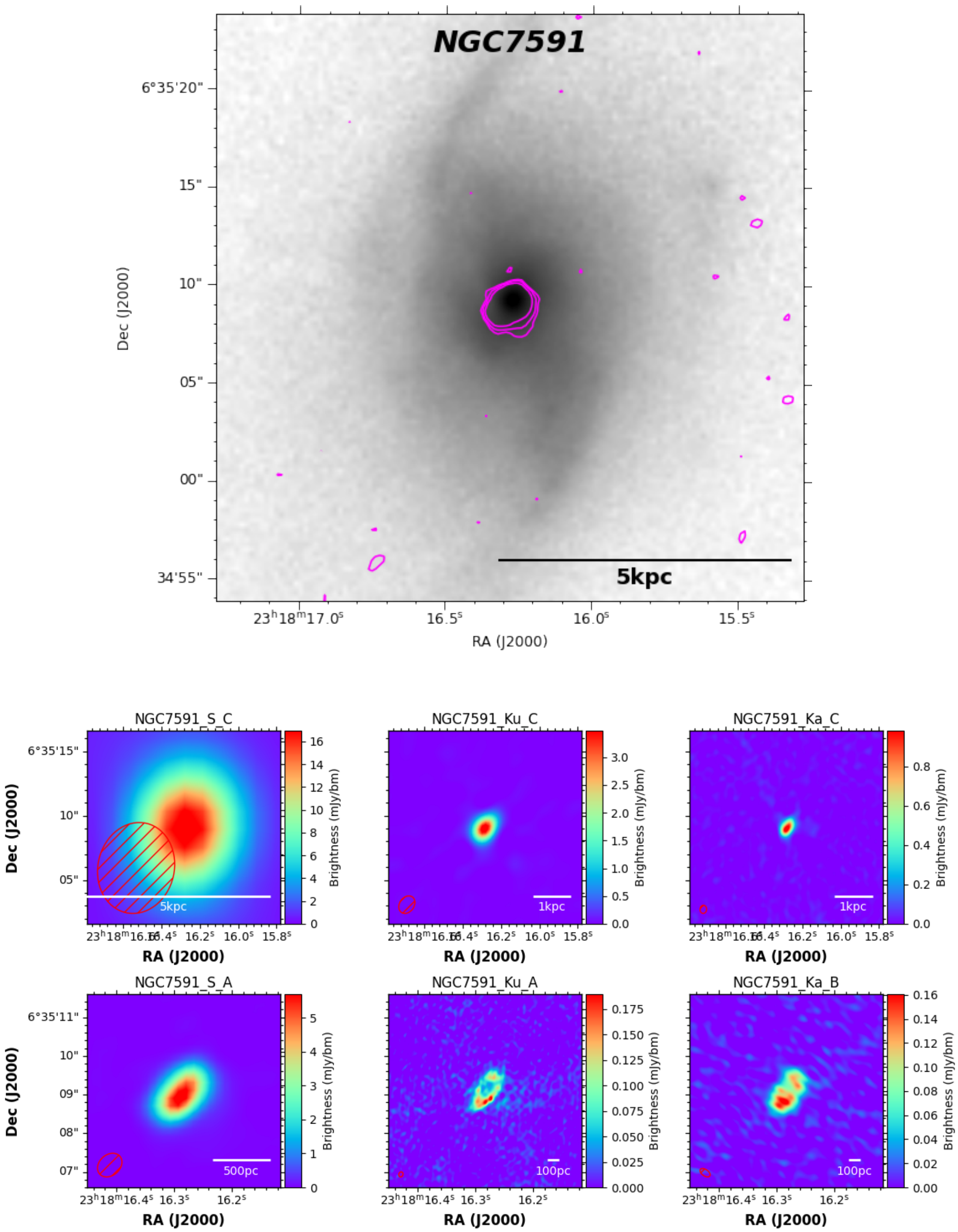

Figure 2.61: NGC 7591

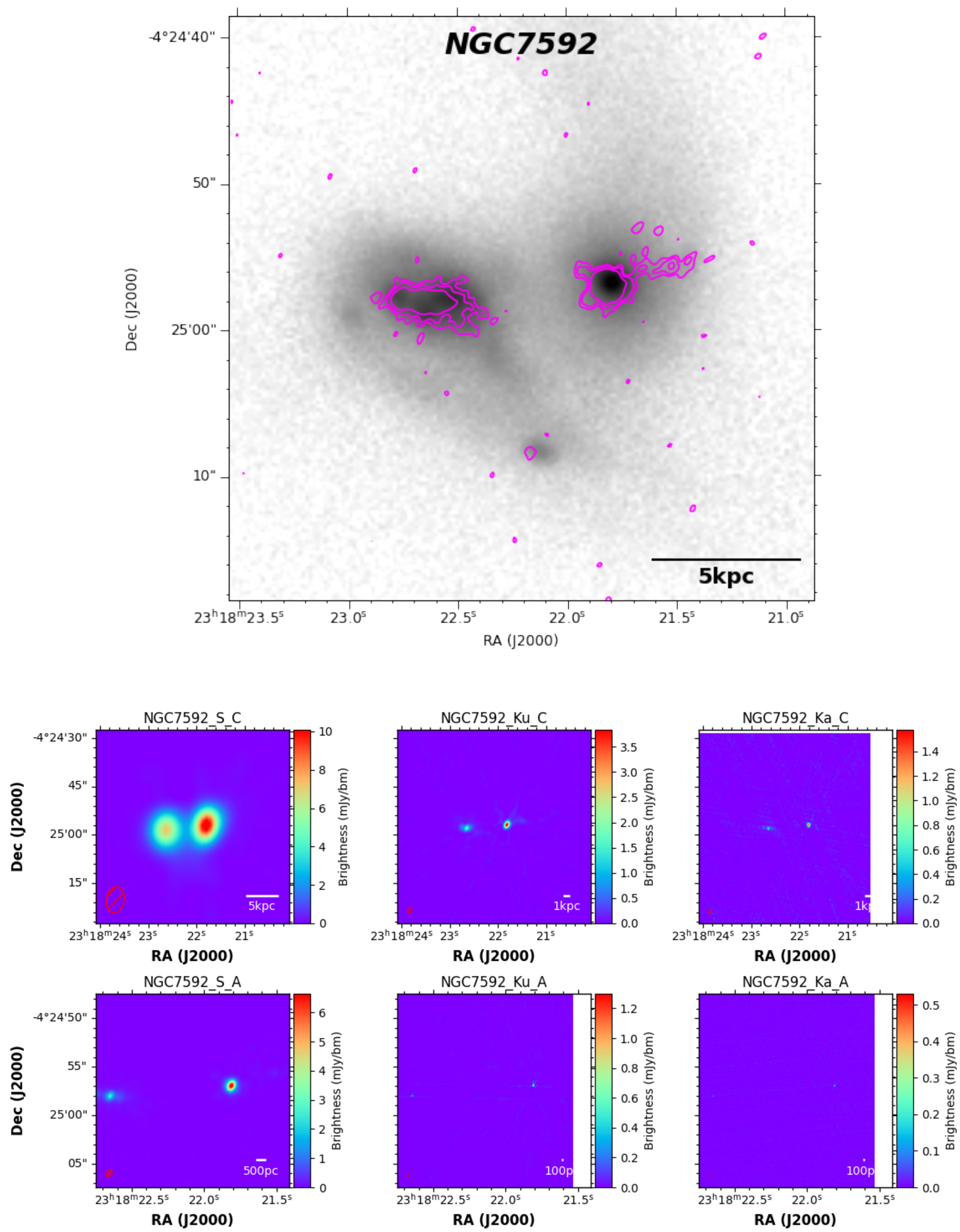

Figure 2.62: NGC 7592

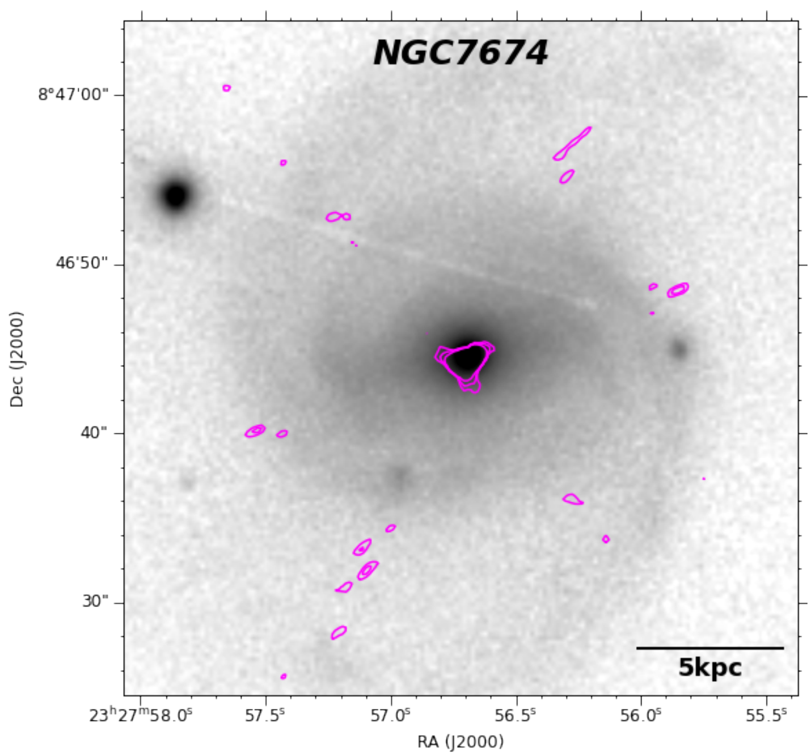

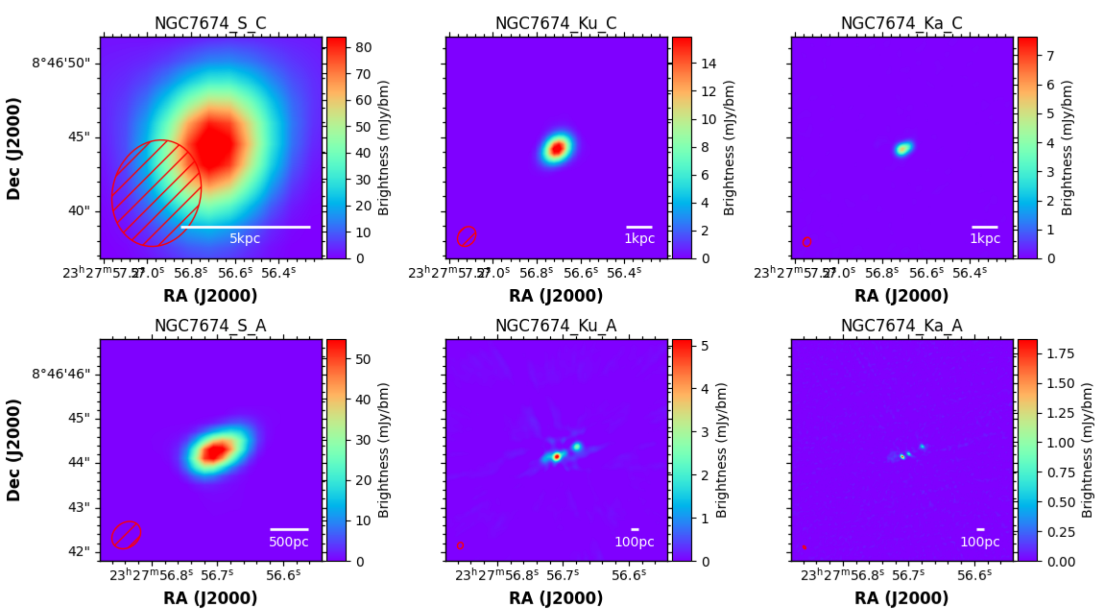

Figure 2.63: NGC 7674

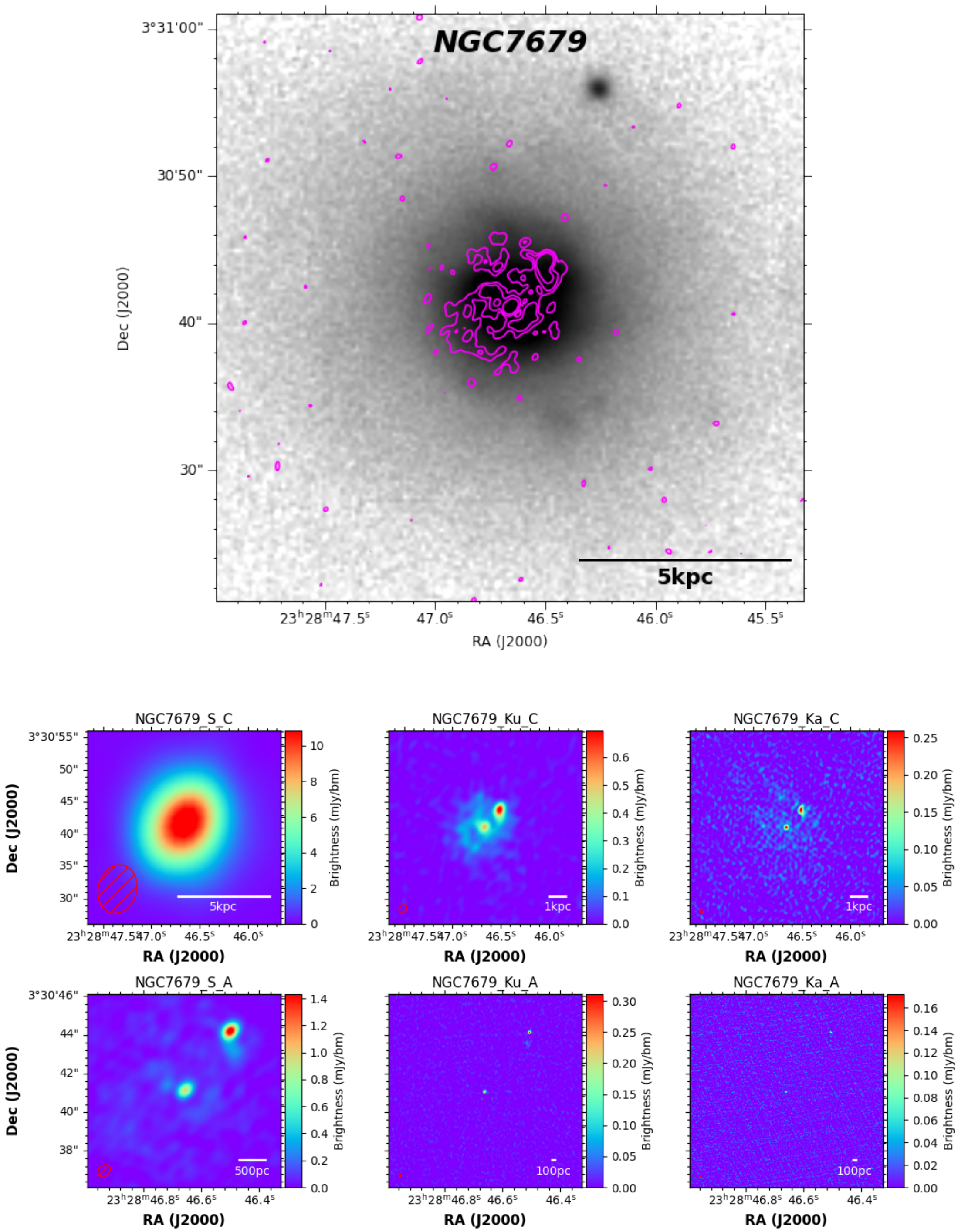

Figure 2.64: NGC 7679

Chapter 3

A Comparison between Nuclear Ring Star Formation in LIRGs and Normal Galaxies with the Very Large Array

[1]

3.1 Introduction

At least one fifth of disk galaxies host star-forming nuclear rings (Knapen, 2005). It is commonly accepted that nuclear rings result from a non-axisymmetric gravitational potential in galaxy centers, which can be induced by the presence of a stellar bar, strong spiral arms or tidal interaction (e.g. Combes & Gerin, 1985; Shlosman et al., 1990; Athanassoula, 1994; Buta & Combes, 1996; Combes, 2001). Such non-

[1]This chapter has been published in the The Astrophysical Journal, Volume 916, Issue 2, id.73, 23 pp. Authors: Song, Y.; Linden, S. T.; Evans, A. S.; Barcos-Muñoz, L.; Privon, G. C.; Yoon, I.; Murphy, E. J.; Larson, K. L.; Díaz-Santos, T.; Armus, L.; Mazzarella, Joseph M.; Howell, J.; Inami, H.; Torres-Albà, N.; U, V.; Charmandaris, V.; McKinney, J.; Kunneriath, D.; Momjian, E.

axisymmetry can drive large amounts of gas into the central region and eventually develop a ring of dense gas and intense star formation (SF) surrounding the galactic nucleus, likely at the location of the Inner Lindblad Resonance (Kim & Stone, 2012; Li et al., 2015) or Nuclear Lindblad Resonance (Fukuda et al., 1998). Optical and infrared (IR) studies of nuclear rings in nearby galaxies indicate that they are prolific in producing young ($< 100\,\mathrm{Myr}$) and massive ($\sim 10^5\,M_\odot$) star clusters in episodic starbursts (e.g. Maoz et al., 1996; Buta et al., 2000; Maoz et al., 2001). With large reservoirs of dense gas present, nuclear rings are predicted to be long-lived despite the enhanced massive SF (Barreto et al., 1991; Regan & Teuben, 2003; Allard et al., 2006; Sarzi et al., 2007). Simulations have been used to predict that even when subject to supernovae feedback, nuclear rings may persist at Gyr timescales (Knapen et al., 1995; Seo & Kim, 2013, 2014). Therefore, nuclear rings provide excellent opportunities to study extreme cases of SF in nearby systems.

As a result of long-lasting SF activity, nuclear rings can account for a large fraction of the stellar mass and bolometric luminosity in their host galaxies (e.g. Barreto et al., 1991; Genzel et al., 1995). In the process of secular evolution, nuclear ring SF (NRSF) often emerges as galactic pseudo-bulges slowly assemble from disk material (Kormendy & Kennicutt, 2004). Meanwhile, powerful NRSF has also been seen in high-resolution observations of galaxy mergers (e.g. Genzel et al., 1995; Knapen et al., 2004; Haan et al., 2013; Herrero-Illana et al., 2014), which is a comparatively more dramatic evolutionary process. Simulations of galaxy mergers have also proposed nuclear rings as a potential fueling mechanism of quasars (Hopkins & Quataert, 2010). Therefore formation of nuclear rings may represent a common and critical phase in galaxy evolution, and properties of NRSF may provide insights into the key dynamical processes associated with various evolutionary paths.

While nuclear rings in nearby disk galaxies have been extensively investigated in the optical and IR, studies of nuclear rings in galaxy mergers are relatively scarce, making a consistent comparison of the two galaxy populations difficult. Luminous and Ultra-luminous Infrared Galaxies (LIRGs: $L_{\rm IR}(8-1000\mu{\rm m}) > 10^{11}L_{\odot}$; ULIRGs: $L_{\rm IR}(8-1000\mu{\rm m}) > 10^{12}L_{\odot}$) in the local Universe, which are often interacting or merging gas-rich spirals, have provided excellent opportunities to study SF in mergers. However, heavy dust obscuration makes the centers of these systems elusive at optical wavelengths (Sanders & Mirabel, 1996). Meanwhile, measurements of the nuclei in U/LIRGs can still be heavily affected by non-uniform dust extinction even in the IR (Díaz-Santos et al., 2011; Piqueras López et al., 2013; U et al., 2019).

With the advancement of high-frequency radio interferometry, a highly detailed, extinction-free view of the heavily obscured hearts of local LIRGs becomes possible. In the present study, we make use of high-resolution ($\sim 100\,{\rm pc}$) VLA observations to characterize and compare the SF properties of nuclear rings hosted in five normal disk galaxies and four LIRGs in the local Universe. Observations of these LIRGs are part of a new VLA campaign for the Great Observatories All-sky LIRG Survey (GOALS; Armus et al., 2009) that contains 68 local U/LIRGs, and the normal galaxies are observed with the Star Formation in Radio Survey (SFRS; Murphy et al., 2012, 2018; Linden et al., 2020) of 56 nearby normal star-forming disk galaxies. These two projects together provide a direct, high-resolution comparison of SF activity in interacting and isolated galaxies in the local Universe. In this paper, we focus on comparing properties of NRSF observed in these two surveys using high-frequency radio continuum as an extinction-free tracer. A full study of the nuclear SF properties in the GOALS VLA campaign will be presented in a forthcoming paper.

This paper is divided into 7 sections. We present our sample selection, observations and calibration procedures in Section 3.2 and 3.3. In Section 4.3, we describe the measurements we perform to characterize the properties of the nuclear rings and the individual NRSF regions, the results of which are presented in Section 4.4. In Section 4.5, we discuss the limitations and implications of the results. Finally, Section 4.6 summarizes major findings and conclusions.

Throughout this work we adopt $H_0 = 70\,\mathrm{km/s/Mpc}$, $\Omega_{\mathrm{matter}} = 0.28$ and $\Omega_\Lambda = 0.72$ based on the five-year WMAP result (Hinshaw et al., 2009). These parameters are used with the 3-attractor model (Mould et al., 2000) to calculate the luminosity distances and physical scales of the LIRGs in the sample.

3.2 Sample Selection

The GOALS "equatorial" VLA campaign (Linden et al., 2019, ; Song et al. in prep) is a multi-frequency, multi-resolution snapshot survey designed to map the brightest radio continuum emission in all 68 U/LIRGs from GOALS that are within declination $|\delta| < 20°$ at Ka (33 GHz), Ku (15 GHz) and S (3 GHz) bands at kpc and $\sim 100\,\mathrm{pc}$ scales. These observations serve as a companion to SFRS, which imaged 56 nearby ($D_L < 30\,\mathrm{Mpc}$) normal star-forming galaxies (i.e. non-U/LIRGs) from SINGS (Kennicutt et al., 2003) and KINGFISH (Kennicutt et al., 2011) at matched frequencies and also at both kpc (Murphy et al., 2012) and $\sim 100\,\mathrm{pc}$ scales (Murphy et al., 2018; Linden et al., 2020). Using the kpc resolution observations from the GOALS equatorial survey, Linden et al. (2019) studied extra-nuclear star formation in 25 local LIRGs, and concluded that the high global SFR of these systems, relative to the Star Formation Main Sequence (e.g. Elbaz et al., 2011; Speagle et al., 2014) occupied by normal galaxies in SFRS, must be driven by extreme nuclear SF.

In this work we focus on studying and comparing star-forming properties of nuclear rings at $\sim 100\,\mathrm{pc}$ scales in a sample of nine galaxies from SFRS and GOALS. While the term "nuclear ring" is traditionally reserved for rings forming at the Nuclear Lindblad Resonance (Fukuda et al., 1998), it has also been more broadly used

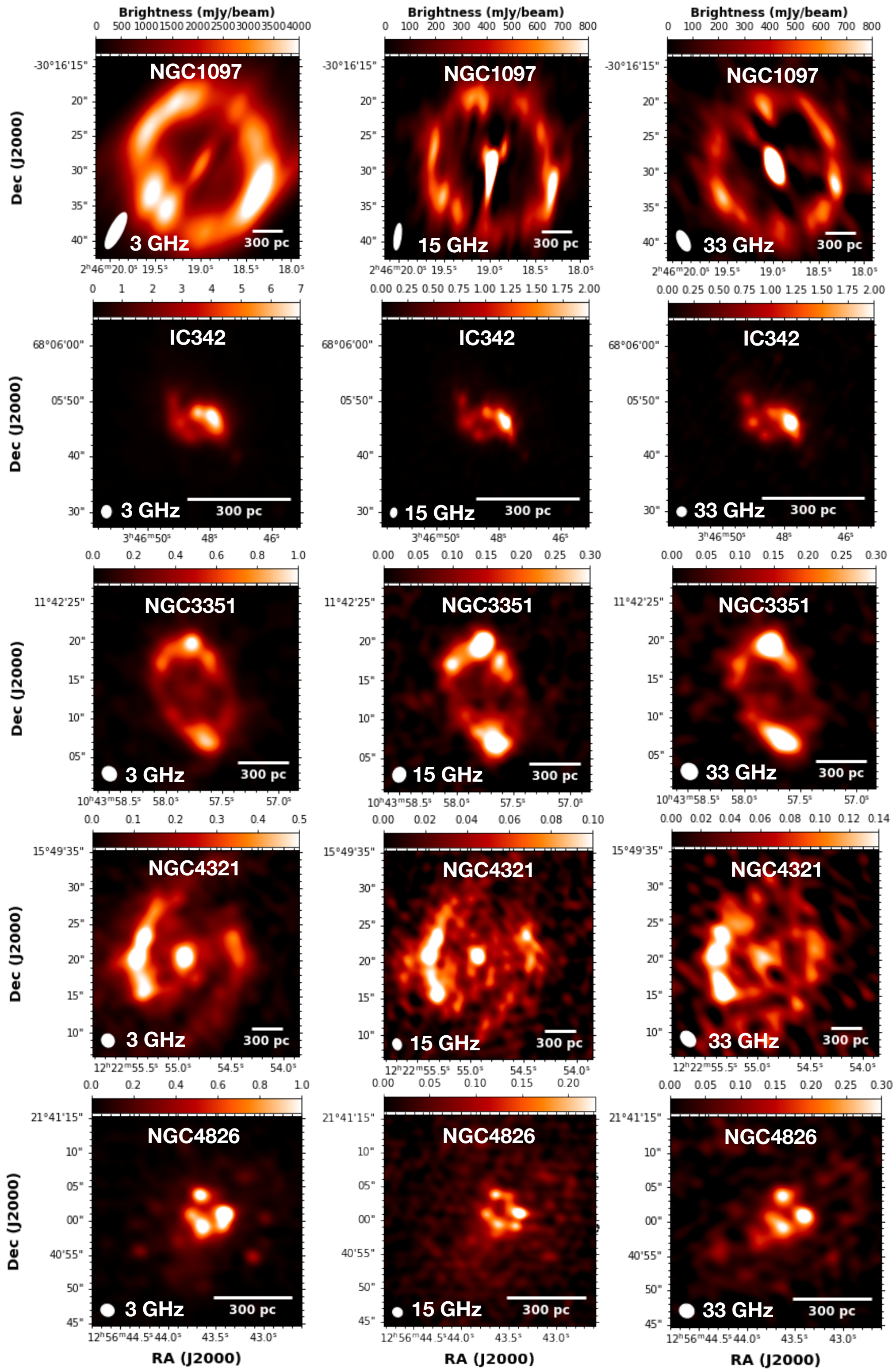

Figure 3.1: Highest resolution Ka, Ku, and S band images of the five nuclear rings hosted in the normal galaxies from SFRS. Each image is displayed with bilinear interpolation, in units of mJy/beam, and the synthesized beam is represented by the white filled ellipse on the lower left corner. The nuclear rings are well detected and resolved at all three bands.

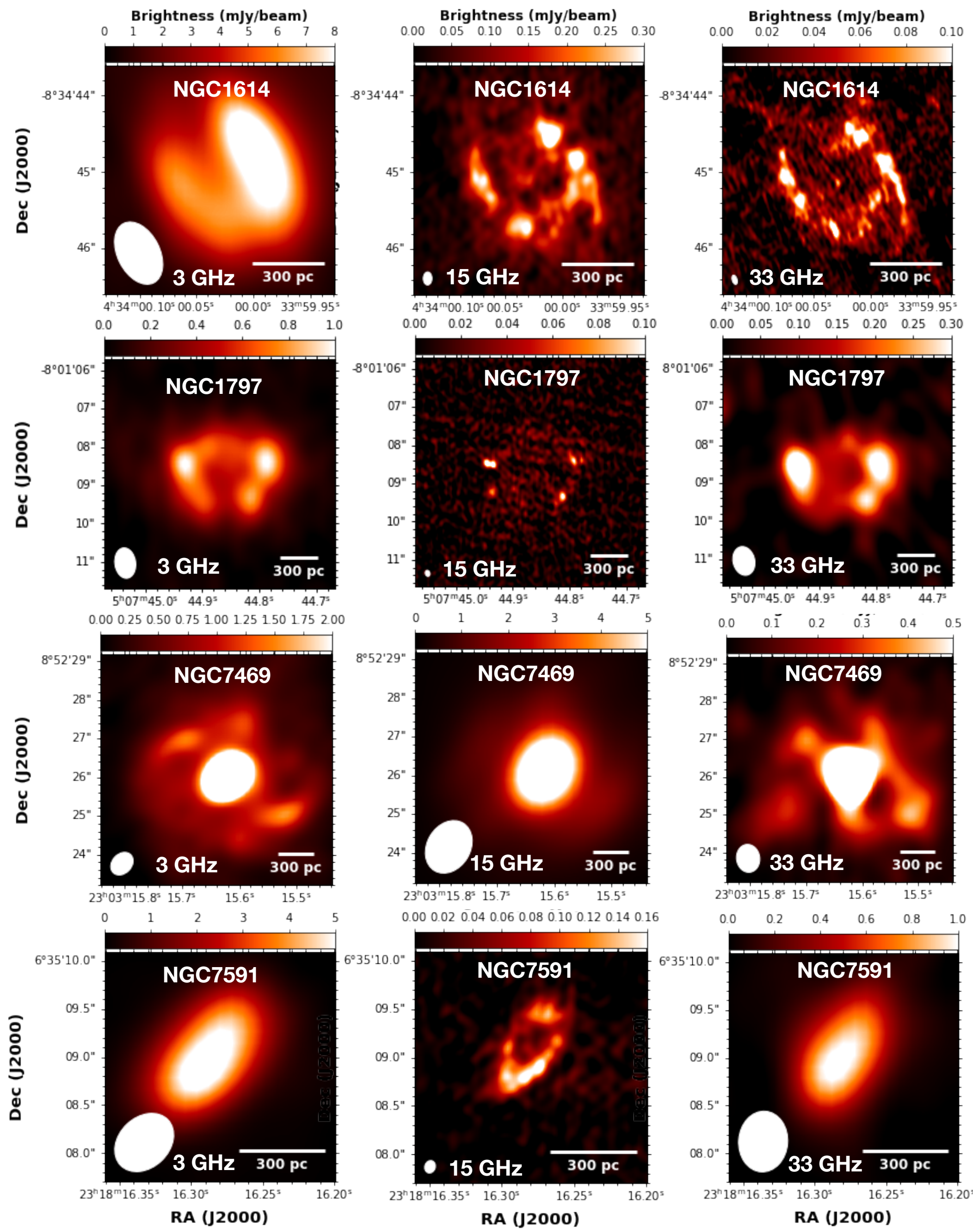

Figure 3.2: Highest resolution Ka, Ku, and S band images for the four nuclear rings hosted in LIRGs from GOALS. Each image is displayed with bilinear interpolation, in units of mJy/beam, and the synthesized beam is represented by the white filled ellipse on the lower left corner. All rings are detected and resolved at all three bands except for NGC 7591, whose nuclear ring was only resolved at Ku Band.

to describe the innermost star-forming rings in galaxies (e.g. Böker et al., 2008). In this paper, we follow the definition and size measurements given in a study of 113 nearby nuclear rings by Comerón et al. (2010), and use "nuclear ring" to describe ring-like emission within the central 2 kpc of a galaxy detected in our surveys at 3, 15 or 33 GHz in radio continuum. With the exceptions of the rings in NGC 1797 and NGC 7591, which are resolved for the first time with the GOALS equatorial survey, all other rings reported here have previously been identified and separately studied as "nuclear rings" at various wavelengths (e.g. Mazzuca et al., 2008; Comerón et al., 2010; Ma et al., 2018). In some other studies, these rings have also been referred to as "circumnuclear rings" (e.g. Xu et al., 2015; Prieto et al., 2019). Figure 3.1 and 3.2 show the VLA images of the sample, and Table 3.1 lists the basic properties of the host galaxies.

We note that due to the sensitivity limit of our VLA observations, we were only able to identify the nine nuclear rings that show consistently bright ($\gtrsim$ 0.1mJy/beam) high-frequency (15 or 33 GHz) emission among the combined total of 124 targets from SFRS and the GOALS equatorial survey. Several other galaxies, such as NGC 1068 (LIRG) and NGC 5194 (normal), are also known nuclear ring hosts from optical studies (e.g. Telesco & Decher, 1988; Laurikainen & Salo, 2002), but their ring structures were not detected in our observations. We further discuss the potential biases of the sample selection in Section 3.6.1.

3.3 Observations & Data Reduction

3.3.1 VLA data

Each galaxy was observed with the VLA at S (3 GHz), Ku (15 GHz) and Ka Band (33 GHz). Observations of the five normal galaxies are acquired from the SFRS. This survey observed all galaxies at S, Ku, and Ka Band in B, C and D configuration, respectively, to achieve a common angular resolution of $\sim 2''.0$ at each frequency. Details of SFRS observations and data calibration procedures are described in Murphy et al. (2018) and Linden et al. (2020).

The four LIRGs were observed with both A ($0''.06 - 0''.6$) and C ($0''.6 - 7''.0$) configurations at 3, 15 and 33 GHz. The observations were carried out with projects VLA/14A-471 (PI: A. Evans) and VLA/16A-204 (PI: S. Linden). The raw VLA datasets were first reduced and calibrated with the standard calibration pipelines using the Common Astronomy Software Applications (CASA, v4.7.0; McMullin et al., 2007). Each measurement set was visually inspected and data related to bad antennas, time and frequency ranges (including RFI) were manually flagged. The above two steps were repeated until all bad data were removed.

Before imaging, we performed data combination on the reduced A and C configuration measurement sets at each frequency using CASAv4.7.0 `concat` task with a weighting scale of 100:1 (A:C). This was done to enhance the image sensitivity while maximizing resolution, as well as maintaining good PSF shapes (i.e. Gaussian-like), accounting for the fact that the uv-plane distribution of C configuration data is ~ 100 times denser than A configuration. The concatenated measurement sets were then imaged using CASAv4.7.0 `tclean` task, using Briggs weighting with a robust parameter of 1.0 and (Multi-Scale) Multi-Frequency Synthesis deconvolving algorithm.

Due to short on-source times, high resolution A configuration imaging is unable to recover the nuclear ring emission at 33 GHz for NGC 1797 and NGC 7591, and at both 15 and 33 GHz For NGC 7469. Therefore, in these cases, we use images made from C configuration measurement sets only, using the same `tclean` parameters as above. Additionally, bright nuclear emission in NGC 7469 allowed for self-calibration of the C Configuration data at 3, 15 and 33 GHz. Native resolution images of all data

Table 3.1: Properties of Sample Galaxies

Host (1)	RA (J2000) (2)	Dec (J2000) (3)	D_L (Mpc) (4)	$\log_{10}(L_{\rm IR})$ (5)	Scale (pc/″) (6)	Type (7)	$f^{\rm bol}_{\rm AGN}$ (%) (8)	Survey (9)	Morphology (10)	Merger Stage (11)
NGC 1097	02h46m19.0s	-30d16m30s	14.2	10.56	69	LINER/Sy1	-	SFRS	SBb	N*
IC 342	03h46m48.5s	+68d05m47s	3.3	9.87	16	HII	-	SFRS	SABcd	N
NGC 3351	10h43m57.7s	+11d42m14s	9.3	9.77	45	HII	-	SFRS	SBb	N
NGC 4321	12h22m54.8s	+15d49m19s	14.3	10.33	70	HII/LINER	-	SFRS	SABbc	N
NGC 4826	12h56m43.6s	+21d40m59s	5.3	9.54	26	LINER	-	SFRS	SAab	N
NGC 1614	04h33m59.8s	-08d34m44s	67.8	11.65	323	HII	12±8	GOALS	SBc pec	d
NGC 1797	05h07m44.9s	-08d01m09s	63.4	11.04	303	HII	6±3	GOALS	SBa pec	a
NGC 7469	23h03m15.6s	+08d52m26s	70.8	11.58	332	Sy1	24±6	GOALS	SABa	a
NGC 7591	23h18m16.3s	+06d35m09s	71.4	11.12	335	LINER	9±2	GOALS	SBbc	N

* 15 GHz images were used for measurements due to poor detections at 33 GHz.

NOTE — (1): Host galaxy of the nuclear ring. (2)&(3): coordinates of the host galaxy. (4): Distance to the host galaxy. For SFRS galaxies, we use redshift-independent distances reported in Kennicutt et al. (2011). For GOALS galaxies, we use luminosity distances reported in Armus et al. (2009) where they adopted the 3-attractor model (Mould et al., 2000). (5): Total infrared luminosity (8-1000μm) of the host galaxy in $\log_{10}$ Solar units ($L_\odot = 3.826 \times 10^{33}$ erg/s), calculated using distances from (4) and IRAS flux densities in Sanders et al. (2003) with recipes given in Sanders & Mirabel (1996). NGC 7469 is in a close interacting pair, so we use instead the value for the resolved major component from Howell et al. (2010). (6): Angular to physical scale conversion factor. For LIRGs, this is calculated using Ned Wright's Cosmology Calculator (Wright, 2006) in combination with the 3-attractor model (Mould et al., 2000). (7): References for active type classification: NGC 1097: Phillips et al. (1984); Storchi-Bergmann et al. (1993); NGC 3351: Planesas et al. (1997); NGC 4321:Ho et al. (1997); NGC 4826: García-Burillo et al. (2003); NGC 1614: Herrero-Illana et al. (2017); NGC 1797:Balzano (1983); NGC 7469: Osterbrock & Martel (1993); NGC 7591: Pereira-Santaella et al. (2010). (8): AGN contribution to the bolometric luminosity of the host galaxy, estimated by Díaz-Santos et al. (2017) for the GOALS galaxies using five different mid-IR AGN diagnostics. AGN contribution to the bolometric light is expected to be negligible in the SFRS galaxies (e.g. Dale et al., 2009). (9): Survey with which nuclear ring observations were taken. (10): Morphology classification of the host galaxy from the NASA/IPAC Extragalactic Database (NED). (11): Merger stages for the GOALS galaxies are determined by Stierwalt et al. (2013) via visual inspection of the Spitzer IRAC 3.6μm observations (N:non-merger, a:pre-merger, d:late-merger). Using the same criteria, we classify all SFRS galaxies as non-mergers, given the lack of massive neighbors in their proximity. *However, NGC 1097 is actively interacting with at least one dwarf companion (Bowen et al., 2016).

referred in this work are displayed in Figure 3.1 and 3.2, and descriptions of these images and extra information on individual sources are provided in Appendix 3.8.1. The characteristics of these images and associated observation information are listed in Table 3.2.

3.3.2 Archival CO(J=1-0) Data

To better understand the properties of star formation in nuclear rings, it is informative to study the molecular environments that give rise to this activity. For each host galaxy in the sample, we searched for archival CO(J=1-0) observations with resolutions that are comparable to or higher than our VLA observations to directly compare SF and cold molecular gas properties in its nuclear ring. Four galaxies in our sample have publicly available archival ALMA data that meet the above criteria, from ALMA projects 2012.1.00001.S (NGC 1097, PI: K. Sheth; unpublished), 2013.1.00885.S (NGC 3351, PI: K. Sandstrom; Leaman et al., 2019), 2015.1.00978.S (NGC 4321, PI: K. Sandstrom; unpublished), 2016.1.00972.S (NGC 4321, PI: K. Sandstrom; unpublished) and 2013.1.00218.S (NGC 7469, PI: T. Izumi; Zaragoza-Cardiel et al., 2017; Wilson et al., 2019). Each ALMA dataset was first re-processed using the appropriate CASA version and data calibration pipeline that are specified in the project's data calibration note from the archive. Continuum subtraction was performed using the `uvcontsub` task in CASA (version consistent with reduction pipeline). The reduced measurement sets were then re-imaged using `tclean` in CASAv4.7.0, using Briggs weighting with robust parameter of 0.5 and Högbom cleaning algorithm. For NGC 1097, because the native angular resolution of the dataset is about four times higher than the VLA data, we also tapered the *uv*-distribution of the measurement sets with a $3''.0$ Gaussian kernel to better compare with the VLA data. We then produced moment 0 maps from the continuum-subtracted CO(J=1-0)

Table 3.2: Observations and Image Characteristics of VLA Data

Galaxy	Project ID	Band	Configuration	Beam	PA (°)	Physical Resolution[a] (pc)	$\sigma_{\rm rms}$ (μJy/bm)
NGC 1097	11B-032	Ka	D	$3''.17 \times 1''.55$	26.7	107	40.4
	13B-215	Ku	C	$3''.81 \times 0''.99$	-7.6	69	20.0
	13B-215	S	B	$5''.76 \times 1''.80$	-27.4	125	46.3
IC 342	11B-032	Ka	D	$1''.76 \times 1''.72$	-34.3	28	35.2
	13B-215	Ku	C	$1''.72 \times 1''.13$	-9.5	18	15.1
	13B-215	S	B	$2''.23 \times 1''.76$	-0.8	28	38.5
NGC 3351	11B-032, 13A-129	Ka	D	$2''.27 \times 2''.04$	47.2	92	17.2
	13B-215	Ku	C	$1''.95 \times 1''.67$	-17.5	75	14.1
	13B-215	S	B	$2''.01 \times 1''.75$	43.6	79	17.2
NGC 4321	13A-129	Ka	D	$2''.41 \times 1''.77$	42.3	123	18.5
	13B-215	Ku	C	$1''.53 \times 1''.17$	17.0	82	9.7
	13B-215	S	B	$1''.89 \times 1''.72$	30.6	120	15.0
NGC 4826	13A-129	Ka	D	$2''.16 \times 1''.98$	65.9	51	13.4
	13B-215	Ku	C	$1''.46 \times 1''.33$	61.3	34	10.4
	13B-215	S	B	$1''.97 \times 1''.75$	67.3	45	14.0
NGC 1614	14A-471, 16A-204	Ka	A,C	$0''.12 \times 0''.06$	16.8	19	13.5
	14A-471	Ku	A,C	$0''.17 \times 0''.11$	-0.4	36	18.8
	14A-471	S	A,C	$0''.87 \times 0''.55$	26.8	178	12.3
NGC 1797	14A-471	Ka	C	$0''.76 \times 0''.56^{*}$	13.7	170	16.5
	14A-471	Ku	A,C	$0''.13 \times 0''.12$	15.6	36	10.0
	14A-471	S	A,C	$0''.80 \times 0''.54$	7.6	164	19.4
NGC 7469	14A-471	Ka	C	$0''.63 \times 0''.52^{*}$	2.4	173	21.1
	14A-471	Ku	C	$1''.44 \times 1''.12^{*}$	-30.8	372	13.5
	14A-471	S	A,C	$0''.65 \times 0''.50$	-43.4	166	40.2
NGC 7591	14A-471	Ka	C	$0''.63 \times 0''.51^{*}$	-4.1	171	17.9
	14A-471	Ku	A,C	$0''.13 \times 0''.11$	-17.6	37	9.4
	14A-471	S	A,C	$0''.68 \times 0''.54$	-50.7	181	27.9

[*] C configuration image was used due to limited dynamic range at A configuration.

[a] The smallest physical scale resolved by the synthesized beam at the distance of the galaxy, given the FWHM of the minor axis of the beam.

Note — The central frequencies for Ka, Ku and S bands are 33 GHz, 15 GHz, and 3 GHz respectively. The root-mean-square error $\sigma_{\rm rms}$ was measured manually on each image before primary beam correction in an emission-free region. A and C configuration datasets are weighted with 100:1 (A:C) before combined imaging to account for differences in uv-plane distribution.

line cubes using the `immoments` task in CASAv4.7.0.

Additionally, we downloaded high-resolution CO (J=1-0) moment 0 maps for NGC 4826 (Casasola et al., 2015) and IC 342 (Ishizuki et al., 1990) from NED. The map for NGC 4826 was observed by the IRAM Plateau de Bure Interferometer (PdBI), and provided in units of $\mathrm{M_\odot\,pc^{-2}}$. We used information from Table 1 and Equation 2 in Casasola et al. (2015) to convert the data to units of Jy/beam km/s. The map for IC 342 was observed using the 10-m sub-millimeter telescope (NRO10m) at Nobeyama Radio Observatory, and provided in units of Jy/beam m/s in B1950 coordinates. We used the `imregrid` task in CASA to re-map the datasets to match the coordinates of our VLA data (J2000), after which we converted the data to units of Jy/beam km/s.

Characteristics of these moment 0 maps are listed in Table 3.3. In Section 3.4.3, we utilize these moment 0 maps to estimate the cold molecular gas densities and gas depletion times in these six nuclear rings.

3.4 Data Analysis

Here we mainly use the 33 GHz continuum images for our analysis of the nuclear rings and individual NRSF regions because radio continuum emission above 30 GHz has been shown to effectively trace thermal free-free emission associated with ongoing massive SF in both normal galaxies and LIRGs (e.g. Murphy et al., 2012; Linden et al., 2019, 2020). For NGC 7591, we use the 15 GHz image instead because the available 33 GHz image does not resolve the ring structure.

3.4.1 Integrated ring measurements

To measure the integrated ring properties, we first quantify the spatial extent of each ring by defining an inner, peak, and outer radius/semi-major axis ($R_{\rm in}$, $R_{\rm peak}$, $R_{\rm out}$) based on its azimuthally-averaged light profile, as shown in Figure 3.3. These

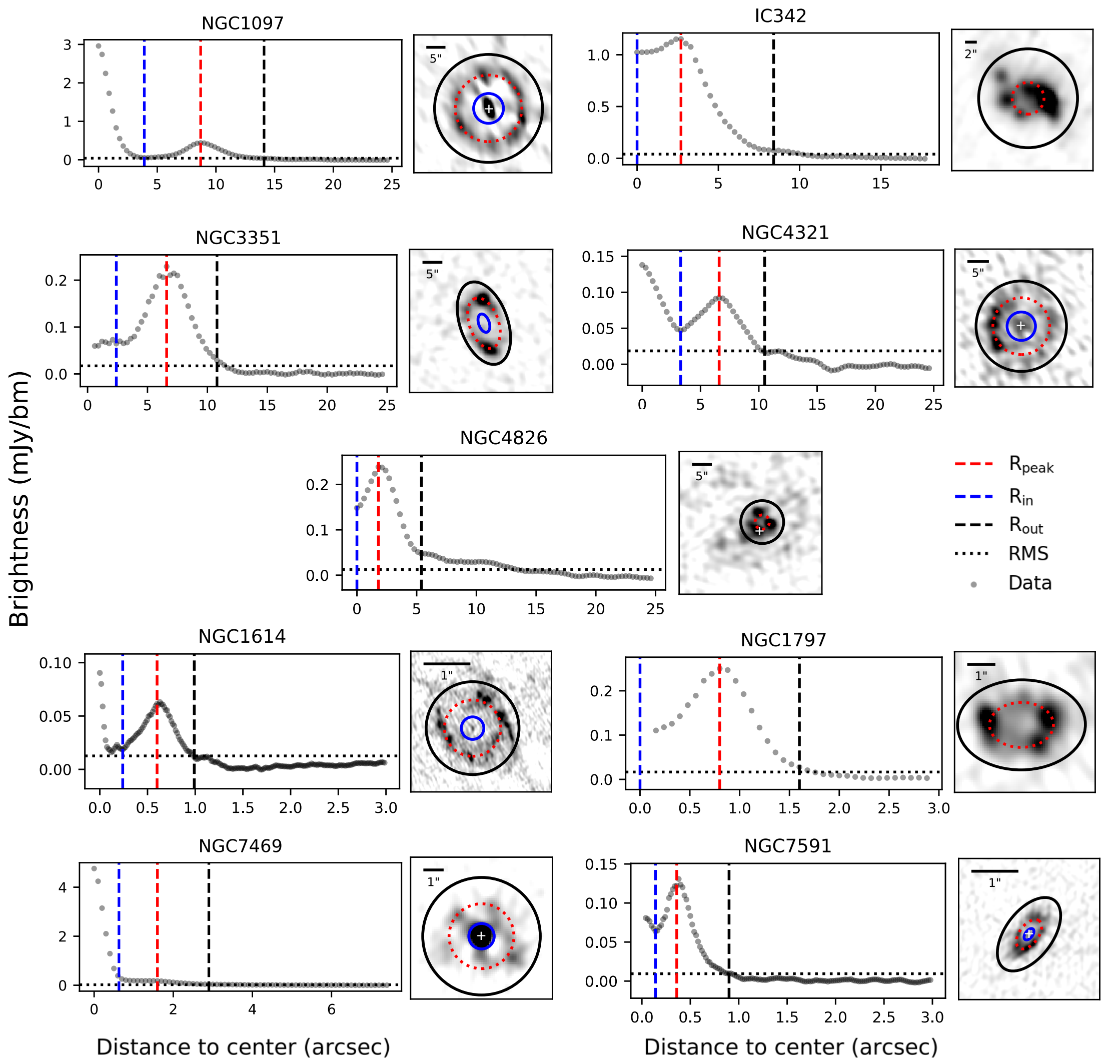

Figure 3.3: *Left column*: azimuthally-averaged light profile (in grey dotted line) from the 33 GHz image of each nuclear ring in the sample. The red dashed vertical line shows the radius of the ring ($R_{\rm peak}$), and the blue and black dashed vertical lines mark the inner and outer radius ($R_{\rm in}$, $R_{\rm out}$), respectively. See Section 3.4.1 for definitions of the different radii. *right column*: 33 GHz image of the nuclear ring shown in grey scale. Circles/ellipses overlaid in dotted red, solid blue and black mark $R_{\rm peak}$, $R_{\rm in}$ and $R_{\rm out}$, respectively. White "+" mark the locations of AGN. For NGC 7591, observation and measurements at 15 GHz are used here because the available 33 GHz image does not resolve the ring structure.

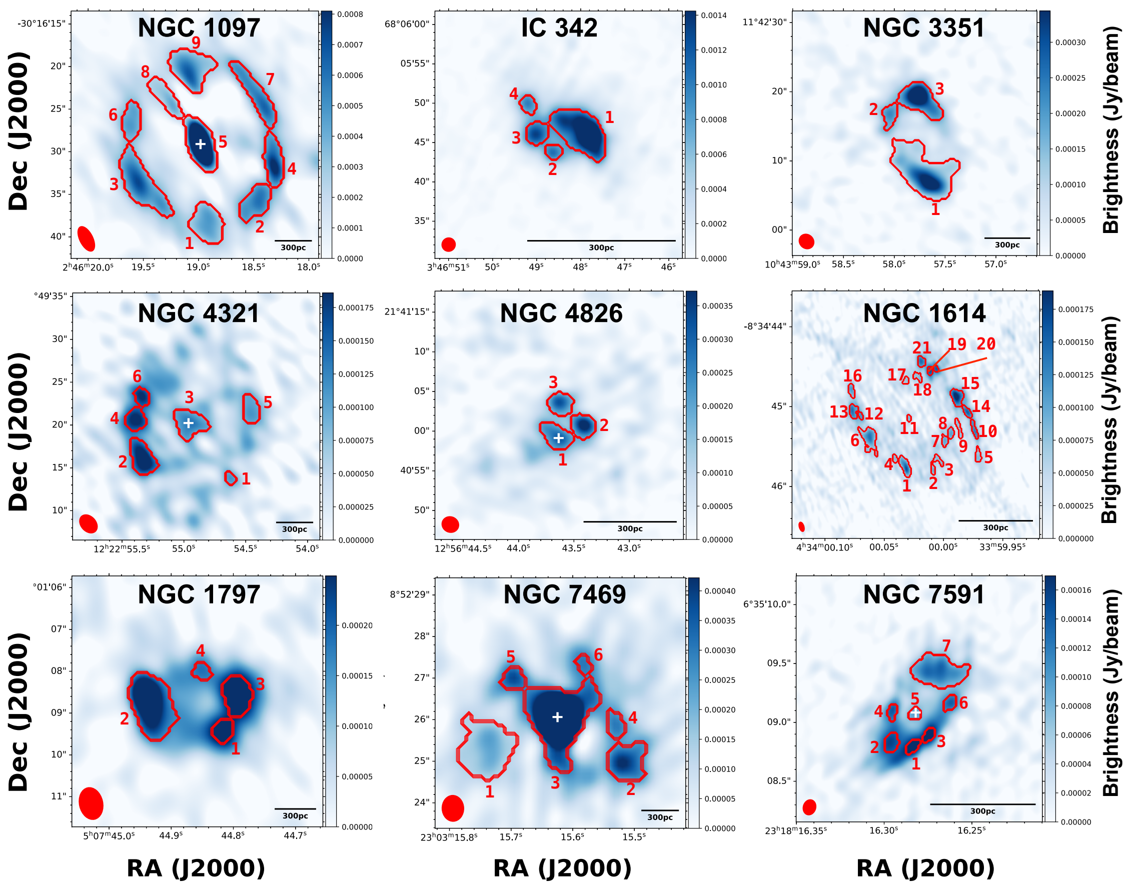

Figure 3.4: 33 GHz images of the sample galaxies (15 GHz for NGC 7591) with nuclei and NRSF regions identified with *Astrodendro* outlined in red. Region IDs (labeled in red) are assigned in ascending order based on region declinations. Red ellipses on the bottom left of the images represent the shapes and sizes of synthesized beams. Scale bars shown on the lower right reflect the physical scales of the observed structures at the distance of the host galaxy. White "+" signs mark the locations of known AGN.

Table 3.3: Observations and Image Characteristics of Ancillary CO (J=1-0) Data

Galaxy	Telescope	Project ID/Reference	Beam	PA (°)	Physical Resolution [a] (pc)	$\sigma_{\rm rms}$ (mJy/bm km/s)
NGC 1097	ALMA	2012.1.00001.S	$2''.85 \times 2''.57$	72.6	178	2.8
IC 342	NRO10m	Ishizuki et al. (1990)	$2''.39 \times 2''.27$	-31	36	3.5
NGC 3351	ALMA	2013.1.00885.S	$2''.03 \times 1''.22$	27.8	55	0.5
NGC 4321	ALMA	2015.1.00978.S	$2''.40 \times 2''.24$	-31.0	156	0.4
	ALMA	2016.1.00972.S				
NGC 4826	IRAM	Casasola et al. (2015)	$2''.53 \times 1.''.80$	39.0	156	0.25
NGC 7469	ALMA	2013.1.00218.S	$0''.91 \times 0''.51$	-48.8	169	0.2

[a] The smallest physical scale resolved by the synthesized beam at the distance of the galaxy, given the FWHM of the minor axis of the beam.

Note — For NGC 4321, we combined the measurement sets from two different ALMA projects to produce CO(J=1-0) moment 0 maps. For ALMA datasets, the root-mean-square error $\sigma_{\rm rms}$ was measured manually on each continuum-subtracted line cube before primary beam correction in an emission-free region across all channels. For NGC 4826 and IC 342, $\sigma_{\rm rms}$ were taken from the original references. ALMA datasets for NGC 1097 and NGC 4321 are unpublished. Dataset for NGC 3351 is published in Leaman et al. (2019), and dataset for NGC 7469 is published in Zaragoza-Cardiel et al. (2017) and Wilson et al. (2019).

light profiles are measured from the central coordinates of the host galaxies using 1-pixel wide circular annuli. Elliptical annuli are used for highly elliptical rings (NGC 3351, NGC 1797, NGC 7591). Details on the relevant procedures are provided in Appendix 3.8.2. In general, we locate $R_{\rm in}$ at the first local minimum of the light profile, and define $R_{\rm peak}$ at the local maximum outside of $R_{\rm in}$. To account for diffuse emission from the ring that is not necessarily axis-symmetric, we define $R_{\rm out}$ to be where the averaged light profile flattens towards the image noise level (i.e. $\sigma_{\rm rms}$ in Table 3.2). An exception to this is NGC 4826, whose averaged light profile contains contribution from a faint spiral structure that surrounds the ring, which we exclude from further analysis by setting $R_{\rm out}$ at the local minimum immediately outside $R_{\rm peak}$. Due to the limited resolution of the observations, light profiles of IC 342, NGC 4826 and NGC 1797 do not yield a well defined local minimum, therefore we do not use $R_{\rm in}$ for rings in these three galaxies. See Appendix 3.8.1 for more details on individual sources.

The flux of each ring is then measured within the area characterized by $R_{\rm in}$ and $R_{\rm out}$ via aperture photometry. For NGC 4826, a LINER AGN likely contributes to the ring emission due to $m = 1$ perturbation (García-Burillo et al., 2003), therefore we additionally mask the image at the reported AGN location ($\alpha_{\rm J2000}$ =12h56m43.64s, $\delta_{\rm J2000}$ =21d40m 59.30s) with a beam-sized aperture before performing aperture photometry. In Figure 3.3, we also mark the locations of known AGN with "+". We do not find similar cases of AGN emission contributing to the nuclear ring in the rest of the sample.

3.4.2 NRSF Region identification & measurements

Given the high resolution of our VLA observations, all nine nuclear rings are resolved at sub-kpc scales at 33 GHz or 15 GHz, thus allowing us to further characterize the properties of individual star-forming regions in these rings.

To identify and measure the flux of individual NRSF regions in each nuclear ring, we use the software *Astrodendro* (Robitaille et al., 2019), which measures hierarchical structures in an astronomical image using dendrograms. *Astrodendro* identifies and categorizes structures in an image into `trunk`, `branch` and `leaf`, based on three input parameters: the minimum brightness required for a structure to be physically meaningful (`min_value`), the minimum number of pixels in a structure (`min_npix`), and the minimum brightness relative to the local background required for a structure to be considered independent (`min_delta`). Structures identified as `leaf` are of the highest hierarchical order, which are the individual NRSF regions that we are interested in, while `branch` and `trunk` are the less luminous diffuse ring emission connecting the SF regions. Therefore here we only focus on the derived properties of `leaf` structures.

We run *Astrodendro* on the 33 GHz image of each nuclear ring (15 GHz for NGC 7591) with `min_value`$= 5\sigma_{\rm rms}$ and `min_delta`$=1\sigma_{\rm rms}$ to identify physically meaningful `leaf` structures, where $\sigma_{\rm rms}$ is the rms noise measured in an emission-free region of the image before primary beam correction (see Table 3.2). We set `min_npix` to be

1/4 the area of the synthesized beam, to avoid identifying noise spikes yet allowing detection of small, unresolved regions. Afterwards, we manually eliminate regions identified beyond the outer radius ($R_{\rm out}$) of the ring, to ensure we only include NRSF regions or nuclei in subsequent analyses. Figure 3.4 shows all the identified regions using *Astrodendro*. We note that varying `min_npix` by small amounts does not significantly alter the population of identified `leaf` structures. For example, setting `min_npix` to be 1/2 or 3/4 of the beam area only blends together Region 1 and 3 in NGC 1797, and Region 3 and 6 in NGC 7469, and the rest of region identification remains exactly the same, in terms of numbers, sizes and shapes.

The flux density and angular area of each identified region are also measured by *Astrodendro*, which can be heavily dependent on the signal-to-noise level of the region. To characterize the effect of image noise on the region size and flux measurements, we use a Monte Carlo method and re-run *Astrodendro* 1000 times randomly adjusting the brightness of each pixel sampling from a Gaussian distribution defined by the rms noise $\sigma_{\rm rms}$ and the assumed VLA flux calibration error ($\sim$ 10%). The standard deviations of the results from the 1000 runs are used to quantify the uncertainties in the flux and size measurements. For unresolved regions that have *Astrodendro*-measured sizes smaller than the beam areas after accounting for uncertainties, we instead measure their flux using beam-sized apertures and use the beam areas as upper-limits for their sizes.

Additionally, to estimate the ratio of thermal free-free emission to total radio continuum emission in these NRSF regions at 33 GHz, we measure radio spectral index between 15 and 33 GHz associated with each region. To do so, we smooth and regrid the native resolution 15 GHz and 33 GHz images of each nuclear ring (shown in Figure 3.1 and 3.2) to a common circular beam and pixel scale for consistent measurements of flux densities across the two frequencies. Assuming a single power-law model representing the combination of flat-spectrum thermal emission and steep-spectrum non-thermal emission $S \sim \nu^{\alpha}$, we can calculate the spectral index α associated with each region by measuring the linear slope between flux densities measured at 15 and 33 GHz with respect to frequency. Due to the coarser resolutions of the beam-matched images, the exact region areas identified with *Astrodendro* using native resolution images cannot be used here to extract spectral indices. As an approximation, for each region we measure its beam-matched 15 and 33 GHz flux using a common circular aperture with area equivalent to the region size as measured by *Astrodendro*. For regions with sizes smaller than the matched circular beams, we instead use beam-sized apertures to extract their associated spectral indices. Uncertainties in the spectral indices are calculated with error propagation.

3.4.3 Measurements of CO(J=1-0) maps

For the six galaxies that have high-resolution ancillary CO(J=1-0) data (see Section 3.3.2), we smooth and regrid the native resolution CO (J=1-0) moment 0 map and 33 GHz radio continuum map of the nuclear ring to a common circular beam and pixel scale for consistent flux measurements. We measure the total CO (J=1-0) and 33 GHz continuum flux of each ring using apertures defined by $R_{\rm in}$ and $R_{\rm out}$ (See Section 3.4.1). These values are used to derive the integrated molecular gas mass, average surface densities and gas depletion times in the ring in Section 3.5.5. For individual NRSF regions, we measure the CO (J=1-0) and 33 GHz flux using circular apertures with area equivalent to the region size as measured by *Astrodendro*. For regions with sizes smaller than the matched circular beams, we use beam-sized apertures instead.

3.5 RESULTS

Here we describe the results of the above measurements and further derive SFR, SFR surface density and gas depletion time for each ring as a whole, as well as for individual NRSF regions identified using *Astrodendro*. We also use the measured 15 – 33 GHz spectral index to derive the ratio of thermal free-free emission to total radio emission at 33 GHz associated with each NRSF regions. The measured and derived quantities for the nuclear rings are summarized in Table 3.4, and the ones for individual NRSF regions are reported in Table 3.6. In total, 63 regions are identified and measured with *Astrodendro*, as shown in Figure 3.4, including 58 NRSF regions (22 in normal galaxies, and 35 in LIRGs) and 5 nuclei (4 known AGN and 1 nuclear starburst). For completeness, in Table 3.6 we report measurements for all 63 identified regions, but only the 58 NRSF regions are included in the final analysis.

3.5.1 Ring size, SFR & SFR surface density

We use $R_{\rm peak}$, defined in Section 3.4.1, as an estimate for the radius/semi-major axis of the ring. The five nuclear rings in the sample of normal galaxies have radii of 43 – 599 pc, and the four nuclear rings in the LIRGs have radii of 121 – 531 pc.

Using flux measured with $R_{\rm in}$ and $R_{\rm out}$, we can calculate the integrated SFR within each ring using Equation 10 in Murphy et al. (2012):

$$\left(\frac{\rm SFR}{\rm M_{\odot}yr^{-1}}\right) = 10^{-27}\Big[2.18\left(\frac{T_e}{10^4{\rm K}}\right)^{0.45}\left(\frac{\nu}{\rm GHz}\right)^{-0.1} + 15.1\left(\frac{\nu}{\rm GHz}\right)^{\alpha^{\rm NT}}\Big]^{-1}\left(\frac{L_\nu}{\rm ergs^{-1}Hz^{-1}}\right) \tag{3.1}$$

where a Kroupa Initial Mass Function (IMF) is assumed. In this equation, L_ν is the spectral luminosity at the observed frequency ν, given by $L_\nu = 4\pi D_L^2 S_\nu^r$, where

S_ν^r is the measured total flux of the ring in Jy, D_L is the luminosity distance of the host galaxy (column 4 in Table 3.1), T_e is the electron temperature and $\alpha^{\rm NT}$ is the non-thermal spectral index. Here we adopt $T_e = 10^4\,{\rm K}$ and $\alpha^{\rm NT} = -0.85$, which have been extensively used to describe SF regions in normal galaxies and LIRGs (e.g. Murphy et al., 2012; Linden et al., 2019, 2020).

The integrated SFR has a range of 0.03 – 2.0 and 6.1 – 29 $\rm M_\odot\ yr^{-1}$ for rings in the normal galaxies and in the LIRGs, respectively. For the normal galaxies, the estimated nuclear ring radii and SFR are in agreement with previous measurements of the same galaxies at optical and IR wavelengths (e.g. Mazzuca et al., 2008; Comerón et al., 2010; Hsieh et al., 2011; Ma et al., 2018). Only a handful of similar measurements exist for the nuclear rings hosted in LIRGs because they are farther away and more obscured by dust. Our radio measurement is also consistent with extinction-corrected Paα measurement for the nuclear ring in NGC 1614 by Alonso-Herrero et al. (2001a), which confirms the effectiveness of using high-frequency radio continuum as extinction-free SFR tracer in these nuclear rings.

We further calculate the average SFR surface density, $\Sigma_{\rm SFR}$, in each ring, by dividing the integrated SFR over the area of the ring as defined in Figure 3.3, with $R_{\rm in}$ and $R_{\rm out}$. For rings with undefined $R_{\rm in}$ due to lack of resolution, we use the areas defined by their $R_{\rm out}$ minus the areas of the synthesized beams (Table 3.2) to account for the central cavities. The resulted range of $\Sigma_{\rm SFR}$ is 0.27 – 2.90 $\rm M_\odot\ yr^{-1}\ kpc^{-2}$ for nuclear rings in the normal galaxies, with a median value of $0.59\pm0.21\,\rm M_\odot\ yr^{-1}$ $\rm kpc^{-2}$. For rings in the LIRGs, $\Sigma_{\rm SFR}$ is higher by at least a factor of two, with a range of 6.0 – 97 $\rm M_\odot\ yr^{-1}\ kpc^{-2}$ and a median of $30\pm22\,\rm M_\odot\ yr^{-1}\ kpc^{-2}$.

3.5.2 Ring SFR vs. Host SFR

Here we estimate the fraction of total SFR of the host galaxy contributed by the nuclear ring. The relevant results are tabulated in Table 3.4 and 3.5. The total SFR of the galaxy is calculated from both FUV and IR emission to account for obscured and unobscured SF (Murphy et al., 2012):

$$\mathrm{SFR_{tot}} = \mathrm{SFR_{FUV}} + \mathrm{SFR_{IR}} \tag{3.2}$$

To calculate $\mathrm{SFR_{FUV}}$, we use GALEX FUV measurements from Clark et al. (2018) for the normal galaxies and from Howell et al. (2010) and Brown et al. (2014) for the LIRGs, along with Equation (2) from Murphy et al. (2012) assuming Kroupa IMF:

$$\mathrm{SFR_{FUV}} = 4.42 \times 10^{-44} L_{\mathrm{FUV}} \tag{3.3}$$

No GALEX FUV measurements are available for NGC 1614 and NGC 1797. For NGC 1614, SFR based on monochromatic UV measurement ($\lambda = 2800$Å) is available from U et al. (2012). Due to the different calibrations adopted, UV SFR from U et al. (2012) are consistently higher than values estimated using FUV measurements from Howell et al. (2010) among U/LIRGs studied in both works, by at least a factor of two. Therefore, for NGC 1614, here we adopt the SFR reported in U et al. (2012), but scaled down by a factor of two as an estimate for its FUV SFR. The FUV contribution to the total SFR is overall very low ($\sim 4\%$) in local U/LIRGs (Howell et al., 2010) therefore does not affect our estimates significantly. For the IR component, we applied L_{IR} from Table 3.1 to Equation (15) in Murphy et al. (2012), modified to account for

AGN emission:

$$\mathrm{SFR_{IR}} = 3.15 \times 10^{-44} L_{\mathrm{IR,SF}} \tag{3.4}$$

$$= 3.15 \times 10^{-44} L_{\mathrm{IR}}(1 - f_{\mathrm{AGN}}) \tag{3.5}$$

where f_{AGN} is the fraction of the bolometric luminosity of the host galaxy contributed by AGN emission (see Table 3.1 and Díaz-Santos et al., 2017). Because the above relations presented in Murphy et al. (2012) are calibrated against 33 GHz measurements, we can directly estimate the fraction of total SFR contributed by the nuclear ring by dividing the ring SFR, derived in the last Section, over $\mathrm{SFR_{tot}}$. The fractions are 7% – 39% for rings in the normal galaxies, and 49 – 60% for rings in the LIRGs, with median values of 12±9% and 56%±6%, respectively. We visualize this result in Figure 3.7 and discuss its implication in Section 3.6.2. For NGC 1614, a similar fraction has also been estimated by Xu et al. (2015). Even though measurements are made at 15 GHz for NGC 7591, we do not expect new measurements at 33 GHz to significantly alter our result.

3.5.3 Region size, SFR and SFR surface density

For each identified NRSF region, we calculate its SFR and Σ_{SFR} using the flux density and area measured in Section 3.4.2, along with Equation 5.4. For regions smaller than the beam areas accounting for uncertainties (i.e. unresolved), Σ_{SFR} calculated here are lower-limits. To compare the region size with values from the literature, we compute and report the effective radius $R_e = \sqrt{\mathrm{area}/\pi}$, which has a range of 16 – 184 pc for the 22 NRSF regions in the normal galaxies and 13 – 221 pc for the 35 NRSF regions in the LIRGs. Regions in the normal galaxies have SFR of 0.01 – 0.21 $\mathrm{M_\odot yr^{-1}}$, with a median of 0.04±0.03 $\mathrm{M_\odot yr^{-1}}$. Regions in the LIRGs

Table 3.4: Integrated Nuclear Ring Properties

Galaxy (1)	ν(GHz) (2)	$R_{\rm in}$(pc) (3)	$R_{\rm peak}$(pc) (4)	$R_{\rm out}$(pc) (5)	S_ν^r(mJy) (6)	SFR($M_\odot$ yr^{-1}) (7)	$\Sigma_{\rm SFR}$($M_\odot$ yr^{-1} kpc^{-2}) (8)	$\rm SFR_{ring}/SFR_{tot}$(%) (9)
NGC 1097	33	269	599	970	19 ±2.0	2.0 ±0.20	0.73±0.07	39±4
IC 342	33	-	43	134	29 ±2.9	0.16±0.02	2.90±0.29	7 ±1
NGC 3351	33	109	299	489	4.5±0.46	0.20±0.02	0.51±0.05	24±2
NGC 4321	33	229	458	728	3.9±0.42	0.41±0.04	0.27±0.03	13±1
NGC 4826	33	-	46	138	2.5±0.26	0.03±0.01	0.69±0.07	7 ±1
NGC 1614	33	77	194	319	12 ±1.3	29 ±3.0	97 ±9.9	60±8
NGC 1797	33	-	242	485	3.0±0.30	6.1 ±0.63	6.0 ±0.62	49±5
NGC 7469	33	208	531	963	8.1±0.83	21 ±2.1	7.6 ±0.78	57±7
NGC 7591	15	47	121	301	4.2±0.43	8.0 ±0.82	53 ±5.3	59±6

Note — (1): Host galaxy of the nuclear ring. (2): Frequency at which sizes and SFR are measured. (3)-(5): inner, peak and outer radius of the ring, as defined in Section 3.4.1. Details on individual source are described in Appendix 3.8.1.(6): Flux density enclosed by apertures with $R_{\rm out}$ and $R_{\rm in}$. For NGC 4826, off-centered AGN emission is excluded. (7): Star formation rates calculated using Eq.5.4 and values from (6). (8): Star formation rate surface densities of each ring, calculated by dividing (7) over the area the ring extends. See Section 3.5.1 for details. (9): Fraction of the total SFR of the host galaxy in the nuclear ring. See Section 3.5.2 and Table 3.5 for details.

Table 3.5: Host Galaxy Star Formation Rates

Galaxy (1)	$\mathrm{SFR_{FUV}}$ ($\mathrm{M_\odot\ yr^{-1}}$) (2)	$\mathrm{SFR_{IR}}$ ($\mathrm{M_\odot\ yr^{-1}}$) (3)	$\mathrm{SFR_{tot}}$ ($\mathrm{M_\odot\ yr^{-1}}$) (4)
NGC 1097	0.69±0.03	4.4±0.0	5.1±0.0
IC 342	1.50±0.07	0.9±0.0	2.4±0.0
NGC 3351	0.15±0.01	0.7±0.0	0.86±0.01
NGC 4321	0.7±0.03	2.6±0.1	3.3±0.1
NGC 4826	0.04±0.01	0.4±0.0	0.46±0.01
NGC 1614	1.5*	47±4.3	48±4
NGC 1797	-*	12±0.4	12±0.4
NGC 7469	1.7±0.0	37±3.0	39±3
NGC 7591	0.4±0.1	13±0.3	14±0.3

Note — (1): Host galaxy name. (2): Star formation rates derived from GALEX FUV flux measurements by Clark et al. (2018), Howell et al. (2010) and Brown et al. (2014), using Eq.(3).*GALEX measurements are not available for NGC 1614 and NGC 1797. For NGC 1614, we use monochromatic UV SFR from U et al. (2012) scaled down by a factor of two as an estimate for FUV SFR. (3): Star formation rates derived from total IR luminosity, accounting for AGN contribution to the bolometric luminosity of the LIRGs (Table 3.1), using Eq.5. (4): Total star formation rates of the host galaxy. See Section 3.5.2 for more details.

have SFR of 0.08 – 1.7 $\mathrm{M_\odot yr^{-1}}$, with a median of 0.25±0.12 $\mathrm{M_\odot yr^{-1}}$. Consequently, Σ_{SFR} for regions in the LIRGs ranges from 7 – 402 $\mathrm{M_\odot yr^{-1} kpc^{-2}}$ with a median of 197±78 $\mathrm{M_\odot yr^{-1} kpc^{-2}}$, about an order of magnitude higher compared to regions in the normal galaxies, whose Σ_{SFR} ranges from 0.4 – 9.2 $\mathrm{M_\odot yr^{-1} kpc^{-2}}$ with a median of 1.4±0.9 $\mathrm{M_\odot yr^{-1} kpc^{-2}}$. We discuss the potential effect of resolution on the results in Section 3.6.3.

3.5.4 Thermal Fractions at 33 GHz

Radio continuum captures both non-thermal synchrotron emission of cosmic ray electrons accelerated by supernovae, and thermal free-free emission associated with HII regions of massive stars (< 10 Myr). At high radio frequencies, radio emission has been directly related to ionizing photon produced by young massive stars (Murphy et al., 2012), with thermal fractions (i.e. ratio of thermal free-free emission to total radio continuum emission) $\gtrsim 90\%$ at 33 GHz in individual star-forming regions in nearby spiral galaxies (Linden et al., 2020). However, it has been shown that even at 33 GHz, radio continuum emission in local U/LIRGs may be largely non-thermal, due to dust absorption of ionizing photons (Barcos-Muñoz et al., 2015, 2017).

To understand what is driving the 33 GHz radio continuum emission in our sample of nuclear rings on sub-kpc scales, we estimate thermal fractions at 33 GHz, $f_{\rm th}$, using spectral index measured between 15 and 33 GHz (see Section 3.4.2), and Equation (11) from Murphy et al. (2012):

$$f_{\rm th}^{\nu_1} = \frac{\left(\frac{\nu_2}{\nu_1}\right)^{\alpha} - \left(\frac{\nu_2}{\nu_1}\right)^{\alpha_{\rm NT}}}{\left(\frac{\nu_2}{\nu_1}\right)^{-0.1} - \left(\frac{\nu_2}{\nu_1}\right)^{\alpha_{\rm NT}}} \tag{3.6}$$

where α is the spectral index measured between ν_1 and ν_2 (33 and 15 GHz), and $\alpha_{\rm NT}$ is the non-thermal spectral index. Almost all regions have $-0.85 < \alpha < -0.1$ within uncertainties, therefore we adopt $\alpha_{\rm NT} = -0.85$ for our calculations following Murphy et al. (2012). Out of the total 58 NRSF regions, three have $\alpha \lesssim -0.85$, which means their radio continuum spectra between 15 and 33 GHz are steeper than the typical non-thermal spectrum. In these cases we set $\alpha_{\rm NT} = \alpha - 0.1$ based on previous measurements of the maximum dispersion of non-thermal spectral index given by $\sigma_{\alpha_{\rm NT}} \simeq 0.1$ (Niklas et al., 1997; Murphy et al., 2011b, 2012). Additionally, three NRSF regions have $\alpha \gtrsim -0.1$, in which cases we set $f_{\rm th}$ to 100%, assuming the spectral flattening is caused by increasing thermal fraction. Alternatively, it may have originated from $\alpha_{\rm NT}$ flattening or anomalous microwave emission (e.g. Dickinson et al., 2018), which will require future matched-resolution observations at more than two radio frequencies to confirm.

Here we use only 15 and 33 GHz images to estimate $f_{\rm th}$ because 3 GHz observations from the GOALS equatorial survey do not resolve the ring structures except for in NGC 7469. Linden et al. (2020) observed similar spectral steepness at 3 – 33 GHz and 15 – 33 GHz for the full SFRS sample, therefore we do not expect to overestimate 33 GHz thermal fractions in NRSF regions in the normal galaxies by using only 15 and 33 GHz measurements. However, in a study of extra-nuclear SF regions in local LIRGs, Linden et al. (2019) observed steeper spectral profile at 3 – 33 GHz compared to 15 – 33 GHz on kpc scales. Therefore the thermal fractions estimated at 33 GHz for the sample of NRSF regions in LIRGs may be higher than reported here when matched-resolution observations at 3 GHz are included, despite that we did not observe significant spectral flattening at 15 – 33 GHz compared to 3 – 33 GHz in NGC 7469.

To better visualize the free-free emission distribution in these rings, we additionally construct pixel-by-pixel maps of $f_{\rm th}$, as shown in Figure 3.5. We mask all values below $5\sigma_{\rm rms}$ for 15 and 33 GHz beam-matched images to ensure reliable outputs, after which we calculate α and $f_{\rm th}$ at each pixel. These maps show significant spatial variation in the distribution of thermal emission in these nuclear rings, with areas of high $f_{\rm th}$ mostly corresponding to the identified NRSF regions. Variations in $f_{\rm th}$ on scales smaller than the matched beams are highly correlated and therefore not physically significant.

The estimated $f_{\rm th}$ has a range of 35 – 100% and 4 – 100% for NRSF regions in the normal galaxies and in the LIRGs, respectively. We note that low resolution ($\sim$ 0".6 or 200pc) 15 and 33 GHz images were used to calculate $f_{\rm th}$ for NGC 1797, NGC 7469 and NGC 7591 because the high resolution images do not have strong enough detection for robust measurements. This means that the physical scales at which $f_{\rm th}$

are measured are 2-5 times larger than the spatial extent of the identified regions, likely including areas with little SF or diffuse non-thermal emission (i.e. cosmic rays accelerated by supernovae). This can skew $f_{\rm th}$ towards lower values, and therefore values reported in Table 3.6 may be interpreted as lower-limits. We further discuss the implications of these results in Section 3.6.5.

3.5.5 Gas depletion times

In the left panels of Figure 3.6, we show the beam-matched CO (J=1-0) moment 0 maps (in color) and 33 GHz continuum data (in contour) for the six nuclear rings in the sample that have archival CO (J=1-0) data at resolutions comparable to the VLA data (Section 3.3.2). We can see that the nuclear rings observed in the radio continuum are largely co-spatial with the cold molecular gas, and molecular spiral arms are visible beyond the rings in NGC 1097, IC 342, NGC 3351 and NGC 4321. Using the measurements of CO (J=1-0) and 33 GHz continuum emission on these resolution-matched maps, we can calculate the cold molecular gas mass ($M_{\rm mol}$) and surface densities ($\Sigma_{\rm mol}$) in these six nuclear rings and their individual NRSF regions, and make direct comparisons with the SFR and $\Sigma_{\rm SFR}$ to estimate the timescale at which SF depletes the molecular gas, which is used in both observational and theoretical studies to quantify star formation efficiencies (i.e. $\tau_{\rm dep} = 1/{\rm SFE} = \Sigma_{\rm mol}/\Sigma_{\rm SFR}$; e.g. Bigiel et al., 2008; Wilson et al., 2019; Moreno et al., 2021).

We follow Herrero-Illana et al. (2019) and use equation from Solomon et al. (1992) to convert the measured CO(J=1-0) flux to molecular gas mass:

$$M_{\rm mol} = \alpha_{\rm CO} L'_{\rm CO} \tag{3.7}$$

$$= 2.45 \times 10^3 \alpha_{\rm CO} \left(\frac{S_{\rm CO}\Delta\nu}{\rm Jy\ km/s}\right)\left(\frac{D_L}{\rm Mpc}\right)^2 (1+z)^{-1} \tag{3.8}$$

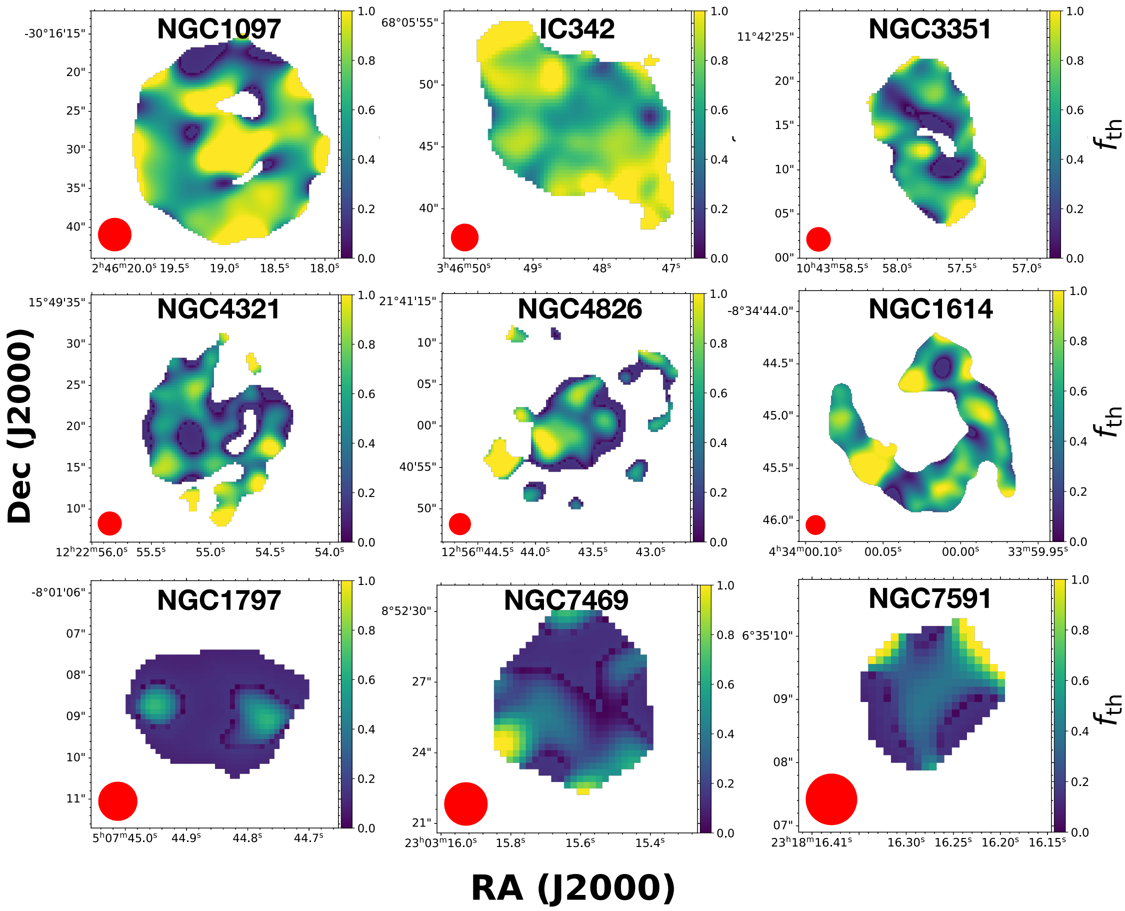

Figure 3.5: Maps of thermal fractions at 33 GHz of the sample galaxies. Each map was calculated from a pair of beam-matched 15 and 33 GHz images as described in Section 3.5.4. Red filled circles on the lower left of the maps represent the final matched beam. These maps show significant spatial variation in the distribution of thermal emission in these nuclear rings. Lower resolution images are used for NGC 1797, NGC 7469 and NGC 7591.

where $M_{\rm mol}$ is in units of $\rm M_\odot$, $S_{\rm CO}\Delta\nu$ is the integrated line flux in Jy km/s and D_L is the luminosity distance in Mpc reported in Table 3.1 given the redshift z. Finally, $\alpha_{\rm CO}$ is the CO-to-$\rm H_2$ conversion factor, in units of $\rm M_\odot(K\ km\ s^{-1}\ pc^{-2})^{-1}$. We adopt $\alpha_{\rm CO} = 4.3\ \rm M_\odot(K\ km\ s^{-1}\ pc^{-2})^{-1}$ for the five nuclear rings hosted in normal galaxies following previous resolved studies of nearby disk galaxies (Bigiel et al., 2008; Leroy et al., 2013), and we use the U/LIRG value $\alpha_{\rm CO} = 1.8\ \rm M_\odot(K\ km\ s^{-1}\ pc^{-2})^{-1}$ from Herrero-Illana et al. (2019) for the nuclear ring in NGC 7469. We use Equation 5.4 to convert the 33 GHz continuum flux to SFR, and $\Sigma_{\rm SFR}$ and $\Sigma_{\rm mol}$ are calculated using the physical areas of the adopted apertures (See Section 3.4.3). In Table 3.7 we summarize the derived quantities for the nuclear rings and the individual NRSF regions.

Based on calculations using previous global CO (J=1-0) measurements (Young et al., 1996; Crosthwaite, 2001; Crosthwaite et al., 2001; García-Burillo et al., 2003; Davies et al., 2004), these six nuclear rings contain $\sim 10-30\%$ of the total molecular gas mass of their host galaxies; this gas is available to fuel the active starbursts that are responsible for $\sim 10-60\%$ of the total SFR of the host galaxies. The average $\Sigma_{\rm mol}$ has a range of $280 \pm 40 - 900 \pm 90\,\rm M_\odot yr^{-1}pc^{-2}$ in these nuclear rings, and $84 \pm 180 - 1970 \pm 200\,\rm M_\odot yr^{-1}pc^{-2}$ in the NRSF regions. The gas depletion times $\tau_{\rm dep}$ associated with the individual NRSF regions range from $0.07 - 1.4$ Gyr. The median $\tau_{\rm dep}$ for regions in the normal galaxies is 0.6 ± 0.5 Gyr. This is almost an order of magnitude longer than regions in NGC 7469, which has a median $\tau_{\rm dep}$ of 0.08 ± 0.01 Gyr. These values agree with results from previous sub-kpc studies of normal galaxies (Bigiel et al., 2008; Leroy et al., 2013) and U/LIRGs (Wilson et al., 2019). Despite that our measurements are made on scales larger than the region sizes measured using native-resolution radio maps, the median $\tau_{\rm dep}$ for the NRSF regions is largely consistent with $\tau_{\rm dep}$ measured over the entire ring for each galaxy, therefore higher-resolution measurements may increase the scatter of $\tau_{\rm dep}$ estimated for these regions but will not significantly change the results. In the right panels of Figure 3.6, we also show pixel-by-pixel map of $\tau_{\rm dep}$ for each nuclear ring for more direct visualization. We note that $\tau_{\rm dep}$ derived near AGN is not meaningful as the 33 GHz emission is not associated solely with star formation, and hence we also do not report $\Sigma_{\rm SFR}$ and $\tau_{\rm dep}$ in Table 3.7 for regions containing AGN. We further discuss these results in the context of universal star formation relation (e.g. Kennicutt, 1998) in Section 3.6.6.

3.6 Discussion

Our selection criteria has resulted in the identification of NRSF in four LIRGs and five normal galaxies. The NRSF in our sample exhibits diverse spatial distributions (Figure 3.1 and 3.2). For examples, NGC 1097 and NGC 1614 have more randomly distributed NRSF regions along the rings compared to NGC 3351 and NGC 1797, where bright regions occur on opposite sides of the ring. Several studies have discussed the potential mechanisms that may give rise to certain alignments of bright NRSF regions, such as orbit crowding of gas clouds at the ends of nuclear stellar bars (e.g., Kenney & Lord, 1991; Mazzarella et al., 1994; Englmaier & Shlosman, 2004), or specific gas inflow rates into the ring (e.g., Seo & Kim, 2013). Depending on how gas accumulates, NRSF can either take place stochastically in the ring due to gravitational instability, resulting in random spatial distribution of "hot spots", or close to the contact points between the ring and dust lanes in multiple bursts (e.g. Böker et al., 2008). Given the limited sample size, we do not further discuss the implications associated with the NRSF spatial distribution, but simply provide descriptions of our observations and relevant information from previous studies on individual nuclear rings in Appendix A. Instead, we focus our discussions on the implications of the results in Section 4.4, and the limitations of the present sample.

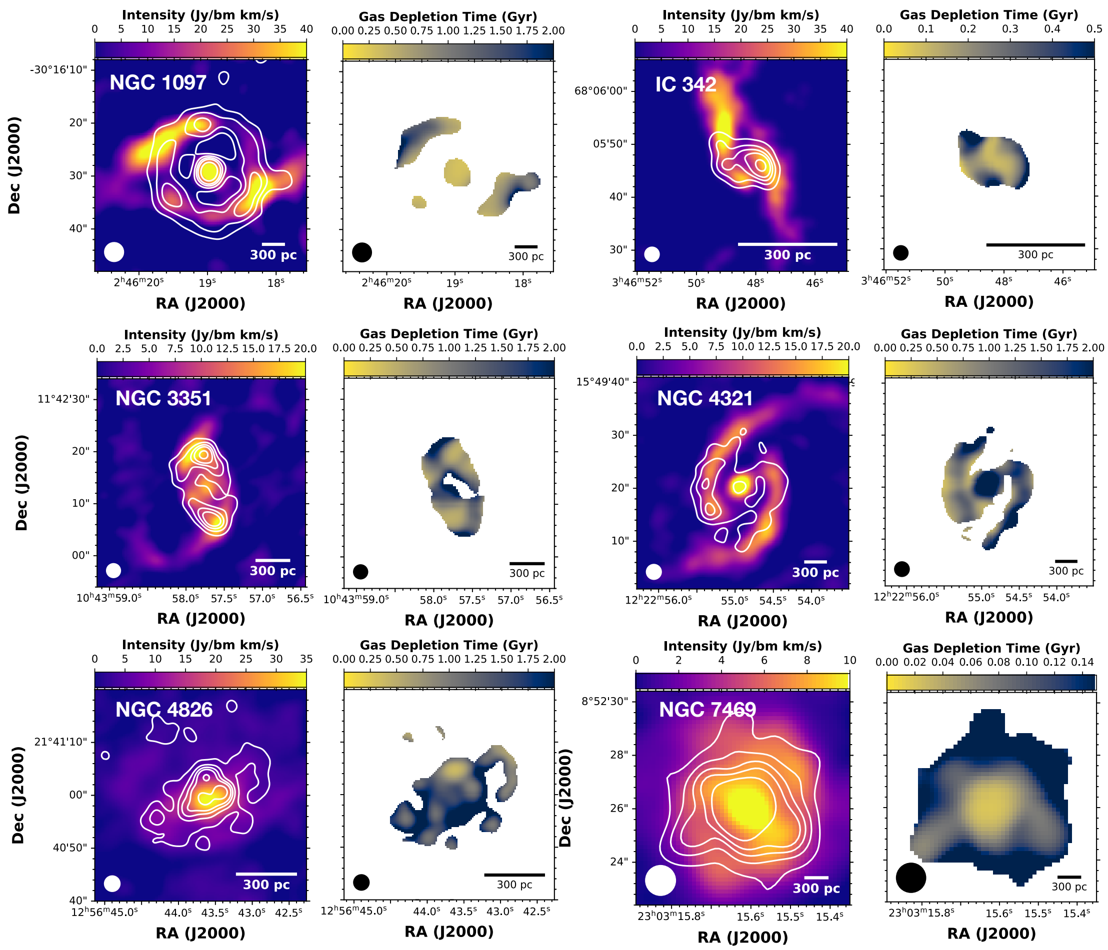

Figure 3.6: Six nuclear rings with high-resolution archival CO (J=1-0) datasets. For each galaxy panel, *left:* Beam-matched archival CO(J=1-0) moment 0 map (in color) and VLA 33 GHz continuum image (white contour). The contours corresponds to $5, 10, 15, 20, 30\,\sigma_{\rm rms}$ levels in 33 GHz intensity; *right:* Maps of gas depletion time $\tau_{\rm dep} = \Sigma_{\rm mol}/\Sigma_{\rm SFR}$, using maps shown on the *left*. Matched beams are represented by white/black filled circles on the lower left of each image in the left/right panel. The radio continuum is largely co-spatial with cold molecular gas. In NGC 1097, IC 342, NGC 3351, and NGC 4321, prominent spiral structures overlap with the SF nuclear rings and extend farther out into the galactic disks. The spiral structure in NGC 7469 is much more tightly wound and less distinct, and its nuclear ring has an order of magnitude shorter gas depletion times on average.

3.6.1 Sample limitation

The sample presented in this work is limited by several effects. Given the resolution of the observations, a nuclear ring has to have an angular radius larger than the synthesized beam in order for the ring structure to be resolved. An example is NGC 4579, a known nuclear ring host in SFRS, whose ring radius is estimated to be 1.6" from HST optical and near-IR observations (Comerón et al., 2010), which is smaller than the 33 GHz beam size of $\sim$ 2", and therefore not included in our sample. Additionally, the surface brightness of the nuclear ring must be high enough above the sensitivity limits of the observations for the ring structure to be visually distinct. NGC 4736 and NGC 5194 are two other galaxies from SFRS that are included in Comerón et al. (2010) but excluded from our sample because many of their NRSF regions are too faint for the ring structure to be visually distinct. This may be due to overall lower level of SF activity, and/or a lack of sensitivity of the observations. For example, with an estimated angular radius of 50"(1.2 kpc, Comerón et al., 2010), the ring in NGC 4736 is detected close to the edge of the 33 GHz primary beam, where sensitivity is significantly worse compared to the phase center, which results in incomplete detection of the ring structure.

For observations from the GOALS equatorial survey, rings at very close distances such as the one in NGC 1068 become too highly-resolved at A configuration to be detected given the sensitivity limit and rings that are far away may either have been unresolved or lack consistent detection of NSRF regions for the ring structure to be visually identified. The fact that all four LIRGs in our sample have similar luminosity distances at $\sim$ 70 Mpc may be the result of such a trade-off between physical resolution and sensitivity. Finally, rings that are highly inclined may appear linear and therefore are not represented in our sample. High-resolution kinematics studies

Table 3.6: Region Properties

Galaxy (1)	ν(GHz) (2)	ID (3)	S_ν(mJy) (4)	R_e(pc) (5)	SFR($M_\odot$ yr^{-1}) (6)	Σ_{SFR}($M_\odot yr^{-1} kpc^{-2}$) (7)	α (8)	f_{th}(%) (9)	Nucleus (10)
NGC 1097	33	1	0.92±0.12	142±22	0.10±0.01	1.5±0.1	-0.18±0.23	91±24	
..	33	2	0.85±0.16	117±25	0.09±0.02	2.0±0.1	-0.25±0.22	84±24	
..	33	3	2.00±0.25	184±27	0.21±0.03	1.9±0.1	-0.44±0.20	62±26	
..	33	4	1.09±0.08	123±12	0.11±0.01	2.4±0.1	-0.50±0.21	54±28	
..	33	5	3.48±0.04	163±6	N/A	N/A	-0.02±0.19	100±17	AGN
..	33	6	0.64±0.11	113±21	0.07±0.01	1.6±0.1	-0.52±0.23	51±32	
..	33	7	0.89±0.60	121±85	0.09±0.06	2.0±0.5	-0.32±0.23	77±27	
..	33	8	0.42±0.07	104±18	0.04±0.01	1.3±0.1	-0.05±0.30	100±28	
..	33	9	1.40±0.08	164±14	0.15±0.01	1.7±0.1	-0.40±0.21	66±26	
IC 342	33	1	12.3±0.42	49±3	0.07±0.01	9.2±0.2	-0.33±0.18	75±21	
..	33	2	0.86±0.12	16±3	0.01±0.01	5.9±0.3	-0.36±0.19	72±23	
..	33	3	2.10±0.25	23±3	0.01±0.01	6.8±0.3	-0.27±0.18	82±20	
..	33	4	0.86±0.12	17±3	0.01±0.01	5.4±0.3	-0.20±0.19	90±20	
NGC 3351	33	1	1.50±0.07	167±15	0.07±0.01	0.78±0.02	-0.44±0.19	62±24	
..	33	2	0.19±0.04	58±13	0.01±0.01	0.82±0.06	-0.62±0.22	37±33	
..	33	3	1.20±0.05	118±8	0.05±0.01	1.2±0.1	-0.43±0.18	62±24	
NGC 4321	33	1	0.06±0.01	<72	0.01±0.01	>0.42	-0.30±0.35	79±40	
..	33	2	0.33±0.03	119±15	0.04±0.01	0.79±0.04	-0.35±0.21	73±25	
..	33	3	0.20±0.04	110±26	N/A	N/A	-0.63±0.24	35±36	AGN
..	33	4	0.17±0.03	85±17	0.02±0.01	0.80±0.06	-0.52±0.22	51±31	
..	33	5	0.09±0.03	77±25	0.01±0.01	0.51±0.06	-0.61±0.29	38±42	
..	33	6	0.11±0.03	68±19	0.01±0.01	0.78±0.07	-0.47±0.23	57±31	
NGC 4826	33	1	0.47±0.05	44±6	N/A	N/A	-0.47±0.19	58±26	AGN
..	33	2	0.44±0.03	40±4	0.01±0.01	1.3±0.1	-0.51±0.19	53±26	
..	33	3	0.34±0.03	38±4	0.01±0.01	1.1±0.1	-0.30±0.21	78±24	
NGC 1614	33	1	0.27±0.03	27±4	0.65±0.07	275±47	-0.55±0.31	47±44	
..	33	2	0.06±0.01	15±3	0.14±0.03	213±68	-0.38±0.39	68±48	
..	33	3	0.05±0.04	14±9	0.13±0.08	208±193	-0.31±0.38	77±44	
..	33	4	0.04±0.01	<14	0.10±0.03	>149	-0.79±0.36	10±60	

Table 3.6 continued

Table 3.6: Region Properties (continued)

Galaxy (1)	ν(GHz) (2)	ID (3)	S_ν(mJy) (4)	R_e(pc) (5)	SFR($M_\odot$ yr^{-1}) (6)	Σ_{SFR}($M_\odot$yr^{-1}kpc^{-2}) (7)	α (8)	f_{th}(%) (9)	Nucleus (10)
..	33	5	0.08±0.02	18±5	0.20±0.06	204±83	-0.28±0.44	81±50	
..	33	6	0.17±0.19	22±26	0.41±0.45	266±433	-0.07±0.30	100±29	
..	33	7	0.08±0.02	16±5	0.19±0.06	241±110	-0.33±0.34	76±39	
..	33	8	0.08±0.02	16±4	0.19±0.04	249±88	-0.43±0.32	63±40	
..	33	9	0.03±0.02	<14	0.08±0.03	>136	-0.74±0.34	18±55	
..	33	10	0.10±0.06	16±10	0.25±0.15	306±277	-0.39±0.33	67±41	
..	33	11	0.04±0.01	<14	0.09±0.03	>135	-0.85±0.57	15±86	Starburst
..	33	12	0.06±0.01	<14	0.15±0.03	>241	-0.46±0.29	59±38	
..	33	13	0.20±0.03	22±4	0.48±0.08	311±82	-0.27±0.30	82±33	
..	33	14	0.15±0.03	18±6	0.36±0.07	327±94	-0.36±0.28	71±34	
..	33	15	0.45±0.07	31±4	1.1±0.16	366±85	-0.26±0.25	83±27	
..	33	16	0.12±0.02	19±3	0.28±0.05	236±66	-0.45±0.40	60±52	
..	33	17	0.04±0.01	13±4	0.10±0.03	197±83	-0.03±0.43	100±40	
..	33	18	0.07±0.02	17±6	0.17±0.06	207±103	-0.36±0.33	71±40	
..	33	19	0.10±0.03	14±4	0.25±0.06	402±150	-0.89±0.24	15±34	
..	33	20	0.09±0.02	<14	0.21±0.04	>326	-0.80±0.24	8±41	
..	33	21	0.16±0.03	19±4	0.38±0.07	316±92	-0.55±0.27	47±38	
NGC 1797	33	1	0.18±0.02	<100	0.38±0.05	>12	-0.78±0.21	11±35	
..	33	2	0.68±0.03	194±12	1.4±0.05	12±1	-0.67±0.19	28±30	
..	33	3	0.35±0.04	126±17	0.73±0.08	14±3	-0.68±0.20	28±32	
..	33	4	0.11±0.02	<99	0.23±0.04	>7.4	-1.19±0.22	12±26	
NGC 7469	33	1	0.64±0.11	221±45	1.7±0.29	11±3	-0.57±0.18	43±27	
..	33	2	0.60±0.07	157±24	1.6±0.19	20±4	-0.79±0.18	10±31	
..	33	3	6.06±0.20	268±30	N/A	N/A	-0.74±0.18	19±29	AGN
..	33	4	0.17±0.04	90±23	0.45±0.11	18±6	-0.83±0.18	4±32	
..	33	5	0.24±0.04	96±20	0.61±0.11	21±6	-0.74±0.18	17±30	
..	33	6	0.19±0.03	<95	0.49±0.07	>17	-0.88±0.18	15±27	
NGC 7591	15	1	0.14±0.03	21±5	0.27±0.07	197±69	-0.64±0.18	34±27	
..	15	2	0.12±0.04	21±7	0.22±0.07	165±77	-0.66±0.18	30±28	

Table 3.6 continued

Table 3.6: Region Properties (continued)

Galaxy (1)	ν(GHz) (2)	ID (3)	S_ν(mJy) (4)	R_e(pc) (5)	SFR($M_\odot$ yr^{-1}) (6)	Σ_{SFR}($M_\odot$yr^{-1}kpc^{-2}) (7)	α (8)	f_{th}(%) (9)	Nucleus (10)
..	15	3	0.12±0.02	19±5	0.22±0.05	197±63	-0.63±0.18	35±27	
..	15	4	0.09±0.02	19±5	0.17±0.04	139±46	-0.65±0.18	32±28	
..	15	5	0.05±0.01	18±5	N/A	N/A	-0.63±0.18	35±27	AGN
..	15	6	0.11±0.02	22±6	0.21±0.04	130±43	-0.63±0.18	35±27	
..	15	7	0.40±0.24	46±30	0.76±0.47	115±103	-0.64±0.18	34±28	

Note — (1): Host galaxy of the nuclear ring; (2): Frequency at which regions were identified and SFR and sizes were measured. For NGC 7591, 15GHz image was used instead. (3): Identifier of the region in reference to Figure 3.4. (4): Flux density of the region. (5): Effective radius of the region assuming region is circular (Section 3.5.3). Beam areas are used for unresolved regions as upper-limits for their sizes, indicated by "<". (6): SFR calculated using Eq.5.4 and (5) for non-AGN regions; (7): Σ_{SFR} estimated by dividing (6) over region area $A = \pi R_e^2$ (in kpc^2). Unresolved regions are given lower-limits for their Σ_{SFR}, indicated by ">"; (8): Spectral index associated with the region (Section 3.5.4) measured from 15 to 33 GHz. (9): Fraction of thermal emission at 33 GHz estimated using α (Section 3.4.2). Given the coarser resolution of the beam-matched 15 and 33 GHz images on which α were measured, the reported 33 GHz thermal fractions may be considered as lower-limits. See Section 3.6.5 for discussion. (10): Whether the region corresponds to a galactic nucleus (AGN/starburst), see Table 3.1 for references.

Table 3.7: Quantities derived from resolution-matched 33 GHz and CO(J=1-0) maps

	Galaxy (1)	ID (2)	$A_{ap}('' ^2)$ (3)	$M_{mol}(10^6\,M_\odot)$ (4)	$\Sigma_{mol}(M_\odot yr^{-1}pc^{-2})$ (5)	$\Sigma_{SFR}(M_\odot yr^{-1}kpc^{-2})$ (6)	τ_{dep}(Gyr)
6*Ring	NGC 1097	-	577	760±100	280±40	0.72±0.07	0.38±0.06
	IC 342	-	213	47±5	860±90	2.9±0.3	0.29±0.04
	NGC 3351	-	170	190±20	550±60	0.55±0.05	1.0±0.1
	NGC 4321	-	312	430±40	280±30	0.26±0.03	1.1±0.2
	NGC 4826	-	82	50±5	790±80	0.58±0.06	1.4±0.2
	NGC 7469	-	25	2500±1	890±90	8.8±0.9	0.10±0.01
30*Region	NGC 1097	1	13.4	26±10	410±20	1.2±0.1	0.35±0.14
	..	2	10.14	47±10	970±200	1.6±0.2	0.61±0.15
	..	3	22.5	49±14	450±130	1.5±0.2	0.32±0.09
	..	4	10.1	61±11	1260±220	1.5±0.2	0.82±0.17
	..	5	17.6	90±15	1070±170	N/A	N/A
	..	6	10.1	35±10	730±190	1.2±0.1	0.63±0.18
	..	7	10.1	14±9	290±180	1.3±0.1	0.23±0.15
	..	8	10.1	4.1±8.7	84±180	0.68±0.10	0.12±0.27
	..	9	18.0	63±13	740±150	1.3±0.1	0.58±0.14
	IC 342	1	29.4	11±3	1460±150	7.7±0.8	0.19±0.03
	..	2	5.93	2.5±1.1	1610±160	4.6±0.5	0.35±0.05
	..	3	6.80	1.7±1.2	990±100	5.1±0.6	0.19±0.03
	..	4	5.93	3.0±1.1	1970±200	4.0±0.5	0.49±0.08
	NGC 3351	1	43.0	54±6	620±70	0.66±0.07	0.94±0.14
	..	2	5.72	7.8±1.1	680±100	0.71±0.08	0.95±0.17
	..	3	21.4	34±4	780±90	1.0±0.1	0.75±0.11
	NGC 4321	1	6.31	20±2	660±80	0.29±0.05	2.30±0.46
	..	2	9.26	26±3	580±70	0.61±0.07	0.94±0.15
	..	3	7.86	49±5	1270±130	N/A	N/A
	..	4	6.31	14±2	440±60	0.62±0.07	0.70±0.13
	..	5	6.31	16±2	530±70	0.38±0.05	1.4±0.3
	..	6	6.31	18±2	590±70	0.57±0.07	1.0±0.2
	NGC 4826	1	9.39	9.2±0.9	1450±150	N/A	N/A
	..	2	7.58	5.8±0.6	1140±120	1.0±0.1	1.1±0.2
	..	3	6.94	1.9±0.3	420±60	0.74±0.07	0.57±0.09
	NGC 7469	1	1.40	280±30	750±100	8.5±0.9	0.09±0.01
	..	2	0.98	290±30	1130±130	12±1	0.09±0.01
	..	3	2.04	800±80	1480±150	N/A	N/A
	..	1	0.98	290±30	1110±130	17±2	0.07±0.01
	..	2	0.98	270±30	1060±120	12±1	0.08±0.01
	..	3	0.98	280±30	1090±130	13±1	0.09±0.01

Note — (1): Host galaxy of the nuclear ring. (2): Identifier of the region in reference to Figure 3.4. (3): Area of the circular aperture used to measure 33 GHz and CO(J=1-0) flux of the nuclear ring/NRSF region. For IC 342 and NGC 4826, beam areas are subtracted from the ring areas defined by R_{out} to account for the central unresolved cavities.(4): Molecular gas mass derived from CO (J=1-0) flux measurements (see Section 3.5.5). (5): Molecular gas surface density over the physical areas of the adopted apertures. (6): Star formation rate surface density over the physical areas of the adopted apertures for non-AGN regions. (7) Gas depletion time calculated using (5) and (6) for non-AGN regions.

are needed to reveal these edge-on rings.

Given the above, our sample represents a lower-limit of the number of nuclear rings in both surveys, and thus the results derived in this study may not represent the full range of NRSF properties in SFRS and the GOALS equatorial survey.

3.6.2 The majority of SF in these LIRGs takes place in their nuclear rings

Figure 3.7 shows the fraction of total SFR contributed by the nuclear ring with respect to $L_{\rm IR}$ of the host galaxy, as calculated in Section 3.5.2. Each galaxy is color-coded by its $L_{\rm IR}$, with darker blue and darker red representing the lower and higher $L_{\rm IR}$, respectively. Nuclear rings hosted in the LIRGs have up to six times higher $\frac{\rm SFR_{ring}}{\rm SFR_{tot}}$ than the ones hosted in the normal galaxies. Furthermore, we can also see that high $\frac{\rm SFR_{ring}}{\rm SFR_{tot}}$ in general corresponds to galaxies with high $L_{\rm IR}$. This result echoes previous studies which found that local galaxies with higher $L_{\rm IR}$ have more centrally concentrated emission (Díaz-Santos et al., 2010, 2011), and that the nuclear SF in LIRGs can dominate the properties of their host galaxies (e.g. Veilleux et al., 1995; Soifer et al., 2001). However, the nuclear rings we study here may only represent the most extreme cases, and it is possible that in many LIRGs, the total star formation is less centrally concentrated. We will present results on various nuclear SF structures in the entire GOALS equatorial survey in a upcoming paper to further investigate this.

It is also worth noting that NGC 1097, which is interacting with a dwarf companion, has both the highest $L_{\rm IR}$ and the highest $\frac{\rm SFR_{ring}}{\rm SFR_{tot}}$ among the normal galaxies. This trend is consistent with studies that observed excess nuclear SFR in interacting galaxies relative to isolated systems (e.g. Lonsdale et al., 1984; Bushouse, 1986),

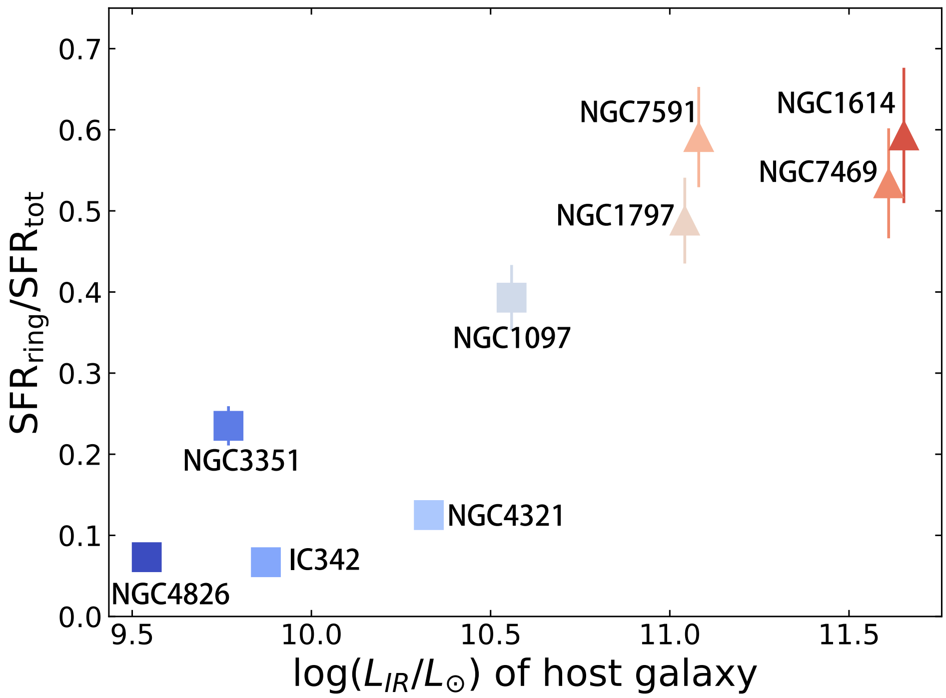

Figure 3.7: Fraction of total SFR contributed by the nuclear ring with respect to $L_{\rm IR}$ of the host galaxy. See Section 3.4.1, Table 3.4 and 3.5 for details. Each galaxy is color-coded by its $L_{\rm IR}$, with darker blue and darker red representing the lower and higher $L_{\rm IR}$, respectively. Squares and triangles represent normal galaxies and LIRGs respectively. **Nuclear rings in the LIRGs consistently contribute higher fractions of the total SFR of their host galaxies compared to rings in the normal galaxies.**

which is also predicted in simulations of galaxy interaction (Moreno et al., 2021).

3.6.3 High SFR and $\Sigma_{\rm SFR}$ in NRSF regions in the sample of LIRGs

The consistently higher nuclear ring contribution to the total SFR, as discussed in the last Section, points to more active NRSF in our sample of LIRGs. In Figure 3.8, we show, in filled symbols, the SFR and $\Sigma_{\rm SFR}$ of all 58 NRSF regions with respect to their effective radius R_e (reported in Table 3.6), and in non-filled symbols, the integrated values for the entire rings (Table 3.4). Note that for the integrated values,

$R_e = \sqrt{\mathrm{area}/\pi}$ measures the effective area extended by the ring, and is different from R_{peak} defined in Section 3.4.1.

Despite the different angular resolutions of the observations, the physical resolutions achieved (marked in short vertical lines on the horizontal axis) and the effective sizes of NRSF regions measured are similar between the normal galaxies and the LIRGs. We can see that at similar or smaller effective sizes, the integrated rings and NRSF regions in the LIRGs (triangles) both have at least an order of magnitude higher SFR and Σ_{SFR} than their counterparts in the normal galaxies (squares), confirming that NRSF in these LIRGs are indeed more active than in the normal galaxies. Additionally, most NRSF regions in these LIRGs have SFR as high as the integrated ring values of the normal galaxies, with 1–2 dex smaller effective sizes, exhibiting extremely high spatial concentration of SF activities.

It is worth noting that for both the normal galaxies and the LIRGs, regions measured at the highest physical resolutions (i.e. those in IC 342 and NGC 1614) have the highest Σ_{SFR}, which demonstrates the importance of high-resolution observations in accurate characterization of these regions. Lower resolution observations would likely result in diluted (and thus lower) measures of the intrinsic Σ_{SFR}. Assuming the extreme case where Σ_{SFR} is diluted by quiescent regions with no active SF when measured within larger area (i.e. $\Sigma_{\mathrm{SFR}} \propto 1/R_e^2$, hatched in red in Figure 3.8), NRSF regions in NGC 1614 may appear to have similar Σ_{SFR} to resolved regions in the normal galaxies even at 0".3 resolution (100 pc). The fact that regions in NGC 1797 and NGC 7469 share similar Σ_{SFR} with regions in IC 342 is likely a result of such dilution effect, given that observations of these two galaxies have much lower physical resolutions.

Furthermore, many regions in the LIRGs, especially in NGC 1614 are unresolved by the beam (marked with arrows), which means that their sizes can be even smaller, and their $\Sigma_{\rm SFR}$ can be even higher. Additionally, the integrated ring values for these LIRGs all lie above the ranges spanned by their NRSF regions, suggesting that active SF takes place throughout these nuclear rings, not only in the NRSF regions that we characterized here. Indeed, the sum of SFR in the NRSF regions only account for about 20 – 50% of the total SFR of the rings. If higher resolution deep observations were to be made available for these rings, we would expect to detect more NRSF regions that are less luminous or much smaller.

In summary, the NRSF regions studied in our sample of LIRGs intrinsically have higher SFR and $\Sigma_{\rm SFR}$ with sizes similar to or smaller than their counterparts in the sample of normal galaxies. Observations with consistent, high physical resolution are crucial for accurate characterization of these extreme, compact NRSF regions.

We note that within our sample, we do not find evidence associating AGN activity with NRSF, as SFR or $\Sigma_{\rm SFR}$ in NRSF regions do not appear consistently higher or lower in AGN hosts. Existing measurements of AGN strength indicators in the IR and X-ray of the host galaxies (Stierwalt et al., 2013; Dale et al., 2006; Grier et al., 2011) also do not reveal any correlation with the NRSF properties studied here.

3.6.4 NRSF in these LIRGs have SFR and $\Sigma_{\rm SFR}$ comparable to luminous SF regions at high-z

Using high-resolution HST Paα and Paβ observations, Larson et al. (2020) measured the SFR and effective radii of 751 extra-nuclear SF regions and 59 nuclei in 48 local LIRGs from GOALS. The authors showed that SF in local LIRGs bridges the gap between the local and the high-z Universe, with a wide range of SFR overlapping with those found in luminous SF clumps in $z = 1-4$ lensed galaxies. In Figure 3.9, we reproduce Figure 5 and 6 from Larson et al. (2020), overlaid with radio measurements for the individual NRSF regions from this study. Note that the most luminous regions

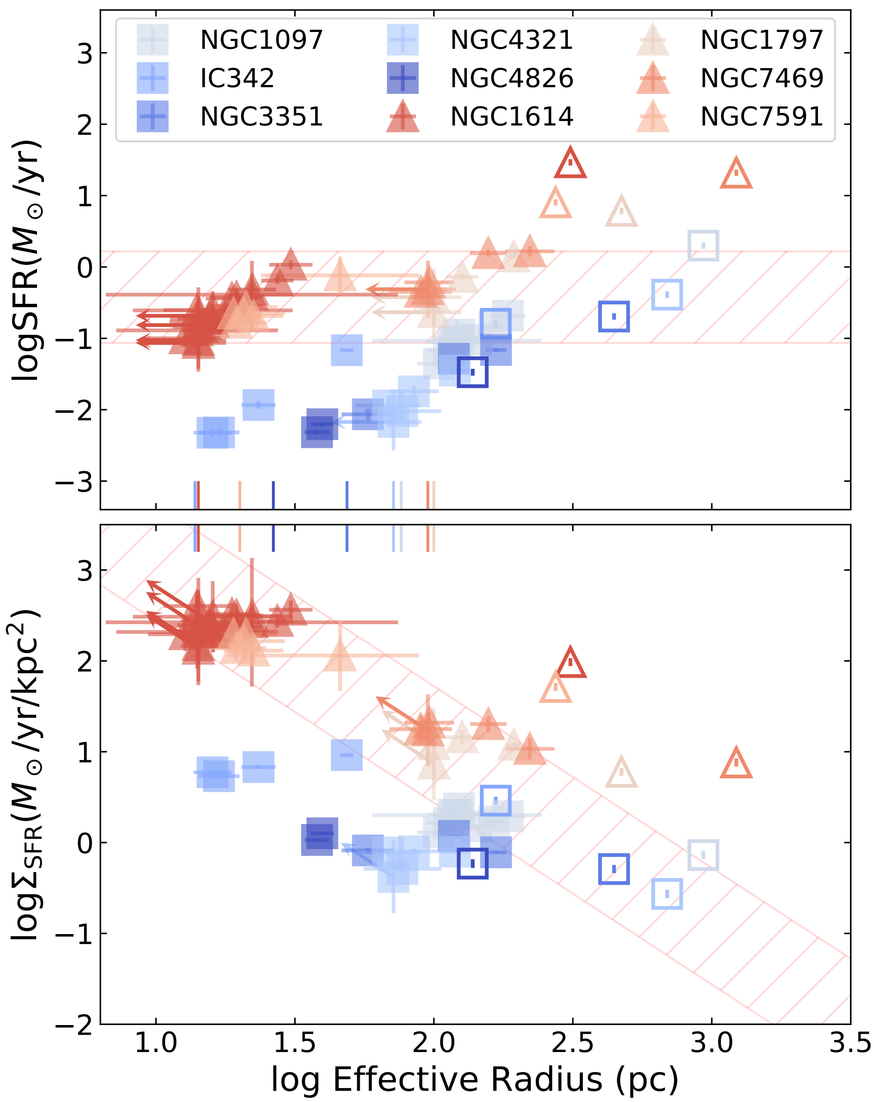

Figure 3.8: Effective radius R_e vs. SFR (*top*) and $\Sigma_{\rm SFR}$ (*bottom*). Values for the 58 NRSF regions are shown in filled symbols, and integrated ring values are in non-filled symbols, both color-coded by $L_{\rm IR}$ of the host galaxy, with squares and triangles representing normal galaxies and LIRGs, respectively. Arrows indicate upper-limits in R_e for unresolved regions, which translate into lower-limits in $\Sigma_{\rm SFR}$ given the measured SFR. Short vertical lines on the horizontal axis mark the resolution limits of the observations. The red hatching represents the range of SFR and expected range of $\Sigma_{\rm SFR}$ spanned by the smallest and largest NRSF regions in the sample of LIRGs, assuming the extreme case where $\Sigma_{\rm SFR}$ is diluted by quiescent areas when measured within larger region size (i.e. $\Sigma_{\rm SFR} \propto 1/R_e^2$). **The NRSF regions studied in our sample of LIRGs have higher SFR and $\Sigma_{\rm SFR}$ with sizes similar to or smaller than their counterparts in the sample of normal galaxies.**

in Larson et al. (2020) are the nuclei, most of which have SFR $> 0.1\,\mathrm{M_\odot/yr}$ and $\Sigma_{\rm SFR}$ $> 0.2\,\mathrm{M_\odot/yr/kpc^2}$ with effective radii greater than 300 pc. The dashed vertical line in orange marks the resolution limit of 90 pc for measurements from Larson et al. (2020). There are several conclusions that can be drawn from this Figure:

- For the five normal galaxies from SFRS, the NRSF regions (black squares) have higher SFR and $\Sigma_{\rm SFR}$ than the ensemble of SINGS regions (grey dots), which are measured in the disk of normal galaxies. Similarly, for the sample of LIRGs from the GOALS equatorial survey, the NRSF regions (red triangles) have higher SFR and $\Sigma_{\rm SFR}$ than the ensemble of GOALS regions (orange "+") detected in the near-IR, over 90% of which are extra-nuclear. These two results together suggest that NRSF can be more extreme than extra-nuclear SF in the disk of the host galaxy, supporting findings from Linden et al. (2019).

- At similar measured sizes, NRSF regions in the sample of normal galaxies overlap with the extra-nuclear GOALS regions in Larson et al. (2020) and lower-luminosity lensed regions at high-z (purple "x"). On the other hand, NRSF regions in the sample of LIRGs lie above the extra-nuclear GOALS regions from Larson et al. (2020), and their SFR and $\Sigma_{\rm SFR}$ are comparable to many luminous high-z regions. Note that if we consider the same dilution analysis as shown in Figure 3.8 (in red hatching), we would still find that the NRSF regions in the LIRGs have $\Sigma_{\rm SFR}$ comparable to many high-z SF regions with lower resolution measurements. We will investigate whether this applies more broadly to other nuclear SF regions in the GOALS equatorial survey in the upcoming paper. Future surveys with the capability of detecting fainter and smaller NRSF regions will allow a more comprehensive understanding of NRSF in LIRGs.

We also note that the different SFR tracers used for data presented in Figure 3.9 are sensitive to dust obscuration at different levels, which can affect the above interpretation of our results. While heavy non-uniform extinction in the nuclei of LIRGs can lead to underestimation of SFR and $\Sigma_{\rm SFR}$ by 1 - 1.5 dex even in the near-IR (U et al., 2019), over 90% of the GOALS regions being compared here are extra-nuclear and expected to be mildly extincted (Larson et al., 2020). Therefore we do not expect extinction correction to change our conclusions.

3.6.5 Thermal fractions in the NRSF regions at 33 GHz

In Figure 3.10, we show the estimated thermal fractions at 33 GHz, $f_{\rm th}$, associated with the NRSF regions in the sample nuclear rings with respect to the physical radii of the apertures within which these measurements were made (see Section 3.4.2 and 3.5.4). For context, we also overlay the expected values from Barcos-Muñoz et al. (2017) for luminous nuclei in U/LIRGs (hatched red), and the median values from Linden et al. (2020) for the nuclear regions in SFRS (hatched blue), both measured at sub-kpc scales.

The median value of $f_{\rm th}$ associated with the NRSF regions in the sample of normal galaxies is $\sim$ 69$\pm$19%, in agreement with the median value of $\sim$ 71% for all nuclear regions (i.e. having galactocentric radii $r_G < 250$ pc) in the full SFRS sample, reported in Linden et al. (2020). As discussed in Linden et al. (2020), excess non-thermal emission is present in the circum-nuclear SF regions in SFRS compared to the extra-nuclear regions ($r_G >= 1$ kpc; median $f_{\rm th} \sim 90\%$), likely due to prolonged SF activities. As illustrated in Figure 7 of Linden et al. (2020) using Starburst99 models, continuous SF for over 100 Myr can decrease the thermal fraction to $\sim$ 50% due to accumulation of non-thermal emission from supernovae, while instantaneous starburst can dramatically bring down thermal fraction to much lower levels within 10 Myr. Given that nuclear rings have prolific episodic starbursts (e.g. Buta et al., 2000; Maoz et al., 2001), and can persist at Gyr timescales (Knapen et al., 1995; Seo

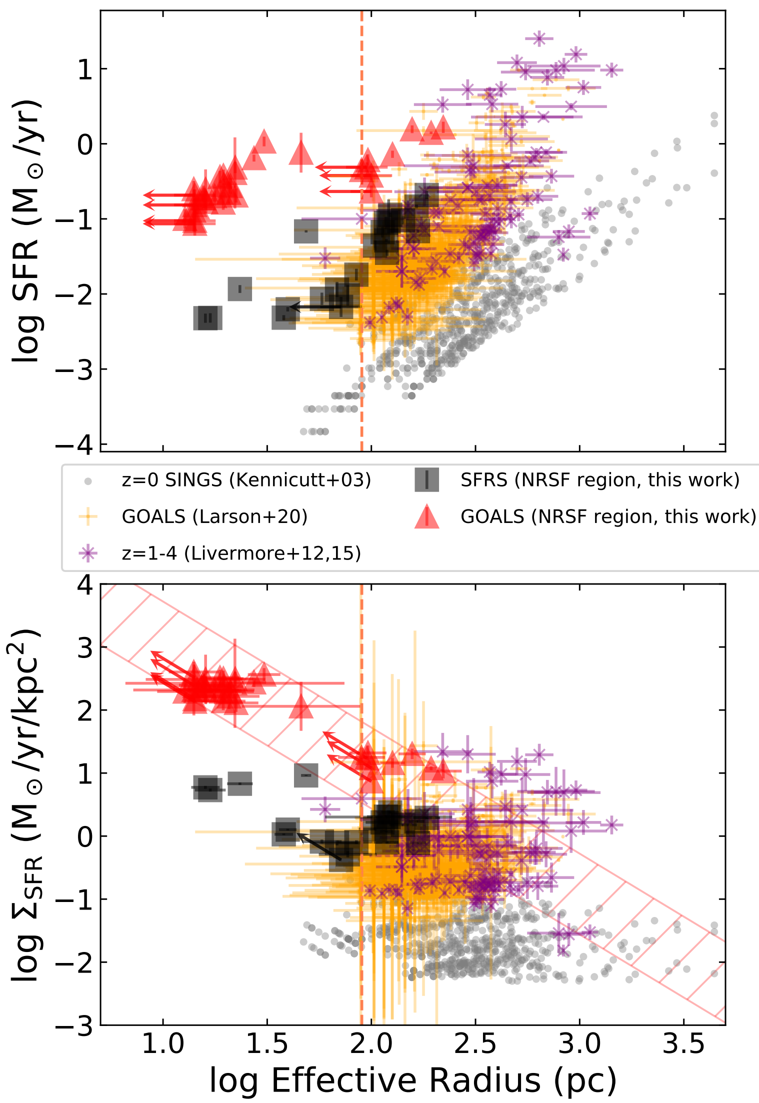

Figure 3.9: Effective radius R_e vs. SFR (*top*) and $\Sigma_{\rm SFR}$ (*bottom*) for SF regions in galaxies at different redshifts, reproduced from Figure 5 and 6 in Larson et al. (2020). Triangles and squares are radio continuum measurements of individual NRSF regions in the LIRGs from the GOALS equatorial survey (red) and the normal galaxies from SFRS (black). Arrows indicate lower-limits in R_e and upper-limits in $\Sigma_{\rm SFR}$ for unresolved regions. Purple "x" represent Hα measurements of SF regions in lensed galaxies at $z \simeq 1-4$ (Livermore et al., 2012, 2015). Orange "+" mark the Paα and Paβ measurements of 59 nuclei and 751 extra-nuclear SF regions in 48 local LIRGs from GOALS (Larson et al., 2020), with a resolution limit of 90 pc (orange dashed vertical line). Grey dots are Hα measurements of SF regions in SINGS galaxies. **NRSF regions in the sample of local LIRGs have SFR and $\Sigma_{\rm SFR}$ comparable to or higher than luminous SF regions at high-z.**

& Kim, 2013), the relatively low $f_{\rm th}$ observed in the NRSF regions in these normal galaxies may be driven by a combination of continuous and "bursty" SF.

In Figure 3.10 we also see that at similar physical scales, $f_{\rm th}$ can be even lower for NRSF regions in the sample of LIRGs compared to those in the normal galaxies, except for NGC 1614, whose NRSF regions span a wide range in $f_{\rm th}$. The median $f_{\rm th}$ in the NRSF regions in the sample of LIRGs is $\sim 35{\pm}36\%$ including NGC 1614, and $\sim 29{\pm}9\%$ excluding NGC 1614, which are much lower than the median of 69% measured in the normal galaxies. This is in agreement with findings from Barcos-Muñoz et al. (2015) and Barcos-Muñoz et al. (2017) that the nuclear regions in U/LIRGs are mostly dominated by non-thermal emission. These authors suggest that thermal emission in the nuclei of U/LIRGs may be suppressed via the absorption of ionizing photons by dust. However, in our case, the lower $f_{\rm th}$ can also be explained by beam dilution due to low resolutions of the beam-matched images, i.e., measurements for most regions in NGC 1797, NGC 7469 and NGC 7591 are at scales 2 - 5 times larger than the sizes of the NRSF regions characterized using *Astrodendro*. The wide range of $f_{\rm th}$ observed in the nuclear ring of NGC 1614, which is measured at physical scales smaller than 50 pc, has also been observed by Herrero-Illana et al. (2014). The authors conclude that this large variation reflects the different ages of starbursts in the NRSF regions, with regions of extremely young starbursts (< 4 Myr) having thermal fractions $\sim 100\%$, and regions of old starbursts (> 8 Myr) having much lower thermal fractions. This explanation is also consistent with Figure 7 in Linden et al. (2020). As demonstrated in previous Sections, the NRSF regions in the sample of LIRGs are likely more compact than the ones in the normal galaxies. Therefore, measurements at $100 - 300$ pc scales in these LIRGs may average over areas of young and old starbursts that have drastically different thermal content. Additionally, as mentioned in Section 3.5.4, non-thermal emission associated with supernovae can be more diffuse than thermal emission (e.g. Condon, 1992), hence low resolution measurements are more likely to represent non-thermal emission. It is possible that, at high resolutions (e.g. $< 100\,\mathrm{pc}$), we may also see very high f_{th} in some of the NRSF regions in NGC 1797, NGC 7469 and NGC 7591, as observed in NGC 1614.

3.6.6 Star formation relation

Global measurements of Σ_{SFR} and Σ_{mol} of galaxies of various types indicate the existence of a universal SF relation, i.e. $\Sigma_{\mathrm{SFR}} = A\Sigma_{\mathrm{mol}}^{N}$, with $N{\sim}1.4$ (e.g. Kennicutt, 1998). According to this relation, SF efficiency increases (i.e. gas depletion time decreases) towards high Σ_{mol} for all types of galaxies. However, several studies argue for a bimodal SF relation which predicts constant star formation efficiency among galaxies of similar types, with gas depletion times in normal spiral galaxies 4 - 10 times longer than in U/LIRGs or high-z sub-millimeter galaxies (e.g. Bigiel et al., 2008; Daddi et al., 2010; Genzel et al., 2010; Kennicutt & de los Reyes, 2020). As we show in Figure 3.11, this bimodality is also present in our results for the nuclear rings (non-filled) and the NRSF regions (filled) derived from extinction-free measurements at sub-kpc scales (see Section 3.5.5). Despite having 1 - 2 dex higher Σ_{mol}, the rings and the NRSF regions in the normal galaxies (square symbols) have similar gas depletion times ($\tau_{\mathrm{dep}} \sim 1\,\mathrm{Gyr}$) with normal spiral disks. The ring and NRSF regions in NGC 7469 also show consistent $\tau_{\mathrm{dep}}(\sim 100\,\mathrm{Myr})$ with circumnuclear disk measurements for U/LIRGs, being up to an order of magnitude shorter than rings and NRSF regions in the normal galaxies. This is similar to values measured in other sub-kpc scale studies of U/LIRGs (e.g. Xu et al., 2015; Pereira-Santaella et al., 2016), but 4 - 6 times shorter than τ_{dep} estimated from global measurements of GOALS galaxies (Herrero-Illana et al., 2019). In a resolved study of five U/LIRGs, Wilson et al. (2019) demonstrated that τ_{dep} decreases more rapidly at increasing Σ_{mol} above $\Sigma_{\mathrm{mol}} > 10^3\mathrm{M}_{\odot}/\mathrm{pc}^2$ in these

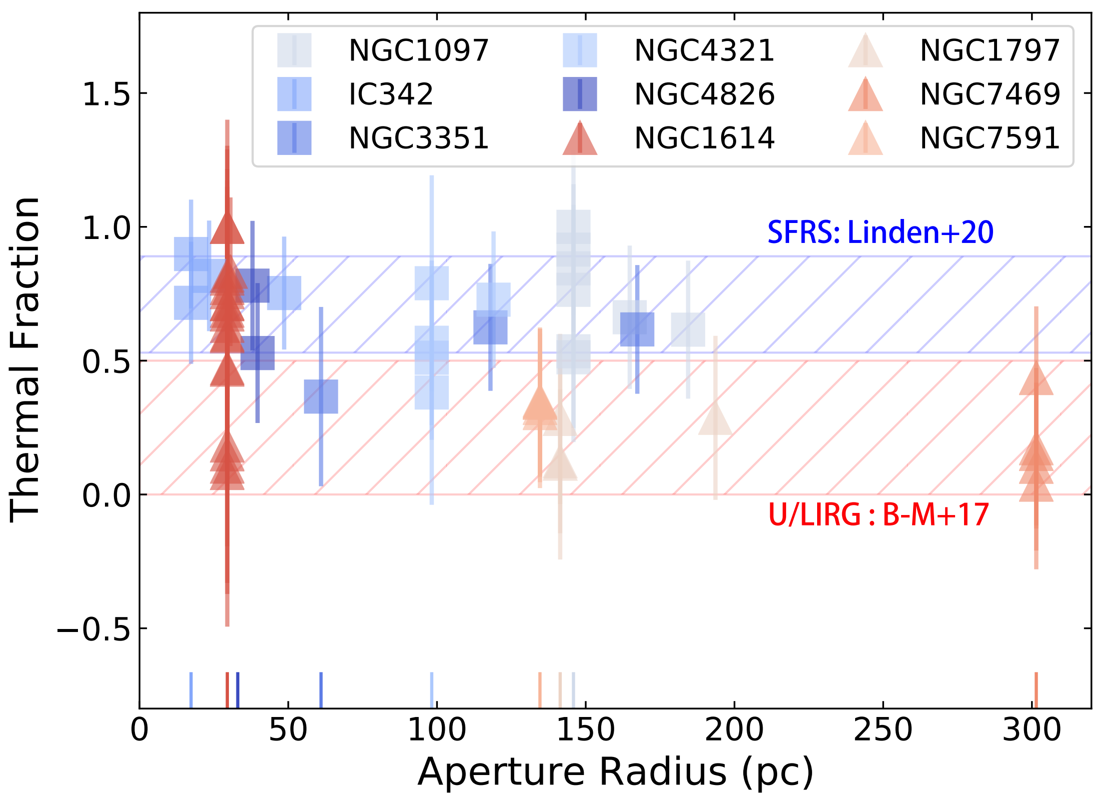

Figure 3.10: Thermal fraction at 33 GHz with respect to the physical size of the aperture used for the measurements for the NRSF regions. Each region is color-coded by L_{IR} of its host galaxy, and squares and triangles represent normal galaxies and LIRGs separately. Short vertical lines on the horizontal axis indicate resolution limits of the spectral index measurements (see Section 3.5.3). Blue hatched area marks the median values and median absolute deviation of 71% and ± 18% measured by Linden et al. (2020) on 100 ∼ 500 pc scales for the nuclear regions ($r_G < 250$ pc) in the SFRS sample, and red hatched area represent the values for the nuclei in the most luminous local U/LIRGs (≤50%) predicated by Barcos-Muñoz et al. (2017) at similar physical scales. **When measured at similar physical scales, NRSF regions in the sample of LIRGs have lower thermal fractions compared to regions in the sample of normal galaxies. NRSF regions in NGC 1614, which are measured at the smallest physical scales, span a wide range in thermal fraction.**

extreme systems. In an upcoming paper, we will present sub-kpc measurements for a larger sample of nuclear SF regions in the GOALS equatorial survey to further explore the sub-kpc SF relation in local U/LIRGs.

The nuclear rings in IC 342 and NGC 1097 also have relatively high SFE compared to spiral disks and other nuclear rings hosted in normal galaxies, with $\tau_{\rm dep} \sim 0.4\,{\rm Gyr}$. This central enhancement of SFE has also been observed in other studies of IC 342 (Sage & Solomon, 1991; Pan et al., 2014) and in surveys of normal galaxies (e.g. Leroy et al., 2013; Utomo et al., 2017). Meanwhile, at similar $\Sigma_{\rm SFR}$, NRSF regions in NGC 1097 span $\sim 1\,{\rm dex}$ in $\tau_{\rm dep}$. Tabatabaei et al. (2018) discovered that this large scatter in SFE is closely tied to local build-up of the magnetic field that support molecular clouds against gravitational collapse. Overall, our results show that, in these nuclear rings, at similar $\Sigma_{\rm mol}$, $\tau_{\rm dep}$ is shorter in the LIRG NGC 7469 compared to in the normal galaxies, but it varies among the normal galaxies as well, likely reflecting variation in local SF conditions. Tentatively, this supports the idea of a multi-modal star formation relation on sub-kpc scales. We note that adopting a normal galaxy $\alpha_{\rm CO}$ for NGC 7469, or environmentally-dependent $\alpha_{\rm CO}$(Narayanan et al., 2012; Sandstrom et al., 2013), can potentially produce a more continuous SF relation among these nuclear rings, but more statistics are needed to explore this.

3.7 Summary

In this paper we present analyses of sub-kpc resolution VLA radio continuum observations of nine nuclear rings hosted in four local LIRGs from the GOALS equatorial survey (NGC 1614, NGC 1797, NGC 7469, NGC 7591) and five nearby normal galaxies from the Star Formation in Radio Survey (NGC 1097, IC 342, NGC 3351, NGC 4321, NGC 4826). These two surveys map the brightest 3, 15 and 33 GHz radio continuum emission in 56 nearby normal galaxies and 68 local U/LIRGs at matched

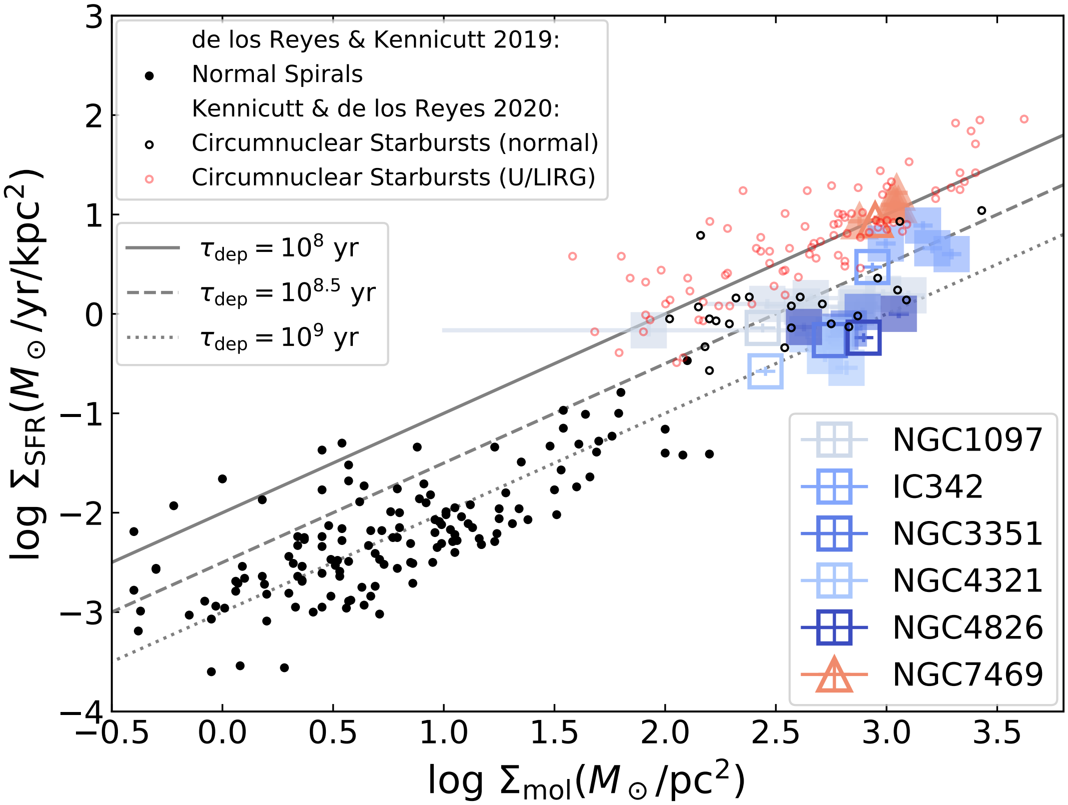

Figure 3.11: $\Sigma_{\rm mol}$ vs. $\Sigma_{\rm SFR}$ for the integrated nuclear rings (non-filled) and NRSF regions (filled), color-coded by the $L_{\rm IR}$ of the host galaxy. Also shown are global measurements for the normal spiral galaxies (black filled circles) from de los Reyes & Kennicutt (2019), and circum-nuclear starbursts in normal galaxies (black non-filled circles) and U/LIRGs (red non-filled circles) from Kennicutt & de los Reyes (2020), converted to match with the $\alpha_{\rm CO}$ we adopted. Solid, dashed, and dotted grey lines represent gas depletion time $\tau_{\rm dep}$ of 10^8, $10^{8.5}$, and 10^9 yr. **The estimated $\tau_{\rm dep}$ is shortest in the nuclear ring of NGC 7469, and has a large scatter among nuclear rings in the normal galaxies at similar $\Sigma_{\rm mol}$.**

physical resolution, and hence allow direct, extinction-free comparison of nuclear star formation across different host environments. Using high-resolution maps of 33 or 15 GHz continuum, we characterize the size, SFR and $\Sigma_{\rm SFR}$ of these nine detected nuclear rings and 58 individual NRSF regions at $\sim$ 100 scales. We summarize our main findings as follows:

1. The five nuclear rings in normal galaxies contribute 7 - 40% of the total SFR of their host galaxies, with radii, SFR and $\Sigma_{\rm SFR}$ in the range of 43 – 599 pc, 0.03 – 2.0 $M_\odot$ yr^{-1} and 0.27 – 2.90 $M_\odot$ yr^{-1} kpc^{-2}, respectively. By comparison, the four nuclear rings in the LIRGs have much more dominant contributions to the total star formation of their host galaxies, at 49 - 60%, with radii, SFR and $\Sigma_{\rm SFR}$ in the range of 121 – 531 pc, 6.1 – 29 $M_\odot$ yr^{-1} and 6.0 – 97 $M_\odot$ yr^{-1} kpc^{-2}, respectively.

2. We identified a total of 58 individual NRSF regions using *Astrodendro*, 22 of which are hosted in the five normal galaxies, and 35 are in the LIRGs. NRSF regions in the normal galaxies have effective radii, SFR and $\Sigma_{\rm SFR}$ in the range of 16 – 184 pc, 0.01 – 0.21 $M_\odot$yr^{-1} and 0.4 – 9.2 $M_\odot$yr^{-1}kpc^{-2}, respectively. NRSF regions in the LIRGs have similar range of effective radii, of 13 – 221 pc, but their SFR and $\Sigma_{\rm SFR}$ are an order of magnitude higher, with a range of 0.08 – 1.7 $M_\odot$yr^{-1} and 7 – 402 $M_\odot$yr^{-1}kpc^{-2}, respectively. Many of these NRSF regions in the LIRGs are unresolved by our observations, so they may be more compact with higher intrinsic $\Sigma_{\rm SFR}$. We also found that these NRSF regions in the LIRGs have SFR and $\Sigma_{\rm SFR}$ as extreme as measured in lensed high-z SF galaxies from the literature.

3. The median ratio of thermal emission to the total 33 GHz radio continuum emission (i.e. thermal fraction) associated with the NRSF regions is 69±19% in the

normal galaxies, and 35±36% in the LIRGs, which is lower than estimates for extra-nuclear SF regions, but consistent with results from previous studies. The dominant presence of non-thermal emission in the LIRGs may originate from suppression of thermal emission due to absorption of ionizing photons by highly concentrated dust in HII regions. In our case, it is more likely due to insufficient resolution of the measurements that results in the inclusion of more diffuse non-thermal emission from cosmic rays accelerated by supernovae. A wide range of thermal fractions were observed in NGC 1614 at high resolution ($< 100\,\mathrm{pc}$), which likely reflects different ages of the starbursts along the nuclear ring.

4. For all five normal galaxies and one LIRG (NGC 7469), we use available archival CO(J=1-0) data with comparable resolutions to our 33 GHz observations to further study star formation efficiencies in these nuclear rings at sub-kpc scales. The nuclear rings and NRSF regions in the normal galaxies have gas depletion times $\tau_{\mathrm{dep}} \sim 1\,\mathrm{Gyr}$, about an order magnitude longer than in the nuclear ring and NRSF regions of NGC 7469 ($\tau_{\mathrm{dep}} \sim 100\,\mathrm{Myr}$), which is consistent with results from previous studies on kpc and global scales. However, τ_{dep} estimated for rings and regions with similar Σ_{mol} have fair amount of scatter, which may point to a multi-modal star formation relation on sub-kpc scales. More statistics are needed to explore this.

In this work we have demonstrated the ability to study embedded nuclear ring star-forming regions on sub-kpc scales in local LIRGs using high frequency radio continuum as an extinction-free tracer of star formation. This makes it possible to directly compare star formation properties in the heavily obscured hearts of local U/LIRGs with those at the center of normal galaxies. We also show that to fully resolve and characterize these extremely compact NRSF regions in the local LIRGs, observations at even higher resolutions and better sensitivity are needed. Future facilities such as the ngVLA will greatly improve our understanding of deeply embedded compact nuclear structures in these systems.

3.8 Appendix

3.8.1 Notes on Individual Galaxies

Here we provide description of individual sources based on data used in this work, as displayed in Figure 3.1, 3.2, 3.3 and 3.6. Where relevant, we include descriptions from prior studies of each nuclear ring.

NGC 1097: In all three VLA bands, we clearly see a nearly circular star-forming ring with diameter (D) $\sim 17''$ (1.2 kpc) made of multiple bright SF knots, surrounding a luminous nucleus. Emission from the nucleus and the ring are well separated in the azimuthally averaged light profile at 33 GHz, which allows us to characterize the spatial extent of the ring. A nuclear spiral inside the ring, which is transporting gas into the nucleus through the ring, has been revealed with multi-wavelength observations by Prieto et al. (2019). Our radio images also show three faint streamer-like structures that connect the central nucleus to the ring, with the brightest streamer on the west of the nucleus extending few arcseconds beyond the ring. This extension has a bright counterpart in the ALMA CO(J=1-0) data, which coincides with the contact point of a kpc gas streamer feeding in ring, as discovered by Prieto et al. (2019). The host galaxy ($cz = 1270\,\mathrm{km/s}$) is interacting with at least one dwarf companion (1097A: $cz = 1368\,\mathrm{km/s}$; Bowen et al., 2016).

IC 342: A small asymmetric nuclear star-forming ring ($D \sim 6'', 160\,\mathrm{pc}$) made of at least four distinct SF knots is detected at all three VLA bands. At 33 GHz, diffuse emission from the ring covers the central region, as seen in the azimuthally-averaged light profile. No bright nuclear emission is detected at any VLA Band, and the ring morphology has previously been confirmed in near-IR and CO observations (Boker et al., 1997; Schinnerer et al., 2003). Therefore we do not assign an inner radius for this nuclear ring when calculating its SFR to account for the diffuse emission, but the area of the synthesized beam is subtracted from the area defined by the outer radius when estimating $\Sigma_{\rm SFR}$ to account for the central cavity. In a previous molecular gas study, Ishizuki et al. (1990) suggest that the nuclear ring outlines the ends of a pair of molecular ridges, which may have formed due to shock-waves from a bar-like gravitational potential.

NGC 3351: An elliptical nuclear ring ($D \sim 13'', 600\,\mathrm{pc}$) with an inclination angle of $\sim 59°$ is clearly present in images at all three VLA bands, with two bright SF knots lying on the north and south tips of the ring separately, accompanied by smaller, fainter SF knots on the east and west sides. The azimuthally-averaged light profile at 33 GHz reveals a faint nuclear component, which outlines the inner radius of the ring. This component is most visible at 3 GHz. A comparison of the radio-detected ring with archival Spitzer IRAC 3.6μm image of the galaxy reveals a bar-like stellar structure connecting the brightest radio "hotspots" along the north-south direction. Low resolution ($\sim 7''$) molecular observations have suggested the presence of a molecular nuclear bar (Devereux et al., 1992), which is absent from the ALMA CO(J=1-0) observation.

NGC 4321: The nuclear ring ($D \sim 14'', 1\,\mathrm{kpc}$) was detected at all three bands, along with the central LINER nucleus. The ring appears fairly clumpy, with three bright knots making up the east half of the ring and relatively faint diffuse emission on the west half. At 3 GHz more diffuse emission is detected, and the ring reveals itself to be part of a tightly wound spiral structure, which is also evident in the ALMA CO(J=1-0) data. The ends of the molecular spiral arms correspond to the location of bright SF knots, which connects the ring to a nuclear bar that is prominent in both archival Spitzer IRAC 3.6 μm image, and CO data (Sakamoto et al., 1995). Numeric simulations predict that such nuclear bars exert strong gravitational torques on molecular gas to effectively feed the SMBHs and nuclear/circum-nuclear starbursts (Wada et al., 1998).

NGC 4826: The small nuclear ring ($D \sim 5'', 120\,\mathrm{pc}$) is most apparent at 15 GHz, where we see five distinct knots lying close together to form a nearly circular structure. The brightest knot is the off-center LINER nucleus (García-Burillo et al., 2003). At 33 and 3 GHz, the emission from the two fainter knots is blended into the brighter knot in between them. The bright nuclear ring is also closely surrounded by a series of much fainter SF regions, which show up in the azimuthally-averaged light profile at $\sim 10''$ (250 pc) away from the center (we exclude them from our analyses). At 33 GHz, diffuse emission from the ring covers the central region, as seen in the light profile. No bright nuclear emission is detected at any VLA Band, and the ring morphology has previously been confirmed in CO observation (García-Burillo et al., 2003). Therefore we do not assign an inner radius for this nuclear ring when calculating its SFR to account for the diffuse emission, but the area of the synthesized beam is subtracted from the area defined by R_{out} when estimating Σ_{SFR} to account for the central cavity.

NGC 1614: A clumpy, almost circular nuclear star-forming ring ($D \sim 1.5'', 400\,\mathrm{pc}$), made of knots with various sizes and brightness, is detected at 33 and 15GHz. One faint elongated knot on the west extends beyond the ring by $\sim 0.5''$ (150 pc). A faint nucleus surrounded by the ring is also detected at 33 GHz, which outlines the inner radius of the ring. At 3 GHz, the ring is unresolved. Prominant dust lanes have been observed to be connected to the northern tip of the nuclear ring where molecular gas is potentially streaming into the ring and fueling the starbursts (Olsson et al., 2010; König et al., 2013).

NGC 1797: The ring structure is resolved for the very first time with the GOALS equatorial survey. At 33 GHz, we clearly see three bright SF knots connected by diffuse emission, forming an elliptical ring ($D \sim 2'', 800\,\mathrm{pc}$) with an inclination angle of $\sim 45°$. At 15 GHz, the brightest region on the east half of the ring is further resolved into three smaller distinct SF knots, with two brighter ones on the north connected to each other. The ring morphology at 3 GHz follows that at 33 GHz, but the diffuse emission connecting the east and west half the ring becomes more prominent. No bright nuclear emission is detected at any VLA Band, therefore we do not assign an inner radius for this nuclear ring when calculating its SFR to account for the diffuse emission, but the area of the synthesized beam is subtracted from the area defined by R_{out} when estimating Σ_{SFR} to account for the central cavity.

NGC 7469: The ring structure ($D \sim 3'', 1000\,\mathrm{pc}$) containing five SF knots is clearly detected at 33GHz, surrounding a much brighter Seyfert 1 nucleus, which outlines the inner radius of the ring. The ring appears more spiral-like at 3 GHz, where the northern and southern components are much more pronounced and extending beyond the ring. A similar morphology is also seen in ALMA CO(J=1-0) data. Due to low angular resolution, the ring appears as faint diffuse emission surrounding the bright nucleus at 15 GHz. Mazzarella et al. (1994) observed the nuclear ring in the near-IR, and found the brightest SF "hotspots" coincide with the ends of a nuclear stellar bar revealed in K-band continuum, which may be transporting gas from the ring to the luminous Seyfert 1 nucleus (e.g. Wada et al., 1998).

NGC 7591: The elliptical ring ($D \sim 1'', 300\,\mathrm{pc}$) has an inclination angle of $\sim 62°$, and is detected at all three bands but was only resolved with at least $3\sigma_{\mathrm{rms}}$ at 15 GHz, with the southern part of the ring brighter than the rest. At 3 and 33 GHz, the ring becomes completely unresolved. The nuclear ring has also been observed in the near-IR Paschen observations by Larson et al. (2020), but NRSF regions in the rings are resolved for the first time with the GOALS equatorial survey.

3.8.2 Integrated measurements for highly elliptical rings

For all but three galaxies (NGC 1797, NGC 3351 and NGC 7591), we measured the azimuthally-averaged light profiles of each nuclear ring by computing the averaged brightness per pixel on a series of 1 pixel wide concentric circles overlaid on top of 33GHz images, with their centers aligned with the central coordinates of the host galaxy, with minor adjustments to visually match the ring center. Due to relatively high ellipticities of the nuclear rings in NGC 1797, NGC 3351 and NGC 7591, we used the following procedures to more accurately depict their light profiles: After each image is masked to only preserve emission with SNR$>$ 5 , the coordinates of the unmasked pixels were extracted and then fitted with a 2D ellipse model using the least square fitting method suggested in Fitzgibbon et al. (1996). Note that 15 GHz image was used for NGC 7591 instead due to low resolution of the available 33 GHz image. The model describes a generic quadratic curve:

$$ax^2 + 2bxy + cy^2 + 2dx + 2fy + g = 0 \tag{3.9}$$

where the fitted ellipse's center coordinate (x_0, y_0), semi-major and semi-minor axes lengths (a', b') and the counterclockwise angle of rotation from the x-axis to the major axis of the ellipse could be calculated as follows:

$$
\begin{aligned}
x_0 &= \frac{cd - bf}{b^2 - ac} \\
y_0 &= \frac{af - bd}{b^2 - ac} \\
a' &= \sqrt{\frac{2(af^2 + cd^2 + gb^2 - 2bdf - acg)}{(b^2 - ac)[\sqrt{(a-c)^2 + 4b^2} - (a+c)]}} \\
b' &= \sqrt{\frac{2(af^2 + cd^2 + gb^2 - 2bdf - acg)}{(b^2 - ac)[-\sqrt{(a-c)^2 + 4b^2} - (a+c)]}} \\
\phi &= \begin{cases} 0, & \text{for } b = 0 \text{ and } a < c \\ \frac{\pi}{2}, & \text{for } b = 0 \text{ and } a > c \\ \frac{1}{2}\cot^{-1}\left(\frac{a-c}{2b}\right), & \text{for } b \neq 0 \text{ and } a < c \\ \frac{\pi}{2} + \frac{1}{2}\cot^{-1}\left(\frac{a-c}{2b}\right), & \text{for } b \neq 0 \text{ and } a > c \end{cases}
\end{aligned}
$$

The above method works under the condition that $\begin{vmatrix} a & b & d \\ b & c & f \\ d & f & g \end{vmatrix} \neq 0$, $\begin{vmatrix} a & b \\ b & c \end{vmatrix} > 0$ and $(a + c) < 0$, which makes Eq.3.9 the general expression for 2D ellipses. The caveat is that this method does not work well for circular fits, therefore we only adopt it to extrapolate the properties of the highly elliptical rings in NGC 1797, NGC 3351 and NGC 7591. Based on the ellipticity estimated from the model fitting result, we then produced a series of concentric 1-pixel-wide elliptical annuli to calculate the adjusted azimuthally-averaged brightness of the ring.

Chapter 4

Characterizing Compact 15 - 33 GHz Radio Continuum Emission in local U/LIRGs

[1]

4.1 Introduction

Luminous Infrared Galaxies (LIRGs; $10^{11} \leq L_{\rm IR}[8–1000\mu{\rm m}] < 10^{12} L_{\odot}$) and Ultra-luminous Infrared Galaxies (ULIRG; $L_{\rm IR}[8–1000\mu{\rm m}] \geq 10^{12} L_{\odot}$) are an important class of objects for understanding massive galaxy evolution. Despite their rarity in the local Universe, U/LIRGs are the dominant contributors to the co-moving infrared (IR) luminosity density and star formation rate (SFR) density at $z \gtrsim 1$ (Chary & Elbaz, 2001; Le Floc'h et al., 2005; Magnelli et al., 2011, 2013; Gruppioni et al., 2013), and

[1]This chapter has been submitted to The Astrophysical Journal. Authors: Y. Song; S. T. Linden; A. S. Evans; L. Barcos-Muñoz; E. J. Murphy; E. Momjian; T. Díaz-Santos; K. L. Larson; G. C. Privon; X. Huang; L. Armus; J. M. Mazzarella; V. U; H. Inami; V. Charmandaris; C. Ricci; K. L. Emig; J. McKinney; I. Yoon; D. Kunneriath;T. S.-Y. Lai; E. E. Rodas-Quito;M. A. Saravia; T. Gao; W. Meynardie; D. B. Sanders

ULIRGs are about a thousand times more common at $z \sim 2$ relative to at $z \sim 0$ (e.g. Chapman et al., 2005; Magnelli et al., 2013).

Observations of U/LIRGs in the local Universe revealed that a significant fraction of local LIRGs and nearly all local ULIRGs are interacting or merging gas-rich spirals (e.g. Lonsdale et al., 1984; Armus et al., 1987; Sanders & Mirabel, 1996). Simulations of galaxy interactions suggest that such a process typically drives large fractions of interstellar materials into the central kpc of each galaxy (e.g. Barnes & Hernquist, 1992), which can trigger intense nuclear starbursts (e.g. Mihos & Hernquist, 1996; Moreno et al., 2020) and/or fueling of powerful Active Galactic Nuclei (AGN) (e.g. Di Matteo et al., 2005). This nuclear activity is thought to play a key role in the transformation of gas-rich systems into massive elliptical galaxies, the formation of quasars and the co-evolution of supermassive black holes (SMBH) and stellar bulges (e.g. Sanders et al., 1988; Hopkins et al., 2006). While the discovery of heavily-obscured luminous AGN in local U/LIRGs (Treister et al., 2012; Ricci et al., 2017; Koss et al., 2018; Ricci et al., 2021) has provided strong supporting evidence for this evolutionary scenario, details regarding the interplay between star formation and AGN activity, as well as how they together (or separately) act upon the transformation of these extreme systems, still remain ambiguous. Importantly, the extraordinary star-forming properties of local U/LIRGs relative to nearby normal galaxies (i.e. galaxies with $L_{\rm IR} < 10^{11} L_{\odot}$; e.g. Condon et al., 1991; Lonsdale et al., 1984; Howell et al., 2010; Stierwalt et al., 2014; Piqueras López et al., 2016; Díaz-Santos et al., 2017; Linden et al., 2019; Larson et al., 2020; Song et al., 2021; Linden et al., 2021), and the prevalence of outflows observed in starburst-dominated local U/LIRGs (e.g. Rupke et al., 2005; Cazzoli et al., 2016; Barcos-Muñoz et al., 2018; Fluetsch et al., 2019; U et al., 2019; Fluetsch et al., 2020) highlight the pivotal role of star formation-driven feedback in regulating their evolution. To better quantify the physical processes governing the evolution of local

U/LIRGs, a robust characterization of the most energetic regions in these systems is necessary.

Due to heavy dust obscuration, especially in the central kpc of U/LIRGs, radio interferometric observations provide the best tools for probing into the most obscured but energetically-dominant regions in these systems. Condon et al. (1991) conducted the first sub-kpc scale radio continuum study of a sample of 40 local U/LIRGs at 8.4 GHz using the Very Large Array, and concluded that most of their dust-obscured nuclei are powered by starbursts, with many as compact as 100 pc in radius. With the upgraded bandwidth of the Karl G. Jansky Very Large Array (VLA), observations at higher frequencies are now possible, allowing access to the faint, thermal free-free emission directly arising from ionizing photons from HII regions (Condon, 1992; Murphy et al., 2011b) at sub-arcsecond resolutions. Using 33 GHz continuum VLA observations, Barcos-Muñoz et al. (2015, 2017) constrained the sizes and star formation rates (SFR) for the nuclei of the 22 most luminous local U/LIRGs. In the western nucleus of ULIRG Arp 220, the authors derived a SFR surface density of $10^{4.1}$ $M_\odot\,yr^{-1}\,kpc^{-2}$, the highest value ever measured, and far exceeding the theoretical limits for starbursts supported by supernovae feedback and dust-reprocessed radiation (Thompson et al., 2005; Kim & Ostriker, 2015). What drives these extreme SFR surface densities, and are such conditions also observed in LIRGs at lower IR luminosity?

This paper aims to investigate the above question. We present results from the high-resolution ($0''.1 - 0''.2$) portion of a new multi-frequency multi-resolution radio continuum snapshot survey of 68 local U/LIRGs from the Great Observatories All-sky LIRG Survey (GOALS; Armus et al., 2009). In contrast to the previous radio surveys (e.g. Condon et al., 1991; Barcos-Muñoz et al., 2017) that focused on the most luminous objects, these 68 U/LIRGs span the entire IR luminosity range of the full GOALS sample of all 201 U/LIRGs in the local Universe (i.e. $10^{11} - 10^{12.5} L_{\odot}$), as demonstrated in Figure 2.1 (see Chapter 2 for details), and therefore represents a more diverse range of physical environments, including ones that more closely resemble nearby normal galaxies. These new observations also serve as an excellent companion to the Star Formation in Radio Survey (SFRS; Murphy et al., 2012, 2018; Linden et al., 2020), a study of 56 nearby normal galaxies observed at the same frequencies and physical scales as this work.

Linden et al. (2019) presented the first results from our new U/LIRG survey based on $\sim$ 1".0 resolution observations. Despite finding star formation enhancement relative to SFRS galaxies on kpc scales, we concluded that nuclear star formation must drive GOALS systems above the Star Formation Main Sequence (SFMS; e.g. Elbaz et al., 2011; Speagle et al., 2014) occupied by the SFRS galaxies. Subsequently in Song et al. (2021), we examined four nuclear rings detected in our survey at $\sim$100 pc ($0''.1$) scales and compared their properties to five nuclear rings detected in the SFRS galaxies. We found that nuclear ring star formation contributes more significantly to the total star formation of the host galaxies for LIRGs compared with normal galaxies. In this paper, we extend the methodology adopted in Song et al. (2021) to study $\sim$ 100 pc-scale compact radio continuum emission detected in 63 U/LIRGs in the survey, with the aim to constrain the nature and physical properties of these energetic regions unimpeded by dust extinction.

This paper is divided into six sections. We describe our sample, data, observation information and reduction procedures in Section 4.2. In Section 4.3, we describe the methods used to identify and characterize individual regions of compact radio continuum emission. We further classify individual regions in each U/LIRG system into different types using ancillary multi-wavelength datasets and information from the literature in Section 4.4, and present the derived region quantities for different region types. In Section 4.5, we discuss the limitations and implications of our results, complemented by results derived from observations of other U/LIRGs and nearby normal galaxies. Finally, Section 4.6 summarizes major results and conclusions.

Throughout this work we adopt $H_0 = 70\,\mathrm{km/s/Mpc}$, $\Omega_{\mathrm{matter}} = 0.28$ and $\Omega_{\mathrm{vacuum}} = 0.72$ based on the five-year WMAP result (Hinshaw et al., 2009). These parameters are used with the 3-attractor model (Mould et al., 2000) to calculate the luminosity distances of the sample.

4.2 Sample & Data

We use 15 and 33 GHz continuum observations of 68 local U/LIRGs from the GOALS "Equatorial" VLA Survey (GOALS-ES), which is described in details in Chapter 2, where information on the sample, VLA observations and data reduction procedures can be found. To study the most compact radio continuum emission in these systems, here we only use the $A-/B-$configuration 15 and 33 GHz GOALS-ES observations that reach angular resolution of FWHM $\lesssim 0''.2$ ($\sim 100\,\mathrm{pc}$ at median $D_L \sim 100\,\mathrm{Mpc}$). Characteristics of these images are given in Table 2.2 in Chapter 2.

4.2.1 Ancillary VLA Data

To expand our study, in Section 4.5 we include comparisons between properties of compact radio continuum emission detected in the GOALS-ES systems and of those detected in other local U/LIRGs and nearby normal galaxies. To do this, we utilize VLA continuum observations of 22 of the most luminous local U/LIRGs presented in Barcos-Muñoz et al. (2017) (hereafter as BM17), those of 56 nearby normal galaxies from the SFRS (Murphy et al., 2018; Linden et al., 2020).

Observations for BM17 were taken with all four VLA configurations at both 6 and 33 GHz, but we only utilize the high-resolution (VLA A- or B-configuration)

33 GHz observations here to complement our the A- or B-configuration GOALS-ES observations. Observations for the SFRS were taken with the VLA in D-configuration at 33 GHz, C-configuration at 15 GHz and B-configuration at 3 GHz. We only use the 15 and 33 GHz observations in this work for comparing with our GOALS-ES observations at the same frequencies. These ancillary VLA observations were reduced using CASA by BM17 and the SFRS team, and relevant details are provided in the original publications. The synthesized beams have FWHM $\sim 0''.06 - 0''.2$ for the BM17 images, and FWHM $\sim 2''$ for the SFRS images. At the distances of the BM17 ($D_L \sim 170$ Mpc) and SFRS galaxies ($D_L \sim 11$ Mpc), these values corresponding to spatial resolutions of $20 - 200$ pc and 30–290 pc, respectively, which are similar to the $10 - 160$ pc resolutions reached by the GOALS-ES observations.

To ensure consistent comparisons, we re-analyzed these ancillary VLA images from BM17 and the SFRS using the same methods adopted here for the GOALS-ES images, described in Section 4.3 and Section 4.4. We present the results of these ancillary analysis in Appendix 4.7.2, and compare them with the GOALS-ES results (see Section 4.4) in Section 4.5.

4.3 Analysis

4.3.1 Regions identification & measurements

To characterize the properties of compact radio emission detected in our VLA observations, we use the Python package *Astrodendro* (Robitaille et al., 2019) for region identification and measurements. *Astrodendro* identifies and categorizes structures in an image into `trunk`, `branch` and `leaf`, based on three input parameters: the minimum brightness required for a structure to be physically meaningful (`min_value`), the minimum number of pixels in a structure (`min_npix`), and the minimum brightness

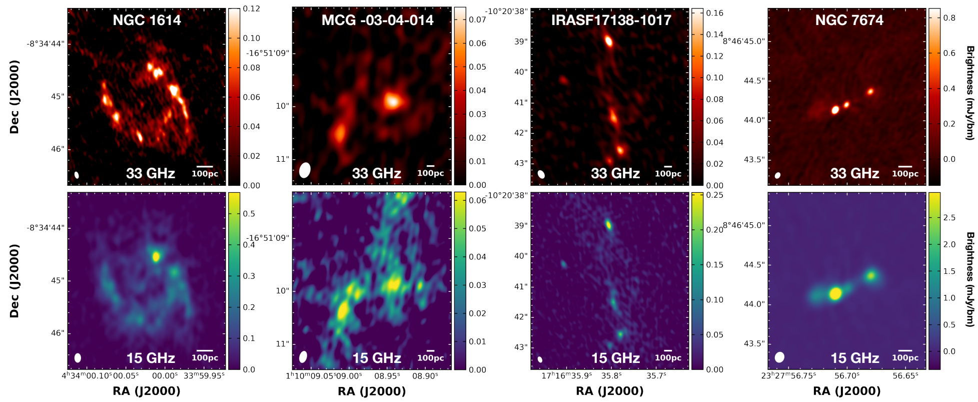

Figure 4.1: Examples of native resolution 33 (top) and 15 GHz (bottom) images used in this work. Each image is displayed in linear stretch with bilinear interpolation, and the colorbars show the brightness of the radio continuum emission, in the range of 0 to 80% of the peak pixel value, in units of mJy beam^{-1}. Synthesized beams (lower left) and scale bars of 100 pc (lower right) are shown.

relative to the local background required for a structure to be considered independent (`min_delta`). Structures identified as `leaf` are of the highest hierarchical order, which are the independent regions of compact radio emission that we are interested in, while `branch` and `trunk` are the surrounding relatively diffuse emission.

To ensure that we only identify physically meaningful structures, we ran *Astrodendro* on both the 15 and 33 GHz images of each system with `min_value`$= 5\sigma_{\rm rms}$ and `min_delta`$=1\sigma_{\rm rms}$ where $\sigma_{\rm rms}$ is the rms noise measured in an emission-free region of the image before primary beam correction. We follow Song et al. (2021) and set `min_npix` to be a quarter of the area of the synthesized beam, to avoid identifying noise spikes yet allowing detection of small unresolved regions. Despite that extended diffuse emission is largely filtered out in these observations, complex structures encompassing `trunk`, `branch`, and `leaf` are identified in several systems. For our purpose of characterizing the most compact radio emission, we only focus on the identified `leaf` structures in subsequent analysis.

Because the 33 GHz radio continuum more directly traces thermal free-free emission from star formation (e.g. Condon, 1992), in general we use *Astrodendro* results derived at 33 GHz for region identification and characterization. This also allows more robust constraints on the region sizes and surface brightness, given that 33 GHz observations either have higher native resolutions than 15 GHz observations, or better sensitivity (i.e. observations from 20A-401). In six systems, only the 15 GHz emission is bright enough to be identified via *Astrodendro*, and hence 15 GHz results were used instead. We also visually inspected all images and *Astrodendro* results to ensure that any identified structures associated with image artifacts are excluded from further analysis.

To account for the image noise and its influence on size and flux measurements of the identified regions, we re-ran *Astrodendro* 1000 times, randomly adjusting the brightness of each pixel sampling from a Gaussian distribution defined by the rms noise σ_{rms} and a VLA flux calibration error (10%)[2]. The standard deviations of the results from the 1000 runs are used to quantify the uncertainties in measured flux densities and sizes. Figure 4.2 shows two examples of *Astrodendro* output for a single run.

4.3.2 15 – 33 GHz Spectral Index

To better understand the nature of the identified regions of compact radio continuum emission, we measured the 15 – 33 GHz radio spectral index associated with each region, which can be used to estimate the relative contribution of thermal free-free emission to the total radio continuum emission at 33 GHz. First, we smoothed and re-gridded the 15 and 33 GHz image of each galaxy to have a common resolution and

[2]While the fundamental accuracy of flux density scale calibration is 3-5%, here we conservatively assume an accuracy of 10% instead since flux density calibrators and complex gain calibrators were not observed at similar elevations given the nature of our snapshot observations. See https://science.nrao.edu/facilities/vla/docs/manuals/oss
/performance/fdscale.

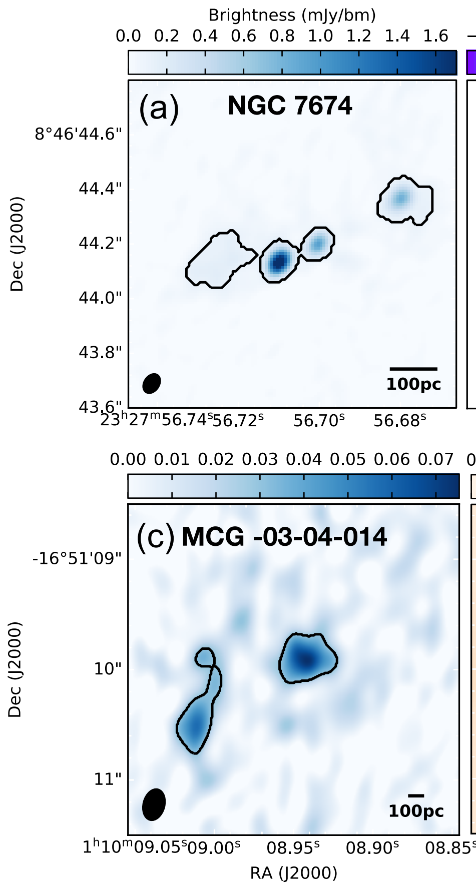

Figure 4.2: Images of NGC 7674 (a,b) and MCG-03-04-014 (c,d), as two examples illustrating the region identification, measurement and classification procedures described in Section 4.3 and 4.4.1. (a) & (c): native-resolution 33 GHz images, as displayed in Figure 4.1, with black contours outlining the areas of individual radio regions identified as `leaf` in a single run of *Astrodendro*. (b) 15 - 33 GHz spectral index map for NGC 7674 allows the identification of synchrotron-dominated radio jets with steep spectra ($\alpha \sim -1$) and AGN with flat-spectrum ($\alpha \sim 0$). Black contours are the same as in (a). (d) Archival *HST/NICMOS* F160W is used to locate the nucleus and off-nuclear star-forming region identified in MCG-03-04-014, as shown in (c). In (b) & (d), region types as classified following Section 4.4.1 are labeled. In each panel, black ellipse represents the native synthesized beam.

pixel scale. Next, we again performed *Astrodendro* analysis on these beam-matched images following the same procedures described in the previous Section. We then use the 15 and 33 GHz flux densities measured for each region within the *Astrodendro*-derived region boundaries to calculate the 15 - 33 GHz spectral index, α, given by the slope between 15 and 33 GHz flux measurements with respect to frequency:

$$\alpha = \frac{\log S_{\nu_1} - \log S_{\nu_2}}{\log \nu_1 - \log \nu_2}$$

where $\nu_1 = 33$ and $\nu_2 = 15$ in our case. Uncertainty of α is calculated via error propagation, accounting for uncertainties in flux density measurements. For most regions, boundaries identified using the 33 GHz images were used to measure their 15 and 33 GHz flux densities. For the 11 systems with regions that were only identified at 15 GHz, either due to limited sensitivity or intrinsic faintness at 33 GHz, boundaries identified from the 15 GHz images were used instead and the derived spectral indices hence are upper-limits. For each unresolved region that has area smaller than the matched-beam, we use the flux density measured within a beam-sized aperture centered on the region to estimate its spectral index.

4.4 Results

For each of the 63 systems with detection, at least one region was identified using *Astrodendro*. In total, we identified and characterized 131 regions at native resolutions at 33 and/or 15 GHz, 17 of which are unresolved by the native beams. Because the 15 – 33 GHz matched-beams are 2-5 times larger than the native beams at 33 GHz, distinct compact regions at native resolutions are blended together into larger, more extended regions at matched resolutions. Therefore, at matched resolutions, only 113 regions were identified, including 10 regions unresolved by the matched beams.

To better distinguish regions identified at native and matched resolutions, for the rest of this paper, we use “native regions” to refer to regions characterized at native resolutions, and refer to those characterized at matched resolutions as “matched regions”. All matched regions encompass at least one native region.

In the following sections, we present the derived properties of the native and matched regions. First, we classify regions into different types on the basis of their AGN activity (Section 4.4.1). In Section 4.4.2 and 4.4.3 we use measurements made for the native regions to constrain the brightness temperatures, physical sizes and luminosity surface densities of various region types. In Section 4.4.4 and 4.4.5 we use measurements for the matched regions that are not associated with AGN activity to estimate their total and thermal-only SFR and surface densities. Measured and derived quantities for the native regions are presented in Table 4.1, and those for the matched regions are in Table 4.2.

4.4.1 Region Classification

Before deriving the physical quantities associated with each region, it is crucial that we first identify the potential source powering the 33 and/or 15 GHz radio continuum emission. Despite that the radio continuum at > 30 GHz is widely used as a tracer of SFR (e.g. Murphy et al., 2012, 2018), emission from AGN, if present, can completely dominate the observed radio emission at a physical scale of ~ 100 pc (Lonsdale et al., 2003), in which case the radio-derived SFR would be over-estimated. Further, separating AGN and SF-dominated regions first will allow us to more clearly examine and better understand the radio properties of each population.

Although high brightness temperature ($T_b > 10^5$ K) is typically used to identify radio AGN (e.g. Condon et al., 1991), beam-dilution may reduce the brightness temperatures observed on 100 pc scales to the level that is characteristic of starbursts (see Section 4.4.2). Since we do not have information on the intrinsic underlying source structures, here we adopt a multi-wavelength approach to classify the native and matched regions characterized in Section 4.3 into different categories based on whether or not they may contain energetically-dominant AGN. We describe this two-step procedure below, which is demonstrated in Figure 4.2 and summarized in Figure 4.3, and provide more details on individual sources in the Appendix.

Region Location

As a first step, we separate regions into three initial categories – "nuclear", "off-nuclear" and "extra-nuclear" – based on their relative location in their host galaxies. These locations are determined visually by first overlaying the 33 and/or 15 GHz radio images on top of optical y-band images of the host galaxy from PanSTARRS1 (Chambers et al., 2016; Flewelling et al., 2020) as well as *Spitzer* IRAC channel 1 and channel 4 maps (J. Mazzarella in prep.). Afterwards, we also overlay an ellipse representing the size of the unresolved Mid-IR (MIR, $\lambda = 13.2\,\mu$m) galaxy "core" reported in Díaz-Santos et al. (2010), which is the FWHM of the Gaussian fit to the *Spitzer* IRS spectra of the galaxy that have spatial resolutions of $\sim 3''.6$. The MIR traces warm dust emission ($\sim 300\,K$) from obscured starburst and/or AGN activity, and hence provides useful constraints on the spatial extent of the most energetic component of the galaxy. The ellipse is then projected using galaxy position angles provided in the HyperLeda database (Makarov et al., 2014) and the Two Micron All Sky Survey (2MASS) Extended Source Catalog (Jarrett et al., 2000), along with galaxy inclination derived from galaxy axis ratio reported in Kim et al. (2013) and Jin et al. (2019) using the recipe given by Dale et al. (1997).

In general, we found agreement between the astrometry of the multi-wavelength images within few arcseconds. Regions that spatially coincide with the optical and

MIR galaxy peak are considered to be the galactic nuclei and hence are classified as "nuclear". Regions that are not "nuclear" but also lie within the MIR galaxy core are "off-nuclear", and regions lying completely outside of the MIR galaxy core are "extra-nuclear". In II Zw 96, the identified region is co-spatial with the brightest MIR component that has previously been identified as a powerful starburst region triggered on the outer edge of the merging galaxy pair (Inami et al., 2010), therefore we classify it as an "extra-nuclear" region. Regions residing within the MIR galaxy core (i.e. "nuclear" and "off-nuclear") are labelled with "n" in Table 4.1 and 4.2 (column 2), and "extra-nuclear" regions are labelled with "e".

Due to the comparatively low spatial resolution of the Pan-STARRS1 and IRAC images, determining whether a given region is "nuclear" or "off-nuclear" can be challenging when there are multiple regions within the MIR galaxy core. For seven galaxies, we were able to rely on direct comparisons with high-resolution *HST* and/or ALMA datasets publicly available from the archives to pinpoint the location of the galactic nuclei (often the kinematic center) and hence separate "nuclear" and "off-nuclear" regions. For 17 native regions residing in eight U/LIRGs without sufficient ancillary information from high-resolution imaging and/or gas kinematics, we assign them a final type "Ud" (undetermined) in Table 4.1 and 4.2 (column 3). Images of these eight systems are shown in the Appendix. We carry out further classification for the remaining 114 native regions (57 "nuclear", 49 "off-nuclear", 8 "extra-nuclear") in the following section.

Host AGN Classification

For the next step, we search in the literature for multi-wavelength (i.e. X-ray, optical, MIR, radio/sub-mm) evidence for AGN presence in each of the 63 U/LIRGs with detection, summarized in Table 4.3 in the Appendix. Mainly, we build upon optical classifications by Veilleux et al. (1995) and Yuan et al. (2010), as well as results from previous surveys of local U/LIRGs with *NuSTAR* (e.g. Ricci et al., 2017, 2021), *Chandra* (Iwasawa et al., 2011; Torres-Albà et al., 2018), *Spitzer* (e.g. Petric et al., 2011; Stierwalt et al., 2013), *AKARI* (e.g. Inami et al., 2018), *VLA* (e.g. at 1.4 and 8.4 GHz; Condon et al., 1995; Vardoulaki et al., 2015) and *VLBA* (e.g. Smith et al., 1998a). The compiled information is used in combination with the initial location classifications to further narrow down whether a region may contain an AGN that could dominate the radio emission:

– For "nucler" regions: if the host galaxies have been identified as AGN in the literature at more than one wavelength range, we classify them as "AGN". For example, we classify the nucleus of NGC 0034 as "AGN", given that the host galaxy is classified as a Seyfert 2 galaxy based on optical line ratios (Veilleux et al., 1995; Yuan et al., 2010) and X-ray spectral analysis with Chandra also reveals excess hard-band X-ray emission from an obscured AGN with absorbing column density $N_{\rm H} \sim 10^{23}{\rm cm}^{-2}$ (Torres-Albà et al., 2018). If the host galaxy has only been identified as AGN at one wavelength range but lacks identification at other wavelengths, or if evidence for AGN is ambiguous or inconsistent across all wavelengths, we classify the "nuclear" regions as "AGN/SBnuc". For example, the nucleus of IRASF 17138-1017 is classified as "AGN/SBnuc", because the X-ray spectral shape of the host galaxy is consistent with either star formation or an obscured AGN (Ricci et al., 2017; Torres-Albà et al., 2018), and the galaxy is classified as LINER in the optical, which may be powered by low-luminosity AGN, evolved stars, or both (Singh et al., 2013). Another example is the nucleus in MCG-03-04-014, which we classify as "AGN/SBnuc" given that the observed nuclear optical line ratios indicates emission from both AGN and starburst (Yuan et al., 2010), despite that the 3.3 and 6.2 μm PAH feature have large equivalent widths consistent with starburst-dominated emission (Stierwalt et al., 2013;

Inami et al., 2018). Lastly, if no AGN evidence has been found at any wavelength range for the host galaxy, we then classify the region as starburst-dominated nucleus ("SBnuc"). An example of this is NGC 5257 (Arp 240N).

– For "off-nuclear" regions: if they form a linear structure with an identified "AGN" and show steep 15 - 33 GHz spectral indices ($\alpha \lesssim -0.8$) indicating synchrotron-dominated emission (e.g. Condon et al., 1991), then we classify them as radio jets ("Jets") associated with the AGN. An example of this is NGC 7674 (see Figure 4.2). While "off-nuclear" regions next to "AGN/SBnuc" may be jets from unconfirmed AGN or star-forming clumps, here assume them as the latter ("SF") for simplicity, given that AGN with jets tend to dominate the nuclear emission and therefore likely to have been identified at other wavelengths. This reasoning has been adopted to classify the "SF" regions in IC 1623B, MCG-03-04-014, CGCG 436-030, III Zw 035 and IRAS F17138-1017, which also all have optical/IR counterparts.

– For "extra-nuclear" regions: if they are detected in the X-rays or have visible optical/IR counterparts, then we classify them as star-forming regions ("SF"). Only one "extra-nuclear" region, in IC 0214, does not show any X-ray, optical or IR counterpart. Hence, it is likely a background radio source ("Bg") that is not associated with the galaxy and therefore eliminated from further analysis.

In summary, out of the 114 native regions with identified locations (i.e. not "Ud"), 17 "AGN", 9 "Jet", 8 "SBnuc", 31 "AGN/SBnuc", 48 "SF" (41 "off-nuclear" and 7 "extra-nuclear") regions are classified, excluding one "Bg" region detected near IC 0214. At matched resolutions, many "off-nuclear" native regions are blended with the "nuclear" native regions, in which cases, the larger blended matched regions are designated with the "nuclear" classifications (i.e. "AGN", "AGN/SBnuc", "SBnuc"). As a result, 17 "AGN", 6 "Jet", 29 "AGN/SBnuc", 8 "SBnuc" and 39 "SF" (34 "off-nuclear" and 5 "extra-nuclear") matched regions are classified. Figure 4.3 summarizes our region classification scheme, and all region classifications are reported in Table 4.1 and 4.2, and described in the Appendix in more details. We note that only two systems in the sample (MCG-03-34-064, NGC 7674) have previously been classified as "radio-loud" AGN based on the excess radio over FIR emission on galaxy scales (Condon & Broderick, 1991; Condon et al., 1995), which emphasizes the necessity of the above two-step approach in constraining the sources of radio emission at resolved scales. In the upcoming survey paper we will further investigate the kpc-scale radio-IR correlations in the GOALS-ES systems for the different region types classified here.

4.4.2 Brightness Temperature

Condon et al. (1991) derived the maximum brightness temperature T_b for an optically-thick starburst radio source to be:

$$T_b \leq T_e(1 + 10(\frac{\nu}{\mathrm{GHz}})^{0.1+\alpha_{\mathrm{NT}}})$$

where $T_e \sim 10^4\,\mathrm{K}$ is the thermal electron temperature characteristic of massive star-formation, ν is the radio frequency at which measurements are made, and α_{NT} is the non-thermal spectral index characteristic of synchrotron emission generated by electrons accelerated by Type II supernovae. This limit allowed Condon et al. (1991) to confirm the AGN nature of the compact radio source they detected in UGC 08058 (Mrk 231), which has $T_b \gtrsim 10^6\,\mathrm{K}$ at 8.4 GHz. Here we assume $\alpha_{\mathrm{NT}} \sim -0.85$, based on resolved measurements of star-forming regions in the nearby disk galaxy NGC 6946 by (Murphy et al., 2011b), which gives a maximum starburst T_b of $10^{4.2}\,\mathrm{K}$ at 33 GHz, and $10^{4.4}\,\mathrm{K}$ at 15 GHz.

Using the Rayleigh-Jeans approximation, the brightness temperature T_b of each

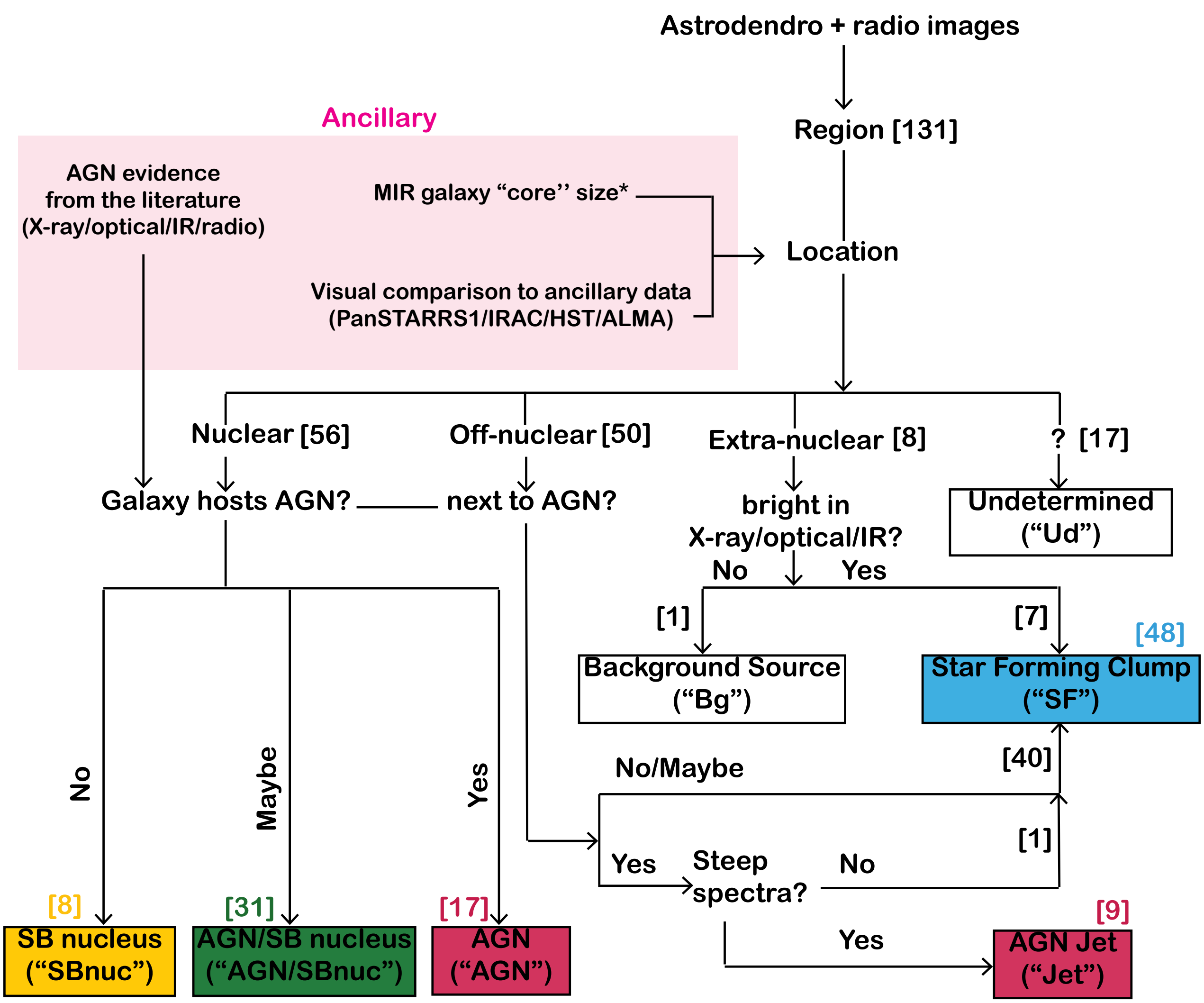

Figure 4.3: Region classification scheme described in Section 4.4.1 and demonstrated in Figure 4.2. Descriptions of individual galaxies are provided in the Appendix, including their multi-wavelength AGN classifications and and the ancillary datasets used. Numbers of native regions classified at each step are shown in brackets. *MIR galaxy "core" sizes are measured by Díaz-Santos et al. (2010).

native region can be calculated via (Condon, 1992; Pérez-Torres et al., 2021):

$$T_b = (\frac{S_\nu}{\Omega})\frac{c^2}{2k\nu^2} \\ \simeq 1.6 \times 10^3 (\frac{S_\nu}{\text{mJy}})(\frac{\nu}{\text{GHz}})^{-2}(\frac{\theta_M\theta_m}{\text{arcsec}^2})\ \text{K} \tag{4.1}$$

where c is the speed of light, k is the Boltzmann constant, S_ν is the region flux density measured at frequency ν, $\Omega = \pi\theta_M\theta_m/(4\ln 2)$ is the region area assuming a Gaussian morphology, with θ_M and θ_m corresponding to the FWHM of the major and minor axis of the Gaussian.

Because the identified regions have irregular morphology with unknown sub-beam structures, here we calculate the brightness temperature of each native region using two different methods. First, we directly use region flux density and area measured with *Astrodendro* for S_ν and Ω in Equation 4.1. Second, we perform Gaussian fitting and deconvolution on all native-resolution images using CASA task `imfit`, and calculate the deconvolved brightness temperature T_b^{imfit} of each region, using the flux density of the fitted Gaussian model and the deconvolved θ_M and θ_m, following Condon et al. (1991). We note that via assuming an simple Gaussian morphology, the latter method allows tighter constraints on the intrinsic sizes on marginally-resolved regions, but does not reflect the observed diverse region morphology or the varying degree of surrounding diffuse emission present in each system, which leads to poor flux recovery especially for extended regions. Gaussian-fitting was also unsuccessful for 16 regions in 8 systems. Therefore we use the latter method only in this Section to illustrate the possible effect of beam dilution, but continue to use results derived with *Astrodendro* (Section 4.3) throughout the rest of the paper. Values of T_b and T_b^{imfit} are reported in Table 4.1 and compared in Figure 4.4.

Figure 4.4 shows that, regardless of the method used, "AGN" and "AGN/SBnuc" have higher brightness temperatures than "SF". The ranges of T_b for "AGN", "AGN/SBnuc" and "SF" are 19 – 950 K, 1 – 360 K and 1 – 160 K, respectively. However, all regions, including "AGN", have $T_b < 10^4$ K. For "SF", the overall low T_b is expected from optically-thin emission associated with star formation. For "AGN" and "AGN/SBnuc", the observed emission may come from a combination of AGN emission and nuclear star formation, which may be further diluted by the beam. The effect of such beam dilution is also demonstrated in Figure 4.4, where we see that T_b^{imfit} for "AGN" (50 – 11900 K), "AGN/SBnuc" (3 – 2500 K) and "SBnuc" (70 – 1710 K) are higher than T_b by up to ~ 1 dex. Nevertheless, no "AGN" has T_b^{imfit} greater than 10^6 K, and the only "AGN" with $T_b^{\mathrm{imfit}} > 10^4$ K is the one in NGC 1068, which is the most nearby Seyfert in GOALS. Additionally, 17 regions (including the "AGN/SBnuc" in IRAS 17208-0014) are unresolved by the beam, and 18 regions (including 3 "AGN" and 2 "AGN/SBnuc") are separately determined as point-sources by CASA `imfit`. For these regions, the calculated T_b and T_b^{imfit} are lower-limits and indicated in Table 4.1.

Our results are similar to those found by Barcos-Muñoz et al. (2017), who measured an overall low T_b ($\sim 100 - 1000$ K) in the nuclei of the most luminous local U/LIRGs at 100 pc scales at 33 GHz. These results also demonstrate the limitation of the current VLA observations for directly identifying AGN using brightness temperatures. Future VLBI follow-up of the "AGN/SBnuc" regions would significantly improve our ability to identify AGN in many more local U/LIRGs, as well as isolate AGN emission from the compact circumnuclear star formation prevalent in these systems (e.g. Condon et al., 1991).

4.4.3 Size, Luminosity and Luminosity Surface Density

For each native region, *Astrodendro* measures its angular area A and flux density S_ν at frequency ν using the region boundary identified by the algorithm (i.e. black

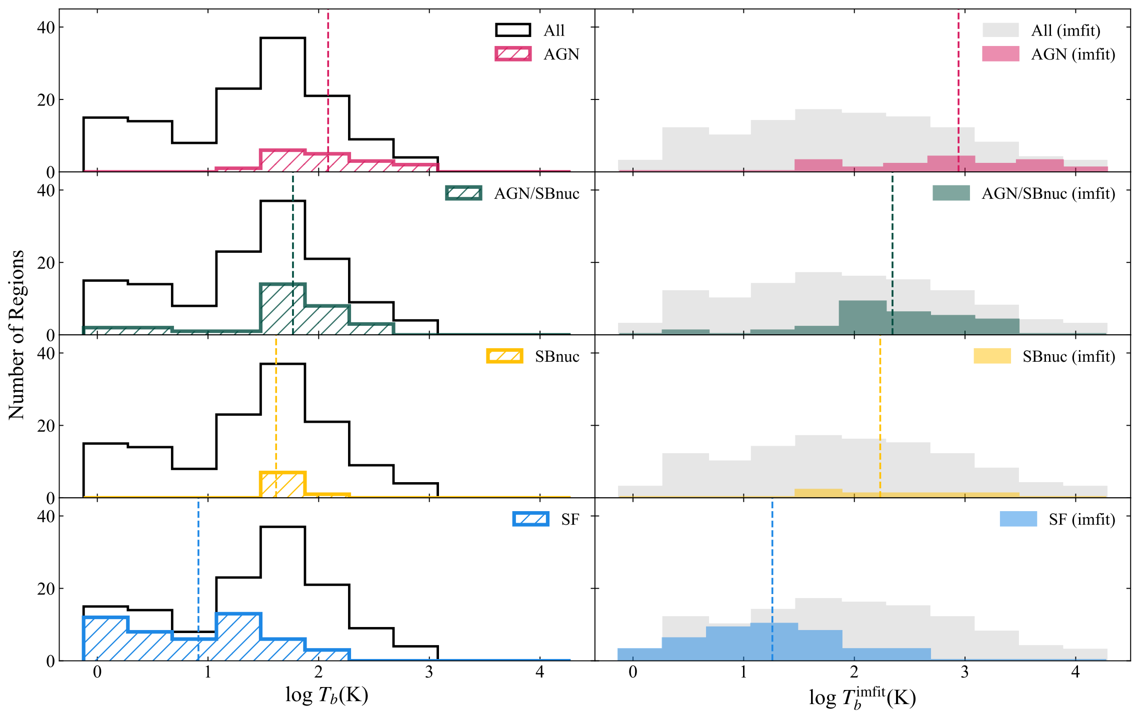

Figure 4.4: Distribution of brightness temperatures of regions identified at native resolutions at 15 or 33 GHz. *Left:* values derived from *Astrodendro* measurements of region areas and flux densities. Distribution for all 131 native regions are shown in black un-filled histogram. *Right:* values derived from Gaussian-fitting results using CASA `imfit` task. Distribution for 115 regions with successful fits are shown in black filled histogram. In both panels, distributions for "AGN" (magenta), "AGN/SBnuc" (green), "SBnuc" (yellow) and "SF" (blue) are shown separately for comparison, with dashed lines marking the median values. Overall, "AGN" have the highest brightness temperatures and Gaussian-fitting yields higher values, but only one "AGN" (in NGC 1068) exceeds the maximum starburst brightness temperature ($\sim 10^4$ K), likely due to beam dilution.

contours in Figure 4.1). We use the mean values of these measurements from 1000 runs of *Astrodendro* (see Section 4.3) to calculate the spectral luminosity ($L_\nu = 4\pi S_\nu D_L^2$), effective radius ($R_e = \sqrt{(A/\pi)}$), and spectral luminosity surface density Σ_{L_ν} of each region, using the luminosity distance (D_L) and angular-to-physical conversion factor derived for each system, as listed in Table 3.1. For the 17 native regions with areas smaller than the synthesized beams accounting for uncertainty, we use the beam areas as upper-limit estimates for the region sizes, and the corresponding Σ_{L_ν} are lower-limits. The derived properties of a total of 131 native regions in 63 systems are reported in Table 4.1, of which 14 regions in 10 systems were measured at 15 GHz due to poor or non-detection at 33 GHz. In Figure 4.5, we show the distributions of the derived properties of 99 native regions with 33 GHz measurements, excluding the "Bg" in IC 0214 and 17 unresolved regions.

The effective radii (R_e) of these 99 native regions span from 8 to 170 pc, with no significant size differences among the region types, except for "AGN/SBnuc" regions, which have the largest sizes at a median value of 80 pc compared with $\sim$ 40 pc for "AGN", "SBnuc" and "SF". As shown in Figure 4.5, the 33 GHz luminosity (L_{33}) span three orders of magnitude, ranging from 3.0×10^{26} to 3.4×10^{29} erg s^{-1} Hz^{-1}. Unsurprisingly, "AGN" regions are overall more luminous, with a $L_{33} = 8.0 \times 10^{26} - 1.7 \times 10^{29}$ erg s^{-1} Hz^{-1} and a median of 1.7×10^{28} erg s^{-1} Hz^{-1}, compared with "SF" regions which have $L_{33} = 2.0 \times 10^{26} - 3.4 \times 10^{28}$ erg s^{-1} Hz^{-1} and a median of 1.1×10^{27} erg s^{-1} Hz^{-1}, about an order of magnitude lower. This difference is also evident in distribution of spectral luminosity surface density $\Sigma_{L_{33}}$: "AGN" regions have $\Sigma_{L_{33}}$ ranging from 1.1×10^{30} to 3.0×10^{31} erg s^{-1} Hz^{-1} kpc^{-2} with a median of 4.2×10^{30} erg s^{-1} Hz^{-1} kpc^{-2}, which is also an order of magnitude higher than 2.3×10^{29} erg s^{-1} Hz^{-1} kpc^{-2} for the "SF" regions. When considering all 99 native regions, including 15 "AGN", 9 "Jet", 28"AGN/SBnuc", 5 "SBnuc", 36 "SF" (31 "off-nuclear" and 5 "extra-nuclear") and 9 "Ud" regions, the median for $\Sigma_{L_{33}}$ is around 1.1×10^{30} erg s^{-1} Hz^{-1} kpc^{-2}, below which the distribution is almost completely dominated by "SF" regions. In Section 4.5.1 we further discuss the implication of the differences we observe between the "AGN" and "SF" native regions, in the theoretical context of radiation feedback-regulated star formation in the dusty environments of U/LIRGs.

4.4.4 Thermal Fraction at 33 GHz

Assuming a typical radio continuum SED for star-forming galaxies (e.g. Condon, 1992), the 33 GHz radio continuum emission can be decomposed into thermal free-free emission with a flat spectrum ($S_\nu \propto \nu^{-0.1}$) and non-thermal synchrotron emission with a steep spectrum ($S_\nu \propto \nu^{\alpha_{\rm NT}}$), where a non-thermal spectral index of $\alpha_{\rm NT} \sim -0.85$ has been found to be widely applicable in resolved star-forming regions detected in nearby disk galaxies (Murphy et al., 2011b, 2012). For each matched region, we derive the 33 GHz thermal fraction $f_{\rm th}$, which measures the fractional contribution of thermal free-free emission generated from plasma around massive young stars (i.e. HII regions) using the measured 15 - 33 GHz spectral index α_{15-33} (see Section 4.3), and Equation (11) from Murphy et al. (2012):

$$f_{\rm th} = \frac{\left(\frac{\nu_2}{\nu_1}\right)^{\alpha} - \left(\frac{\nu_2}{\nu_1}\right)^{\alpha_{\rm NT}}}{\left(\frac{\nu_2}{\nu_1}\right)^{-0.1} - \left(\frac{\nu_2}{\nu_1}\right)^{\alpha_{\rm NT}}} \tag{4.2}$$

where we set the spectral index α between ν_1 and ν_2 (33 and 15 GHz) to be our measured α_{15-33}, and use error propagation to derive the uncertainties associated with flux calibration and image noise levels. We note that 16 matched regions in 11 systems were not identified with *Astrodendro* at 33 GHz due to insufficient sensitivity, so the measured α_{15-33} for these regions are likely steeper than the intrinsic values.

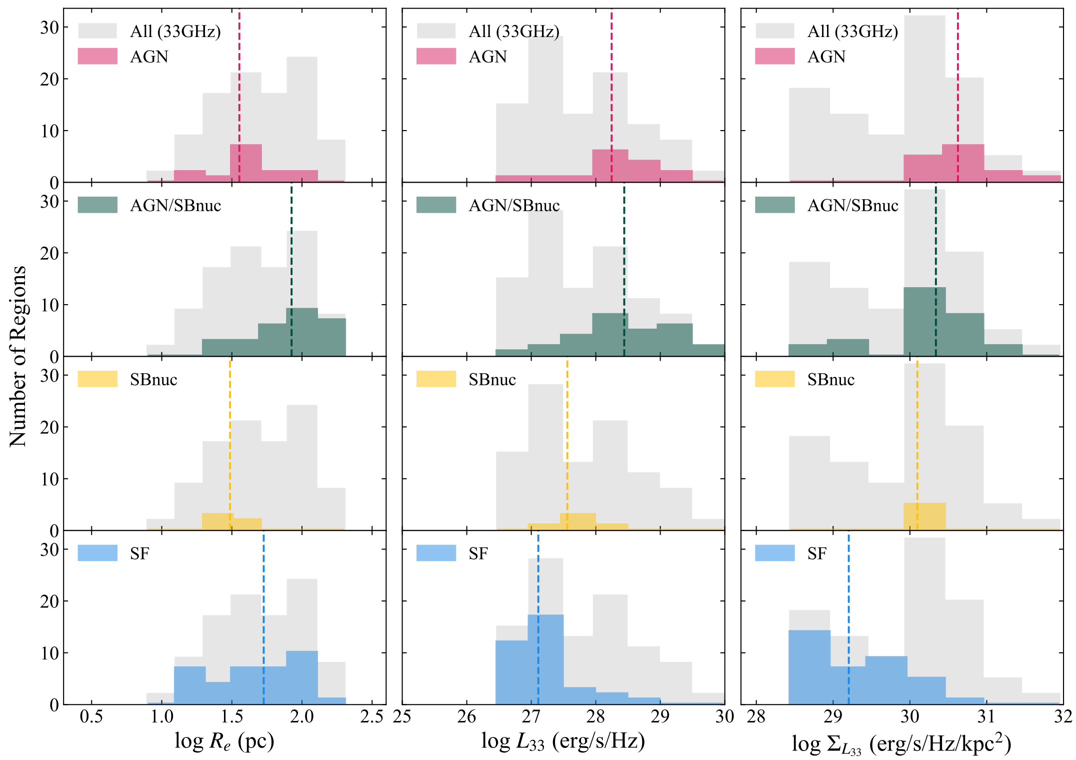

Figure 4.5: Distribution of derived properties of regions identified and characterized at native resolutions using *Astrodendro*. For direct comparison, we only show results derived from 33 GHz measurements, available for 117 native regions, excluding the "Bg" source in IC 0214. *Left:* Effective radius R_e. *Middle:* 33 GHz luminosity L_{33}. *Right:* 33 GHz luminosity surface density $\Sigma_{L_{33}}$. In all three columns, we also show distributions for "AGN" (magenta), "AGN/SBnuc" (green), "SBnuc" (yellow) and "SF" regions (blue), and the corresponding median values (dashed lines), overlaid on the distributions of all 117 native regions (grey). Results for "Jet" and "Ud" regions are not separately shown for simplicity. While all regions types share similar sizes, "AGN" and "AGN/SBnuc" have higher L_{33} and $\Sigma_{L_{33}}$ than "SF" by an order of magnitude.

We label these values in Table 4.2 as upper-limits, and mark the host systems with "*".

Of the 97 matched regions that were identified at both 15 and 33 GHz (excluding "Bg" in IC 0214), 10 regions have steep spectra with $\alpha_{15-33} \lesssim -0.85$ after accounting for the estimated uncertainties, including four "Jet", three "SF" and three "AGN/SBnuc". This suggests that the observed 33 GHz emission in these regions are dominated by non-thermal synchrotron emission produced by relativistic electrons accelerated in AGN jets or supernovae. The "AGN/SBnuc" in UGC 02238 and NGC 5104 have the steepest spectra, with $\alpha_{15-33} \sim -1.6 \pm 0.3$. In these cases we follow Linden et al. (2020) and set $\alpha_{\rm NT} = \alpha_{15-33}$, which gives $f_{\rm th} \sim 0\%$, on the basis that negative $f_{\rm th}$ are not physically meaningful. For three "SF" regions, IC1623B_n4, NGC5257_e1 and IC2810_e1, $\alpha_{15-33} \gtrsim 0$ after accounting for uncertainties, which is unexpected from optically-thin thermal free-free emission. Given that all "SF" regions have brightness temperatures much lower than the optically-thick starburst temperature of $\sim 10^4$ K (see Section 4.4.2), a potential cause for the higher than expected 33 GHz continuum flux may be anomalous microwave emission from spinning dust particles in heavily-obscured young starburst (Murphy et al., 2020), which will require more high-resolution observations above and below 33 GHz to confirm. We note that the extra-nuclear region in NGC 5257 also shows the flattest 3 - 33 GHz spectrum among 48 extra-nuclear regions hosted in 25 U/LIRGs in the equatorial sample when measured on kpc scale, consistent with our measurement (Linden et al., 2019). For regions with $\alpha_{15-33} \gtrsim -0.1$ we assume $f_{\rm th} \sim 100\%$.

indent Figure 4.6 shows the resulted distribution of $f_{\rm th}$ for all 97 matched regions as well as for different region types, which all span a wide range from $\sim 0\%$ (dominated by non-thermal emission) to 100% (dominated by thermal emission). However, the median values for "AGN" and "AGN/SBnuc", at $f_{\rm th} \sim 30\%$, are noticeably lower than

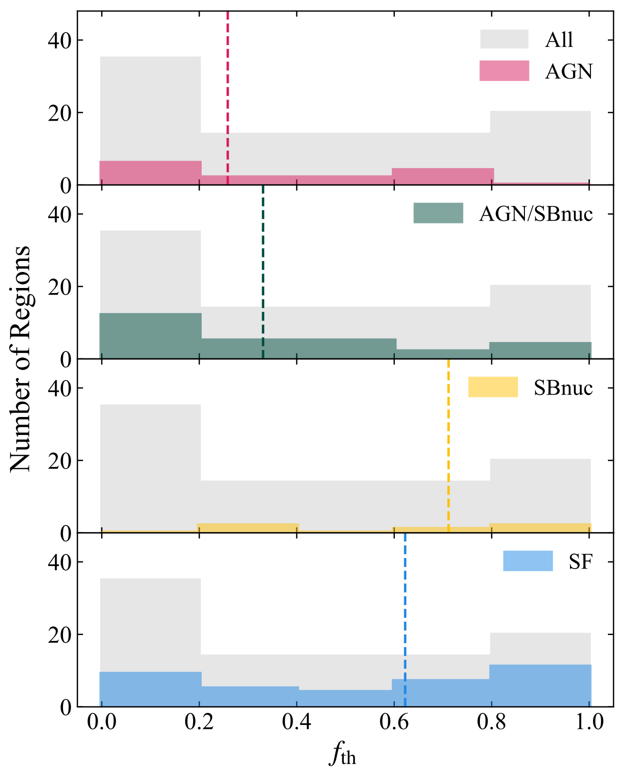

Figure 4.6: Distribution of the derived 33 GHz thermal fraction $f_{\rm th}$, for 97 matched regions identified at both 15 and 33 GHz (in gray) excluding "Bg", and for "AGN" (magenta), "AGN/SBnuc" (green), "SBnuc" (yellow) and "SF" regions (blue). The median values are $\sim$ 25%, 33%, 71% and 62%, respectively, and shown in dashed lines. Results for "Jet" and "Ud" regions are not separately shown. While $f_{\rm th}$ spans a wide range for all region types compared, "AGN" and "AGN/SBnuc" have lower median $f_{\rm th}$ than "SBnuc" and "SF" regions.

those for "SBnuc" and "SF", at $f_{\rm th} \sim 65\%$. This result is consistent with kpc-scale measurements of extra-nuclear star-forming regions by Linden et al. (2019) using GOALS-ES C-configuration observations. For "AGN" and "AGN/SBnuc", mechanisms other than star formation may be producing excess non-thermal emission at 33 GHz (e.g. Panessa et al., 2019). Overall, the wide range of $f_{\rm th}$ spanned by different region types demonstrates that a simple two-frequency spectral index is insufficient for inferring the nature of radio emission in a given region at 100 pc scales. In Section 4.5.2 we further discuss the potential mechanisms that may be contributing to the 15 – 33 GHz radio continuum emission in these local U/LIRGs at 100 pc scales.

4.4.5 Star Formation Rates and Surface Densities

For all matched "SF" and "SBnuc" regions, we use Equation (10) in Murphy et al. (2012) to convert the measured 33 or 15 GHz continuum flux density to a total star formation rate (SFR), accounting for both thermal free-free emission from HII regions (< 10 Myr) and non-thermal synchrotron emission from supernovae ($\sim$10–100 Myr):

$$\left(\frac{\rm SFR}{\rm M_{\odot}yr^{-1}}\right) = 10^{-27}\Big[2.18\left(\frac{T_e}{10^4{\rm K}}\right)^{0.45}\left(\frac{\nu}{\rm GHz}\right)^{-0.1} + 15.1\left(\frac{\nu}{\rm GHz}\right)^{\alpha^{\rm NT}}\Big]^{-1}\left(\frac{L_\nu}{\rm erg s^{-1}Hz^{-1}}\right) \tag{4.3}$$

where a Kroupa Initial Mass Function (IMF) and continuous and constant star-forming history over 100 Myr is assumed. In Equation 5.4, L_ν is the spectral luminosity at the observed frequency ν, given by $L_\nu = 4\pi D_L^2 S_\nu$, where S_ν is the measured flux density. Here we again adopt an electron temperature $T_e = 10^4$ K and a non-thermal spectral index $\alpha^{\rm NT} = -0.85$, as following the previous Sections. If we only consider the thermal free-free emission from young massive stars, Equation 5.4

becomes (Equation 6 in Murphy et al., 2012):

$$\left(\frac{\mathrm{SFR_{th}}}{\mathrm{M_{\odot}yr^{-1}}}\right) = 4.6\times10^{-28}\left(\frac{T_e}{10^4\mathrm{K}}\right)^{-0.45}\left(\frac{\nu}{\mathrm{GHz}}\right)^{0.1} \times\left(\frac{L_{\nu}^{\mathrm{T}}}{\mathrm{ergs^{-1}Hz^{-1}}}\right) \tag{4.4}$$

where $L_{\nu}^{\mathrm{T}} = f_{\mathrm{th}}L_{\nu}$ is the thermal-only spectral luminosity. For regions with $f_{\mathrm{th}} \simeq 100\%$, thermal emission from young massive stars completely dominates the radio continuum, and $L_{\nu}^{\mathrm{T}} \simeq L_{\nu}$. For $f_{\mathrm{th}} \simeq 0\%$, $\mathrm{SFR_{th}} \simeq 0\,M_{\odot}\mathrm{yr}^{-1}$.

For the 38 matched "SF" regions, SFR ranges from 0.14 to $12\,M_{\odot}\mathrm{yr}^{-1}$, with a median of $\sim 0.7\,M_{\odot}\mathrm{yr}^{-1}$. The $\mathrm{SFR_{th}}$ spans from $\sim 0\,M_{\odot}\mathrm{yr}^{-1}$ to $12\,M_{\odot}\mathrm{yr}^{-1}$, corresponding to $f_{\mathrm{th}} \simeq 0\%$ to $f_{\mathrm{th}} \simeq 100\%$. The median SFR_{th} is $0.4\,M_{\odot}\mathrm{yr}^{-1}$. For the 8 "SBnuc", the ranges of SFR and $\mathrm{SFR_{th}}$ are $0.2 - 13\,M_{\odot}\mathrm{yr}^{-1}$ and $0 - 11\,M_{\odot}\mathrm{yr}^{-1}$, similar to the "SF" regions, but with higher median values, at 3.5 and $2\,M_{\odot}\mathrm{yr}^{-1}$, respectively. When taking account of the physical sizes of these matched regions, as calculated from the region boundaries defined by *Astrodendro* with which flux density and spectral index of each region was measured, the SFR and $\mathrm{SFR_{th}}$ surface densities, Σ_{SFR} and $\Sigma_{\mathrm{SFR_{th}}}$, range from 13 – $1.6\times10^{3}\,M_{\odot}\mathrm{yr}^{-1}\mathrm{kpc}^{-2}$ and 0 – $1.7\times10^{3}\,M_{\odot}\mathrm{yr}^{-1}\mathrm{kpc}^{-2}$ for the "SF" regions including 6 unresolved regions. For "SBnuc", Σ_{SFR} and $\Sigma_{\mathrm{SFR_{th}}}$ have ranges of 22 – $540\,M_{\odot}\mathrm{yr}^{-1}\mathrm{kpc}^{-2}$ and 0 – $400\,M_{\odot}\mathrm{yr}^{-1}\mathrm{kpc}^{-2}$, including 1 unresolved region. The median values for the "SBnuc" regions are higher than those for the "SF" regions by about a factor of five. However, this result may not be representative given the limited numbers of "SBnuc" identified in the sample. We report the above derived values in Table 4.2. For all other region types, given the unknown contribution of star formation to the observed radio continuum, we do not report values of SFR and $\mathrm{SFR_{th}}$. In Section 4.5.2 we compare these results to those derived for star-forming regions in nearby normal galaxies observed with the SFRS at ~ 100 pc scales.

4.5 Discussion

4.5.1 What powers the compact 33 GHz continuum emission in local U/LIRGs?

As demonstrated in Section 4.4.2, the radio data at hand does not allow for direct AGN identification using brightness temperatures, and multi-frequency VLBI observations at milli-arcsecond resolutions are needed to pinpoint the location of AGN and isolate its emission from the circumnuclear star formation in “AGN” and “AGN/SBnuc” regions. Nevertheless, it is evident from Figure 4.4 and 4.5 that “AGN” and “SF” respectively dominate the upper and lower end of the distributions in brightness temperature and 33 GHz luminosity surface density. In Figure 4.7, we further illustrate this difference by showing the luminosity and luminosity surface density with respect to the effective radius characterized with *Astrodendro* at 33 GHz (filled symbols), including additional 23 regions from BM17 (see Section 4.2.1 and Appendix 4.7.2).

Figure 4.7 shows that “AGN” and “AGN/SBnuc” almost always have higher L_{33} and $\Sigma_{L_{33}}$ relative to “SF” across the entire size range probed and by up to ~ 3 dex. This result suggests that more extreme mechanisms may be driving the observed radio emission in the “AGN” and “AGN/SBnuc” regions compared with the “SF” and “SBnuc” regions. In the following sections we discuss two mechanisms that may be simultaneously contributing to the elevated 33 GHz emission observed in these “AGN” and “AGN/SBnuc” regions.

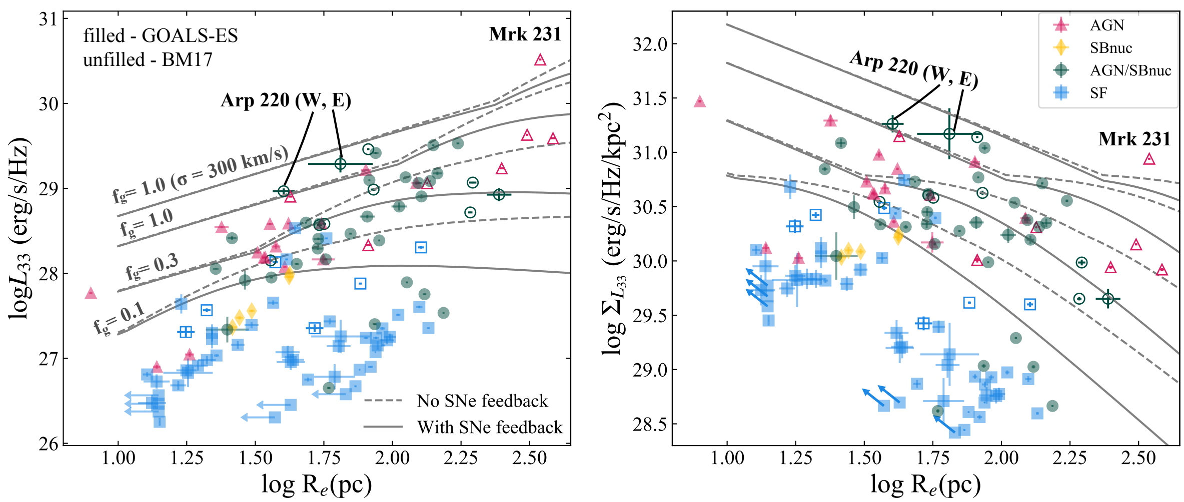

Figure 4.7: 33 GHz luminosity L_{33} (left) and surface density $\Sigma_{L_{33}}$ (right) vs. effective radius for 95 native regions from GOALS-ES (filled symbols) and of additional 23 native regions characterized using observations of the most luminous U/LIRGs from Barcos-Muñoz et al. (2017) (BM17; unfilled symbols). In both panels, we show "AGN" (magenta triangle), "AGN/SBnuc" (green circles), "SBnuc" (yellow diamonds) and "SF" regions (blue squares). Regions classified as "Jet" or "Ud" are not shown for simplicity. Upper-limits in size measurements are indicated with arrows. Dashed grey curves are models for a steady-state radiation feedback-supported maximal starburst disk from Thompson et al. (2005) with assumed molecular gas fraction $f_g = 0.1, 0.3, 1.0$ and stellar velocity dispersion $\sigma = 200\,\mathrm{km\ s^{-1}}$, as well as for $f_g = 1.0$ and $\sigma = 300\,\mathrm{km\ s^{-1}}$. Solid grey curves show the same models with a modified term to include supernovae feedback, as adopted in Barcos-Muñoz et al. (2017). Compared to "SF" and "SBnuc" regions, "AGN" and "AGN/SBnuc" regions have higher L_{33} and $\Sigma_{L_{33}}$ by up to 3 dex across the entire size range probed, but only the "AGN" in Mrk 231 clearly exceeds the predicted L_{33} and $\Sigma_{L_{33}}$ for a maximally star-forming nuclear disk.

Radiation pressure-supported nuclear starburst

Using analytical models, Thompson et al. (2005) (hereafter as TQM05) demonstrated that intense starbursts triggered in the dust-obscured gas-rich nuclear environments of local U/LIRGs can potentially radiate at the Eddington-limit (for dust). In this scenario, IR radiation from dust-reprocessed UV or optical emission from massive young stars provides the dominant vertical support against gravitational collapse in the optically-thick starburst disk. The authors compared the models to IR luminosity surface density estimated from radio observations of local U/LIRGs by Condon et al. (1991) and found a general agreement. These models have also been invoked to interpret compact radio/sub-mm emission observed in the most luminous local U/LIRGs on $\sim$ 100 pc scales (e.g. Barcos-Muñoz et al., 2015, 2017; Pereira-Santaella et al., 2021). In Figure 4.7 we compare our 33 GHz measurements to a simplified version of the radiation pressure-supported starburst disk models presented in Thompson et al. (2005) to investigate the possibility that the observed compact radio emission is driven by such radiation pressure-supported optically-thick starbursts.

Following BM17, we also present additional solutions incorporating vertical support from supernovae feedback that can be approximated as $10 \mathrm{n_{mol}}^{-1/7}$(Faucher-Giguère et al., 2013; Kim & Ostriker, 2015), where $\mathrm{n_{mol}}$ is the volume number density of the molecular gas of the modelled marginally-stable one-zone disk (Equation 1 and 7 from Thompson et al., 2005). The predicted IR luminosities are then converted into 33 GHz luminosities by assuming both come from star formation, using Equation 10 and 15 from Murphy et al. (2012). With this assumption, we expect that excess 33 GHz emission from AGN activity would bring the "AGN" and "AGN/SBnuc" regions above the predicted values for maximal starbursts.

However, as shown in Figure 4.7, only the nucleus in Mrk 231 has L_{33} and ΣL_{33}

exceeding the model prediction for the highest molecular gas fraction and velocity dispersion assumed, suggesting dominant AGN contribution to the 33 GHz emission at 100 pc scales. While this result is unsurprising given that Mrk 231 hosts the closest quasar (Adams, 1972), the fact that all other "AGN" and "AGN/SBnuc" do not exceed the model predictions points to the possibility that their 33 GHz emission could be attributed to star formation. Most of the "AGN/SBnuc" regions cluster around the solutions for a constant molecular gas fraction of 0.3, which is also the average value for local U/LIRGs derived by Larson et al. (2016) based on results from galaxy SED fitting by (U et al., 2012) (for stellar mass) and global molecular gas mass estimates from the literature. Therefore, in the context of this model comparison, the higher L_{33} and $\Sigma_{L_{33}}$ of the "AGN" and "AGN/SBnuc" regions relative to the "SF" regions reflect a more extreme mode of star formation that maintains a radiation pressure-supported nuclear starburst disk, compared with star formation in relatively isolated Giant Molecular Clouds in the outskirts of the systems.

We note that many of these compact nuclei may have higher gas fractions at 100 pc scales as molecular gas likely dominates the nuclear environments of local U/LIRGs (Downes et al., 1993; Larson et al., 2020). Additionally, radiation pressure may exceed the Eddington limit and drives outflows (e.g. Murray et al., 2005), in which case measurements will also lie above the model predictions (e.g. Pereira-Santaella et al., 2021). A notable example is the two nuclei in Arp 220 ($f_g \sim 0.5, \sigma \sim 165$ km/s; Genzel et al., 2001; Downes & Solomon, 1998), around which outflows have been detected in different tracers (e.g. Sakamoto et al., 2009; Tunnard et al., 2015; Sakamoto et al., 2017; Barcos-Muñoz et al., 2018; Perna et al., 2020). Although these outflows have collimated morphology that indicates an AGN origin (Sakamoto et al., 2017; Barcos-Muñoz et al., 2018), VLBI observation does not show evidence for a bright AGN core (e.g. Smith et al., 1998b; Lonsdale et al., 2006; Parra et al., 2007; Varenius et al., 2019), which suggests that the elevated radio continuum emission of these two nuclei are likely powered by nuclear starbursts. Future follow-up high-resolution extinction-free measurements of the stellar and molecular gas distribution and kinematics in these nuclei are required to conduct more extensive comparisons to these models.

(Obscured) AGN activity

Aside from an extreme mode of nuclear starburst, AGN activity likely contributes to the elevated 33 GHz emission in "AGN" and "AGN/SBnuc" regions. TQM05 showed that efficient AGN fueling on pc scales is accompanied by intense star formation in the nuclear disk over 100 pc scales above a critical rate. This prediction may explain the relatively low L_{33} and $\Sigma_{L_{33}}$ of the "SBnuc" regions relative to "AGN" and "AGN/SBnuc" regions: star formation in "SBnuc" do not yet reach the rates required to trigger efficient AGN fueling. In the theoretical context of a merger-quasar evolutionary sequence (e.g. Di Matteo et al., 2005) where tidal torque of gas-rich galaxy merger drives nuclear fueling, we then would expect the"SBnuc" regions to reside in systems at earlier interacting stages, and the luminosities of the nuclei to increase towards later interacting stages due to contribution from triggered AGN activity.

In the top panel of Figure 4.8, we present a histogram of the region types represented in galaxies from GOALS-ES at different merger stages, normalized by the total number of systems at each stage. We see that the "SBnuc" regions are indeed preferentially found in early-stage mergers (stage "b"), which supports the proposed scenario. Additionally, "AGN/SBnuc" regions are found at all stages but most frequently in late-stage mergers (stage "d"). This is consistent with results from MIR analysis of the GOALS systems by Stierwalt et al. (2013), who found that among the local U/LIRGs, the fraction of AGN-starburst composite systems increases among late stage mergers. Among the merging systems, "AGN" regions are also most frequently found in late-stage mergers. As shown in the the lower panel of Figure 4.8, it is also at the late-stage that the nuclei have the highest median L_{33}. These results are in agreement with the scenario that powerful AGN activity is triggered during gas-rich galaxy-mergers. The marked increase in "AGN/SBnuc" towards the later stages may reflect increased level of dust obscuration that makes AGN identification more difficult at shorter wavelengths, as suggested in previous GOALS studies in the MIR and X-rays (e.g. Stierwalt et al., 2013; Ricci et al., 2017, 2021). We note that nuclei from BM17 were not included in Figure 4.8 because they primarily reside in late-stage mergers, but including them does not alter the overall trend seen in the GOALS-ES sample.

To further investigate whether the elevated 33 GHz emission is correlated with more powerful AGN activity, we compare AGN diagnostics in the X-rays (hardness ratio, $L_{2-10\mathrm{keV}}$; Iwasawa et al., 2011; Torres-Albà et al., 2018) and MIR (6.2μm PAH equivalent width, MIR slope; Stierwalt et al., 2013) with L_{33} of "AGN" and "AGN/SBnuc" regions in Figure 4.9. We also mark systems with [Ne V] (14.3 μm), Fe K (6.4 keV), and hard X-ray (> 10 keV) detections (Petric et al., 2011; Iwasawa et al., 2011; Ricci et al., 2021), which are commonly used indicators of AGN activity. The latter two are used to identify heavily-obscured AGN.

As shown in Figure 4.9, while L_{33} does not exhibit clear correlation with the X-ray hardness ratio, nuclei with higher L_{33} show higher $L_{2-10\mathrm{keV}}$, smaller 6.2μm PAH equivalent width (EW), and steeper MIR slope. The Kendall's Tau correlation coefficients are 0.08, 0.27, -0.29 and 0.29, respectively for comparisons presented in Figure (a), (b), (c) and (d), indicating stronger (anti)correlations between L_{33} and MIR diagnostics. Nuclei with the highest L_{33} mostly reside in ULIRGs, and they also have the smallest 6.2μm PAH EW and highest $L_{2-10\mathrm{keV}}$, which suggests that the 33 GHz continuum is tracing AGN activity that produces strong hard X-ray emission and weak PAH emission. The steeper MIR slope of these nuclei, as shown in Stierwalt et al. (2013), suggest that they are heavily-embedded in thick layers of cool dust, which can absorb significant amount of X-ray emission and cause reduced correlation between the radio and observed X-ray luminosity.

In Figure 4.9(b) we also show the expected range of X-ray luminosities for radio-quiet AGN (shaded in grey; Panessa et al., 2019) and star-forming galaxies (black dashed line; Ranalli et al., 2003) at the given L_{33}. Many "AGN/SBnuc" follow the relation established for star-forming galaxies, suggesting that both $L_{2-10\mathrm{keV}}$ and L_{33} could be tracing star formation in these nuclei. However, some of them may also host highly-embedded AGN whose X-ray emission is significantly absorbed. Comparison between the observed $L_{2-10\mathrm{keV}}$ (Iwasawa et al., 2011; Torres-Albà et al., 2018) and intrinsic $L_{2-10\mathrm{keV}}$ derived from spectral model-fitting by Ricci et al. (2021) for a handful of overlapping systems shows that the latter could be higher by up to two orders of magnitude. Correcting for the effect of host obscuration will allow a more robust comparison between these nuclei to radio-quiet AGN (shaded area), and would require more sensitive X-ray observations and spectral analysis.

The above results that the elevated 33 GHz emission in "AGN" and "AGN/SBnuc" with the highest 33 GHz-luminosities are likely dominated by AGN contribution that is obscured in the X-rays. We note that the overall weak correlations between L_{33} and various AGN diagnostics presented above are likely driven by the $> 5-10$, times lower resolutions of the X-ray/MIR observations compared to our 33 GHz observations.

In summary, the elevated 33 GHz continuum emission of "AGN" and "AGN/SBnuc" regions relative to "SF" regions in local U/LIRGs likely come from a combination of extreme nuclear starburst and AGN activity, with the nuclei with higher 33 GHz luminosities more dominated by AGN but also suffer more severely from dust obscuration at shorter wavelengths. This conclusion is in agreement with X-ray studies which show that AGN accretion is accompanied by intense circumnuclear star formation(e.g. Lutz et al., 2018), and that powerful AGN accretion in mergers are heavily obscured by dust, especially in the final ULIRG stage (e.g. Ricci et al., 2017, 2021). However, follow-up observations at higher resolutions are required to fully disentangle the contribution from AGN and starburst.

4.5.2 How does star formation in U/LIRGs compare with that in nearby normal galaxies?

In Section 4.4.4 and Figure 4.6 we showed that all regions in the GOALS-ES span a wide range in $f_{\rm th}$, but the median values for "SF" and "SBnuc" are significantly higher compared to those for "AGN" and "AGN/SBnuc" regions. We note that similarly low $f_{\rm th}$ ($< 50\%$) have also been observed by Barcos-Muñoz et al. (2015) and BM17 in the most luminous local U/LIRGs including Arp 220, using 6 – 33 GHz measurements. The authors suggest that in these heavily-obscured systems, thermal emission from the nuclear starburst could be suppressed via dust absorption of ionizing photons, which may be responsible for the apparent dominance of non-thermal emission. Meanwhile, given the discussion in Section 4.5.1,"AGN" and "AGN/SBnuc" regions may also contain excess non-thermal emission from unresolved jets and/or wind/outflows associated with AGN activity (e.g. Panessa et al., 2019; Hayashi et al., 2021). Therefore, In this Section we only focus on the comparing 46 "SF"/"SBnuc" regions in the GOALS-ES with 129 star-forming regions identified in the SFRS (see Section 4.2.1 and Appendix 4.7.2).

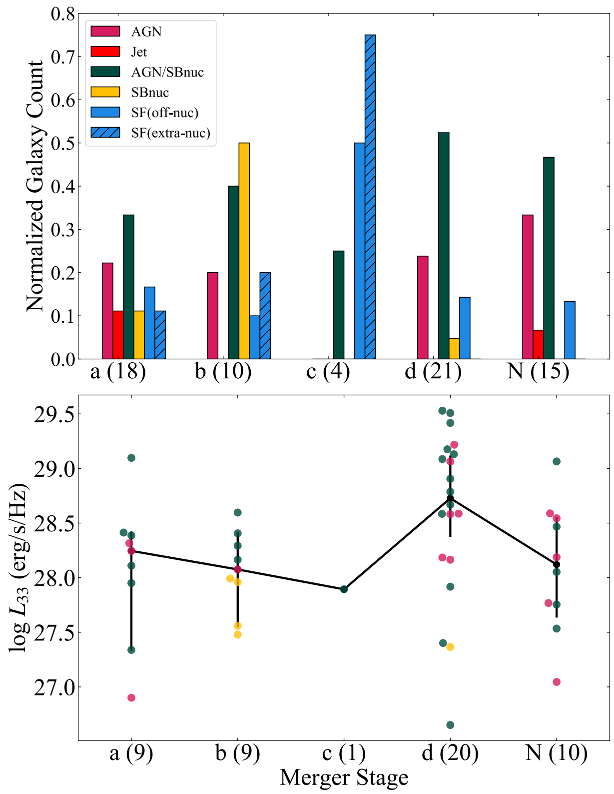

Figure 4.8: Fraction of systems hosting different region types (upper) and nuclear luminosity distribution (lower) vs. merger stage classification of the host system (a (pre-merging), b (early-merger), c (mid-merger), d (late-merger), N (non-merger); Stierwalt et al., 2013). Upper: For each merger stage, the number of galaxies hosting each region type is normalized by the total number of galaxies with the specific merger classification, shown in parentheses on the horizontal axis. Galaxies often host more than one types of regions, therefore the normalized galaxy counts at each merger stage do not add to 1. All 113 native regions identified at 15 or 33 GHz from GOALS-ES are shown, excluding "Ud" and "Bg". Lower: Individual values are color-coded by the nuclear region types ("AGN" - magenta, "AGN/SBnuc" - green, "SBnuc" - yellow), and median values and uncertainties at each merger stages are represented in solid black lines. The numbers of systems included at each merger stages are shown in parentheses on the horizontal axis. Only nuclei identified at 33 GHz from GOALS-ES are included. Overall, "AGN" and "AGN/SBnuc" are more frequently found and are more luminous at 33 GHz at the final merging stage.

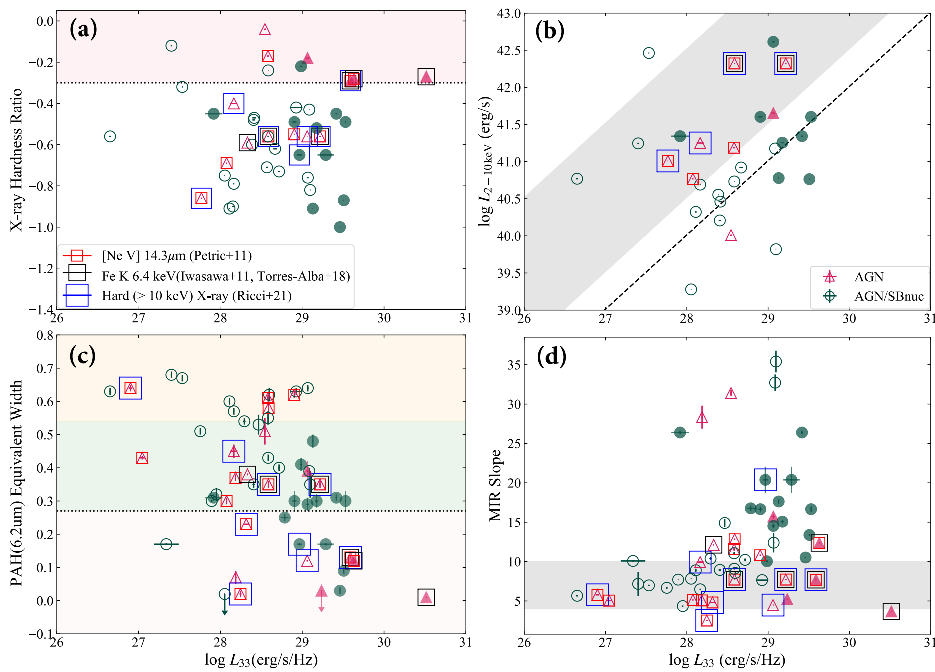

Figure 4.9: 33 GHz continuum luminosity of nuclei in GOALS-ES and BM17 vs. AGN diagnostics in the X-rays (a,b) and Mid-IR (c,d). *(a):* X-ray hardness ratios measured by Iwasawa et al. (2011) and Torres-Albà et al. (2018) using *Chandra* observations, defined as HR=(H-S)/(H+S), where H is the hard-band (2-7 keV) flux and S is the soft-band (0.5 - 2 keV) flux. Dotted horizontal line mark the empirical threshold above which the nucleus is considered to host AGN due to excess hard X-ray emission (pink shaded area). *(b):* X-ray luminosity at 2-10 keV from Iwasawa et al. (2011) and Torres-Albà et al. (2018), corrected for galactic extinction. Grey shaded area represents the radio/X-ray luminosity ratio range for radio-quiet AGN from Panessa et al. (2019) (i.e. $\nu L_\nu / L_{2-10\,\mathrm{keV}} = 10^{-2} - 10^{-4}$, $\nu = 90 - 100\,\mathrm{GHz}$), assuming $L_{33} \sim L_{100}$. Black dashed line represents the radio/X-ray luminosity ratio for star-forming galaxies from Ranalli et al. (2003) (i.e. $\log L_{2-10\,\mathrm{keV}} = \log L_{1.4} + 11.12$), assuming $\alpha_{1.4-33} \sim \alpha_{15-33} \sim -0.65$, as measured among "AGN/SBnuc" in this work. *(c):* 6.2 μm PAH equivalent widths (EW) measured Stierwalt et al. (2013) using *Spitzer* observations. Horizontal dotted line marks the empirical threshold, 0.27 μm, below which the MIR nuclear emission is considered to be dominated by AGN (pink shaded area). The green shaded area represents the empirical range (0.27 μm - 0.54 μm) where the nuclear emission is considered to have some but non-dominant AGN contribution, and nuclei in the yellow shaded area are considered to be starburst-dominated and have low to no AGN contribution on kpc scales. *(d):* MIR slope from Stierwalt et al. (2013), defined as the logarithmic flux density ratio between 30 and 15 mum. Grey shaded area represents the range spanned by the majority of LIRGs in GOALS. In all panels, filled symbols represent ULIRGs, and system with [Ne V] 14.3 μm, Fe K 6.4 keV, and hard (> 10 keV) X-ray detections reported in Petric et al. (2011); Iwasawa et al. (2011); Torres-Albà et al. (2018); Ricci et al. (2021) are marked in square symbols in red, black and blue with increasing sizes. Nuclei with the highest L_{33} also have higher observed $L_{2-10\,\mathrm{keV}}$, smallest 6.2 μm PAH EW, and steepest MIR, suggesting (dust-obscured) AGN contribution to the 33 GHz emission in "AGN" and "AGN/SBnuc" regions.

Radio spectral indices & 33 GHz thermal fraction

Studies of nearby normal galaxies with the SFRS have shown that their 33 GHz continuum emission is largely dominated by thermal free-free emission from HII regions on both kpc and 100 pc scales, which make 33 GHz continuum an ideal extinction-free tracer of ongoing massive star formation (Murphy et al., 2011b, 2012; Linden et al., 2020). Linden et al. (2019) shows that for extra-nuclear star-forming regions in the GOALS-ES, thermal emission accounts for ∼65% of the 33 GHz emission on kpc scales, which is similar to values derived for the SFRS galaxies on the same physical scales ($f_{\rm th}$ ∼60% ; Murphy et al., 2012). To investigate whether this agreement is also seen on 100 pc-scales, in Figure 4.10(right) we compare the distributions of 15 – 33 GHz spectral indices (α_{15-33}) measured for the GOALS-ES ("SF"/"SBnuc") regions and SFRS star-forming regions. We also show the effective radius of the area we use to measure α_{15-33} for each matched region. We note that α_{15-33} instead of $f_{\rm th}$ is presented because the former can be more straight-forwardly compared without considering any underlying assumptions about the intrinsic non-thermal and thermal spectral shapes.

Figure 4.10 shows that star-forming regions in GOALS-ES and SFRS both exhibit a wide range of α_{15-33}, from -2.06 ± 0.43 to 1.38 ± 0.72 for GOALS-ES and -0.98 ± 1.20 to $\gtrsim 2$ for SFRS. The median spectral index of the SFRS regions is $-0.08{\pm}0.27$, which is consistent with values derived by Linden et al. (2020) using different method for photometry. In contrast, the median value for the GOALS-ES regions is $-0.46{\pm}0.25$, suggesting higher contribution from steep-spectrum non-thermal emission. This value is also steeper than the median value derived on kpc scales for extra-nuclear star-forming regions in the GOALS-ES ($-0.27{\pm}0.23$; Linden et al., 2019). A two-sample K-S test on the distributions of α_{15-33} for the GOALS-ES

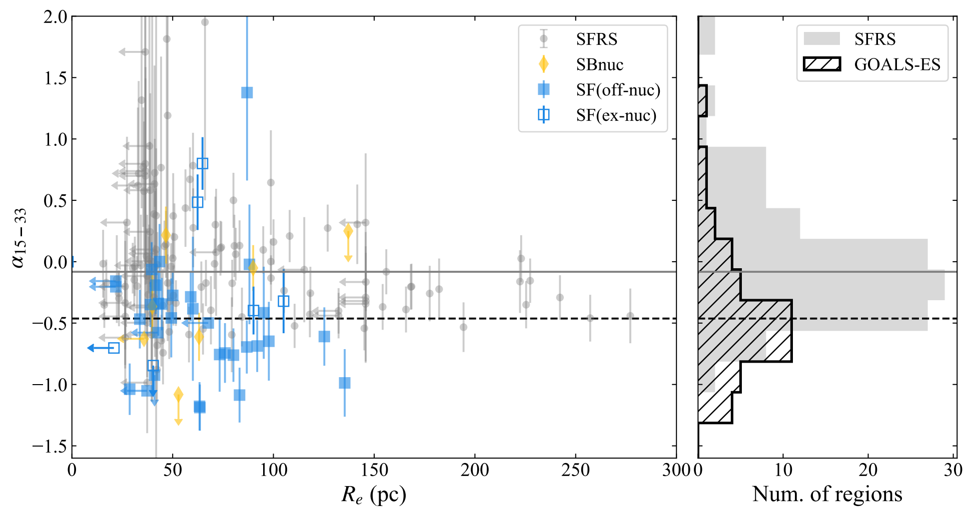

Figure 4.10: The 15 - 33 GHz spectral indices (α_{15-33}) measured for matched regions identified in nearby star-forming galaxies from the SFRS and local U/LIRGs from GOALS-ES. *Left*: α_{15-33} vs. effective radii, R_e, of the region area used to measure α_{15-33}. SFRS regions are in grey, GOALS-ES regions are colored in yellow ("SBnuc") and blue ("SF"), with extra-nuclear "SF" regions in non-filled symbols. Upper-limits in size and *Right*: Distribution of α_{15-33} for GOALS-ES regions (hatched black) and for SFRS regions (filled grey). In both panels, the median values for the SFRS (-0.08 ± 0.27) and GOALS-ES regions (-0.46 ± 0.25) are shown in solid grey and dashed black lines, respectively. Overall, α_{15-33} spans a wide range for star-forming regions in both local U/LIRGs and normal galaxies, especially at $R_e < 100$ pc. Regions in U/LIRGs have steeper median α_{15-33} compared with those in nearby normal galaxies, suggesting more dominant non-thermal contribution at 33 GHz.

and SFRS regions yields a p-value of << 1, which means that the differences we see between the two sample of regions are likely intrinsic. Several mechanisms may be responsible for the comparatively steep α_{15-33} of the 100 pc-scale GOALS-ES regions:

First, because U/LIRGs are dusty, thermal free-free emission from HII regions may have been suppressed via dust absorption (Barcos-Muñoz et al., 2015, 2017). However, this effect likely only becomes important in the most heavily-obscured systems such as in the ULIRGs, and we also do not find any correlation between α_{15-33} and the MIR 9.7 μm silicate depths estimated by Stierwalt et al. (2013), which measure the level of dust obscuration on kpc scales in these systems. Matched-resolution comparison between the resolved dust and the spectral index distribution will shed light on how much dust absorption affects the 100 pc scale high-frequency radio properties of local U/LIRGs.

Second, the ages of the starbursts also affect the relative contribution of non-thermal and thermal emission (e.g. Rabidoux et al., 2014; Linden et al., 2019, 2020). Using Starburst99 models, Linden et al. (2020) showed that non-thermal synchrotron emission from supernovae can quickly dominate the radio emission of an instantaneous starburst within 10 Myr compared with steady continuous star formation that maintains high thermal contribution with relatively flat radio spectrum. Using the same models and NIR hydrogen recombination line observations, Larson et al. (2020) estimated that star-forming clumps in local U/LIRGs have an age range of 6 - 10 Myr. Therefore the overall higher non-thermal contribution at 33 GHz measured in local U/LIRGs could be a reflection of the more recent star formation triggered in local U/LIRGs on 100 pc scales.

Third, the dense ISM in the compact starbursts in local U/LIRGs may produce non-thermal synchrotron spectrum than is intrinsically steeper that those characterized in star-forming regions in nearby normal galaxies (i.e. $\alpha_{\rm NT} \sim -0.85$; Murphy et al., 2011b). For example, $\alpha_{\rm NT} \sim -1.5$ have been measured in nearby starburst NGC 4945 via multi-frequency analysis (e.g. Bendo et al., 2016; Emig et al., 2020). Additionally, spectral steepening of synchrotron emission above 10 GHz have also been observed in nearby star-forming galaxies (e.g. Klein et al., 2018), local U/LIRGs (e.g. Clemens et al., 2008; Leroy et al., 2011) as well as high-z star-forming and starburst galaxies (e.g. Thomson et al., 2019; Algera et al., 2021). As discussed in Klein et al. (2018), steep synchrotron spectra either result from energy losses of high-energy electrons due to inverse-Compton scattering and synchrotron radiation in dense ISM environments, or intrinsic lack of high-energy electrons. Therefore, the steeper α_{15-33} measured in GOALS-ES regions may simply reflect intrinsically steep non-thermal spectrum, and does not necessarily require excess non-thermal emission. We note that if we assume a simple two-component power law model without spectral steepening (i.e. Equation 5.3), for $f_{\rm th}$ to be as high as measured in the SFRS regions ($\sim 90\%$) at $\alpha_{15-33} \sim -0.46$, $\alpha_{\rm NT}$ will have to be ~ -2, which is also the steepest α_{15-33} measured in the GOALS-ES region. Matched resolution observations at lower radio frequencies are needed to recover the intrinsic non-thermal spectral shape in these extreme systems.

Finally, tidal shocks associated with galaxy mergers may have produced excess non-thermal synchrotron emission in local U/LIRGs (Murphy, 2013). While it is possible that we are detecting traces of shock-driven synchrotron emission, given the high-resolution of our observations, large-scale diffuse emission driven by such dynamical effects are likely to have been resolved out, and would play relatively minimal role in producing the steep α_{15-33} we measure on 100 pc scales.

We emphasize that while the median α_{15-33} of the GOALS-ES regions is significantly steeper than that of the SFRS regions, the wide range of values seen in both samples, especially at $R_e < 100$ pc, suggests that the balancing between thermal and non-thermal emission is more complicated at small scales. Large uncertainties in our measurements due to sparse frequency coverage and short on-source time also limit our ability to draw more definitive conclusions. Matched resolution radio continuum observations at more than two different frequencies are needed to more robustly characterize the radio continuum spectrum of compact star-forming regions in local U/LIRGs. This will also allow us to better understand the whether and how the extreme ISM conditions in these dense starbursts may alter the synchrotron production and propagation processes.

Star formation rates and surface densities

In Figure 4.11 we show star formation rates and surface densities with respect to effective radii for "SF" and "SBnuc" regions in GOALS-ES (see Section 4.4.5) and SFRS. We show values derived from both the total 33 GHz flux (a,b) and the free-free component via 15 – 33 GHz spectral decomposition (c,d), as described in Section 4.4.4. The star-forming regions in local U/LIRGs have 1-3 dex higher SFR and $\Sigma_{\rm SFR}$ than similarly-sized regions in the nearby normal galaxies, even after accounting for the steeper α_{15-33} measured in the GOALS-ES regions. The median values for SFR and $\Sigma_{\rm SFR}$ for the GOALS-ES regions are $0.8{\pm}0.5\,{\rm M_\odot yr^{-1}}$ and $86 \pm 65\,{\rm M_\odot yr^{-1} kpc^{-2}}$, which is roughly 10 times higher than the median values for the SFRS regions (SFR $\sim 0.1\,{\rm M_\odot yr^{-1}}$ and $\Sigma_{\rm SFR} \sim 10\,{\rm M_\odot yr^{-1} kpc^{-2}}$). As expected, the median values for $\rm SFR_{th}$ and $\Sigma_{\rm SFR_{th}}$ are lower, at $\sim 0.4\,{\rm M_\odot yr^{-1}}$ and $\sim 50\,{\rm M_\odot yr^{-1} kpc^{-2}}$, but still significantly higher than those for the SFRS regions, despite that the latter is more dominated by thermal free-free emission. Given that this comparison is made at the scales of Giant Molecular Clouds (GMC; 10 – 100 pc), our result suggests that GMCs in local U/LIRGs are forming more stars compared to those in nearby normal galaxies, at least in these most active star-forming regions detected in these systems that

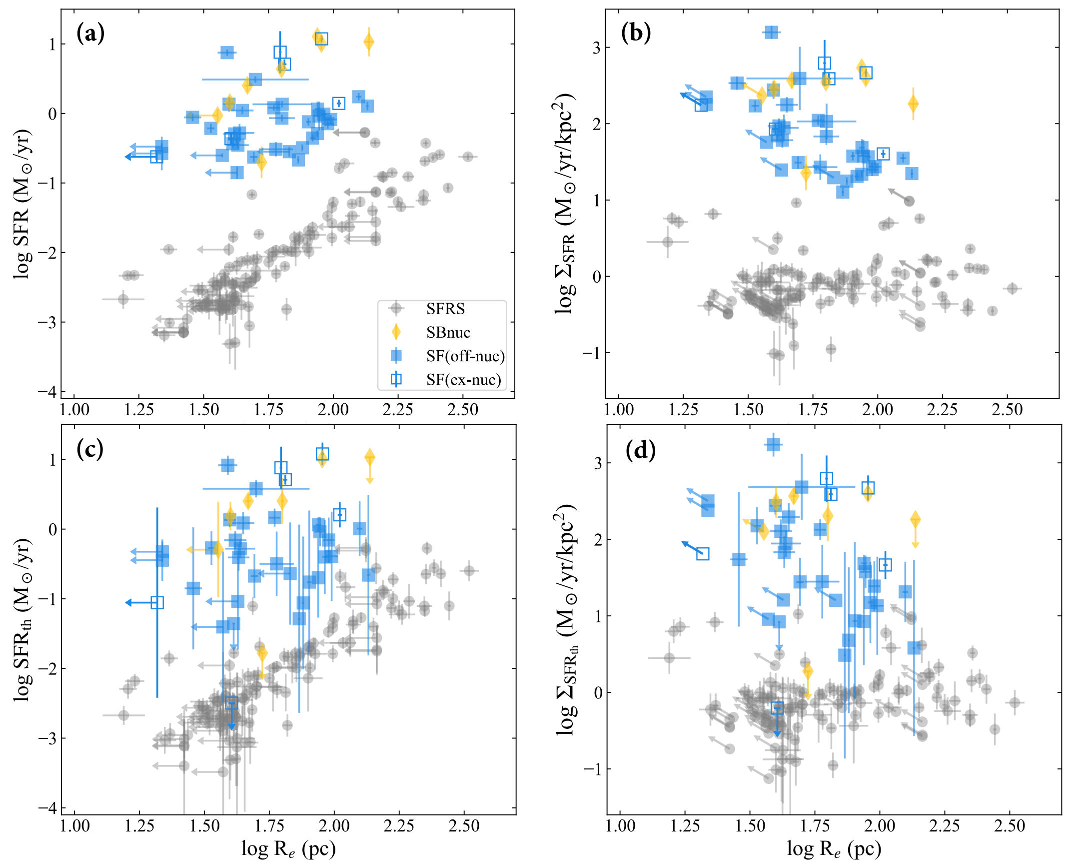

Figure 4.11: Star formation rates and surface densities vs. effective radii for "SF" and "SBnuc" regions characterized in local U/LIRGs in this work, as well as for star-forming regions in nearby normal galaxies from the SFRS characterized using the same methods outlined in Section 4.3. Values derived for the SFRS sample are in grey triangles. We show values derived both from the total 33 GHz flux (a, b) and thermal free-free only flux based on the measured 15-33 GHz spectral indices (c, d). Star-forming clumps and starburst nuclei in the GOALS-ES have up to 3 dex higher star formation rates and surface densities compared with star-forming clumps in the SFRS on ~ 100 pc scales.

are mostly "nuclear" and "off-nuclear".

Using HST NIR hydrogen recombination line (i.e. Paα, Paβ) observations of 48 local U/LIRGs smoothed at a common resolution of 90 pc, Larson et al. (2020) identified 751 extra-nuclear star-forming clumps in these systems with median SFR$\sim$ $0.03\,\mathrm{M_{\odot}yr^{-1}}$ and $\Sigma_{\mathrm{SFR}} \sim 0.3\,\mathrm{M_{\odot}yr^{-1}kpc^{-2}}$. These values are over 10 times lower than the values derived for the GOALS-ES regions, which may be due to intrinsic differences between nuclear and extra-nuclear star formation as suggested in Linden et al. (2019), or systematic offsets introduced by the use of different SFR tracers. However, due to the 90 pc resolution limit, the clumps studied in Larson et al. (2020) are at least five times larger than the GOALS-ES regions characterized in this work, which complicates the interpretation.

To investigate whether the different SFR tracers used may have introduced a systematic offset, we acquired continuum-subtracted Paα or Paβ images used in Larson et al. (2020) for 9 non-AGN U/LIRGs also included in the GOALS-ES and directly compare the Paα/β emission with the radio continuum, without smoothing the HST images, as demonstrated in the upper panels of Figure 4.12. We calculate SFR at each matched region identified in the radio using the the same circular apertures on the NIR, 15 and 33 GHz maps, following Equation 5.4, 5.5 and the prescription provided in Larson et al. (2020). Due to lack of multi-line observations, these NIR images are not corrected for extinction, which has minimal effect on the measurements of extra-nuclear clumps studied in Larson et al. (2020) but could affect measurements within the central kpc (Piqueras López et al., 2013).

As shown in the lower panel of Figure 4.12, SFR derived from the total 33 GHz continuum are consistently higher than values derived from the Paα/β emission by up to $\sim$ 1 dex, with the "AGN/SBnuc" in IRAS F16399-0937 showing the highest discrepancy, possibly due to AGN activity or extreme nuclear obscuration. When only considering the thermal component, the radio-derived values for "SF" regions show better agreement, with $\mathrm{SFR_{th}/SFR_{NIR}} \sim 0.5 - 15$ and a median of ~ 2, which would correspond to $A_v \sim 4$ if we assume thermal radio emission is tracing the the same emission. This value is consistent with nuclear extinction estimated from NIR line ratios in previous works (e.g. Alonso-Herrero et al., 2006; Piqueras López et al., 2013). This suggests that thermal free-free radio continuum is indeed tracing ionized plasma in HII regions that is producing the hydrogen recombination lines, and that radio continuum is more reliably tracing star formation in the dusty nuclear environments of local U/LIRGs.

Given the above, while the limited sensitivity of our current radio observations only allow detections of the most energetic regions of nuclear star formation, we expect that radio- and NIR-derived SFR for the mildly obscured extra-nuclear star-forming clumps in local U/LIRGs to be largely consistent with each other. Therefore, nuclear star formation in local U/LIRGs, as probed by the extremely high SFR and Σ_{SFR} derived in this work and previous studies (e.g. Barcos-Muñoz et al., 2017; U et al., 2019), are likely proceeding at much faster rates at GMC scales than those in the outskirts of local U/LIRGs, as well as those in nearby normal galaxies. Such extreme activity is likely driven by the high molecular gas surface densities in the central kpc of local U/LIRGs, as have been measured with ALMA at ~ 100 pc scales (e.g. Wilson et al., 2019; Sánchez-García et al., 2021, 2022). These studies also show that molecular gas forms stars more efficiently in these high density environments, potentially driven by cloud-cloud collisions (Jog & Solomon, 1992) and/or gravitational instability induced by the high stellar mass density (e.g. Romeo & Fathi, 2016).

Meanwhile, it has also been shown that local U/LIRGs host a higher fraction of young (< 10 Myr) and massive ($\gtrsim 10^6\,\mathrm{M_\odot}$) star clusters compared to normal galaxies (e.g. Alonso-Herrero et al., 2002; Linden et al., 2017, 2021). Therefore, the elevated

SFR and Σ_{SFR} of GOALS-ES regions characterized in this work relative to the SFRS regions may be a reflection of the higher numbers of massive star clusters being produced in the former. These massive clusters better samples the stellar initial mass function (IMF) and contains more massive stars that generate synchrotron emission via supernovae explosions, which possibly contributes to the steep α_{15-33} measured in the GOALS-ES regions, as discussed in Section 4.5.2.

Finally, as shown in Figure 4.11, while SFR and $\mathrm{SFR_{th}}$ is clearly correlated with R_e for the SFRS regions, values for the GOALS-ES regions show relatively weak dependence on the region sizes. Fitting the data with a power-law model SFR $\propto L_{\mathrm{radio}} \propto r^{\eta}$ yields $\eta \sim 2.3$ for the SFRS regions and $\eta \sim 1.1$ for the GOALS-ES regions, with similar values derived using $\mathrm{SFR_{th}}$. While the limited sensitivity of the radio observations prevents a direct comparison to luminosity-size relation established in the optical/NIR (e.g. Piqueras López et al., 2016; Cosens et al., 2018), the relatively weak size dependence of SFR and $\mathrm{SFR_{th}}$ among the GOALS-ES regions is consistent with a scenario where the HII region is density-bounded with its luminosity set by the local gas volume density. In this case, hydrogen atoms in the region recombine faster than they are ionized and hence a fraction of ionizing photons are not absorbed and escape the region, resulting in lower luminosity than expected at a given region size (e.g. Beckman et al., 2000; Wisnioski et al., 2012). Hence the relatively constant SFR and $\mathrm{SFR_{th}}$ of the GOALS-ES regions may be reflecting the high density environments that they reside in. In comparison, the SFRS regions may more closely resemble photon-bounded HII regions (i.e. Stŕomgren spheres) in low-density environments, whose luminosities are more or less proportional to the region volumes as hydrogen recombination balances ionization.

A similar dichotomy was also observed by Cosens et al. (2018) in a large sample of star-forming clumps, and the authors found that clumps with $\Sigma_{\mathrm{SFR}} > 1\,\mathrm{M_{\odot} yr^{-1}\,kpc^{-2}}$

show weaker size dependence in Hα luminosity than clumps with $\Sigma_{\mathrm{SFR}} < 1\,\mathrm{M_\odot yr^{-1}}$ $\mathrm{kpc^{-2}}$, which are consistent with the ranges of Σ_{SFR} and $\Sigma_{\mathrm{SFR_{th}}}$ represented by the GOALS-ES and SFRS regions, respectively. Deeper radio observations capable of sampling a wider range of star-forming clumps would allow a more quantitative comparison between the luminosity - size relation observed in the radio and at shorter wavelengths.

4.6 Summary

In this study we have used high-resolution ($\sim 0''.1$) 33 and 15 GHz radio continuum VLA observations of 68 local U/LIRGs from the GOALS "equatorial" VLA Survey (GOALS-ES) to study the properties of AGN and star formation in these extreme systems at 100 pc scales. The GOALS-ES sample spans the entire range of IR luminosities, distances and merger stages represented in the local U/LIRG population. Below we provide a summary of our major results and conclusions:

• Among the 68 systems in the GOALS-ES sample, compact radio continuum emission were detected in 63 systems with our high-resolution VLA observations at either 33 or 15 GHz. Using *Astrodendro*, we identified and characterized a total of 131 regions of compact radio continuum emission in these systems at the native resolutions, and found the effective radii (R_e) range from 8 to 170 pc. These regions were further classified as 17 "AGN" (AGN), 9 "Jet" (AGN jet), 31 "AGN/SBnuc" (AGN-starburst composite nucleus), 8 "SBnuc" (starburst nucleus), 48 "SF"(star-forming clump) and 17 "Ud" (unsure) based on their locations in the host galaxies as well as multi-wavelength AGN classifications from the literature. While all regions have low brightness temperatures ($T_b \lesssim 10^4\,K$), "AGN" and "AGN/SBnuc" regions have consistently higher 33 GHz luminosities (L_{33}) and surface densities ($\Sigma_{L_{33}}$) compared

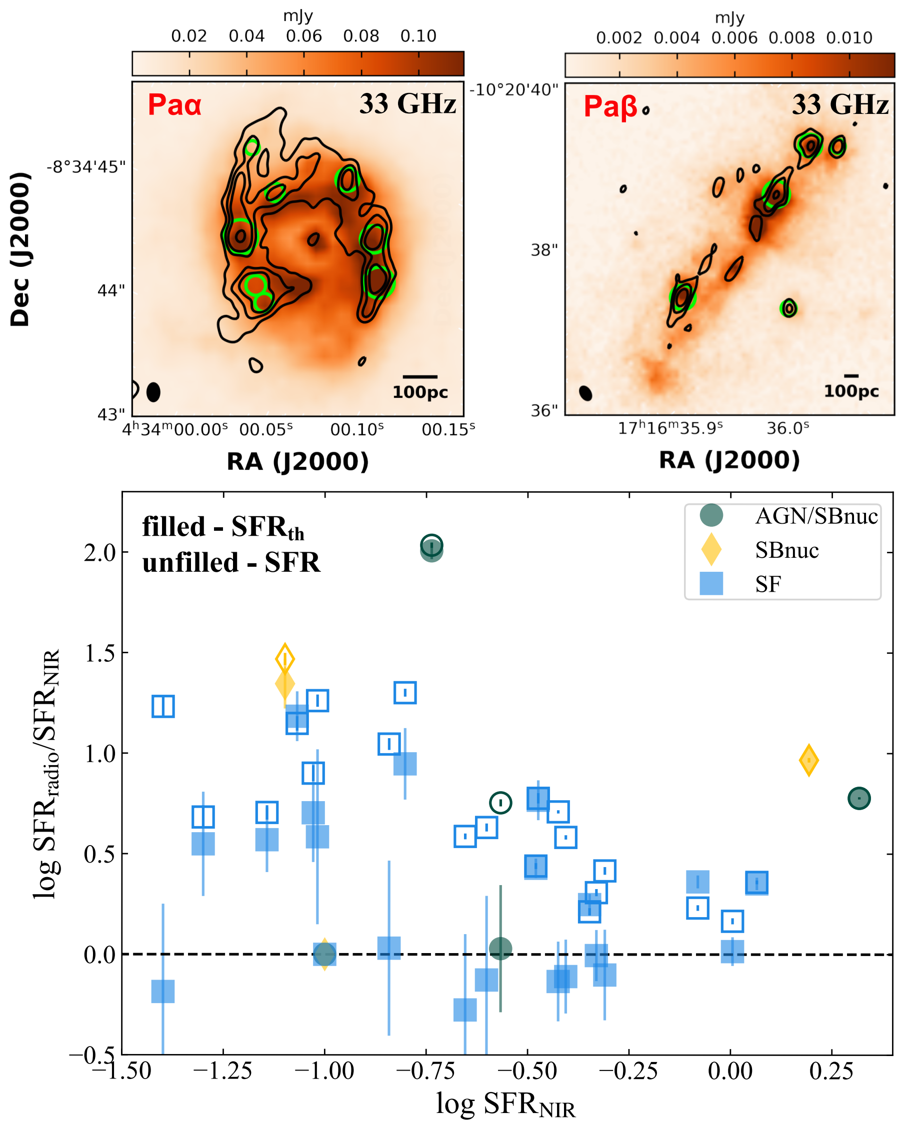

Figure 4.12: Comparison between radio continuum and Paα/β as SFR tracer. (Upper) Continuum-subtracted *HST* Paα image of NGC 1614 (*left*) and Paβ image of IRAS F17138-1017(*right*) from (Larson et al., 2020). Black contours show 33 GHz radio continuum at matched resolutions with 15 GHz continuum, and the matched beams are shown in the lower left corners in black ellipses. Contour levels are 0.075, 0.15, 0.23, 0.45 mJy/beam for NGC 1614, and 0.032, 0.065, 0.13 mJy/beam for IRAS F17138-1017. Lime circles show the apertures used for measuring and comparing radio- and Paα/β-derived SFR. (Lower) Ratio between radio-derived and NIR-derived SFR for 9 U/LIRGs in the sample. SFR derived from thermal free-free radio continuum (filled) shows better agreement with NIR-derived SFR than those derived from total 33 GHz continuum (unfilled), and deviations from 1:1 relation (dashed line) are likely due to nuclear dust extinction.

with "SF" and "SBnuc" regions of similar sizes by up to ~ 3 dex. Comparison with analytical models of radiation pressure-supported nuclear starburst and with lower resolution X-ray and IR AGN diagnostics suggests that both extreme mode of nuclear starburst and AGN activity may contribute to the elevated 33 GHz emission in "AGN" and "AGN/SBnuc".

• We used resolution-matched 15 and 33 GHz images to measure the 15 – 33 spectral indices (α_{15-33}) of a total of 113 regions, with which we estimated the fractional contribution of thermal free-free emission to the total 33 GHz continuum (thermal fraction; $f_{\rm th}$) in these regions. The 15 - 33 GHz spectral indices for these regions span a wide range, from -2.06±0.43 to 1.38±0.72, corresponding to $f \sim 0-100\%$ assuming a constant non-thermal spectral index of -0.85. While all region types span a wide range of α_{15-33}, "SF" and "SBnuc" have flatter median spectral indices compared with "AGN" and "AGN/SBnuc" regions. However, the median spectral index for "SF" and "SBnuc" ($\alpha_{15-33} \sim -0.46\pm0.25$) are significantly steeper than star-forming regions in nearby normal galaxies measured at similar physical scales, suggesting higher contribution of non-thermal synchrotron emission at 33 GHz in local U/LIRGs.

• For the 46 "SF" and "SBnuc" regions measured at matched resolution, we estimated their star formation rates and surface densities from both total 33 GHz flux densities as well as thermal free-free emission extracted using the estimated $f_{\rm th}$ for each region. We found that with effective radii of 20 - 140 pc, these regions have star formation rates and surface densities of 0.14 - 13 $M_\odot$/yr and 12 - 1600 $M_\odot$/yr/kpc^2, respectively, which are consistently higher than similarly-sized star-forming regions in nearby normal galaxies. Even after accounting for the relatively low estimated 33 GHz thermal fractions, the estimated thermal-only star formation rates and surface densities still have median values of 0.4 $M_\odot$/yr and 50 $M_\odot$/yr/kpc^2, respectively, and are at least 2 dex higher than star-forming regions in normal galaxies.

Through this study we have demonstrated the elevated star-forming activities in local U/LIRGs relative to nearby normal galaxies at the scales of giant molecular clouds, which motivates comprehensive investigation of the cold molecular gas properties at high resolution in these extreme environments. We have also shown the ubiquity of compact and powerful nuclear activity in local U/LIRGs with a wide range of host properties, despite that the origin for these luminous high-frequency radio emission remains highly debatable. Future multi-frequency high-resolution observations with wider frequency coverage will allow more accurate characterization of the radio SED of these compact emission to future investigate their nature, and VLBI observations will help determine the prevalence and contribution from AGN activity. Meanwhile, the upcoming JWST will provide crucial information of dust and multi-phase ISM at matched resolutions.

4.7 Appendix

4.7.1 Notes on Individual Systems

Here we provide details on the regions identified in each system, along with their classifications via comparisons with archival optical and IR datasets as well as information from the literature, when available. Unless otherwise specified, merger stage classifications are from Stierwalt et al. (2013), descriptions of the optical and IR comparisons are based on y-band images from the Pan-STARRS1 database (Flewelling et al., 2020), and channel maps from *Spitzer* IRAC (Mazzarella in prep). When describing 6.2μm PAH equivalent width (EW) as an AGN diagnostic, we follow Stierwalt et al. (2013) and Vardoulaki et al. (2015) and consider sources with 6.2μm PAH EW $< 0.27\mu$m to be AGN-dominated, and those with $0.27 < 6.2\mu$m PAH EW $< 0.54\mu$m

Table 4.1: Measured and Derived Properties of Regions Identified at Native Resolution

ID (1)	Region (2)	Type (3)	RA (J2000) (°) (4)	Dec (J2000) (°) (5)	S_ν (mJy) (6)	log R_e (pc) (7)	log L_ν (erg/s/Hz) (8)	log Σ_{L_ν} (erg/s/Hz/kpc^2) (9)	log T_b (K) (10)	log T_b^{imfit} (K) (11)
1	n1	AGN	2.777289	-12.107661	1.70±0.17	1.75±0.04	28.16±0.04	30.17±0.09	1.65±0.09	1.65±0.09
2	n1	SBnuc	4.712000	-10.376830	1.10±0.07	2.14±0.02	28.27±0.03	29.49±0.04	1.66±0.04	-
3	n1	SF	16.947427	-17.507269	0.20±0.01	1.94±0.01	27.24±0.01	28.86±0.03	0.35±0.03	0.92±0.21
	n2	SF	16.947899	-17.507178	0.13±0.02	1.62±0.04	27.07±0.08	29.34±0.12	0.82±0.12	0.93±0.05
	n3	SF	16.947995	-17.507169	0.31±0.03	1.77±0.02	27.43±0.04	29.4±0.06	0.88±0.06	1.5±0.17
	n4	SF	16.947943	-17.507019	0.10±0.02	1.63±0.05	26.96±0.09	29.2±0.14	0.68±0.14	-0.31±0.03
	n5	SF	16.948030	-17.506986	0.11±0.02	1.64±0.04	26.98±0.07	29.21±0.11	0.69±0.11	0.68±0.04
	n6	AGN/SBnuc	16.948336	-17.506803	0.89±0.01	2.05±0.01	27.89±0.01	29.29±0.01	0.77±0.01	2.12±0.06
4	n1	SF	17.537546	-16.852919	0.08±0.01	2.13±0.01	27.36±0.01	28.6±0.01	0.05±0.01	0.17±0.23
	n2	AGN/SBnuc	17.537256	-16.852756	0.12±0.01	2.19±0.01	27.53±0.01	28.66±0.01	0.12±0.01	0.4±0.14
5	n1	SF	20.010986	14.361711	0.09±0.02	< 1.34	27.30±0.10	> 30.12	> 1.58	> 2.16
	n2	SF	20.010978	14.361733	0.08±0.02	< 1.34	27.23±0.11	> 30.04	> 1.51	1.33±0.08
	n3	AGN/SBnuc	20.010989	14.361786	1.20±0.04	1.73±0.02	28.41±0.02	30.45±0.04	1.91±0.04	2.92±0.1
6	n1	AGN/SBnuc	24.720291	-10.453247	2.30±0.02	2.14±0.01	29.09±0.01	30.31±0.01	1.75±0.01	2.49±0.11
7	n1	SF	26.127251	17.102370	0.27±0.07	< 1.23	27.64±0.11	> 30.68	> 2.15	2.52±0.02
	n2	AGN/SBnuc	26.127263	17.102392	1.60±0.08	1.42±0.02	28.41±0.02	31.09±0.04	2.56±0.04	> 2.45
8	n1	SF	32.411082	-10.146978	0.05±0.01	< 1.15	26.25±0.05	> 29.45	> 0.95	> 1.42
9	e1	Bg	33.523529	5.171878	0.60±0.01	1.59±0.01	28.08±0.01	30.41±0.01	1.88±0.01	> 2.26
	n1	SBnuc	33.522890	5.173353	0.12±0.01	1.42±0.02	27.36±0.03	30.03±0.04	1.50±0.04	1.85±0.26
12	n1	AGN	40.669625	-0.013322	18±0.18	0.9±0.01	27.77±0.01	31.47±0.01	2.98±0.01	4.08±0.01
	n2	Jet	40.669639	-0.013244	31±0.29	0.99±0.01	28.01±0.01	31.54±0.01	3.04±0.01	3.89±0.01
	n3	Jet	40.669689	-0.013158	20±0.22	1.04±0.01	27.82±0.01	31.24±0.02	2.75±0.02	3.5±0.01
13	n1	AGN/SBnuc	41.572942	13.095758	0.04±0.01	1.77±0.01	26.65±0.01	28.62±0.02	0.10±0.02	-
14	n1	AGN/SBnuc	43.507581	14.970808	0.68±0.01	1.76±0.01	28.16±0.01	30.15±0.01	1.62±0.01	2.24±0.05
	n2	SBnuc	43.507247	14.976514	0.46±0.01	1.63±0.01	27.99±0.01	30.24±0.01	1.71±0.01	3.23±0.2
15	n1	AGN/SBnuc	54.696273	15.548194	1.70±0.08	1.91±0.03	28.67±0.02	30.35±0.06	1.81±0.06	2.36±0.03
16*	e1	SF	58.567399	15.929631	0.16±0.01	1.72±0.01	27.22±0.01	29.29±0.02	1.45±0.02	-
18	n1	AGN/SBnuc	65.333298	-18.810889	1.00±0.01	1.95±0.01	28.39±0.01	29.99±0.01	1.45±0.01	2.09±0.04

Table 4.1 continued

Table 4.1: Measured and Derived Properties of Regions Identified at Native Resolution (continued)

ID	Region	Type	RA (J2000) (°)	Dec (J2000) (°)	S_ν (mJy)	log R_e (pc)	log L_ν (erg/s/Hz)	log Σ_{L_ν} (erg/s/Hz/kpc^2)	log T_b (K)	log T_b^{imfit} (K)
(1)	(2)	(3)	(4)	(5)	(6)	(7)	(8)	(9)	(10)	(11)
19	n1	SF	68.500131	-8.579383	0.19±0.01	1.36±0.01	27.03±0.02	29.82±0.02	1.31±0.02	1.86±0.39
	n2	SF	68.500257	-8.579275	0.26±0.03	1.44±0.02	27.16±0.05	29.79±0.07	1.28±0.07	1.38±0.11
	n3	SF	68.499996	-8.579283	0.05±0.01	1.12±0.05	26.47±0.10	29.73±0.14	1.22±0.14	0.94±0.09
	n4	SF	68.499973	-8.579261	0.09±0.01	1.22±0.03	26.68±0.05	29.75±0.08	1.24±0.08	1.26±0.23
	n5	SF	68.499889	-8.579256	0.12±0.05	1.25±0.09	26.83±0.17	29.82±0.25	1.31±0.25	1.31±0.08
	n6	SF	68.500288	-8.579200	0.04±0.01	< 1.15	26.37±0.11	> 29.58	> 1.07	1.92±1.27
	n7	SF	68.500322	-8.579181	0.15±0.02	1.29±0.04	26.91±0.06	29.83±0.09	1.32±0.09	1.49±0.13
	n8	SF	68.499917	-8.579186	0.13±0.02	1.25±0.04	26.86±0.06	29.86±0.1	1.35±0.10	> 1.36
	n9	SF	68.499954	-8.579133	0.44±0.04	1.49±0.03	27.39±0.04	29.92±0.06	1.41±0.06	1.73±0.12
	n10	SF	68.500325	-8.579106	0.05±0.01	< 1.15	26.47±0.05	> 29.67	> 1.16	1.59±0.35
	n11	SF	68.500046	-8.579042	0.10±0.02	1.14±0.05	26.73±0.08	29.95±0.13	1.44±0.13	1.44±0.13
	n12	SF	68.500024	-8.579036	0.07±0.02	< 1.15	26.56±0.11	> 29.77	> 1.26	0.82±0.12
	n13	SF	68.500080	-8.579008	0.17±0.02	1.32±0.03	26.98±0.05	29.84±0.08	1.32±0.08	1.17±0.12
20	n1	AGN	68.890888	19.171595	0.08±0.01	1.26±0.02	27.05±0.03	30.03±0.04	1.50±0.04	> 1.70
21	n1	SF	76.936725	-8.019272	0.15±0.01	1.88±0.01	26.87±0.01	28.61±0.01	0.10±0.01	-
	n2	SF	76.937236	-8.019239	0.09±0.01	1.87±0.01	26.67±0.01	28.44±0.01	-0.07±0.01	-
	n3	SF	76.937247	-8.019033	0.24±0.01	1.94±0.01	27.07±0.01	28.7±0	0.19±0.01	-
	n4	SF	76.936644	-8.019017	0.16±0.01	1.92±0.01	26.90±0.01	28.56±0.02	0.05±0.02	-
22	n1	AGN/SBnuc	77.088371	17.368975	2.80±0.10	1.73±0.02	28.29±0.02	30.34±0.04	1.83±0.04	2.33±0.02
23	n1	AGN/SBnuc	80.277259	-10.246119	1.60±0.02	1.85±0.01	28.47±0.01	30.28±0.01	1.74±0.01	2.21±0.05
24	n1	Ud	86.796939	17.562867	0.24±0.01	1.96±0.01	27.29±0.01	28.87±0.02	0.35±0.02	0.43±0.06
	n2	Ud	86.796356	17.562908	0.57±0.02	1.97±0.01	27.65±0.01	29.22±0.02	0.70±0.02	1.11±0.05
	n3	Ud	86.796706	17.562911	0.11±0.01	1.78±0.01	26.92±0.02	28.86±0.04	0.35±0.04	0.41±0.09
	n4	Ud	86.796563	17.562983	0.36±0.01	1.98±0.01	27.45±0.01	28.99±0.03	0.47±0.03	0.59±0.05
	n5	Ud	86.796260	17.563022	0.16±0.01	1.76±0.02	27.10±0.03	29.1±0.04	0.58±0.04	0.52±0.05
25*	n1	SBnuc	97.946724	-17.621568	1.90±0.01	2.00±0.01	28.31±0.01	29.82±0.01	1.99±0.01	2.82±0.02
26	n1	AGN/SBnuc	111.906720	-2.915072	1.70±0.02	2.15±0.01	29.51±0.01	30.71±0.01	2.08±0.01	3.01±0.05
27	n1	Ud	113.930986	11.709761	0.03±0.01	< 1.10	26.29±0.10	> 29.60	> 1.08	-

Table 4.1 continued

Table 4.1: Measured and Derived Properties of Regions Identified at Native Resolution (continued)

ID	Region	Type	RA (J2000)	Dec (J2000)	S_ν	log R$_e$	log L_ν	log Σ_{L_ν}	log T_b	log $T_b^{\rm imfit}$
			(°)	(°)	(mJy)	(pc)	(erg/s/Hz)	(erg/s/Hz/kpc^2)	(K)	(K)
(1)	(2)	(3)	(4)	(5)	(6)	(7)	(8)	(9)	(10)	(11)
	n2	Ud	113.931001	11.709783	0.05±0.01	$<$ 1.10	26.53±0.09	$>$ 29.84	$>$ 1.33	-
	n3	AGN/SBnuc	113.930955	11.709811	0.34±0.12	1.40±0.08	27.34±0.15	30.05±0.22	1.53±0.22	-
28*	n1	Ud	138.411783	-10.322264	0.11±0.02	2.10±0.04	27.91±0.08	29.2±0.12	1.31±0.12	-
	n2	AGN	138.411817	-10.322197	0.06±0.02	1.97±0.07	27.62±0.12	29.18±0.18	1.29±0.18	-
	n3	Ud	138.411893	-10.322031	0.21±0.01	2.20±0.01	28.18±0.01	29.27±0.02	1.38±0.02	-
29*	n1	SBnuc	146.584648	3.045767	0.18±0.01	1.72±0.01	27.27±0.02	29.33±0.03	1.48±0.03	-
31	n1	AGN/SBnuc	155.000861	8.226089	2.10±0.02	1.92±0.01	29.1±0.01	30.77±0.01	2.20±0.01	3.39±0.06
32	n1	AGN/SBnuc	170.300994	-2.984111	0.55±0.01	1.56±0.01	27.95±0.01	30.34±0.01	1.81±0.01	$>$ 2.28
33	e1	SF	171.437174	14.675178	0.49±0.01	1.61±0.01	28.16±0.01	30.44±0.01	1.89±0.01	$>$ 2.26
	n1	AGN/SBnuc	171.437757	14.676531	0.44±0.01	1.65±0.01	28.11±0.01	30.31±0.02	1.77±0.02	2.37±0.13
34	n1	AGN/SBnuc	183.441419	2.810864	0.58±0.03	2.11±0.01	28.91±0.02	30.2±0.04	1.59±0.04	1.94±0.07
	n2	AGN/SBnuc	183.441903	2.811542	2.40±0.02	2.24±0.01	29.53±0.01	30.55±0.01	1.94±0.01	2.91±0.03
35	n1	AGN	186.266292	-6.681283	0.84±0.02	1.54±0.01	28.19±0.01	30.62±0.02	2.09±0.02	3.28±0.22
36	n1	AGN/SBnuc	186.727556	-0.877617	7.50±0.08	1.36±0.01	28.05±0.01	30.85±0.02	2.35±0.02	3.40±0.01
37	n1	Ud	195.459577	4.333481	0.07±0.01	1.45±0.02	27.39±0.04	29.99±0.06	1.44±0.06	1.17±0.10
	n2	Ud	195.459488	4.333506	0.07±0.01	1.46±0.03	27.39±0.06	29.97±0.09	1.42±0.09	$>$ 1.30
	n3	Ud	195.459516	4.333522	0.06±0.01	1.42±0.04	27.31±0.07	29.96±0.11	1.41±0.11	0.92±0.20
38	n1	SBnuc	195.581962	-15.767778	1.30±0.04	1.62±0.01	27.96±0.01	30.22±0.03	1.70±0.03	2.30±0.05
39	n1	AGN/SBnuc	200.346350	0.342328	0.59±0.01	2.12±0.01	27.75±0.01	29.02±0.02	0.50±0.02	-
40	n1	Jet	200.601899	-16.728475	1.80±0.11	1.47±0.02	28.13±0.03	30.69±0.05	2.18±0.05	2.52±0.02
	n2	Jet	200.601934	-16.728439	0.39±0.06	$<$ 1.16	27.48±0.07	$>$ 30.66	$>$ 2.14	2.36±0.01
	n3	Jet	200.601952	-16.728417	0.62±0.13	$<$ 1.16	27.68±0.09	$>$ 30.86	$>$ 2.34	3.32±0.06
	n4	Jet	200.601966	-16.728397	0.57±0.14	$<$ 1.16	27.64±0.11	$>$ 30.82	$>$ 2.31	2.96±0.02
41	e1	SF	204.970597	0.836818	0.32±0.02	1.57±0.02	27.66±0.03	30.03±0.05	1.50±0.05	1.52±0.08
	n1	SBnuc	204.970514	0.840113	0.26±0.01	1.49±0.01	27.56±0.01	30.09±0.02	1.56±0.02	2.15±0.17
42	n1	SF	208.067729	2.101314	0.06±0.01	1.99±0.02	27.25±0.04	28.77±0.06	0.23±0.06	0.35±0.13
	n2	SF	208.067588	2.101339	0.14±0.01	2.1±0.01	27.6±0.02	28.91±0.03	0.37±0.03	$>$ 1.20
	n3	SF	208.067488	2.101405	0.05±0.01	1.95±0.03	27.15±0.05	28.76±0.08	0.22±0.08	0.52±0.22

Table 4.1 continued

Table 4.1: Measured and Derived Properties of Regions Identified at Native Resolution (continued)

ID (1)	Region (2)	Type (3)	RA (J2000) (°) (4)	Dec (J2000) (°) (5)	S_ν (mJy) (6)	log R$_e$ (pc) (7)	log L_ν (erg/s/Hz) (8)	log Σ_{L_ν} (erg/s/Hz/kpc^2) (9)	log T_b (K) (10)	log $T_b^{\rm imfit}$ (K) (11)
	n4	SF	208.067337	2.101547	0.06±0.01	1.98±0.02	27.21±0.05	28.76±0.07	0.21±0.07	0.60±0.26
	n5	SF	208.067346	2.101630	0.02±0.01	1.79±0.08	26.78±0.15	28.71±0.21	0.17±0.21	0.10±0.13
	n6	SF	208.067212	2.101680	0.01±0.00	$<$ 1.83	26.58±0.09	$>$ 28.42	$>$ -0.12	$>$ -0.04
	e1	SF	208.067513	2.102364	0.11±0.01	2.02±0.01	27.51±0.01	28.97±0.02	0.43±0.02	1.43±0.26
43	n1	AGN	219.409501	-15.006728	0.65±0.04	2.09±0.02	29.07±0.02	30.39±0.04	1.77±0.04	2.02±0.06
	n2	AGN/SBnuc	219.409984	-15.005906	0.34±0.04	2.02±0.03	28.79±0.05	30.24±0.07	1.61±0.07	1.79±0.08
44	n1	AGN	228.304564	7.225519	7.10±0.18	1.38±0.03	28.54±0.01	31.29±0.05	2.78±0.05	3.77±0.01
45*	n1	AGN/SBnuc	232.503449	12.989301	0.17±0.01	1.51±0.01	26.95±0.02	29.43±0.03	1.60±0.03	1.55±0.1
46*	n1	AGN	236.568233	2.415485	0.18±0.01	1.46±0.01	26.93±0.01	29.52±0.02	1.70±0.02	2.54±0.25
47	n1	SF	244.799038	-7.900803	1.80±0.13	1.65±0.02	28.53±0.03	30.74±0.05	2.21±0.05	2.35±0.02
	n2	AGN	244.799097	-7.900789	2.00±0.05	1.55±0.01	28.58±0.01	30.98±0.03	2.44±0.03	$>$ 2.57
48	n1	Ud	247.735558	4.083006	0.03±0.01	$<$ 1.7	26.59±0.10	$>$ 28.69	$>$ 0.16	0.29±0.1
49	n1	AGN/SBnuc	250.667232	-9.720342	2.00±0.02	1.73±0.01	28.58±0.01	30.62±0.01	2.09±0.01	3.11±0.06
50	n1	AGN	253.245372	2.400925	10.0±0.2	1.90±0.02	29.22±0.01	30.91±0.04	2.38±0.04	3.66±0.01
	n2	AGN	253.245514	2.401328	2.50±0.03	1.62±0.01	28.59±0.01	30.85±0.01	2.32±0.01	$>$ 2.93
51*	e1	Ud	253.599241	-9.889218	0.04±0.01	1.63±0.02	26.76±0.03	29.01±0.05	1.16±0.05	-
52	n1	SF	259.149184	-10.345253	0.07±0.01	1.69±0.01	26.75±0.02	28.87±0.04	0.35±0.04	0.89±0.3
	n2	SF	259.149083	-10.345153	0.21±0.01	1.9±0.01	27.24±0.01	28.94±0.02	0.42±0.02	0.83±0.14
	n3	SF	259.149142	-10.344861	0.28±0.01	1.96±0.01	27.35±0.01	28.93±0.02	0.41±0.02	0.59±0.08
	n4	SF	259.149608	-10.344511	0.04±0.01	$<$ 1.63	26.45±0.04	$>$ 28.70	$>$ 0.18	$>$ 0.35
	n5	AGN/SBnuc	259.149193	-10.344161	0.31±0.01	1.94±0.01	27.40±0.01	29.03±0.02	0.52±0.02	1.14±0.09
53	n1	AGN/SBnuc	260.841483	-0.283581	5.70±0.13	1.94±0.01	29.42±0.01	31.04±0.02	2.48±0.02	3.02±0.02
	n2	Ud	260.841533	-0.283589	0.37±0.07	1.48±0.05	28.23±0.08	30.77±0.12	2.21±0.12	1.59±0.03
	n3	AGN/SBnuc	260.841567	-0.283583	0.18±0.05	$<$ 1.46	27.92±0.11	$>$ 30.5	$>$ 1.94	2.24±0.05
54	n1	AGN/SBnuc	270.132691	-4.014867	7.30±0.05	1.68±0	28.60±0.01	30.73±0.01	2.22±0.01	3.33±0.01
55*	n1	Ud	272.889204	1.528424	0.13±0.02	1.7±0.03	27.45±0.06	29.56±0.09	1.71±0.09	1.92±0.1
	n2	Ud	272.889146	1.528432	0.22±0.01	1.76±0.02	27.68±0.02	29.66±0.04	1.80±0.04	2.44±0.15
	e1	SF	272.888671	1.529303	0.07±0.01	1.61±0.01	27.15±0.02	29.44±0.03	1.59±0.03	$>$ 1.77

Table 4.1 continued

Table 4.1: Measured and Derived Properties of Regions Identified at Native Resolution (continued)

ID	Region	Type	RA (J2000)	Dec (J2000)	S_ν	log R_e	log L_ν	log Σ_{L_ν}	log T_b	log T_b^{imfit}
			(°)	(°)	(mJy)	(pc)	(erg/s/Hz)	(erg/s/Hz/kpc^2)	(K)	(K)
(1)	(2)	(3)	(4)	(5)	(6)	(7)	(8)	(9)	(10)	(11)
56	n1	AGN/SBnuc	293.092944	-4.000269	0.81±0.04	2.16±0.02	29.18±0.02	30.35±0.04	1.72±0.04	2.12±0.07
57	n1	AGN/SBnuc	299.149109	11.318064	1.10±0.04	2.09±0.01	29.06±0.02	30.38±0.03	1.78±0.03	2.00±0.05
58	n1	AGN	308.275475	-2.027358	1.60±0.02	1.53±0.01	28.19±0.01	30.63±0.01	2.11±0.01	3.78±0.11
59	e1	SF	314.351562	17.127561	0.84±0.01	1.76±0.01	28.41±0.01	30.4±0.01	1.85±0.01	2.48±0.07
60*	n1	AGN/SBnuc	337.856224	-19.034481	0.54±0.00	1.93±0	27.89±0.01	29.53±0.01	1.69±0.01	2.63±0.09
61	n1	AGN/SBnuc	342.955627	-17.873369	0.92±0.01	2.05±0	29.13±0.01	30.54±0.01	1.92±0.01	3.07±0.26
62	n1	AGN	345.815075	8.873903	3.50±0.24	1.58±0.02	28.32±0.03	30.67±0.04	2.16±0.04	2.95±0.04
63	n1	AGN/SBnuc	346.235651	19.552303	2.70±0.03	1.74±0.01	28.59±0.01	30.61±0.01	2.08±0.01	2.76±0.02
64	n1	SF	349.567859	6.585778	0.30±0.14	1.81±0.11	27.26±0.20	29.14±0.29	0.63±0.29	0.85±0.05
	n2	SF	349.567884	6.585861	0.03±0.01	< 1.57	26.31±0.11	> 28.67	> 0.15	> 0.44
	n3	SF	349.567767	6.585894	0.23±0.04	1.80±0.04	27.14±0.08	29.04±0.12	0.53±0.12	0.69±0.07
65	n1	SBnuc	349.594360	-4.416128	0.23±0.01	1.44±0.01	27.48±0.02	30.1±0.03	1.57±0.03	1.86±0.20
	n2	AGN	349.590885	-4.415828	0.89±0.02	1.61±0.01	28.07±0.01	30.36±0.02	1.84±0.02	2.99±0.15
66	n1	Jet	351.986339	8.778928	0.15±0.28	1.34±0.43	27.45±0.82	30.27±1.19	1.74±1.19	1.85±0.07
	n2	Jet	351.986291	8.778925	2.30±0.04	1.60±0.01	28.63±0.01	30.93±0.02	2.40±0.02	3.99±0.17
	n3	AGN	351.986252	8.778944	0.94±0.03	1.51±0.01	28.24±0.01	30.73±0.03	2.20±0.03	3.29±0.16
	n4	Jet	351.986165	8.778992	1.30±0.06	1.68±0.02	28.39±0.02	30.54±0.05	2.01±0.05	2.77±0.07
67	n1	AGN	352.194425	3.511397	0.12±0.01	1.14±0.01	26.90±0.02	30.12±0.03	1.61±0.03	> 1.81
	e1	SF	352.193779	3.512247	0.10±0.01	1.11±0.02	26.81±0.03	30.10±0.04	1.59±0.04	> 1.76

* 15 GHz images were used for measurements due to poor detections at 33 GHz.

NOTE — (1) Identifier for the IRAS system, corresponding to column (1) in Table 3.1. For systems marked with *, 15 GHz measurements are reported, due to either non- or poor detection (SNR < 5) at 33 GHz. For all other regions, 33 GHz measurements are used (i.e. $\nu = 33$). (2) Identifier for regions within each IRAS system identified and characterized using *Astrodendro*, with"nuclear" and "off-nuclear" regions labeled with "n" and "extra-nuclear" regions labeled with "e". Regions within each system are numbered following the order of ascending declination. (3) Region type indicating the most likely source for the detected radio emission. See Section 4.4.1 and the Appendix notes for details. (4) & (5): J2000 coordinates of the emission peak of the region, in degrees. (6): Measured flux density of the region at 33 GHz in mJy. For regions in systems marked with * in column (1), 15 GHz measurements are reported instead. (7) Region effective radius. For unresolved regions smaller than the synthesized beam accounting for uncertainties, the effective radius of the beam is reported instead as an upper-limit for the region size, indicated with "<", as described in Section 4.4.3. (8) Spectral luminosity calculated from column (6) and Table 3.1. (9) Spectral luminosity surface density. For unresolved regions, the reported values are lower-limits and marked with ">". (10) & (11) Brightness temperature of the region in K, derived using `Astrodendro` measurements, and via Gaussian-fitting using CASA `imfit`, in $\log_{10}$ units. Values for unresolved regions are marked with ">". See Section 4.4.2.

Table 4.2: Measured and Derived Properties of Regions Identified at Matched Resolution

ID	Region	Type	S_{33}	S_{15}	α_{15-33}	$f_{\rm th}$	log R$_e$	log SFR	log $\Sigma_{\rm SFR}$	log SFR$_{\rm th}$	log $\Sigma_{\rm SFR_{th}}$
			(mJy)	(mJy)		(%)	(pc)	(M$_\odot$/yr)	(M$_\odot$/yr/kpc^2)	(M$_\odot$/yr)	(M$_\odot$/yr/kpc^2)
(1)	(2)	(3)	(4)	(5)	(6)	(7)	(8)	(9)	(10)	(11)	(12)
1	n1	AGN	3.54±0.37	5.01±0.51	-0.44±0.19	62±24	2.08±0.01				
2*	n1	SBnuc	< 1.34	1.10±0.11	< 0.25	< 100	2.14±0.02	1.03±0.21	2.26±0.21	< 1.03	< 2.26
3	n1	SF	0.20±0.02	0.07±0.04	1.38±0.72	100	1.94±0.01	0.06±0.11	1.69±0.11	0.06±0.11	1.69±0.11
	n2	SF	0.13±0.01	0.15±0.02	-0.19±0.24	91±9	1.62±0.04	-0.29±0.05	1.97±0.10	-0.16±0.13	2.11±0.15
	n3	SF	0.31±0.03	0.39±0.05	-0.29±0.20	80±20	1.77±0.02	0.08±0.05	2.04±0.06	0.16±0.13	2.13±0.14
	n4	SF	0.09±0.01	0.09±0.02	0.00±0.31	100±0	1.64±0.06	-0.28±0.13	1.95±0.17	-0.28±0.13	1.95±0.17
	n5	SF	0.09±0.01	0.12±0.02	-0.34±0.26	74±26	1.63±0.04	-0.46±0.05	1.78±0.10	-0.41±0.19	1.83±0.21
	n6	AGN/SBnuc	0.89±0.09	0.90±0.10	-0.01±0.19	100±0	2.05±0.01				
4	n1	SF	0.09±0.01	0.19±0.03	-0.99±0.28	14±14	2.13±0.01	0.11±0.06	1.35±0.06	-0.66±1.15	0.58±1.15
	n2	AGN/SBnuc	0.13±0.02	0.23±0.04	-0.76±0.25	16±16	2.19±0.01				
5	n1,n2,n3	AGN/SBnuc	2.50±0.26	3.43±0.35	-0.40±0.18	67±23	2.1±0.01				
6	n1	AGN/SBnuc	2.59±0.27	4.78±0.48	-0.78±0.18	12±12	2.31±0.01				
7	n1, n2	AGN/SBnuc	5.25±0.53	10.8±1.1	-0.91±0.18	15±15	1.98±0.01				
8*	n1	SF	< 0.13	0.27±0.03	< -0.92	< 8	1.61±0.01	-0.44±0.06	1.84±0.06	< -1.36	< 0.92
9	e1	Bg	0.52±0.06	1.10±0.11	-0.95±0.20	14±14	1.73±0.01				
	n1	SBnuc	0.11±0.02	0.18±0.02	-0.63±0.38	36±36	< 1.55	-0.03±0.09	> 2.37	-0.29±0.68	> 2.1
12	n1	AGN	13.1±1.3	18.7±1.9	-0.45±0.18	60±23	0.89±0.01				
	n2	Jet	26.6±2.7	60.3±6.0	-1.04±0.18	0	0.98±0.01				
	n3	Jet	17.7±1.8	44.5±4.5	-1.17±0.18	0	1.03±0.01				
13	n1	AGN/SBnuc	0.05±0.01	0.16±0.02	-1.61±0.28	0	1.77±0.01				
14	n1	AGN/SBnuc	0.81±0.09	1.32±0.13	-0.62±0.19	37±28	1.93±0.01				
	n2	SBnuc	0.43±0.05	0.70±0.07	-0.61±0.20	38±29	1.8±0.01	0.64±0.05	2.54±0.05	0.4±0.33	2.31±0.33
15	n1	AGN/SBnuc	1.69±0.18	2.65±0.27	-0.57±0.18	44±26	2.01±0.01				
18	n1	AGN/SBnuc	1.11±0.12	2.28±0.23	-0.91±0.19	15±15	2.06±0.01				
19	n1	SF	0.25±0.04	0.36±0.04	-0.47±0.24	58±31	1.53±0.01	-0.21±0.07	2.23±0.07	-0.27±0.24	2.18±0.24
	n3, n4	SF	0.11±0.06	0.13±0.07	-0.20±0.34	89±11	< 1.34	-0.58±0.24	> 2.25	-0.45±0.30	> 2.38
	n2	SF	0.37±0.05	0.39±0.05	-0.06±0.22	100±0	1.60±0.02	0.13±0.11	2.44±0.12	0.13±0.11	2.44±0.12
	n5,n8,n9	SF	1.26±0.14	1.57±0.16	-0.27±0.19	82±18	1.70±0.21	0.49±0.05	2.59±0.41	0.58±0.12	2.68±0.43
	n6,n7,n10	SF	0.45±0.06	0.60±0.06	-0.35±0.21	74±25	1.65±0.04	0.04±0.06	2.25±0.10	0.09±0.16	2.29±0.18
	n11,n12	SF	0.28±0.04	0.64±0.07	-1.04±0.21	14±14	1.46±0.03	-0.06±0.06	2.53±0.09	-0.85±0.88	1.74±0.88
	n13	SF	0.14±0.02	0.16±0.01	-0.16±0.29	94±6	< 1.34	-0.48±0.05	> 2.35	-0.32±0.15	> 2.5
20*	n1	AGN	< 0.18	0.30±0.03	< -0.66	< 20	1.78±0.01	0.10±0.05	2.04±0.05	< -0.3	< 1.63
21	n1	SF	0.15±0.02	0.27±0.04	-0.74±0.24	18±18	1.88±0.01	-0.49±0.05	1.25±0.05	-1.06±0.95	0.68±0.95
	n2	SF	0.10±0.01	0.18±0.04	-0.76±0.30	16±16	1.87±0.01	-0.67±0.05	1.10±0.05	-1.29±1.35	0.49±1.35
	n3	SF	0.24±0.03	0.41±0.06	-0.69±0.22	26±26	1.94±0.01	-0.29±0.05	1.34±0.05	-0.7±0.57	0.93±0.57
	n4	SF	0.16±0.02	0.37±0.05	-1.09±0.22	0	1.92±0.01	-0.35±0.05	1.31±0.05	0	0
22	n1	AGN/SBnuc	3.19±0.33	3.63±0.36	-0.16±0.18	94±6	1.84±0.01				
23	n1	AGN/SBnuc	2.05±0.22	5.03±0.50	-1.14±0.19	0	2.03±0.01				
24	n1	Ud	0.24±0.03	0.38±0.05	-0.57±0.22	45±32	1.96±0.01				
	n2	Ud	0.57±0.06	1.08±0.11	-0.81±0.19	8±8	1.97±0.01				
	n3	Ud	0.11±0.01	0.16±0.03	-0.49±0.28	56±37	1.78±0.01				
	n4	Ud	0.36±0.04	0.65±0.07	-0.76±0.2	15±15	1.98±0.01				
	n5	Ud	0.16±0.02	0.23±0.03	-0.46±0.23	59±29	1.76±0.02				
25*	n1	SBnuc	< 0.40	2.05±0.21	< -2.06	0	1.94±0.01	1.11±0.04	2.73±0.04	0	0
26	n1	AGN/SBnuc	1.72±2.77	0.18±0.28	-0.61±0.18	39±27	2.34±0.01				
27	n1	AGN/SBnuc	0.97±1.23	0.12±0.12	-0.30±0.20	79±23	1.70±0.06				
28*	n1	Ud	< 0.13	0.04±0.02	< 0.15	< 100	2.10±0.04				
	n2	AGN	< 0.07	0.03±0.01	< 0.29	< 100	1.97±0.07				
	n3	Ud	< 0.15	0.05±0.03	< -0.38	< 55	2.20±0.01				
29*	n1	AGN/SBnuc	< 0.07	0.04±0.02	< -1.08	< 6	1.72±0.01				
31		AGN/SBnuc	2.03±3.10	0.21±0.31	-0.53±0.18	49±25	2.11±0.01				
32	n1	AGN/SBnuc	0.53±0.07	1.15±0.12	-0.98±0.21	14±14	1.89±0.01				

Table 4.2 continued

Table 4.2: Measured and Derived Properties of Regions Identified at Matched Resolution (continued)

ID (1)	Region (2)	Type (3)	S_{33} (mJy) (4)	S_{15} (mJy) (5)	α_{15-33} (6)	f_{th} (%) (7)	log R_e (pc) (8)	log SFR ($M_\odot$/yr) (9)	log Σ_{SFR} ($M_\odot$/yr/kpc^2) (10)	log $\mathrm{SFR_{th}}$ ($M_\odot$/yr) (11)	log $\Sigma_{\mathrm{SFR_{th}}}$ ($M_\odot$/yr/kpc^2) (12)
33		SF	0.39±0.27	0.05±0.03	0.48±0.23	100	1.79±0.01	0.88±0.30	2.79±0.30	0.88±0.3	2.79±0.3
		AGN/SBnuc	0.61±0.58	0.08±0.06	0.06±0.21	100	1.92±0.01				
34	n1	AGN/SBnuc	0.66±0.08	0.75±0.08	-0.17±0.20	92±8	2.31±0.01				
	n2	AGN/SBnuc	2.63±0.27	4.05±0.41	-0.55±0.18	48±25	2.45±0.01				
35	n1	AGN	1.13±0.13	2.01±0.20	-0.73±0.19	20±20	1.95±0.01				
36	n1	AGN/SBnuc	8.19±0.83	12.9±1.3	-0.57±0.18	44±26	1.60±0.01				
37	n1	Ud	0.22±0.04	0.27±0.03	-0.26±0.26	83±17	1.89±0.06				
	n2, n3	Ud	0.30±0.05	0.36±0.04	-0.22±0.23	88±12	1.95±0.04				
38	n1	SBnuc	2.21±0.24	2.30±0.23	-0.05±0.19	100	1.95±0.01	1.00±0.09	2.60±0.09	1±0.09	2.6±0.09
39	n1	AGN/SBnuc	0.59±0.06	1.15±0.12	-0.84±0.19	0	2.12±0.01				
40	n1,n2,n3,n4	Jet	10.3±1.0	22.4±2.24	-0.98±0.18	14±14	2.04±0.01				
41	e1	SF	0.56±0.07	0.30±0.03	0.80±0.21	100±0	1.81±0.01	0.71±0.07	2.59±0.07	0.71±0.07	2.59±0.07
	n1	SBnuc	0.28±0.04	0.23±0.03	0.22±0.23	100±0	1.67±0.01	0.40±0.1	2.57±0.10	0.4±0.1	2.57±0.1
42	n1	SF	0.07±0.01	0.11±0.02	-0.65±0.32	33±33	1.99±0.02	-0.09±0.07	1.44±0.08	-0.39±0.64	1.13±0.64
	n2	SF	0.14±0.02	0.23±0.03	-0.61±0.24	39±35	2.1±0.01	0.24±0.05	1.55±0.06	0.01±0.39	1.31±0.39
	n3	SF	0.05±0.01	0.05±0.02	-0.02±0.49	100±0	1.94±0.02	-0.04±0.21	1.58±0.21	-0.04±0.21	1.58±0.21
	n4	SF	0.06±0.01	0.08±0.02	-0.42±0.38	65±35	1.98±0.02	-0.15±0.07	1.40±0.08	-0.16±0.32	1.39±0.33
	n5	SF	0.02±0.01	0.03±0.01	-0.38±0.59	69±31	1.78±0.07	-0.52±0.1	1.43±0.17	-0.5±0.46	1.45±0.48
	n6	SF	0.02±0.01	0.03±0.01	-0.50±0.68	54±46	< 1.83	-0.55±0.07	> 1.29	-0.64±0.73	> 1.2
	e1	SF	0.11±0.01	0.15±0.02	-0.32±0.26	76±24	2.02±0.01	0.14±0.05	1.60±0.06	0.21±0.18	1.67±0.18
43	n1	AGN	1.01±0.12	2.02±0.2	-0.88±0.19	15±15	2.38±0.02				
	n2	AGN/SBnuc	0.66±0.09	1.27±0.13	-0.83±0.21	4±4	2.35±0.01				
44	n1	AGN	8.17±0.83	13.0±1.3	-0.59±0.18	42±26	1.69±0.01				
45*	n1	AGN/SBnuc	< 0.24	0.17±0.02	< 0.42	< 100	1.51±0.01				
46*	n1	AGN	< 0.15	0.18±0.02	< -0.24	< 77	1.46±0.01				
47	n1	SF	0.89±0.09	1.18±0.12	-0.35±0.18	73±22	1.59±0.04	0.87±0.05	3.20±0.09	0.92±0.14	3.24±0.16
	n2	AGN	1.98±0.20	3.57±0.36	-0.75±0.18	17±17	1.72±0.02				
48	n1	Ud	0.03±0.01	0.04±0.01	-0.27±0.65	82±18	< 1.7				
49	n1	AGN/SBnuc	2.05±0.21	2.97±0.30	-0.47±0.18	58±24	1.94±0.01				
50	n1	AGN	11.0±1.11	14.6±1.5	-0.36±0.18	72±22	2.04±0.01				
	n2	AGN	2.15±0.23	4.64±0.47	-0.98±0.19	14±14	1.78±0.01				
51*	e1	Ud	< 0.06	0.05±0.01	< 0.41	< 100	1.63±0.02				
52	n1	SF	0.07±0.01	0.10±0.02	-0.46±0.32	60±40	1.69±0.01	-0.63±0.07	1.49±0.08	-0.67±0.31	1.44±0.31
	n2	SF	0.21±0.03	0.39±0.05	-0.76±0.22	15±15	1.90±0.01	-0.12±0.05	1.58±0.06	-0.76±1.03	0.93±1.03
	n3	SF	0.28±0.03	0.47±0.06	-0.69±0.21	27±27	1.96±0.01	-0.01±0.05	1.57±0.06	-0.4±0.53	1.18±0.53
	n4	SF	0.04±0.01	0.06±0.01	-0.58±0.48	43±43	< 1.63	-0.85±0.09	> 1.39	-1.04±0.69	> 1.21
	n5	AGN/SBnuc	0.31±0.03	0.60±0.07	-0.86±0.20	15±15	1.94±0.01				
53	n1,n2,n3	AGN/SBnuc	12.2±1.2	21.1±2.1	-0.69±0.18	26±26	2.41±0.01				
54	n1	AGN/SBnuc	7.49±0.76	12.7±1.3	-0.67±0.18	30±28	1.77±0.01				
55*	n1	Ud	< 0.18	0.14±0.02	< 0.3	< 100	1.70±0.03				
	n2	Ud	< 0.18	0.22±0.03	< -0.24	< 76	1.76±0.02				
	e1	SF	< 0.03	0.06±0.01	< -0.85	0	1.61±0.01	-0.36±0.08	1.93±0.08	0	0
56	n1	AGN/SBnuc	0.94±0.11	1.53±0.15	-0.62±0.19	37±29	2.33±0.01				
57	n1	AGN/SBnuc	1.69±0.19	3.20±0.32	-0.81±0.19	7±7	2.34±0.01				
58	n1	AGN	1.72±0.18	3.13±0.31	-0.76±0.18	16±16	1.77±0.01				
59	e1	SF	0.89±0.10	1.22±0.12	-0.40±0.19	67±24	1.95±0.01	1.07±0.05	2.67±0.05	1.08±0.16	2.67±0.16
60*	n1	AGN/SBnuc	< 0.16	0.54±0.06	< -1.52	0	1.93±0.01				
61	n1	AGN/SBnuc	0.87±0.10	1.60±0.16	-0.78±0.20	12±12	2.25±0.01				
62	n1	AGN	3.34±0.34	6.93±0.69	-0.93±0.18	15±15	1.68±0.01				
63	n1	AGN/SBnuc	2.97±0.31	4.99±0.50	-0.66±0.18	31±28	1.89±0.01				
64	n1	SF	0.38±0.04	0.97±0.10	-1.19±0.19	0	1.80±0.11	0.13±0.05	2.03±0.23	0	0
	n2	SF	0.07±0.01	0.17±0.01	-1.05±0.26	13±13	< 1.57	-0.6±0.03	> 1.76	-1.40±1.08	> 0.96

Table 4.2 continued

Table 4.2: Measured and Derived Properties of Regions Identified at Matched Resolution (continued)

ID (1)	Region (2)	Type (3)	S_{33} (mJy) (4)	S_{15} (mJy) (5)	α_{15-33} (6)	$f_{\rm th}$ (%) (7)	log R$_e$ (pc) (8)	log SFR (M$_\odot$/yr) (9)	log $\Sigma_{\rm SFR}$ (M$_\odot$/yr/kpc^2) (10)	log SFR$_{\rm th}$ (M$_\odot$/yr) (11)	log $\Sigma_{\rm SFR_{th}}$ (M$_\odot$/yr/kpc^2) (12)
	n3	SF	0.24±0.03	0.61±0.07	-1.18±0.20	0	1.80±0.05	-0.07±0.05	1.83±0.11	0	0
65	n1	SBnuc	0.24±0.04	0.33±0.03	-0.37±0.26	71±29	1.60±0.01	0.16±0.08	2.46±0.08	0.19±0.2	2.49±0.21
	n2	AGN	0.88±0.10	1.69±0.17	-0.83±0.19	4±4	1.77±0.01				
66	n1	Jet	1.68±0.17	4.20±0.42	-1.16±0.18	0	1.65±0.01				
	n2	Jet	0.27±0.04	0.66±0.07	-1.13±0.23	0	1.51±0.06				
	n3	AGN	0.59±0.03	0.88±0.03	-0.51±0.20	53±27	$<$ 1.54				
	n4	Jet	1.57±0.17	3.52±0.35	-1.02±0.19	14±14	1.87±0.01				
67	n1	AGN	0.10±0.02	0.13±0.01	-0.38±0.44	69±31	$<$ 1.32				
	e1	SF	0.08±0.02	0.15±0.01	-0.70±0.49	25±25	$<$ 1.32	-0.62±0.08	$>$ 2.24	-1.06±1.37	$>$ 1.81

* 15 GHz images were used for measurements due to poor detections at 33 GHz.

Note — (1) Identifier for the IRAS system, corresponding to column (1) in Table 3.1. (2) Identifier for regions corresponding to column (2) in Table 4.1. Due to the lower-resolution of the beam-matched 15 and 33 GHz images, several regions identified at native-resolution are blended together. In these cases, multiple region identifiers are provided for a single measurement. (3) Region type indicating the most likely source for the detected radio emission. See Section 4.4.1 and the Appendix for details. (4): Measured flux of the beam-matched region at 33 GHz. For regions identified at 15 GHz, upper-limits on the 33 GHz flux densities are provided. (5): Measured flux of the beam-matched region at 15 GHz (6): Measured 15 - 33 GHz spectral index within the beam-matched region. (7) Thermal fraction at 33 GHz derived from (6). (8) Effective radius for the beam-matched region, based on region area (A) computed by *Astrodendro*, defined as $R_e = \sqrt{A/\pi}$. For unresolved regions that are smaller than the matched-beam accounting for uncertainties, the effective radius of the matched-beam is reported instead as an upper-limit for the region size, indicated with "$<$". (8) Star formation rates of the beam-matched region derived from 33 GHz flux density in column (4). (10) Star formation rate surface density. For unresolved regions, the reported values are lower-limits, indicated with "$>$". (11) Thermal-only star formation rate derived from 33 GHz flux in column (4) and 15 - 33 GHz spectral index from column (6). (12) Thermal-only star formation rate surface density. For regions identified at 15 GHz, upper-limits are provided for (6), (7), (11) and (12). For unresolved regions, the reported values are lower-limits, indicated with "$>$". For column (9) - (12), we only report values for "SF" and "SBnuc".

to have mixed contribution from AGN and starburst, and those with 6.2μm PAH EW $> 0.54\mu$m to be starburst-dominated. For galaxies with regions with undetermined nature due to lack of high-resolution ancillary data, we also show comparison between the ancillary data and our radio images for clarity.

(*1*) *NGC 0034* : This system is a late-stage merger. We identified one bright nuclear region in this system at both 15 and 33 GHz. This region aligns with the galaxy center in the optical and IR. X-ray study suggests that this galaxy hosts a buried AGN ($N_{\rm H} \sim 10^{23}{\rm cm}^{-2}$; Torres-Albà et al., 2018), and this galaxy is classified as a type-2 Seyfert in the optical (Veilleux et al., 1995; Yuan et al., 2010). Therefore we classify the nuclear region identified in the radio as "AGN".

(*2*) *MCG -02-01-051* : This galaxy is the southern component of the early stage interacting pair Arp 256. Two nuclear regions were identified at 33 GHz at native resolution, but the image quality is poor (SNR $\lesssim$ 5), therefore in Table 4.1 we report region properties characterized using the native resolution 15 GHz image where the two regions blend together into one larger region. Note that the 15 – 33 GHz spectral index of this region, reported in Table 4.2, is an upper-limit given the low SNR of the detection at 33 GHz. This region aligns with the optical and IR peak, and no evidence of AGN activity has been reported, therefore here we classify this region as "SBnuc".

(*3*) *IC 1623 (VV 114)* : We detect the eastern component of this mid-stage merger at both 15 and 33 GHz. In total, 7 nuclear regions are identified with *Astrodendro*. The brightest region aligns with the optical center and is identified as an AGN by Iono et al. (2013) based on elevated HCN/HCO$^+$ ratio. However, no clear signatures of AGN have been found in the X-rays, optical or MIR. Given the uncertainties, we classify the brightest region as "AGN/SBnuc", and the rest as off-nuclear "SF".

(*4*) *MCG -03-04-014* : Two nuclear regions are identified at both 15 and 33 GHz in this non-interacting galaxy. The brighter region aligns with the optical and IR peak, as well as the dynamical center of the warm molecular gas as revealed in ALMA CO(J=3-2) dataset (2013.1.01165.S, PI: S. Haan). The fainter region lies on a nuclear spiral arm that connects to the dynamical center. No clear detection of AGN has been reported for this galaxy but it has been classified as an AGN/SB composite system in the optical by Yuan et al. (2010). Therefore we classify the brighter region as "AGN/SBnuc" and the fainter region as off-nuclear "SF".

(*5*) *CGCG 436-030* : In the native resolution 33 GHz image, we detect one bright and two faint knots at the optical and IR peak of this western component of an early-stage merger. At matched resolution at 15 and 33 GHz, these three knots are blended together and were identified as one larger extended nuclear region with *Astrodendro*. This nuclear region is detected in soft and hard X-ray with *Chandra* (Torres-Albà et al., 2018), and the nuclear Mid-IR spectra (slit width $\sim 4''$) indicate clear dominance of emission from star formation (Díaz-Santos et al., 2017; Inami et al., 2018). However, this galaxy is classified as an AGN/SB composite system in the optical (Vega et al., 2008) and radio (Vardoulaki et al., 2015). VLBI observations of this galaxies revealed a high brightness temperature ($T_b > 10^7$ K) component that can be explained with a clustered radio supernovae model (Smith et al., 1998a). Given these uncertainties, here we classify this nuclear region as an "AGN/SBnuc".

(*6*) *IRAS F01364-1042* : In this late-stage merger, we detect one bright nuclear region close to the optical and IR peak of the galaxy. *Chandra* detected both soft and hard X-ray at the center of this galaxy, and (Iwasawa et al., 2011) attributed their origin to highly-obscured high mass X-ray binaries or AGN. This system is classified as an LINER in the optical (Veilleux et al., 1995; Yuan et al., 2010), and as a likely AGN candidate in the radio due to the compactness of its 33 GHz emission (Barcos-Muñoz et al., 2017). Given the above, here we classify this nuclear region as "AGN/SB nuc".

(*7*) *III Zw035* : We detect the northern component of this pre-merger at both 15 and 33 GHz. At native resolution, one bright knot and a much fainter knot are identified at 33 GHz. Analysis of 0".03 resolution ALMA Band 6 continuum (2018.1.01123.S, PI: A. Medling) suggests that the brighter northern region likely hosts the AGN, while the fainter region in the south is part of a clumpy dust ring-like structure that is also producing strong OH maser emission (Pihlström et al., 2001). At matched resolution, these two knots are blended and were identified as one extended nuclear region. This region aligns with the optical and IR peak. While no direct evidence for AGN currently exists, González-Martín et al. (2009) found indirect X-ray signatures for a Compton-thick AGN, which is supported by an extremely high gas surface density estimated by Barcos-Muñoz et al. (2017), who also reported that this galaxy has the most compact 33 GHz emission among U/LIRGs in the GOALS sample. Given the above, here we classify this extended nuclear region as "AGN/SBnuc". More precisely, the nucleus is located at the brighter knot detected at native resolution, which coincides with the dynamical center of the molecular gas as revealed by ALMA (2018.1.01123.S, PI: A. Medling). Observation with e-MERLIN at 5 GHz reveals compact continuum emission at the location of the "AGN/SBnuc" with peak brightness temperature of $10^{4.8}$ K (J. Molden, private communication).

(*8*) *NGC 0838* : This galaxy is the north-east component of a complex pre-merging system with three components, one of which is a closely interacting galaxy pair formed by NGC 0833 and NGC 0835. A bright region lying within the MIR galaxy "core" is visible at both 15 and 33 GHz in NGC 0838. This region is also detected in the hard X-ray with *Chandra* (Torres-Albà et al., 2018), and lies to the south of the optical and IR peak, with a faint counterpart in the NIR as revealed by archival *HST* NICMOS images (11080, PI: D. Calzetti). The soft X-ray emission of this system is very extended, likely associated with wind from a starburst(Turner et al., 2001; Torres-Albà et al., 2018), which also shows up in our low resolution $C-$configuration image. Given the above, here we tentatively classify this region as off-nuclear "SF". At matched resolution, detection at 33 GHz is poor (SNR < 5), therefore spectral index reported in Table 4.2 is an upper-limit.

(*9*) *IC 0214* : Two regions are identified in this late-stage merger at both 15 and 33 GHz. The fainter region aligns with the optical and IR peak of the system, and the brighter region lies outside of the galaxy, with no visible IR or optical counterpart. No evidence for AGN has been reported in the literature and the high PAH 6.2μm equivalent width measured with *Spitzer* indicates that this system is dominated by star formation, which is consistent with optical BPT diagnostics using VLT/MUSE (ID: 097.B-0427, PI: G. Privon). Therefore here we classify the fainter region as the starburst-dominated nucleus. The bright extra-nuclear radio source does not have bright counterparts in optical or IR, therefore we tentatively classify this region as "Bg". We report its measured quantities in Table 4.1 and 4.2 for completeness but exclude it from further analysis.

(*10*) *NGC 0877* : Due to the limited sensitivity of the *A*-configuration observations, we did not detect any 15 or 33 GHz emission in this pre-merging system.

(*11*) *NGC 0958* : Due to the limited sensitivity of the *A*-configuration observations, we did not detect any 15 or 33 GHz emission in this isolated galaxy.

(*12*) *NGC 1068* : This well-studied isolated Seyfert 2 galaxy (Yuan et al., 2010, e.g.) is the nearest LIRG in our sample. At both 15 and 33 GHz, three luminous nuclear regions are identified with *Astrodendro*. These regions are aligned almost linearly along the N-S direction, with the central region being the brightest at both 15 and 33 GHz. All three regions have been previously identified as radio jets associated with a highly obscured AGN, which is likely located within the southern region (e.g. Gallimore et al., 1996, 2004). Therefore we have classified the southern region as “AGN”, and the other two as “Jet”.

(*13*) *UGC 02238* : We detect one nuclear region in this late-stage merger at both 15 and 33 GHz. This bright region aligns with the optical and IR peak of the galaxy. This region is also detected in the soft and hard X-ray with *Chandra*, but clear X-ray AGN signature was not found (Torres-Albà et al., 2018). The galaxy also does not show excess radio emission relative to FIR emission, as expected from radio AGN (Condon et al., 1995). However, optical observations have classified this system as a LINER (Veilleux et al., 1995) or AGN/SB composite galaxy (Yuan et al., 2010). Given the above, we classify this nuclear region as “AGN/SBnuc”.

(*14*) *UGC 02369* : In this pair of early-stage merger, we detect two nuclear regions that coincide with the optical and IR peaks of the two galaxies at both 15 and 33 GHz. The nucleus of the southern galaxy is detected in both soft and hard X-ray with *Chandra*, and is classified as an AGN by Vardoulaki et al. (2015) based on steep radio spectral index between 1.4 and 8.4 GHz. The northern nucleus is very faint in the X-ray and IR, with no reported signatures of AGN. The entire interacting system has been classified as HII (Veilleux et al., 1995) or AGN/SB composite system (Yuan et al., 2010) in the optical, and MIR diagnostics indicate that the system is dominated by star formation (Stierwalt et al., 2013; Inami et al., 2018). Given the above, we classify the southern nucleus as "AGN/SBnuc", and the northern nucleus as "SBnuc".

(*15*) *IRAS F03359+1523* : We detect one bright nuclear region in this edge-on eastern component of a late-stage merger at both 15 and 33 GHz. This radio source is classified as AGN/SB composite based on 1.4 - 8.4 GHz spectral index profile in Vardoulaki et al. (2015), but the galaxy is classified as starburst-dominated based on optical (Veilleux et al., 1995; Yuan et al., 2010) and MIR diagnostics (Inami et al., 2018). Observation with e-MERLIN at 5 GHz reveals compact continuum emission at the nucleus with a peak brightness temperature of $10^{4.5}$ K (J. Molden, private communication). Given the above, here we tentatively classify this region as "AGN/SBnuc".

(*16*) *CGCG 465-012* : In this mid-stage merger, one bright extra-nuclear region is detected and identified at 15 GHz. No emission is detected at 33 GHz, therefore we do not report measurements of this region in Table 4.2. This extra-nuclear region lies in the tidal tail of the merger and has a bright counterpart in the X-ray (Torres-Albà et al., 2018). We classify this region as extra-nuclear "SF" following Torres-Albà et al. (2018).

(*17*) *UGC 02982* : Due to the limited sensitivity of the *A*-configuration observations, we did not detect any 15 or 33 GHz emission in this late-stage merger.

(*18*) *ESO 550-IG025* : We detect the two nuclei of this pair of pre-merger at both 15 and 33 GHz. However, nuclear emission from the southern galaxy is much fainter and more diffuse and does not have good detection, therefore we only report measurements for the nucleus of the northern galaxy in Table 4.1 and 4.2. Both nuclei are detected in the X-rays with *Chandra* in Torres-Albà et al. (2018). While no clear signatures of AGN have been reported, both galaxies have been separately classified as LINER/composite system by Veilleux et al. (1995) and Yuan et al. (2010) in the optical. Given the above, here we tentatively classify the identified nucleus of the northern component as "AGN/SBnuc".

(*19*) *NGC 1614* : We detect 13 individual star-forming regions along the nuclear star-forming ring of this late-stage minor merger at native resolution 33 GHz. At matched resolution, several smaller regions are blended together, resulting a total of 8 regions identified at both 15 and 33 GHz. A faint nucleus is visible at 33 GHz, but the detection is poor, therefore not characterized in this work. The property of the nuclear star-forming ring has been studied at various wavelengths (e.g. Alonso-Herrero et al., 2001b; König et al., 2013; Xu et al., 2015), and analysis of the ring based on radio datasets used in this work is presented in Song et al. (2021). Although this galaxy has been classified as an AGN/SB composite system in the optical (Yuan et al., 2010), deep VLBI observation has found no evidence for AGN (Herrero-Illana et al., 2017), and the lack of molecular gas at the nucleus also excludes the possibility of a Compton-thick AGN (Xu et al., 2015). Following these studies, we classify all these nuclear ring regions as off-nuclear "SF".

(*20*) *UGC 03094* : We detect one nuclear region in this isolated spiral galaxy at both 15 and 33 GHz. This region aligns with the optical and IR peak of the galaxy center, and was detected in the ultra-hard X-ray with *SWIFT*/BAT (Koss et al., 2013). While this galaxy does not show excess radio emission relative to FIR emission as expected for radio AGN (Condon et al., 1995), fine-structure gas emission line [Ne V] 14.3 μm is clearly detected with *Spitzer* in this galaxy, which is a strong signature of AGN presence (Petric et al., 2011). Given the above, here we classify the identified radio nucleus as "AGN".

(*21*) *NGC 1797* : This galaxy is in a pre-merging system IRAS F05053-0805, together with NGC 1799. We detected four nuclear regions at both 15 and 33 GHz, which are star-forming regions along a nuclear star-forming ring, whose diffuse emission is detected in $C-$configuration 33 and 15 GHz observations (Song et al., 2021). This galaxy is classified as a starburst galaxy in the optical (Veilleux et al., 1995; Yuan et al., 2010) and based on PAH 6.2μm equivalent width (Stierwalt et al., 2013), with no emission detected at the center of the ring in our radio observations. We classify these four nuclear regions as off-nuclear "SF".

(*22*) *CGCG 468-002* : In this mid-merging galaxy pair, we detect the nuclei of both galaxies at 15 and 33 GHz. Detection of hard X-ray emission with *NuSTAR* (Ricci et al., 2017) and [Ne V] 14.3μm line emission with *Spitzer* (Petric et al., 2011) in the southwestern galaxy strongly suggests AGN presence, which is not detected in the eastern galaxy. Based on the PAH 6.2μm equivalent width, the northeastern galaxy is dominated by star formation. Pereira-Santaella et al. (2015) classified the northeastern galaxy as an AGN/SB composite galaxy based on optical diagnostics. Because only the northeastern component is a LIRG, here we only report measurements of the northeastern nucleus, which we tentatively classify as "AGN/SBnuc".

(*23*) *IRAS F05187-1017* : We detect one nuclear region in this isolated galaxy at both 15 and 33 GHz. This region coincides with with the optical and IR peak of the galaxy. This galaxy is classified as a LINER in the optical (Veilleux et al., 1995; Yuan et al., 2010) and the PAH 6.2 μm equivalent width indicates that both AGN and star formation could be contributing to the emission in this galaxy. Given the above, we classify the detected radio nucleus as "AGN/SBnuc".

(*24*) *IRAS 05442+1732* : We detect 5 nuclear regions in this east-most component of a pre-merging system at both 15 and 33 GHz. This galaxy is likely dominated by star formation given the relatively high PAH 6.2 μm equivalent width (Stierwalt et al., 2013), and its IR SED agrees well with a pure starburst model (Dopita et al., 2011). These regions have counterparts in the NIR of various brightness based on comparison with archival high-resolution WFC3 F110W *HST* image (15241, PI: K. Larson). Given the lack of evidence for AGN, these regions are likely "SBnuc" and off-nuclear "SF". However, currently available ancillary information does not allow us to determine the precise nature of radio emission in these regions.

(*25*) *ESO 557-G002* : We detect the nucleus of this northern component of a pre-merging galaxy pair at both 15 and 33 GHz. Detection at 33 GHz is poor (S/N $<$ 5), therefore we use the 15 GHz image to measure the properties of the detected nucleus, and the reported 15 - 33 GHz spectral index is an upper-limit. Emission in this galaxy is dominated by star formation based on optical

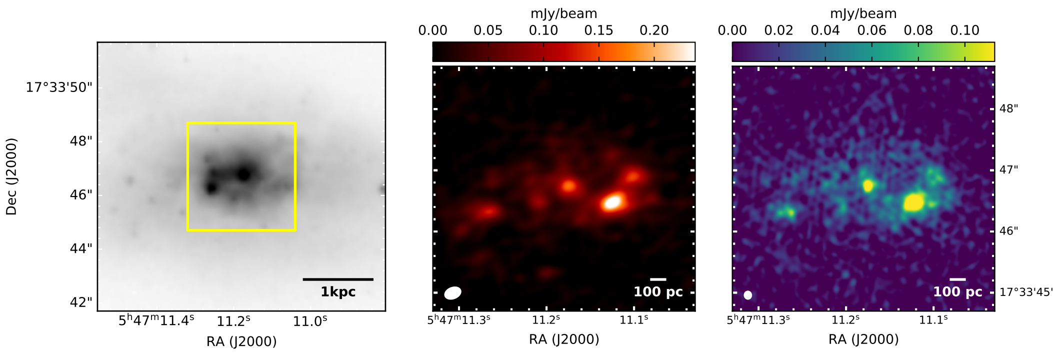

Figure 4.13: IRAS 05442+1732: *left:* Archival HST 110W image, displayed in arcsinh stretch with bilinear interpolation. Yellow square outlines the field-of-view of *middle:* 33 GHz VLA continuum observed with *B*-configuration. *right:* 15 GHz VLA continuum observed with *A*-configuration.

(Corbett et al., 2003) and MIR PAH 6.2 μm equivalent width (Stierwalt et al., 2013), and no clear signatures for AGN have been reported. Therefore here we tentatively classify this radio nucleus as “SBnuc”.

(*26*) *IRAS F07251-0248* : In this late-stage merger we detect one nuclear region at 33 GHz. Observation at 15 GHz was severely affected by malfunction of the re-quantizer therefore we do not report matched resolution measurements of this region in Table 4.2. This region lies within the optical and IR peak of the galaxy, and is detected in the soft X-ray with *Chandra*. This galaxy is classified as a “hard X-ray quiet (HXQ)” source by Iwasawa et al. (2009), and the X-ray emission may come from obscured high-mass X-ray binary or AGN. The low PAH 6.2 μm equivalent width detected in this galaxy (Stierwalt et al., 2013) also indicates potential AGN presence. Given the above, we classify the radio nucleus as “AGN/SB nucleus”.

(*27*) *MCG +02-20-003* : In this northern component of a pre-merging system, we identify 3 radio regions at 33 GHz. Observation at 15 GHz was severely affected by malfunction of the re-quantizer therefore we do not report matched resolution measurements of these regions in Table 4.2. These regions all coincide with the optical and IR peak of the galaxy, and lie within the elongated galaxy nucleus detected in Paα with *HST* NICMOS ((10169, PI: A. Alonso-Herrero); Alonso-Herrero et al., 2009; Larson et al., 2020) (see Figure 4.14). This galaxy is classified as an AGN/SB composite galaxy in the optical by Alonso-Herrero et al. (2009). While a low PAH 6.2 μm is detected (Stierwalt et al., 2013), Alonso-Herrero et al. (2012) did not find evidence for AGN via IR spectral decomposition. Currently available ancillary information does not allow us to determine the precise nature of radio emission in these regions.

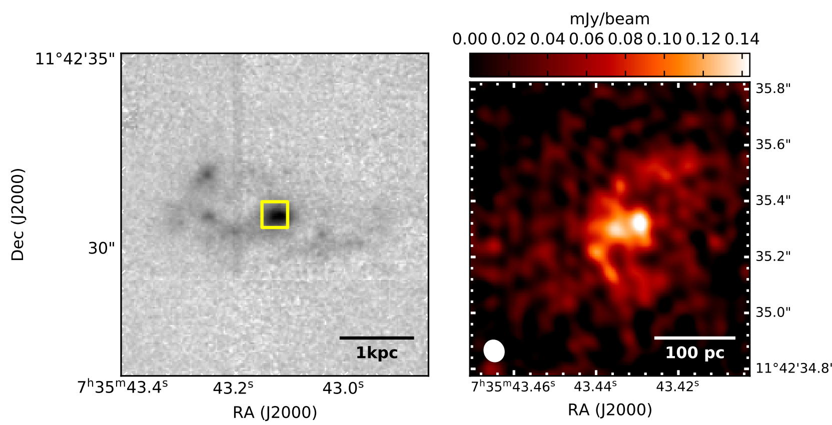

Figure 4.14: MCG +02-20-003: HST Paα image (*left*), displayed in arcsinh stretch with bilinear interpolation. The yellow square outlines the field-of-view of the 33 GHz VLA continuum observed with *B*-configuration (*right*), showing bright clumpy nuclear star-forming structures.

(*28*) *IRAS 09111-1007* : Due to the limited sensitivity of the *A*-configuration observation, we did not detect 33 GHz emission in this mid-stage merging galaxy pair. At 15 GHz, we detect three regions within the MIR peak of the eastern component, with the central region aligned with optical peak. This galaxy was not classified as X-ray AGN, but strong SI XIII line was detected with Chandra (Iwasawa et al., 2011), which may come from a buried AGN. [Ne V] 14.3μm line is detected in the MIR on kpc scales (Petric et al., 2011), and the system is classified as an Seyfert 2 or LINER in the optical (Duc et al., 1997). Therefore we classify the central region as "AGN", and the other two regions as "Ud" as we do not have sufficient information from other wavelengths to identify the nature of their radio emission.

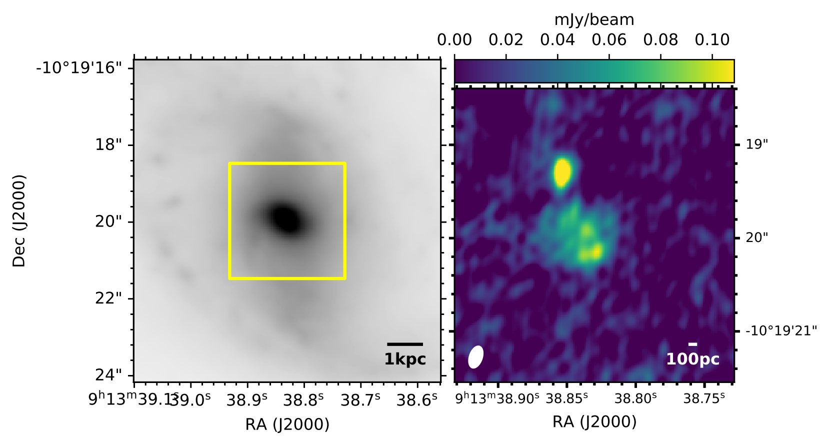

Figure 4.15: IRAS 09111-1007: *left:* Archival HST 160W image, displayed in arcsinh stretch with bilinear interpolation. *right:* 15 GHz VLA continuum observed with A-configuration.

(*29*) *Arp 303 (IC 0563/4)* : Due to the limited sensitivity of the A-configuration observation, we did not detect 33 GHz emission in this pre-merging galaxy pair. Only the nucleus of the southern component (IC 0563) is detected at 15 GHz. The southern galaxy show excess hard X-ray coming from an off-nuclear ULX region, which is possibly a background AGN. Given that no AGN evidence has been reported in this system, we classify the detected nucleus as "SBnuc".

(*30*) *NGC 3110* : Due to the limited sensitivity of the A-configuration observations, we did not detect emission in this late-stage merger at 33 or 15 GHz.

(*31*) *IRAS F10173+0828* : We detect the nucleus of this galaxy in pre-merging stage at both 15 and 33 GHz. This nucleus is faint in the soft X-ray and is classified as an HXQ source by Iwasawa et al. (2009), potentially containing a Compton-thick AGN. Optical (Vardoulaki et al., 2015) and MIR diagnostics (Stierwalt et al., 2013) indicate a mixture of AGN- and SB-driven emission in this galaxy, which also hosts 26 OH mega-masers (Yu, 2005). Vardoulaki et al. (2015) classified this galaxy as a radio AGN based on its negative 1.4 - 8.4 GHz spectral index, a signature for face-on AGN with jets. Given the above, here we classify the nucleus as "AGN/SBnuc".

(*32*) *CGCG 011-076* : We detect one nuclear region in this pre-merging galaxy at both 15 and 33 GHz. This region coincides with the optical and IR peak of the galaxy. While no clear evidence for AGN presence has been reported, its intermediate MIR PAH equivalent widths (Stierwalt et al., 2013; Yamada et al., 2013) indicate potential contribution from an AGN. Given the above, we classify the radio nucleus as "AGN/SBnuc".

(*33*) *IC 2810* : We detect one nuclear and one extra-nuclear region in this northwestern component of a per-merging galaxy pair at both 15 and 33 GHz. The fainter region aligns with the optical and IR peak of the galaxy, while the brighter region lies in the galaxy disk about 5"south to the nucleus. Optical, MIR and radio diagnostics all indicate a mixture of AGN- and SB-driven emission in the galaxy (Imanishi et al., 2010; Stierwalt et al., 2013; Vardoulaki et al., 2015), therefore we classify the fainter region as "AGN/SBnuc", and the brighter region as extra-nuclear "SF".

(*34*) *IRAS F12112+0305* : In this late-stage merger ULIRG, we detect the two nuclei of the north-south aligned galaxy pair at both 15 and 33 GHz, with the southern nucleus about 5 times fainter than the northern nucleus. Both nuclei are detected with *Chandra* in the hard X-ray but the northern nucleus is slightly fainter and has softer spectrum than the southern nucleus (Iwasawa et al., 2011). Neither of the two nuclei was detected with *NuSTAR* and analysis of the *Chandra/XMM-Newton* spectrum indicates no presence of AGN (Ricci et al., 2021). While no clear AGN signatures are present, this system has been classified as a type-2 Seyfert in the optical (Yuan et al., 2010), and the southern nucleus is classified as AGN/SB in the radio by Vardoulaki et al. (2015). Given the above, here we tentatively classify both nuclei as "AGN/SBnuc".

(*35*) *IRAS F12224-0624* : In this isolated galaxy, we detect one nuclear region, at both 15 and 33 GHz, that coincides with the galaxy's optical and IR peak. Small equivalent width of PAH emission at both 6.2 and 3.3 μm strongly suggests AGN presence (Stierwalt et al., 2013; Yamada et al., 2013), and this galaxy has also been classified as a Seyfert 2 galaxy in the optical (Yuan et al., 2010). Therefore here we classify the nucleus as "AGN".

(*36*) *NGC 4418* : We detect one nuclear region in this isolated galaxy at both 15 and 33 GHz. This region coincides with the optical and IR peak of the galaxy, and the nature of this nucleus has been under active debate. While small equivalent widths of PAH emission at both 6.2 and 3.3 μm indicate AGN-dominated emission (Stierwalt et al., 2013; Yamada et al., 2013), this galaxy is not detected in the ultra-hard X-rays (Koss et al., 2013; Ricci et al., 2021). The flat hard X-ray spectrum potentially points to an Compton-thick AGN (Maiolino et al., 2003), and VLBI observation at 5 GHz with *EVN* indicates that the nuclear radio emission in this galaxy comes from a mixture of AGN and star formation (Varenius et al., 2014). Given the above, we classify this nucleus as "AGN/SBnuc".

(*37*) *CGCG 043-099* : We detect 3 nuclear regions in this late-stage merger at 33 GHz at native resolution, two of which blend into one at 15 - 33 GHz matched resolution. All these regions coincides with the IR and optical peak of the system, whose emission is dominated by star formation given the relatively large PAH 6.2 μm equivalent width. Optical studies have classified this system as an type-2 Seyfert (Toba et al., 2013), or a shock-dominated starburst (Rich et al., 2015). Archival *HST*/WFC3 F160W image (11235, PI: J. Surace) shows a unresolved galaxy nucleus that encompass all radio regions (Figure 4.16). Given the late merger stage, we are likely detecting the obscured double/triple nuclei of this system. However, currently available ancillary information does not allow us to determine the precise nature of radio emission in these regions.

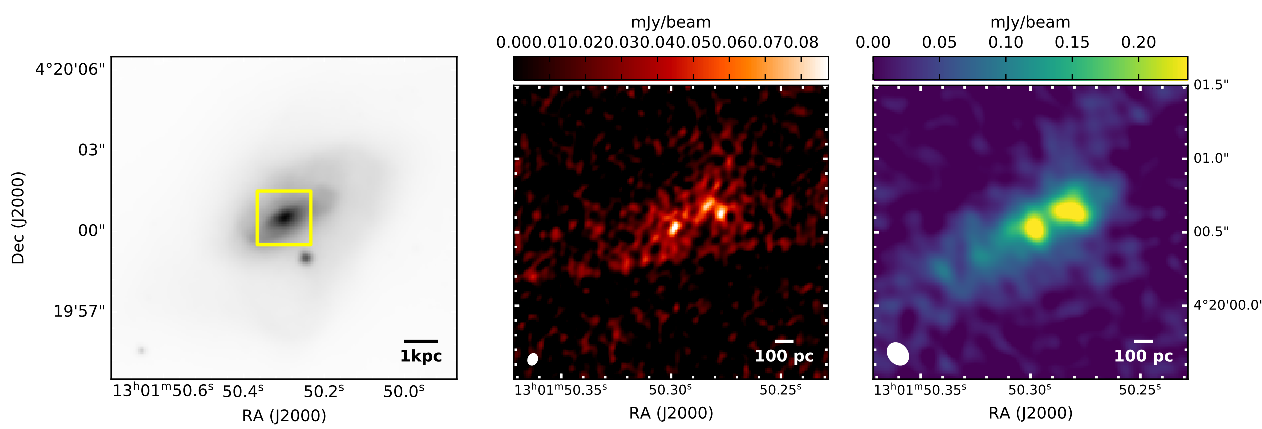

Figure 4.16: CGCG 043-099: *left:* Archival HST 160W image, displayed in arcsinh stretch with bilinear interpolation. *middle:* 33 GHz VLA continuum observed with *A*-configuration. *right:* 15 GHz VLA continuum observed with *A*-configuration.

(*38*) *MCG-02-33-098* : We detect the nucleus of this western component of the early-stage merger IRAS F12596-1529 at both 15 and 33 GHz. Based on optical and MIR diagnostics (Veilleux et al., 1995; Yuan et al., 2010; Stierwalt et al., 2013), emission in this galaxy is dominated by star formation, and no AGN is detected in the ultra-hard X-rays with *Swift*/BAT (Koss et al., 2013). Therefore we classify this nucleus as an SB-dominated nucleus.

(*39*) *NGC5104* : In this isolated galaxy, we detect one nuclear region at the location of the optical and IR peak of the galaxy at both 15 and 33 GHz. While no signatures of AGN are present in the X-rays (Koss et al., 2013; Privon et al., 2020), this galaxy is classified as a LINER (Veilleux et al., 1995) or AGN/SB composite system (Yuan et al., 2010) in the optical, which is supported by an intermediate PAH 6.2 μm equivalent width (Stierwalt et al., 2013). Give the above, we classify the radio nucleus as "AGN/SBnuc".

(*40*) *MCG-03-34-064* : In this southern component of a pre-merging galaxy pair, we detect four nuclear regions aligned linearly on NE-SW direction in native resolution 33 GHz image. At 15 and 33 GHz with matched resolutions, these four regions are blended together into one elongated region that lies within the IR and optical peak of the galaxy. Clear signatures of AGN are present in the X-rays (Torres-Albà et al., 2018; Ricci et al., 2017), optical (Corbett et al., 2002) and MIR (Petric et al., 2011). This galaxy also show significant radio excess relative to the radio-FIR correlation (Condon et al., 1995; Corbett et al., 2003), therefore the four linearly aligned regions we observe at native resolution are very likely AGN and radio jets, which is confirmed by steep 15 - 33 GHz spectral index (< -0.9) measured at matched resolution. Although the precise location of the AGN is unclear from the currently available observations, the morphology of radio emission resembles commonly observed one-sided radio jets, with the brighter and more compact knots resulting from Doppler boosting effect from relativistic jets traveling close to the line-of-sight (e.g. Bridle & Perley, 1984; Singal, 2016). Given the above, we tentatively attribute the nuclear radio emission detected in this galaxy to radio "jets".

(*41*) *Arp 240 (NGC 5257/8)* : Although both the eastern and western components in this early-stage merger have been observed, we only detect two regions in the western component NGC 5257, both at native and at matched resolutions due to limited sensitivity. These two regions are about 12"apart along the N-S direction, and the northern region coincides with the optical and IR peak of the galaxy while the southern region lies at the tip of a spiral arm. This galaxy is classified as a starburst galaxy in the optical (Veilleux et al., 1995), MIR (Stierwalt et al., 2013) and radio (Vardoulaki et al., 2015), therefore we classify the northern region as "SBnuc" and the southern region as extra-nuclear "SF".

(*42*) *NGC 5331* : In this mid-merging galaxy pair, we only detect radio emission in the southern galaxy NGC 5331S given the sensitivity limits. At both 15 and 33 GHz, we identify 7 regions in total in NGC 5331S, with 6 regions residing within the bulk of MIR emission at the galaxy center, and 1 region on the northern spiral arm. Comparison with high-resolution ALMA CO(J=2-1) data (2017.1.00395.S, PI: T. Díaz-Santos) indicates that the nuclear radio knots lie along the edge of a inclined rotating nuclear disk. This galaxy is classified as a starburst galaxy in the optical (Wu et al., 1998), in agreement with a high PAH 6.2 μm equivalent width(Stierwalt et al., 2013), and no AGN is detected in the X-rays (Torres-Albà et al., 2018). Therefore we classify the nuclear regions as off-nuclear "SF", and the region on the spiral arm as extra-nuclear "SF".

(*43*) *IRAS 14348-1447* : In this late-stage merger, we detect the two nuclei of the SW-NE aligned merging galaxy pair at both 15 and 33 GHz. Both galaxies have been separately classified as LINERs (Veilleux et al., 1995) or AGN/SB composite galaxies (Yuan et al., 2010) in the optical, as well as in the radio (Vardoulaki et al., 2015). Both nuclei are detected in the X-rays with *Chandra*, but only the southwestern nucleus is bright in the hard X-ray with a spectrum consist with the model for buried AGN (Iwasawa et al., 2011). Therefore we classify the southern nucleus as "AGN", and the northern nucleus as "AGN/SBnuc".

(44) *CGCG 049-057* : In this isolated galaxy we detect one nuclear region at both 15 and 33 GHz. This region coincides with the optical and IR peak of the galaxy. While no AGN signatures are present based on IR and optical studies (e.g. Stierwalt et al., 2013; Imanishi et al., 2010; Alonso-Herrero et al., 2012), this galaxy likely contains an buried AGN based on X-ray (Torres-Albà et al., 2018) and radio (Baan & Klöckner, 2006) analysis, which is supported by the high gas column density measured in the nucleus (Falstad et al., 2015). Therefore we classify this nucleus as "AGN".

(45) *NGC 5936* : In this isolated galaxy we detect the nucleus at both 15 and 33 GHz. However, detection at 33 GHz is poor (S/N < 5), so we only report measurements at 15 GHz for this nucleus in Table 4.1 and its spectral index reported in 4.2 is an upper-limit. This galaxy has relatively large PAH 6.2 μm equivalent width indicating SB-dominated emission, but it has been classified as an AGN/SB composite galaxy in the optical (Yuan et al., 2010; Alonso-Herrero et al., 2012). Given the above, we tentatively classify this nucleus as "AGN/SBnuc".

(46) *NGC 5990* : We detect the nucleus of the bright southern component of this pre-merger at both 15 and 33 GHz. However, detection at 33 GHz is poor (S/N

< 5), so we only report measurements at 15 GHz for this nucleus in Table 4.1 and its spectral index reported in 4.2 is an upper-limit. While this galaxy does not show excess radio emission relative to FIR emission as expected for radio AGN (Condon et al., 1995), it has been classified as a type-2 Seyfert in the optical (Yuan et al., 2010) and [Ne V] 14.3 μm line is detected at the nucleus on kpc scale (Petric et al., 2011), which is a clear signature of AGN. Therefore we classify this nucleus as "AGN".

(47) *IRAS F16164-0746* : In this late-stage merger, at both 15 and 33 GHz we detect a compact luminous nuclear region with faint elongated emission on its sides along the E-W direction and perpendicular to the galaxy's optical disk. Only emission on the west side of this region has strong enough detection to be characterized with *Astrodendro*, along with the bright region itself. Despite having a relatively large PAH 6.2 μm equivalent width Stierwalt et al. (2013), this galaxy is classified as an AGN in the X-rays (Torres-Albà et al., 2018) and [Ne V] 14.3 μm line is detected at the nucleus on kpc scales (Petric et al., 2011), which is a clear signature for AGN. It has also been classified as a LINER (Veilleux et al., 1995), or Seyfert 2 (Yuan et al., 2010) in the optical. The bright region coincides with the dynamical center of the molecular gas as revealed by ALMA (2017.1.00395.S, PI: T. Díaz-Santos), therefore here we assume it to be the location of the AGN. The ALMA data also shows an edge-on rotating nuclear molecular disk, with the west side of the disk coinciding with the fainter elongated radio region, which has a relatively flat 15 - 33 GHz spectral index (~ -0.3). Therefore here we tentatively classify this fainter region as off-nuclear "SF".

(48) *CGCG 052-037* : In this isolated galaxy, multiple nuclear regions were detected

at native resolutions, but only one region has high enough S/N to be consistently identified with *Astrodendro* at both 15 and 33 GHz. No clear signatures of AGN have been reported in the literature, and existing MIR studies classify this galaxy as a starburst galaxy (Imanishi et al., 2010; Yamada et al., 2013; Stierwalt et al., 2013). Therefore this region is likely "SBnuc", or off-nuclear "SF". However, currently available information does not allow us to determine the nature of the radio emission.

(*49*) *IRAS F16399-0937N* : In this late-stage interacting pair we detect the northern nucleus at both 33 and 15 GHz. While no clear evidence for AGN has been presented, a buried AGN possibly exists and is producing the OH mega-maser observed in this system Sales et al. (2015); Torres-Albà et al. (2018). Given the above, we classify this nucleus as "AGN/SBnuc".

(*50*) *NGC 6240* : In this well-studied late-stage merger, we detect the two nuclei of the merging galaxy pair at both 15 and 33 GHz. This system has been classified as a LINER in the optical (Veilleux et al., 1995; Yuan et al., 2010). Despite having a relatively large PAH 6.2 μm equivalent width, MIR line diagnostics on kpc scales indicate a strong presence of one or two buried AGN Armus et al. (2006). Analysis in the X-rays show that both nuclei have clear AGN signatures (Iwasawa et al., 2011). These two active nuclei have also been resolved with radio VLBI (Gallimore et al., 2004). Therefore here we classify these two nuclei as "AGN".

(*51*) *IRAS F16516-0948* : In this late-stage merger, we detect two regions that lie outside of the MIR galaxy "core" at both 15 and 33 GHz. These two extra-nuclear radio-emitting regions were also identified by Herrero-Illana et al. (2017)

at 8 GHz. However, only the region to the east has good enough detection to be identified by *Astrodendro* and only at 15 GHz, hence we only report the 15 GHz measurements in Table 4.1 and the spectral index reported in Table 4.2 are upper-limits. This region lies outside the bulk of optical and 3.5μm IR emission (*Spitzer* IRAS Channel 1), yet coincides with the peak of 8μm IR emission (*Spitzer* IRAS Channel 4), as shown in Figure 4.17. While relatively large PAH 6.2 μm equivalent width was measured in this system (Stierwalt et al., 2013), the measurement was performed centering on the optical peak of the system and misses the region we identify at 15 GHz, which may be a highly-obscured nucleus or off-nuclear "SF". Currently available ancillary information does not allow us to determine the precise nature of radio emission in this region.

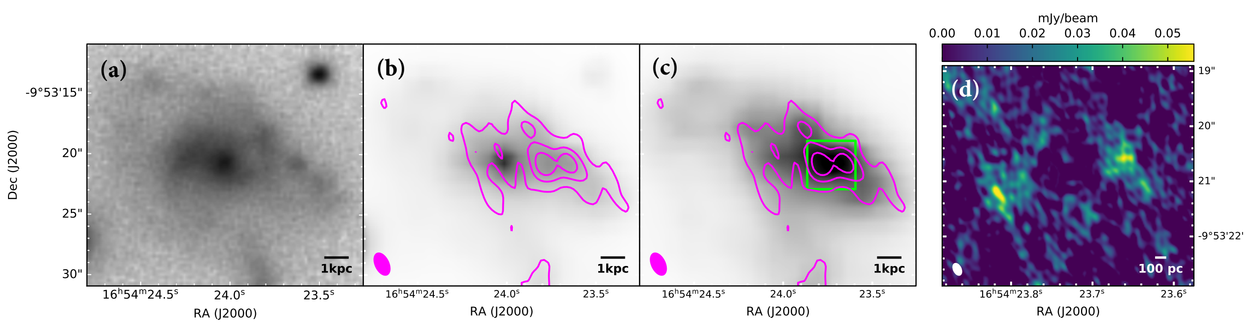

Figure 4.17: IRAS F16516-0948: *(a):* PanSTARRS1 y band image, displayed in arcsinh stretch with bilinear interpolation. *(b):* Spitzer channel 1 image, overlaid with 33 GHz VLA continuum (magenta contours) observed with *C*-configuration (beam shown on the lower left in magenta). *(c):* Same as *(b)* but on Spitzer channel 4 image. Lime square outlines the field-of-view of *(d):* 15 GHz VLA continuum observed with *A*-configuration.

(*52*) *IRAS F17138-1017* : In this late-stage merger, we detect 5 regions at both 15 and 33 GHz, 4 of which are aligned along N-S direction following bulk of the nuclear optical and IR emission in the galaxy. The north-most region is at the location of the nucleus (Colina et al., 2015), and is also the brightest among all regions. Although this galaxy is detected in hard X-ray with *NuSTAR* and *Chandra*, it is inconclusive from analysis of the X-ray spectra whether a buried AGN is present (Ricci et al., 2017; Torres-Albà et al., 2018). In the optical this galaxy is classified as an AGN/SB composite galaxy (Yuan et al., 2010), while the PAH 6.2 μm equivalent width and NIR line diagnostics indicate that its nuclear emission is dominated by SF (Stierwalt et al., 2013; Colina et al., 2015). Give the above, we classify the north-most region as "AGN/SBnuc", the rest 4 nuclear regions as off-nuclear "SF".

(*53*) *IRAS 17208-0014* : In this late-stage merger, we detect three nuclear regions at native resolutions at both 15 and 33 GHz. These regions are aligned linearly along the E-W direction, and the west-most region appears much more luminous than the rest. At matched resolution, these regions are blended together into a larger elongated region at 15 and 33 GHz. Prominent shock features have been observed in this galaxy (Medling et al., 2015; U et al., 2019), which has been attributed to star formation (Rich et al., 2015). While VLBI observations do not find compact radio cores indicative of AGN activity (Momjian et al., 2003b, 2006), the system has been classified as a AGN-starburst composite systems in the optical (Yuan et al., 2010) and based on an intermediate 6.2 μm PAH equivalent width (Stierwalt et al., 2013). It has been argued in several studies that the system likely hosts buried AGN (e.g. Iwasawa et al., 2011; Falstad et al., 2021; Baba et al., 2022). The brightest region on the west is located at the dynamical center of the molecular gas as revealed by ALMA (2018.1.00486.S, PI: M. Pereira-Santaella). This region and the faint radio region on the east coincide with the locations of the merging dual nuclear disks revealed in milli-arcsecond resolution Keck observations (Medling et al., 2015). Therefore we classify these two regions as "AGN/SBnuc". The other faint region in between may be associated with shock or clumpy star formation in one of the nuclear disk, but currently available information is not sufficient to clearly identify its nature. Figure 4.18 shows the HST image of the galaxy along with VLA radio continuum images of the nuclear regions studied in this work.

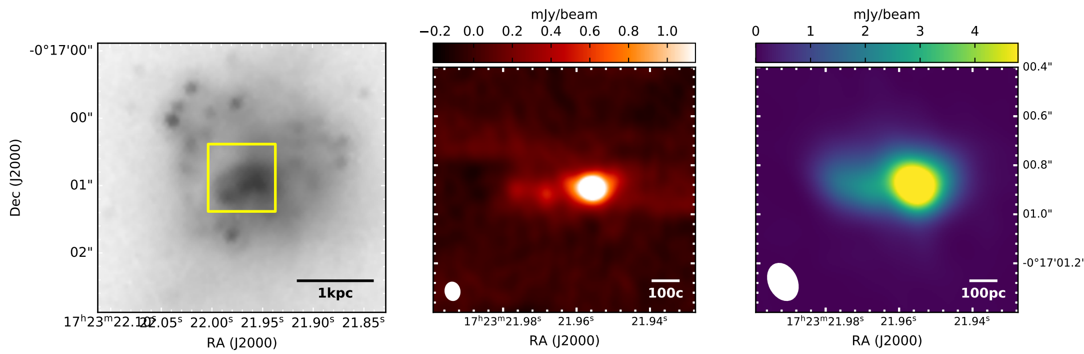

Figure 4.18: IRAS F17207-0014: *(a):* HST/NICMOS F160W image, displayed in arcsinh stretch with bilinear interpolation. Yellow square outlines the field-of-view of *(middle):* 33 GHz VLA continuum observed with A-configuration (beam shown on the lower left in white). *(right):* 15 GHz VLA continuum observed with A-configuration.

(*54*) *IRAS 17578-0400* : In the northern component of this early-stage merging galaxy triplet, we detect one nuclear region at both 15 and 33 GHz. This region aligns with the optical and IR peak of this galaxy. This galaxy is not detected in the ultra-hard X-rays with *SWIFT*/BAT (Koss et al., 2013), and it has a large PAH 6.2 μm equivalent width (Stierwalt et al., 2013), indicating SB-dominated emission, which is also consistent with the optical classification (Rich et al., 2015). However, this galaxy may host a highly embedded AGN (Falstad et al., 2021). Therefore we tentatively classify this nucleus as "AGN/SBnuc".

(*55*) *IRAS 18090+0130W* : We detect two nuclear regions and one extra-nuclear region in this western component of a early-stage merger at both 15 and 33

GHz. However, the detection at 33 GHz is poor (S/N < 5), therefore we only report measurements made at 15 GHz in Table 4.1 and the derived spectral indices reported in Table 4.2 are upper-limits. The two nuclear regions lie closely besides each other, and both are located at the IR and optical peak of the galaxy. Archival HST 132N image (ID: 14095, PI: G. Brammer) shows an unresolved galaxy nucleus encompassing the radio regions we detect, as shown in Figure 4.19. This galaxy is not detected in the X-rays with *Chandra* or *SWIFT*/BAT (Koss et al., 2013; Torres-Albà et al., 2018), but an intermediate PAH 6.2 μm equivalent width (Stierwalt et al., 2013) indicates that the emission in this galaxy may be partially driven by AGN. Therefore the two nuclear regions that we detect are likely the AGN/SB nucleus and a off-nuclear SF region or a radio jet. Archival However, currently available ancillary information does not allow us to determine the precise nature of radio emission in these two nuclear regions.

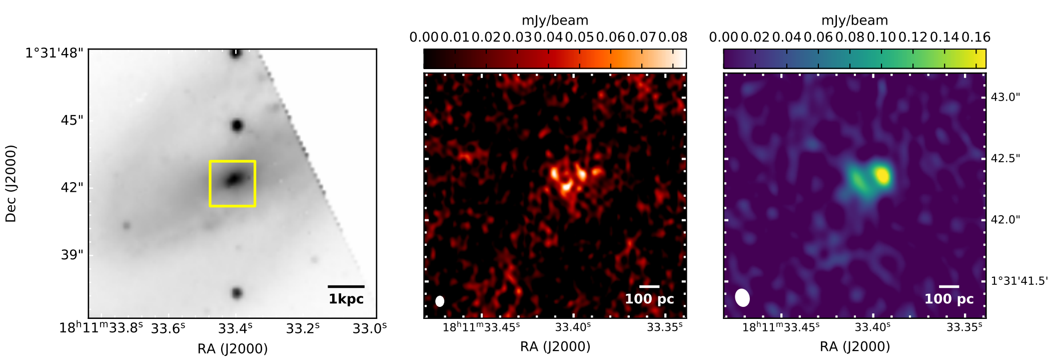

Figure 4.19: IRAS 18090+0130: HST F132N image (*left*), displayed in arcsinh stretch with bilinear interpolation. The yellow square outlines the field-of-view of the 33 GHz (*middle*) and 15 GHz (*right*) VLA continuum observed with *A*-configuration, showing at least two radio components of undetermined nature.

(*56*) *IRAS F19297-0406* : We detect the nucleus of this late-stage merger at both 15 and 33 GHz. This galaxy is detected in both soft and hard X-rays with *Chandra*, and Iwasawa et al. (2009) classified it as an HXQ, and may contain an buried AGN. Optical and MIR diagnostics all point to an AGN/SB composite system (Yuan et al., 2010; Stierwalt et al., 2013). Therefore we classify this nucleus as "AGN/SBnuc".

(*57*) *IRAS 19542+1110* : In this isolated galaxy we detect its nucleus at both 15 and 33 GHz. While MIR diagnostics do not clearly identify AGN signatures (Imanishi et al., 2010; Stierwalt et al., 2013), this galaxy is compact and bright in the hard X-ray and has a very steep spectrum and hence was classified as an AGN by Iwasawa et al. (2011). AGN signatures were not detected in the optical (Fluetsch et al., 2020). Therefore here we classify this nucleus as "AGN/SBnuc".

(*58*) *NGC 6926* : We detect the nucleus of this late-stage merger at both 15 and 33 GHz. This galaxy is an optical type-2 Seyfert (Veilleux et al., 1995; Yuan et al., 2010), and has clear detection of [Ne V] 14.3 μm line at the nucleus on kpc scale, which is a clear signature of AGN presence. Therefore we classify this nucleus as AGN.

(*59*) *II Zw96* : In this mid-stage merger, we detect one region at both 15 and 33 GHz. This region coincides with the site of an extremely obscured off-nuclear starburst that is responsible for 70% of the IR luminosity of this system (Inami et al., 2010), which also has the hardest X-ray spectrum among all X-rays sources detected in this system due to the obscuration (Iwasawa et al., 2011). Here we tentatively classify this region as an extra-nuclear "SF" following (Inami et al., 2010). We note that while VLBI observations of the OH megamaser in this region have suggested that it may host an obscured AGN (Migenes et al., 2011), recent multi-frequency analysis of the radio spectrum shows that it is well described by pure star formation (Wu et al., 2022).

(*60*) *ESO 602-G025* : In this isolated galaxy we detect its nucleus at both 15 and 33 GHz. However, detection at 33 GHz is poor therefore we report the 15 GHz measurements instead in Table 4.1 and its spectral index reported in 4.2 is highly uncertain. Both MIR and optical diagnostics point to an AGN/SB composite scenario (Yuan et al., 2010; Stierwalt et al., 2013; Yamada et al., 2013), therefore we classify this nucleus as "AGN/SBnuc"

(*61*) *IRAS F22491-1808* : We detect the eastern nucleus of this late-stage merger at both 33 and 15 GHz. This nucleus is detected in both soft and hard X-rays with *Chandra*, and is classified as an HXQ by Iwasawa et al. (2011) which may contain a buried AGN. This system is classified as SB-dominated in the optical (Veilleux et al., 1995; Yuan et al., 2010), but MIR diagnostics indicate potential AGN contribution to the emission (Stierwalt et al., 2013). Given the above, we classify this nucleus as "AGN/SBnuc".

(*62*) *NGC 7469* : In this southern component of a pre-merging galaxy pair we detect its nucleus at both 15 and 33 GHz. This galaxy does not show excess radio emission relative to FIR emission, as expected for radio AGN(Condon et al., 1995), but it is a well-studied optical Seyfert 1 galaxy (e.g. Veilleux et al., 1995; Yuan et al., 2010), and [Ne V] 14.3 μm line is clearly detected at its nucleus on kpc scales (Petric et al., 2011). Therefore we classify the detected radio nucleus as "AGN".

(*63*) *CGCG 453-062* : In this isolated galaxy we detect the nucleus at both 33 and 15 GHz. While MIR diagnostics point to a SB-dominated scenario (Imanishi et al., 2010; Stierwalt et al., 2013; Yamada et al., 2013), this galaxy has been classified as a LINER (Veilleux et al., 1995) or Seyfert 2 (Yuan et al., 2010) in the optical and strong [Ne V] 14.3 μm line emission has been detected at the nuclear position at kpc scales (Petric et al., 2011). Therefore we classify this nucleus as an "AGN".

(*64*) *NGC 7591* : In this isolated galaxy, we detect a nuclear star-forming ring at both 33 and 15 GHz. The nucleus and 6 individual star-forming regions along the ring are resolved only at 15 GHz at native resolution, and analysis of these regions is presented in Song et al. (2021). This ring has also been detected and studied in NIR hydrogen recombination lines by Larson et al. (2020). For consistency, here we mainly use the 33 GHz measurements for our analysis. At 33 GHz, the circum-nuclear ring was observed at lower resolution (i.e. *B*-configuration), and 3 distinct regions were identified by *Astrodendro*, which we classify as off-nuclear "SF".

(*65*) *NGC 7592* : In this early-stage merging galaxy triplet, we detect the nuclei of the eastern and western components at both 15 and 33 GHz. While [Ne V] 14.3 μm line is clearly detected for the entire unresolved system with *Spitzer* (Petric et al., 2011), only the western galaxy is classified as a Seyfert 2 in the optical (Veilleux et al., 1995; Yuan et al., 2010), which also shows compact emission in the X-rays with hard X-ray excess Torres-Albà et al. (2018) and MIR AGN signatures (Imanishi et al., 2010). The eastern component is classified as a starburst galaxy in the optical (Veilleux et al., 1995; Yuan et al., 2010), and no AGN signatures have been identified in the X-ray or MIR (Torres-Albà et al., 2018; Imanishi et al., 2010; Stierwalt et al., 2013). Therefore here we classify the eastern nucleus as "SBnuc", and the western nucleus as an "AGN".

(*66*) *NGC 7674* : In this western component of a pre-merging galaxy pair, we detect four nuclear regions at both 33 and 15 GHz. These regions are aligned almost linearly along the E-W direction. This galaxy is detected with *NuSTAR* (Gandhi et al., 2017) and classified as a Seyfert 2 in the optical (Veilleux et al., 1995; Yuan et al., 2010), with a strong detection of [Ne V] 14.3 μm line (Petric et al., 2011) and small PAH equivalent widths (Imanishi et al., 2010; Stierwalt et al., 2013). This galaxy also shows excess radio emission relative to FIR emission, as expected from radio AGN (Condon et al., 1995). Using VLBI, Momjian et al. (2003a) also concluded that the nuclear radio continuum emission are mostly likely all associated with AGN activity and that the AGN itself is located in between the brightest two radio components. At 15 and 33 GHz, we detect a faint region in between the two brightest radio continuum sources that were observed by Momjian et al. (2003a), and this is the only region that shows a flat 15 - 33 GHz spectral index ($\alpha \sim -0.35$) among all four regions, which likely marks the location of the AGN. Therefore we classify this faint region as "AGN", and the others as "Jet".

(*67*) *NGC 7679* : In this pre-merging galaxy, we detect one nuclear region and one extra-nuclear region at 15 and 33 GHz. The nuclear region coincides with the optical and IR peak of the galaxy. Observations in the X-ray revealed that this galaxy hosts an unobscured AGN (Della Ceca et al., 2001), while it is classified as a Seyfert 2 in the optical (Veilleux et al., 1995; Yuan et al., 2010). Although the large PAH 6.2 μm equivalent width (Stierwalt et al., 2013) indicates that this galaxy is dominated by star formation, [Ne V] 14.3 μm line is clearly detected at the nucleus on kpc scales (Petric et al., 2011), supporting the optical and X-ray classification. Therefore we classify the nuclear region as AGN, and the extra-nuclear region as extra-nuclear "SF".

(*68*) *MCG -01-60-022*: We did not detect any radio continuum emission in this pre-merging galaxy due to incorrect pointing setup.

4.7.2 Analysis result for ancillary VLA Data

Images from BM17 and SFRS (see Section 4.2.1) were re-analyzed following methods described in Section 4.3. Five of the 22 systems in BM17 are also in the GOALS-ES sample, and emission in two other systems are resolved out in the *A*- or *B*-configuration), therefore we only include results derived for 26 regions in 15 systems from BM17 to complement our discussions in Section 4.5. These regions are classified into seven "AGN", ten "AGN/SBnuc", six "SF", two "Ud" and one "Bg", using procedures described in Section 4.4.1. Regions classified as "Ud" and "Bg" were further removed from comparison. One galaxy in the SFRS, NGC 2146, is a LIRG included in the full GOALS sample (Armus et al., 2009), and hence was also excluded from re-analysis and comparison to the GOALS-ES results. A total of 187 regions are identified at characterized at both 15 and 33 GHz in 35 SFRS galaxies, but we remove 58 regions identified as AGN, background galaxies and AME candidates by Linden et al. (2020) from comparison to the GOALS-ES "SF" and "SBnuc" regions in Section 4.5.2 and Section 4.5.2. Below we present measured and derived quantities for a total of 152 regions identified in the BM17 and SFRS sample that were included in Figure 4.7, 4.9, 4.10 and 4.11 in Section 4.5.

Table 4.3: Multi-wavelength AGN Classification for the GOALS-ES Sample

ID (1)	X-Ray (2)	Optical (3)	MIR (4)	Radio (5)	Reference(X-ray/Optical/MIR/Radio) (6)	Adopted (7)
1	Y	Y	N, M, M	Y	T18/V95,Y10/I10, S13, I18/V15	Y
2	N	N	N*	-	R17/V95,Y10/I10, S13, I18/-	N
3	M	N	N, M	N, Y, Y	G06, G20/V95,Y10/I10, S13/C95, V15, I13	M
4	N	N,M	N	-	K13/V95,Y10/I10, S13, I18/-	M
5	N	M	N, M	M	T18/V08/I10, S13/V15	M
6	M	M	M, Y	M	I11/V95,Y10/S13, I18/V15	M
7	N,M	N	N*	M	G09, TA18/V95,Y10/I18/PC	M
8	N	N	N	-	T18,T01/T01/S13/-	N
9	N	N	N	-	K13/PC/S13/-	N
12	Y	Y	Y	Y	T18/V95,Y10/P11/G96	Y
13	N	M	N	N	T18/V95,Y10/I10, S13, I18/C95	M
14	N	N,M	N*	Y(S)	T18/V95,Y10/S13, I18/V15	M(S), N(N)
15	N	N	N	M	T18/V95,Y10/I10, I18/V15, PC	M
18	N	M	-	Y(S), M(N)	T18/V95,Y10/-/V15	M(S), M(N)
19	N	M	N	N	T18/V95,Y10/I10, S13, I18/H17	N
20	Y	-	Y, M	-	K13/-/P11, S13/C95	Y
21	N	N	N	-	K13/V95,Y10/S13/-	N
22	N	M	N	-	R17/P15/S13/-	M
23	N	M	M	-	K13/V95,Y10/S13/-	M
24	-	-	N	-	-/-/S13/-	N
25	N	N	N	-	K13/C03/S13/-	N
26	M	-	Y	-	I09, I11/-/S13/-	M
27	N	M	Y, N	-	K13/A09/S13, A12/-	M
31	M	M	N, M, N	Y	I09, I11/V15/I10, S13, I18/V15	M
32	-	-	M	-	-/-/S13/-	M
33	N	M	Y, N	M	T18/V08,V15/I10, S13/V15	M
34	M	Y*	M*	N(N), M(S)	I09, I11/V95,Y10/S13/V15	M
35	N	Y	Y	-	K13/V95,Y10/I10, S13, Y13/-	Y
36	N	-	Y	M	K13, R21/-/I10, S13, Y13/V13	M
37	N	Y, N	N	-	T18/T13, R15/S13/-	M
38	N	N	N	-	K13/V95,Y10/S13/-	N
39	N	M	M	-	K13,P20/V95,Y10/S13/-	M
40	Y	Y	Y	Y	R17, T18/R93/P11, S13/C95, C03	Y
41	N	N	N	N	K13/V95/S13/V15	N
42	N	N	N	-	T18/W98/S13/-	N
43	Y(SW), N(NE)	M	Y*	M	I11/V95,Y10/I10, S13/V15	Y(SW), M(NE)
44	Y	N, M	N, M	Y	T18/V95,A12/I10, S13/BK06, F15	Y
45	N	N, M	N	-	K13/V95,Y10/S13/-	M
46	N	Y	Y	N	K13/Y10/P11, S13/C95	Y
47	Y	M, Y	Y, N	-	T18/V95,Y10/P11, S13/-	Y
48	-	-	N	-	-/-/I10, S13, Y13/-	M
49	M	M	M	N	T18/Y10, R15/S13/BK06	M
50	Y	M	Y*, M*	Y	I11/V95,Y10/A06, S13/G04	Y
51	-	-	N	N	-/-/S13/C02	N
52	M	M	N	-	R17, T18/Y10/S13, C15/-	M
53	M	M, N	M	-	I11/Y10, R15/S13, M15/-	M
54	N	N	N	M	K13/R15/S13/F21	M
55	N	-	M	-	T18/-/S13/-	M
56	M	N, M	M	-	I11/V95,Y10/S13/-	M
57	Y	N	N,M	-	I11/F20/I10, S13/-	M
58	Y	Y	Y, M	-	K13/V95,Y10/P11, S13/-	Y
60	N	M	M	-	K13/V95,Y10/S13, Y13/-	M
61	N	N	N, M	-	I11/V95,Y10/I10, S13/-	M
62	Y	Y	Y	N	B86/V95,Y10/I10, S13, Y13/C95	Y
63	-	M, Y	Y	-	-/V95,Y10/P11/-	Y
65	Y(W), N(E)	Y(W), N(E)	Y(W), N(E)	-	T18/V95,Y10/I10, P11/-	Y(W), N(E)
66	Y	Y	Y	Y	K13,G17/V95,Y10/P11, S13, I13/M03, K17	Y
67	Y	Y	Y, N	-	D01,K13/V95,Y10/P11, S13/-	Y

Table 4.3 continued

Table 4.3: Multi-wavelength AGN Classification for the GOALS-ES Sample (continued)

ID (1)	X-Ray (2)	Optical (3)	MIR (4)	Radio (5)	Reference(X-ray/Optical/MIR/Radio) (6)	Adopted (7)

Note — (1): Identifier for each IRAS system matched with Table 2.1. (2): Whether any AGN has been detected in the X-ray (i.e. ultra-hard X-ray detection, hardness ratio, Fe line detection) where Y=Yes, N=No, M=Maybe (i.e. analysis is unable to identify origin of X-ray emission). (3) Whether AGN has been detected in the system at optical wavelengths via optical line ratios (i.e. BPT diagram). We consider "LINER" to be potentially hosting AGN (i.e. classified as "M). (4): Whether any AGN has been detected via Mid-IR diagnostics (i.e. 6.2 μm PAH equivalent width, 15 - 30μm spectral slope, [Ne V] 14.3 μm line detection). (5) Whether AGN has been detected in the radio. For (2) - (5): If AGN classifications from multiple studies conducted at the same wavelength range disagree, the classification from individual studies is presented, separated by comma. (6): Coded references for AGN identification in the X-ray/Optical/Mid-IR/Radio. See end of the table caption for full references. (7): Adopted AGN classification in this study. If an AGN has been identified at least two different wavelength ranges, then we consider the system as an AGN host in this work (i.e. labeled as Y=Yes); if evidence for AGN is identified at only one wavelength range (Y or M), or if evidence is ambiguous at all wavelengths, then we consider the system as an potential AGN host (i.e. classified as M=Maybe); If no AGN evidence is currently identified at any wavelength ranges (i.e. classified as N=No). * indicates classification for the entire IRAS system instead of individual galaxy components.

References — PC: private communication, A06 (Armus et al., 2006), A09 (Alonso-Herrero et al., 2009), A12 (Alonso-Herrero et al., 2012), B86 (Barr, 1986), BK06 (Baan & Klöckner, 2006), C02 (Corbett et al., 2002),C03 (Corbett et al., 2003), C15 (Colina et al., 2015), C95 (Condon et al., 1995) D01 (Della Ceca et al., 2001), F15 (Falstad et al., 2015), F20 (Fluetsch et al., 2020), F21 (Falstad et al., 2021), G04 (Gallimore et al., 2004), G06 (Grimes et al., 2006), G09 (González-Martín et al., 2009), G17 (Gandhi et al., 2017), G20 (Garofali et al., 2020), G96 (Gallimore et al., 1996), H17 (Herrero-Illana et al., 2017), I09 (Iwasawa et al., 2009), I10 (Imanishi et al., 2010), I11 (Iwasawa et al., 2011), I13 (Iono et al., 2013), I18 (Inami et al., 2018), K13 (Koss et al., 2013), K17 (Kharb et al., 2017), M03 (Momjian et al., 2003a), M15 (Medling et al., 2015), P10 (Petric et al., 2011), P15 (Pereira-Santaella et al., 2015), P20 (Privon et al., 2020), R15 (Rich et al., 2015), R17 (Ricci et al., 2017), R21 (Ricci et al., 2021), R93 (Rush et al., 1993), S13 (Stierwalt et al., 2013), T01 (Turner et al., 2001), T13 (Toba et al., 2013), T18 (Torres-Albà et al., 2018), V08 (Vega et al., 2008), V14 (Varenius et al., 2014), V15 (Vardoulaki et al., 2015), V95 (Veilleux et al., 1995), W98 (Wu et al., 1998), Y10 (Yuan et al., 2010), Y13 (Yamada et al., 2013).

Table 4.4: Measured and derived quantities for BM17 regions

Region (1)	Type (2)	RA (°) (3)	Dec (°) (4)	log R$_e$ (pc) (5)	S_{33} (mJy) (6)	log L_{33} (erg s^{-1} Hz^{-1}) (7)	log $\Sigma_{L_{33}}$ (erg s^{-1} Hz^{-1} kpc^{-2}) (8)
IRASF08572+3915_n1	AGN	135.105726	39.065042	2.40±0.01	2.08±0.04	29.24±0.01	29.94±0.01
UGC04881_n1	AGN/SB	138.981308	44.332764	2.28±0.01	1.39±0.03	28.72±0.01	29.65±0.02
UGC05101_n1	AGN	143.964993	61.35325	2.59±0.01	10.4±0.12	29.59±0.01	29.92±0.01
MCG+07-23-019_n1	AGN/SB	165.974877	40.849986	2.29±0.01	3.95±0.09	29.07±0.01	29.99±0.03
NGC3690_e1	SF	172.127739	58.563694	1.72±0.03	0.72±0.08	27.35±0.05	29.42±0.06
NGC3690_n1	AGN	172.129125	58.561333	1.91±0.01	6.82±0.1	28.33±0.01	30.01±0.02
NGC3690_e2	SF	172.130562	58.563889	1.88±0.01	2.41±0.04	27.88±0.01	29.62±0.01
NGC3690_n2	AGN	172.140122	58.562958	2.13±0.01	36.54±0.32	29.06±0.01	30.31±0.01
UGC08058_n1	AGN	194.059319	56.873681	2.54±0.01	74.7±1.07	30.52±0.01	30.94±0.01
VV250A_n1	AGN/SB	198.895668	62.124661	2.39±0.04	3.59±0.63	28.93±0.08	29.65±0.09
UGC08387_n1	SF	200.147075	34.139639	1.32±0.01	0.26±0.01	27.57±0.02	30.42±0.03
UGC08387_n2	AGN	200.147159	34.139542	1.63±0.01	5.69±0.06	28.9±0.01	31.15±0.01
UGC08387_n3	SF	200.147216	34.139494	1.25±0.03	0.14±0.02	27.31±0.06	30.32±0.06
UGC08387_n4	SF	200.147307	34.139381	1.57±0.01	0.96±0.03	28.13±0.01	30.49±0.02
UGC08696_n1	AGN	206.175541	55.887083	2.49±0.01	12.32±0.13	29.63±0.01	30.15±0.01
UGC08696_n2	SF	206.175739	55.886889	2.10±0.01	0.58±0.02	28.31±0.01	29.60±0.02
VV705_n1	AGN	229.525484	42.745851	1.73±0.01	0.91±0.02	28.57±0.01	30.60±0.02
VV705_n2	AGN/SB	229.526365	42.743917	1.56±0.01	0.35±0.01	28.15±0.01	30.54±0.02
IRASF15250+3608_n1	AGN/SB	231.747596	35.97707	1.91±0.01	3.78±0.04	29.46±0.01	31.14±0.01
UGC09913_n1	AGN/SB	233.738441	23.503215	1.81±0.12	20.8±4.83	29.29±0.10	31.17±0.24
UGC09913_n2	AGN/SB	233.738729	23.503168	1.60±0.04	9.94±0.77	28.97±0.03	31.26±0.08
IRAS21101+5810_n1	AGN/SB	317.872035	58.385519	1.75±0.01	1.06±0.02	28.58±0.01	30.58±0.01
IRASF23365+3604_n1	AGN/SB	354.755258	36.352366	1.93±0.01	0.98±0.04	28.99±0.02	30.63±0.02

NOTE — (1) Region identifier including galaxy name, with "n" and "e" indicating region location: "n" - within the MIR galaxy core measured by Díaz-Santos et al. (2010), "e" - extra-nuclear (outside MIR galaxy core). (2) Region type indicating the most likely source for the detected radio emission, classified following Section 4.4.1. (3) & (4) J2000 coordinates of the emission peak of the region. (5) Region effective radius. (6) 33 GHz flux density. (7) 33 GHz spectral luminosity calculated from column (6). (8) 33 GHz spectral luminosity surface density, calculated from (5) and (7).

Table 4.5: Measured and derived quantities for SFRS star-forming regions

Region (1)	RA (°) (2)	Dec (°) (3)	log R_e (pc) (4)	S_{15} (mJy) (5)	S_{33} (mJy) (6)	α_{15-33} (7)	$f_{\rm th}$ (%) (8)	log SFR ($M_\odot$ yr^{-1}) (9)	log $\Sigma_{\rm SFR}$ ($M_\odot$ yr^{-1} kpc^{-2}) (10)	log SFR$_{\rm th}$ ($M_\odot$ yr^{-1}) (11)	log $\Sigma_{\rm SFR_{th}}$ ($M_\odot$ yr^{-1} kpc^{-2}) (12)
NGC0337_e4	14.95841	-7.57622	2.25±0.01	0.34±0.04	0.28±0.04	-0.26±0.23	83±17	-1.27±0.06	-0.26±0.06	-1.17±0.14	-0.16±0.14
NGC0337_e1	14.96135	-7.58297	2.52±0.04	1.66±0.17	1.24±0.13	-0.37±0.19	70±23	-0.62±0.05	-0.16±0.09	-0.6±0.15	-0.13±0.17
NGC0337_e3	14.96622	-7.57672	< 2.06	0.09±0.01	0.08±0.02	-0.07±0.43	100	-1.63±0.20	> -0.25	-1.63±0.2	> -0.25
NGC0337_e2	14.96757	-7.57772	2.15±0.02	0.11±0.02	0.14±0.03	0.30±0.32	100	-1.40±0.13	-0.20±0.13	-1.4±0.13	-0.20±0.13
NGC0628_e1	24.14878	15.83535	< 1.53	0.07±0.01	0.07±0.02	-0.03±0.41	100	-2.56±0.19	> -0.13	-2.56±0.19	> -0.13
NGC0628_e1	24.15686	15.75200	1.63±0.01	0.16±0.02	0.16±0.03	-0.02±0.27	100	-2.19±0.13	0.06±0.13	-2.19±0.13	0.06±0.13
NGC1097_e5	41.57669	-30.27344	< 2.16	0.91±0.04	0.70±0.05	-0.32±0.24	76±24	-1.14±0.03	> 0.04	-1.07±0.16	> 0.10
NGC1097_e2	41.57698	-30.27661	2.35±0.02	2.60±0.26	1.97±0.22	-0.35±0.19	73±23	-0.69±0.05	0.11±0.06	-0.65±0.14	0.15±0.15
NGC1097_e1	41.57891	-30.27736	< 2.16	0.82±0.05	0.72±0.06	-0.17±0.24	93±7	-1.13±0.04	> 0.05	-0.98±0.12	> 0.20
NGC1097_e6	41.57949	-30.27228	2.29±0.02	1.81±0.18	1.19±0.15	-0.53±0.2	50±28	-0.91±0.05	0.02±0.07	-1.04±0.25	-0.11±0.25
NGC1097_e3	41.58142	-30.27603	2.41±0.01	3.53±0.36	2.46±0.27	-0.46±0.19	59±25	-0.59±0.05	0.09±0.06	-0.64±0.19	0.04±0.19
IC342_e1	56.69650	68.09453	1.19±0.08	0.26±0.03	0.25±0.05	-0.02±0.28	100	-2.67±0.14	0.45±0.21	-2.67±0.14	0.45±0.21
IC342_n2	56.69918	68.09611	1.69±0.01	15.8±1.58	12.3±1.23	-0.32±0.18	76±21	-1.17±0.04	0.96±0.05	-1.11±0.13	1.02±0.13
IC342_n3	56.70253	68.09544	1.21±0.03	1.10±0.11	0.84±0.09	-0.35±0.19	73±22	-2.33±0.05	0.76±0.08	-2.29±0.14	0.80±0.16
IC342_n4	56.70432	68.09611	1.36±0.03	2.44±0.24	1.99±0.20	-0.26±0.18	84±16	-1.96±0.04	0.82±0.08	-1.86±0.11	0.92±0.13
IC342_n5	56.70499	68.09719	1.23±0.04	0.97±0.10	0.85±0.09	-0.17±0.19	93±7	-2.33±0.05	0.71±0.09	-2.18±0.1	0.86±0.13
NGC1482_e2	58.66209	-20.50219	< 2.12	2.83±0.10	2.00±0.08	-0.44±0.19	62±24	-0.28±0.02	> 0.98	-0.31±0.17	> 0.95
NGC1482_e1	58.66280	-20.50236	< 2.12	2.79±0.13	2.03±0.11	-0.40±0.19	67±23	-0.27±0.02	> 0.99	-0.27±0.15	> 0.99
NGC2403_e1	114.11956	65.56339	< 1.7	0.53±0.06	0.54±0.06	0.03±0.21	100	-2.36±0.09	> -0.26	-2.36±0.09	> -0.26
NGC2403_e2	114.17505	65.61433	1.37±0.01	0.23±0.03	0.18±0.02	-0.30±0.23	79±21	-3.01±0.06	-0.25±0.06	-2.94±0.15	-0.17±0.16
NGC2403_e3	114.18999	65.61717	1.69±0.01	1.00±0.11	0.97±0.10	-0.04±0.19	100	-2.11±0.09	0.01±0.09	-2.11±0.09	0.01±0.09
NGC2403_e1	114.20492	65.61442	1.49±0.01	0.36±0.04	0.32±0.04	-0.15±0.21	95±5	-2.77±0.05	-0.25±0.06	-2.61±0.11	-0.09±0.11
NGC2403_e2	114.21716	65.61344	1.48±0.02	0.38±0.04	0.36±0.04	-0.05±0.21	100	-2.54±0.1	0.01±0.11	-2.54±0.1	0.01±0.11
NGC2403_e2	114.27855	65.61075	1.61±0.01	2.15±0.22	2.07±0.21	-0.04±0.18	100	-1.78±0.09	0.5±0.09	-1.78±0.09	0.50±0.09
NGC2403_e1	114.32559	65.56303	1.66±0.03	0.48±0.06	0.53±0.06	0.13±0.21	100	-2.37±0.09	-0.19±0.11	-2.37±0.09	-0.19±0.11
NGC2798_e1	139.34511	42.00036	< 2.61	0.07±0.01	0.04±0.01	-0.65±0.42	32±64	-1.82±0.12	> -1.53	-2.13±0.87	> -1.85
NGC2976_e2	146.77163	67.93094	1.58±0.01	0.42±0.05	0.42±0.06	-0.02±0.22	100	-2.39±0.11	-0.05±0.11	-2.39±0.11	-0.05±0.11
NGC2976_e3	146.78139	67.93186	1.82±0.01	1.85±0.19	1.61±0.17	-0.17±0.19	93±7	-1.98±0.05	-0.12±0.05	-1.84±0.1	0.02±0.11
NGC2976_e1	146.78272	67.93011	1.35±0.04	0.11±0.02	0.10±0.02	-0.14±0.36	96±4	-3.19±0.1	-0.38±0.13	-3.03±0.19	-0.22±0.21
NGC2976_e2	146.84798	67.89875	1.49±0.02	0.30±0.04	0.29±0.04	-0.04±0.24	100	-2.54±0.12	-0.03±0.13	-2.54±0.12	-0.03±0.13
NGC2976_e1	146.85152	67.89858	1.51±0.03	0.34±0.04	0.29±0.04	-0.20±0.25	90±10	-2.73±0.07	-0.24±0.09	-2.59±0.14	-0.11±0.15
NGC3049_n1	148.70650	9.27114	< 2.37	1.28±0.13	0.96±0.10	-0.37±0.19	71±23	-0.74±0.05	> 0.03	-0.71±0.15	> 0.06
NGC3190_e1	154.51795	21.82553	2.36±0.01	2.19±0.22	1.94±0.20	-0.15±0.18	95±5	-0.43±0.04	0.36±0.05	-0.28±0.1	0.51±0.10
NGC3184_n1	154.57036	41.42425	1.96±0.01	0.17±0.02	0.14±0.02	-0.23±0.27	87±13	-2.01±0.07	-0.42±0.07	-1.89±0.16	-0.30±0.16
NGC3198_e1	154.97923	45.54981	1.82±0.02	0.19±0.02	0.08±0.02	-1.03±0.30	14±39	-1.97±0.09	-0.11±0.10	-2.76±1.26	-0.90±1.26
IC2574_e2	157.18191	68.47422	1.61±0.02	0.18±0.03	0.31±0.05	0.72±0.28	100	-2.46±0.09	-0.18±0.10	-2.46±0.09	-0.18±0.10
IC2574_n1	157.20167	68.46764	1.57±0.01	0.31±0.04	0.32±0.04	0.05±0.23	100	-2.44±0.10	-0.08±0.10	-2.44±0.1	-0.08±0.10
NGC3351_e1	160.99024	11.70189	2.22±0.02	2.17±0.22	1.60±0.17	-0.39±0.19	68±23	-1.14±0.05	-0.08±0.06	-1.13±0.15	-0.07±0.16
NGC3351_n3	160.99066	11.70539	2.07±0.01	1.56±0.16	1.11±0.12	-0.43±0.19	63±24	-1.30±0.05	0.06±0.05	-1.32±0.17	0.04±0.17
NGC3351_e2	160.99186	11.70464	1.76±0.05	0.31±0.04	0.19±0.03	-0.59±0.23	41±33	-2.06±0.06	-0.08±0.12	-2.27±0.35	-0.29±0.37
NGC3627_e1	170.06784	12.96367	< 2.23	1.94±0.20	1.65±0.17	-0.21±0.19	89±11	-1.13±0.05	> -0.07	-1±0.11	> 0.05
NGC3627_e1	170.06826	12.97881	2.38±0.01	6.43±0.65	5.11±0.52	-0.29±0.18	80±20	-0.63±0.04	0.1±0.05	-0.55±0.12	0.18±0.12
NGC3773_n1	174.55459	12.11242	2.26±0.03	0.67±0.08	0.60±0.07	-0.14±0.21	96±4	-1.32±0.05	-0.33±0.08	-1.16±0.11	-0.17±0.12
NGC4254_e1	184.69229	14.40531	1.99±0.01	0.06±0.02	0.10±0.02	0.64±0.43	100	-1.79±0.12	-0.27±0.12	-1.79±0.12	-0.27±0.12
NGC4321_e5	185.72693	15.82258	1.90±0.06	0.18±0.02	0.11±0.02	-0.60±0.3	41±44	-1.93±0.09	-0.22±0.14	-2.14±0.48	-0.44±0.49
NGC4321_e1	185.72762	15.82050	< 1.85	0.06±0.01	0.06±0.01	0.08±0.52	100	-1.99±0.2	> -0.20	-1.99±0.2	> -0.20
NGC4321_e2	185.73048	15.82108	2.07±0.03	0.39±0.04	0.32±0.04	-0.26±0.22	84±16	-1.47±0.06	-0.11±0.08	-1.37±0.14	-0.01±0.15
NGC4321_e6	185.73057	15.82317	1.84±0.05	0.13±0.02	0.10±0.02	-0.40±0.28	67±33	-1.99±0.08	-0.16±0.13	-1.98±0.23	-0.15±0.26
NGC4321_e4	185.73074	15.82242	1.93±0.05	0.24±0.03	0.17±0.02	-0.45±0.24	61±31	-1.75±0.06	-0.10±0.11	-1.79±0.23	-0.14±0.25
NGC4536_e2	188.61225	2.18881	2.16±0.02	5.33±0.53	3.47±0.35	-0.54±0.18	48±25	-0.42±0.04	0.76±0.06	-0.56±0.23	0.62±0.23
NGC4536_e1	188.61375	2.18772	2.04±0.04	2.66±0.27	1.76±0.18	-0.52±0.18	51±25	-0.72±0.04	0.70±0.09	-0.83±0.21	0.58±0.23
NGC4559_e3	188.98410	27.96125	< 1.61	0.02±0.01	0.04±0.01	0.63±0.97	100	-2.82±0.24	> -0.54	-2.82±0.24	> -0.54

Table 4.5 continued

Table 4.5: Measured and derived quantities for SFRS star-forming regions (continued)

Region (1)	RA (°) (2)	Dec (°) (3)	log R_e (pc) (4)	S_{15} (mJy) (5)	S_{33} (mJy) (6)	α_{15-33} (7)	f_{th} (%) (8)	log SFR ($M_\odot$ yr^{-1}) (9)	log Σ_{SFR} ($M_\odot$ yr^{-1} kpc^{-2}) (10)	log SFR_{th} ($M_\odot$ yr^{-1}) (11)	log $\Sigma_{SFR_{th}}$ ($M_\odot$ yr^{-1} kpc^{-2}) (12)
NGC4559_e2	188.99353	27.95775	1.62±0.02	0.04±0.01	0.05±0.01	0.38±0.55	100	-2.7±0.18	-0.44±0.19	-2.7±0.18	-0.44±0.19
NGC4631_e7	190.51391	32.53819	< 1.60	0.24±0.02	0.24±0.02	0.01±0.22	100	-1.96±0.09	> 0.35	-1.96±0.09	> 0.35
NGC4631_e2	190.51470	32.53703	< 1.60	0.08±0.01	0.05±0.01	-0.60±0.54	41±59	-2.82±0.07	> -0.52	-3.04±0.84	-0.73±0.84
NGC4631_e5	190.51490	32.53786	1.71±0.02	0.80±0.08	0.61±0.06	-0.34±0.19	75±22	-1.74±0.05	0.34±0.06	-1.69±0.14	0.39±0.14
NGC4631_e3	190.51747	32.53736	1.65±0.03	0.14±0.02	0.11±0.02	-0.36±0.29	72±28	-2.49±0.07	-0.29±0.1	-2.45±0.22	-0.26±0.23
NGC4631_e8	190.51776	32.54036	2.19±0.01	2.88±0.30	2.70±0.28	-0.08±0.18	100	-0.91±0.09	0.20±0.09	-0.91±0.09	0.2±0.09
NGC4631_e4	190.52103	32.53736	< 1.60	0.08±0.01	0.06±0.01	-0.36±0.51	72±28	-2.76±0.09	> -0.45	-2.72±0.38	> -0.41
NGC4631_e3	190.59043	32.54675	< 1.59	0.02±0.01	0.04±0.01	0.58±0.79	100	-2.75±0.21	> -0.43	-2.75±0.21	> -0.43
NGC4631_e1	190.59132	32.54567	2.03±0.05	0.44±0.05	0.52±0.06	0.21±0.21	100	-1.63±0.09	-0.20±0.13	-1.63±0.09	-0.2±0.13
NGC4631_e2	190.59478	32.54625	1.7±0.1	0.09±0.02	0.12±0.02	0.37±0.35	100	-2.26±0.12	-0.16±0.24	-2.26±0.12	-0.16±0.24
NGC4736_e4	192.73461	41.12214	< 1.44	0.05±0.02	0.07±0.01	0.32±0.70	100	-2.96±0.23	> -0.33	-2.96±0.23	> -0.33
NGC4736_e3	192.73472	41.12056	1.68±0.01	0.38±0.05	0.33±0.04	-0.17±0.23	93±7	-2.43±0.05	-0.28±0.06	-2.28±0.13	-0.14±0.13
NGC4736_e2	192.73605	41.11797	1.81±0.02	0.87±0.10	0.56±0.07	-0.55±0.21	47±29	-2.20±0.05	-0.32±0.06	-2.34±0.27	-0.47±0.27
NGC4736_e1	192.73693	41.11314	1.68±0.01	0.54±0.06	0.34±0.04	-0.57±0.22	44±31	-2.42±0.06	-0.28±0.06	-2.59±0.31	-0.46±0.31
NGC4826_e8	194.17897	21.68550	< 1.42	0.06±0.01	0.05±0.01	-0.20±0.51	90±10	-3.14±0.09	> -0.49	-3.01±0.28	> -0.36
NGC4826_e5	194.17897	21.68342	< 1.42	0.06±0.01	0.05±0.01	-0.34±0.51	75±25	-3.16±0.08	> -0.50	-3.1±0.36	> -0.45
NGC4826_e1	194.17960	21.68183	< 1.42	0.08±0.01	0.06±0.01	-0.45±0.42	61±39	-3.08±0.09	> -0.42	-3.12±0.4	> -0.46
NGC4826_e7	194.17996	21.68500	< 1.42	0.08±0.01	0.05±0.01	-0.62±0.46	37±63	-3.15±0.08	> -0.49	-3.4±0.8	> -0.74
NGC4826_e4	194.18085	21.68358	1.6±0.02	0.60±0.06	0.43±0.05	-0.42±0.19	64±24	-2.21±0.05	0.09±0.06	-2.23±0.17	0.08±0.17
NGC4826_n6	194.18184	21.68433	1.58±0.02	0.42±0.05	0.34±0.04	-0.27±0.20	82±18	-2.31±0.05	0.04±0.07	-2.21±0.13	0.13±0.13
NGC4826_e2	194.18453	21.68208	1.61±0.01	0.12±0.02	0.16±0.02	0.39±0.31	100	-2.46±0.11	-0.18±0.11	-2.46±0.11	-0.18±0.11
NGC5194_e1	202.41397	47.14339	< 1.58	0.02±0.01	0.04±0.01	0.94±1.13	100	-2.80±0.23	> -0.47	-2.8±0.23	> -0.47
NGC5194_e2	202.41397	47.14464	1.91±0.01	0.20±0.03	0.23±0.03	0.13±0.25	100	-1.99±0.10	-0.3±0.11	-1.99±0.1	-0.3±0.11
NGC5194_e3	202.43203	47.16686	< 1.56	0.03±0.01	0.05±0.01	0.74±0.76	100	-2.69±0.18	> -0.31	-2.69±0.18	> -0.31
NGC5194_e2	202.43559	47.16644	< 1.56	0.02±0.01	0.04±0.01	0.70±0.89	100	-2.77±0.21	> -0.39	-2.77±0.21	> -0.39
NGC5194_e1	202.43816	47.16578	1.85±0.01	0.23±0.03	0.29±0.03	0.30±0.23	100	-1.89±0.09	-0.09±0.09	-1.89±0.09	-0.09±0.09
NGC5194_e3	202.44604	47.22797	1.67±0.01	0.01±0.01	0.04±0.01	1.81±2.01	100	-2.78±0.21	-0.62±0.22	-2.78±0.21	-0.62±0.22
NGC5194_e1	202.44813	47.22364	1.62±0.02	0.01±0.01	0.01±0.01	2.04±4.47	100	-3.30±0.39	-1.04±0.39	-3.3±0.39	-1.04±0.39
NGC5194_e7	202.45647	47.23331	1.68±0.01	0.01±0.01	0.02±0.01	1.19±1.84	100	-3.06±0.31	-0.91±0.31	-3.06±0.31	-0.91±0.31
NGC5194_e2	202.45647	47.22439	< 1.56	0.01±0.02	0.04±0.01	1.71±2.19	100	-2.73±0.25	> -0.35	-2.73±0.25	> -0.35
NGC5194_e1	202.45806	47.19194	1.70±0.01	0.19±0.02	0.15±0.02	-0.28±0.24	82±18	-2.35±0.06	-0.25±0.07	-2.26±0.16	-0.16±0.16
NGC5194_e8	202.45928	47.19761	< 1.57	0.08±0.01	0.05±0.01	-0.50±0.44	54±46	-2.81±0.08	> -0.45	-2.89±0.48	> -0.54
NGC5194_e5	202.46027	47.22914	1.65±0.02	0.02±0.01	0.04±0.01	0.77±0.90	100	-2.75±0.22	-0.54±0.22	-2.75±0.22	-0.54±0.22
NGC5194_e6	202.46064	47.23222	< 1.56	0.02±0.02	0.03±0.01	0.80±1.43	100	-2.84±0.34	> -0.46	-2.84±0.34	> -0.46
NGC5194_e11	202.46112	47.19886	1.61±0.02	0.10±0.02	0.08±0.01	-0.29±0.33	80±20	-2.64±0.08	-0.36±0.09	-2.56±0.22	-0.27±0.22
NGC5194_e4	202.46224	47.22881	1.54±0.02	0.03±0.02	0.08±0.01	1.32±0.88	100	-2.43±0.14	0.00±0.15	-2.43±0.14	0±0.15
NGC5194_e12	202.46468	47.20028	1.65±0.03	0.41±0.05	0.25±0.03	-0.64±0.21	34±32	-2.13±0.05	0.08±0.08	-2.42±0.41	-0.21±0.41
NGC5194_e6	202.46811	47.19678	< 1.57	0.11±0.01	0.05±0.01	-0.99±0.41	14±55	-2.72±0.09	> -0.36	-3.49±1.72	> -1.13
NGC5194_e10	202.46836	47.19878	1.63±0.07	0.13±0.02	0.08±0.01	-0.68±0.28	28±44	-2.63±0.08	-0.38±0.16	-3.01±0.68	-0.76±0.70
NGC5194_e9	202.46909	47.19819	1.66±0.05	0.19±0.02	0.10±0.02	-0.74±0.26	18±42	-2.5±0.07	-0.31±0.13	-3.06±0.99	-0.87±1.00
NGC5194_e7	202.46983	47.19769	1.63±0.08	0.22±0.03	0.11±0.02	-0.88±0.26	15±37	-2.43±0.07	-0.18±0.17	-3.13±1.07	-0.88±1.08
NGC5194_e2	202.47952	47.19294	< 1.57	0.06±0.01	0.05±0.01	-0.12±0.50	98±2	-2.82±0.09	> -0.46	-2.64±0.24	> -0.29
NGC5194_e5	202.48258	47.19578	1.91±0.01	0.38±0.05	0.39±0.05	0.06±0.22	100	-1.75±0.1	-0.07±0.1	-1.75±0.1	-0.07±0.1
NGC5194_e1	202.49846	47.23328	1.55±0.03	0.04±0.01	0.07±0.02	0.77±0.49	100	-2.47±0.14	-0.07±0.16	-2.47±0.14	-0.07±0.16
NGC5194_e1	202.49934	47.18683	1.67±0.01	0.15±0.02	0.17±0.03	0.14±0.27	100	-2.11±0.12	0.05±0.12	-2.11±0.12	0.05±0.12
NGC5194_e1	202.50630	47.21428	1.81±0.01	0.43±0.05	0.37±0.04	-0.21±0.21	89±11	-1.96±0.05	-0.07±0.06	-1.83±0.12	0.06±0.12
NGC5194_e1	202.50993	47.16361	1.71±0.01	0.15±0.02	0.18±0.03	0.20±0.27	100	-2.09±0.11	0.00±0.12	-2.09±0.11	0.00±0.12
TOL89_n1	210.33377	-33.06967	< 2.35	1.44±0.15	1.47±0.16	0.03±0.19	100	-1.17±0.09	> -0.37	-1.17±0.09	> -0.37
M101_e6	210.61708	54.27697	1.55±0.11	0.06±0.02	0.10±0.02	0.57±0.57	100	-2.48±0.17	-0.08±0.27	-2.48±0.17	-0.08±0.27
M101_e5	210.61765	54.27397	1.9±0.01	0.40±0.05	0.59±0.06	0.50±0.22	100	-1.69±0.08	0.01±0.08	-1.69±0.08	0.01±0.08
M101_e4	210.62293	54.27214	< 1.59	0.05±0.02	0.06±0.01	0.24±0.73	100	-2.71±0.25	> -0.39	-2.71±0.25	> -0.39
M101_e3	210.62351	54.27097	1.92±0.01	0.59±0.07	0.66±0.07	0.13±0.21	100	-1.64±0.09	0.02±0.09	-1.64±0.09	0.02±0.09

Table 4.5 continued

Table 4.5: Measured and derived quantities for SFRS star-forming regions (continued)

Region (1)	RA (°) (2)	Dec (°) (3)	log R_e (pc) (4)	S_{15} (mJy) (5)	S_{33} (mJy) (6)	α_{15-33} (7)	f_{th} (%) (8)	log SFR ($M_\odot$ yr^{-1}) (9)	log Σ_{SFR} ($M_\odot$ yr^{-1} kpc^{-2}) (10)	log SFR_{th} ($M_\odot$ yr^{-1}) (11)	log $\Sigma_{SFR_{th}}$ ($M_\odot$ yr^{-1} kpc^{-2}) (12)
M101_e2	210.62750	54.26939	1.87±0.01	0.40±0.05	0.44±0.05	0.11±0.22	100	-1.81±0.09	-0.05±0.1	-1.81±0.09	-0.05±0.1
M101_e1	210.62764	54.26697	1.75±0.01	0.15±0.03	0.21±0.03	0.44±0.32	100	-2.14±0.11	-0.14±0.11	-2.14±0.11	-0.14±0.11
M101_e1	210.75487	54.24147	< 2.10	1.23±0.14	1.53±0.16	0.27±0.19	100	-1.27±0.08	> 0.02	-1.27±0.08	> 0.02
M101_n1	210.80179	54.34850	< 1.52	0.03±0.01	0.05±0.01	0.72±0.75	100	-2.78±0.18	> -0.32	-2.78±0.18	> -0.32
M101_e1	210.91608	54.31569	2.02±0.01	8.37±0.84	6.95±0.70	-0.24±0.18	86±14	-0.79±0.04	0.66±0.05	-0.68±0.11	0.78±0.11
M101_e1	210.97111	54.36558	< 1.52	0.04±0.01	0.06±0.01	0.62±0.63	100	-2.69±0.17	> -0.22	-2.69±0.17	> -0.22
M101_e2	210.97139	54.36850	1.78±0.01	0.17±0.03	0.31±0.04	0.78±0.27	100	-1.97±0.08	-0.03±0.08	-1.97±0.08	-0.03±0.08
M101_e3	210.97497	54.36983	1.77±0.01	0.17±0.03	0.29±0.04	0.67±0.26	100	-1.99±0.08	-0.03±0.08	-1.99±0.08	-0.03±0.08
NGC5713_e5	220.04292	-0.28892	2.26±0.05	0.23±0.03	0.19±0.03	-0.22±0.25	87±13	-1.34±0.06	-0.36±0.12	-1.22±0.15	-0.24±0.18
NGC5713_e3	220.04325	-0.29125	< 2.16	0.09±0.02	0.07±0.01	-0.34±0.47	74±26	-1.78±0.09	> -0.60	-1.73±0.34	> -0.56
NGC5713_e1	220.04400	-0.29675	< 2.16	0.08±0.01	0.06±0.01	-0.29±0.53	80±20	-1.83±0.08	> -0.66	-1.75±0.34	> -0.58
NGC5713_e8	220.04475	-0.28883	2.23±0.02	0.70±0.07	0.59±0.06	-0.20±0.19	90±10	-0.85±0.05	0.2±0.06	-0.72±0.11	0.33±0.11
NGC5713_e2	220.04550	-0.29333	2.44±0.01	0.51±0.06	0.36±0.05	-0.44±0.22	62±29	-1.07±0.06	-0.45±0.06	-1.1±0.21	-0.48±0.21
NGC5713_e9	220.04608	-0.28867	2.19±0.03	0.70±0.07	0.53±0.05	-0.37±0.19	71±23	-0.91±0.05	0.22±0.08	-0.88±0.15	0.25±0.16
NGC5713_e7	220.04750	-0.28875	2.39±0.01	2.59±0.26	1.95±0.20	-0.36±0.18	71±22	-0.34±0.04	0.38±0.05	-0.3±0.14	0.42±0.14
NGC5713_e6	220.05150	-0.28900	< 2.16	0.06±0.01	0.08±0.01	0.32±0.56	100	-1.56±0.19	> -0.39	-1.56±0.19	> -0.39
NGC5713_e4	220.05267	-0.28867	2.35±0.03	0.27±0.04	0.24±0.03	-0.16±0.26	94±6	-1.25±0.06	-0.44±0.09	-1.1±0.14	-0.29±0.15
NGC6946_e2	308.58284	60.16850	< 1.99	1.30±0.13	1.48±0.15	0.16±0.18	100	-1.27±0.08	> 0.23	-1.27±0.08	> 0.23
NGC6946_e4	308.58921	60.17167	< 1.99	0.70±0.08	0.61±0.06	-0.18±0.19	92±8	-1.84±0.05	> -0.13	-1.69±0.1	> 0.01
NGC6946_e5	308.59457	60.17608	< 1.99	1.22±0.13	1.10±0.11	-0.13±0.19	97±3	-1.58±0.04	> -0.07	-1.42±0.09	> 0.1
NGC6946_e1	308.63450	60.17194	< 1.99	0.86±0.09	0.93±0.10	0.10±0.19	100	-1.48±0.08	> 0.07	-1.48±0.08	> 0.07
NGC6946_e1	308.66384	60.08131	1.78±0.01	0.11±0.02	0.14±0.02	0.28±0.32	100	-2.31±0.12	-0.36±0.13	-2.31±0.12	-0.36±0.13
NGC6946_e1	308.70777	60.21131	1.60±0.03	0.01±0.01	0.01±0.01	2.24±3.38	100	-3.31±0.29	-1.01±0.3	-3.31±0.29	-1.01±0.3
NGC6946_e2	308.71331	60.21172	< 1.62	0.05±0.01	0.06±0.01	0.10±0.50	100	-2.69±0.19	> -0.43	-2.69±0.19	> -0.43
NGC6946_e3	308.71767	60.21214	1.82±0.02	0.01±0.01	0.04±0.01	1.95±1.45	100	-2.82±0.16	-0.95±0.17	-2.82±0.16	-0.95±0.17
NGC6946_n1	308.71775	60.15397	< 2.23	19.4±1.94	12.7±1.27	-0.54±0.18	49±25	-0.52±0.04	> 0.52	-0.65±0.23	> 0.39
NGC6946_e2	308.77567	60.18233	1.58±0.05	0.11±0.02	0.11±0.02	0.02±0.28	100	-2.41±0.13	-0.07±0.16	-2.41±0.13	-0.07±0.16
NGC6946_e1	308.77936	60.17925	< 1.62	0.11±0.01	0.08±0.02	-0.37±0.40	70±30	-2.69±0.09	> -0.42	-2.67±0.31	> -0.4
NGC6946_e3	308.79619	60.14929	< 1.99	1.23±0.13	1.23±0.13	0.01±0.19	100	-1.35±0.09	> 0.16	-1.35±0.09	> 0.16
NGC6946_e1	308.80389	60.14729	1.85±0.01	0.46±0.05	0.46±0.05	-0.02±0.21	100	-1.78±0.10	0.02±0.1	-1.78±0.1	0.02±0.1
NGC6946_e2	308.80875	60.14771	< 1.62	0.06±0.01	0.07±0.01	0.07±0.51	100	-2.61±0.20	> -0.34	-2.61±0.2	> -0.34
NGC6946_e1	308.81984	60.18342	1.87±0.01	0.42±0.05	0.46±0.06						

NOTE — (1) Region identifier, with "n" and "e" indicating the location of the region within the galaxy: "n" – nuclear (within 250 pc of the galaxy center), "e" – extra-nuclear. (2) & (3) region coordinates. (4) Region effective radius. For regions with area smaller than the matched 15 – 33 GHz synthesized beam (i.e. unresolved), the effective radius of the synthesized beam is reported and marked as upper-limits ("<"). (5) 15 GHz flux density. (6) 33 GHz flux density. (7) 15 – 33 GHz spectral index. (8) Thermal fraction at 33 GHz, estimated from (6) using Equation 5.3. (9) Star formation rates derived from total 33 GHz continuum emission from (6) using Equation 5.4. (10) Star formation rate surface density. For unresolved regions, the reported values are lower-limits, indicated with ">". (11) Thermal-only star formation rate derived from 33 GHz flux in column (6) and 15 - 33 GHz spectral index from column (7), using Equation 5.5. (12) Thermal-only star formation rate surface density. For unresolved regions, the reported values are lower-limits, indicated with ">".

Chapter 5

Resolved Kpc-Scale 3-33 GHz SED and Radio-IR Correlation

5.1 Introduction

Luminous Infrared Galaxies (LIRGs; $10^{11} \leq L_{\rm IR}[8–1000\mu{\rm m}] < 10^{12} L_{\odot}$) and Ultra-luminous Infrared Galaxies (ULIRG; $L_{\rm IR}[8–1000\mu{\rm m}] \geq 10^{12} L_{\odot}$) are the most prolific star-forming galaxies in the local Universe, having the highest star formation rates (SFR) per stellar mass (Howell et al., 2010). From an cosmological perspective, U/LIRGs are also an important class of objects for understanding massive galaxy evolution, as they are the dominant contributors to the co-moving infrared (IR) luminosity density and star formation rate (SFR) density at $z \gtrsim 1$ (Chary & Elbaz, 2001; Le Floc'h et al., 2005; Murphy et al., 2011a; Magnelli et al., 2011, 2013; Gruppioni et al., 2013), when half of the stellar mass of the Universe was produced (Madau & Dickinson, 2014). Furthermore, detailed observations of local U/LIRGs reveal them to be interacting and merging gas-rich spirals (Armus et al., 1987; Sanders & Mirabel, 1996), which may represent an important starburst transition phase precedent to the formation of luminous quasars and massive elliptical galaxies (e.g. Di Matteo et al., 2005; Springel & Hernquist, 2005; Hopkins et al., 2006). Therefore, local U/LIRGs provide the ideal laboratories to conduct detailed investigation into the evolution process of massive galaxies and the extreme star-forming environments common at high-z.

One major obstacle in characterizing the properties of local U/LIRGs is the heavy extinction of UV/optical and even near-IR photons by the large amounts of dust generated by ongoing starburst activity. It is estimated that only $\sim 4\%$ of star formation in local U/LIRGs is unobscured (Howell et al., 2010), and the rest can only be accounted for by FIR observations that capture thermal emission from dust heated by massive stars. An alternative solution lies in the radio regime where the emission is largely unaffected by foreground dust extinction, and can be mapped at extremely high resolutions that are yet to be achieved in the FIR, using radio interferometers such as the Karl G. Jansky Very Large Array (VLA). Furthermore, radio continuum emission, like FIR emission, largely comes from massive stars (Condon, 1992): in ionized gas immediately surrounding young massive stars ($< 10\,\mathrm{Myr}$), free electrons scatter off ions and emit thermal free-free emission. In addition, as massive stars reach the supernovae stage, electrons are accelerated to high velocity and energy in the explosion, emitting synchrotron radiation. The connection of FIR and radio emission to star formation is empirically reflected in the tight correlation between radio continuum and FIR luminosities that has been widely observed among galaxies spanning four orders of magnitude in luminosity, including local U/LIRGs (e.g. de Jong et al., 1985; Helou et al., 1985; Condon & Broderick, 1991; Yun et al., 2001; Bell, 2003). This FIR-radio correlation (FRC) has allowed radio continuum emission to be used an extinction-free tracer of SFR.

Because the FRC operates on the basis that both radio continuum and FIR emission come from star formation, deviation from the FRC has been used as a diagnostic for AGN activity: excess radio emission from the AGN relative to FIR emission from star formation will bring galaxies that are dominated by AGN activity above the FRC (e.g. Condon & Broderick, 1991). However, it has been shown that galaxies hosting "radio-quiet"(RQ) AGN can still lie on the FRC among star-forming galaxies (Morić et al., 2010), but with their radio and IR emission both dominated by star formation, or even, AGN activity (Zakamska et al., 2016). This introduces complications for using radio continuum as SFR diagnostics. Meanwhile, most studies of the FRC utilize observations of the 1.49 GHz radio continuum, thanks to large-scale 1.49 GHz surveys such as NVSS (Condon et al., 1998) and FIRST (Becker et al., 1994) conducted with the VLA. However, the 1.49 GHz radio continuum of a star-forming galaxy is largely dominated by non-thermal synchrotron emission, which is a less direct tracer of star formation (Condon et al., 1990), as it is also governed by complex processes of the cosmic ray production and propagation, as well as local magnetic field strengths (e.g. Murphy, 2009; Lacki et al., 2010; Lacki & Thompson, 2010). Non-linearity of FRC have been reported in several studies on global scales (e.g. Bell, 2003; Molnár et al., 2021; Matthews et al., 2021), and variations on resolved scales have been observed widely in studies of nearby star-forming galaxies (e.g. Hughes et al., 2006; Murphy et al., 2006, 2008). These latter studies also demonstrate that the resolved FRC reflect the timescales on which ionizing photons heat the dust relative to those on which cosmic ray electrons escape their birth sites, which are closely related to the balance between thermal and non-thermal radio continuum emission.

In this study we present analysis of the spatially-resolved FRC and radio spectra of a representative sample of local U/LIRGs from the Great Observatories All-sky LIRG Survey (Armus et al., 2009), with the goal of investigating the kpc-scale variations of the ISM conditions in these extreme local starbursts that could shed light on the properties of more distant dusty star-forming galaxies, as well as the interpretation of the observed FRC at high$-z$ (e.g. Ivison et al., 2010; Murphy, 2009; Sargent et al., 2010b,a; Magnelli et al., 2015). Importantly, we utilize newly-acquired multi-frequency (3, 15, 33 GHz) VLA observations, complemented by multi-wavelength (24, 70, 100μm) Mid- and Far-IR ancillary observations with Spitzer (Mazzarella in prep.) and Herschel (Chu et al., 2017), which allow direct comparisons among thermal and non-thermal dominated radio emission, as well as IR emission from hot (MIR) and cold dust (FIR) components.

This paper is organized as the following: §5.2 describes the sample and the radio and IR observations used, as well as the relevant data reduction procedures; §5.3 describes the methods for aligning the radio and IR images and performing aperture photometry; §5.4 presents the resulted 3 – 33 GHz radio spectra and FRC characterized at different radio frequencies and IR wavelengths, as well as for the identified kpc-scale regions with different levels of AGN contribution. Lastly, §5.5 discusses the implication of our results and summarizes major conclusions. Throughout this work we adopt $H_0 = 70\,\mathrm{km/s/Mpc}$, $\Omega_{\mathrm{matter}} = 0.28$ and $\Omega_{\mathrm{vacuum}} = 0.72$ based on the five-year WMAP result (Hinshaw et al., 2009). These parameters are used with the 3-attractor model (Mould et al., 2000) to calculate the luminosity distances of the sample.

5.2 Observations & Data Reduction

5.2.1 Sample & VLA data

We use 3, 15 and 33 GHz continuum observations of 68 local U/LIRGs from the GOALS "Equatorial" VLA Survey (GOALS-ES), which is described in details in Chapter 2, where information on the sample, VLA observations and data reduction procedures can be found. To compare fairly with IR observations of these systems taken with Spitzer and Herschel, we used the A-configuration S-Band (3 GHz), and C-configuration Ku- (15 GHz) and Ka-Band (33 GHz) observations from GOALS-ES, which have native synthesized beam FWHM of $\sim 0''.6, 1''.5$ and $0''.6$ and with a largest angular scales of $\sim 10''$ (using conservative estimates based on the 5$^{\mathrm{th}}$ percentile of the uv distance)[1]. At the distances of these local U/LIRGs (~ 100 Mpc), these observations are probe radio emission down to ~ 1 kpc scales, but will likely miss most flux from diffuse emission beyond ~ 10 kpc.

5.2.2 IR observations

All galaxies observed with the GOALS-ES have ancillary MIR and FIR imaging from GOALS. In particular, we use the processed 24μm Spitzer/MIPS images from Mazzarella et al. (in prep) and 70 and 100μm Herschel/PACS images from Chu et al. (2017). Information on the relevant observations and data reduction are provided in the respective survey papers. We also converted the Spitzer images to units of Jy pixel^{-1} to be consistent with the Herschel images.

5.3 Analysis

5.3.1 Resolution-Matching & Image Alignment

To prepare for matched-aperture photometry and analysis, we first matched the resolution of all radio and IR images to a FWHM of $7''$, which is slightly larger the PSF of the 100μm Herschel images (6".8 Chu et al., 2017). For the VLA images from GOALS-ES, this is done using the Common Astronomy Software Applications (CASA; McMullin et al., 2007) with the task `imsmooth` by setting the target resolu-

[1] ALMA Cycle 4 technical handbook: https://almascience.nrao.edu/documents-and-tools/cycle4/alma-technical-handbook

tion to a Gaussian beam with the FWHM of both the major and minor axis at 7″. For the IR images, we utilized the kernel convolution IDL code and custom kernels provided by Aniano et al. (2011)[2], and convolved the Spitzer and Herschel images with respective custom kernels with FWHM of 7″.

Due to the different instrument properties, the resulted smoothed images do not always align with each other, which could bias the radio-IR comparison. To ensure that matched-aperture photometry can produce robust measurements, we also performed image registration and alignment on the radio and IR images for each U/LIRG system in the sample, using the Python package `image_registration`[3], which is a toolkit for registering images of astronomical images containing primarily extended flux (e.g., nebulae, radio and millimeter maps). We visually inspected the aligned images after each run to ensure that no mismatch between the images have occurred and the aligned emission across the different frequencies and wavelengths indeed come from the same emitting galaxy structures.

5.3.2 Region Identification & Aperture Photometry

To perform matched-aperture photometry for measuring the radio and IR emission of the various galactic structures observed in local U/LIRGs in the sample, we first used the Python package *Astrodendro* (Robitaille et al., 2019) to identify regions of significant radio emission in the smoothed 7" resolution VLA images for each system. Because the VLA observations have short integration times and have limited sensitivity, selecting regions using the radio observations ensures good detection in both radio and IR. Further, these radio observations also capture the most energetic activity in these systems, therefore the FRC derived from these radio regions would help evaluate whether and how the FRC changes under extreme physical conditions

[2]see https://www.astro.princeton.edu/ draine/Kernels.html
[3]https://github.com/keflavich/image_registration

when compared to those observed in nearby normal galaxies that are forming stars at slower rates.

Astrodendro identifies and categorizes structures in an image into `trunk`, `branch` and `leaf`, based on three input parameters: the minimum brightness required for a structure to be physically meaningful (`min_value`), the minimum number of pixels in a structure (`min_npix`), and the minimum brightness relative to the local background required for a structure to be considered independent (`min_delta`). Structures identified as `leaf` are of the highest hierarchical order, while `branch` and `trunk` are the surrounding relatively diffuse emission.

To ensure that we only identify physically meaningful structures, we ran *Astrodendro* on beam-matched 3, 15 and 33 GHz images of each system with `min_value`$= 5\sigma_{\rm rms}$ and `min_delta`$=1\sigma_{\rm rms}$ where $\sigma_{\rm rms}$ is the rms noise measured in an emission-free region of the smoothed image without primary beam correction. We follow Song et al. (2021) and set `min_npix` to be a quarter of the area of the synthesized beam, to avoid identifying noise spikes yet allowing detection of slightly unresolved regions. Despite that we detected diffuse emission that encompass `trunk`, `branch`, and `leaf` structures in several systems, we restrict region identification to only `leaf` structures as measurements of the `branch` and `trunk` structures likely miss significant amounts of flux due to the limited LAS of the radio observations ($\sim 10''$).

For each identified region, *Astrodendro* also calculates the region location, sizes (major and minor axis) and position angle assuming an elliptical morphology. In most cases, the same regions are identified across 3, 15 and 33 GHz, and we then used the information from *Astrodendro* to construct matched elliptical apertures for measuring the radio and IR flux of each identified region on beam-matched VLA, Spitzer and Herschel images of the same system. In cases where some regions are not uniformly identified across the different radio frequencies due to intrinsic faintness at a certain frequency, we generated apertures from all regions identified at each radio frequency to ensure to include regions with unusual 3 - 33 GHz spectral shapes. The aperture major and minor axis were set to be the FWTM (Full Width Tenth Maximum) of the ellipses calculated by *Astrodendro* with a minimum major and minor axis set to 7" and to 9.5" at maximum. This is to ensure that the apertures do not measure flux within the smoothed beam or beyond the LAS of the observations (10"). Once apertures are generated, we performed aperture photometry using the same apertures on all beam-matched and aligned radio and IR images of a given system in the sample using the Python package *photutils* (Bradley et al., 2022) to measure flux densities of the region at 3, 15, 33 GHz and 24μm, 70μm and 100μm in a common unit of Jy. Figure 5.1 shows two examples of the apertures generated via the process described above.

5.3.3 Radio Spectral Index and Spectral Fitting

The above measurements also allow us to characterize the radio spectra of the most energetic regions in local U/LIRGs in the sample, and to derive the relative contribution of thermal free-free to non-thermal emission at each radio frequency for a given region. For each region, we used two methods to characterize the observed 3 – 33 GHz spectrum:

First, we calculated the 3 – 15 GHz, 15 – 33 GHz and 3 – 33 GHz spectral indices ($\alpha_{3-15}, \alpha_{15-33}, \alpha_{3-33}$) based on the the measured 3, 15 and 33 GHz flux densities on $\sim$ 7" scales (see previous Section), defined as:

$$\alpha_{\nu_1-\nu_2} = \frac{\log S_{\nu_1} - \log S_{\nu_2}}{\log \nu_1 - \log \nu_2} \tag{5.1}$$

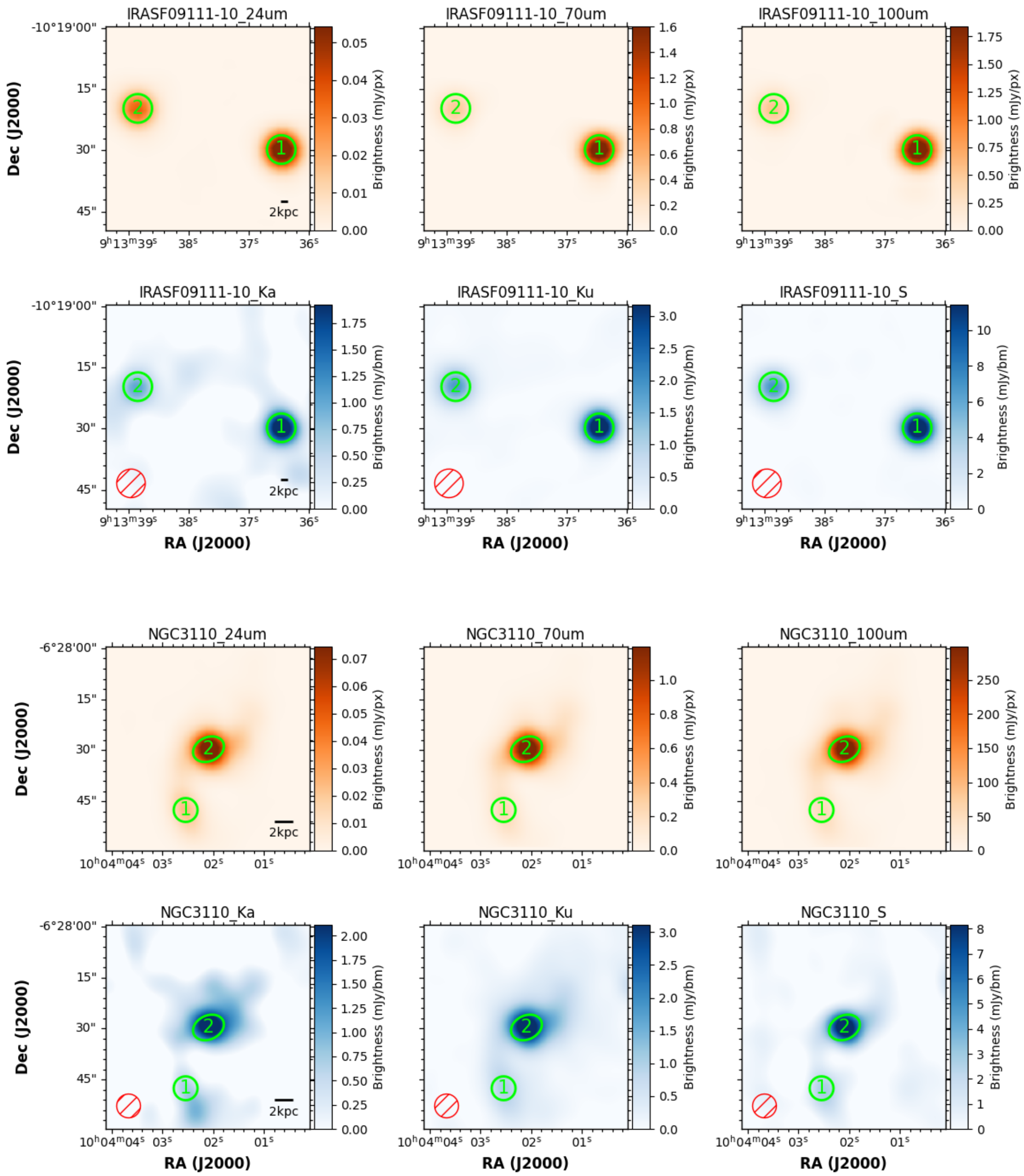

Figure 5.1: Examples of apertures generated from matched-resolution radio and IR images, for IRAS F09111-1007 (upper) and NGC 3110 (lower). For each system, the top row displays in orange the IR images from Spitzer (24μm) and Herschel, and the bottom row displays in blue the radio images from VLA (3, 15, 33 GHz). All images are convolved to a common Gaussian beam of 7$''$ (indicated with red hatched circles), set by the native resolution of the Herschel 100μm images (Chu et al., 2017). Apertures are labeled by increasing declinations.

where ν_1 and ν_2 are two different observing frequencies. Uncertainty of α is calculated via error propagation, accounting for uncertainties in flux density measurements.

Second, we directly fitted the measured flux densities at 3, 15, 33 GHz with a parametric function that represents the sum of two power-law components: the optically-thin thermal free-free and and non-thermal emission, defined as:

$$S_\nu = S_{\rm syn} + S_{\rm ff} = A\nu^{-0.85} + B\nu^{-0.1} \tag{5.2}$$

where $S_{\rm ff} \propto \nu^{-0.1}$ represents the optically-thin thermal free-free component, and $S_{\rm syn} \propto \nu^{-0.85}$ represents the non-thermal component, where we assume an non-thermal spectral index of -0.85, following resolved measurements in nearby galaxy NGC 6946 (Murphy et al., 2011b). We performed least square fitting accounting for uncertainty in the flux density measurements using the `optimize.curve_fit` function from *Scipy* (Virtanen et al., 2019), and the best-fitted parameters, A and B, hence providing a prescription for estimating the relative contribution of thermal and non-thermal component at any radio frequency for a given region.

Because our radio observations reach much higher native resolutions (FWHM $\sim 1''$) compared to the existing IR observations, we can analyze the resolved $3-33$ GHz radio spectral properties of compact radio-emitting regions at much smaller scales. To do this, for each system in the sample we also performed the region identification and matched-aperture photometry procedures, as described in the previous Section, on 3, 15 and 33 GHz images matched to a common largest circular beam of $\sim 2''$ (determined by the 15 GHz images which have the largest native synthesized beams). We then repeated the procedures above to calculate the spectral indices and performed spectral fitting using these new measurements made with smaller apertures (with a minimum size set to the FWTM of the common Gaussian beam shared by the

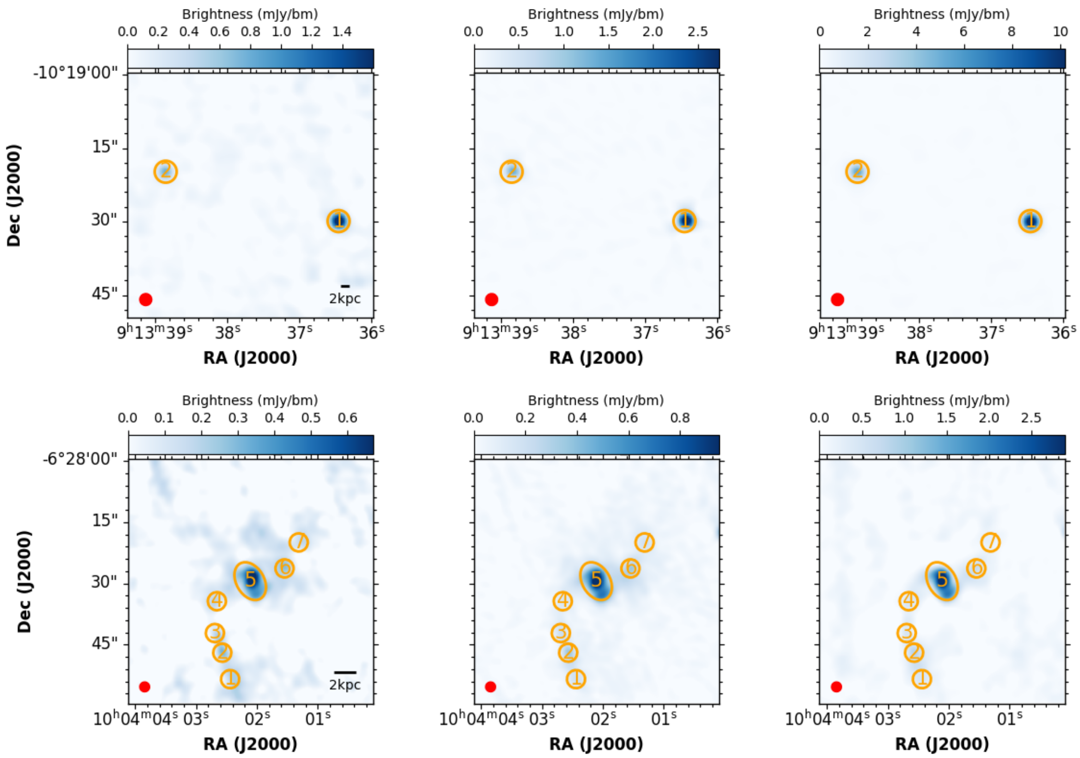

Figure 5.2: Examples of apertures generated from matched-resolution radio images, for IRAS F09111-1007 (upper) and NGC 3110 (lower). For each system, the radio images from VLA (3, 15, 33 GHz from left to right) are displayed in blue. All images are convolved to a common circular Gaussian beam of 7″ (indicated with red filled circles), set by the native resolution of the 15 GHz images (see Chapter 2). Apertures are labeled by increasing declinations.

resolution-matched radio images). Figure 5.2 shows two examples of the apertures made from the beam-matched VLA images.

5.4 Results

In total, we identified and performed aperture photometry as described above for 87 regions at 7″ and 127 regions at $\sim 2''$, with 80 regions having complete measurements across all radio and IR frequencies/wavelengths at 7″. All regions are further classified into "AGN" (AGN-dominated nucleus), "Jet" (AGN jet),"AGN/SBnuc" (AGN-starburst composite nucleus), "SBnuc" (starburst-dominated nucleus), "SF" (star-forming region) and “Bg”(background galaxy) based on classification schemes described in Chapter 4. The only exceptions to the current classification schemes are the regions along the ionized bubbles surrounding the double AGN in NGC 6240 (see Figure 2.47 in Appendix), which have been previously studied at various wavelengths (e.g. Medling et al., 2021) but to our knowledge have not been captured in the radio at such high frequencies. This is also the only system in the sample where we see the ionized wind bubbles from the intense starburst/AGN activity at the targeted frequencies (3 - 33 GHz). Therefore we classified these regions in NGC 6240 as “wind” but excluded them from analysis in the work for simplicity. Results from aperture photometry and spectral analysis at $7''$ and $\sim 2''$ are reported in Table 5.2 and 5.1 respectively, including region classification.

5.4.1 3 – 33 GHz Spectral Indices

In Figure 5.3 and 5.4 we show the distributions of α_{3-15}, α_{15-33} and α_{3-33} for all regions characterized at $\sim 2''$ and $7''$ respectively, which have median values of $\alpha_{3-15} \sim -0.65 \pm 0.11$, $\alpha_{15-33} \sim -0.50 \pm 0.23$ and $\alpha_{3-33} \sim -0.60 \pm 0.11$ at $\sim 2''$, and $\alpha_{3-15} \sim -0.64 \pm 0.11$, $\alpha_{15-33} \sim -0.55 \pm 0.16$ and $\alpha_{3-33} \sim -0.62 \pm 0.08$ at $7''$.

As shown in Figure 5.3, α_{3-15} spans a broader range compared to α_{3-33} and α_{15-33}, which are mainly due to the larger variations among “SF" regions. Overall, α_{3-15} and α_{3-33} mostly follow the 1:1 ratio line for all region types, which is expected from spectra with no curvatures. However, α_{15-33} is consistently flatter (larger) than α_{3-15} and α_{3-33} for “SBnuc" and especially “SF” regions, indicating spectral flattening towards 33 GHz from 15 GHz in these regions. The median α_{15-33} are $\sim -0.45 \pm 0.12$ and $\sim -0.26 \pm 0.15$ for “SBnuc” and “SF”, which are significantly higher than those of “AGN” and “AGN/SBnuc”, with $\alpha_{15-33} \sim -0.67 \pm 0.12$ and $\alpha_{15-33} \sim -0.65 \pm 0.13$, respectively.

At 7″ measurements, the above trends remain but the number of "SF" regions that can be directly measured are significantly reduced due to the larger beam and measurements also have larger uncertainties due to the inclusion of more background noise. The effect of beam dilution can be observed more directly in Figure 5.5 where we show the median 3 – GHz spectrum for each region type measured at both 7″ and $\sim 2''$, normalized by 15 GHz flux density. While "SF" regions have flattest median spectra in both plots, the spectral curvature is more prominent at $\sim 2''$, where we also see the distinction between "SF" and "SBnuc". However, while all region types show similar 3 – 15 GHz median spectra at 2″, the median spectra of "SF" and "SBnuc" also become flatter than those of "AGN" and "AGN/SBnuc".

5.4.2 33 GHz Thermal Fractions

Studies of nearby normal star-forming galaxies and starbursts show that radio continuum emission at 33 GHz is largely dominated by thermal free-free emission from HII regions, which makes the 33 GHz radio continuum an excellent tracer of recent star formation (Murphy et al., 2011b, 2012; Linden et al., 2020). Using the best-fitted parameters acquired from Equation 5.2 from §5.3, we can estimate the fractional contribution of thermal free-free emission at 33 GHz, $f_{\rm th}^{\rm fit}$, by calculating the ratio $A\nu^{-0.1}/(A\nu^{-0.1} + B\nu^{-0.85})$. The distributions of the resulted $f_{\rm th}^{\rm fit}$ are reported in Table 5.1 and 5.2 for the 2″ and 7″ measurements respectively, and shown in Fig 5.6. As shown in Figure 5.6, while "SF" regions have the highest $f_{\rm th}^{\rm fit}$, all region types span the full range in thermal fraction, from 0 – 100%. At 2″, the median $f_{\rm th}^{\rm fit}$ is $53 \pm 15\%$ for all regions combined, and $41 \pm 15\%, 40 \pm 10\%, 57 \pm 8\%$ and $61 \pm 14\%$ for "AGN" "AGN/SBnuc" "SBnuc" and "SF" regions. At 7″, the median value is $54 \pm 16\%$ for all regions, and $42 \pm 21\%, 43 \pm 10\%, 60 \pm 9\%$ and $67 \pm 10\%$ respectively

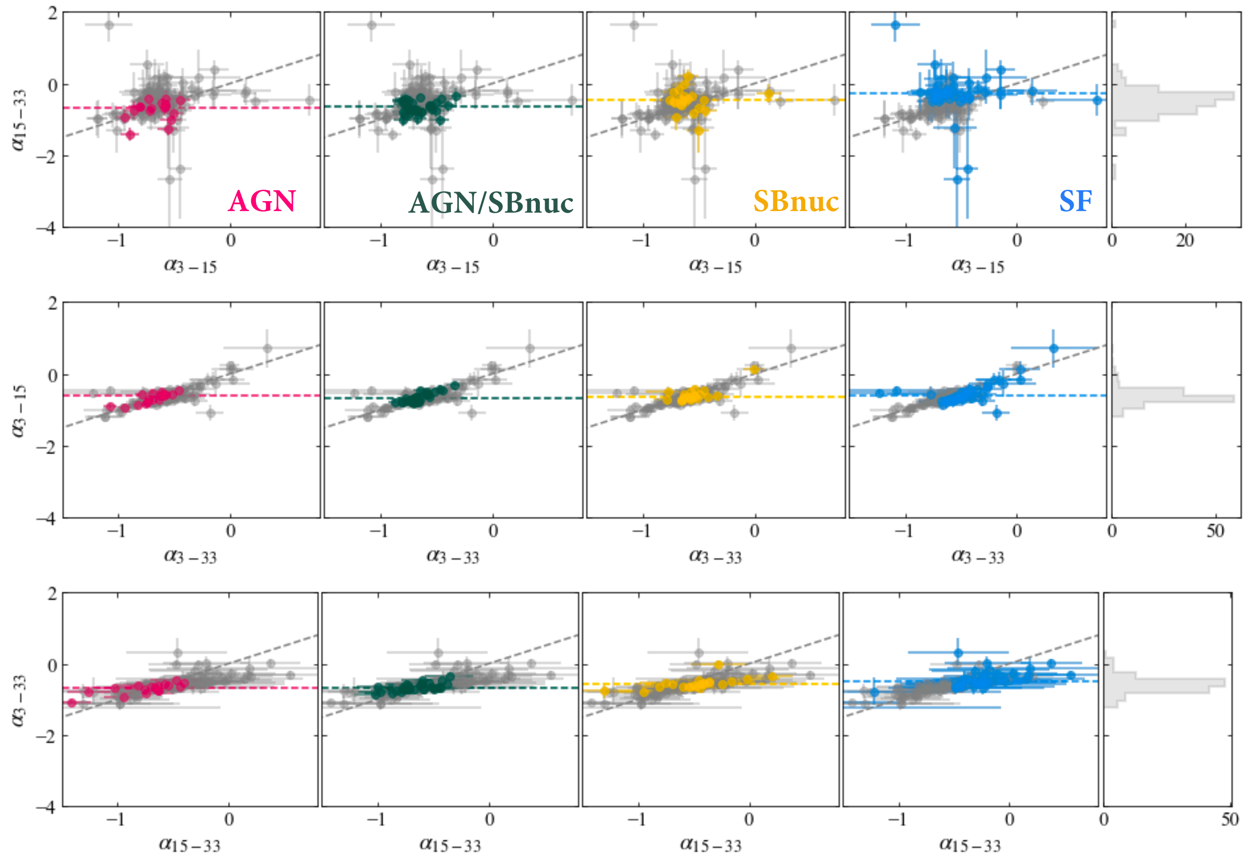

Figure 5.3: Comparison between radio spectral indices measured at $\sim 2''$ between $3-15$, $15-33$ and $3-33$ GHz, shown in grey for all regions. Values for "AGN", "AGN/SBnuc", "SBnuc" and "SF" are shown separately from left to right. The distributions of the spectral indices are shown on the right-most panels. Dashed grey line in each plot mark the 1:1 ratio (i.e. no spectral curvature), and colored dash lines mark the median values for the respective region types. Spectral index between $15-33$ GHz shows the most variation among the sample, and "SBnuc" and "SF" exhibit significant spectral flattening towards 33 GHz.

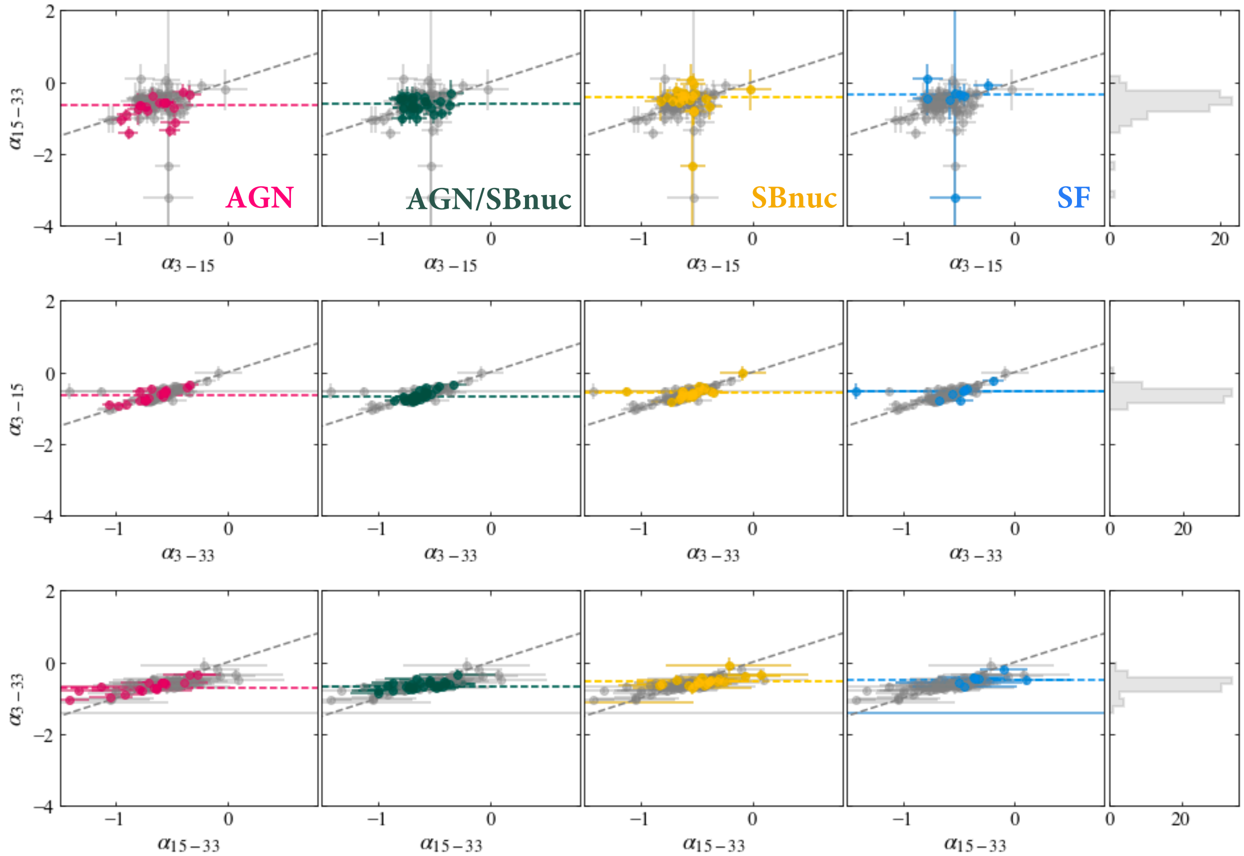

Figure 5.4: Same as Figure 5.3 but measured at 7″ resolution.

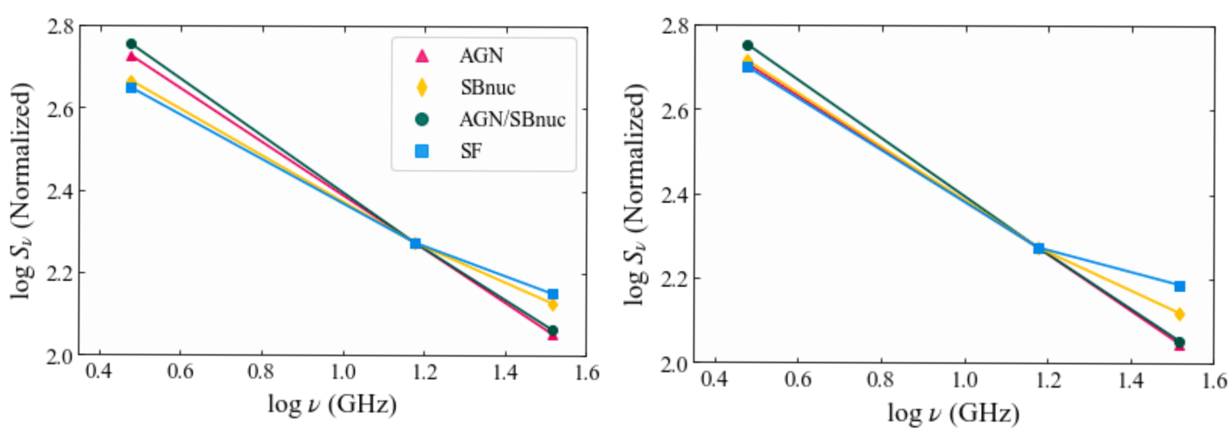

Figure 5.5: Comparison between spectral shapes as characterized at 7″ (left) and $\sim 2''$ (right) for different regions types. Flux densities are normalized by the brightest 15 GHz flux density measured among all regions. Spectral flattening towards 33 GHz for "SF" and "SBnuc" are more prominent at $\sim 2''$ than at 7″.

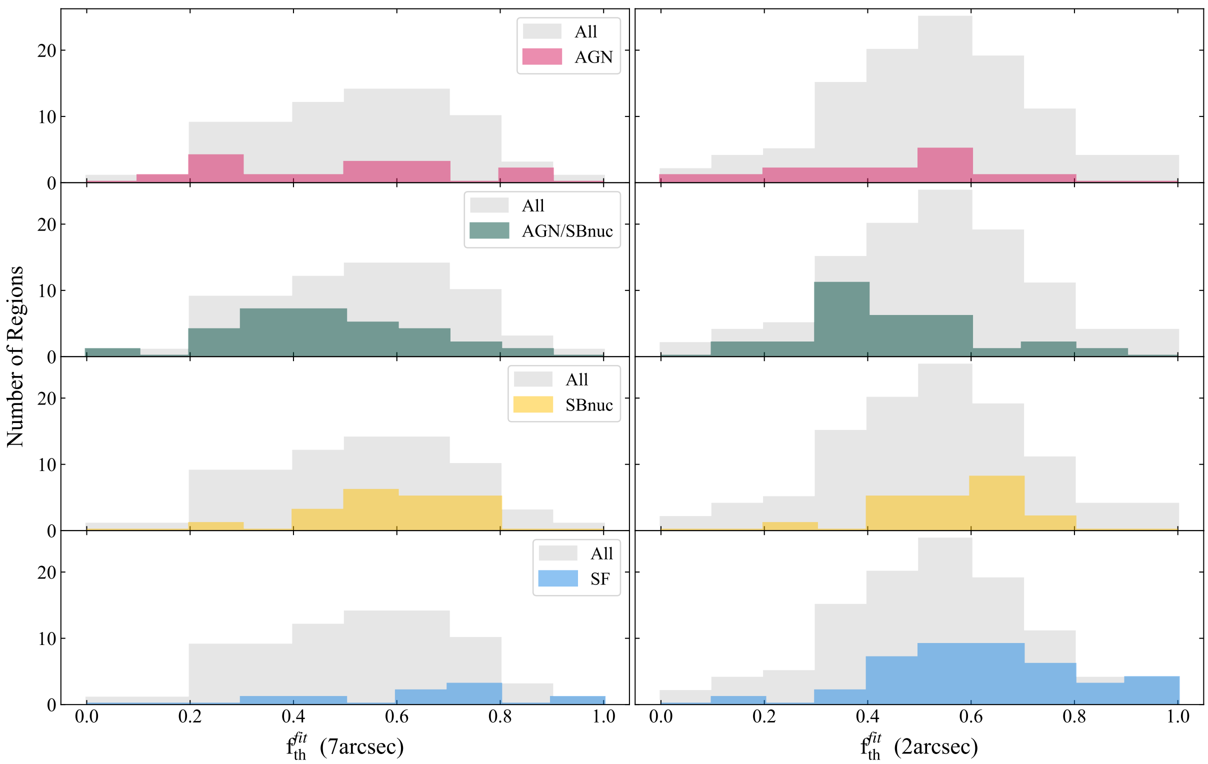

Figure 5.6: Thermal fraction at 33 GHz derived from spectral fitting, $f_{\rm th}^{\rm fit}$, assuming a two component power-law model with non-thermal spectral index set to -0.85, based on measurements at $7''$ (left) and $\sim 2''$ (right). Distributions for all regions are shown in grey, with those for each region type separately shown in color. While "SF" regions have the highest fitted 33 GHz thermal fractions, all region types span the full range of thermal fractions from $0 - 100\%$.

for "AGN" "AGN/SBnuc" "SBnuc" and "SF" regions. These values derived for the "SF" are consistent with previous estimates made by Linden et al. (2019) on a subset of the current dataset.

Additional to spectral fitting, as a comparison, we also derive alternative estimates for the 33 GHz thermal fraction directly using the measured 15 - 33 GHz spectral index α_{15-33} (see Section 5.3), and Equation (11) from Murphy et al. (2012):

$$f_{\rm th} = \frac{\left(\frac{\nu_2}{\nu_1}\right)^{\alpha} - \left(\frac{\nu_2}{\nu_1}\right)^{\alpha_{\rm NT}}}{\left(\frac{\nu_2}{\nu_1}\right)^{-0.1} - \left(\frac{\nu_2}{\nu_1}\right)^{\alpha_{\rm NT}}} \tag{5.3}$$

where we set the spectral index α between ν_1 and ν_2 (33 and 15 GHz) to be our measured α_{15-33}, and use error propagation to derive the uncertainties associated with flux calibration and image noise levels. The derived values for $f_{\rm th}$ are restricted to within 0 – 100% to be physically meaningful. At 2″, the median $f_{\rm th}$ is $55 \pm 29\%$ for all regions combined, and $30 \pm 19\%, 33 \pm 20\%, 59 \pm 20\%$ and $84 \pm 15\%$ for "AGN" "AGN/SBnuc" "SBnuc" and "SF" regions. At 7″, the median $f_{\rm th}$ is $48 \pm 22\%$ for all regions combined, and $33 \pm 21\%, 37 \pm 18\%, 63 \pm 15\%$ and $71 \pm 14\%$ for "AGN" "AGN/SBnuc" "SBnuc" and "SF" regions. Compared to results from spectral fitting, the values for "AGN"/"AGN/SBnuc" are slightly lower and values for "SF" are slightly higher but overall agree within uncertainty. These results are in agreement with estimates previously made in Linden et al. (2019) and confirm that star-forming regions and nuclei in local U/LIRGs are dominated by thermal free-free emission at 33 GHz.

5.4.3 IR-Radio Correlations

In Figure 5.8 we compare flux measurements made at 3, 15 and 33 GHz from our VLA observations with those at 24, 70 and 100μm from Spitzer and Herschel obser-

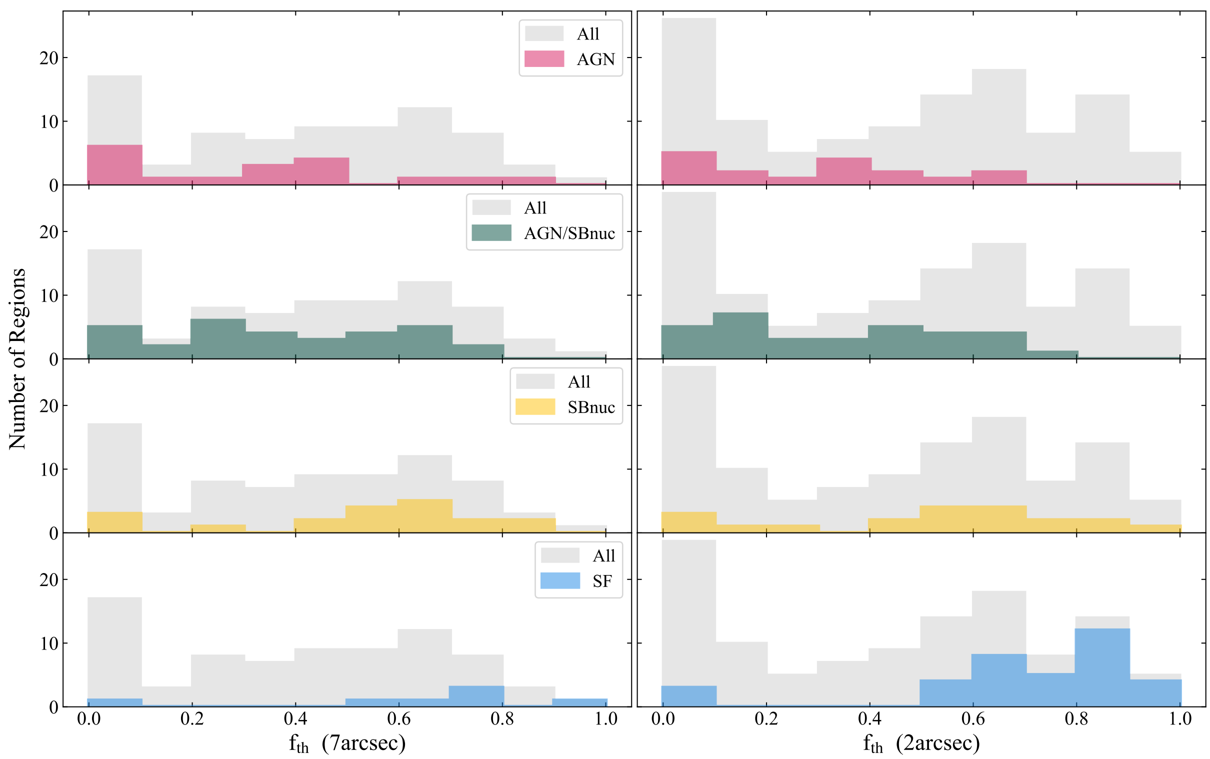

Figure 5.7: Thermal fraction at 33 GHz derived from 15 – 33 GHz spectral indices, $f_{\rm th}$, assuming a two component power-law model with non-thermal spectral index set to -0.85, based on measurements at 7″ (left) and $\sim$ 2″ (right). Distributions for all regions are shown in grey, with those for each region type separately shown in color. While "SF" regions have the highest fitted 33 GHz thermal fractions, all region types span the full range of thermal fractions from 0 – 100%.

vations using matched apertures. We can see that the radio and IR flux densities are well correlated with each other across all frequencies/wavelengths. After excluding "AGN" regions, the Pearson coefficients for these correlations are all $\gtrsim 0.6$ with $p-$values close to 0, meaning that all observed correlations are statistically-significant. The strongest correlation is seen between the radio flux densities and the 70μm flux density, the 100μm flux density shows the weakest correlation with the radio flux densities, especially with 33 GHz flux density. The derived linear relation between 24μm and 33 GHz flux density measurements is also consistent with results from Murphy et al. (2012) based on resolved measurements in nearby normal star-forming galaxies.

5.5 Discussion & Conclusion

5.5.1 Resolution effect on the observed 3 – 33 GHz spectral shape

As shown in Figure 5.3 and 5.4, spectral indices measured between 3 – 15, 15 – 33 and 3 –33 GHz for "SF" and "SBnuc" are flatter than "AGN" and "AGN/SBnuc" regions, indicating more dominant contributions from thermal free-free emission across 3 – 33 GHz. However, measurements made with apertures with larger physical sizes could include more diffuse emission that is dominated by synchrotron emission from cosmic-rays that have traveled away from their birth sites. To investigate whether beam dilution may be biasing our results, in Figure 5.9 we show the calculated spectral indices based on photometry performed at $\sim 2''$ with respect to the physical diameters of the apertures used for photometry. We can see that "SF" are all measured with apertures smaller than 5 kpc, while "AGN" and "AGN/SBnuc" are measured with apertures from < 1 kpc to over 10 kpc. This means that "SF" are identified in

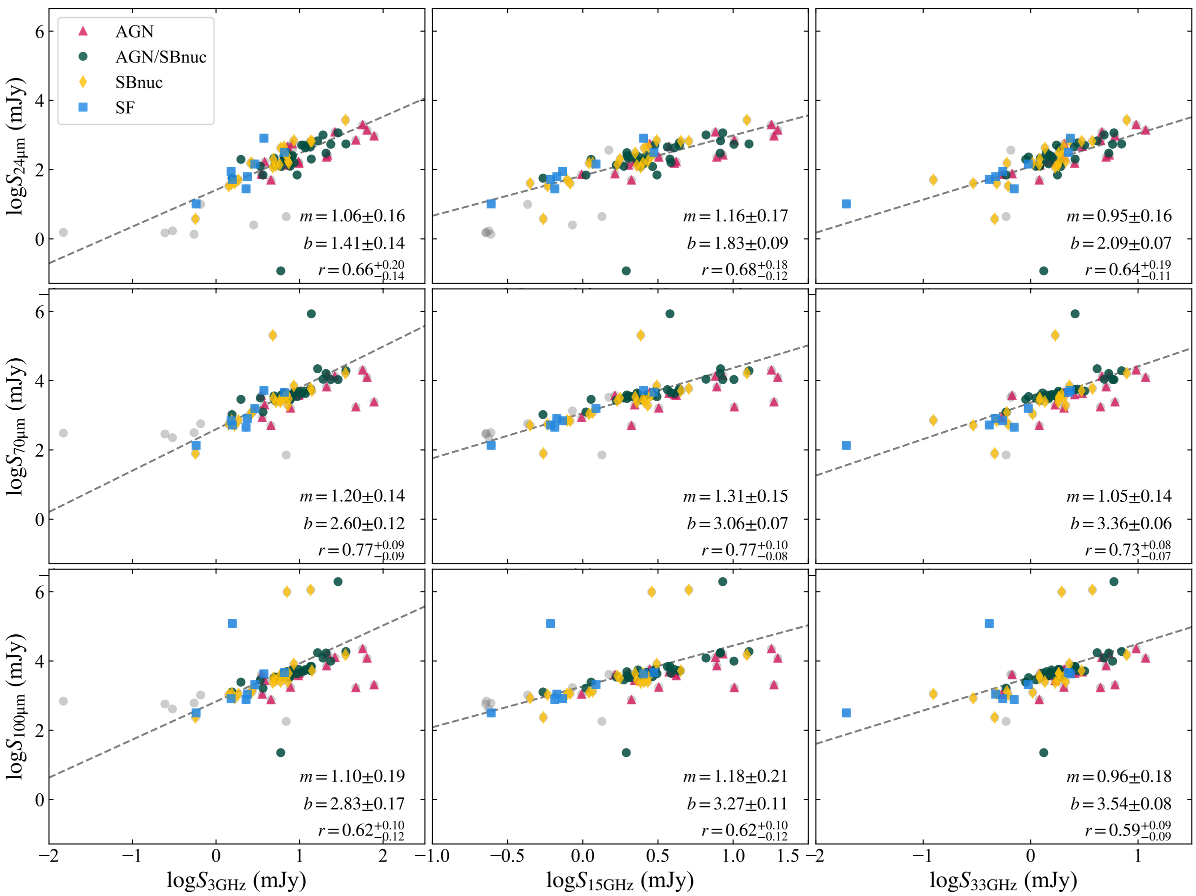

Figure 5.8: Correlation between radio (3, 15 and 33 GHz from left to right) and IR (24, 70, 100μm from top to bottom) flux density measurements at 7″, shown in grey for all regions and in color for different region types. The fitted slope m and intercept b of each linear relation, as well as the Pearson correlation efficient r are displayed on the lower right corner of each panel. All correlations between radio-IR flux measurements are statistically-significant, with $p \sim 0$. Radio flux measurements show strongest correlation with 70μm flux measurements for non-AGN regions in local U/LIRGs in the sample.

the more nearby systems in the sample, where emission from star-forming regions can be isolated from the typically brighter nuclear emission. The uncertainties of the spectral indices for "SF" regions are also larger compared to other region types, which is likely introduced by the brighter diffuse emission from spiral arms or tidal tails where these star-forming regions are located. However, "SF" and "SBnuc" overall do have flatter spectral indices compared to "AGN" and "AGN/SBnuc" regions that are measured on similar physical scales, which means that "SF" and "SBnuc" regions in these local U/LIRGs intrinsically have flatter $3-33$ GHz radio spectra compared to "AGN" and "AGN/SBnuc" regions. At $1-10$ kpc scales, the spectral indices of the "AGN" and "AGN/SBnuc" are relatively constant at ~ -0.7. In comparison, the spectral indices for "SF" and "SBnuc" have larger scatter, potentially reflecting the different timescales of the starburst activity among these regions, as demonstrated in Linden et al. (2019). The $15-33$ GHz spectral indices of "SF" and "SBnuc" are particularly flat, as also illustrated in Figure 5.5. These results confirm that the flatter $3-33$ GHz radio continuum spectra of "SF" and "SBnuc" regions are driven by high contribution from thermal free-free emission, especially at 33 GHz, instead of flattening of intrinsic non-thermal spectra.

Meanwhile, as shown in Figure 5.5, the larger aperture sizes used at $7''$ resolution may have introduced more diffuse non-thermal emission into the measurements of "SF" and "SBnuc" regions, hence the spectral flatness at $15-33$ GHz is reduced relative to that observed at $\sim 2''$. However, the $3-15$ GHz median spectrum for "SF" becomes flatter at $7''$ relative to at $\sim 2''$, which is contrary to our expectation that larger apertures dilute the thermal free-free contribution. A possible explanation for this is that the "SF" regions identified are surrounded by more regions of massive star formation that are either fainter or smaller which contributes to maintaining a relatively high level of thermal free-free emission and relatively flat spectra when

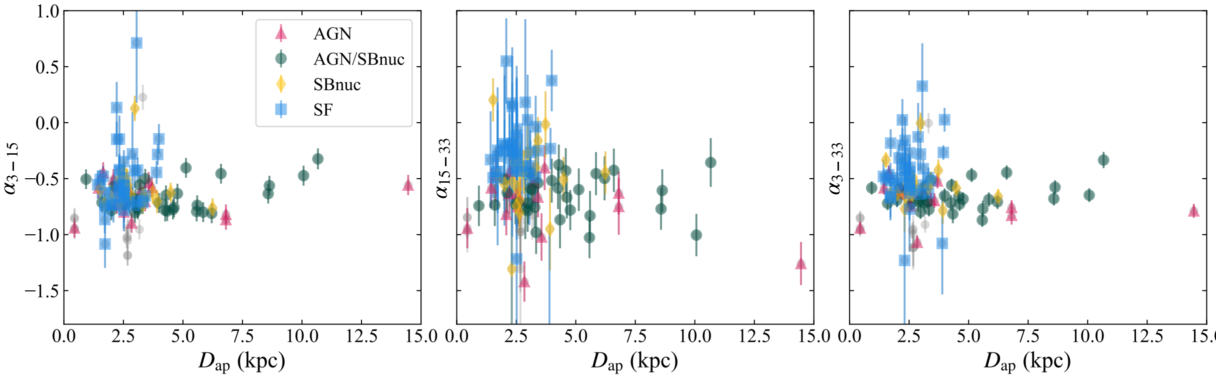

Figure 5.9: Radio spectral indices measured between 3 – 15, 15 – 33 and 3 – 33 GHz vs. linear diameter of the aperture used for photometry at 2″. Region symbols are the same as in Figure 5.8. Spectral indices for "AGN" and "AGN/SBnuc" regions, which are measured with apertures with diameters of 1-10 kpc, are relatively constant at ~ -0.7, while those for "SF" and "SBnuc" are flatter and with larger scatter. The 15 – 33 GHz spectral indices of "SF" regions are the flattest.

measured with larger apertures. In this scenario, for 3 - 15 GHz to be noticeably flatter when measured on larger scales, many of the identified "SF" regions would also likely to have gone through relatively recent starburst activity, with the cosmic rays produced in supernovae still close to the birth sites. This is also consistent with the overall flatter 15 – 33 GHz spectra of the "SF" regions.

In summary, beam dilution could reduce the estimated thermal emission at 33 GHz for "SF" and "SBnuc" regions, but their overall 3 – 33 GHz spectral shapes would remain relatively flat compared to "AGN/SBnuc" and "AGN" regions up to $\sim$ 10 kpc scales.

Several "SF" and "SBnuc" regions (in IC 2810, NGC 6926, IRAS 05442+1732 and CGCG 468-002) show 15 – 33 GHz flatter than 0, suggesting rising spectra towards higher frequencies. This may be caused by spinning dust in highly embedded star-forming regions (Murphy et al., 2020) or high electron opacity. Follow-up observations with ALMA at $\sim$ 100 GHz will aid in revealing their nature.

5.5.2 IR-Radio correlations

As shown in Figure 5.8, using the observed radio-IR correlations to identify AGN is not straight-forward, as many "AGN" lie on or very close to the "SF" and "SB-nuc" regions. However, deviations of "AGN" regions from the correlations are more noticeable at far-IR wavelengths (70, 100μm) instead of mid-IR (24μm), and at 3 and 15 GHz instead of 33 GHz at 7″. This suggests that at least on 10 kpc scales, these "AGN" are more dominated by non-thermal emission and do not contribute significantly to cool dust emission. For the other "AGN" and most "AGN/SBnuc" regions that follow the observed correlations, their emission may be dominated by star formation rather than AGN activity. It is also possible that some of these nuclei with higher radio and IR flux densities may host heavily obscured yet powerful AGN or starbursts that produce high level of radio emission as well as cool dust emission due to green house effect (González-Alfonso & Sakamoto, 2019).

Given the observed radio-IR correlations among non-AGN regions, we can also estimate how much of the total SFR of these local U/LIRGs, as traced by their total IR luminosities, are recovered by the star-forming regions detected in our radio observations. To do this, we use the 33 GHz flux measurements given that the 33 GHz continuum is dominated by thermal free-free emission for "SF" and "SBnuc" regions, as discussed in the previous section. Using the sum of the 33 GHz continuum flux densities for non-AGN regions identified and measured in individual systems, we can calculate their combined SFR using Equation (10) from Murphy et al. (2012), accounting for both thermal free-free emission from HII regions (< 10 Myr) and non-thermal synchrotron emission from supernovae ($\sim$10–100 Myr):

$$\left(\frac{\mathrm{SFR}}{\mathrm{M}_{\odot}\mathrm{yr}^{-1}}\right) = 10^{-27}\Bigg[2.18\left(\frac{T_e}{10^4\mathrm{K}}\right)^{0.45}\left(\frac{\nu}{\mathrm{GHz}}\right)^{-0.1} + 15.1\left(\frac{\nu}{\mathrm{GHz}}\right)^{\alpha^{\mathrm{NT}}}\Bigg]^{-1}\left(\frac{L_\nu}{\mathrm{ergs}^{-1}\mathrm{Hz}^{-1}}\right) \tag{5.4}$$

where a Kroupa Initial Mass Function (IMF) and continuous and constant star-forming history over 100 Myr is assumed. In Equation 5.4, L_ν is the spectral luminosity at the observed frequency ν, given by $L_\nu = 4\pi D_L^2 S_\nu$, where S_ν is the measured flux density. Here adopt an electron temperature $T_e = 10^4$ K and a non-thermal spectral index $\alpha^{\mathrm{NT}} = -0.85$, following the previous Chapters. If we only consider the thermal free-free emission from young massive stars, Equation 5.4 becomes (Equation 6 in Murphy et al., 2012):

$$\left(\frac{\mathrm{SFR_{th}}}{\mathrm{M}_{\odot}\mathrm{yr}^{-1}}\right) = 4.6\times 10^{-28}\left(\frac{T_e}{10^4\mathrm{K}}\right)^{-0.45}\left(\frac{\nu}{\mathrm{GHz}}\right)^{0.1} \times \left(\frac{L_\nu^{\mathrm{T}}}{\mathrm{ergs}^{-1}\mathrm{Hz}^{-1}}\right) \tag{5.5}$$

where $L_\nu^{\mathrm{T}} = f_{\mathrm{th}} L_\nu$ is the thermal-only spectral luminosity. For regions with $f_{\mathrm{th}} \simeq$ 100%, thermal emission from young massive stars completely dominates the radio continuum, and $L_\nu^{\mathrm{T}} \simeq L_\nu$. For $f_{\mathrm{th}} \simeq 0\%$, $\mathrm{SFR_{th}} \simeq 0\, M_{\odot}\mathrm{yr}^{-1}$.

In Figure 5.10 (top) we show the ratio between the summed SFR derived from the 33 GHz radio continuum flux density from non-AGN regions measured at 7″ and the total SFR derived from the total IR luminosity of the host galaxy, as given by

$$\mathrm{SFR_{IR}} = 3.15\times 10^{-44} L_{\mathrm{IR,SF}} \tag{5.6}$$

$$= 3.15\times 10^{-44} L_{\mathrm{IR}}(1 - f_{\mathrm{AGN}}) \tag{5.7}$$

which is a modified version of Equation (15) in Murphy et al. (2012), accounting for the AGN contribution to the total IR luminosity, $f_{\rm AGN}$, as estimated by Díaz-Santos et al. (2017) using MIR diagnostics. As shown in Figure 5.10 (top), the fraction of total SFR recovered by the 33 GHz continuum emission from all non-AGN regions in a galaxy span a wide range from 10 – 80%, with a median recovery rate of 41% for total 33 GHz continuum emission and 28% for thermal-only 33 GHz emission for LIRGs, and 32% and 10% For ULIRGs, though there are fewer data points from ULIRGs. For LIRGs, especially those with $L_{\rm IR} < 10^{11.5} L_{\odot}$, the recovery rate has the largest scatter. Because we are only measuring the brightest radio regions at $7''$, the low recovery rate at low IR luminosity is likely due to the fact that star formation is widespread in these systems such as in extended dusty spiral arms and disks, which are not captured by our radio measurements. The high recovery rate in some low luminosity systems suggest that their obscured star formation is more concentrated. At moderate IR luminosity ($10^{11.5} L_{\odot} < L_{\rm IR} < 10^{12} L_{\odot}$), the recovery rate has the highest median value, at $\sim 45\%$, which likely reflect the overall compact morphology of the star-forming activity in these systems. However, in ULIRGs where emission is known to be compact, the 33 GHz does not recover well the total SFR traced by the IR emission. One possibility is that AGN actually contributes to much higher level of IR emission than previously estimated by (Díaz-Santos et al., 2017) using MIR diagnostics. ULIRGs are more heavily obscured compared to LIRGs (Stierwalt et al., 2013), and the MIR emission from a heavily obscured AGN could be absorbed and re-emitted at longer wavelengths González-Alfonso & Sakamoto (2019). In this case, the AGN fraction of the system would be underestimated using MIR diagnostics, and the total SFR would be over estimated, resulting low radio recovery rate. However, it is also possible that we are missing extended emission from these systems due to the limited LAS ($10''$) of our radio observations. Using VLA D-configuration observations with LAS as large as 22″, Barcos-Muñoz et al. (2017) showed that for 22 of the most luminous local U/LIRGs, SFRs derived from 33 GHz emission and total IR emission are roughly consistent with one another. This effect of missing flux may also explain the very low recovery rates in some low-luminosity systems. Additionally, some "AGN" regions may account for significant fraction of star formation in the host systems and excluding these regions would also lower the recovery rate in these systems.

Given that we also have measurements of the mid- and far-IR flux densities of individual radio regions, we can also directly compare the SFR derived from the 33 GHz continuum emission and those from the total IR luminosity extrapolated from 24, 70 and 100μm flux densities for each non-AGN region. To do this, we adopt the empirical calibration provided in Galametz et al. (2013) based on *Spitzer* and *Herschel* measurements of 61 nearby galaxies (< 31 Mpc) from the KINGFISH sample (Kennicutt et al., 2011) at the same wavelengths (i.e. 24, 70 and 100μm):

$$L_{\rm IR} = 2.192 \pm 0.114 \nu L_\nu(24\mu{\rm m}) + 0.187 \pm 0.035 \nu {\rm L}_\nu(70\mu{\rm m}) + 1.314 \pm 0.016 \nu {\rm L}_\nu(100\mu{\rm m})$$

where $L_{\rm IR}$ and νL_ν are in units of $L_\odot$. The resulted $L_{\rm IR}$ can then be converted to $\rm SFR_{IR}$ using Equation 5.6. As shown in Figure 5.10 (bottom), for non-AGN regions in our sample, the SFR derived from the 33 GHz continuum and those derived from $L_{\rm IR}$ are largely consistent with one another. This result confirms that the 33 GHz radio continuum is indeed tracing the star-forming activities that are powering the mid- and far-IR dust emission on 10 kpc scales.

In this study we have demonstrated that on kpc to 10 kpc scales, star-forming regions and nuclei in local U/LIRGs are dominated by thermal free-free emission at

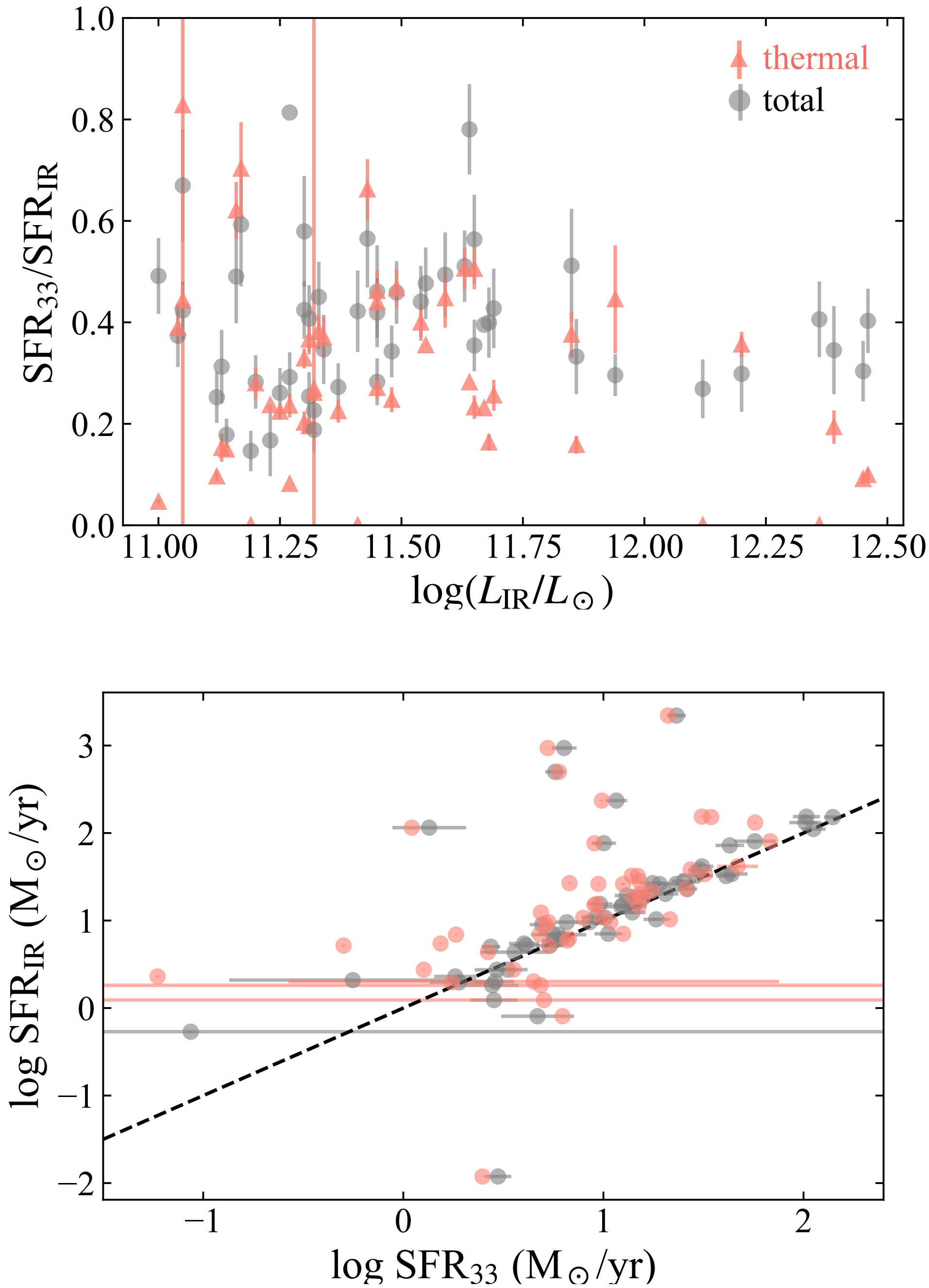

Figure 5.10: Comparison between star formation rates derived from 33 GHz radio continuum and those derived from total IR luminosity. *Top:* Ratio between combined star formation rates derived from 33 GHz radio continuum density measured at 7″ resolution for non-AGN regions and total IR luminosity of the host galaxy. *Bottom:* Star formation rates derived from 33 GHz radio continuum and total IR luminosity for individual non-AGN regions, measured at 7″ resolution. Values derived from the total 33 GHz continuum are shown in grey, and those from thermal free-free component are shown in pink. In both panels, values derived from the total 33 GHz continuum are shown in grey, and those from thermal free-free component are shown in pink. Black dashed line mark the 1:1 ratio line. Overall, the 33 GHz continuum emission coming from non-AGN regions together traces $\sim 40\%$ of the total SFR of the host galaxies. The recovery rate has a larger scatter among LIRGs than ULIRGs. Values derived from the radio emission are consistent with those from total IR luminosities.

33 GHz, with significant spectral flattening near 33 GHz that is more prominent on kpc scales. This confirms the utility of 33 GHz radio continuum as an useful SFR tracer in the dusty environments of both local U/LIRGs and potentially their high-z counterparts. We find that the combined SFR of the non-AGN regions as derived from the 33 GHz continuum emission on 10 kpc scales recover $\sim 40\%$ of the total SFR of each host system as traced by their total IR emission, which is likely an underestimate given the limited largest angular scales of our radio observations. Direct comparison between SFR derived from the 33 GHz radio continuum and those derived from total IR luminosity extrapolated from 24, 70 and 100μm flux densities for individual non-AGN regions yields consistent values. We also show that the radio-IR correlations hold on 10 kpc scales in these local U/LIRGs and that AGN is more easily identified towards lower radio frequency and longer IR wavelengths, which extends the utility of FRC as an AGN diagnostics to resolved scales. However, many known AGN also fall on the radio-IR correlations, which necessitates the need for multi-wavelength approach in identifying AGN in these systems. With upcoming observations from the JWST, we will be able to investigate the relation between radio and MIR dust emission on 100 pc scales.

Table 5.1: Aperture Photometry at $\sim 2''$ at 3, 15 and 33 GHz

Region (1)	Type (2)	RA (°) (3)	Dec (°) (4)	S_3 (mJy) (5)	S_{15} (mJy) (6)	S_{33} (mJy) (7)	α_{3-15} (8)	α_{15-33} (9)	α_{3-33} (10)	$f_{\rm th}$ (%) (11)	$f_{\rm th}^{\rm fit}$ (%) (12)
CGCG011-076_1	AGN/SBnuc	170.30098	-2.98411	12.16 ± 1.22	4.1 ± 0.43	1.89 ± 0.21	-0.67 ± 0.09	-0.98 ± 0.19	-0.78 ± 0.06	0	21 ± 7
CGCG043-099_1	AGN/SBnuc	195.45959	4.33347	13.58 ± 1.36	4.02 ± 0.42	2.37 ± 0.25	-0.76 ± 0.09	-0.67 ± 0.19	-0.73 ± 0.06	30 ± 30	31 ± 0
CGCG049-057_1	AGN	228.30458	7.22553	38.5 ± 3.85	15.06 ± 1.51	9.51 ± 0.95	-0.58 ± 0.09	-0.58 ± 0.18	-0.58 ± 0.06	43 ± 43	57 ± 8
CGCG052-037_1	AGN/SBnuc	247.73558	4.08289	14.09 ± 1.42	3.89 ± 0.39	2.72 ± 0.31	-0.8 ± 0.09	-0.46 ± 0.19	-0.69 ± 0.06	60 ± 60	37 ± 8
CGCG436-030_1	AGN/SBnuc	20.01099	14.36175	21.46 ± 2.15	7.14 ± 0.71	4.05 ± 0.43	-0.68 ± 0.09	-0.72 ± 0.18	-0.7 ± 0.06	22 ± 22	38 ± 5
CGCG453-062_1	AGN	346.23565	19.55232	16.57 ± 1.66	6.52 ± 0.65	3.96 ± 0.41	-0.58 ± 0.09	-0.63 ± 0.18	-0.6 ± 0.06	35 ± 35	56 ± 10
CGCG465-012_1	SF	58.56731	15.92642	0.53 ± 0.09	0.19 ± 0.03	0.16 ± 0.09	-0.63 ± 0.15	-0.21 ± 0.71	-0.49 ± 0.24	89 ± 11	60 ± 10
CGCG465-012_2	SF	58.56638	15.92736	0.71 ± 0.1	0.22 ± 0.03	0.19 ± 0.09	-0.72 ± 0.13	-0.19 ± 0.61	-0.55 ± 0.2	91 ± 9	45 ± 11
CGCG465-012_3	SBnuc	58.56651	15.92869	3.81 ± 0.39	1.29 ± 0.13	0.84 ± 0.12	-0.67 ± 0.09	-0.55 ± 0.22	-0.63 ± 0.07	47 ± 47	49 ± 1
CGCG465-012_4	SF	58.56738	15.92966	2.06 ± 0.22	0.63 ± 0.07	0.51 ± 0.1	-0.74 ± 0.09	-0.26 ± 0.28	-0.58 ± 0.09	84 ± 16	48 ± 14
CGCG468-002_1	SBnuc	77.0821	17.36334	3.95 ± 0.41	1.51 ± 0.15	1.78 ± 0.2	-0.59 ± 0.09	0.2 ± 0.19	-0.33 ± 0.06	100	78 ± 22
CGCG468-002_2	SF	77.08835	17.36898	10.78 ± 1.08	4.76 ± 0.48	3.23 ± 0.34	-0.51 ± 0.09	-0.49 ± 0.18	-0.5 ± 0.06	55 ± 55	69 ± 9
ESO550-IG02_1	AGN/SBnuc	65.33351	-18.81583	6.15 ± 0.62	1.73 ± 0.18	0.87 ± 0.15	-0.79 ± 0.09	-0.87 ± 0.25	-0.82 ± 0.08	0	12 ± 1
ESO550-IG02_2	AGN/SBnuc	65.33329	-18.81092	9.71 ± 0.98	2.96 ± 0.3	1.54 ± 0.22	-0.74 ± 0.09	-0.83 ± 0.22	-0.77 ± 0.07	3 ± 3	24 ± 4
ESO557-G002_1	SBnuc	97.94672	-17.62157	7.29 ± 0.73	2.57 ± 0.26	1.82 ± 0.21	-0.65 ± 0.09	-0.44 ± 0.2	-0.58 ± 0.06	62 ± 62	57 ± 3
ESO602-G025_1	AGN/SBnuc	337.85631	-19.03457	12.02 ± 1.21	3.45 ± 0.35	2.46 ± 0.3	-0.78 ± 0.09	-0.43 ± 0.2	-0.66 ± 0.07	63 ± 63	41 ± 9
IC0214_1	Bg	33.52349	5.17192	0.9 ± 0.14	1.3 ± 0.13	0.89 ± 0.14	0.23 ± 0.11	-0.48 ± 0.24	0 ± 0.09	57 ± 57	100
IC0214_2	SBnuc	33.52289	5.17335	4.49 ± 0.46	1.39 ± 0.14	1.15 ± 0.16	-0.73 ± 0.09	-0.24 ± 0.22	-0.57 ± 0.07	85 ± 15	53 ± 17
IC0214_3	SF	33.52212	5.17455	3.19 ± 0.33	1.04 ± 0.11	0.71 ± 0.13	-0.7 ± 0.09	-0.49 ± 0.27	-0.63 ± 0.09	56 ± 56	48 ± 3
IC0214_4	SF	33.52092	5.17488	2.23 ± 0.25	0.71 ± 0.08	0.69 ± 0.13	-0.72 ± 0.1	-0.04 ± 0.28	-0.49 ± 0.09	100	56 ± 25
IC0563_1	SF	146.586	3.04463	0.9 ± 0.12	0.38 ± 0.05	0.05 ± 0.1	-0.54 ± 0.11	-2.65 ± 2.58	-1.23 ± 0.85	0	54 ± 44
IC0563_2	SBnuc	146.58467	3.0458	1.29 ± 0.15	0.57 ± 0.06	0.2 ± 0.1	-0.51 ± 0.1	-1.31 ± 0.63	-0.77 ± 0.21	0	60 ± 36
IC0563_3	SF	146.58306	3.04717	1.89 ± 0.23	0.93 ± 0.1	0.14 ± 0.15	-0.44 ± 0.1	-2.37 ± 1.38	-1.08 ± 0.46	0	59 ± 41
IC0563_4	SBnuc	146.5879	3.07133	2.2 ± 0.25	0.8 ± 0.09	0.79 ± 0.16	-0.63 ± 0.1	-0.01 ± 0.29	-0.43 ± 0.1	100	67 ± 25
IC1623_1	SF	16.94491	-17.50769	9.63 ± 0.99	3.13 ± 0.32	2.53 ± 0.3	-0.7 ± 0.09	-0.27 ± 0.2	-0.56 ± 0.07	83 ± 17	57 ± 15
IC1623_2	AGN/SBnuc	16.94798	-17.50709	30.99 ± 3.11	9.2 ± 0.92	6.47 ± 0.67	-0.75 ± 0.09	-0.45 ± 0.18	-0.65 ± 0.06	61 ± 61	44 ± 7
IC2810_1	SF	171.43716	14.67517	0.62 ± 0.11	0.49 ± 0.06	0.66 ± 0.12	-0.14 ± 0.13	0.38 ± 0.27	0.03 ± 0.11	100	100
IC2810_2	AGN/SBnuc	171.43774	14.67661	7.76 ± 0.78	2.45 ± 0.25	1.63 ± 0.19	-0.72 ± 0.09	-0.52 ± 0.2	-0.65 ± 0.06	52 ± 52	45 ± 3
IIIZW035_1	AGN/SBnuc	26.12725	17.10236	29.13 ± 2.91	12.12 ± 1.21	6.83 ± 0.69	-0.54 ± 0.09	-0.73 ± 0.18	-0.6 ± 0.06	21 ± 21	55 ± 15
IIZW096_1	SF	314.35034	17.12643	2.15 ± 0.32	1.09 ± 0.11	0.8 ± 0.12	-0.42 ± 0.11	-0.39 ± 0.23	-0.41 ± 0.09	69 ± 69	79 ± 11
IIZW096_2	SF	314.3516	17.12757	5.77 ± 0.65	3.66 ± 0.37	3.05 ± 0.32	-0.28 ± 0.09	-0.23 ± 0.19	-0.27 ± 0.06	86 ± 14	91 ± 8
IRAS05442+173_1	SBnuc	86.79648	17.56297	23.94 ± 2.4	7.61 ± 0.76	5.02 ± 0.52	-0.71 ± 0.09	-0.53 ± 0.18	-0.65 ± 0.06	50 ± 50	45 ± 2
IRAS05442+173_2	SF	86.79522	17.56281	0.59 ± 0.09	0.1 ± 0.03	0.38 ± 0.1	-1.08 ± 0.21	1.66 ± 0.51	-0.18 ± 0.12	100	0
IRAS10173+08_1	AGN/SBnuc	155.00085	8.22608	6.18 ± 0.62	3.23 ± 0.32	2.01 ± 0.22	-0.4 ± 0.09	-0.6 ± 0.19	-0.47 ± 0.06	40 ± 40	74 ± 24
IRAS17578-040_1	AGN/SBnuc	270.13268	-4.01487	37.76 ± 4	15.11 ± 1.52	9.23 ± 0.94	-0.57 ± 0.09	-0.63 ± 0.18	-0.59 ± 0.06	36 ± 36	57 ± 10
IRAS18090+013_1	AGN/SBnuc	272.88921	1.52846	2.55 ± 0.27	0.86 ± 0.09	0.47 ± 0.09	-0.67 ± 0.09	-0.77 ± 0.27	-0.71 ± 0.09	14 ± 14	39 ± 7
IRAS18090+013_2	SF	272.88861	1.52926	0.2 ± 0.1	0.13 ± 0.04	0.15 ± 0.07	-0.28 ± 0.37	0.18 ± 0.74	-0.13 ± 0.3	100	95 ± 131
IRAS19542+1110_1	AGN/SBnuc	299.14909	11.31806	13.61 ± 1.36	3.79 ± 0.38	1.69 ± 0.18	-0.79 ± 0.09	-1.03 ± 0.18	-0.87 ± 0.06	0	0
IRASF01364-104_1	AGN/SBnuc	24.72026	-10.45327	10.8 ± 1.09	5.19 ± 0.52	3.71 ± 0.43	-0.46 ± 0.09	-0.43 ± 0.19	-0.45 ± 0.06	64 ± 64	75 ± 9
IRASF03359+15_1	AGN/SBnuc	54.69624	15.54821	9.78 ± 0.98	4 ± 0.4	2.49 ± 0.26	-0.56 ± 0.09	-0.6 ± 0.18	-0.57 ± 0.06	40 ± 40	60 ± 10
IRASF05187-10_1	AGN/SBnuc	80.27725	-10.24614	16.47 ± 1.65	5.49 ± 0.55	3.03 ± 0.33	-0.68 ± 0.09	-0.75 ± 0.19	-0.71 ± 0.06	16 ± 16	36 ± 6
IRASF07251-024_1	AGN/SBnuc	111.90669	-2.91509	8.63 ± 0.87	3.49 ± 0.35	2.17 ± 0.24	-0.56 ± 0.09	-0.61 ± 0.19	-0.58 ± 0.06	39 ± 39	59 ± 10
IRASF09111-10_1	AGN	138.40191	-10.32497	12.45 ± 1.25	3.33 ± 0.34	2.03 ± 0.23	-0.82 ± 0.09	-0.63 ± 0.19	-0.76 ± 0.06	36 ± 36	23 ± 3
IRASF09111-10_2	AGN	138.41187	-10.32217	5.77 ± 0.59	1.43 ± 0.15	0.79 ± 0.14	-0.87 ± 0.09	-0.75 ± 0.25	-0.83 ± 0.08	17 ± 17	4 ± 0
IRASF12112+03_1	AGN/SBnuc	183.44183	2.81166	14.51 ± 1.46	6.78 ± 0.7	3.07 ± 0.33	-0.47 ± 0.09	-1 ± 0.19	-0.65 ± 0.06	0	49 ± 25
IRASF12224-06_1	AGN	186.26629	-6.68128	6.35 ± 0.64	2.68 ± 0.3	1.2 ± 0.15	-0.54 ± 0.09	-1.02 ± 0.21	-0.69 ± 0.07	0	41 ± 19
IRASF14348-14_1	AGN	219.40953	-15.0067	14.87 ± 1.49	6.07 ± 0.64	2.25 ± 0.25	-0.56 ± 0.09	-1.26 ± 0.19	-0.79 ± 0.06	0	18 ± 11
IRASF16164-07_1	AGN	244.79909	-7.90078	35.73 ± 3.58	13.22 ± 1.32	8.66 ± 0.87	-0.62 ± 0.09	-0.54 ± 0.18	-0.59 ± 0.06	49 ± 49	56 ± 3
IRASF16399-09_1	SBnuc	250.66683	-9.7218	3.06 ± 0.33	1.03 ± 0.11	0.9 ± 0.12	-0.68 ± 0.09	-0.16 ± 0.21	-0.51 ± 0.07	94 ± 6	62 ± 21
IRASF16399-09_2	SF	250.66592	-9.72083	2.14 ± 0.24	0.75 ± 0.08	0.61 ± 0.1	-0.65 ± 0.1	-0.25 ± 0.24	-0.52 ± 0.08	84 ± 16	61 ± 14
IRASF16399-09_3	AGN/SBnuc	250.66727	-9.7204	8.54 ± 0.86	3.81 ± 0.38	2.49 ± 0.26	-0.5 ± 0.09	-0.54 ± 0.18	-0.51 ± 0.06	49 ± 49	68 ± 12
IRASF16516-09_1	SF	253.59938	-9.89191	0.64 ± 0.13	0.32 ± 0.05	0.33 ± 0.09	-0.43 ± 0.16	0.03 ± 0.4	-0.28 ± 0.14	100	84 ± 16

Table 5.1 continued

Table 5.1: Aperture Photometry at $\sim 2''$ at 3, 15 and 33 GHz (continued)

Region (1)	Type (2)	RA (°) (3)	Dec (°) (4)	S_3 (mJy) (5)	S_{15} (mJy) (6)	S_{33} (mJy) (7)	α_{3-15} (8)	α_{15-33} (9)	α_{3-33} (10)	$f_{\rm th}$ (%) (11)	$f_{\rm th}^{\rm fit}$ (%) (12)
IRASF16516-09_2	SBnuc	253.59904	-9.88911	11.08 ± 1.15	5.37 ± 0.55	3.74 ± 0.44	-0.45 ± 0.09	-0.46 ± 0.2	-0.45 ± 0.07	59 ± 59	75 ± 12
IRASF17138-10_1	AGN/SBnuc	259.14911	-10.34442	27.58 ± 2.77	9.71 ± 0.97	7.21 ± 0.74	-0.65 ± 0.09	-0.38 ± 0.18	-0.56 ± 0.06	70 ± 70	59 ± 6
IRASF17207-00_1	AGN/SBnuc	260.84151	-0.28358	63.36 ± 6.34	22.87 ± 2.29	12.36 ± 1.24	-0.63 ± 0.09	-0.78 ± 0.18	-0.68 ± 0.06	12 ± 12	41 ± 9
IRASF19297-04_1	AGN/SBnuc	293.09295	-4.00027	10.86 ± 1.09	3.91 ± 0.39	2.13 ± 0.23	-0.63 ± 0.09	-0.77 ± 0.19	-0.68 ± 0.06	14 ± 14	42 ± 9
IRASF22491-18_1	AGN/SBnuc	342.9556	-17.87333	3.44 ± 0.37	2.04 ± 0.21	1.54 ± 0.21	-0.32 ± 0.09	-0.36 ± 0.22	-0.33 ± 0.07	72 ± 72	86 ± 14
MCG-02-01-051_1	SBnuc	4.71197	-10.37681	11.35 ± 1.15	3.91 ± 0.39	2.84 ± 0.31	-0.66 ± 0.09	-0.4 ± 0.19	-0.58 ± 0.06	67 ± 67	57 ± 6
MCG-02-20-003_1	AGN/SBnuc	113.93098	11.70977	17.34 ± 1.74	5.34 ± 0.54	3.04 ± 0.33	-0.73 ± 0.09	-0.72 ± 0.19	-0.73 ± 0.06	23 ± 23	31 ± 2
MCG-02-33-098_1	SBnuc	195.58188	-15.76777	10.43 ± 1.05	4.31 ± 0.44	2.28 ± 0.25	-0.55 ± 0.09	-0.81 ± 0.19	-0.63 ± 0.06	7 ± 7	50 ± 16
MCG-02-33-098_2	SBnuc	195.58489	-15.76647	4.07 ± 0.43	1.8 ± 0.21	1.04 ± 0.14	-0.51 ± 0.1	-0.69 ± 0.23	-0.57 ± 0.07	26 ± 26	62 ± 17
MCG-03-04-014_1	AGN/SBnuc	17.5373	-16.85276	14.04 ± 1.41	3.81 ± 0.38	2.57 ± 0.3	-0.81 ± 0.09	-0.5 ± 0.2	-0.71 ± 0.06	54 ± 54	33 ± 7
MCG-03-34-064_1	AGN	200.60192	-16.72845	138.87 ± 13.89	32.85 ± 3.29	10.73 ± 1.08	-0.9 ± 0.09	-1.42 ± 0.18	-1.07 ± 0.06	0	0
NGC0034_1	AGN	2.77729	-12.10764	32.69 ± 3.27	9.05 ± 0.91	5.49 ± 0.57	-0.8 ± 0.09	-0.63 ± 0.18	-0.74 ± 0.06	35 ± 35	27 ± 2
NGC0838_1	SBnuc	32.4109	-10.14654	25.21 ± 2.55	9.58 ± 0.96	6.95 ± 0.74	-0.6 ± 0.09	-0.41 ± 0.19	-0.54 ± 0.06	66 ± 66	63 ± 2
NGC1068_1	Jet	40.66838	-0.01482	147.82 ± 14.8	37.05 ± 3.71	18.95 ± 1.97	-0.86 ± 0.09	-0.85 ± 0.18	-0.86 ± 0.06	0	0
NGC1068_2	Jet	40.66921	-0.01428	143.25 ± 14.34	30.89 ± 3.09	14.34 ± 1.53	-0.95 ± 0.09	-0.97 ± 0.19	-0.96 ± 0.06	0	0
NGC1068_3	Jet	40.66963	-0.01319	853.75 ± 85.38	188.11 ± 18.81	89.48 ± 8.96	-0.94 ± 0.09	-0.94 ± 0.18	-0.94 ± 0.06	0	0
NGC1068_4	AGN	40.67025	-0.01219	606.86 ± 60.69	155.03 ± 15.5	79.84 ± 8	-0.85 ± 0.09	-0.84 ± 0.18	-0.85 ± 0.06	1 ± 1	1 ± 0
NGC1614_1	SBnuc	68.50012	-8.57919	64.29 ± 6.43	22.56 ± 2.26	14.14 ± 1.42	-0.65 ± 0.09	-0.59 ± 0.18	-0.63 ± 0.06	41 ± 41	49 ± 4
NGC1797_1	SBnuc	76.93691	-8.01907	10.75 ± 1.09	3.89 ± 0.39	2.93 ± 0.33	-0.63 ± 0.09	-0.36 ± 0.19	-0.54 ± 0.06	72 ± 72	62 ± 6
NGC3110_1	SF	151.01017	-6.48151	0.82 ± 0.14	0.33 ± 0.05	0.38 ± 0.11	-0.57 ± 0.14	0.17 ± 0.42	-0.32 ± 0.15	100 ± 0	73 ± 27
NGC3110_2	SF	151.0107	-6.47971	1.32 ± 0.18	0.5 ± 0.06	0.41 ± 0.12	-0.6 ± 0.11	-0.24 ± 0.38	-0.48 ± 0.13	85 ± 15	65 ± 10
NGC3110_3	SF	151.01121	-6.47838	0.67 ± 0.14	0.33 ± 0.05	0.24 ± 0.11	-0.43 ± 0.15	-0.41 ± 0.61	-0.42 ± 0.21	66 ± 34	80 ± 9
NGC3110_4	SF	151.01107	-6.47621	0.76 ± 0.14	0.26 ± 0.04	0.29 ± 0.11	-0.67 ± 0.15	0.14 ± 0.53	-0.4 ± 0.18	100 ± 0	59 ± 29
NGC3110_5	SBnuc	151.00879	-6.47484	12.06 ± 1.23	4.41 ± 0.45	2.96 ± 0.36	-0.63 ± 0.09	-0.51 ± 0.2	-0.59 ± 0.07	53 ± 53	57 ± 2
NGC3110_6	SF	151.00644	-6.47398	1.16 ± 0.17	0.59 ± 0.07	0.48 ± 0.12	-0.42 ± 0.11	-0.25 ± 0.34	-0.36 ± 0.12	84 ± 16	82 ± 2
NGC3110_7	SF	151.00547	-6.47221	0.41 ± 0.12	0.32 ± 0.05	0.28 ± 0.11	-0.15 ± 0.21	-0.18 ± 0.54	-0.16 ± 0.21	92 ± 8	98 ± 2
NGC4418_1	AGN/SBnuc	186.72755	-0.87762	29.4 ± 2.94	13.04 ± 1.31	7.26 ± 0.73	-0.5 ± 0.09	-0.74 ± 0.18	-0.58 ± 0.06	18 ± 18	58 ± 19
NGC5104_1	AGN/SBnuc	200.34633	0.34248	14.32 ± 1.45	4.12 ± 0.41	2.59 ± 0.28	-0.77 ± 0.09	-0.59 ± 0.19	-0.71 ± 0.06	42 ± 42	33 ± 3
NGC5257_1	SF	204.97058	0.83677	1.25 ± 0.16	0.72 ± 0.08	0.66 ± 0.09	-0.35 ± 0.1	-0.11 ± 0.21	-0.27 ± 0.08	99 ± 1	89 ± 11
NGC5257_2	SF	204.96882	0.838	1.17 ± 0.15	0.4 ± 0.05	0.32 ± 0.06	-0.66 ± 0.11	-0.28 ± 0.29	-0.54 ± 0.1	81 ± 19	59 ± 12
NGC5257_3	SF	204.96758	0.8396	0.71 ± 0.12	0.26 ± 0.04	0.21 ± 0.06	-0.63 ± 0.13	-0.25 ± 0.39	-0.51 ± 0.13	85 ± 15	62 ± 12
NGC5257_4	SBnuc	204.97052	0.8401	1.71 ± 0.19	0.85 ± 0.09	0.47 ± 0.07	-0.44 ± 0.1	-0.74 ± 0.24	-0.54 ± 0.08	18 ± 18	68 ± 28
NGC5257_5	SF	204.96808	0.84033	0.47 ± 0.1	0.13 ± 0.03	0.1 ± 0.06	-0.78 ± 0.19	-0.32 ± 0.73	-0.63 ± 0.24	77 ± 23	34 ± 9
NGC5257_6	SF	204.97302	0.8414	0.52 ± 0.11	0.2 ± 0.03	0.14 ± 0.06	-0.61 ± 0.16	-0.43 ± 0.55	-0.55 ± 0.19	63 ± 37	61 ± 1
NGC5258_1	SF	204.98808	0.82897	2.2 ± 0.24	1 ± 0.1	0.77 ± 0.09	-0.49 ± 0.09	-0.33 ± 0.2	-0.44 ± 0.07	75 ± 75	75 ± 0
NGC5258_2	SF	204.98845	0.82973	2.53 ± 0.27	0.85 ± 0.09	0.6 ± 0.08	-0.68 ± 0.09	-0.43 ± 0.22	-0.6 ± 0.07	63 ± 63	53 ± 5
NGC5258_3	SF	204.99242	0.831	0.39 ± 0.1	0.16 ± 0.03	0.06 ± 0.05	-0.55 ± 0.19	-1.22 ± 1.14	-0.77 ± 0.38	0	57 ± 31
NGC5258_4	SF	204.99018	0.83163	0.45 ± 0.1	0.16 ± 0.03	0.15 ± 0.06	-0.63 ± 0.18	-0.15 ± 0.54	-0.47 ± 0.19	95 ± 5	63 ± 18
NGC5258_5	SF	204.99345	0.8323	0.41 ± 0.1	0.12 ± 0.03	0.1 ± 0.06	-0.74 ± 0.2	-0.22 ± 0.72	-0.57 ± 0.24	88 ± 12	45 ± 14
NGC5331_1	SBnuc	208.0675	2.10144	10.32 ± 1.05	3.02 ± 0.31	2.12 ± 0.23	-0.76 ± 0.09	-0.45 ± 0.19	-0.66 ± 0.06	61 ± 61	42 ± 8
NGC5331_2	SBnuc	208.0684	2.10864	1.64 ± 0.2	0.53 ± 0.06	0.25 ± 0.07	-0.7 ± 0.1	-0.95 ± 0.37	-0.78 ± 0.12	0	28 ± 8
NGC5936_1	Bg	232.49543	12.98221	14.3 ± 1.45	2.72 ± 0.28	1.42 ± 0.19	-1.03 ± 0.09	-0.83 ± 0.21	-0.96 ± 0.07	4 ± 4	0
NGC5936_2	Bg	232.49693	12.98687	11.88 ± 1.21	2.56 ± 0.26	1.34 ± 0.19	-0.95 ± 0.09	-0.82 ± 0.22	-0.91 ± 0.07	5 ± 5	0
NGC5936_3	AGN/SBnuc	232.50353	12.98931	10.01 ± 1.02	2.84 ± 0.29	1.9 ± 0.21	-0.78 ± 0.09	-0.51 ± 0.19	-0.69 ± 0.06	53 ± 53	37 ± 6
NGC5990_1	SF	236.56891	2.41324	2.62 ± 0.3	1.05 ± 0.11	1.01 ± 0.15	-0.57 ± 0.1	-0.06 ± 0.24	-0.4 ± 0.08	100 ± 0	74 ± 26
NGC5990_2	AGN	236.56824	2.41544	9.83 ± 0.99	3.06 ± 0.31	2.17 ± 0.24	-0.73 ± 0.09	-0.44 ± 0.19	-0.63 ± 0.06	62 ± 62	48 ± 7
NGC5990_3	SF	236.56694	2.41727	0.73 ± 0.11	0.3 ± 0.04	0.23 ± 0.07	-0.55 ± 0.13	-0.33 ± 0.43	-0.48 ± 0.15	75 ± 25	69 ± 3
NGC6240_1	Wind	253.24518	2.39971	7.15 ± 0.75	1.07 ± 0.11	0.49 ± 0.2	-1.18 ± 0.09	-0.98 ± 0.54	-1.12 ± 0.18	0	0
NGC6240_2	Wind	253.24277	2.40028	6.21 ± 0.66	1.2 ± 0.12	0.43 ± 0.2	-1.02 ± 0.09	-1.31 ± 0.61	-1.11 ± 0.2	0	0
NGC6240_3	AGN	253.24541	2.40104	106.79 ± 10.68	34.43 ± 3.44	20.38 ± 2.05	-0.7 ± 0.09	-0.67 ± 0.18	-0.69 ± 0.06	30 ± 30	38 ± 3
NGC6240_4	Wind	253.24167	2.40061	7.69 ± 0.8	1.68 ± 0.17	0.79 ± 0.21	-0.95 ± 0.09	-0.95 ± 0.36	-0.95 ± 0.12	0	0
NGC6240_5	Wind	253.24254	2.40158	9.02 ± 0.93	1.66 ± 0.17	0.83 ± 0.21	-1.05 ± 0.09	-0.88 ± 0.35	-1 ± 0.12	0	0

Table 5.1 continued

Table 5.1: Aperture Photometry at $\sim 2''$ at 3, 15 and 33 GHz (continued)

Region (1)	Type (2)	RA (°) (3)	Dec (°) (4)	S_3 (mJy) (5)	S_{15} (mJy) (6)	S_{33} (mJy) (7)	α_{3-15} (8)	α_{15-33} (9)	α_{3-33} (10)	$f_{\rm th}$ (%) (11)	$f_{\rm th}^{\rm fit}$ (%) (12)
NGC6240_6	Wind	253.24391	2.40221	8.29 ± 0.86	1.22 ± 0.13	0.57 ± 0.2	-1.19 ± 0.09	-0.98 ± 0.48	-1.12 ± 0.16	0	0
NGC6926_1	SF	308.27419	-2.03597	0.78 ± 0.13	0.24 ± 0.05	0.37 ± 0.09	-0.74 ± 0.15	0.55 ± 0.38	-0.31 ± 0.12	100	64 ± 36
NGC6926_2	AGN	308.27549	-2.02737	7.93 ± 0.8	3.52 ± 0.35	1.85 ± 0.2	-0.5 ± 0.09	-0.82 ± 0.19	-0.61 ± 0.06	6 ± 6	55 ± 21
NGC6926_3	SF	308.27452	-2.0193	2.71 ± 0.3	0.86 ± 0.1	0.63 ± 0.12	-0.71 ± 0.1	-0.39 ± 0.28	-0.61 ± 0.09	68 ± 32	49 ± 8
NGC7469_1	AGN	345.81508	8.8739	68.59 ± 6.86	21.76 ± 2.18	12.06 ± 1.22	-0.71 ± 0.09	-0.75 ± 0.18	-0.73 ± 0.06	17 ± 17	31 ± 4
NGC7591_1	AGN/SBnuc	349.56783	6.58584	13.72 ± 1.38	4.36 ± 0.44	2.44 ± 0.27	-0.71 ± 0.09	-0.74 ± 0.19	-0.72 ± 0.06	19 ± 19	33 ± 4
NGC7592_1	SBnuc	349.59435	-4.41612	6.82 ± 0.69	2.78 ± 0.28	2.08 ± 0.24	-0.56 ± 0.09	-0.36 ± 0.2	-0.49 ± 0.06	71 ± 71	68 ± 2
NGC7592_2	AGN	349.59087	-4.41582	12.53 ± 1.26	4.84 ± 0.49	2.8 ± 0.31	-0.59 ± 0.09	-0.69 ± 0.19	-0.62 ± 0.06	26 ± 26	52 ± 11
NGC7679_1	AGN	352.19445	3.51142	2.47 ± 0.27	1.2 ± 0.13	0.83 ± 0.13	-0.45 ± 0.09	-0.47 ± 0.23	-0.46 ± 0.08	57 ± 57	75 ± 13
NGC7679_2	SF	352.19378	3.51212	2.86 ± 0.31	1.32 ± 0.14	0.94 ± 0.13	-0.48 ± 0.09	-0.44 ± 0.22	-0.46 ± 0.07	62 ± 62	74 ± 8
UGC02238_1	AGN/SBnuc	41.57298	13.09573	18.24 ± 2.3	5.18 ± 0.52	3.27 ± 0.35	-0.78 ± 0.1	-0.58 ± 0.19	-0.72 ± 0.07	42 ± 42	33 ± 3
UGC02369_1	SF	43.50783	14.96998	3.5 ± 0.36	1.07 ± 0.11	0.76 ± 0.12	-0.74 ± 0.09	-0.44 ± 0.23	-0.64 ± 0.08	62 ± 62	44 ± 7
UGC02369_2	AGN/SBnuc	43.50752	14.97078	13.82 ± 1.38	3.79 ± 0.38	2.04 ± 0.22	-0.8 ± 0.09	-0.79 ± 0.19	-0.8 ± 0.06	11 ± 11	14 ± 0
UGC02369_3	SBnuc	43.50721	14.97648	0.64 ± 0.09	0.79 ± 0.08	0.63 ± 0.11	0.13 ± 0.11	-0.28 ± 0.26	-0.01 ± 0.09	82 ± 18	100
UGC02982_1	SBnuc	63.09408	5.54729	2.96 ± 0.31	0.93 ± 0.1	0.63 ± 0.11	-0.72 ± 0.09	-0.48 ± 0.25	-0.64 ± 0.08	57 ± 57	45 ± 4
UGC02982_2	SF	63.09301	5.54762	2.1 ± 0.23	0.64 ± 0.07	0.45 ± 0.1	-0.74 ± 0.1	-0.44 ± 0.3	-0.64 ± 0.1	62 ± 38	43 ± 6
UGC02982_3	SF	63.0916	5.54789	0.88 ± 0.13	0.32 ± 0.04	0.25 ± 0.09	-0.62 ± 0.12	-0.3 ± 0.48	-0.52 ± 0.16	79 ± 21	61 ± 7
UGC02982_4	SF	63.09347	5.54926	1.03 ± 0.14	0.26 ± 0.04	0.21 ± 0.09	-0.87 ± 0.12	-0.25 ± 0.56	-0.66 ± 0.18	85 ± 15	11 ± 5
UGC02982_5	SF	63.09153	5.54892	0.97 ± 0.13	0.28 ± 0.04	0.19 ± 0.09	-0.76 ± 0.12	-0.49 ± 0.6	-0.67 ± 0.2	55 ± 45	33 ± 4
UGC03094_1	SF	68.89096	19.16609	0.17 ± 0.15	0.54 ± 0.06	0.38 ± 0.13	0.71 ± 0.53	-0.46 ± 0.45	0.33 ± 0.38	59 ± 41	100
UGC03094_2	SF	68.89128	19.16949	0.53 ± 0.12	0.42 ± 0.05	0.33 ± 0.09	-0.15 ± 0.16	-0.31 ± 0.39	-0.2 ± 0.15	77 ± 23	97 ± 3
UGC03094_3	AGN	68.89089	19.17159	7.49 ± 0.77	2.95 ± 0.3	2.15 ± 0.26	-0.58 ± 0.09	-0.4 ± 0.2	-0.52 ± 0.07	67 ± 67	65 ± 1
UGC03094_4	SF	68.89064	19.17336	0.32 ± 0.11	0.4 ± 0.05	0.34 ± 0.09	0.14 ± 0.23	-0.2 ± 0.39	0.02 ± 0.19	90 ± 10	100

NOTE — Photometry are performed on 3, 15 and 33 GHz images smoothed to a common circular Gaussian beam determined by the 15 GHz images. (1): Region identifier including the host galaxy name (2): Region type indicating the most likely source for the detected radio emission. (3) & (4): Region location, J2000 RA and Dec. (5): 3 GHz flux density. (6): 15 GHz flux density. (7): 33 GHz flux density. (8): Measured 3 - 15 GHz spectral index. (9): Measured 15 - 33 GHz spectral index. (10): Measured 3 - 33 GHz spectral index. (11) Thermal fraction at 33 GHz derived from (9). (12) Thermal fraction at 33 GHz derived from spectral fitting, assuming a two component power-law (thermal free-free, synchrotron).

Table 5.2: Aperture Photometry on Radio and IR Data at 7″

Region (1)	Type (2)	S_3 (mJy) (3)	S_{15} (mJy) (4)	S_{33} (mJy) (5)	S_{24} (Jy) (6)	S_{70} (Jy) (7)	S_{100} (Jy) (8)	α_{3-15} (9)	α_{15-33} (10)	$f_{\rm th}$ (%) (11)	$f_{\rm th}^{\rm fit}$ (%) (12)
CGCG011-076_1	AGN/SBnuc	11.79 ± 1.19	4.07 ± 0.5	1.85 ± 0.26	0.43 ± 0.02	4.29 ± 0.21	5.69 ± 0.28	-0.66 ± -0.1	-1 ± -0.23	0	24 ± 8
CGCG043-099_1	AGN/SBnuc	7.78 ± 0.79	2.53 ± 0.31	1.47 ± 0.21	0.15 ± 0.01	3.31 ± 0.17	4.13 ± 0.21	-0.7 ± -0.1	-0.69 ± -0.24	27 ± 27	38 ± 3
CGCG049-057_1	AGN	21.61 ± 2.18	8.55 ± 0.87	5.39 ± 0.55	0.26 ± 0.01	14.17 ± 0.71	15.92 ± 0.8	-0.58 ± -0.09	-0.58 ± -0.18	42 ± 26	58 ± 8
CGCG052-037_1	AGN/SBnuc	7 ± 0.72	1.96 ± 0.2	1.4 ± 0.2	0.31 ± 0.02	3.87 ± 0.19	4.92 ± 0.25	-0.79 ± -0.09	-0.43 ± -0.22	64 ± 28	38 ± 9
CGCG436-030_1	AGN/SBnuc	13.47 ± 1.37	4.38 ± 0.44	2.72 ± 0.38	0.59 ± 0.03	5.73 ± 0.29	5.31 ± 0.27	-0.7 ± -0.09	-0.6 ± -0.22	40 ± 32	43 ± 1
CGCG453-062_1	AGN	9.84 ± 1.01	4.07 ± 0.41	2.57 ± 0.37	0.15 ± 0.01	3.91 ± 0.2	4.42 ± 0.22	-0.55 ± -0.09	-0.58 ± -0.22	42 ± 32	63 ± 11
CGCG465-012_1	SBnuc	6.62 ± 0.69	2.23 ± 0.23	1.83 ± 0.3	0.3 ± 0.02	3.39 ± 0.17	4.34 ± 0.22	-0.68 ± -0.09	-0.25 ± -0.25	84 ± 16	58 ± 14
CGCG468-002_1	SBnuc	2.59 ± 0.36	1.1 ± 0.13	1.04 ± 0.23	0.15 ± 0.01	1.09 ± 0.05	1.24 ± 0.06	-0.53 ± -0.11	-0.07 ± -0.32	100	76 ± 23
CGCG468-002_2	SF	6.57 ± 0.7	2.97 ± 0.3	2.24 ± 0.3	0.32 ± 0.02	4.67 ± 0.23	4.7 ± 0.24	-0.49 ± -0.09	-0.36 ± -0.22	72 ± 26	74 ± 2
ESO550-IG02_1	AGN/SBnuc	3.65 ± 0.38	1.05 ± 0.12	0.59 ± 0.19	0.07 ± 0	1.25 ± 0.06	1.64 ± 0.08	-0.77 ± -0.09	-0.73 ± -0.43	20 ± 20	25 ± 1
ESO550-IG02_2	AGN/SBnuc	7.72 ± 0.79	2.42 ± 0.25	1.22 ± 0.26	0.13 ± 0.01	2.82 ± 0.14	3.51 ± 0.18	-0.72 ± -0.09	-0.87 ± -0.3	0	28 ± 6
ESO557-G002_1	SBnuc	4.85 ± 0.5	1.77 ± 0.19	1.22 ± 0.21	0.2 ± 0.01	3.16 ± 0.16	3.24 ± 0.16	-0.63 ± -0.09	-0.48 ± -0.26	57 ± 34	58 ± 0
ESO602-G025_1	AGN/SBnuc	6.48 ± 0.68	1.97 ± 0.21	1.47 ± 0.24	0.25 ± 0.01	3.07 ± 0.15	3.8 ± 0.19	-0.74 ± -0.09	-0.37 ± -0.25	71 ± 29	46 ± 10
IC0214_1	SBnuc	7.25 ± 0.75	2.71 ± 0.28	2.12 ± 0.31	0.17 ± 0.01	1.95 ± 0.1	2.55 ± 0.13	-0.61 ± -0.09	-0.31 ± -0.23	78 ± 22	64 ± 8
IC0563_1	SBnuc	1.85 ± 0.24	0.79 ± 0.1	0.12 ± 0.18	0.05 ± 0	0.72 ± 0.04	1.12 ± 0.06	-0.53 ± -0.11	-2.34 ± -1.81	0	53 ± 43
IC0563_2	SF	0.58 ± 0.16	0.25 ± 0.06	0.02 ± 0.18	0.01 ± 0	0.14 ± 0.01	0.32 ± 0.02	-0.53 ± -0.23	-3.23 ± -11.61	0	63 ± 37
IC0563_3	SBnuc	1.42 ± 0.21	0.58 ± 0.08	0.62 ± 0.19	0.03 ± 0	0.55 ± 0.03	1.06 ± 0.05	-0.55 ± -0.12	0.07 ± -0.42	100	73 ± 27
IC1623_1	AGN/SBnuc	28.88 ± 2.91	8.53 ± 0.86	5.96 ± 0.64	1.16 ± 0.06	10.76 ± 0.54	1963.44 ± 98.2	-0.76 ± -0.09	-0.45 ± -0.19	60 ± 24	43 ± 7
IC2810_1	AGN/SBnuc	5.07 ± 0.53	1.67 ± 0.18	1.22 ± 0.21	0.14 ± 0.01	2.71 ± 0.14	3.43 ± 0.17	-0.69 ± -0.09	-0.4 ± -0.26	67 ± 32	52 ± 6
IIIZW035_1	AGN/SBnuc	23.63 ± 2.37	10.12 ± 1.02	5.8 ± 0.66	0.54 ± 0.03	10.84 ± 0.54	9.91 ± 0.5	-0.53 ± -0.09	-0.71 ± -0.19	24 ± 24	59 ± 16
IIZW096_1	SF	3.74 ± 0.66	2.54 ± 0.26	2.34 ± 0.3	0.81 ± 0.04	5.27 ± 0.26	4.24 ± 0.21	-0.24 ± -0.13	-0.1 ± -0.21	100	95 ± 5
IRAS05442+173_1	SBnuc	14.05 ± 1.41	4.49 ± 0.45	2.98 ± 0.36	0.67 ± 0.03	5.11 ± 0.26	5.26 ± 0.26	-0.71 ± -0.09	-0.52 ± -0.2	51 ± 27	46 ± 2
IRAS10173+08_1	AGN/SBnuc	3.39 ± 0.38	1.88 ± 0.2	1.12 ± 0.22	0.13 ± 0.01	3.18 ± 0.16	2.85 ± 0.14	-0.37 ± -0.1	-0.66 ± -0.28	32 ± 32	79 ± 21
IRAS17578-040_1	AGN/SBnuc	20.72 ± 2.85	8.2 ± 0.84	5.34 ± 0.59	0.3 ± 0.01	16.24 ± 0.81	17.04 ± 0.85	-0.58 ± -0.11	-0.54 ± -0.19	48 ± 27	59 ± 8
IRAS18090+013_1	AGN/SBnuc	1.55 ± 0.26	0.54 ± 0.09		0.06 ± 0	1.05 ± 0.05	1.27 ± 0.06	-0.65 ± -0.34	0		
IRAS19542+1110_1	AGN/SBnuc	7.49 ± 0.78	2.1 ± 0.22	0.96 ± 0.16	0.23 ± 0.01	3.5 ± 0.17	3.3 ± 0.17	-0.79 ± -0.09	-1 ± -0.25	0	1 ± 0
IRASF01364-104_1	AGN/SBnuc	6.02 ± 0.63	2.91 ± 0.3	1.91 ± 0.35	0.12 ± 0.01	3.84 ± 0.19	3.54 ± 0.18	-0.45 ± -0.09	-0.54 ± -0.27	49 ± 37	75 ± 17
IRASF03359+15_1	AGN/SBnuc	6.62 ± 0.68	2.57 ± 0.26	1.69 ± 0.25	0.19 ± 0.01	3.62 ± 0.18	3.73 ± 0.19	-0.59 ± -0.09	-0.53 ± -0.23	49 ± 31	60 ± 5
IRASF05187-10_1	AGN/SBnuc	9.33 ± 0.95	3.11 ± 0.32	1.78 ± 0.27	0.07 ± 0	3.46 ± 0.17	4.31 ± 0.22	-0.68 ± -0.09	-0.71 ± -0.23	23 ± 23	40 ± 5
IRASF07251-024_1	AGN/SBnuc	4.96 ± 0.52	2.01 ± 0.21	1.23 ± 0.23	0.21 ± 0.01	3.63 ± 0.18	3.31 ± 0.17	-0.56 ± -0.09	-0.62 ± -0.27	37 ± 37	61 ± 11
IRASF09111-10_1	AGN	7.18 ± 0.74	2.01 ± 0.21	1.22 ± 0.21	0.13 ± 0.01	3.7 ± 0.18	4.42 ± 0.22	-0.79 ± -0.09	-0.63 ± -0.25	35 ± 35	26 ± 2
IRASF09111-10_2	AGN	3.57 ± 0.39	0.98 ± 0.11	0.54 ± 0.18	0.07 ± 0	0.86 ± 0.04	1.1 ± 0.05	-0.8 ± -0.1	-0.76 ± -0.45	15 ± 15	17 ± 0
IRASF12112+03_1	AGN/SBnuc	8.64 ± 0.88	3.86 ± 0.45	1.88 ± 0.26	0.16 ± 0.01	4.51 ± 0.23	4.47 ± 0.22	-0.5 ± -0.1	-0.91 ± -0.23	0	53 ± 22
IRASF12224-06_1	AGN	3.48 ± 0.39	1.64 ± 0.28	0.67 ± 0.15	0.08 ± 0	3.73 ± 0.19	4 ± 0.2	-0.47 ± -0.13	-1.13 ± -0.36	0	48 ± 25
IRASF14348-14_1	AGN	9.69 ± 0.98	4.18 ± 0.47	1.47 ± 0.19	0.17 ± 0.01	3.75 ± 0.19	3.74 ± 0.19	-0.52 ± -0.09	-1.33 ± -0.21	0	21 ± 14
IRASF16164-07_1	AGN	21.04 ± 2.12	7.79 ± 0.79	5.05 ± 0.52	0.23 ± 0.01	6.62 ± 0.33	7.21 ± 0.36	-0.62 ± -0.09	-0.55 ± -0.18	47 ± 26	55 ± 4
IRASF16399-09_1	AGN/SBnuc	11.29 ± 1.16	4.4 ± 0.44	3.18 ± 0.36	0.51 ± 0.03	5.04 ± 0.25	5.13 ± 0.26	-0.59 ± -0.09	-0.41 ± -0.19	66 ± 24	64 ± 1
IRASF16516-09_1	SBnuc	4.78 ± 0.52	2.43 ± 0.25	1.69 ± 0.24	0.12 ± 0.01	205.43 ± 10.28	2.4 ± 0.12	-0.42 ± -0.09	-0.46 ± -0.22	60 ± 29	78 ± 15
IRASF17138-10_1	AGN/SBnuc	19.09 ± 1.93	6.6 ± 0.67	4.84 ± 0.52	1.01 ± 0.05	11.07 ± 0.55	12.21 ± 0.61	-0.66 ± -0.09	-0.39 ± -0.19	68 ± 23	57 ± 6
IRASF17207-00_1	AGN/SBnuc	35.86 ± 3.6	12.75 ± 1.28	7.04 ± 0.72	0.55 ± 0.03	19.41 ± 0.97	18.82 ± 0.94	-0.64 ± -0.09	-0.75 ± -0.18	16 ± 16	41 ± 8
IRASF19297-04_1	AGN/SBnuc	6.46 ± 0.67	2.29 ± 0.24	1.29 ± 0.2	0.19 ± 0.01	4.43 ± 0.22	4.48 ± 0.22	-0.64 ± -0.09	-0.73 ± -0.24	20 ± 20	45 ± 8
IRASF22491-18_1	AGN/SBnuc	1.99 ± 0.28	1.14 ± 0.14	0.9 ± 0.22	0.2 ± 0.01	2.89 ± 0.14	2.45 ± 0.12	-0.35 ± -0.12	-0.3 ± -0.34	79 ± 21	86 ± 8
MCG-02-01-051_1	SBnuc	6.52 ± 0.71	2.73 ± 0.28	2.03 ± 0.29	0.46 ± 0.02	3.25 ± 0.16	3.37 ± 0.17	-0.54 ± -0.09	-0.38 ± -0.22	70 ± 27	70 ± 0
MCG-02-20-003_1	AGN/SBnuc	9.72 ± 0.99	3.04 ± 0.31	1.82 ± 0.27		4.97 ± 0.25	5.77 ± 0.29	-0.72 ± -0.09	-0.65 ± -0.23	32 ± 32	37 ± 1
MCG-02-33-098_1	SBnuc	5.94 ± 0.62	2.56 ± 0.29	1.36 ± 0.19	0.42 ± 0.02	2.5 ± 0.12	2.53 ± 0.13	-0.52 ± -0.1	-0.8 ± -0.23	8 ± 8	56 ± 19
MCG-02-33-098_2	SBnuc	2.7 ± 0.32	1.16 ± 0.18	0.6 ± 0.15	0.15 ± 0.01	1.21 ± 0.06	1.33 ± 0.07	-0.52 ± -0.12	-0.84 ± -0.36	2 ± 2	58 ± 20
MCG-03-04-014_1	AGN/SBnuc	13.46 ± 1.37	3.65 ± 0.37	2.55 ± 0.34	0.45 ± 0.02	5.52 ± 0.28	6.92 ± 0.35	-0.81 ± -0.09	-0.46 ± -0.21	60 ± 28	34 ± 8
MCG-03-34-064_1	AGN	77.98 ± 7.81	18.69 ± 1.87	6.1 ± 0.63	0.94 ± 0.05	2.43 ± 0.12	2.04 ± 0.1	-0.89 ± -0.09	-1.42 ± -0.18	0	0
NGC0034_1	AGN	26.48 ± 2.66	7.63 ± 0.77	4.61 ± 0.55	1.22 ± 0.06	13.52 ± 0.68	12.67 ± 0.63	-0.77 ± -0.09	-0.64 ± -0.2	34 ± 30	30 ± 1
NGC0838_1	SBnuc	13.56 ± 1.39	5.07 ± 0.52	3.76 ± 0.43	0.67 ± 0.03	5.98 ± 0.3	1137.08 ± 56.86	-0.61 ± -0.09	-0.38 ± -0.19	69 ± 24	63 ± 4
NGC0877_1	SF	2.82 ± 0.35	0.85 ± 0.1			1.35 ± 0.07	1.71 ± 0.09	-0.74 ± -0.25			
NGC0958_1	SF	0.55 ± 0.14	0.25 ± 0.05			0.32 ± 0.02	0.61 ± 0.03	-0.5 ± -0.48			

Table 5.2 continued

Table 5.2: Aperture Photometry on Radio and IR Data at 7″ (continued)

Region (1)	Type (2)	S_3 (mJy) (3)	S_{15} (mJy) (4)	S_{33} (mJy) (5)	S_{24} (Jy) (6)	S_{70} (Jy) (7)	S_{100} (Jy) (8)	α_{3-15} (9)	α_{15-33} (10)	$f_{\rm th}$ (%) (11)	$f_{\rm th}^{\rm fit}$ (%) (12)
NGC0958_2	SF	0.24 ± 0.13	0.23 ± 0.05			0.29 ± 0.01	0.57 ± 0.03	−0.05 ± −0.84			
NGC0958_3	AGN/SBnuc	0.01 ± 0.13	0.23 ± 0.05			0.31 ± 0.02	0.69 ± 0.03	1.7 ± −12.43			
NGC0958_4	SF	0.3 ± 0.13	0.24 ± 0.05			0.23 ± 0.01	0.41 ± 0.02	−0.15 ± −0.71			
NGC0958_5	SF	0.65 ± 0.16	0.43 ± 0.07		0.01 ± 0	0.57 ± 0.03	1.04 ± 0.05	−0.26 ± −0.43			
NGC1068_1	AGN	1007.09 ± 100.72	235.3 ± 23.53	114.22 ± 11.48		51.69 ± 2.59	0	−0.9 ± −0.09	−0.92 ± −0.18	0	0
NGC1614_1	SBnuc	35.45 ± 3.55	12.35 ± 1.24	7.84 ± 0.81	2.71 ± 0.14	16.5 ± 0.83	15.16 ± 0.76	−0.66 ± −0.09	−0.58 ± −0.18	44 ± 26	50 ± 3
NGC1797_1	SBnuc	8.54 ± 0.89	3.1 ± 0.32	2.3 ± 0.33	0.7 ± 0.03	7.14 ± 0.36	8.24 ± 0.41	−0.63 ± −0.09	−0.38 ± −0.22	69 ± 27	60 ± 5
NGC3110_1	SF	1.57 ± 0.24	0.61 ± 0.08	0.41 ± 0.17	0.05 ± 0	0.53 ± 0.03	122.38 ± 6.15	−0.59 ± −0.13	−0.5 ± −0.56	54 ± 46	63 ± 3
NGC3110_2	SBnuc	7.06 ± 0.74	2.87 ± 0.29	1.95 ± 0.28	0.25 ± 0.01	3.98 ± 0.2	996.48 ± 49.84	−0.56 ± −0.09	−0.49 ± −0.22	55 ± 30	65 ± 6
NGC4418_1	AGN/SBnuc	16.43 ± 1.65	8.25 ± 0.87	4.16 ± 0.45	0.68 ± 0.03	22.22 ± 1.11	17.39 ± 0.87	−0.43 ± −0.09	−0.87 ± −0.19	0	61 ± 28
NGC5104_1	AGN/SBnuc	8.06 ± 0.85	2.33 ± 0.24	1.57 ± 0.21	0.24 ± 0.01	3.97 ± 0.2	5.51 ± 0.28	−0.77 ± −0.09	−0.5 ± −0.22	54 ± 29	38 ± 5
NGC5257_1	SF	1.52 ± 0.24	0.73 ± 0.09	0.55 ± 0.12	0.09 ± 0	0.69 ± 0.04	0.83 ± 0.04	−0.45 ± −0.12	−0.37 ± −0.32	71 ± 29	78 ± 6
NGC5257_2	SBnuc	1.54 ± 0.24	0.82 ± 0.09	0.48 ± 0.12	0.04 ± 0	0.69 ± 0.03	1.15 ± 0.06	−0.39 ± −0.12	−0.68 ± −0.35	29 ± 29	77 ± 23
NGC5258_1	SF	2.91 ± 0.34	1.22 ± 0.13	0.95 ± 0.14	0.15 ± 0.01	1.59 ± 0.08	2.1 ± 0.11	−0.54 ± −0.1	−0.32 ± −0.23	77 ± 23	71 ± 4
NGC5331_1	SBnuc	5.77 ± 0.61	1.69 ± 0.18	1.21 ± 0.16	0.14 ± 0.01	2.65 ± 0.13	3.73 ± 0.19	−0.76 ± −0.09	−0.43 ± −0.22	63 ± 28	42 ± 8
NGC5331_2	SBnuc	1.67 ± 0.27	0.45 ± 0.07	0.29 ± 0.11	0.04 ± 0	0.52 ± 0.03	0.85 ± 0.04	−0.82 ± −0.14	−0.54 ± −0.53	49 ± 49	21 ± 4
NGC5936_1	Bg	8.21 ± 0.87	1.49 ± 0.16	0.65 ± 0.17	0.37 ± 0.02	3.31 ± 0.17	4.1 ± 0.21	−1.06 ± −0.09	−1.05 ± −0.35	0	0
NGC5936_2	Bg	6.93 ± 0.74	1.34 ± 0.15	0.59 ± 0.16	0	0.07 ± 0	0.18 ± 0.01	−1.02 ± −0.1	−1.04 ± −0.38	0	0
NGC5936_3	AGN/SBnuc	5.95 ± 0.65	1.95 ± 0.2	1.32 ± 0.2	0	−0.02 ± 0	0.02 ± 0	−0.69 ± −0.09	−0.49 ± −0.24	56 ± 31	49 ± 3
NGC5990_1	AGN	8.21 ± 0.85	2.79 ± 0.29	2.05 ± 0.27	0.56 ± 0.03	4.66 ± 0.23	5.76 ± 0.29	−0.67 ± −0.09	−0.39 ± −0.21	68 ± 26	56 ± 7
NGC6240_1	AGN	64.19 ± 6.43	19.8 ± 1.98	11.76 ± 1.24	1.39 ± 0.07	12.46 ± 0.62	12.07 ± 0.6	−0.73 ± −0.09	−0.66 ± −0.18	31 ± 28	35 ± 1
NGC6926_1	SF	2.29 ± 0.32	0.65 ± 0.11	0.7 ± 0.19	0.03 ± 0	0.46 ± 0.02	0.78 ± 0.04	−0.78 ± −0.14	0.1 ± −0.41	100	48 ± 28
NGC6926_2	AGN	4.55 ± 0.49	2.11 ± 0.22	1.2 ± 0.19	0.05 ± 0	0.51 ± 0.03	0.76 ± 0.04	−0.48 ± −0.09	−0.71 ± −0.25	23 ± 23	66 ± 22
NGC6926_3	SF	2.37 ± 0.3	0.67 ± 0.1	0.47 ± 0.16	0.06 ± 0	0.81 ± 0.04	1.1 ± 0.06	−0.78 ± −0.12	−0.45 ± −0.47	61 ± 39	32 ± 6
NGC7469_1	AGN	56.93 ± 5.71	17.98 ± 1.8	9.61 ± 1	1.98 ± 0.1	20.33 ± 1.02	22.42 ± 1.12	−0.72 ± −0.09	−0.8 ± −0.18	9 ± 9	28 ± 4
NGC7591_1	AGN/SBnuc	8.23 ± 0.86	2.65 ± 0.27	1.53 ± 0.27	0.26 ± 0.01	3.78 ± 0.19	4.71 ± 0.24	−0.7 ± −0.09	−0.7 ± −0.26	25 ± 25	38 ± 4
NGC7592_1	SBnuc	5.22 ± 0.56	2.29 ± 0.24	1.81 ± 0.29	0.13 ± 0.01	2.44 ± 0.12	2.79 ± 0.14	−0.51 ± −0.09	−0.3 ± −0.24	79 ± 21	74 ± 4
NGC7592_2	AGN	7.78 ± 0.81	3.2 ± 0.33	2.04 ± 0.3	0.23 ± 0.01	1.62 ± 0.08	1.75 ± 0.09	−0.55 ± −0.09	−0.57 ± −0.23	44 ± 32	63 ± 10
NGC7674_1	AGN	47.16 ± 4.74	10.18 ± 1.02	4.47 ± 0.5	0.71 ± 0.04	1.75 ± 0.09	1.7 ± 0.08	−0.95 ± −0.09	−1.04 ± −0.19	0	0
NGC7679_1	AGN	7.2 ± 0.79	3.75 ± 0.39	3.02 ± 0.4	0.46 ± 0.02	4.27 ± 0.21	4.79 ± 0.24	−0.41 ± −0.09	−0.27 ± −0.21	82 ± 18	83 ± 1
UGC02238_1	AGN/SBnuc	13.82 ± 1.4	3.8 ± 0.38	2.59 ± 0.32	0.2 ± 0.01	857.96 ± 42.9	7.02 ± 0.35	−0.8 ± −0.09	−0.48 ± −0.2	56 ± 27	34 ± 7
UGC02369_1	AGN/SBnuc	10.57 ± 1.07	3.01 ± 0.31	1.74 ± 0.26	0.51 ± 0.03	4.27 ± 0.21	4.78 ± 0.24	−0.78 ± −0.09	−0.7 ± −0.23	26 ± 26	25 ± 0
UGC02369_2	SBnuc	0.57 ± 0.16	0.55 ± 0.08	0.46 ± 0.19	0	0.08 ± 0	0.24 ± 0.01	−0.02 ± −0.2	−0.21 ± −0.56	89 ± 11	100
UGC02982_1	SBnuc	7.44 ± 0.78	2.52 ± 0.26	1.82 ± 0.27	0.16 ± 0.01	3.02 ± 0.15	4.38 ± 0.22	−0.67 ± −0.09	−0.41 ± −0.23	66 ± 29	54 ± 6
UGC03094_1	AGN	3.82 ± 0.45	2.21 ± 0.23	1.69 ± 0.26	0.17 ± 0.01	1.99 ± 0.1	2.76 ± 0.14	−0.34 ± −0.1	−0.34 ± −0.23	74 ± 26	86 ± 14

NOTE — Photometry are performed on 3, 15 and 33 GHz VLA images, 24μm Spitzer and 70, 100μm Herschel images, all smoothed to a common circular Gaussian beam with FWHM = 7″, determined by the native resolution of 100μm images. (1): Region identifier including the host galaxy name (2): Region type indicating the most likely source for the detected radio emission. (3): 3 GHz flux density. (4): 15 GHz flux density. (5): 33 GHz flux density. (6): 24μ flux density. (7): 70μ flux density. (8): 100μ flux density. (9): Measured 3 - 15 GHz spectral index. (10): Measured 15 - 33 GHz spectral index. (11) Thermal fraction at 33 GHz derived from (9). (12) Thermal fraction at 33 GHz derived from spectral fitting, assuming a two component power-law (thermal free-free, synchrotron).

Chapter 6

Summary

Using multi-frequency VLA radio continuum observations of a representative sample of local U/LIRGs from the GOALS Equatorial VLA Survey (GOALS-ES; Chapter 2), we have investigated the most energetic star-forming and AGN activity in these most extreme star-forming systems on both $\sim$100 pc and kpc scales. As presented in Chapter 5, we found that the $\sim$kpc-scale radio emission from star-forming structures in these local U/LIRGs to be well correlated with MIR and FIR emission as observed by Spitzer and Herschel, which extends the correlations widely-observed on unresolved scales and confirm that both radio and IR emission from these structures are tracing massive star formation. This is directly supported by the fact that the same structures have relatively flat 3 – 33 GHz radio spectra, with prominent spectral flattening towards 33 GHz, indicating that their 3 – 33 GHz radio continuum emission contain higher contribution from thermal free-free emission from HII regions that become dominant at 33 GHz.

Using the 33 GHz continuum as an extinction-free tracer of SFR, we characterized the properties of four star-forming nuclear rings detected in the GOALS-ES and compared them with those derived for five nuclear rings in nearby normal galaxies that have been observed in the Star Formation in Radio Survey (SFRS; Murphy et al., 2018; Linden et al., 2020), in Chapter 3. We found that nuclear rings in these four local U/LIRGs contribute more than half of the total SFR of the host galaxies as traced by IR and UV emission, where in the normal galaxies the nuclear rings only account for a moderate fraction of the total SFR. Due to the high resolutions of our 33 GHz observations, we were able to characterize the sizes and SFR of individual star-forming regions in these rings on 100 pc scales. These regions not only have 10 times higher SFR relative to nuclear ring regions in the normal galaxies with similar sizes, but their SFR surface density also rival star-forming clumps observed in lensed high-z galaxies that have larger sizes.

Extending the ~ 100 pc-scale study to the entire GOALS-ES sample in Chapter 4, we characterized over 100 regions of compact radio continuum emission at 15 and/or 33 GHz. After classifying these regions into different types based on multi-wavelength AGN identifications of the host galaxies based on the literature, we found that AGN-dominated and AGN-starburst composite nuclei in local U/LIRGs have up to 3 dex higher 33 GHz luminosity and surface density relative to starburst-dominated nuclei and star-forming clumps. Comparisons with models for radiation pressure supported starbursts (Thompson et al., 2005) indicate that such elevated 33 GHz emission in the former could be associated with intense nuclear starburst activity, but comparisons with X-ray and MIR AGN diagnostics measured on $\sim$ kpc scales also indicate AGN contribution, especially in nuclei with the highest 33 GHz luminosities. When only focusing on the star-forming nuclei and clumps, we found their $15 - 33$ GHz spectra to be overall steeper than those in nearby normal galaxies identified in the SFRS, possibly suggesting relatively lower contribution from thermal free-free emission. Nevertheless, the SFR and surface densities derived for these regions in local U/LIRGs are ~ 100 times higher than those in normal galaxies, even after accounting for the comparatively low estimates for thermal contribution. Comparison between SFR derived using thermal radio emission and NIR hydrogen recombination lines yield largely consistent results considering dust extinction of the NIR emission, which confirms the utility of thermal radio continuum emission as an extinction-free tracer of recent massive star formation.

This dissertation has revealed the prevalence of extreme star-forming activity in local U/LIRGs on the scales of giant molecular clouds, which are the fundamental building blocks of star-forming galaxies. Much work remains to be done to better understand what drives the molecular clouds in local U/LIRGs to form stars at rates ~ 100 times faster than those in nearby normal galaxies. Molecular gas observations at matched resolutions with ALMA, NOEMA and the SMA will provide critical information on the temperature, density, kinematics and chemical composition of the star-forming gas clouds in local U/LIRGs and shed light on this matter. The large amount of available archival ALMA data already provides such opportunity, which is further complemented by the public release of the Physics at High Angular resolution in Nearby Galaxies (PHANGS) survey which have revealed the environmental dependence of cloud properties in nearby normal galaxies (e.g. Sun et al., 2018, 2022). Meanwhile, our studies also show that many local U/LIRGs host even more extreme activity in their nuclei that may be powered by intense nuclear starburst at maximal capacity and/or heavily-obscured AGN activity. These nuclei provide ideal opportunities for investigating the interplay between AGN and nuclear star formation in the evolution of massive galaxies for both mergers and non-mergers. Follow-up VLBI observations will be crucial for direct identification of AGN on 1 pc scales and isolating its contribution to the observed radio emission from surrounding starburst. Upcoming observations with the JWST will unveil the physical conditions of the dust, ionized and warm molecular gas at matched physical resolution with our radio observations and allow us to study the effect of such intense nuclear activity on their local environments, and subsequently the evolution of their host systems.

References

Adams, T. F. 1972, The Astrophysical Journal Letters, 176, L1

Aird, J., Nandra, K., Laird, E. S., et al. 2010, Monthly Notices of the Royal Astronomical Society, 401, 2531

Algera, H. S. B., Hodge, J. A., Riechers, D. A., et al. 2021, arXiv e-prints, arXiv:2111.01153

Allard, E. L., Knapen, J. H., Peletier, R. F., & Sarzi, M. 2006, Monthly Notices of the Royal Astronomical Society, 371, 1087

Alonso-Herrero, A., Engelbracht, C. W., Rieke, M. J., Rieke, G. H., & Quillen, A. C. 2001a, The Astrophysical Journal, 546, 952

—. 2001b, The Astrophysical Journal, 546, 952

Alonso-Herrero, A., García-Marín, M., Monreal-Ibero, A., et al. 2009, Astronomy and Astrophysics, 506, 1541

Alonso-Herrero, A., Pereira-Santaella, M., Rieke, G. H., & Rigopoulou, D. 2012, The Astrophysical Journal, 744, 2

Alonso-Herrero, A., Rieke, G. H., Rieke, M. J., et al. 2006, The Astrophysical Journal, 650, 835

Alonso-Herrero, A., Rieke, G. H., Rieke, M. J., & Scoville, N. Z. 2002, The Astronomical Journal, 124, 166

Aniano, G., Draine, B. T., Gordon, K. D., & Sandstrom, K. 2011, Publications of the Astronomical Society of the Pacific, 123, 1218

Armus, L., Heckman, T., & Miley, G. 1987, The Astronomical Journal, 94, 831

Armus, L., Charmandaris, V., Spoon, H. W. W., et al. 2004, The Astrophysical Journal Supplement Series, 154, 178

Armus, L., Bernard-Salas, J., Spoon, H. W. W., et al. 2006, The Astrophysical Journal, 640, 204

Armus, L., Mazzarella, J. M., Evans, A. S., et al. 2009, Publications of the Astronomical Society of the Pacific, 121, 559

Athanassoula, E. 1994, in Mass-Transfer Induced Activity in Galaxies, ed. I. Shlosman, 143

Baan, W. A., & Klöckner, H. R. 2006, Astronomy and Astrophysics, 449, 559

Baba, S., Imanishi, M., Izumi, T., et al. 2022, The Astrophysical Journal, 928, 184

Balzano, V. A. 1983, The Astrophysical Journal, 268, 602

Barcos-Muñoz, L., Leroy, A. K., Evans, A. S., et al. 2015, The Astrophysical Journal, 799, 10

—. 2017, The Astrophysical Journal, 843, 117

Barcos-Muñoz, L., Aalto, S., Thompson, T. A., et al. 2018, The Astrophysical Journal Letters, 853, L28

Barnes, J. E., & Hernquist, L. 1992, Annual Review of Astronomy and Astrophysics, 30, 705

Barr, P. 1986, Monthly Notices of the Royal Astronomical Society, 223, 29P

Barreto, J. A., Downes, D., Combes, F., et al. 1991, Astronomy and Astrophysics, 244, 257

Becker, R. H., White, R. L., & Helfand, D. J. 1994, in Astronomical Society of the Pacific Conference Series, Vol. 61, Astronomical Data Analysis Software and Systems III, ed. D. R. Crabtree, R. J. Hanisch, & J. Barnes, 165

Beckman, J. E., Rozas, M., Zurita, A., Watson, R. A., & Knapen, J. H. 2000, The Astronomical Journal, 119, 2728

Bell, E. F. 2003, The Astrophysical Journal, 586, 794

Bendo, G. J., Henkel, C., D'Cruze, M. J., et al. 2016, Monthly Notices of the Royal Astronomical Society, 463, 252

Bigiel, F., Leroy, A., Walter, F., et al. 2008, The Astronomical Journal, 136, 2846

Blandford, R., Meier, D., & Readhead, A. 2019, Annual Review of Astronomy and Astrophysics, 57, 467

Böker, T., Falcón-Barroso, J., Schinnerer, E., Knapen, J. H., & Ryder, S. 2008, The Astronomical Journal, 135, 479

Boker, T., Forster-Schreiber, N. M., & Genzel, R. 1997, The Astronomical Journal, 114, 1883

Bowen, D. V., Chelouche, D., Jenkins, E. B., et al. 2016, The Astrophysical Journal, 826, 50

Bradley, L., Sipőcz, B., Robitaille, T., et al. 2022, astropy/photutils:, v.1.4.0, Zenodo, doi:10.5281/zenodo.6385735

Bridle, A. H., & Perley, R. A. 1984, Annual Review of Astronomy and Astrophysics, 22, 319

Brown, M. J. I., Moustakas, J., Smith, J. D. T., et al. 2014, The Astrophysical Journal Supplement Series, 212, 18

Burbidge, E. M., Burbidge, G. R., Fowler, W. A., & Hoyle, F. 1957, Reviews of Modern Physics, 29, 547

Bushouse, H. A. 1986, The Astronomical Journal, 91, 255

Buta, R., & Combes, F. 1996, , 17, 95

Buta, R., Treuthardt, P. M., Byrd, G. G., & Crocker, D. A. 2000, The Astronomical Journal, 120, 1289

Casasola, V., Hunt, L., Combes, F., & García-Burillo, S. 2015, Astronomy and Astrophysics, 577, A135

Cazzoli, S., Arribas, S., Maiolino, R., & Colina, L. 2016, Astronomy and Astrophysics, 590, A125

Chambers, K. C., Magnier, E. A., Metcalfe, N., et al. 2016, arXiv e-prints, arXiv:1612.05560

Chapman, S. C., Blain, A. W., Smail, I., & Ivison, R. J. 2005, The Astrophysical Journal, 622, 772

Chary, R., & Elbaz, D. 2001, The Astrophysical Journal, 556, 562

Chu, J. K., Sanders, D. B., Larson, K. L., et al. 2017, The Astrophysical Journal Supplement Series, 229, 25

Clark, C. J. R., Verstocken, S., Bianchi, S., et al. 2018, Astronomy and Astrophysics, 609, A37

Clemens, M. S., Vega, O., Bressan, A., et al. 2008, Astronomy and Astrophysics, 477, 95

Colina, L., Piqueras López, J., Arribas, S., et al. 2015, Astronomy and Astrophysics, 578, A48

Combes, F. 2001, in Advanced Lectures on the Starburst-AGN, ed. I. Aretxaga, D. Kunth, & R. Mújica, 223

Combes, F., & Gerin, M. 1985, Astronomy and Astrophysics, 150, 327

Comerón, S., Knapen, J. H., Beckman, J. E., et al. 2010, Monthly Notices of the Royal Astronomical Society, 402, 2462

Condon, J. J. 1992, Annual Review of Astronomy and Astrophysics, 30, 575

Condon, J. J., Anderson, E., & Broderick, J. J. 1995, The Astronomical Journal, 109, 2318

Condon, J. J., & Broderick, J. J. 1991, The Astronomical Journal, 102, 1663

Condon, J. J., Cotton, W. D., Greisen, E. W., et al. 1998, The Astronomical Journal, 115, 1693

Condon, J. J., Helou, G., Sanders, D. B., & Soifer, B. T. 1990, The Astrophysical Journal Supplement Series, 73, 359

Condon, J. J., Huang, Z. P., Yin, Q. F., & Thuan, T. X. 1991, The Astrophysical Journal, 378, 65

Corbett, E. A., Norris, R. P., Heisler, C. A., et al. 2002, The Astrophysical Journal, 564, 650

Corbett, E. A., Kewley, L., Appleton, P. N., et al. 2003, The Astrophysical Journal, 583, 670

Cosens, M., Wright, S. A., Mieda, E., et al. 2018, The Astrophysical Journal, 869, 11

Crosthwaite, L. P. 2001, PhD thesis, University of California, Los Angeles

Crosthwaite, L. P., Turner, J. L., Hurt, R. L., et al. 2001, The Astronomical Journal, 122, 797

Daddi, E., Elbaz, D., Walter, F., et al. 2010, The Astrophysical Journal Letters, 714, L118

Dale, D. A., Giovanelli, R., Haynes, M. P., et al. 1997, The Astronomical Journal, 114, 455

Dale, D. A., Smith, J. D. T., Armus, L., et al. 2006, The Astrophysical Journal, 646, 161

Dale, D. A., Smith, J. D. T., Schlawin, E. A., et al. 2009, The Astrophysical Journal, 693, 1821

Davies, R. I., Tacconi, L. J., & Genzel, R. 2004, The Astrophysical Journal, 602, 148

de Jong, T., Klein, U., Wielebinski, R., & Wunderlich, E. 1985, Astronomy and Astrophysics, 147, L6

de los Reyes, M. A. C., & Kennicutt, Robert C., J. 2019, The Astrophysical Journal, 872, 16

Della Ceca, R., Pellegrini, S., Bassani, L., et al. 2001, Astronomy and Astrophysics, 375, 781

Delvecchio, I., Gruppioni, C., Pozzi, F., et al. 2014, Monthly Notices of the Royal Astronomical Society, 439, 2736

Devereux, N. A., Kenney, J. D., & Young, J. S. 1992, The Astronomical Journal, 103, 784

Di Matteo, T., Springel, V., & Hernquist, L. 2005, Nature, 433, 604

Díaz-Santos, T., Charmandaris, V., Armus, L., et al. 2010, The Astrophysical Journal, 723, 993

—. 2011, The Astrophysical Journal, 741, 32

Díaz-Santos, T., Armus, L., Charmandaris, V., et al. 2017, The Astrophysical Journal, 846, 32

Dickinson, C., Ali-Haïmoud, Y., Barr, A., et al. 2018, , 80, 1

Dopita, M. A., Armus, L., Kewley, L. J., et al. 2011, , 333, 225

Downes, D., & Solomon, P. M. 1998, The Astrophysical Journal, 507, 615

Downes, D., Solomon, P. M., & Radford, S. J. E. 1993, The Astrophysical Journal Letters, 414, L13

Duc, P. A., Mirabel, I. F., & Maza, J. 1997, Astronomy and Astrophysics Supplement Series, 124, 533

Elbaz, D., Dickinson, M., Hwang, H. S., et al. 2011, Astronomy and Astrophysics, 533, A119

Emig, K. L., Bolatto, A. D., Leroy, A. K., et al. 2020, The Astrophysical Journal, 903, 50

Englmaier, P., & Shlosman, I. 2004, The Astrophysical Journal Letters, 617, L115

Falstad, N., González-Alfonso, E., Aalto, S., et al. 2015, Astronomy and Astrophysics, 580, A52

Falstad, N., Aalto, S., König, S., et al. 2021, Astronomy and Astrophysics, 649, A105

Faucher-Giguère, C.-A., Quataert, E., & Hopkins, P. F. 2013, Monthly Notices of the Royal Astronomical Society, 433, 1970

Fitzgibbon, A. W., Pilu, M., & Fisher, R. B. 1996, in Proceedings of 13th International Conference on Pattern Recognition, Vol. 1, 253–257 vol.1

Flewelling, H. A., Magnier, E. A., Chambers, K. C., et al. 2020, The Astrophysical Journal Supplement Series, 251, 7

Fluetsch, A., Maiolino, R., Carniani, S., et al. 2019, Monthly Notices of the Royal Astronomical Society, 483, 4586

—. 2020, arXiv e-prints, arXiv:2006.13232

Freiburghaus, C., Rosswog, S., & Thielemann, F. K. 1999, The Astrophysical Journal Letters, 525, L121

Fukuda, H., Wada, K., & Habe, A. 1998, Monthly Notices of the Royal Astronomical Society, 295, 463

Galametz, M., Kennicutt, R. C., Calzetti, D., et al. 2013, Monthly Notices of the Royal Astronomical Society, 431, 1956

Gallimore, J. F., Baum, S. A., & O'Dea, C. P. 2004, The Astrophysical Journal, 613, 794

Gallimore, J. F., Baum, S. A., O'Dea, C. P., & Pedlar, A. 1996, The Astrophysical Journal, 458, 136

Gandhi, P., Annuar, A., Lansbury, G. B., et al. 2017, Monthly Notices of the Royal Astronomical Society, 467, 4606

García-Burillo, S., Combes, F., Hunt, L. K., et al. 2003, Astronomy and Astrophysics, 407, 485

Garofali, K., Lehmer, B. D., Basu-Zych, A., et al. 2020, The Astrophysical Journal, 903, 79

Genzel, R., Tacconi, L. J., Rigopoulou, D., Lutz, D., & Tecza, M. 2001, The Astrophysical Journal, 563, 527

Genzel, R., Weitzel, L., Tacconi-Garman, L. E., et al. 1995, The Astrophysical Journal, 444, 129

Genzel, R., Tacconi, L. J., Gracia-Carpio, J., et al. 2010, Monthly Notices of the Royal Astronomical Society, 407, 2091

González-Alfonso, E., & Sakamoto, K. 2019, The Astrophysical Journal, 882, 153

González-Martín, O., Masegosa, J., Márquez, I., Guainazzi, M., & Jiménez-Bailón, E. 2009, Astronomy and Astrophysics, 506, 1107

Grier, C. J., Mathur, S., Ghosh, H., & Ferrarese, L. 2011, The Astrophysical Journal, 731, 60

Grimes, J. P., Heckman, T., Hoopes, C., et al. 2006, The Astrophysical Journal, 648, 310

Gruppioni, C., Pozzi, F., Rodighiero, G., et al. 2013, Monthly Notices of the Royal Astronomical Society, 432, 23

Haan, S., Armus, L., Surace, J. A., et al. 2013, Monthly Notices of the Royal Astronomical Society, 434, 1264

Hayashi, T. J., Hagiwara, Y., & Imanishi, M. 2021, Monthly Notices of the Royal Astronomical Society, 504, 2675

Helou, G., Soifer, B. T., & Rowan-Robinson, M. 1985, The Astrophysical Journal Letters, 298, L7

Herrero-Illana, R., Alberdi, A., Pérez-Torres, M. Á., et al. 2017, Monthly Notices of the Royal Astronomical Society, 470, L112

Herrero-Illana, R., Pérez-Torres, M. Á., Alonso-Herrero, A., et al. 2014, The Astrophysical Journal, 786, 156

Herrero-Illana, R., Privon, G. C., Evans, A. S., et al. 2019, Astronomy and Astrophysics, 628, A71

Hinshaw, G., Weiland, J. L., Hill, R. S., et al. 2009, The Astrophysical Journal Supplement Series, 180, 225

Ho, L. C., Filippenko, A. V., & Sargent, W. L. W. 1997, The Astrophysical Journal Supplement Series, 112, 315

Hollenbach, D. J., & Tielens, A. G. G. M. 1999, Reviews of Modern Physics, 71, 173

Hopkins, P. F., Hernquist, L., Cox, T. J., et al. 2006, The Astrophysical Journal Supplement Series, 163, 1

Hopkins, P. F., & Quataert, E. 2010, Monthly Notices of the Royal Astronomical Society, 407, 1529

Howell, J. H., Armus, L., Mazzarella, J. M., et al. 2010, The Astrophysical Journal, 715, 572

Hoyle, F., & Fowler, W. A. 1960, The Astrophysical Journal, 132, 565

Hsieh, P.-Y., Matsushita, S., Liu, G., et al. 2011, The Astrophysical Journal, 736, 129

Hughes, A., Wong, T., Ekers, R., et al. 2006, Monthly Notices of the Royal Astronomical Society, 370, 363

Imanishi, M., Nakagawa, T., Shirahata, M., Ohyama, Y., & Onaka, T. 2010, The Astrophysical Journal, 721, 1233

Inami, H., Armus, L., Surace, J. A., et al. 2010, The Astronomical Journal, 140, 63

Inami, H., Armus, L., Charmandaris, V., et al. 2013, The Astrophysical Journal, 777, 156

Inami, H., Armus, L., Matsuhara, H., et al. 2018, Astronomy and Astrophysics, 617, A130

Iono, D., Saito, T., Yun, M. S., et al. 2013, Publications of the Astronomical Society of Japan, 65, L7

Ishizuki, S., Kawabe, R., Ishiguro, M., Okumura, S. K., & Morita, K.-I. 1990, Nature, 344, 224

Ivison, R. J., Magnelli, B., Ibar, E., et al. 2010, Astronomy and Astrophysics, 518, L31

Iwasawa, K., Sanders, D. B., Evans, A. S., et al. 2009, The Astrophysical Journal Letters, 695, L103

Iwasawa, K., Sanders, D. B., Teng, S. H., et al. 2011, Astronomy and Astrophysics, 529, A106

Jarrett, T. H., Chester, T., Cutri, R., et al. 2000, The Astronomical Journal, 119, 2498

Jin, J.-J., Zhu, Y.-N., Wu, H., et al. 2019, The Astrophysical Journal Supplement Series, 244, 33

Jog, C. J., & Solomon, P. M. 1992, The Astrophysical Journal, 387, 152

Johnson, J. A. 2019, Science, 363, 474

Karakas, A. I., & Lattanzio, J. C. 2014, , 31, e030

Kellermann, K. I., Sramek, R., Schmidt, M., Shaffer, D. B., & Green, R. 1989, The Astronomical Journal, 98, 1195

Kenney, J. D. P., & Lord, S. D. 1991, The Astrophysical Journal, 381, 118

Kennicutt, Robert C., J. 1998, The Astrophysical Journal, 498, 541

Kennicutt, Robert C., J., & de los Reyes, M. A. C. 2020, arXiv e-prints, arXiv:2012.05363

Kennicutt, Robert C., J., Armus, L., Bendo, G., et al. 2003, Publications of the Astronomical Society of the Pacific, 115, 928

Kennicutt, R. C., Calzetti, D., Aniano, G., et al. 2011, Publications of the Astronomical Society of the Pacific, 123, 1347

Kessler, M. F., Steinz, J. A., Anderegg, M. E., et al. 1996, Astronomy and Astrophysics, 315, L27

Kharb, P., Lal, D. V., & Merritt, D. 2017, Nature Astronomy, 1, 727

Kim, C.-G., & Ostriker, E. C. 2015, The Astrophysical Journal, 815, 67

Kim, D. C., Evans, A. S., Vavilkin, T., et al. 2013, The Astrophysical Journal, 768, 102

Kim, W.-T., & Stone, J. M. 2012, The Astrophysical Journal, 751, 124

Klein, U., Lisenfeld, U., & Verley, S. 2018, Astronomy and Astrophysics, 611, A55

Knapen, J. H. 2005, Astronomy and Astrophysics, 429, 141

Knapen, J. H., Beckman, J. E., Heller, C. H., Shlosman, I., & de Jong, R. S. 1995, The Astrophysical Journal, 454, 623

Knapen, J. H., Whyte, L. F., de Blok, W. J. G., & van der Hulst, J. M. 2004, Astronomy and Astrophysics, 423, 481

König, S., Aalto, S., Muller, S., Beswick, R. J., & Gallagher, J. S. 2013, Astronomy and Astrophysics, 553, A72

Kormendy, J., & Ho, L. C. 2013, Annual Review of Astronomy and Astrophysics, 51, 511

Kormendy, J., & Kennicutt, Robert C., J. 2004, Annual Review of Astronomy and Astrophysics, 42, 603

Korobkin, O., Rosswog, S., Arcones, A., & Winteler, C. 2012, Monthly Notices of the Royal Astronomical Society, 426, 1940

Koss, M., Mushotzky, R., Baumgartner, W., et al. 2013, The Astrophysical Journal Letters, 765, L26

Koss, M. J., Blecha, L., Bernhard, P., et al. 2018, Nature, 563, 214

Lacki, B. C., & Thompson, T. A. 2010, The Astrophysical Journal, 717, 196

Lacki, B. C., Thompson, T. A., & Quataert, E. 2010, The Astrophysical Journal, 717, 1

Larson, K. L., Sanders, D. B., Barnes, J. E., et al. 2016, The Astrophysical Journal, 825, 128

Larson, K. L., Díaz-Santos, T., Armus, L., et al. 2020, The Astrophysical Journal, 888, 92

Larson, R. B., & Tinsley, B. M. 1978, The Astrophysical Journal, 219, 46

Laurikainen, E., & Salo, H. 2002, Monthly Notices of the Royal Astronomical Society, 337, 1118

Le Floc'h, E., Papovich, C., Dole, H., et al. 2005, The Astrophysical Journal, 632, 169

Leaman, R., Fragkoudi, F., Querejeta, M., et al. 2019, Monthly Notices of the Royal Astronomical Society, 488, 3904

Leroy, A. K., Evans, A. S., Momjian, E., et al. 2011, The Astrophysical Journal Letters, 739, L25

Leroy, A. K., Walter, F., Sandstrom, K., et al. 2013, The Astronomical Journal, 146, 19

Li, Z., Shen, J., & Kim, W.-T. 2015, The Astrophysical Journal, 806, 150

Linden, S., Evans, A., Larson, K., et al. 2021, arXiv e-prints, arXiv:2110.03638

Linden, S. T., Murphy, E. J., Dong, D., et al. 2020, The Astrophysical Journal Supplement Series, 248, 25

Linden, S. T., Evans, A. S., Rich, J., et al. 2017, The Astrophysical Journal, 843, 91

Linden, S. T., Song, Y., Evans, A. S., et al. 2019, The Astrophysical Journal, 881, 70

Livermore, R. C., Jones, T., Richard, J., et al. 2012, Monthly Notices of the Royal Astronomical Society, 427, 688

Livermore, R. C., Jones, T. A., Richard, J., et al. 2015, Monthly Notices of the Royal Astronomical Society, 450, 1812

Lonsdale, C. J., Diamond, P. J., Thrall, H., Smith, H. E., & Lonsdale, C. J. 2006, The Astrophysical Journal, 647, 185

Lonsdale, C. J., Lonsdale, C. J., Smith, H. E., & Diamond, P. J. 2003, The Astrophysical Journal, 592, 804

Lonsdale, C. J., Persson, S. E., & Matthews, K. 1984, The Astrophysical Journal, 287, 95

Lutz, D., Shimizu, T., Davies, R. I., et al. 2018, Astronomy and Astrophysics, 609, A9

Ma, C., de Grijs, R., & Ho, L. C. 2018, The Astrophysical Journal, 857, 116

Madau, P., & Dickinson, M. 2014, Annual Review of Astronomy and Astrophysics, 52, 415

Magnelli, B., Elbaz, D., Chary, R. R., et al. 2011, Astronomy and Astrophysics, 528, A35

Magnelli, B., Popesso, P., Berta, S., et al. 2013, Astronomy and Astrophysics, 553, A132

Magnelli, B., Ivison, R. J., Lutz, D., et al. 2015, Astronomy and Astrophysics, 573, A45

Maiolino, R., Comastri, A., Gilli, R., et al. 2003, Monthly Notices of the Royal Astronomical Society, 344, L59

Makarov, D., Prugniel, P., Terekhova, N., Courtois, H., & Vauglin, I. 2014, Astronomy and Astrophysics, 570, A13

Maoz, D., Barth, A. J., Ho, L. C., Sternberg, A., & Filippenko, A. V. 2001, The Astronomical Journal, 121, 3048

Maoz, D., Barth, A. J., Sternberg, A., et al. 1996, The Astronomical Journal, 111, 2248

Matthews, A. M., Condon, J. J., Cotton, W. D., & Mauch, T. 2021, The Astrophysical Journal, 914, 126

Mazzarella, J. M., Voit, G. M., Soifer, B. T., et al. 1994, The Astronomical Journal, 107, 1274

Mazzuca, L. M., Knapen, J. H., Veilleux, S., & Regan, M. W. 2008, The Astrophysical Journal Supplement Series, 174, 337

McConnell, N. J., & Ma, C.-P. 2013, The Astrophysical Journal, 764, 184

McKinney, J., Armus, L., Pope, A., et al. 2021, The Astrophysical Journal, 908, 238

McMullin, J. P., Waters, B., Schiebel, D., Young, W., & Golap, K. 2007, in Astronomical Society of the Pacific Conference Series, Vol. 376, Astronomical Data Analysis Software and Systems XVI, ed. R. A. Shaw, F. Hill, & D. J. Bell, 127

Medling, A. M., U, V., Rich, J. A., et al. 2015, Monthly Notices of the Royal Astronomical Society, 448, 2301

Medling, A. M., Kewley, L. J., Calzetti, D., et al. 2021, The Astrophysical Journal, 923, 160

Meyer, B. S., Mathews, G. J., Howard, W. M., Woosley, S. E., & Hoffman, R. D. 1992, The Astrophysical Journal, 399, 656

Migenes, V., Coziol, R., Cooprider, K., et al. 2011, Monthly Notices of the Royal Astronomical Society, 416, 1267

Mihos, J. C., & Hernquist, L. 1996, The Astrophysical Journal, 464, 641

Molnár, D. C., Sargent, M. T., Leslie, S., et al. 2021, Monthly Notices of the Royal Astronomical Society, 504, 118

Momjian, E., Romney, J. D., Carilli, C. L., & Troland, T. H. 2003a, The Astrophysical Journal, 597, 809

—. 2006, The Astrophysical Journal, 653, 1172

Momjian, E., Romney, J. D., Carilli, C. L., Troland, T. H., & Taylor, G. B. 2003b, The Astrophysical Journal, 587, 160

Moreno, J., Torrey, P., Ellison, S. L., et al. 2020, Monthly Notices of the Royal Astronomical Society, arXiv:2009.11289

—. 2021, Monthly Notices of the Royal Astronomical Society, 503, 3113

Morić, I., Smolčić, V., Kimball, A., et al. 2010, The Astrophysical Journal, 724, 779

Mould, J. R., Huchra, J. P., Freedman, W. L., et al. 2000, The Astrophysical Journal, 529, 786

Murphy, E. J. 2009, The Astrophysical Journal, 706, 482

—. 2013, The Astrophysical Journal, 777, 58

Murphy, E. J., Chary, R. R., Dickinson, M., et al. 2011a, The Astrophysical Journal, 732, 126

Murphy, E. J., Dong, D., Momjian, E., et al. 2018, The Astrophysical Journal Supplement Series, 234, 24

Murphy, E. J., Helou, G., Kenney, J. D. P., Armus, L., & Braun, R. 2008, The Astrophysical Journal, 678, 828

Murphy, E. J., Hensley, B. S., Linden, S. T., et al. 2020, The Astrophysical Journal Letters, 905, L23

Murphy, E. J., Helou, G., Braun, R., et al. 2006, The Astrophysical Journal Letters, 651, L111

Murphy, E. J., Condon, J. J., Schinnerer, E., et al. 2011b, The Astrophysical Journal, 737, 67

Murphy, E. J., Bremseth, J., Mason, B. S., et al. 2012, The Astrophysical Journal, 761, 97

Murray, N., Quataert, E., & Thompson, T. A. 2005, The Astrophysical Journal, 618, 569

Narayanan, D., Krumholz, M. R., Ostriker, E. C., & Hernquist, L. 2012, Monthly Notices of the Royal Astronomical Society, 421, 3127

Neugebauer, G., Habing, H. J., van Duinen, R., et al. 1984, The Astrophysical Journal Letters, 278, L1

Niklas, S., Klein, U., & Wielebinski, R. 1997, Astronomy and Astrophysics, 322, 19

Olsson, E., Aalto, S., Thomasson, M., & Beswick, R. 2010, Astronomy and Astrophysics, 513, A11

Osterbrock, D. E., & Martel, A. 1993, The Astrophysical Journal, 414, 552

Padovani, P., Alexander, D. M., Assef, R. J., et al. 2017, , 25, 2

Pan, H.-A., Kuno, N., & Hirota, A. 2014, Publications of the Astronomical Society of Japan, 66, 27

Panessa, F., Baldi, R. D., Laor, A., et al. 2019, Nature Astronomy, 3, 387

Parra, R., Conway, J. E., Diamond, P. J., et al. 2007, The Astrophysical Journal, 659, 314

Pereira-Santaella, M., Diamond-Stanic, A. M., Alonso-Herrero, A., & Rieke, G. H. 2010, The Astrophysical Journal, 725, 2270

Pereira-Santaella, M., Alonso-Herrero, A., Colina, L., et al. 2015, Astronomy and Astrophysics, 577, A78

Pereira-Santaella, M., Colina, L., García-Burillo, S., et al. 2016, Astronomy and Astrophysics, 587, A44

—. 2021, Astronomy and Astrophysics, 651, A42

Pérez-Torres, M., Mattila, S., Alonso-Herrero, A., Aalto, S., & Efstathiou, A. 2021, , 29, 2

Perna, M., Arribas, S., Catalán-Torrecilla, C., et al. 2020, Astronomy and Astrophysics, 643, A139

Petric, A. O., Armus, L., Howell, J., et al. 2011, The Astrophysical Journal, 730, 28

Phillips, M. M., Pagel, B. E. J., Edmunds, M. G., & Diaz, A. 1984, Monthly Notices of the Royal Astronomical Society, 210, 701

Pihlström, Y. M., Conway, J. E., Booth, R. S., Diamond, P. J., & Polatidis, A. G. 2001, Astronomy and Astrophysics, 377, 413

Piqueras López, J., Colina, L., Arribas, S., & Alonso-Herrero, A. 2013, Astronomy and Astrophysics, 553, A85

Piqueras López, J., Colina, L., Arribas, S., Pereira-Santaella, M., & Alonso-Herrero, A. 2016, Astronomy and Astrophysics, 590, A67

Planesas, P., Colina, L., & Perez-Olea, D. 1997, Astronomy and Astrophysics, 325, 81

Prieto, M. A., Fernandez-Ontiveros, J. A., Bruzual, G., et al. 2019, Monthly Notices of the Royal Astronomical Society, 485, 3264

Privon, G. C., Ricci, C., Aalto, S., et al. 2020, The Astrophysical Journal, 893, 149

Rabidoux, K., Pisano, D. J., Kepley, A. A., Johnson, K. E., & Balser, D. S. 2014, The Astrophysical Journal, 780, 19

Ranalli, P., Comastri, A., & Setti, G. 2003, Astronomy and Astrophysics, 399, 39

Rau, U., & Cornwell, T. J. 2011, Astronomy and Astrophysics, 532, A71

Regan, M. W., & Teuben, P. 2003, The Astrophysical Journal, 582, 723

Ricci, C., Bauer, F. E., Treister, E., et al. 2017, Monthly Notices of the Royal Astronomical Society, 468, 1273

Ricci, C., Privon, G. C., Pfeifle, R. W., et al. 2021, Monthly Notices of the Royal Astronomical Society, 506, 5935

Rich, J. A., Kewley, L. J., & Dopita, M. A. 2015, The Astrophysical Journal Supplement Series, 221, 28

Robitaille, T., Rice, T., Beaumont, C., et al. 2019, astrodendro: Astronomical data dendrogram creator, , , ascl:1907.016

Robitaille, T. P., & Whitney, B. A. 2010, The Astrophysical Journal Letters, 710, L11

Romeo, A. B., & Fathi, K. 2016, Monthly Notices of the Royal Astronomical Society, 460, 2360

Rupke, D. S., Veilleux, S., & Sanders, D. B. 2005, The Astrophysical Journal Supplement Series, 160, 87

Rush, B., Malkan, M. A., & Spinoglio, L. 1993, The Astrophysical Journal Supplement Series, 89, 1

Sage, L. J., & Solomon, P. M. 1991, The Astrophysical Journal, 380, 392

Sakamoto, K., Okumura, S., Minezaki, T., Kobayashi, Y., & Wada, K. 1995, The Astronomical Journal, 110, 2075

Sakamoto, K., Aalto, S., Wilner, D. J., et al. 2009, The Astrophysical Journal Letters, 700, L104

Sakamoto, K., Aalto, S., Barcos-Muñoz, L., et al. 2017, The Astrophysical Journal, 849, 14

Sales, D. A., Robinson, A., Axon, D. J., et al. 2015, The Astrophysical Journal, 799, 25

Sánchez-García, M., García-Burillo, S., Pereira-Santaella, M., et al. 2022, Astronomy and Astrophysics, 660, A83

Sánchez-García, M., Pereira-Santaella, M., García-Burillo, S., et al. 2021, arXiv e-prints, arXiv:2111.03876

Sanders, D. B., Mazzarella, J. M., Kim, D. C., Surace, J. A., & Soifer, B. T. 2003, The Astronomical Journal, 126, 1607

Sanders, D. B., & Mirabel, I. F. 1996, Annual Review of Astronomy and Astrophysics, 34, 749

Sanders, D. B., Soifer, B. T., Elias, J. H., et al. 1988, The Astrophysical Journal, 325, 74

Sandstrom, K. M., Leroy, A. K., Walter, F., et al. 2013, The Astrophysical Journal, 777, 5

Sargent, M. T., Schinnerer, E., Murphy, E., et al. 2010a, The Astrophysical Journal Letters, 714, L190

—. 2010b, The Astrophysical Journal Supplement Series, 186, 341

Sarzi, M., Allard, E. L., Knapen, J. H., & Mazzuca, L. M. 2007, Monthly Notices of the Royal Astronomical Society, 380, 949

Schinnerer, E., Böker, T., & Meier, D. S. 2003, The Astrophysical Journal Letters, 591, L115

Seo, W.-Y., & Kim, W.-T. 2013, The Astrophysical Journal, 769, 100

—. 2014, The Astrophysical Journal, 792, 47

Shankar, F., Weinberg, D. H., & Miralda-Escudé, J. 2009, The Astrophysical Journal, 690, 20

Shlosman, I., Begelman, M. C., & Frank, J. 1990, Nature, 345, 679

Singal, A. K. 2016, The Astrophysical Journal, 827, 66

Singh, R., van de Ven, G., Jahnke, K., et al. 2013, Astronomy and Astrophysics, 558, A43

Smith, H. E., Lonsdale, C. J., & Lonsdale, C. J. 1998a, The Astrophysical Journal, 492, 137

Smith, H. E., Lonsdale, C. J., Lonsdale, C. J., & Diamond, P. J. 1998b, The Astrophysical Journal Letters, 493, L17

Soifer, B. T., & Neugebauer, G. 1991, The Astronomical Journal, 101, 354

Soifer, B. T., Neugebauer, G., Matthews, K., et al. 2001, The Astronomical Journal, 122, 1213

Solomon, P. M., Downes, D., & Radford, S. J. E. 1992, The Astrophysical Journal Letters, 398, L29

Song, Y., Linden, S. T., Evans, A. S., et al. 2021, The Astrophysical Journal, 916, 73

Speagle, J. S., Steinhardt, C. L., Capak, P. L., & Silverman, J. D. 2014, The Astrophysical Journal Supplement Series, 214, 15

Spoon, H. W. W., Tielens, A. G. G. M., Armus, L., et al. 2006, The Astrophysical Journal, 638, 759

Springel, V., Di Matteo, T., & Hernquist, L. 2005, Monthly Notices of the Royal Astronomical Society, 361, 776

Springel, V., & Hernquist, L. 2005, The Astrophysical Journal Letters, 622, L9

Stierwalt, S., Armus, L., Surace, J. A., et al. 2013, The Astrophysical Journal Supplement Series, 206, 1

Stierwalt, S., Armus, L., Charmandaris, V., et al. 2014, The Astrophysical Journal, 790, 124

Storchi-Bergmann, T., Baldwin, J. A., & Wilson, A. S. 1993, The Astrophysical Journal Letters, 410, L11

Sun, J., Leroy, A. K., Schruba, A., et al. 2018, The Astrophysical Journal, 860, 172

Sun, J., Leroy, A. K., Rosolowsky, E., et al. 2022, arXiv e-prints, arXiv:2206.07055

Tabatabaei, F. S., Minguez, P., Prieto, M. A., & Fernández-Ontiveros, J. A. 2018, Nature Astronomy, 2, 83

Tacconi, L. J., Genzel, R., & Sternberg, A. 2020, Annual Review of Astronomy and Astrophysics, 58, 157

Telesco, C. M., & Decher, R. 1988, The Astrophysical Journal, 334, 573

Thompson, T. A., Quataert, E., & Murray, N. 2005, The Astrophysical Journal, 630, 167

Thomson, A. P., Smail, I., Swinbank, A. M., et al. 2019, The Astrophysical Journal, 883, 204

Toba, Y., Oyabu, S., Matsuhara, H., et al. 2013, Publications of the Astronomical Society of Japan, 65, 113

Torres-Albà, N., Iwasawa, K., Díaz-Santos, T., et al. 2018, Astronomy and Astrophysics, 620, A140

Treister, E., Schawinski, K., Urry, C. M., & Simmons, B. D. 2012, The Astrophysical Journal Letters, 758, L39

Tunnard, R., Greve, T. R., Garcia-Burillo, S., et al. 2015, The Astrophysical Journal, 800, 25

Turner, M. J. L., Reeves, J. N., Ponman, T. J., et al. 2001, Astronomy and Astrophysics, 365, L110

U, V., Sanders, D. B., Mazzarella, J. M., et al. 2012, The Astrophysical Journal Supplement Series, 203, 9

U, V., Medling, A. M., Inami, H., et al. 2019, The Astrophysical Journal, 871, 166

Utomo, D., Bolatto, A. D., Wong, T., et al. 2017, The Astrophysical Journal, 849, 26

Vardoulaki, E., Charmandaris, V., Murphy, E. J., et al. 2015, Astronomy and Astrophysics, 574, A4

Varenius, E., Conway, J. E., Martí-Vidal, I., et al. 2014, Astronomy and Astrophysics, 566, A15

Varenius, E., Conway, J. E., Batejat, F., et al. 2019, Astronomy and Astrophysics, 623, A173

Vartanyan, D., Burrows, A., Radice, D., Skinner, M. A., & Dolence, J. 2019, Monthly Notices of the Royal Astronomical Society, 482, 351

Vega, O., Clemens, M. S., Bressan, A., et al. 2008, Astronomy and Astrophysics, 484, 631

Veilleux, S., Kim, D. C., Sanders, D. B., Mazzarella, J. M., & Soifer, B. T. 1995, The Astrophysical Journal Supplement Series, 98, 171

Virtanen, P., Gommers, R., Oliphant, T. E., et al. 2019, arXiv e-prints, arXiv:1907.10121

Wada, K., Sakamoto, K., & Minezaki, T. 1998, The Astrophysical Journal, 494, 236

Werner, M. W., Roellig, T. L., Low, F. J., et al. 2004, The Astrophysical Journal Supplement Series, 154, 1

Wilson, C. D., Elmegreen, B. G., Bemis, A., & Brunetti, N. 2019, The Astrophysical Journal, 882, 5

Wisnioski, E., Glazebrook, K., Blake, C., et al. 2012, Monthly Notices of the Royal Astronomical Society, 422, 3339

Wright, E. L. 2006, Publications of the Astronomical Society of the Pacific, 118, 1711

Wu, H., Zou, Z. L., Xia, X. Y., & Deng, Z. G. 1998, Astronomy and Astrophysics Supplement Series, 132, 181

Wu, H., Wu, Z., Sotnikova, Y., et al. 2022, arXiv e-prints, arXiv:2203.00276

Xu, C. K., Cao, C., Lu, N., et al. 2015, The Astrophysical Journal, 799, 11

Yamada, R., Oyabu, S., Kaneda, H., et al. 2013, Publications of the Astronomical Society of Japan, 65, 103

Young, J. S., Allen, L., Kenney, J. D. P., Lesser, A., & Rownd, B. 1996, The Astronomical Journal, 112, 1903

Yu, Z.-Y. 2005, Chinese Physics Letters, 22, 780

Yuan, T. T., Kewley, L. J., & Sanders, D. B. 2010, The Astrophysical Journal, 709, 884

Yun, M. S., Reddy, N. A., & Condon, J. J. 2001, The Astrophysical Journal, 554, 803

Zakamska, N. L., Lampayan, K., Petric, A., et al. 2016, Monthly Notices of the Royal Astronomical Society, 455, 4191

Zaragoza-Cardiel, J., Beckman, J., Font, J., et al. 2017, Monthly Notices of the Royal Astronomical Society, 465, 3461